ESCOLA DE DOUTORAMENTO
INTERNACIONAL DA USC

Luis Javier
Pérez Pérez

Tese de doutoramento

Contributions to the mathematical modelling and numerical simulation of some problems related to blast furnace ironmaking

Santiago de Compostela, 2022

Programa de Doutoramento en Métodos Matemáticos e Simulación Numérica en Enxeñaría e Ciencias Aplicadas

USC
UNIVERSIDADE
DE SANTIAGO
DE COMPOSTELA

TESE DE DOUTORAMENTO

CONTRIBUTIONS TO THE MATHEMATICAL MODELLING AND NUMERICAL SIMULATION OF SOME PROBLEMS RELATED TO BLAST FURNACE IRONMAKING

Luis Javier Pérez Pérez

ESCOLA DE DOUTORAMENTO INTERNACIONAL DA UNIVERSIDADE DE SANTIAGO DE COMPOSTELA

PROGRAMA DE DOUTORAMENTO EN MÉTODOS MATEMÁTICOS E SIMULACIÓN NUMÉRICA EN ENXEÑERÍA E CIENCIAS APLICADAS

SANTIAGO DE COMPOSTELA

2022

USC
UNIVERSIDADE
DE SANTIAGO
DE COMPOSTELA

AUTORIZACIÓN DAS DIRECTORAS DA TESE

Contributions to the mathematical modelling and numerical simulation of some problems related to blast furnace ironmaking

Dna. Patricia Barral Rodiño
Dna. Peregrina Quintela Estévez

INFORMAN:

Que a presente tese, correspóndese co traballo realizado por D. Luis Javier Pérez Pérez, baixo a miña dirección, e autorizo a súa presentación, considerando que reúnen os requisitos esixidos no Regulamento de Estudos de Doutoramento da USC, e que como director desta non incorre nas causas de abstención establecidas na Lei 40/2015.

De acordo co indicado no Regulamento de Estudos de Doutoramento, declara tamén que a presente tese de doutoramento é idónea para ser defendida en base á modalidade de Monográfica con reproducción de publicacións, nos que a participación do doutorando foi decisiva para a súa elaboración e as publicacións se axustan ao Plan de Investigación.

En Santiago de Compostela, 14 de xullo de 2022

Asdo. Patricia Barral Rodiño

Asdo. Peregrina Quintela Estévez

USC
UNIVERSIDADE
DE SANTIAGO
DE COMPOSTELA

DECLARACIÓN DO AUTOR/A DA TESE

D./Dna. **Luis Javier Pérez Pérez**

Título da tese: **Contributions to the mathematical modelling and numerical simulation of some problems related to blast furnace ironmaking**

Presento a miña tese, seguindo o procedemento axeitado ao Regulamento, e declaro que:

1) A tese abarca os resultados da elaboración do meu traballo.
2) De ser o caso, na tese faise referencia ás colaboracións que tivo este traballo.
3) Confirmo que a tese non incorre en ningún tipo de plaxio doutros autores nin de traballos presentados por min para a obtención doutros títulos.
4) A tese é a versión definitiva presentada para a súa defensa e coincide a versión impresa coa presentada en formato electrónico

E comprométome a presentar o Compromiso Documental de Supervisión no caso de que o orixinal non estea na Escola.

En **Santiago de Compostela**, **22 xullo de 2022**.

Asdo. Luis Javier Pérez Pérez

USC
UNIVERSIDADE
DE SANTIAGO
DE COMPOSTELA

Agradecimientos

Este manuscrito es el fruto de innumerables horas de trabajo, pero también del esfuerzo desinteresado de múltiples personas que han estado siempre ahí para ayudarme. Sin su apoyo, aliento y orientación, no habría sido posible completarlo. Quisiera que estas líneas sirviesen como reconocimiento a todos ellos.

En primer lugar, deseo expresar mi más profundo agradecimiento a *Patricia Barral Rodiño* y *Peregrina Quintela Estévez*, directoras de esta tesis doctoral, no solo por haberme ofrecido la posibilidad de realizar este trabajo, sino también por su confianza y, sobre todo, por su inagotable paciencia y generosidad. Su conocimiento y experiencia han resultado de inestimable ayuda. Gracias por no perder la fe en mí y por darme un empujón en la dirección correcta cuando más lo necesitaba. Me siento afortunado de haber podido trabajar con vosotras.

A lo largo de estos años, he tenido el privilegio de compartir lugar de trabajo con los miembros del Departamento de Mátematica Aplicada. Me gustaría agradecer a todos ellos su disposición todo este tiempo para cualquier tipo de problema, duda o necesidad. Ha sido un placer compartir con vosotros docencia, charlas, congresos, seminarios, comidas... Especialmente, gracias *Dolores*, por facilitarme el aterrizaje en la docencia y por estar siempre ahí para inyectarme algo de autoestima. Gracias también, *José Luis* y *Jerónimo*, por iniciarme en esto de la Matemática Aplicada. También querría agradecer a *Carlos*, por su asistencia con los múltiples problemas informáticos, así como a *Elisa* y *Manolo* por su disponibilidad para echar una mano con las habituales trabas burocráticas y complicaciones administrativas.

Asimismo, me gustaría agradecer a mis compañeros en el Departamento de Ingeniería Geológica y Minera de la UPM por su cariñosa y cálida acogida este último año de Tesis, y, en particular, a *Arturo* y *Elena* por su ayuda y comprensión.

No quiero olvidarme de todas las personas con las que he compartido despacho y todo tipo de peripecias durante esta etapa: *Saray*, *Alejandra*, *Begoña*, *Cristina*, *Marta*, *Alba*, *Fran*... Me gustaría dedicar un especial agradecimiento a *Óscar*, con quién he tenido el placer de "remar" los últimos años de tesis y a *Alfredo*, que lleva soportándome desde el principio de los tiempos. Gracias a ambos por entender mis locuras y por vuestro apoyo.

Por supuesto, también quisiera agradecer a todas las personas a las que nunca supe explicar muy bien qué diantres he estado haciendo todo este tiempo, que han tenido que sufrir mis agonías interminables sin una buena justificación. A todos ellos les estoy muy agradecido de veras y lamento haber estado ausente: a mis amigos más cercanos y, en particular, a mis padres. Es gracias a su esfuerzo permanente que me he convertido en la persona que soy hoy. Gracias por estar siempre ahí.

Finalmente, a *Ruth*, que ha tenido que compartir todos los malos momentos, el estrés, las crisis... Sin tu cariño, apoyo y comprensión incondicionales durante todo este viaje, no estaría redactando estas líneas. Gracias por todo.

En definitiva, a todas las personas que han hecho que esta etapa haya sido menos dura: gracias.

This work was financially supported by the Ministerio de Ciencia, Innovación y Universidades through the Plan Nacional de I+D+i (MTM2015-68275-R) and the grant BES-2016-077228, by the ERDF and Xunta de Galicia funds under the ED431C 2017/60 and 2021/15 grants, and by the Agencia Estatal de Investigación through project PID2019-10561RB-I00/AEI/10.13039/501100011033.

USC
UNIVERSIDADE
DE SANTIAGO
DE COMPOSTELA

Contents

List of Figures xv

List of Tables xix

Preface xxi
1. Motivation and objectives . . . xxi
2. Methodology . . . xxiii
3. List of publications . . . xxiv

I. Mathematical modelling of the blast furnace main trough 1

Introduction 5

1. Physical problem. Blast furnace main trough 9
1.1. Blast furnace steelmaking . . . 9
1.2. Tapping process . . . 11
1.3. Main trough . . . 12
1.4. Trough refractory linings . . . 14
1.4.1. Castable refractories . . . 14
1.4.2. Wear mechanisms . . . 15
1.4.3. Critical isotherms . . . 16
1.5. Setting of the mathematical models . . . 16
1.5.1. Material properties . . . 17

2. Transient 3D hydrodynamic model of the BF main trough 19
2.1. General conservation equations . . . 20
2.1.1. Mass conservation . . . 21
2.1.2. Momentum conservation . . . 21
2.1.3. Constitutive law . . . 21
2.1.4. Additional assumptions . . . 22
2.2. Turbulence modelling . . . 23
2.2.1. RANS models . . . 23
2.2.2. SST $K-\omega$ turbulence model . . . 25
2.2.3. Near wall turbulence . . . 27
2.3. Volume of fluid . . . 29
2.4. Mathematical model . . . 32
2.4.1. Computational domain . . . 32
2.4.2. Model equations . . . 34
2.4.3. Boundary conditions . . . 34
2.4.4. Initial conditions . . . 36
2.4.5. Mesh of the domain . . . 37
2.4.6. Discretisation and numerical methodology . . . 38
2.4.7. Analysed cases . . . 39
2.5. Results and discussion . . . 40
2.5.1. Grid validation . . . 41
2.5.2. Runs A-C . . . 47

USC UNIVERSIDAD DE SANTIAGO DE COMPOSTELA

2.5.3. Run A* . . . 56

3. Steady 3D thermo-hydrodynamic model **59**
3.1. Mathematical model . . . 60
3.1.1. Computational domain . . . 61
3.1.2. Energy conservation and equation of state . . . 62
3.1.3. Radiation modelling . . . 66
3.1.4. Model equations . . . 68
3.1.5. Boundary conditions . . . 70
3.2. Numerical solution . . . 74
3.2.1. Mesh . . . 75
3.3. Results and discussion . . . 76
3.3.1. Grid validation . . . 76
3.3.2. Main results . . . 77
3.3.3. Sensitivity to the air velocity . . . 80
3.3.4. Comparison with experimental measurements . . . 82

4. Non-local radiation model **85**
4.1. General thermal radiation . . . 86
4.1.1. Radiative heat transfer equation . . . 86
4.1.2. Boundary condition . . . 88
4.2. Non-local radiation problem . . . 89
4.2.1. Derivation of the integral kernel . . . 90
4.2.2. Non-local radiation integral equation . . . 92
4.2.3. Model problem of coupled conduction and non-local radiation . . . 93
4.3. Plane problem . . . 94
4.3.1. Cylindrical domain . . . 94
4.3.2. Plane integral kernel . . . 95
4.4. Numerical solution . . . 100
4.4.1. Spatial discretisation . . . 100
4.4.2. Time discretisation . . . 101
4.4.3. Adaptive time stepping . . . 103
4.4.4. Algorithm . . . 103
4.5. Derivation of a 2D coupled manufactured solution test . . . 104
4.5.1. Simplified integral kernel . . . 106
4.5.2. Cauchy problem for non-local radiation . . . 107
4.5.3. Test by Blackwell et al. . . . 108
4.5.4. New manufactured solution test . . . 111
4.6. Numerical experiments with the manufactured solution test . . . 112
4.6.1. Fixed step size . . . 114
4.6.2. Adaptive step size . . . 117

5. Transient 2D thermal model of the BF trough campaign cycle **121**
5.1. Mathematical model . . . 121
5.1.1. Tapping cycles . . . 122
5.1.2. Computational domain . . . 124
5.1.3. Model equations . . . 126
5.1.4. Boundary conditions . . . 126
5.1.5. Initial condition . . . 129
5.1.6. Strong formulation . . . 130
5.1.7. Variational formulation . . . 131
5.2. Numerical solution . . . 132
5.2.1. Spatial discretisation . . . 133
5.2.2. Newton method . . . 134

USC UNIVERSIDADE DE SANTIAGO DE COMPOSTELA

5.2.3. Algorithm . . . 135
5.3. Results . . . 135
5.3.1. Sensitivity test . . . 135
5.3.2. Single BF tapping . . . 139
5.3.3. Simulation of two campaign cycles . . . 141
5.4. Assessment of thermocouple positions . . . 146
5.4.1. Motivation . . . 146
5.4.2. Minimisation problem . . . 147
5.4.3. Hybrid GRSA algorithm . . . 148
5.4.4. Application to the BF main trough problem validation . . . 153

Conclusions and perspectives **157**
Future research . . . 158

II. Equivalent material for the ceramic cup masonry 161

Introduction **165**

6. Preliminaries. Some results related to linear elasticity **167**
6.1. Basic notation . . . 167
6.2. Linear elasticity . . . 168
6.2.1. Constitutive law . . . 168
6.2.2. Infinitesimal rigid motions . . . 170
6.2.3. Model problem . . . 172
6.3. Pure Neumann boundary condition . . . 173
6.3.1. Existence and uniqueness of solution . . . 173
6.3.2. Saddle point formulation . . . 176
6.3.3. Existence and uniqueness of solution to the saddle point problem . . . 177
6.3.4. Numerical solution . . . 180
6.3.5. Other solution strategies . . . 181
6.3.6. Preconditioning of the saddle point system . . . 182
6.3.7. Numerical experiments . . . 183

7. Mathematical homogenisation. A classical result in linear elasticity **189**
7.1. Basic terminology . . . 189
7.2. Homogenisation in linear elasticity . . . 190
7.2.1. Auxiliary periodic problems . . . 191
7.2.2. Homogenisation result . . . 191
7.3. Numerical solution of the auxiliary problems . . . 192

8. Stress basic tests **195**
8.1. Introduction . . . 195
8.2. Statement of the stress basic tests . . . 197
8.3. Numerical experiments . . . 198
8.3.1. Test problems . . . 199
8.3.2. Cell A. Square brick and mortar masonry . . . 200
8.3.3. Cell B. Hexagonal brick layout with mortar joints . . . 206
8.3.4. Cell C. Layered composite . . . 209

9. Displacement basic tests **213**
9.1. Symmetry results . . . 213
9.1.1. Weak auxiliary problem . . . 214
9.1.2. Normal displacements . . . 215

9.1.3. Tangential displacements . . . 217
9.2. Basic tests . . . 218
9.2.1. Lifting functions . . . 219
9.2.2. Traction tests . . . 221
9.2.3. Shear tests . . . 222
9.3. Equivalence with the corrector problems . . . 223
9.3.1. Equivalent linear system . . . 226
9.4. Numerical experiments . . . 228
9.4.1. Cell C. Layered composite . . . 228
9.4.2. Cell D. Blast furnace ceramic cup . . . 230
9.4.3. Cell E. Running bond masonry . . . 237

Conclusions and perspectives **241**

Resumo **247**

Bibliography **249**

Nomenclature **257**

USC UNIVERSIDADE DE SANTIAGO DE COMPOSTELA

List of Figures

I. Mathematical modelling of the blast furnace main trough **1**

1.1. Blast furnace and schematic diagram of its parts. . . . 10
1.2. Sketch of the BF trough. . . . 13
1.3. Schematic diagram of the main trough. . . . 14
1.4. Drawings of the main trough 18
2.1. Computational domain and jet trajectory 33
2.2. Boundaries of the computational domain Ω. . . . 35
2.3. Schematic diagram of the height values used to compute initial volume fractions. . . . 36
2.4. Mesh 4. . . . 37
2.5. Outflow rates for the meshes considered in the grid sensitivity study. . . . 41
2.6. Contour $\alpha_{hm} = 0.5$ at $t = 25$ s for the meshes considered in the grid sensitivity study. 42
2.7. Wall shear and pressure on line crossing the jet impingement area. . . . 43
2.8. Wall shear stress and pressure on the wall at the jet impingement, $t = 100$ s. . . . 44
2.9. Averaged wall shear stress and pressure on the jet impingement zone for the different grids. . . . 45
2.10. Computed solution for the different grids along the line $x_1 = 1.5$ m, $x_3 = 4$ m, $t = 100$ s. 46
2.11. Plane cross-section of the computational domain ($x_3 = 7.35$ m), velocity magnitude contours. . . . 46
2.12. Evolution of the interface height for Runs A-C. . . . 48
2.13. Contour $\alpha_{slag} = 0.5$ at $t = 150$ s for Runs A-C and $\alpha_{hm} = 0.5$ at $t = 100$ s for Run A* . 49
2.14. Median height of the interfaces at various time values for Runs A, B and C. . . . 50
2.15. Jet impingement zone: velocity vectors on the plane $x_1 = 1.5$ m. . . . 51
2.16. Skimmer and slag runner zone: velocity vectors on the plane $x_1 = 1.5$ m. . . . 52
2.17. Jet impingement zone: velocity vectors on the plane $x_2 = 1.15$ m, with velocity magnitude contours. . . . 53
2.18. Jet impingement zone: velocity vectors on the plane $x_2 = 1.5$ m. . . . 54
2.19. Plane cross-section at $x_3 = 7.35$ m, v_3 velocity. . . . 54
2.20. Plane cross-section at $x_3 = 11$ m, v_3 velocity. . . . 55
2.21. Averaged wall shear stress and pressure on the wall at the jet impingement zone at $t = 150$ s, Runs A-C. . . . 55
2.22. Averaged wall shear and pressure at line crossing the jet impingement area at different time values for Runs A-C. . . . 56
2.23. Run A*: Wall shear and pressure at line crossing the jet impingement area at various time values. . . . 56
2.24. Run A*: Wall shear stress and pressure on the jet impingement area at $t = 25$ s. . . . 57
3.1. Solid (Ω_S) and slag/hot metal subdomains (Ω_L). . . . 60
3.2. Fluid subdomain (Ω_F). . . . 61
3.3. Interfaces and boundaries involving the fluid subdomain (Ω_F). . . . 69
3.4. External and symmetry boundaries of the computational domain. . . . 71
3.5. Mesh 4 of the computational domain. . . . 75
3.6. Temperature contours in the cross-section $x_3 = 8$ m, the grid sensitivity study. . . . 76
3.7. Velocity magnitude contours in the cross-section $x_3 = 8$ m, grid sensitivity study. . . . 77
3.8. Temperature and velocity magnitude along the line $x_1 = 1.5$ m and $x_3 = 11$ m on selected parts of the computational domain, grid sensitivity study. . . . 78
3.9. Velocity magnitude contours and streamlines in Ω_A and Ω_L, $v_{air} = 2$ m/s. . . . 79

USC UNIVERSIDADE DE SANTIAGO DE COMPOSTELA

3.10. Temperature contours and critical isotherms in the solid subdomain and hot metal/slag subdomain, $v_{air} = 2$ m/s. . . . 79
3.11. Temperature contours in the plane $x_1 = 1.5$ m, $v_{air} = 2$ m/s. . . . 79
3.12. Temperature and velocity magnitude contours in the cross-sections $x_3 = 8$ m and $x_3 = 11$ m of the hot metal and slag subdomain (Ω_L). . . . 80
3.13. Temperature contours in the working lining and Σ_{free}, seen from above and hiding the air subdomain and the refractory cover, for various v_{air} values. . . . 81
3.14. Temperature contours in the cross-section $x_3 = 8$ m of the air subdomain (Ω_A), for various v_{air} values. . . . 81
3.15. Air aspiration temperature measurements during the first tappings of a campaign cycle. 83
3.16. Average temperature on air outlet (Γ^A_{outlet}) and on the surfaces corresponding to the thermocouple positions, with respect to v_{air}. . . . 84
4.1. Sketch of a 2D section of the problem domain. . . . 86
4.2. Schematic of specular and diffuse reflection on an opaque surface. . . . 88
4.3. Cross-section of the problem setting, displaying the relation between the points $\mathbf{y}, \mathbf{x}$ and the unit vector $\mathbf{s}$. . . . 90
4.4. Schematic of a cylindrical domain. . . . 94
4.5. Sketch depicting the angles used in the derivation of the plane integral kernel. . . . 97
4.6. Set-up for the plane integral kernel derivation. . . . 98
4.7. Flow diagram of the algorithm. . . . 104
4.8. Manufactured solution test domain. . . . 105
4.9. Radiosity, temperature and heat flux due to radiation on γ^a_R, test by Blackwell et al. . 110
4.10. Radiosity, temperature and heat flux due to radiation on γ^a_R, new manufactured solution test. . . . 112
4.11. Mesh 5 (left) and T_{exact} at $t = 5$ s (right). . . . 113
4.12. Approximated radiosity for Problem $(\mathcal{P}^a_{PR})$, with implicit Euler and different step size values at $t = 5$ s with Mesh 5. . . . 114
4.13. Approximated radiosity with ESDIRK 3/2a and different meshes at $t = 5$ s, $\Delta t/128$. 116
4.14. Relative errors in log-log scale. . . . 117
4.15. Computed step size values for the different tolerance values in Mesh 8. . . . 118
4.16. $e^{\Delta t}_{h,L^2}(T_h)$ with Mesh 8 for various tolerance values, using ESDIRK 3/2a with H211b controller. . . . 118
5.1. Temperature schematic at the contact area with fluids of the working lining during a campaign cycle. . . . 122
5.2. Temperature measurements in the insulation lining during a runner lifetime cycle. . 123
5.3. Signal indicating whether the BF is tapping or stopped. . . . 124
5.4. Cross-section of the main trough. . . . 124
5.5. Boundaries of the computational domain. . . . 125
5.6. Computed temperatures in the fluids and proposed fitted temperature profile T_F at different locations. . . . 127
5.7. Temperature profile $T^m_{D,cast}$. . . . 128
5.8. Temperature contours of the initial temperature T_0. . . . 130
5.9. Flow diagram of the algorithm. . . . 136
5.10. Triangulation of the domain ϖ_{stop}, Mesh 2. . . . 136
5.11. Computed numerical solution for the considered mesh sizes. . . . 137
5.12. Step size values. . . . 138
5.13. Number of computed fixed point algorithm iterations for the second RK stage at each time step, different tolerance values. . . . 139
5.14. Temperature contours at various time values, single tapping. . . . 140
5.15. Temperature and radiosity on γ_R at various time values, single tapping. . . . 140
5.16. Continuous cast with $t_{end} = 15$ days. . . . 140
5.17. Computed temperature over time, at selected points in ϖ_{cast}, $t_{end} = 15$ days (Continuous cast). . . . 141

USC UNIVERSIDADE DE SANTIAGO DE COMPOSTELA

5.18. Time step values computed by the H211b controller during the two campaign cycles. 142
5.19. Temperature contours at various time values during Campaign cycle 1. 143
5.20. Temperature evolution at selected points, Campaing cycle 1. 144
5.21. Critical isotherms, Campaign cycle 1. 145
5.22. Computed radiosity on γ_R for various time values for Campaign cycle 1. 145
5.23. Temperature contours at various time values during Campaign cycle 2. 145
5.24. Feasible region for the thermocouples location in the BF runner cross-section. 146
5.25. Temperature over time at the reported thermocouple locations, Campaign cycle 1. . . 147
5.26. Flow chart of the simulated annealing (SA) algorithm. 151
5.27. Test functions for the optimisation algorithm. 151
5.28. Convergence histories of three runs for the Levy function with $N = 1000$. 153
5.29. Thermocouple reported positions and corrected positions after a hybrid GRSA algorithm run using numerical solution for Campaign cycle 1. 154
5.30. Temperature over time at the corrected thermocouple locations. 155

II. Equivalent material for the ceramic cup masonry **161**

1. Ceramic cup reconstruction, showing the taphole zone of the hearth wall. Source: ArcelorMittal. 166
6.1. Reference configuration Ω composed of two disjoint subdomains Ω_1 and Ω_2. 169
6.2. Element face highlighted in red corresponding to the Dirichlet boundary for the *pinning* approach, for the computational domain considered in Test 2. 184
6.3. Computed solutions using Lagrange multipliers (SPP). 185
6.4. Test 2. Relative error approximating the displacements. 187
7.1. Masonry wall obtained repeating a representative element. 190
8.1. Square brick and mortar masonry (Cell A). 199
8.2. Square brick and mortar reference cell, Mesh 4. 200
8.3. Von Mises stress norm on the deformed configuration of Y for the approximation of the solution to the basic tests $(\mathcal{P}_{PN})^m$, $m = 1, 4, 5$; Mesh 4. 201
8.4. Computed coefficients of the stiffness matrix $\overline{\mathbf{C}}_h$ with respect to the maximum element size h_{max}. 202
8.5. Modulus of the computed approximation of $\boldsymbol{\mathcal{X}}^{lk}$, Mesh 4. 203
8.6. Contours of the numerical solution to Problem 1, Cell A, considering the homogenised material predicted by the S-BT, the correctors, and the real heterogeneus material. . . 204
8.7. Solution for Cell A, along the line $[\mathbf{x}_{min}, \mathbf{x}_{max}]$. 205
8.8. Contours of the von Mises stress in Problem 2, Cell A, considering different approaches to characterise the equivalent material and the heterogeneous material. 205
8.9. Hexagonal brick layout with mortar joints (Cell B). 207
8.10. Contours of the numerical solution to Problem 1, Cell B, considering the homogenised material predicted by the S-BT, correctors and mixture rule, and the heterogeneous material. 208
8.11. Numerical solution for Cell B, along the line $[\mathbf{x}_{min}, \mathbf{x}_{max}]$. 209
8.12. Layered composite (Cell C). 210
8.13. Numerical solution of Problem 1, Cell C, considering the homogenised material predicted by S-BT (1,1,1), the correctors, and the heterogeneous material. The results are displayed on the deformed configuration. 210
8.14. Solution for Cell C and Problem 1 along the line $[\mathbf{x}_{min}, \mathbf{x}_{max}]$. 211
9.1. Reference cell Y satisfying the symmetry hypotheses (H.2). 214
9.2. Meshes of reference cell C. 230
9.3. Schematic of the hearth of a BF. 230
9.4. Ceramic cup of the BF (Cell D). 231
9.5. Reference cell Y for the ceramic cup of the BF (Cell D); mesh and dimensions. 232
9.6. Contours of the VM stress norm corresponding to the solutions $\mathbf{u}^m$ for the D-BT. . . 232

9.7. Cell D. Contours of the numerical solution to Problem 3. 233
9.8. Cell D. Numerical solution to Problem 3 along the line $[\mathbf{x}_{min}, \mathbf{x}_{max}]$. 234
9.9. Cell D. Contours of the numerical solution to Problem 1. 235
9.10. Cell D. Solution to Problems 1 and 2 along the line $[\mathbf{x}_{min}, \mathbf{x}_{max}]$. 236
9.11. Running bond masonry (Cell E). 237
9.12. Dimensions (in mm) of the reference period for Cell E. 238
9.13. Cell E. Contours of the numerical solution to Problem 2. 238
9.14. Cell E. Solution to Problems 1 and 2 along the line $[\mathbf{x}_{min}, \mathbf{x}_{max}]$. 239

USC
UNIVERSIDADE DE SANTIAGO DE COMPOSTELA

List of Tables

I. Mathematical modelling of the blast furnace main trough **1**

1.1. Properties of the materials. . . . 17
2.1. Turbulence model constants. Source: Ansys, Inc. (2019). . . . 26
2.2. Computational grids, with mesh quality metrics and maximum specified time-step size used in the adaptive time-stepping method. . . . 39
2.3. Amount of tapped hot metal and slag in each run, in % of the total tapping volumetric flow rate and mass flow rate ($\dot{m}_{tap}$). . . . 39
2.4. Initial and final median height of the interfaces, for Runs A,B and C. . . . 47
3.1. Air properties at 350 K. Source: Bergman et al. (2011). . . . 71
3.2. Heat transfer coefficient obtained with a flat plate correlation and modified heat transfer coefficient for the external boundaries. . . . 72
3.3. Computational grids chosen for the mesh sensitivity study, with mesh quality metrics. 75
3.4. Average radiative heat flux (q_{rad}) [W/m^2], average total heat flux (q) [W/m^2] and temperature (T) [K] on several parts of the radiation cavity, for various inlet air velocity values (v_{air}). . . . 82
3.5. Heat transfer coefficients on the parts of the radiation cavity, for various v_{air} values. . 83
3.6. Thermocouple (TC) temperature measurements, numerical temperature values, absolute error and relative error, $v_{air} = 8$ m/s . . . 84
4.1. Maximum element size, minimum element size, number of elements in the triangulation of ϖ^a and number of edge elements in the mesh of γ_R^a. . . . 113
4.2. Implicit Euler scheme: $e^{\Delta t}_{h,L^2}(T_h)$ (top), $e^{\Delta t}_{h,H^1}(T_h)$ (middle) and $e^{\Delta t}_{h,L^2}(R_h)$ (bottom) relative errors. . . . 115
4.3. ESDIRK 3/2a: $e^{\Delta t}_{h,L^2}(T_h)$ (top), $e^{\Delta t}_{h,H^1}(T_h)$ (middle) and $e^{\Delta t}_{h,L^2}(R_h)$ (bottom) relative errors. 116
4.4. Maximum step size, number of accepted steps and rejected steps and acceptance rate using the H211b controller. . . . 118
4.5. ESDIRK 3/2a with H211b controller for adaptive step size.: $e^{\Delta t}_{h,L^2}(T_h)$ (top), $e^{\Delta t}_{h,H^1}(T_h)$ (middle) and $e^{\Delta t}_{h,L^2}(R_h)$ (bottom) relative errors. . . . 119
5.1. Example of BF activity values. . . . 123
5.2. Heat transfer coefficients. . . . 129
5.3. Meshes used for the mesh sensitivity test, maximum element size, minimum element size, number of triangle elements in the grid of the domain and number of edge elements on the non-local radiation boundary. . . . 137
5.4. Maximum step size, number of accepted steps, number of rejected steps and acceptance rate using the H211b controller with $tol = 10^{-4}$ for the different mesh sizes, grid sensitivity test. . . . 138
5.5. Maximum step size, number of accepted steps, number of rejected steps and acceptance rate using the H211b controller for various tolerance values. . . . 139
5.6. Start date, end date and total number of casts (M) for each solved campaign cycle. . 142
5.7. Maximum step size, number of accepted steps, number of rejected steps and acceptance rate using the H211b controller for the considered campaign cycles. . . . 142
5.8. Parameter values for GRSA algorithm. . . . 149
5.9. Results for the GRSA algorithm on the test examples . . . 152
5.10. Originally reported thermocouple positions, corrected positions and functional value at both locations for the three thermocouples, Campaign cycle 1. . . . 154

USC UNIVERSIDADE DE SANTIAGO DE COMPOSTELA

5.11. Originally found (for Campaign cycle 1) thermocouple positions, corrected positions and functional value at both locations. 155

II. Equivalent material for the ceramic cup masonry 161

6.1. Errors for the saddle point formulation (top), supplying a nullspace basis to a CG solver (middle) and artificially constraining the displacement on the degrees of freedom corresponding to an element face (bottom). 186
8.1. Material properties for the numerical experiments with the square brick and mortar masonry (Cell A), the hexagonal brick layout with mortar joints (Cell B) and the layered composite (Cell C). 198
8.2. Number of vertices in the mesh (N_h), maximum element size (h_{max}) and minimum element size (h_{min}) for the square masonry (Cell A). 200
8.3. Cell A. Comparison of the coefficients of the constant stiffness matrix for the equivalent materials. 206
8.4. Cell B.Comparison of the coefficients of the constant stiffness matrix for the equivalent materials. 207
8.5. Cell C. Comparison of the coefficients of the constant stiffness matrix for the equivalent materials. 211
9.1. Material properties for the numerical experiments. 228
9.2. Cell C: leading order coefficients of the equivalent material stiffness matrix for stress basic tests (S-BT), displacement basic tests (D-BT) and rule of mixtures (Mixture). . 229
9.3. Cell D: leading order coefficients of the equivalent material stiffness matrix for stress basic tests (S-BT), displacement basic tests (D-BT) and rule of mixtures (Mixture). . 232
9.4. Cell E: leading order coefficients of the equivalent material stiffness matrix for stress basic tests (S-BT), displacement basic tests (D-BT) and rule of mixtures (Mixture). . 237

USC UNIVERSIDADE DE SANTIAGO DE COMPOSTELA

Preface

Steel is a deeply rooted material in modern society. The main source of demand for steel is infrastructure, but it is also a key ingredient for various means of transportation, household appliances and many other applications. In addition, steel plays a crucial role in the global economy, with revenues of over $2.5 trillion and employing about 6 million people worldwide. Since 1970, global steel demand has tripled and it is forecast to continue growing by more than a third until 2050 (International Energy Agency, 2020).

The manufacturing of steel is mainly carried out using an intermediate material, known as *hot metal* or *pig iron*, produced in large metallurgical furnaces called *Blast Furnaces* (BF) by reducing iron ore. They are responsible for around 70% of global steel production (Geerdes et al., 2015). According to Cameron et al. (2019), in the foreseeable future, the BF is expected to remain the main source of steel production worldwide, as no other steelmaking process can achieve the scale and efficiency of modern BFs. To maintain the economy of scale of the process, its productivity and campaign life must satisfy an ever-increasing demand. This places higher requirements for the refractory materials used to line steelmaking vessels, as larger BF throughputs lead to higher rates of mechanical erosion, chemical attack and also bigger thermal stresses (Luomala et al., 2001).

1. Motivation and objectives

In the integrated steelworks plant, BF ironmaking is the most expensive process, since the cost of obtaining hot metal is around 75% of all the costs regarding steel production (Cameron et al., 2019). A large amount of these costs are expenses related to the refractory materials used to protect the troughs, ladles and other equipment, which suffer harsh operating conditions, leading to extensive damage and degradation. Furthermore, since the steel manufacturing is an energy-intensive process, there are important environmental concerns regarding the improvement of efficiency and reducing the carbon print of the process. Specifically, the iron and steel industry accounts for approximately 7% of worldwide greenhouse gas emissions and 11% of global CO_2 emissions (Hasanbeigi, 2022).

The hostile operation conditions in most stages of the process and difficulty of access make experimentation costly, both from a safety and capital costs standpoint. Therefore, the industry can largely benefit from the use of mathematical tools to obtain suitable predictions that allow characterising the performance of the refractory vessels involved in different stages of the steel fabrication process. Although the complexities of the process frequently lead to models that require a notable idealisation of the real conditions, in most of these cases valuable conclusions can still be drawn for the steel industry.

On the other hand, considerable efforts have been made in the recent years to incorporate computational techniques to bring new insights into the BF ironmaking process (see e.g. Kuang et al., 2018). These recent developments have brought major changes in the industry. In the last decades casthouses have seen significant changes in BF size, technology, tapping and operation practices, among others (Ranjan et al., 2022). Indeed, these changes have led to sizeable increases in BF efficiency, as since 1960 the energy required to produce a tonne of crude steel is estimated to have reduced by approximately 60% (World Steel, 2022). Nonetheless, there are still many open questions and challenges concerning steel manufacturing that should be addressed to further optimise the process in the coming years.

This manuscript is divided into two parts where different techniques are applied in the modelling and numerical simulation of BF ironmaking-related processes. In the following, a brief description of the contents of each part is provided.

USC UNIVERSIDADE DE COMPOSTELA

Part I: Mathematical modelling of the blast furnace main trough

The scope of the first part is to propose adequate mathematical models to study the thermal and hydrodynamic behaviour of the BF main trough. The primary motivation is to provide a better understanding of the phenomena related to the multiphase flow in the trough, as well as to study the heat transfer in this refractory vessel, used to separate and transport the drained hot metal and slag from the BF. The trough undergoes cyclic thermal loading during its campaign life, which is believed to be related to the degradation of refractory materials (Prompt & Ouedraogo, 2008). Furthermore, chemical attack from the slag and erosion due to the fluid flow play a fundamental role in the refractory wear (Ranjan et al., 2022). The design of the BF trough structures has been frequently based on try-and-error methods (Ouedraogo & Prompt, 2008). Therefore, valuable insights can be provided through numerical simulation. To investigate these phenomena, a CAD model of a BF main trough operated by ArcelorMittal Spain is constructed.

A hierarchy of different mathematical models is proposed and numerically solved. First, a Computational Fluid Dynamics (CFD) model, similar to those that have recently appeared in the literature (see e.g. Monteiro de Oliveira et al., 2020; H. Yao et al., 2021), is used to analyse the flow patterns in the trough. Several knowledge gaps in the existing body of work are addressed, such as the evolution of the estimated position of the fluid interfaces and accurate shear stress characterisation.

The velocity profile obtained by solving the previous model is used to provide an appropriate boundary condition for a subsequent model that aims to investigate the thermal field in the trough. To this end, steady-state conditions are assumed. In addition, only the middle and end parts of the trough are included, where the influence of the impact of the tapping stream in the fluids held in the trough is less significant and the flow is plug-like (He et al., 2002). The thermal model aims to address the conjugate heat transfer between the solid refractory layers and the fluids circulating in the trough, as well as the forced flow generated due to fume aspiration. Moreover, radiative heat transfer is also assessed, considering surface radiation. The results are used to study if the trough design results in the so-called critical temperature isotherms being within the working lining, the trough refractory layer that is in contact with the hot fluids. In addition, the effect of the forced air current velocity on the refractory temperature is investigated. The temperature predictions are validated with a temperature snapshot measured by several thermocouples embedded in the BF trough, showing good agreement levels.

Nevertheless, time-dependent readings of the thermocouple data later supplied by ArcelorMittal Spain show significant temperature oscillations at the reported thermocouple placement locations. These suggest that the temperature field in the back-up refractory layers is highly dependent on the duration of the stops between the BF tappings and that a steady-state assumption is not entirely realistic. To further investigate this issue, the impact of the tapping process stops on the thermal response of the trough is studied during a complete campaign cycle. A novel transient thermal model is introduced, which combines a sequence of problems emulating the cyclic nature of the real BF operation. The model is defined in a 2D cross-section of the trough and uses a non-local radiation model to address the radiative heat transfer. To avoid having to resolve the complexities concerning the fluid flow during the tappings, the results from the previous mathematical models are utilised to set suitable boundary conditions. Using real BF activity data from two different campaign cycles, the proposed methodology allows to study the evolution of the temperature in the trough for the entire duration of its campaign, enhancing previous research studies which assumed that a steady-state was reached or considered rather idealistic conditions for radiative heat transfer (e.g. Vázquez-Fernández et al., 2019). These results show promising lines for further research, as an inverse heat transfer model using the deviations from the thermocouple measurements could produce real-time predictions of the refractory lining wear profile.

USC UNIVERSIDADE DE SANTIAGO DE COMPOSTELA

Part II: Equivalent material for the ceramic cup masonry

In the second part, the spotlight is moved to the blast furnace itself. Some BF hearth walls have an inner masonry formed by corundum refractory bricks separated by joints, called the *ceramic cup*. It helps to protect an outer layer of larger carbon blocks from erosion in the BF hearth. In order to employ computational methods to simulate the mechanical response of such structure, it is not computationally feasible to include each individual brick and joint, which motivates the need of providing a methodology that allows the numerical simulation of the mechanical response of the ceramic cup. Since the structure can be generated by periodic repetition of a reference cell, under the assumption of a linear elastic response, classical tools from periodic homogenisation can be used to obtain a homogenised material, characterised by constant effective properties, with a similar mechanical behaviour to the heterogeneous structure (Cioranescu & Donato, 1999).

To obtain the homogenised material stiffness matrix entries, the so-called corrector functions to the linear elasticity system have to be computed. These are solutions to some problems defined in the periodicity cell, which require to introduce a periodic boundary condition in all the faces of the cell, as well as to constrain the mean displacement. Although the periodic boundary condition is readily set numerically when the mesh is identical in the opposite faces of the boundary, arbitrary meshes require more complicated techniques (see e.g. V.-D. Nguyen et al., 2012). Furthermore, these constraints are not always easy to enforce in most of the software packages used in the engineering practise. Consequently, in this part, two fast and easy-to-use methodologies are proposed, relaxing these constraints and inspired by how uniaxial compression and shear tests are experimentally conducted to characterise the behaviour of materials.

First, a simple technique, called *stress basic tests* (S-BT), is introduced. It features six pure traction problems posed in the periodically repeating cell. Since the pure traction problems are ill-posed, the uniqueness of solution is enforced via a Lagrange multiplier, using a similar formulation to that proposed in Bochev & Lehoucq (2011); Kuchta et al. (2019). It is demonstrated that suitable results can also be obtained by using a Krylov method to solve the arising linear system, removing the requirement to solve the saddle point problem with the Lagrange multiplier. Several numerical experiments are conducted and the performance of the methodology is assessed against that of the classical homogenisation. However, the S-BT is shown to yield unsatisfactory results in some specific situations, and the accuracy of predictions when using the corresponding homogenised material can be severely compromised. Therefore, a different methodology, called *displacement basic tests* (D-BT), is subsequently proposed. Instead of the pure Neumann boundary condition of the S-BT, Dirichlet boundary conditions are set on selected displacement components. Under suitable geometric symmetry assumptions, it is shown that the solutions of these new basic tests are related to the corrector functions of the linear elastic system. Hence, both methodologies are equivalent in the sense that they yield the same stiffness matrix of the homogenised material. Numerical experiments are also conducted in this case. In particular, both methodologies are applied to a masonry with the dimensions and mechanical parameters of the ceramic cup of the BF. It is found to behave as an orthotropic auxetic material, i.e., a material with a negative Poisson's ratio, which has important implications with regard to its mechanical behaviour.

2. Methodology

In Part I, classical tools of continuum mechanics are used to pose mathematical models that address the various phenomena of interest, such as the turbulent, multiphase flow in the BF trough or the radiative heat transfer. On the other hand, in Part II, classical results from periodic homogenisation as well as basic tools from functional analysis are employed to prove that the D-BT technique is equivalent to solving the auxiliary periodic problems for the linear elastic system.

Most of the proposed mathematical models are numerically solved using own-developed code, implemented mainly using the programming language *Python*. To this end, the computing platform *FEniCS* (Alnæs et al., 2015) is utilised, which allows to readily obtain the finite element discretisation of the system of partial differential equations (PDEs) from the corresponding variational formulation,

and also provides adequate interfaces to interact with the *PETSc* library (Balay et al., 2022), used to solve the arising linear systems. Also, for the more complicated models that involve the characterisation of the fluid flow in the BF trough in Part I, their numerical simulation is carried out employing the commercial CFD package *Ansys Fluent*, which uses a cell-centred finite volume method discretisation of the conservation equations. For the postprocessing and further discussion of the computed results, several packages were used, such as *MATLAB*, the open-source code library *Matplotlib* and the software *Paraview*. For the tasks related to numerical simulation, we had access to the *Mariscal* computer cluster, consisting of 21 nodes with diverse specifications hosted at the Centro de Supercomputación de Galicia (CESGA).

To validate the models, the numerical results and the own-developed numerical implementations, various techniques were utilised in Part I. In Chapters 3 and 5, the temperature measurements obtained with several thermocouples embedded in the BF main trough were used. However, since these measurements are not fully reliable due to the uncertainties regarding the placement process of the devices, to ensure the correctness of the numerical implementations, a new methodology to obtain manufactured solution tests for coupled non-local radiation and heat conduction was introduced in Chapter 4. For many parameters, such as the flow patterns of slag and hot metal in the trough studied in Chapter 2, the results are compared with the observations of several researchers using physical scale and CFD models to study the trough hydrodynamics. On the other hand, in Part II, in addition to the mathematical proofs, the performance of the proposed techniques was compared to the classical approach for periodic homogenisation and to a rule of mixtures with numerical experiments. Also, the performance of different methods to solve the pure traction linear elasticity problem was shown with a couple of manufactured solution tests.

This herein presented work was done in the framework of the research projects *MTM2015-68275-R*, financially supported by the Ministerio de Ciencia, Innovación y Universidades, and *PID2019-10561RB-I00/AEI/10.13039/501100011033*, supported by the Agencia Estatal de Investigación. In both projects, the steelmaking company ArcelorMittal was a collaborating entity, which provided real data concerning the BF hearth and trough geometry, as well as physical properties for the involved solid and fluid materials. Active dialogue with engineers from the company was promoted for the identification of parameters, properties and strategies adequate for modelling the various physical phenomena addressed in this manuscript. Furthermore, the experimental measurements and BF operation data supplied by the company were essential for adjusting the models and the validation of the obtained numerical results.

3. List of publications

The following list indicates those articles that have been partially reproduced in this manuscript:

- Chapters 1 and 5 reproduce contents from:

  Barral, P.[*,†], Pérez-Pérez, L.J.[*], & Quintela, P.[*,†] (2022). *Numerical simulation of the transient heat transfer in a blast furnace main trough during its complete campaign cycle*. International Journal of Thermal Sciences. 173, 107349. ISSN: 1290-0729. doi:10.1016/j.ijthermalsci.2021.107349

  Journal rankings: Impact Factor (JCR): 4.779 (2021) Quartile (JCR): Q1, 21/137 (Engineering, Mechanical)

  Author's contribution: Development of the mathematical model and numerical methodology, computer implementation, and writing of the article.

  Permissions: The article is published as open access under a CC BY-NC-ND 4.0 License. The publisher, Elsevier, grants authors the right to include as part of doctoral dissertations without express authorisation, provided that it is not commercially published (see https://www.elsevier.com/about/policies/copyright).

USC UNIVERSIDADE DE SANTIAGO DE COMPOSTELA

- Chapters 1, 4 and 5 reproduce contents from:

  Barral, P.[*,†], Pérez-Pérez, L.J.[*], & Quintela, P.[*,†] (2022). *Transient thermal response with nonlocal radiation of a blast furnace main trough*. Applied Mathematical Modelling. 105, 197 – 225. ISSN: 0307-904X. doi:10.1016/j.apm.2021.12.029

  Journal rankings: Impact Factor (JCR): 5.336 (2021) Quartile (JCR): Q1, 7/108 (Mathematics, Interdisciplinary Applications)

  Author's contribution: Development of the mathematical model and numerical methodology, computer implementation, and writing of the article.

  Permissions: The article is published as open access under a CC BY-NC-ND 4.0 License. The publisher, Elsevier, grants authors the right to include the article as part of doctoral dissertations without express authorisation, provided that it is not commercially published (see https://www.elsevier.com/about/policies/copyright).

In addition, some contents of the subsequent book chapter are reproduced in Chapters 1 and 3:

Barral, P.[*,†], Nicolás, B.[*]; Pérez-Pérez, L.J.[*], & Quintela, P.[*,†] (2019). Numerical Simulation of Wear-Related Problems in a Blast Furnace Runner. In: García Guirao, J., Murillo Hernández, J., Periago Esparza, F. (eds) Recent Advances in Differential Equations and Applications. SEMA SIMAI Springer Series, vol 18. Springer, Cham. ISSN 2199-3041. doi:10.1007/978-3-030-00341-8_14

Author's contribution: Development of the mathematical model concerning the BF trough, numerical solution, and writing of the chapter.

Permissions: The publisher, Springer, grants authors the right to include the publication in their thesis (see https://www.springer.com/gp/rights-permissions/obtaining-permissions/).

USC UNIVERSIDADE DE SANTIAGO DE COMPOSTELA

[*] Department of Applied Mathematics, Universidade de Santiago de Compostela, 15782 Santiago de Compostela, Spain.
[†] Technological Institute for Industrial Mathematics (ITMATI), Rúa Constantino Candeira s/n, 15782 Santiago de Compostela, Spain. (Currently incorporated to CITMAGA).

USC
UNIVERSIDADE
DE SANTIAGO
DE COMPOSTELA

Part I

Mathematical modelling of the blast furnace main trough

USC
UNIVERSIDADE
DE SANTIAGO
DE COMPOSTELA

USC
UNIVERSIDADE
DE SANTIAGO
DE COMPOSTELA

Contents

Introduction **5**

1. Physical problem. Blast furnace main trough **9**
1.1. Blast furnace steelmaking . . . 9
1.2. Tapping process . . . 11
1.3. Main trough . . . 12
1.4. Trough refractory linings . . . 14
1.5. Setting of the mathematical models . . . 16

2. Transient 3D hydrodynamic model of the BF main trough **19**
2.1. General conservation equations . . . 20
2.2. Turbulence modelling . . . 23
2.3. Volume of fluid . . . 29
2.4. Mathematical model . . . 32
2.5. Results and discussion . . . 40

3. Steady 3D thermo-hydrodynamic model **59**
3.1. Mathematical model . . . 60
3.2. Numerical solution . . . 74
3.3. Results and discussion . . . 76

4. Non-local radiation model **85**
4.1. General thermal radiation . . . 86
4.2. Non-local radiation problem . . . 89
4.3. Plane problem . . . 94
4.4. Numerical solution . . . 100
4.5. Derivation of a 2D coupled manufactured solution test . . . 104
4.6. Numerical experiments with the manufactured solution test . . . 112

5. Transient 2D thermal model of the BF trough campaign cycle **121**
5.1. Mathematical model . . . 121
5.2. Numerical solution . . . 132
5.3. Results . . . 135
5.4. Assessment of thermocouple positions . . . 146

Conclusions and perspectives **157**
Future research . . . 158

USC
UNIVERSIDADE DE SANTIAGO DE COMPOSTELA

USC
UNIVERSIDADE
DE SANTIAGO
DE COMPOSTELA

Introduction

In the context of the blast furnace ironmaking process, it is of large interest to assess and minimise the wear suffered by the refractory materials used in the iron and steel industry. Usually, in the experimental and numerical studies about such process, the focus is on different parts of the BF itself, the metallurgical furnace where the iron ore is reduced and smelted to obtain hot metal. However, another important and, arguably, understudied vessel used in ironmaking is the main trough (Monteiro de Oliveira et al., 2020), a trench-like receptacle lined with castable refractories wherein the products of the blast furnace –molten hot metal and slag– are collected after their extraction from the BF and separated by density difference. Avoiding trough breakage and increasing its availability is a major concern for the metallurgical industry (Kumar et al., 2010), as the refractory linings suffer a high degree of degradation. Consequently, they are subject to periodic repairs and operation issues with the consequent costs for the steelmaking companies.

The BF trough is a complicated environment, with different coupled physics involved. First, the high temperatures, around 1500°C, lead to thermal radiation being of high relevance. Also, the produced flow patterns in the trough are complex and intricate. The discharge of the fluids extracted from the BF generates a molten jet stream, which upon its impact onto the BF trough generates a highly turbulent mixed gas-liquid multiphase flow with large amounts of entrained air bubbles (see e.g. Begnis & Brandaleze, 2006). Furthermore, as the BF cast process is not continuous and the fluid discharge conditions are not steady, the structure is subject to cyclic thermal loading during its entire campaign life. Lastly, some chemical reactions, enhanced to some extent by the interaction with the hot fluids, severely affect refractory performance.

To ensure a safe operation and prevent breakouts, the trough campaign life is usually capped after a certain hot metal tonnage is reached, even if no critical damage is detected. After that, the trough is repaired and the most external refractory layer, which is in contact with the hot fluids, known as *working lining*, is replaced. Thus, accurately assessing the wear of refractory materials could allow to increase operation safety, as well as trough productivity by reducing the frequency of repairs. According to He et al. (2002), sizeable savings in refractory costs can be achieved by controlling wear in the regions of high erosion. Modern BF troughs are generally lined with Al_2O_3-SiC-C castable refractories, which have excellent thermal shock, oxidation and slag penetration resistance (Prompt & Ouedraogo, 2008).

Wear of refractory linings in the BF main trough is a complicated phenomenon. The precise mechanisms that lead to lining degradation are not fully understood yet. As mentioned above, chemical corrosion plays a role, both due to chemical attack by the slag and also due to oxidation of the refractory linings. Nonetheless, it is not the sole mechanism responsible for refractory degradation, as the *in situ* observed wear rates are largely non-uniform. Namely, the region where the jet impinges the trough is generally the most damaged one, which is also where higher turbulence and larger shear stress in the liquid metals are observed. Therefore, some researchers have argued that the driving factor in the refractory wear is mechanical erosion, with wall shear stress playing a critical role. However, *post-mortem* analyses of the state of the wear profile in BF troughs at the end of their campaign (Rüther & Lüngen, 1989; Begnis & Brandaleze, 2006) reveal that, while the computed shear stresses are generally found to be larger in the bottom of the trough, the wear profile is much more pronounced in the laterals of the trough. The most worn-out zones are precisely the locations where the hot metal-slag and slag-air interfaces are located, which often dictate the trough campaign life (Cameron et al., 2019). In addition, as refractories are porous materials, the fluids infiltrate the lining through the open pores. This may lead to severe spalling, as cycles of heating and cooling due to the tapping process stops occur with the thermal expansion in the infiltrated refractory being different from that within the non-penetrated refractory (Schacht, 2004). Nowadays, it is generally accepted

that the degradation of the trough refractories is the consequence of the combined action of the fluid flow, chemical reactions and heat and mass transfer phenomena (Ranjan et al., 2022).

Extreme heat in the trough, the difficulty of access to many parts of the industrial units as well as the visual opacity of incandescent molten metals pose a challenge to experimentation. This motivates the use of different tools to better understand the phenomena occurring in the BF trough. One of such tools are physical scale models, which have been used by various researchers to investigate the intricate flow patterns that are generated (e.g. Begnis & Brandaleze, 2006; Monteiro de Oliveira et al., 2020). Generally, oil and water have been used to represent slag and hot metal, respectively. However, the degree to which these results can be extrapolated to the real system is not entirely clear, due to the mismatch of density, viscosity ratio and other simplifications.

Recently, several studies regarding the hydrodynamics in the trough using CFD models have appeared in the scientific literature. Some of them focus on the issue of metal-slag separation (e.g. Kou et al., 2019), as BF troughs need to be appropriately sized to ensure an effective separation of slag from hot metal. On the other hand, other studies have specifically addressed the flow patterns due to the impinging jet generated by the tapping stream of hot metal on the liquid pool held in the trough (Rezende et al., 2007; H. Yao et al., 2021), confirming to some extent the findings that have been observed by researchers using scale models. However, most CFD studies do not include the thick slag layer above the hot metal and, instead, model the trough hydrodynamics considering a two-phase flow (air and hot metal) or a single-phase flow. Those that include the three-phase flow devote themselves to the issue of separation and do not provide many details regarding the flow structures. Furthermore, wall shear appears to have not been carefully studied in the existing body of research, and large differences between the reported results by different researchers are observed (Ranjan et al., 2022).

In addition, some publications have incorporated mathematical models for thermal effects, addressing the phenomena in the trough to some degree. Nonetheless, most researchers have done so in rather idealised conditions. For instance, Ge et al. (2020) neglected the radiative heat transfer or Vázquez-Fernández et al. (2019) addressed only the steady-state case in cross-sections of the trough, disregarding the influence of the refractory lid. Moreover, the impact of forced convection with air due to fume aspiration was not studied. The cyclic thermal loading due to the tapping process stops suffered by the trough also remains to be assessed.

Thereby, this part of the memoir is devoted to present several mathematical models that aim to capture the phenomena related to the thermo-hydrodynamics in the BF trough and to provide additional insight concerning some of the knowledge gaps mentioned above. Different numerical methodologies are introduced and the discussion of the obtained numerical solutions and their possible impact in the iron industry is carried out. To this end, we use the commercial package *Ansys Fluent* (Ansys, Inc., 2019) as well as own-developed code, with the aid of several open-source code libraries, such as *FEniCS* (Alnæs et al., 2015).

The outline of this part is as follows. First, in Chapter 1, the main features of the physical problem are discussed, addressing the BF process and devoting special attention to the fluid drainage from the BF, known as tapping. The general characteristics of the BF main trough are detailed and the current understanding of the main wear mechanisms is briefly reviewed. Moreover, the specific geometric dimensions of the trough that is modelled in this manuscript are introduced, as well as the physical properties of the fluid and solid materials. Then, in Chapter 2, a transient 3D hydrodynamic model of the BF trough is presented. The model is similar to those appearing in several recent studies, but using a slightly more advanced turbulence model and incorporating the three-phase flow. Also, some intricacies of the process that have not yet been analysed in the literature are studied, such as the interface position evolution, or the effect that specific parameters have on the wall shear stress, such as the slag fraction on the tapping stream. Subsequently, Chapter 3 deals with the usage of the results from the previous model to propose a suitable 3D thermo-hydrodynamic model of the middle and end parts of the trough. The scope is to obtain the steady temperature field, assessing the influence of the forced air flow below the refractory cover and the radiative heat transfer due to emission from the high temperature slag-air free surface. In Chapter 4, the non-local radiation model integral equation is formally derived in the 2D setting from the radiative heat transfer equation. A segregated

USC

fixed-point algorithm for the solution of coupled non-local radiation and conduction problem is then proposed and implemented. To assess the performance and to verify the correctness of the numerical implementation, a technique for the derivation of a manufactured solution test is proposed. Lastly, the aim of Chapter 5 is to apply the numerical procedure presented in the previous chapter to solve a simplified transient thermal model on the BF trough defined on a 2D cross-section. The model is used to study the thermal response of the trough during its complete campaign cycle, including the effect of the tapping process stops. It shows ability to reproduce the significant temperature oscillations that are observed in the available experimental measurements, made with several thermocouples embedded in the trough.

USC
UNIVERSIDADE
DE SANTIAGO
DE COMPOSTELA

USC
UNIVERSIDADE
DE SANTIAGO
DE COMPOSTELA

Chapter 1

Physical problem. Blast furnace main trough

In the iron and steel industry, there are two major methods for the production of steel: *electric arc furnace steelmaking* and *blast furnace steelmaking*. The former is also frequently known as the Electric Arc Furnace route (EAF route) while the latter is also called the Blast Furnace-Basic Oxygen Furnace route, or simply the BF-BOF route (see e.g. Babich & Senk, 2019). Both of them are fundamentally different, since the type of final products that can be made and the procedure differ. Furthermore, the raw materials are different, as in blast furnace steelmaking the feed material for steel production is hot metal, obtained from iron ore. In contrast, the EAF route uses scrap metal.

The scope of this chapter is to introduce the main features of the BF steel manufacturing process, specifically addressing the stage of the process that involves the BF main trough. This sets out the fundamental characteristics of the physical problem that is covered in the subsequent chapters. The content related to the BF process description introduced in this chapter mainly follows the textbooks by Geerdes et al. (2015) and Cameron et al. (2019), to which we refer the reader for a more accurate and detailed discussion of the various stages and intricacies of the BF steelmaking procedure. In Section 1.1, the essential features of the steelmaking process inside the BF are described. Subsequently, in Section 1.2, the BF tapping process, i.e., the extraction of hot metal and slag from the BF hearth, is introduced. Section 1.3 is devoted to state the purpose and characteristics of the BF trough, whereas Section 1.4 deals with the general features of the refractory materials used to line the trough and the mechanisms affecting their wear and tear. Lastly, Section 1.5 presents the specific geometrical parameters and physical property values that are used in the following chapters of this part of the manuscript, supplied by ArcelorMittal.

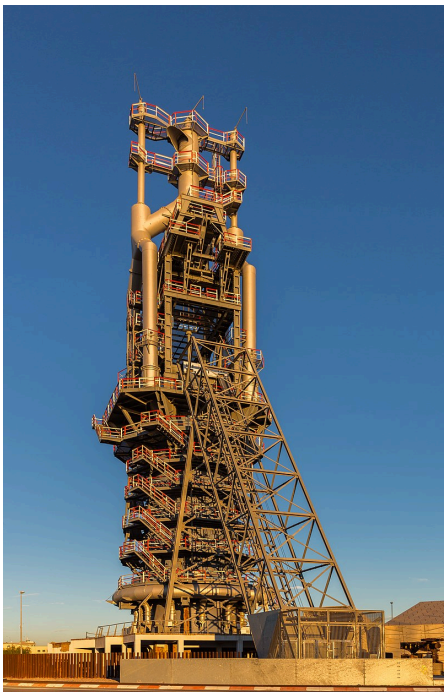
1.1. Blast furnace steelmaking

The blast furnace steelmaking route starts at the BF, a tall cylindrical shaft furnace where iron ores are reduced to obtain *hot metal*, an intermediate material in the steelmaking process. It is also known as *raw*, *molten* or *pig iron* in the specialised literature, and sometimes is simply referred to as metal or iron when there is no risk of confusion. It is a Fe-C alloy, with around a 95% of iron and a 5% in carbon content, respectively, as well as traces of silicon and manganese. Hot metal has few applications as an end-product since it is a brittle and not formable material. Hence, after its drainage from the BF, it is immediately transported to other plant facilities where it is further processed and refined into a lower carbon molten steel. Modern BFs have a diameter ranging from 10-15 m and are 40 m high, achieving hot metal throughputs that typically go from 4000 tonnes/day to 12000 tonnes/day. In Figure 1.1a, the BF No. 2 of *Altos Hornos del Mediterráneo* is shown, located in Sagunto, Spain. The furnace was

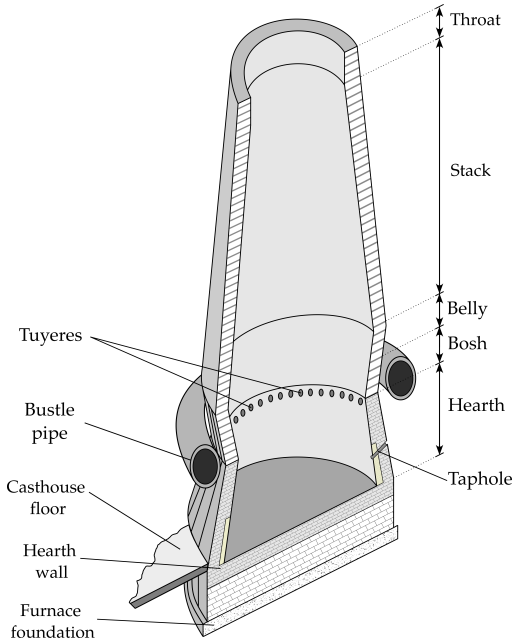
This chapter reproduces contents from the following publications:

- Barral, P., Nicolás, B.; Pérez-Pérez, L.J., & Quintela, P. (2019). *Numerical Simulation of Wear-Related Problems in a Blast Furnace Runner*. In: García Guirao, J., Murillo Hernández, J., Periago Esparza, F. (eds) Recent Advances in Differential Equations and Applications. SEMA SIMAI Springer Series, vol 18. Springer, Cham. ISSN 2199-3041. doi:10.1007/978-3-030-00341-8_14
- Barral, P., Pérez-Pérez, L.J., & Quintela, P. (2022). *Transient thermal response with nonlocal radiation of a blast furnace main trough*. Applied Mathematical Modelling. 105, 197 – 225. ISSN: 0307-904X. doi:10.1016/j.apm.2021.12.029

USC UNIVERSIDADE DE SANTIAGO DE COMPOSTELA



(**a**) Former BF No. 2 of *Altos Hornos del Mediterráneo*. Credits: Diego Delso, *delso.photo*, CC-BY-SA license.



(**b**) Schematic diagram of the BF.

Figure 1.1: Blast furnace and schematic diagram of its parts.

decommissioned in 1984 and was later restored as a tourist attraction. In Figure 1.1b, a schematic diagram of the BF is shown, illustrating its typical conical shape and its main parts.

To reduce the iron-bearing components –sinter, pellets and natural crushed ore– into hot metal, the BF employs the carbon contained in *coke*. Metallurgical coke is a porous, coal-based fuel with few impurities and high carbon content, produced in coke ovens by heating coal in the absence of air. Iron ore and coke are continuously charged in layers through the top of the furnace. In addition, *fluxes* are also added to the furnace burden. They are oxides, such as CaO and MgO, which help removing the alumina and silica impurities in the iron ore and coke. To smelt the ores and fluxes, hot air at around 1200°C is blown into the BF through a series of pipes, called *tuyeres*. They are located around a circumference near the bottom of the furnace. The blast air, distributed to the individual tuyeres through the bustle pipe, burns the coke with a high temperature flame, above 2000°C and hot enough to heat the descending solid charge throughout the BF, providing sufficient heat to reduce the iron oxides. It is injected with gauge pressures up to 420 kPa, reaching speeds around 180-240 m/s, which leads to the formation of a gas space near each tuyere, called the *raceway*. In this void zone, small hurtling coke particles circulate at high velocities.

The ascending gas leaves the furnace through the top, at around 120-200°C. Thus, a countercurrent flow is generated in the interior of the BF, as the descending furnace burden is in contact with the upflow of CO-rich, hot blast air, enhancing the heat and chemical exchange process. Through the tuyeres, cheaper substitute reduction materials for the expensive coke are also injected, such as pulverised coal or natural gas.

As hot metal is produced, a by-product is formed within the furnace, known as *BF slag* or simply *slag*. Its composition is mainly CaO and SiO_2 (around 40% of the mass content in both cases), with 10% of alumina (Al_2O_3) and MgO, as well as traces of other materials. Slag contains little iron, and its composition is carefully controlled by adjusting the added fluxes to guarantee a fluid slag that removes the ore gangue and coke ashes, as well as absorbing alkalis (such as K_2O and Na_2O) and

sulphur. In addition, it must meet suitable conditions that ensure a smooth BF operation and consistent burden descent. Lastly, slag composition must also satisfy the required physical and chemical properties to guarantee that it is easily extracted from the BF. Solidified slag is used as an aggregate for road construction and cement production.

Coke remains solid up to very high temperatures, above 2000°C, and plays an important role in the BF process, not only as a reducing agent and as fuel, but also as an essential structural element, distributing the ascending gas through the burden and allowing the molten slag and hot metal drip down through the coke pieces. During the final stage of the BF process, they attain their final reduced composition and accumulate in the bottom of the furnace, known as the *hearth*. Below the tuyere level, the only solid material that remains inside the furnace are smaller pieces of hot coke and both slag and hot metal are molten at a temperature around 1500°C.

The ironmaking process in the BF is continuous. It only stops to replace the cooling system, for furnace relining (replacing the furnace refractories) or for safety concerns. The rebuilding process is expensive, as iron production must be halted. Generally, a BF operates for 12-15 years continuously before it becomes unsafe, after which it is rebuilt. This period is known as the blast furnace campaign life. According to Cameron et al. (2019), the current longevity record holder is the Blast Furnace No. 1 in Tubarão, Brazil, operated by ArcelorMittal. It produced more than 90 million tonnes of hot metal during over 28 years and 4 months of non-stop activity. To achieve longer campaigns, stable furnace operation as well as good furnace design are key issues.

1.2. Tapping process

The removal of the accumulated molten slag and hot metal in the BF hearth takes place through the taphole, which is a constructed opening in the hearth wall (see Figure 1.1b). This drainage process is frequently known as *tapping*, often simply referred to as *tap* or *cast*. While the taphole is open, the exiting molten stream of hot metal and slag falls onto the BF *main trough* or *runner*, where they separate by density difference. Separation already takes place in the hearth before the liquids are tapped, given the large density difference among slag and hot metal, typically around 7000 kg/m^3 and 2500 kg/m^3, respectively.

Each tap starts as the taphole is drilled open with a powerful hydraulic drill. Since the hot metal and slag are stratified inside the BF hearth, during the beginning of each cast usually only the former is drained, as the metal-slag interface is above the taphole. Eventually, as the removal of iron from the BF lowers its level within the hearth, the slag level reaches the taphole and it is also drained. The elapsed time from the start of the tapping to slag being also discharged is frequently referred to as *slag delay*, and its duration depends largely on the conditions within the BF hearth (see e.g. Shao & Saxén, 2012a). Thereafter, slag and hot metal are drained simultaneously until BF gas bursts out from the taphole (called a *gas blow*), point at which the taphole is closed by forcing a plug of refractory clay into the orifice with a mud gun, sealing it and ending the tapping.

The clay also replaces the worn taphole profile, which may suffer severe wear during each cast. According to Geerdes et al. (2015), the taphole is the most vulnerable zone of the BF due to the exposure to both chemical and physical attack by slag and hot metal, as well as the reliance on consumable materials and manual intervention. In particular, Henriksson et al. (2016, p. 168) obtained a good agreement with tapping flow rate measurements in real BFs by adjusting a mathematical model that predicted sizeable increases in the taphole diameter during the tap, reaching up to 90% enlargement in some cases. On the other hand, Cameron et al. (2019, p. 629) reports that typical wear rates are significantly lower, about 0.11 mm/min, depending on the clay type. The taphole wear is substantial only when the discharge of slag starts, and results in non-constant draining rates of iron and slag. When the taphole is closed, an amount of excess clay deposits in the interior of the hearth, forming the so-called *mushroom*, which protects the original BF wall. Therefore, the use of superior quality taphole clay is essential to achieve consistent removal of slag and hot metal.

The furnace drainage procedure is heavily influenced by the *deadman*, a stable pile of accumulated solid coke that remains in the centre of the BF hearth as a result of the turbulence originated in the

raceway. It impedes liquid flow and can redirect the molten iron and slag during tapping towards the hearth walls (Shao & Saxén, 2012b), which can lead augmented wear rates. Depending on the furnace conditions, the deadman can be sitting (filling the hearth) or floating, and is believed to have a conical shape.

Blast furnaces have usually between 2 or 4 tapholes that are used alternatively. Taphole length is maintained at around 3 m, depending on the hearth diameter, by changing the amount of taphole clay added. The drilling angle is slightly tilted downwards to facilitate drainage, with angles around 10°, which delay BF gas from entering the stream and causing early splashing while also favouring slag removal. Typically, a BF is cast between 8 and 14 times a day, with each cast lasting for about 90 minutes, although the precise durations widely depend on the furnace features. In the world's largest furnaces, it is possible to achieve almost continuous casting or even casting times over 24 h/day by overlapping the tappings, with two tapholes open at once.

The tapping stream exiting the taphole is driven by the furnace pressure, with velocities usually above 5 m/s. It behaves as an unconfined fluid jet, which travels through air describing a parabolic profile. Ideally, it should have a low arch, with minimal splashing to avoid excessive damage in the trough refractories. In He et al. (2002), images of the exiting stream show that the jet remains dense for a certain distance and then breaks in smaller fragments as it approaches the pool in the trough. It was also concluded that blast gas entrainment into the taphole was the most likely cause for an excessively splashy jet stream, which was believed to be the cause of higher wear rates in the refractory cover. In addition, taphole blockages and roughness were found to be contributing factors to the jet spread. It is also believed that clay quality can influence trough refractory performance, as poor quality clay may lead to very uneven erosion profiles in the taphole and produce excessively flared and incoherent jets, with increased splashing on the trough linings (Ranjan et al., 2022).

When slag and hot metal are tapped simultaneously, although density stratification occurs in the hearth, the flow regime in the taphole can become more complicated. Some researchers, such as Iida et al. (2008), have implicitly assumed fully dispersed flow in the taphole, while Stevenson & He (2005) have found that slug flow (a partially dispersed regime) is likely to occur in the taphole with gas-liquid experiments. However, Shao & Saxén (2013a) argue that the density difference between iron and slag makes more natural to assume separated flow, and that the conclusions drawn by gas-liquid physical models may not be fully extrapolable to the real BF, as they are a rather extreme case for the taphole flow characterisation. Moreover, it is stated that clear interfaces are often observed in commercial BFs, which indicates that slag and hot metal remain stratified in the taphole to some extent.

Attempting to match the continuous hot metal production within the furnace and the intermittent tapping process is a challenge for furnace operators. The BF is operated to always keep the molten layers below the tuyeres. To this end, molten liquid depths in the hearth are carefully controlled by adjusting the tapping duration and the outflow rates. The monitoring of the liquid levels is not immediate, as due to the inner pressure in the furnace, the slag and hot metal interfaces during tapping are substantially contorted towards the taphole (Shao & Saxén, 2013b).

1.3. Main trough

The BF main trough is a refractory concrete-lined structure where the molten iron and slag tapping stream is collected. A sketch of the BF and the trough is displayed in Figure 1.2. Its dimensions and specific features widely depend on the casthouse arrangement and its particular needs. However, the general characteristics are common to most modern troughs. The function of the trough is not merely hauling the cast hot metal to the next step in the process, but also to ensure adequate metal-slag separation (Monteiro de Oliveira et al., 2020). Separation is achieved by density difference, as the denser hot metal flows underneath a *skimmer* block, which forces the lighter slag to accumulate on top of it and drain through a smaller runner that goes sideways, the *slag runner*.

The *iron dam* at the end of the trough allows a residual amount of hot metal and slag to be kept inside the trough between tappings. Most modern BF troughs are arranged so that they are *pooling*

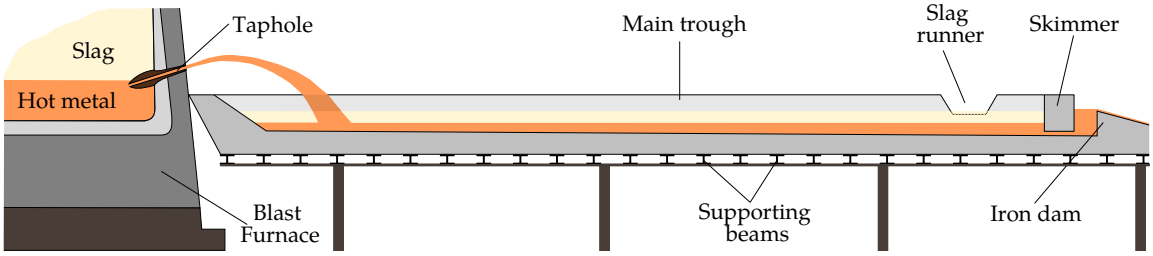


Figure 1.2: Sketch of the BF trough.

troughs (Cameron et al., 2019), meaning that they are only slightly sloped downwards to facilitate liquid sliding, with slopes frequently below 1.5%. In such case, a liquid pool or bath is retained in the trough, with a depth usually over 20 cm. The fluid pool is not only useful to mitigate the kinetic energy of the falling jet stream, but also leads to better preservation of heat (Geyer & Halifa, 2014). In addition, the liquid bath and reduced slope results in lower hot metal velocities, which increases residence time of slag and iron in the trough, allowing for better metal-slag separation. Furthermore, pooling troughs greatly reduce the refractory wear and tear at the jet impact point, and most of the refractory degradation is localised at the laterals of the trough (Rüther & Lüngen, 1989).

During the tapping process, the liquid level in the trough rises and, eventually, the iron dam is overflown by hot metal. Then, it circulates through the smaller *iron runner*, which delivers the molten metal to the *tilting runner*. It distributes and fills torpedo-shaped rail car ladles, whose function is to transport the liquid hot metal to the steel workshop for further processing. When one ladle is full, the tilting runner is repositioned to fill a different torpedo ladle, avoiding the stoppage of the process. On the other hand, slag flows along the slag runner to the granulator or to pits, where it solidifies.

The trough is constructed over a steel casing, which in modern BF troughs is usually suspended in open air, supported by a set of beams, as depicted in Figure 1.2. This allows the trough dissipate large amounts of heat both by free convection with the surrounding ambient air and also by emission of thermal radiation, which becomes relevant due to the high temperature that is reached. Metallic fins and ribs can be added to the laterals and bottom of the casing to enhance the cooling with ambient air. In some cases, the main trough includes cooling ducts through which cold air is blown to further enhance heat dissipation over the trough metallic shell (Cameron et al., 2019).

To effectively control fume emission during the furnace operation, a *refractory cover*, *hood* or *lid* is installed on the BF trough system. The stronger fuming is produced near the taphole, where the molten stream contacting the ambient air produces a substantial amount iron oxide fumes and carbon kish (Cameron et al., 2019). The slag layer sitting on top of hot metal in the trough suppresses the formation of fumes due to hot metal oxidation. However, the slag stream generates a significant amount of sulphur-bearing fumes (Turkdogan, 1984). The cover is formed by several separate pieces to facilitate manipulation and removal for maintenance purposes, and often have specifically designed cranes incorporated near the taphole area to easily remove the cover to drill and plug the taphole. The cover system ensures an effective aspiration of the casthouse, and also avoids excessive cast iron cooling, as it blocks radiation emission to the surroundings by the molten stream circulating in the trough. In Figure 1.3, a 3D schematic diagram of the main trough is depicted, showing the iron and slag runners, as well as the skimmer. The cover has been cut for clarity purposes, but is usually placed over the entire system.

Iron and slag separation is also a central issue in the BF trough operation. It should be correctly sized in order to allow good separation of both liquids. As discussed in Kim & Ozturk (1998), hot metal losses with slag lead to danger of explosion in the slag granulation process, while slag entrainment in hot metal results in a decreased efficiency in the desulphurisation process. Some studies, such as Shestopalov et al. (1988), reported high metal losses with slag, up to 2%. Several factors play a role in separation, such as the droplet settling velocity, the residence time and the amount of generated turbulence in the trough (Kim & Ozturk, 1998; Begnis & Brandaleze, 2006). Furthermore, geometrical parameters of the trough, such as the iron dam, skimmer and slag runner height relative to the bot-

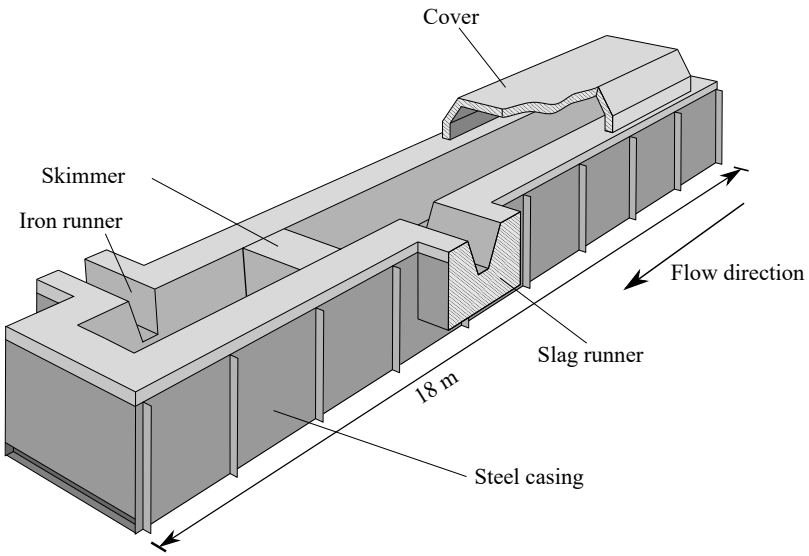


Figure 1.3: Schematic diagram of the main trough.

tom of the trough impact separation, as well as the length of the trough (Luomala et al., 2001). Some exotic trough configurations, such as the additional skimmer described in Shestopalov et al. (1988), have been reported to increase separation efficiency, with a similar effect to that of lengthening the trough. The reduction in the tapping stream energy due to the liquid pool kept in the trough enlarges the region where plug-like flow occurs, frequently referred to as quiet or laminar region. There, the entrained slag droplets in the metal rise at the velocity determined by *Stokes' law*. Therefore, the increased residence time due to lower velocities has a direct influence on the separation of hot metal and slag in the BF trough (Cameron et al., 2019).

1.4. Trough refractory linings

The BF trough is generally lined with different material layers, each with a specific purpose. The outermost layer, referred to as working lining, is usually composed of an alumina based castable refractory with silicon carbide and carbon content (Al_2O_3-SiC-C). It is directly in contact with the molten slag and iron circulating on the trough, and thus sustains harsh conditions that result in severe wear. Usually, an additional refractory layer, the *safety lining*, serves as a back-up refractory and should compensate any working lining perforation. Moreover, an insulating material is often added to maintain the temperature in the external steel shell below suitable values (Prompt & Ouedraogo, 2008).

As mentioned in the previous chapter, it is a major concern for the steel industry to minimise the wear of the blast furnace runner, which usually needs to have the working lining replaced after around two months of usage to avoid greater damage in the layers below. This wear is due to a combination of factors. These include chemical corrosion, erosion due to the liquid metal flow and the impact of the falling jet on the trough, as well as thermal effects, both from thermal shock and cyclic thermal loading.

1.4.1. Castable refractories

Refractories are physically and chemically stable materials at elevated temperatures, used to line vessels designed for the production of other materials, like metals or glass (Lee et al., 2001). Furthermore, they have good mechanical and thermomechanical properties, as well as good corrosion resistance,

making them very useful in the iron and steel industry, which employs around 70% of all refractories that are produced (Garbers-Craig, 2008). Refractories are composed by aggregate particles, held together by a bonding phase. There is a wide range of types of refractory materials, and a variety of complicated microstructures, phase assemblages and aggregates are commercially available. They are porous materials, and the distribution of particles and size directly affect its properties.

Depending on the specific application, shaped or *monolithic* (unshaped) refractories may be used. The former, normally brick-shaped, are more difficult to install and susceptible to joint damage. On the other hand, monolithic refractories are only given a specific shape upon installation, and they have undergone extensive development over the last century, both in composition and installation techniques, evolving into a versatile class of refractory materials (Lee & Moore, 1998). One of the most significant advances in monolithic refractories was the development of *castable* refractories, which are complex formulations of dry granular materials that require water addition. Normally, they use calcium aluminate cement (CAC) as a binder and, although conventional castables with high amounts of cement are still widely used, low cement varieties, known as *low cement castables* (LCC) and *ultra-low cement castables* (ULCC) have shown consistent growth. This is mainly because the CaO present in the cement leads to deterioration of its properties at high temperatures (Lee et al., 2001).

Castables require to add significant amounts of water in order to flow. This water is taken by the porosity of the grain and creates the hydraulic bond. In contrast, low cement varieties use fine particles (≤ 1 μm) to replace cement content, which fill the voids between the coarse grains. This aids to reduce water consumption and porosity. One significant drawback with LCC is that reactions among microsilica particles result in the formation anorthite, which melts at about 1400°C. The formation of such liquid phases contributes to a sudden loss of strength and properties of the castable (Garbers-Craig, 2008). The installation methods of castables are very diverse. Conventional castables are usually poured, while the low-cement varieties require external or internal vibration. More advanced and modern techniques are available, as *self-flowing castables*, which do not need vibration, or *shotcrete*.

Regarding the mechanical behaviour of the castable refractories that compose the trough, Ouedraogo & Prompt (2008) experimentally analysed the response at different temperature values of an Al_2O_3-SiC-SiO_2 castable, with traces of TiO_2, CaO and Fe_2O_3. The material presented a quasi-brittle behaviour up to a temperature around 900°C, with non-linear evolution evidencing the occurrence of thermal damage. For higher temperatures, especially those above 1000°C, the behaviour was viscoplastic. Similar conclusions were drawn in Ouedraogo et al. (2011), where the mechanical response of two different refractories was compared.

1.4.2. Wear mechanisms

As mentioned previously, wear and degradation of the refractory linings is a complex phenomenon, with various interacting factors involved. Some researchers argue that the main driving factor of trough refractory wear is mechanical erosion due to the fluid flow (Ge et al., 2020). In such case, the wear should be closely related to the wall shear stress. This is supported by the observation that the areas with higher turbulence in the liquids are those where increased wear rates are measured, both inside BF hearth (Almeida et al., 2017) and in the main trough itself (Begnis & Brandaleze, 2006). According to He et al. (2002), the wear rate of the blast furnace trough refractory in the impingement region of the taphole stream is approximately three times greater than that further down the trough. This is also noted in Luomala et al. (2001), as the most intense area of wear occurs on the walls at the impact point about 2-3 m from the taphole. However, as it is also mentioned by the authors, in pooling troughs the wear of the bottom is almost negligible. This has been also observed by Begnis & Brandaleze (2006); Rüther & Lüngen (1989), who report *post-mortem* wear profiles in different BF troughs. Over time, the trough refractory lining erodes forming a curvilinear profile, more pronounced in the slag and metal lines, which correspond, respectively, to the slag-air and slag-hot metal interfaces. According to Cameron et al. (2019), the most challenging location to minimise refractory degradation is the slag-hot metal interface. There, the refractory must sustain both oxidation and reduction as the oxidized slag and the carbon-rich hot metal alternate over a small elevation of the

trough hot face.

Since CFD studies have found that the wall shear stress is larger in the bottom of the trough than in the lateral walls (see e.g. Rezende et al., 2007), wear cannot be explained solely on the basis of mechanical erosion, as mentioned in Ranjan et al. (2022), who documented the current state of the art regarding research related to the BF trough process. In particular, addressing the current knowledge concerning refractory wear in the runners, they identify three regions were different wear mechanisms take place. In the first region, which corresponds to the part of the wall above the slag line, the main degradation mechanism is oxidation of SiC and C. Moreover, a second region, called intermediate region, corresponds to the part of the wall exposed to both slag and hot metal. There, some researchers argue that wear can be explained via oxidation due to formed FeO in the bulk of the liquid and its interaction with SiC and C. Nevertheless, according to Ranjan et al. (2022), it seems unlikely that this is the only mechanism responsible for degradation, and other works suggest that dissolution of alumina due to action of the slag is also relevant. Lastly, a third region corresponds to the part of the wall that is primarily in contact with hot metal. There, hot metal penetration is believed to be the main wear mechanism. Also, the fluctuations of liquid levels and temperature due to the discontinuous and non-steady nature of the tapping process can impair the spalling resistance of the refractory linings, creating cracks that lead to higher wear rates.

In summary, refractory degradation is a consequence of fluid flow, chemical attack as well as mass and heat transfer phenomena. For more details concerning the issue of refractory wear, we refer the reader to Ranjan et al. (2022) and the references therein, and to textbooks such as Schacht (2004).

1.4.3. Critical isotherms

The critical isotherms are temperature contours that are related to increased wear in the trough refractory materials. Usually, the position of the temperature isotherms among 1150°C and 1250°C is monitored. In general, it is of interest to ensure that the isotherms are inside the working lining, as preventing them from reaching the back-up refractory helps controlling degradation therein.

The 1150°C isotherm is of particular significance, as it corresponds to the eutectic point of the alloy of Fe-C. Since the composition of hot metal is essentially 95% iron and 5% carbon, with traces of other materials, maintaining this isotherm within the working lining guarantees that any infiltrated iron solidifies, forming a protective layer. This layer of solid hot metal is usually referred to as *skull* in the specialised literature, and helps reducing the possibility of suffering a major trough breakout.

Measures such as increasing the refractory thermal conductivity or reducing the insulation lining thickness can result in better heat extraction from the working lining, which maintains the 1150°C isotherm within the working lining (Kumar et al., 2010). However, this difficults controlling the temperature in the external shell.

1.5. Setting of the mathematical models

The models presented in the subsequent chapters are defined using the data supplied by Arcelor-Mittal Spain, which corresponds to one of their BFs in Gijón. It is a 3-taphole BF, with an estimated hot metal production of 6000 tonnes/day and a working volume around 2625 m^3. In Figure 1.4, the adapted drawings of the troughs operated in the BF are shown. Note that the depicted dimensions are in mm, and that the total length of the runner is about 18 m. The trough is naturally cooled by the surrounding air, supported by a steel casing structure that has several incorporated fins, similar to those depicted in Figure 1.3. In the subsequent models, the formwork of the trough is not included and thereby it is not displayed in the drawings.

A longitudinal cut of the trough along the symmetry axis of its cross-section is represented in Figure 1.4a, where the refractory cover is also shown. In reality, the cover is composed by three different pieces of similar length to facilitate their removal for maintenance purposes. Since the gaps are small, around 5 cm, it has been assumed that is continuous to simplify the mathematical model in Chapter 3. Also, the centreline of the BF taphole is displayed as a discontinuous red line, with a drilling

angle $\gamma_{tap} = 10°$. In Figures 1.4b and 1.4c, the cross-sections of the main trough and slag runner are depicted, respectively. The extent of the working, safety and insulation linings is shown. Notice that, to accommodate the slight inclination of the trough (of 0.5%, approximately), some of the dimensions shown in the cross-section are variable and depend linearly on the distance to the blast furnace.

The fume aspiration is performed next to the taphole. Therefore, a forced circulation of air develops, with the air flowing below the cover from the opposite side of the trough, around 18 m away, and crossing it countercurrent in comparison to the slag and hot metal.

1.5.1. Material properties

The physical properties of the solid materials composing the layers of the trough are shown in Table 1.1a. In this table, we denote as k, c_p and ρ the *thermal conductivity*, the *specific heat* and the *density*, respectively. The values have been supplied by ArcelorMittal, in some cases taken from the data sheets elaborated by the material manufacturer. The constant values are given at the expected operation temperature. In particular, since the technical sheet of the material corresponding to the insulation lining contains temperature-dependent data for the thermal conductivity, we construct the subsequent function, which was obtained fitting the data:

$$k_{in}(T) = \begin{cases} 0.13, & \text{if } T \leq 293, \\ \dfrac{1}{98000}(9T + 10103), & \text{if } 293 < T < 1273, \\ 0.22, & \text{if } T \geq 1273, \end{cases} \tag{1.1}$$

where T denotes the temperature.

Concerning the fluid phases that play a role in the flow on the BF trough (air, slag and hot metal), the properties shown in Table 1.1b are used in the mathematical models introduced in the subsequent chapters. The symbol μ denotes the *dynamic viscosity*, whereas M_w is the molar mass. Notice that most of the properties are considered constant, with the exception of the air density, which in Chapter 3 is modelled as a weakly compressible ideal gas using a temperature dependent function $\rho_A(T)$, defined therein.

Table 1.1: Properties of the materials.

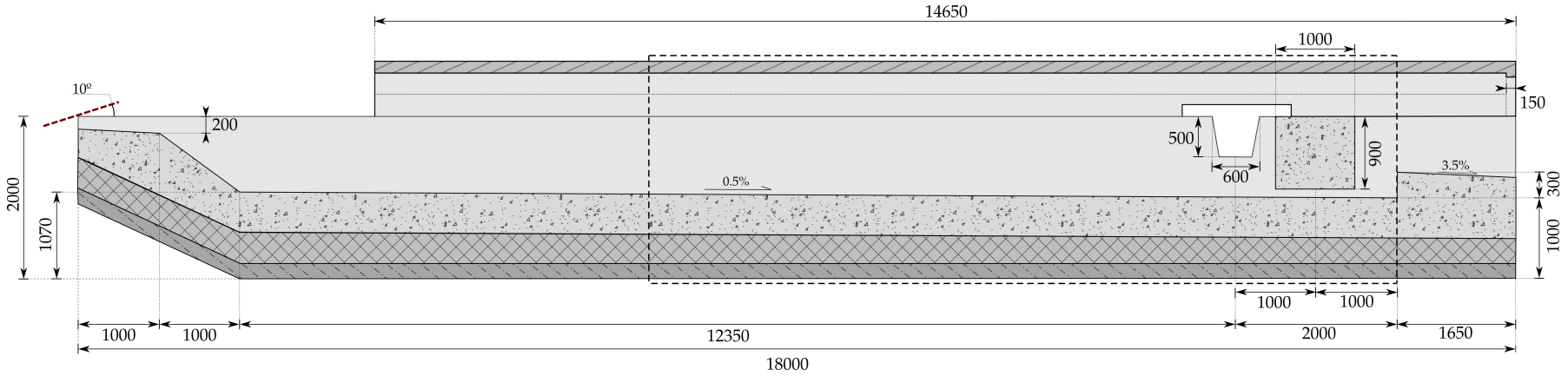
(**a**) Solids.

	k [W/(m · K)]	c_p [J/(kg · K)]	ρ [kg/m^3]
Working lining	2.6	1212	2500
Safety lining	1.8	1172	2900
Insulation lining	$k_{in}(T)$	1050	800
Cover refractory	2.5	1296	2750

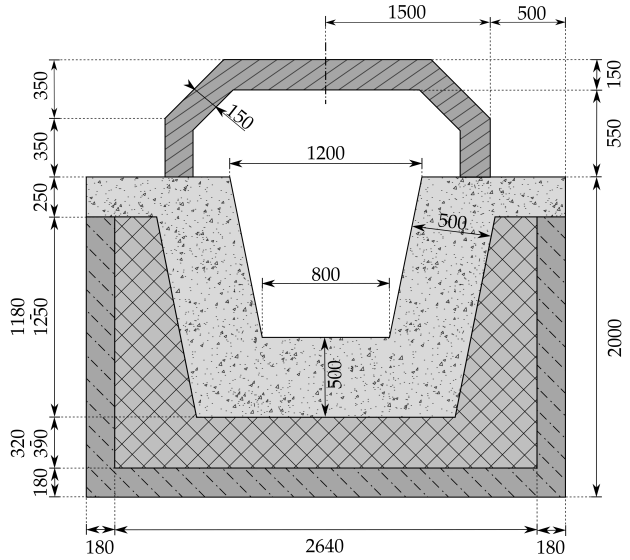
(**b**) Fluids.

	k [W/(m · K)]	c_p [J/(kg · K)]	ρ [kg/m^3]	μ [Pa · s]	M_w [g/mol]
Hot metal	16.5	850	7015	$7.15{\cdot}10^{-3}$	-
Slag	9.7	807	2600	0.5	-
Air	0.0257	1005	$\rho_A(T)$	$1.82{\cdot}10^{-5}$	28

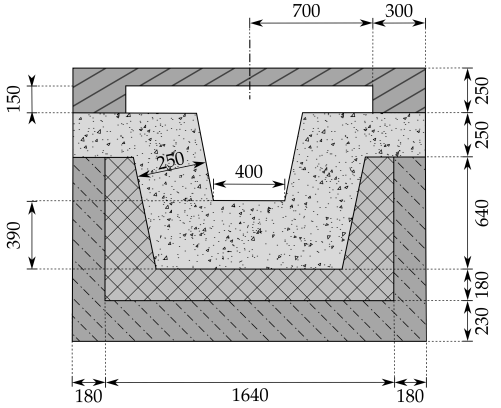
USC UNIVERSIDADE DE SANTIAGO DE COMPOSTELA



(**a**) Longitudinal cut of the BF trough.



(**b**) Main trough cross-section.



(**c**) Slag runner cross-section.

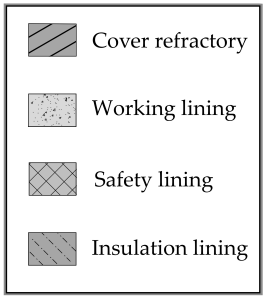


Figure 1.4: Drawings of the main trough used to construct the computational domains. Dimensions are indicated in mm.

Chapter 2

Transient 3D hydrodynamic model of the BF main trough

In this chapter, a mathematical model addressing the flow of hot metal and slag in the trough is presented and solved numerically. The main motivation is to investigate the complicated flow structures that are generated by the impact of the molten jet stream exiting the taphole on the liquid pool held in the trough. These flow patterns have been a matter of research by several authors, as they are believed to have a strong influence on the refractory lining wear (see Section 1.4.2). Some publications have relied on physical scale models, while other researchers have used Computational Fluid Dynamics (CFD) to solve the Navier-Stokes equations with the purpose of characterising the multiphase flow in the trough. From both standpoints, it has been shown that substantial entrainment of air occurs in the jet impact region, generating a highly turbulent mixed gas, metal and slag multiphase flow with intricate features (Ranjan et al., 2022).

Kim & Ozturk (1998) and He et al. (2002) carried out experiments using physical scale models of the BF trough. To emulate slag and hot metal, oil and water were used, respectively. The influence of several process variables in slag and hot metal separation, such as the BF discharge rate or the trough geometry, was investigated in the former. On the other hand, the latter focused in the study of the general flow features. Flow separation, as well as its main structures and characteristics, were also assessed with a scale model by Luomala et al. (2001), using water for the experimental apparatus as hot metal. Return flows, generated by the tapping stream in the water pool, were considered to strongly influence the wear of the refractory wall in the BF trough. The effect of longitudinal pads and other modifications in the flow were analysed. Begnis & Brandaleze (2006) developed a similar physical scale model to investigate the flow patterns. They also inspected the damage on a BF trough between campaigns, finding that the most severely worn zone correlates well with the higher-turbulence regions resulting from the jet impact.

The hostile environment in the trough, posing a significant challenge to experimentation, has motivated the surge of mathematical modelling and numerical simulation applied to the main trough, especially in the recent years. Rezende et al. (2007) solved a CFD model involving the multiphase flow of hot metal and air in the runner, using an algebraic turbulence model. The patterns resulting from the jet stream impingement were studied, showing qualitative agreement among the numerical results and those reported by physical models. L. Wang et al. (2017) used a similar mathematical model to investigate the flow in the trough, including slag as a different fluid phase and buoyancy effects due to thermal expansion of the fluids. Separation efficiency of slag and metal was analysed, concluding that controlling the height level between the slag runner and the iron dam is essential to achieve separation. In Kou et al. (2019), separation was also addressed with a CFD model, incorporating the three-phase flow. Geometry changes, such as decreasing the trough bottom slope, were shown to have a sizeable impact on the slag-metal separation. Moreover, in Monteiro de Oliveira et al. (2020), a CFD model was combined with a physical scale model, which was used to undertake extensive experiments and to validate the numerical findings. Flow modifiers were introduced to contain the region where the mixing is more intense, achieving features similar to those of plug flow in a greater region of the trough. Ge et al. (2020) and H. Yao et al. (2021) considered an analogous approach, but modelling the flow in the trough as a single-phase flow in a fixed domain instead. The former considered a mixture of slag and hot metal, while the latter used cast iron properties for the fluid. In both studies, conjugate heat transfer with the refractory lining was incorporated, and H. Yao

et al. (2021) also assessed the thermal stresses in the solids, considering that the refractory behaves as a linear thermoelastic material. In addition, Barral et al. (2021) numerically investigated the shear stress generated by a planar hot metal jet impact in the BF trough.

As discussed above, there is a significant body of research regarding the flow conditions in the trough. Some researchers, guided by both numerical findings or by scale model predictions, have proposed geometrical modifications to the trough to reduce erosive phenomena, mainly by the addition of baffles or pads to the bottom and sidewalls of the trough. However, most CFD studies do not include the thick slag layer above the hot metal and, instead, the trough hydrodynamics are modelled considering a two-phase flow (air and hot metal) or a single-phase flow. Those studies that include slag and hot metal as different phases do not focus on the shear stress and mainly address the issue of slag entrainment with hot metal (L. Wang et al., 2017; Kou et al., 2019). In this chapter, the scope is to study the influence of the slag bath on the flow dynamics in the BF trough, giving special attention to the evolution of the positions of the interfaces separating the fluid phases. This is done for different taphole stream conditions, considering first a hot metal-only flow, and different volumetric shares of slag in the stream subsequently. Since refractory wear is closely related to wall shear stress (see Section 1.4.2), we also aim to obtain a shear stress estimation for a realistic geometrical model of the trough. Provided that it is not computationally feasible to solve a detailed hydrodynamic model for a full BF tapping, we set a time interval that leads to a solution that can be considered quasi steady. In such case, for the given model conditions, the variations of the variables describing the flow, such as the pressure or velocity, can be regarded as fluctuations around a steady mean value. With this purpose, several simplifying assumptions are introduced. Namely, an incompressible and isothermal flow is considered, and the air circulating above the pool of fluids is assumed to be still. Also, surface tension effects are neglected, and the involved fluid phases are regarded as immiscible and continuous.

This chapter is structured as follows. Aiming to achieve a self-contained document, we provide in Section 2.1 a brief description of the derivation of the conservation equations that are involved in the mathematical model. Section 2.2 deals with the turbulence model that is used to address the influence of the turbulent fluctuations that are generated in the flow. Subsequently, Section 2.3 is devoted to provide a description of the numerical technique that is used to model the multiphase flow of air, hot metal and slag, known as the Volume of Fluid method (VOF). In Section 2.4, the computational domain, as well as the boundary and initial conditions that are used to close the mathematical model, are presented in detail. The numerical procedure is also discussed. Lastly, in Section 2.5, a grid sensitivity study is presented, and the numerical results for the various taphole conditions are examined.

2.1. General conservation equations

This section aims to develop the conservation equations that describe general fluid flow. We do so in a formal way, following the classical framework of continuum mechanics. We adopt the notation introduced in Gurtin (1982), to which we refer the reader for additional details and a more rigorous treatment of the derivation. Alternative approaches to the derivation of the conservation equations can be found, for instance, in Chacón Rebollo & Lewandowski (2014); Kundu et al. (2015).

Let $\mathcal{B}$ be a *body*, i.e, a regular region of the three-dimensional Euclidean space, $\mathcal{E}$ (Gurtin, 1982). Set $X(\mathbf{p}, t)$ as a *motion*, i.e., a $\mathcal{C}^3$ mapping such that $X : \mathcal{B} \times \mathbb{R} \to \mathcal{E}$, where $\mathbf{p}$ is called a *material point* and t is the time. In addition, assume that $\mathcal{P} \subset \mathcal{B}$ is an arbitrary part of the body, and let us denote as $\mathcal{P}_t = X(\mathcal{P}, t)$ the region of the space occupied by the part $\mathcal{P}$ at time t. Moreover, set $\mathcal{T}_X$ as the *trajectory* associated to the motion X, defined as the following set:

$$\mathcal{T}_X = \{(\mathbf{x}, t) |\ \mathbf{x} \in \mathcal{B}_t,\ t \in \mathbb{R}\},$$

where $\mathcal{B}_t = X(\mathcal{B}, t)$.

USC UNIVERSIDADE DE SANTIAGO

2.1.1. Mass conservation

Let $\rho(\mathbf{x}, t)$ be the *mass density*, defined in the trajectory $\mathscr{T}_X$. The mass conservation law asserts that:

$$\frac{d}{dt}\int_{\mathcal{P}_t} \rho(\mathbf{x}, t)\, dV = 0.$$

From the previous expression, it can be shown that the subsequent local form of the mass conservation law holds (Gurtin, 1982):

$$\frac{\partial \rho}{\partial t}(\mathbf{x}, t) + \operatorname{div}(\rho(\mathbf{x}, t)\mathbf{v}(\mathbf{x}, t)) = 0, \tag{2.1}$$

where $\mathbf{v}(\mathbf{x}, t)$ is the *spatial description of the velocity*, i.e., the velocity of the material point $\mathbf{p} \in \mathcal{B}$ that occupies the position $\mathbf{x}$ at time instant t. In the sequel, for the sake of simplicity, we shall simply refer to $\mathbf{v}(\mathbf{x}, t)$ as *velocity*.

2.1.2. Momentum conservation

Let $(\boldsymbol{s}(\boldsymbol{\eta}, \mathbf{x}, t), \mathbf{b}(\mathbf{x}, t))$ be a *system of forces* for the body $\mathcal{B}$ (see e.g. Bermúdez, 2005), where $\boldsymbol{s}$ is a vector field that represents the *density of surface force* and $\mathbf{b}$ is the body force per unit volume. In addition, $\boldsymbol{\eta}$ denotes a unit vector in $\mathbb{R}^3$. Newton's second law leads to the subsequent balance of linear momentum

$$\frac{d}{dt}\int_{P_t} \rho\mathbf{v}\, dV = \int_{P_t} \boldsymbol{s}(\mathbf{n})\, dA + \int_{\partial P_t} \mathbf{b}\, dV,$$

where we have suppressed the dependence on the spatial points and time in the involved fields. Moreover, $\mathbf{n}$ denotes the outward-pointing unit normal vector.

Owing to the Cauchy's theorem, there exists a symmetric second order tensor field $\mathbf{T}$ such that $\boldsymbol{s}(\mathbf{n}(\mathbf{x}), \mathbf{x}, t) = \mathbf{T}(\mathbf{x}, t)\mathbf{n}(\mathbf{x})$. Furthermore, the following equation holds:

$$\frac{\partial}{\partial t}(\rho\mathbf{v}) + \operatorname{div}(\rho\mathbf{v} \otimes \mathbf{v}) = \operatorname{div}(\mathbf{T}) + \mathbf{b}, \tag{2.2}$$

where $\otimes$ denotes the tensor product, defined for $\mathbf{a}, \mathbf{b} \in \mathbb{R}^N$ as the second order tensor such that

$$(\mathbf{a} \otimes \mathbf{b})\mathbf{w} = (\mathbf{b} \cdot \mathbf{w})\mathbf{a},$$

for any $\mathbf{w} \in \mathbb{R}^N$. Equivalently, in component notation, $[\mathbf{a} \otimes \mathbf{b}]_{ij} = a_i b_j$, for any $i, j \in \{1, \ldots, N\}$.

Remark 2.1. *Expressions (2.1) and (2.2) are frequently regarded as the conservative forms of the local conservation laws. From them, the subsequent expressions can be deduced:*

$$\frac{\partial \rho}{\partial t} + grad(\rho) \cdot \mathbf{v} + \rho div(\mathbf{v}) = 0,$$

$$\rho\left(\frac{\partial \mathbf{v}}{\partial t} + grad(\mathbf{v})\mathbf{v}\right) = div(\mathbf{T}) + \mathbf{b},$$

which are known as the non-conservative or convective forms of the conservation laws.

2.1.3. Constitutive law

Constitutive assumptions are required to relate some of the involved unknowns in (2.1) and (2.2). Specifically, we assume that the body $\mathcal{B}$ belongs to the *Newtonian fluid* class, composed of those materials such that

$$\mathbf{T} = -p\mathbf{I} + \mathbf{T}_v = -p\mathbf{I} + \mathbb{C}(\operatorname{grad}(\mathbf{v})), \tag{2.3}$$

USC DE COMPOSTELA

where $p(\mathbf{x}, t)$ is a scalar field, known as *pressure* and $\mathbf{T}_v$ is the viscous part of the stress tensor. Moreover, $\mathbb{C}$ is a fourth order tensor, i.e., a linear operator in $\mathcal{L}(Lin, Lin)$, with Lin being the set of second order tensors.

If the fluid is assumed to be *isotropic*, the *material frame indifference principle* (see Gurtin, 1982) and the linearity of $\mathbb{C}$ lead to

$$\mathbb{C}(\text{grad}(\mathbf{v})) = \xi_v \text{div}(\mathbf{v})\mathbf{I} + \mu(\text{grad}(\mathbf{v}) + \text{grad}(\mathbf{v})^T),$$

where $\mathbf{I}$ is the identity tensor and μ and ξ_v are the *dynamic viscosity* and *second viscosity coefficient*, respectively. The *bulk viscosity* is defined as $\zeta = \xi_v + \frac{2}{3}\mu$. In addition, we adopt the *Stokes' hypothesis* or *assumption*, which asserts that the bulk viscosity is zero. Therefore, the second viscosity coefficient satisfies that

$$\xi_v = -\frac{2}{3}\mu.$$

The Stokes' assumption is accepted as a good approximation in a wide range of applications (Panton, 2013). If it holds, the viscous stress tensor in the fluid is such that

$$\mathbf{T}_v = -\frac{2}{3}\mu \text{div}(\mathbf{v})\mathbf{I} + \mu(\text{grad}(\mathbf{v}) + \text{grad}(\mathbf{v})^T). \tag{2.4}$$

Lastly, substituting (2.4) in (2.3), the final form of the stress tensor for a Newtonian fluid under the Stokes' assumption follows:

$$\mathbf{T} = -p\mathbf{I} + 2\mu\mathbf{D}(\mathbf{v}) - \frac{2}{3}\mu \text{div}(\mathbf{v})\mathbf{I}, \tag{2.5}$$

where $\mathbf{D}(\mathbf{v})$ is the symmetric part of the velocity gradient, i.e.:

$$\mathbf{D}(\mathbf{v}) = \frac{1}{2}(\text{grad}(\mathbf{v}) + \text{grad}(\mathbf{v})^T).$$

The tensor $\mathbf{D}(\mathbf{v})$ is frequently called the *strain-rate tensor* in the fluid dynamics specialised literature and is often denoted as S. Here, we follow the previously introduced notation, similar to that used in Bermúdez (2005).

2.1.4. Additional assumptions

Let $\Omega \subset \mathbb{R}^3$ be a domain with a sufficiently smooth boundary $\partial\Omega$. We assume that a domain is a subset of $\mathbb{R}^3$ which is open, bounded, connected and with a Lipschitz continuous boundary. We refer to Ω as the *computational domain*, and assume that the conservation equations (2.1) and (2.2) hold in $\Omega \times (0, t_{end}]$, where $t_{end} > 0$ denotes the final time value.

In general, the density of the fluid, ρ, as well as the dynamic viscosity, μ, are dependent on the thermodynamic conditions. Thus, both may suffer variations due to changes in temperature or pressure. Nonetheless, we assume that the flow is *incompressible* and neglect any density variation. In particular, we also consider a constant viscosity. Under these assumptions, the mass conservation equation (2.1) reads as

$$\text{div}(\mathbf{v}) = 0, \qquad \text{in } \Omega \times (0, t_{end}], \tag{2.6}$$

and the stress tensor simplifies to

$$\mathbf{T} = -p\mathbf{I} + 2\mu\mathbf{D}(\mathbf{v}). \tag{2.7}$$

Remark 2.2. *Although the velocities of hot metal and slag in the BF trough are below the threshold necessary to induce compressibility effects due to pressure, thermal effects may play a significant role inducing some degree of buoyancy in the flow due to density variations. However, experimental measurements provided by ArcelorMittal taken at the hot metal pool at the end of the trough indicate that it still remains at temperatures very close to 1500°C. This heavily suggests that the bulk of the pool of fluids held in the trough during tappings is at a high and mostly constant temperature, with the exception of the slag-air free surface, where significant heat losses are produced due to radiation emission and convection with the forced flow of air, as discussed in Chapter 1.*

Since the body forces acting on the fluids flowing on the BF trough are only due to gravity, it holds that $\mathbf{b} = \rho\mathbf{g}$. Considering (2.6) and substituting (2.7) in the momentum conservation equation (2.2), we obtain the so-called *Navier-Stokes equations* for an incompressible flow.

Find $\mathbf{v}(\mathbf{x}, t)$ and $p(\mathbf{x}, t)$ such that:

$$\operatorname{div}(\mathbf{v}) = 0, \qquad \text{in } \Omega \times (0, t_{end}], \tag{2.8}$$

$$\frac{\partial(\rho\mathbf{v})}{\partial t} + \operatorname{div}(\rho\mathbf{v} \otimes \mathbf{v}) = -\operatorname{grad}(p) + \operatorname{div}(2\mu\mathbf{D}(\mathbf{v})) + \rho\mathbf{g}, \qquad \text{in } \Omega \times (0, t_{end}], \tag{2.9}$$

where we set that the gravitational acceleration is such that $\mathbf{g} = -9.81\mathbf{e}_2$ m/s^2, with $\{\mathbf{e}_1, \mathbf{e}_2, \mathbf{e}_3\}$ being the canonical basis.

2.2. Turbulence modelling

In this section, the basic properties of turbulent flows are introduced for completeness. Moreover, the essential modelling principles followed in order to obtain the mathematical model accounting for turbulence in the flow are stated. For a detailed treatment of mathematical modelling of turbulence, we refer to e.g. Mohammadi & Pironneau (1994); Wilcox (2006); Chacón Rebollo & Lewandowski (2014).

The features of an incompressible flow are strongly related to the value of the *Reynolds number*, defined as:

$$Re = \frac{\rho\mathscr{L}\mathscr{V}}{\mu}, \tag{2.10}$$

with $\mathscr{L}$ and $\mathscr{V}$ being the length and velocity scales, respectively. Specifically, it is observed that for Reynolds number values below a critical value, Re_c, the flow is smooth as the fluid layers slide over each other in an ordered manner. Additionally, if flow conditions are constant in time, a steady-state is eventually reached. In contrast, if this critical value is surpassed, the flow becomes turbulent. The specific value of Re_c at which the laminar transition to turbulent flow occurs widely depends on the geometric particularities of the flow.

Turbulent flows are characterised by the presence of irregular and chaotic vortex structures, whose scales vary between the characteristic length scale of the flow, $\mathscr{L}$, and the *Kolmogorov length scale*, η_K, for the smallest ones. The vortices due to turbulence absorb energy from the mean flow and transfer it to the smaller ones, where it is dissipated owing to the action of viscous forces, which become increasingly relevant at the smallest scales. The chaotic motion throughout the cascade of scales results in a more efficient mixing of the fluid, which can be regarded as turbulence leading to increased diffusion in the flow. Turbulence is completely described by the Navier-Stokes equations (2.8)-(2.9). This means that, in theory, a complete numerical solution of the equation system would allow to fully characterise all the phenomenology in the flow. This kind of procedure is called *Direct Numerical Simulation* (DNS). However, the computational cost of DNS is extremely high, as to properly capture all the microscales in the flow tiny mesh and time step sizes are required. Therefore, in most real situations it is necessary to use additional modelling hypotheses in order to account for the effects of the smaller scales without resolving them.

2.2.1. RANS models

The most widespread type of techniques to model the effect of turbulence are the RANS models (*Reynolds-Averaged Navier-Stokes*). They are based on solving only the mean flow, modelling the turbulent fluctuations and their effect using additional variables and assumptions. In other turbulence modelling approaches, such as Large Eddy Simulation (LES), the largest turbulent scales of the flow are solved numerically and only the so-called subgrid scales (the smallest ones) are modelled, hence

obtaining a more accurate prediction of the turbulent phenomena, but at a much higher computational cost. In the following, we showcase the procedure to obtain the equations describing the mean flow from (2.8)-(2.9).

Let $\phi(\mathbf{x},t)$ be an arbitrary flow variable. In RANS models, every flow variable is decomposed in a part due to the fluctuations, $\phi'(\mathbf{x},t)$, and a mean field, $\langle\phi\rangle(\mathbf{x},t)$, obtained through a Reynolds average, such that:

$$\phi(\mathbf{x},t) = \langle\phi\rangle(\mathbf{x},t) + \phi'(\mathbf{x},t), \tag{2.11}$$

where the *Reynolds average*, $\langle\phi\rangle$, is obtained through a time averaging operator, defined as follows:

$$\langle\phi\rangle(\mathbf{x},t) = \frac{1}{\mathscr{T}}\int_t^{t+\mathscr{T}} \phi(\mathbf{x},s)\, ds. \tag{2.12}$$

In the previous expression, $\mathscr{T}$ is a suitable temporal scale such that there exist $\mathscr{T}_1$ and $\mathscr{T}_2$ satisfying $\mathscr{T}_1 \ll \mathscr{T} \ll \mathscr{T}_2$. Here, $\mathscr{T}_1$ is the scale of the turbulent fluctuations in the flow and $\mathscr{T}_2$ represents the scale of the slow flow variations that are not due to turbulent effects.

The splitting of ϕ in (2.11) is known as *Reynolds decomposition*. Depending on the characteristics of the turbulence, the Reynolds average (2.12) can be defined in different equivalent manners, such as space averaging or ensemble averaging (Wilcox, 2006). It satisfies several crucial properties for a sufficiently smooth function $\phi(\mathbf{x},t)$, such as linearity and that the fluctuations have zero mean, this is, $\langle\phi'\rangle(\mathbf{x},t) = 0$ (see e.g. Mohammadi & Pironneau, 1994). Nevertheless, note that the product of fluctuations for two arbitrary flow variables ϕ and ψ has a non-zero average in general, i.e., $\langle\phi'\psi'\rangle \neq 0$. In such case, it is said that they are *correlated*.

Replacing in (2.8)-(2.9) the pressure and velocity with their respective Reynolds decompositions, $p = \langle p\rangle + p'$ and $\mathbf{v} = \langle\mathbf{v}\rangle + \mathbf{v}'$, it can be shown that the subsequent system is obtained.

Find $\langle\mathbf{v}\rangle(\mathbf{x},t)$ and $\langle p\rangle(\mathbf{x},t)$ such that:

$$\operatorname{div}(\langle\mathbf{v}\rangle) = 0, \qquad \text{in } \Omega\times(0,t_{end}], \tag{2.13}$$

$$\begin{aligned}\frac{\partial(\rho\langle\mathbf{v}\rangle)}{\partial t} + \operatorname{div}(\rho\langle\mathbf{v}\rangle\otimes\langle\mathbf{v}\rangle) &= -\operatorname{grad}(\langle p\rangle)\\ &\quad - \operatorname{div}(\rho\langle\mathbf{v}'\otimes\mathbf{v}'\rangle) + \operatorname{div}(2\mu\mathbf{D}(\langle\mathbf{v}\rangle)) + \rho\mathbf{g}, \qquad \text{in } \Omega\times(0,t_{end}].\end{aligned} \tag{2.14}$$

The previous equations are frequently known as the RANS equations. Also, since the time dependency has been retained, provided that we expect slow variations of the mean flow, this particular unsteady version is often termed as the URANS equations (*Unsteady Reynolds-Averaged Navier-Stokes*). In (2.14), the term appearing due to the fluctuations of the velocity is called *Reynolds stress tensor*, which we denote as

$$\boldsymbol{\tau}^R = -\rho\langle\mathbf{v}'\otimes\mathbf{v}'\rangle.$$

Note that it is a symmetric tensor where the six new unknowns require additional modelling assumptions to close the model. In particular, we assume that the so-called *Boussinesq approximation* or *assumption* holds, i.e., that

$$\boldsymbol{\tau}^R = 2\mu_T\mathbf{D}\left(\langle\mathbf{v}\rangle\right) - \frac{2}{3}\rho K\mathbf{I}, \tag{2.15}$$

where K is the *turbulent kinetic energy*, with units $\mathrm{m}^2/\mathrm{s}^2$.

The new variable, μ_T, is called *turbulent viscosity* or *eddy viscosity*. It models the enhanced diffusion due to the small scales in the flow that are not solved. Depending on the particularities of the turbulence model, the relation among it and the other flow variables may vary. Furthermore, the turbulent kinetic energy is defined as:

$$K = \frac{1}{2}\langle|\mathbf{v}'|^2\rangle = -\frac{1}{2\rho}\operatorname{Tr}(\boldsymbol{\tau}^R),$$

where $\operatorname{Tr}(\boldsymbol{\tau}^R)$ denotes the trace of the Reynolds stress tensor.

USC UNIVERSIDADE DE SANTIAGO

The Boussinesq assumption (2.15) asserts that the Reynolds stress tensor is proportional to the *mean strain rate* tensor, $\mathbf{D}(\langle \mathbf{v} \rangle)$, with constant of proportionality μ_T. This essentially means that the turbulent viscosity is isotropic, as the proportionality constant is the same in all directions. Hence, turbulence models based on the Boussinesq assumption fail to accurately predict some details appearing in complex flows, such as those with sudden mean strain rate changes (Wilcox, 2006). An alternative to this approach are the so-called *Reynolds Stress equation Models* (RSM), also frequently called second-order closure or second-moment closure models. These models provide a more appropriate description of $\boldsymbol{\tau}^R$, accounting for subtle interactions in turbulent flows such as directional effects of the Reynolds stresses, at the cost of requiring the solution of additional transport equations to model the components of the Reynolds stress tensor. Therefore, there is a significant increase both in computational effort as well as in complexity, and several assumptions are required to close these models. A computationally cheaper approach are the so-called *mixing length models*, which attempt to predict the Reynolds stresses by means of algebraic expressions that directly provide the values of the eddy viscosity (see e.g. Versteeg & Malalasekera, 2007).

In summary, after applying the Reynolds averaging procedure and introducing the Boussinesq assumption, the RANS system (2.13)-(2.14) reads as follows.

Find $\langle \mathbf{v} \rangle(\mathbf{x}, t)$ and $\langle p \rangle(\mathbf{x}, t)$ such that:

$$\begin{aligned}
&\operatorname{div}(\langle \mathbf{v} \rangle) = 0, && \text{in } \Omega \times (0, t_{end}], \\
&\frac{\partial(\rho \langle \mathbf{v} \rangle)}{\partial t} + \operatorname{div}(\rho \langle \mathbf{v} \rangle \otimes \langle \mathbf{v} \rangle) = -\operatorname{grad}(\langle p \rangle) \\
&\qquad + \operatorname{div}\left((\mu + \mu_T) 2\mathbf{D}(\langle \mathbf{v} \rangle) - \frac{2}{3}\rho K \mathbf{I} \right) + \rho \mathbf{g}, && \text{in } \Omega \times (0, t_{end}].
\end{aligned}$$

It still remains to provide a suitable modelling approach for the turbulent kinetic energy and the eddy viscosity, which we address in the next section.

2.2.2. SST $K - \omega$ turbulence model

For the purpose of modelling μ_T and K, there is a wide range of different turbulence models, which are generally based in introducing new variables and transport equations. Here, we use Menter's SST $K - \omega$ (*Shear Stress Transport*) model, originally proposed in Menter (1994). Several modifications to the model were introduced in Menter et al. (2003), based on the experience on its practical application.

The SST $K - \omega$ turbulence model was conceived as a modification of Wilcox's $K - \omega$ model (Wilcox, 2006). To describe the eddy viscosity, in addition to the turbulent kinetic energy, the model introduces the specific dissipation rate, denoted as ω. It has dimensions $[\mathrm{s}^{-1}]$ and may be interpreted as the vorticity associated to the turbulent eddies of larger size. It is effectively a hybrid model, which transforms the $K - \omega$ turbulence model in a $K - \varepsilon$ model away from the walls. To this end, various blending functions are used, which are constructed to obtain a smooth transition between both models. They are typically functions of the wall distance, the turbulent variables and the fluid properties, and are adjusted to be one on the walls and converge to zero far away from them. This allows to maintain the good behaviour of the $K - \omega$ model near the wall while not having to suffer some of its major drawbacks. Namely, Wilcox's $K - \omega$ does not perform well under adverse pressure gradients and has been found to be sensitive to the free stream values of the turbulence variables (Versteeg & Malalasekera, 2007).

The SST model is regarded as robust and of general applicability in the CFD field, capable of solving with acceptable accuracy somewhat complex flows, including these situations where Wilcox's $K - \omega$ is less accurate. It has been used to obtain shear stress predictions in similar applications, showing better accuracy than other two-equation turbulence models when compared to experimental shear stress measurements of impinging jets (Barral et al., 2021). In some cases, it has been claimed that it is able to predict transition from laminar to turbulent boundary layer, although a reliable treatment of that phenomena requires more sophisticated turbulence models. In particular, as other two-equation

Table 2.1: Turbulence model constants. Source: Ansys, Inc. (2019).

a_1	$\sigma_{\omega 1}$	$\sigma_{\omega 2}$	σ_{K1}	σ_{K2}	β_1	β_2	β^*_∞	α_1	α_2	E	κ	C_μ
0.31	2.0	1.168	1.176	1.0	0.075	0.0828	0.09	5/9	0.44	9.793	0.41	0.09

RANS turbulence models, it fails to correctly represent the subtle interactions between turbulence production and stresses due to anisotropy. To this end, more complex models such as the RSM or LES techniques are required.

In the SST $K-\omega$ model, the turbulent viscosity is computed as:

$$\mu_T = \frac{\rho K}{\max\left(\omega, \dfrac{SF_2}{a_1}\right)}, \tag{2.16}$$

where the *mean strain rate magnitude*, S, is defined as $S = \sqrt{2\mathbf{D}(\langle\mathbf{v}\rangle) : \mathbf{D}(\langle\mathbf{v}\rangle)}$ and a_1 is a constant (see Table 2.1). Moreover, F_2 is the subsequent blending function:

$$F_2 = \tanh\left(\max\left(\frac{\sqrt{K}}{0.045\omega y_w}, \frac{500\mu}{\rho y_w^2 \omega}\right)^2\right).$$

In the previous expression, y_w is the distance to the nearest wall. An additional blending function, denoted as F_1, is used in the sequel. It is defined as

$$F_1 = \tanh\left(\min\left(\chi_1, \frac{4\rho K}{\sigma_{\omega 2} D^+_\omega y_w^2}\right)^4\right), \tag{2.17}$$

where

$$\chi_1 = \max\left(\frac{\sqrt{K}}{0.09\omega y_w}, \frac{500\mu}{\rho\omega y_w^2}\right), \qquad D^+_\omega = \max(D^*_\omega, 10^{-10}),$$

with $\sigma_{\omega 2}$ being the constant defined in Table 2.1 and D^*_ω defined as follows:

$$D^*_\omega = 2\rho\frac{1}{\sigma_{\omega 2}}\frac{\mathrm{grad}(K)\cdot\mathrm{grad}(\omega)}{\omega}. \tag{2.18}$$

The model uses the following transport equations to model the evolution of the turbulent kinetic energy and the specific dissipation rate, respectively:

$$\frac{\partial(\rho K)}{\partial t} + \mathrm{div}(\rho K\langle\mathbf{v}\rangle) = \mathrm{div}\left[\left(\mu + \frac{\mu_T}{\sigma_K}\right)\mathrm{grad}(K)\right] + G_K - Y_K, \tag{2.19}$$

$$\frac{\partial(\rho\omega)}{\partial t} + \mathrm{div}(\rho\omega\langle\mathbf{v}\rangle) = \mathrm{div}\left[\left(\mu + \frac{\mu_T}{\sigma_\omega}\right)\mathrm{grad}(\omega)\right] + G_\omega - Y_\omega + D_\omega, \tag{2.20}$$

where the turbulent Prandtl numbers σ_K and σ_ω are defined as

$$\sigma_K = \frac{1}{\dfrac{F_1}{\sigma_{K1}} + \dfrac{1-F_1}{\sigma_{K2}}}, \qquad \sigma_\omega = \frac{1}{\dfrac{F_1}{\sigma_{\omega 1}} + \dfrac{1-F_1}{\sigma_{\omega 2}}}. \tag{2.21}$$

In (2.21) σ_{K1}, σ_{K2} and $\sigma_{\omega 1}$ are model constants that have been calibrated with experimental measurements (see Table 2.1). The production terms of K and ω in (2.19)-(2.20), denoted respectively as G_K and G_ω, are

$$G_K = \min(\mu_T S^2, 10\rho\beta^*_\infty K\omega), \qquad G_\omega = \frac{\rho\alpha^*}{\mu_T}G_K,$$

UNIVERSIDADE DE SANTIAGO DE COMPOSTELA

where α^* is defined using the blending function F_1 as follows:

$$\alpha^* = \alpha_1 F_1 + \alpha_2(1 - F_1).$$

The limiter in the turbulent kinetic energy production term is introduced to avoid excessive build-up of turbulence in the stagnation regions (Versteeg & Malalasekera, 2007; Ansys, Inc., 2019). Additionally, in (2.19)-(2.20), the turbulence dissipation terms Y_K and Y_ω are defined as

$$Y_K = \rho\beta^*_\infty K\omega, \qquad Y_\omega = \rho\beta^*\omega^2,$$

with β^*_∞ being a constant and β^* obtained using the blending function (2.17):

$$\beta^* = F_1\beta_1 + (1 - F_1)\beta_2,$$

where β_1 and β_2 are constants taking the values collected in Table 2.1.

Lastly, the cross diffusion term, D_ω, appearing in (2.20), is such that

$$D_\omega = (1 - F_1)D^*_\omega,$$

where D^*_ω is defined in (2.18).

Remark 2.3. *In the following discussion, with the purpose of simplifying the notation, we omit the Reynolds averaging operator that distinguishes the mean velocity and pressure from the corresponding instantaneous fields, as there is no risk of confusion. Hence, in the sequel,* $\mathbf{v}$ *and* p *should be understood as the Reynolds average of pressure and velocity.*

2.2.3. Near wall turbulence

The presence of boundary layers due to the no-slip boundary conditions at the walls ($\mathbf{v} = \mathbf{0}$) leads to the modelling of turbulent flows requiring special attention. Close to the wall, the effects of the fluid's inertia and pressure gradient become increasingly small, and turbulence-generated flow fluctuations dissipate. A wide number of experimental measurements show that the streamwise velocity in turbulent flows near solid walls is proportional to the logarithm of the distance to the wall, both in internal and external flows (Wilcox, 2006). This relationship can be derived through dimensional analysis. In the sequel, we briefly introduce the main features of the behaviour of turbulent flows near walls, which is essential to provide suitable boundary conditions for the mathematical model.

Let $\mathscr{V}$ be the scale of the velocity of the free stream. Then, dimensional analysis considerations yield that:

$$v^+ = \frac{\mathscr{V}}{v_\tau} = f\left(\frac{\rho v_\tau y_w}{\mu}\right) = f(y^+), \tag{2.22}$$

where v^+ and y^+ are known as *dimensionless velocity* and *dimensionless wall distance*, respectively. The scale of the near wall velocity, v_τ, is known as *friction velocity*, and satisfies

$$v_\tau = \sqrt{\frac{\tau_w}{\rho}},$$

where τ_w is the shear stress on the wall. Expression (2.22) is known as the *law of the wall*. The analysis of this equation reveals that in turbulent flows near solid walls several sublayers with distinct properties are generated. In the outer layer, the flow is free from viscous effects due to the wall, whereas in the inner layer, which spreads over approximately a thickness equal to 10-20% of the boundary layer thickness, three different zones can be observed depending on the dimensionless wall distance (Tennekes & Lumley, 1972; Versteeg & Malalasekera, 2007):

- *Linear* or *viscous sublayer* ($y^+ < 5$): the viscous stresses dominate the flow. The dimensionless velocity satisfies that

$$v^+ = y^+. \tag{2.23}$$

USC UNIVERSIDADE DE SANTIAGO DE COMPOSTELA

- *Buffer layer* ($5 \leq y^+ \leq 30$): the viscous stress and the turbulent stress are of the same order.
- *Logarithmic layer* ($30 < y^+ < 200$): the Reynolds stresses dominate and the following *logarithmic wall law*, also called *log-law*, holds:

$$v^+ = \frac{1}{\kappa}\ln(E_w y^+). \tag{2.24}$$

This multilayer structure is a characteristic of turbulent flows near solid walls, and it has been observed both experimentally and numerically (with DNS studies) for a wide range of flows. In the logarithmic law (2.24), the von Kármán constant κ and the constant E_w have been calibrated through experiments. In particular, the values shown in Table 2.1 have been found satisfactory for smooth walls. The upper limit on the logarithmic layer thickness depends on the Reynolds number and it grows with increasing Reynolds number. In general applications, larger values of this bound, up to 500, lead to reasonably accurate predictions of the near-wall velocity profile.

For highly turbulent flows, it is not feasible to solve all the details of this structure since the boundary layer thickness decreases as the flow Reynolds number increases. Nonetheless, it is possible to use (2.24) to impose a boundary condition for the velocity field at the wall. Thus, it is not necessary to solve all the details of the boundary layer, greatly reducing the computational cost. To assure this is done correctly, it is necessary to guarantee that every cell in the mesh where the boundary condition is imposed has its centroid at an adequate distance to the wall, this is, with y^+ values above 30. In flows with moderate to low Reynolds numbers, it is computationally realisable to resolve the boundary layer up to the viscous sublayer, where the linear relation (2.23) can be applied as a boundary condition. Using the latter approach has the main advantage of solving the flow with a higher degree of accuracy, at the cost of increasing the computational effort, as it requires much finer mesh sizes near the wall. Although it often suffices to have $y^+ < 5$, it is generally desirable to have values satisfying that $y^+ \sim 1$ to improve accuracy.

When a turbulence model is integrated towards the viscous sublayer it is often called a *Low-Reynolds Number* (LRN) model. This is the case of the $K-\omega$ family of RANS models, which contrast with the $K-\varepsilon$ models, whose integration towards the wall require of additional modifications and in their standard form can only be used with the log-law approach. Conversely, if (2.24) is used to impose the no-slip condition on the wall, a turbulence model is labelled as a *High-Reynolds Number* (HRN) model (Bredberg, 2000). Hence, the SST $K-\omega$ can be either used as an HRN or a LRN model, depending on the particularities of the flow and grid size requirements.

So far, we have briefly described the classical method for the wall law. Notice that, to impose the velocity profile corresponding to the log-law (2.24), an iterative procedure is required, as both the friction velocity, v_τ, and the dimensionless wall distance, y^+, are unknown. Launder & Spalding (1974) proposed a modification which performs better in recirculating flows with boundary layer separation and reattachment (Bredberg, 2000). The methodology chooses a slightly different wall dimensionless distance, denoted as y^*:

$$y^* = \frac{\rho C_\mu^{1/4} K^{1/2} y}{\mu},$$

where C_μ is a constant (see Table 2.1).

This approach is the most widely used in general applications and industrial flows nowadays. It is the formulation used in the software package *Ansys Fluent* that is used in subsequent sections to solve the flow in the BF trough (Ansys, Inc., 2019).

In the particular case of the SST $K-\omega$ model, as it can be used both as a LRN and HRN turbulence model, it is possible to switch between the log-law (2.24) and the viscous layer (2.23) in function of the y^+ or y^* values and supply suitable conditions for K and ω accordingly. In practice, this can lead to stability issues. Thus, formulations of the near wall treatment for $K-\omega$ models have been developed that automatically and gradually switch between the wall functions and the linear profile in the viscous sublayer, depending on the wall distance. More specifically, Menter & Esch (2001)

propose the following blending for the friction velocity:

$$v_\tau = \left(\left(\frac{\mathcal{V}}{y^+} \right)^4 + \left(\frac{\mathcal{V}}{\frac{1}{\kappa} \ln(Ey^+)} \right)^4 \right)^{1/4}.$$

Similarly, using that the solutions for the specific dissipation rate, ω, are known both in the viscous sublayer and in the logarithmic region, the following blending for its boundary condition is devised:

$$\omega = \sqrt{\left(\frac{6\mu}{\rho \beta_1 (y^+)^2} \right)^2 + \left(\frac{v_\tau}{C_\mu^{1/2} \kappa y^+} \right)^2}.$$

These expressions are used to impose the velocity and ω boundary conditions on the wall. Lastly, the boundary condition for the turbulent kinetic energy is simply $\frac{\partial K}{\partial \mathbf{n}} = 0$. Thus, the strict requirements on the grid resolution of the LRN turbulence model approach can be relaxed while keeping the error within reasonable bounds. This is of interest in most applications involving complex flows in complicated geometries, where in practice is difficult to either guarantee that all grid centroids are located within either the logarithmic layer or the viscous sublayer.

2.3. Volume of fluid

The conservation equations and the turbulence model described above are suitable to model the behaviour of each of the fluid phases separately. Nonetheless, it is necessary to take into account that the flow in the BF trough has three immiscible fluid phases –air, slag and hot metal– which are separated by density stratification and, therefore, by well-defined interfaces. In this section, we briefly describe the technique that is used to deal with the multiphase flow in the trough, the *Volume of Fluid method* (VOF). For the description of the methodology, we loosely follow Quarteroni (2009) and summarise the main concepts regarding its implementation. A detailed overview of the VOF method can be found in Tryggvason et al. (2011).

The Navier-Stokes equations (2.8)-(2.9) can describe a free surface flow without any further modifications. In such case, the free surfaces are understood as interfaces separating the fluid phases, cutting a fixed domain Ω in open subdomains, one for each different phase. We decompose it as the union of the subdomains that each of the involved phases occupies at a given time $t \in (0, t_{end}]$:

$$\Omega(t) = \Omega_A(t) \cup \Omega_{slag}(t) \cup \Omega_{hm}(t) \cup \Sigma(t),$$

where $\Sigma(t)$ is the set of interfaces separating the phases at time t. We assume that $\Sigma(0) = \Sigma_0$ is known. Moreover, $\Omega_A(t)$, $\Omega_{slag}(t)$ and $\Omega_{hm}(t)$ are the subdomains occupied by air, slag and hot metal at time t, respectively.

On each subdomain, we consider a constant density and viscosity, equal to that of the corresponding fluid (see Table 1.1b). Therefore, these properties are defined as piecewise constant functions. For example, the viscosity reads as follows:

$$\mu(\mathbf{x}, t) = \begin{cases} \mu_A, & \text{in } \Omega_A(t), \\ \mu_{slag}, & \text{in } \Omega_{slag}(t), \\ \mu_{hm}, & \text{in } \Omega_{hm}(t), \end{cases} \tag{2.25}$$

where μ_A, μ_{slag} and μ_{hm} denote the viscosity of air, slag and hot metal. The density, $\rho(\mathbf{x}, t)$, is defined analogously.

Since the properties of the fluid are represented by discontinuous functions such as (2.25), the system (2.8)-(2.9) only holds strongly in the open subdomains corresponding to each phase. Therefore, the equations have to be coupled with interface conditions on $\Sigma(t)$, also called *jump conditions*. These

conditions are constraints that the velocity and pressure need to satisfy at the interface, which enable the coupling between the different phases.

Let $[\cdot]_\Sigma$ denote the jump of a field across the interface $\Sigma(t)$, defined as follows for an arbitrary flow variable ϕ (see Quarteroni, 2009):

$$[\phi]_\Sigma(\mathbf{x},t) = \lim_{\epsilon\to 0^+} \big(\phi(\mathbf{x}+\epsilon\mathbf{n}_\Sigma,t) - \phi(\mathbf{x}-\epsilon\mathbf{n}_\Sigma,t)\big), \tag{2.26}$$

where $\mathbf{n}_\Sigma$ is the unit normal vector at the interface. A consistent orientation for the normal vector is required for each of the interfaces in $\Sigma(t)$. For example, in the slag-hot metal interface, we may assume that $\mathbf{n}_\Sigma$ always points from slag to hot metal. Then, the interface conditions are the following:

$$[\mathbf{v}]_\Sigma = \mathbf{0}, \tag{2.27}$$

$$[\mathbf{T}\mathbf{n}_\Sigma]_\Sigma = [2\mu\mathbf{D}(\mathbf{v})\mathbf{n}_\Sigma - p\mathbf{n}_\Sigma]_\Sigma = \sigma_\Sigma\kappa_\Sigma\mathbf{n}_\Sigma. \tag{2.28}$$

The jump condition (2.27), also called *kinematic interface condition*, expresses that the velocity is continuous at the interface. We remark that it is derived assuming that there is no mass transfer across Σ. In addition, in (2.28), often known as *dynamic interface condition*, κ_Σ is the interface curvature and σ_Σ is the surface or interfacial tension coefficient. Note that the constitutive assumption (2.7) on the stress tensor has been applied. For a formal derivation of (2.27) and (2.28), we refer to Panton (2013).

Remark 2.4. *The importance of surface tension effects can be determined by computing several dimensionless numbers to assess whether the surface tension forces are overcome by other effects in the flow (Tryggvason et al., 2011). Since the flow in the trough is turbulent, especially in the hot metal phase, the value of the Weber number can be analysed, which measures ratio among the inertia and surface tension forces, and is defined as:*

$$We = \frac{\rho\mathscr{L}\mathscr{V}^2}{\sigma_\Sigma},$$

where $\mathscr{L}$ is the characteristic length and $\mathscr{V}$ the characteristic velocity.

Considering a typical value of $\sigma_\Sigma = 1.25\ N/m$ for the interfacial tension between hot metal and air, since $\rho_{hm} = 7015\ kg/m^3$ (see Table 1.1b), it is clear that the surface tension is much less relevant than the inertia forces, both if the length scale and velocity are selected at the taphole or for the characteristic velocity and length scale in the middle of the trough. Hence, in all the results that are presented in this chapter, surface tension is neglected. Nonetheless, it should be noted that in the jet impingement area, the flow structures are intricate and significant bubble entrainment occurs. In the length scale of these bubbles, surface tension effects are indeed relevant, but a detailed resolution of these features of the flow requires much finer meshes and, arguably, the use of more complex turbulence models.

Therefore, if the Navier-Stokes equations are supplied with appropriate boundary conditions, an initial condition and the jump conditions (2.27)-(2.28), the multiphase flow in the trough can be described. However, the presented formulation with discontinuous fields is not appealing for its numerical simulation. Various numerical methodologies to circumvent this issue and yield computational predictions of multiphase flows have been proposed. In the overview provided in Quarteroni (2009), a distinction between techniques that provide *explicit* and *implicit* interface descriptions is made. The former generally use marker points or surfaces that are advected with the fluid velocity to follow the interface positions, whereas the latter use scalar functions to assess whether a point belongs to a phase on a fixed mesh. They are also called *front-tracking* and *front-capturing* methods, respectively.

In particular, the VOF method, which was proposed originally in Hirt & Nichols (1981), is a front-capturing method widely used to solve fluid mechanics problems with several fluid phases. Hence, the interfaces between the immiscible phases are not tracked explicitly by moving the mesh or markers. Instead, the position of the interfaces is described implicitly with suitable scalar functions, assuming a single fluid domain with a fixed boundary. It has been used in various studies featuring the multiphase and turbulent flow in the BF trough (e.g. Rezende et al., 2007; Monteiro de Oliveira et al., 2020; Barral et al., 2021).

Let $\xi_{slag}(\mathbf{x}, t)$ be the following characteristic function associated to the slag phase:

$$\xi_{slag}(\mathbf{x}, t) = \begin{cases} 1, & \mathbf{x} \in \Omega_{slag}(t), \\ 0, & \mathbf{x} \notin \Omega_{slag}(t), \end{cases}$$

and set ξ_{hm} and ξ_A defined analogously. Consequently, the discontinuity points of these functions indicate the position of the interface $\Sigma(t)$ at each time instant t.

To account for the motion of the interface, the evolution of each of these functions needs to be tracked as time advances. Although the shape of the region occupied by each fluid phase may change, each fluid particle belongs to the same phase. Therefore, the material derivative of any of these characteristic functions is zero, which yields an advection equation for each ξ (Tryggvason et al., 2011, p. 76). Numerically, instead of working with these discontinuous functions, the usual procedure is to approximate them by the so-called *colour function* or *volume fraction*, denoted as α_{slag} for the slag phase and α_{hm} as well as α_A for hot metal and air, respectively. The volume fractions are the discrete versions of the characteristic functions. For instance, considering the slag phase, in a cell-centred finite volume discretisation scheme, the corresponding volume fraction is defined as the average of ξ_{slag} in each computational cell of the mesh, i.e., if N_{cell} denotes the number of cells in the mesh, then, for $1 \leq i \leq N_{cell}$, we set that

$$\alpha^i_{slag}(t) = \frac{1}{\mathrm{Vol}(C_i)} \int_{C_i} \xi_{slag}(\mathbf{x}, t)\, dV,$$

where C_i is the ith cell in the computational grid of the domain and $\mathrm{Vol}(C_i)$ denotes the volume of such cell.

Thus, a value of $\alpha^i_{slag}(t) = 1$ represents that slag fills the cell volume. Values of the volume fraction different from 0 and 1 describe the fraction of the cell volume that is occupied by the slag. In such case, a mixture of fluid phases is assumed to fill the cell, indicating the transition region where the interfaces are located.

In the engineering literature, when using the VOF method, it is customary to write the model equations in terms of the volume fractions also in the continuous setting, although they are actually obtained from the characteristic functions after the discretisation is performed, as described above. We also commit this slight abuse of notation and, from the advection equation for the characteristic function, ξ_{slag}, we write that

$$\frac{\partial \alpha_{slag}}{\partial t} + \mathrm{div}(\alpha_{slag}\mathbf{v}) = 0. \tag{2.29}$$

The VOF method only solves one set of conservation equations for all the fluid phases. It considers mixture properties weighted appropriately using the corresponding volume fractions. For an arbitrary scalar property field ϕ it is considered that

$$\widehat{\phi} = \alpha_{slag}\phi_{slag} + \alpha_{hm}\phi_{hm} + (1 - \alpha_{slag} - \alpha_{hm})\phi_A, \tag{2.30}$$

where we recall that ϕ_{slag}, ϕ_{hm} and ϕ_A denote the constant property values corresponding to slag, hot metal and air, respectively. Notice from (2.30) that the volume fraction of air can be directly obtained from the values of the volume fractions of slag and hot metal. Therefore, for the three-phase flow in the BF trough, the VOF method adds two new unknowns, α_{slag} and α_{hm}, with the corresponding two advection equations.

The main difficulty with volume of fluid techniques, as well as with other methodologies to computationally solve multiphase flows, is to advect the marker function without inducing significant numerical diffusion and maintaining a sharp interface. As the fluids are assumed to be immiscible, this behaviour is highly undesired, as it leads to mixing effects spreading across the whole domain instead of being concentrated near the actual position of the interface, which becomes increasingly diffuse. Complex techniques have been developed for the reconstruction of interface normal vectors and curvature to attempt to keep the interface sharp as it is advected using the VOF method.

The VOF method proceeds in two steps: first, the interface is reconstructed using the local values of the volume fraction. For this purpose, several techniques are available, such as the *piecewise linear*

interface construction (PLIC), which essentially reconstructs the interface as a planar surface inside each cell. To this end, the gradient of the volume fraction in the own cell and in the neighbouring ones is used to approximate the normal vector to the interface. Once the interface is reconstructed, it is advected by considering a given velocity field. For more details on the procedure, we refer to Tryggvason et al. (2011).

2.4. Mathematical model

This section is dedicated to the introduction of the mathematical model, as well as some aspects related to the numerical methodology employed to obtain an approximation of its solution. The methodologies and conservation equations presented in the previous sections are posed in a computational domain selected as a portion of the empty space within the BF trough, discussed in Section 2.4.1. The equations of the model are summarised in Section 2.4.2, and the corresponding boundary and initial conditions are introduced in Sections 2.4.3 and 2.4.4, respectively. In Section 2.4.5, we briefly describe some issues concerning the generation of the computational grid. Moreover, in Section 2.4.6, the numerical schemes used for the solution of the mathematical model are stated. Lastly, in Section 2.4.7, we introduce the different conditions that we consider for the studies that are discussed in the next section.

2.4.1. Computational domain

The computational domain is constructed using the measurements provided in the drawings of one of the casthouses operated by ArcelorMittal Spain, as discussed in Section 1.5 (see also Figure 1.4). Note that the dimensions are those of the refractory linings at the time of commissioning a brand new trough and, therefore, the refractory lining is assumed to be in perfect condition for the study. Nonetheless, it is noteworthy that as the BF runner campaign cycle advances, the castable refractory suffers heavy degradation and the boundary delimiting the castable surface lining can be subject to large variations.

Provided that the scope of this chapter is to address the hydrodynamics of the fluid phases in the trough, only the empty space directly within the trough is included in the computational domain Ω, as depicted in Figure 2.1a. Note that the depicted lateral and bottom boundaries of the domain coincide with the surface of the refractories, whereas the top boundary is a fictitious boundary, as any of the fluid phases may freely flow through it. In Figure 2.1c, the relative position of the computational domain with respect to the actual BF trough is shown, omitting the refractory cover for clarity.

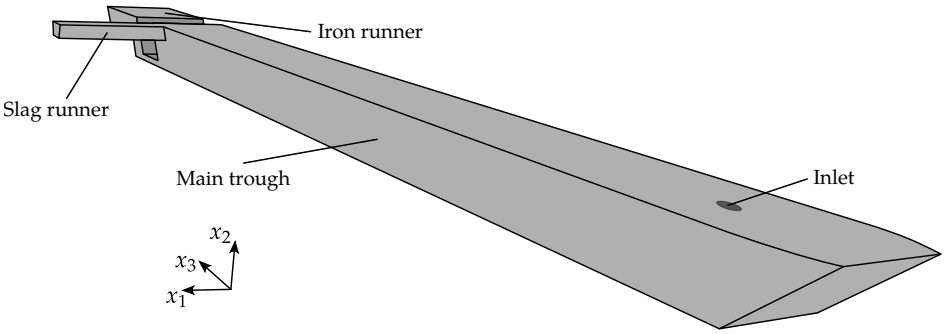
We consider that the taphole has a radius of $R_{tap} = 0.031$ m and that it has an inclination angle $\gamma_{tap} = 10°$. It has been observed numerically and experimentally that the hot metal and slag jet closely follows a parabolic profile, as it flows out at a high velocity value (see e.g. Stevenson & He, 2005). According to the slag and hot metal production data supplied by the company, the velocity at the taphole opening is estimated to be around 6.29 m/s. We set the coordinate axes and the origin, **O**, as in Figure 2.1, and let $\mathbf{x}(t) = (x_1, x_2, x_3)(t)$ denote the trajectory of the jet as a function of the time parameter, t. Hence, the known initial position of the jet, corresponding to the position of the taphole centre, is denoted as:

$$\mathbf{x}(0) = \mathbf{x}^0 = (x_1^0, x_2^0, x_3^0).$$

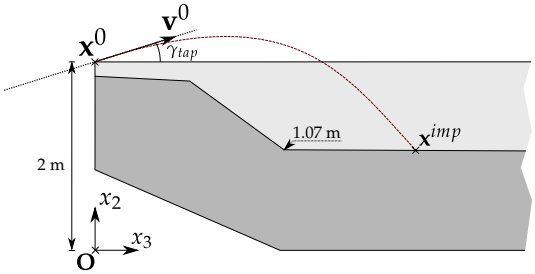
Specifically, for the selected origin of coordinates, it holds that $\mathbf{x}^0 = (1.5, 2, 0)$ m. In addition, the initial velocity is $\mathbf{v}(0) = \mathbf{v}^0 = (v_1^0, v_2^0, v_3^0)$, with $\mathbf{v}^0 = \mathbf{x}'(0)$. A schematic diagram of the jet trajectory is depicted in Figure 2.1b. Neglecting drag forces, the trajectory of the jet exiting the taphole is only affected by gravity. Thus, it is obtained that

$$\begin{aligned} x_1(t) &= x_1^0, \\ x_2(t) &= -9.81\frac{t^2}{2} + v_2^0 t + x_2^0, \\ x_3(t) &= v_3^0 t + x_3^0. \end{aligned}$$

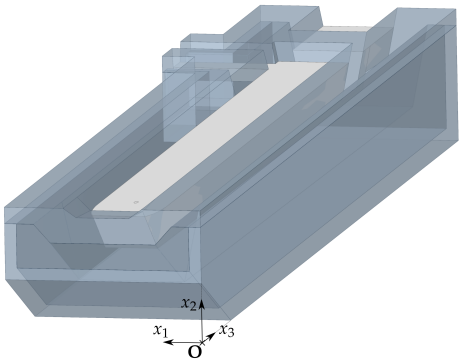
USC UNIVERSIDADE DE SANTIAGO DE COMPOSTELA



(**a**) Computational domain.



(**b**) Schematic of the jet trajectory.



(**c**) Ω (white) and solid refractories (blue, with transparency).

Figure 2.1: Computational domain (Ω), jet trajectory schematic and position of the domain with respect the solid refractory linings.

Using the substitution $t = (x_3 - x_3^0)/v_3^0$, the height of the jet (x_2 coordinate) can be described as a function of the distance to the BF, x_3. The corresponding function is denoted as h_{jet}, which satisfies:

$$h_{jet}(x_3) = -\frac{9.81}{2}\left(\frac{x_3 - x_3^0}{v_3^0}\right)^2 + v_2^0\left(\frac{x_3 - x_3^0}{v_3^0}\right) + x_2^0. \tag{2.31}$$

Recall from Chapter 1 that the trough has an inclination of approximately 0.5%. Specifically, with this choice of coordinate origin, the height of the bottom of the trench through where the hot fluids circulate can be parametrised as a function of the x_3 coordinate as follows

$$h_B(x_3) = 1.07 - (x_3 - 2)\frac{70}{14350}, \tag{2.32}$$

for $x_3 \in [2, 16.35]$ m.

Noting that $\gamma_{tap} = 10^\circ$ and that the initial velocity modulus is $|\mathbf{v}^0| = 6.29$ m/s, we find that $\mathbf{v}^0 = (0, 1.0922, 6.1944)$ m/s. Then, using that $\mathbf{x}^0 = (1.5, 2, 0)$ m, the solution of $h_{jet}(x_3) = h_B(x_3)$ allows to find the theoretical longitudinal coordinate at which the free jet impacts the bottom surface, denoted as x_3^{imp}. In particular, we find that $x_3^{imp} = 3.48$ m. We remark that while the zero drag assumption with air may be reasonable, once the jet reaches the pool of fluids held in the trough, significant drag occurs with the layers of slag and hot metal at rest.

In preliminary studies with 3D jets, we found a similar result to that presented in Barral et al. (2021) for a planar hot metal jet, i.e., that the jet impingement point predicted by the parabolic profile is very similar to the simulated point if the entire jet trajectory is numerically simulated. Therefore, to reduce

the computational cost and to facilitate the mesh generation procedure (see Section 2.4.5), and since it is of little interest for our aims, we do not solve the complete jet starting from the taphole until it reaches the pool of fluids in the BF trough. Instead, we impose an inlet condition at the maximum height of the computational domain using the trajectory (2.31) to find a suitable ingress point and velocity. This approach is similar to that used in the numerical studies by Ge et al. (2020); H. Yao et al. (2021).

2.4.2. Model equations

In this section, we briefly state the equations that are solved in this chapter. As discussed previously, we consider the Reynolds-averaged Navier-Stokes equations coupled with transport equations for the volume fractions of slag and hot metal. To compute the Reynolds stress tensor, the two-equation RANS turbulence model SST $K-\omega$ is used, yielding the subsequent system.

Find $\mathbf{v}$, p, α_{slag}, α_{hm}, K and ω such that:

$$
\begin{aligned}
&\operatorname{div}(\mathbf{v}) = 0, && \text{in } \Omega \times (0, t_{end}],\\
&\frac{\partial \alpha_{slag}}{\partial t} + \operatorname{div}(\alpha_{slag}\mathbf{v}) = 0, && \text{in } \Omega \times (0, t_{end}],\\
&\frac{\partial \alpha_{hm}}{\partial t} + \operatorname{div}(\alpha_{hm}\mathbf{v}) = 0, && \text{in } \Omega \times (0, t_{end}],\\
&\frac{\partial (\widehat{\rho}\mathbf{v})}{\partial t} + \operatorname{div}(\widehat{\rho}\mathbf{v}\otimes\mathbf{v}) = -\operatorname{grad}(p) + \operatorname{div}\left((\widehat{\mu}+\widehat{\mu}_T)2\mathbf{D}(\mathbf{v}) - \frac{2}{3}\widehat{\rho}K\mathbf{I}\right) + \widehat{\rho}\mathbf{g}, && \text{in } \Omega \times (0, t_{end}],\\
&\frac{\partial (\widehat{\rho}K)}{\partial t} + \operatorname{div}(\widehat{\rho}K\mathbf{v}) = \operatorname{div}\left[\left(\widehat{\mu} + \frac{\widehat{\mu}_T}{\sigma_K}\right)\operatorname{grad}(K)\right] + G_K - Y_K, && \text{in } \Omega \times (0, t_{end}],\\
&\frac{\partial (\widehat{\rho}\omega)}{\partial t} + \operatorname{div}(\widehat{\rho}\omega\mathbf{v}) = \operatorname{div}\left[\left(\widehat{\mu} + \frac{\widehat{\mu}_T}{\sigma_\omega}\right)\operatorname{grad}(\omega)\right] + G_\omega - Y_\omega + D_\omega, && \text{in } \Omega \times (0, t_{end}].
\end{aligned}
$$

The various source terms appearing in the K and ω equations have been described in Section 2.2.2. Moreover, the eddy viscosity, $\widehat{\mu}_T$, is computed as:

$$\widehat{\mu}_T = \frac{\widehat{\rho}K}{\max\left(\omega, \dfrac{SF_2}{a_1}\right)}. \tag{2.33}$$

Recall that $\widehat{\mu}$ and $\widehat{\rho}$ denote mixture properties, computed as functions of the volume fractions as follows:

$$
\begin{aligned}
\widehat{\rho} &= \alpha_{slag}\rho_{slag} + \alpha_{hm}\rho_{hm} + (1-\alpha_{slag}-\alpha_{hm})\rho_A,\\
\widehat{\mu} &= \alpha_{slag}\mu_{slag} + \alpha_{hm}\mu_{hm} + (1-\alpha_{slag}-\alpha_{hm})\mu_A.
\end{aligned}
$$

In addition, we remind that $\mathbf{v}$ and p should be understood as the mean velocity and pressure, as noted in Remark 2.3.

2.4.3. Boundary conditions

The boundary of the computational domain is decomposed as shown in Figure 2.2. We set the subsequent boundary conditions:

- On Γ_{wall}, which corresponds to the refractory lining surface, the standard no-slip condition is imposed, i.e., $\mathbf{v} = \mathbf{0}$. Since the SST $K-\omega$ turbulence model is used, this condition is set by blending the linear law valid on the viscous sublayer with the logarithmic wall law as a function of the dimensionless wall distance. A blending function is also used to set a Dirichlet condition on ω, and the normal gradient of K is considered null (see Section 2.2.3).

USA UNIVERSIDAD DE SANTIAGO DE COMPOSTELA

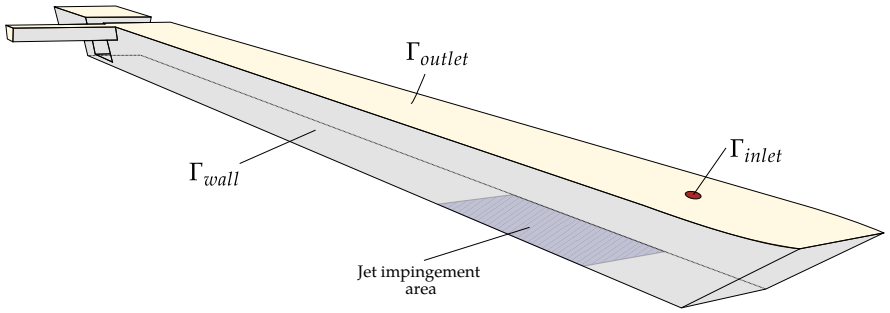


Figure 2.2: Boundaries of the computational domain Ω.

- On Γ_{inlet}, the fluid velocity corresponding to the intersection of the jet with the fictitious boundary at the top of Ω is set. To this end, we note that this boundary corresponds with the intersection between $\overline{\Omega}$ and the plane $x_3 = 1.7$ m. Then, the procedure detailed in Section 2.4.1 leads to the subsequent inlet velocity:

$$\mathbf{v}_{inlet} = (0, -2.66, 6.19) \text{ m/s}.$$

  Moreover, the values of the turbulence model variables, K and ω, are also required. Since the diameter of the taphole is such that $D_{tap} \approx 0.06$ m, we find that the Reynolds number associated to this characteristic length, a characteristic velocity $\mathcal{V} = 6.29$ m/s and the physical properties of hot metal is $Re_{D_{tap}} \approx 3.7 \cdot 10^5$. Following the procedure detailed in Ansys, Inc. (2019), based on the taphole length scale, the *mixing length*, l_{mix}, and the *turbulent intensity*, I_T, are estimated using the following expressions:

$$I_T = 0.16 Re_{D_{tap}}^{-1/8} = 0.032, \qquad l_{mix} = \frac{0.07 D_{tap}}{C_\mu^{3/4}} = 0.026 \text{ m},$$

  being C_μ the constant defined in Table 2.1. We note that the turbulent intensity is defined as the ratio among the magnitudes of the turbulent fluctuations and the mean velocity, i.e., $I_T = |\mathbf{v}'|/|\langle \mathbf{v} \rangle|$.

  Hence, the inlet values of K and ω are estimated using the following relationships:

$$K = \frac{3}{2}(\mathcal{V} I_T)^2 = 0.061 \text{ m}^2/\text{s}^2, \qquad \omega = \frac{K^{1/2}}{C_\mu l_{mix}} = 105.35 \text{ s}^{-1}.$$

  Lastly, adequate α_{slag} and α_{hm} values are set assuming that the hot metal and slag jet reaches the computational domain without spreading. The values are adjusted depending on the analysed case to match different mass flow rates through the taphole (see Section 2.4.7). When slag and hot metal are tapped simultaneously, it is assumed that the flow in the taphole is stratified (see the remark below).

- On Γ_{outlet}, which corresponds to the fictitious boundaries of the computational domain, we specify the so-called *pressure-outlet* boundary condition, imposing a pressure value equal to $p = 0$. The velocity field required to achieve mass conservation given this pressure value is computed. Notice that to achieve this, backflow can occur, i.e., fluid can enter the computational domain through this boundary. In such case, we assume that $\alpha_A = 1$, $K = 0.0001$ m^2/s^2 and $\omega = 0.1$ s^{-1}. Otherwise, if no backflow is required on the corresponding computational cell boundary, the normal gradients of K, ω and $\mathbf{v}$ are assumed to be zero.

Remark 2.5. *The refractory lining profile within the taphole is uneven and substantial roughness due to the severe erosion and the drilling practice may occur. Hence, the exiting stream is highly turbulent, sometimes with entrained gas and non-stratified flow in the taphole, showing significant spreading before reaching the liquid*

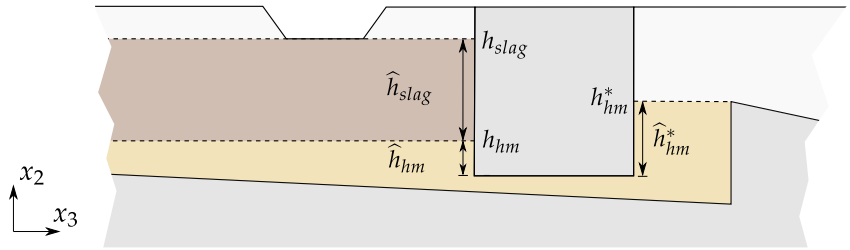


Figure 2.3: Schematic diagram of the height values used in the α_{hm} and α_{slag} initial condition computation.

pool. As discussed in Section 1.2, the precise conditions of the flow in the taphole are not fully understood, but while some degree of dispersed flow may be expected, especially if gas entrainment occurs, the stratified flow pattern that it is implicitly assumed in this chapter, with slag sitting on top of the hot metal, seems a reasonable assumption (see e.g. Shao & Saxén, 2013a).

In any case, it should be noted that the assumptions that the jet enters the computational domain as a cohesive, density-stratified stream when the flow is a combination of slag and hot metal may not be very realistic. An accurate characterisation of the jet flow would require to emulate the taphole conditions and the flow within the BF, as well as the use of more detailed turbulence models, which are out of scope for our aims in this study due to the high computational costs and modelling uncertainties. If the 3D jet is simulated as exiting the taphole with a RANS model, the shearing with the surrounding air is not enough to induce significant spreading until the impact point is reached (see Barral et al., 2021), and the jet closely follows the parabolic profile determined by (2.31), as mentioned previously.

Remark 2.6. *The estimations for the turbulent intensity and mixing length for the inlet condition, obtained above from various correlations, assume fully developed flow within the taphole. This is a quite idealised condition, especially if the flow in the taphole is a combination of slag and hot metal. In any case, one of the advantages of the SST $K-\omega$ is that it is not very sensitive to the specified values of free stream turbulent variables, which in practical problems tend to be somewhat arbitrary (Versteeg & Malalasekera, 2007).*

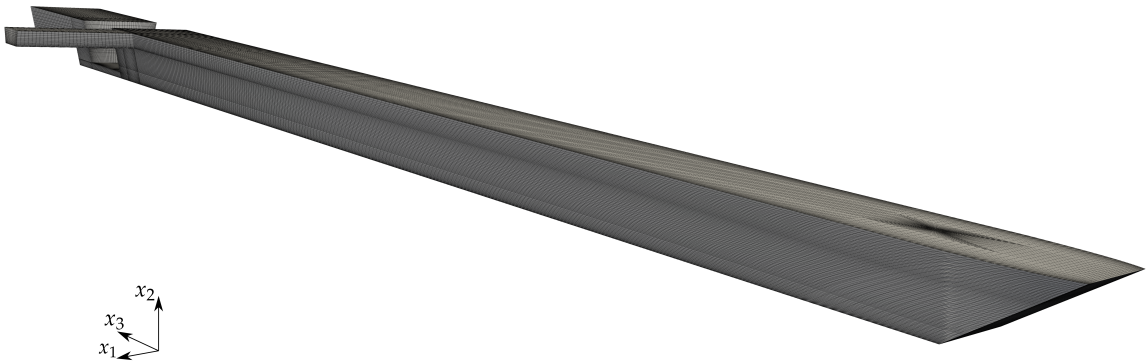
2.4.4. Initial conditions

Recall from Chapter 1 that the trough is only drained when major reparations are required or at the end of its useful life, after two months of campaign, approximately. Thus, at the beginning of each BF tapping, there is a pool of fluids in the trough, which mitigates the impact of the jet on the refractory and also helps slag and hot metal separation. For the initial condition, we assume that the trough is filled with this pool of fluids and, therefore, we set α_{hm} and α_{slag} with non-zero values at $t = 0$ s.

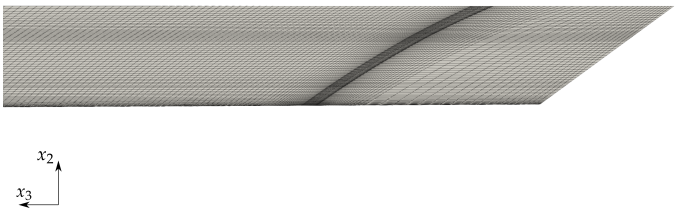
To do so, the positions of the interfaces need to be computed at $t = 0$ s. With this purpose, we follow the approach described in Luomala et al. (2001), which was also used in L. Wang et al. (2017). The trough is assumed to be completely filled with fluids from a previous tapping. Hence, the slag level in the trough should reach the level of the slag runner and the hot metal level after the skimmer should be approximately at the height of the iron dam. These height values are denoted as h_{slag} and h_{hm}, respectively. However, the height of the interface separating slag and hot metal upstream of the skimmer, h_{hm}, is unknown. If equilibrium conditions hold, assuming that the slag and hot metal remain at the constant densities collected in Table 1.1b, the pressure due to the column of slag and hot metal upstream of the skimmer should be equal to that resulting from the column of hot metal downstream (see Figure 2.3). Thus, it holds that:

$$\widehat{h}_{hm}\rho_{hm} + \widehat{h}_{slag}\rho_{slag} = \widehat{h}^*_{hm}\rho_{hm}, \tag{2.34}$$

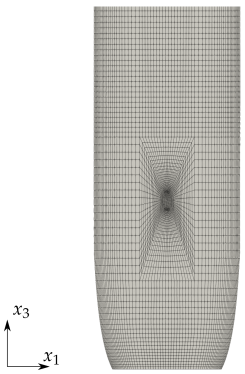
where $\widehat{h}_{slag}$ is the depth of the slag in the trough, $\widehat{h}_{hm}$ denotes the height difference between the slag-hot metal interface and the bottom part of the skimmer, and $\widehat{h}^*_{hm}$ is the height difference between the iron dam and the bottom of the skimmer.



(**a**) Complete view.



(**b**) Lateral view.



(**c**) View from above.

Figure 2.4: Mesh 4.

For our particular configuration of the trough $\widehat{h}^*_{hm} = 0.2$ m and $h_{slag} = 1.5$ m (see the drawings depicted in Figure 1.4). In addition, $\widehat{h}_{hm} + \widehat{h}_{slag} = h_{slag} - h_{skimmer} = 0.4$ m where h_{slag} is the height of the slag trough, as discussed above, and $h_{skimmer}$ is the height of the bottom of the skimmer. Then, from (2.34) it follows that

$$\widehat{h}_{hm} = \frac{\widehat{h}^*_{hm}\rho_{hm} - 0.4\rho_{slag}}{\rho_{hm} - \rho_{slag}} \approx 8.22 \cdot 10^{-2} \text{ m}.$$

Hence, since $h_{skimmer} = 1.1$ m, we find that the free surface separating air and slag is at a height $h_{hm} = 1.182$ m. Using these heights, the values of α_{slag} and α_{hm} are set.

Below, we summarise the remaining initial conditions. Since the fluids are assumed at rest initially, the mean velocity is $\mathbf{v} = \mathbf{0}$ m/s. In addition, the turbulent kinetic energy is $K = 0$ m^2/s^2 and for the specific dissipation rate we consider a standard value of $\omega = 1$ s^{-1}.

2.4.5. Mesh of the domain

A full hexahedral mesh of the computational domain is constructed, which allows to reduce the global number of cells in the domain while improving the general accuracy of the computation. Hexahedral cells lead to a more accurate interface reconstruction with the PLIC algorithm, especially in this specific application, since it is known beforehand that the free surfaces in most of the computational domain will have a normal vector whose direction is approximately that of $\mathbf{e}_2$, similar to the planes specified as initial condition (see Figure 2.3).

Notice that the above-mentioned consideration does not apply to the jet itself and the region where it impinges the liquid pool, since the kinetic energy of the impact leads to significant air and slag entrainment and mixing with hot metal. Therefore, the interfaces become curved and the flow is partially buoyancy-driven due to the rising entrained air bubbles, as it has been observed experimentally with scale models (see e.g. Begnis & Brandaleze, 2006; Monteiro de Oliveira et al., 2020). Hence, the grid is refined in those areas, where the most complicated structures of the flow are generated. We note that the grid generation is not straightforward. Provided that the approximate trajectory of the jet is known (see Section 2.4.1), the mesh is constructed by sweeping a circle along the analytical expression for the trajectory (2.31), starting from the taphole position. Then, the remainder of the mesh is constructed by matching the faces of the hexahedra following the jet trajectory with those in the rest of the trough, as shown in Figure 2.4 for the most refined of the constructed meshes, labelled Mesh 4. Notice that the mesh is finer near the bottom of the trough and at the expected positions of the slag-air and slag-hot metal interfaces downstream of the jet impingement zone.

Since the aim is to study the global characteristics of the flow and simulate a sufficient time to obtain an approximation of the mean flow features in the BF trough, it is not feasible to construct a mesh that fully integrates the viscous layer, achieving everywhere $y^+ \sim 1$, and totally avoid the usage of wall functions in the model (see Section 2.2.3). Mainly, the difficulty lies around the jet impact zone position, where the hot metal and slag impinges the solid refractory. The fluid velocity there is around 7 m/s; for this velocity and considering the properties of hot metal (see Table 1.1b), standard estimations of the friction velocity v_τ (see Versteeg & Malalasekera, 2007) yield that the first cell centroid of the mesh should be located at a distance from the wall around $5 \cdot 10^{-6}$ m. Thus, to comply with the CFL condition (see Section 2.4.6), tiny steps would be required, leading to enormous computational costs that are unfeasible for our aims. However, it has been shown in previous studies (see Barral et al., 2021) that the SST $K - \omega$ with wall functions can provide meaningful shear stress predictions when compared to experimental measurements. In any case, it should be noted that a fully accurate representation of the wall shear stress would require finer meshes, allowing to solve the characteristics of the viscous sublayer also in the jet impingement point, as the logarithmic wall law is a crude simplification in this situation.

In most of the runner, as the flow is far more gentle, with much lower speeds of hot metal (below 0.1 m/s), integration to the viscous sublayer is viable. In particular, since the dynamic viscosity of slag is very large and flows slower than the hot metal in the trough, it is not possible to guarantee an y^+ value above 30. Therefore, the mesh is constructed so that $y^+ \leq 5$ in most of the runner, with higher y^+ values only occurring in the impact zone. There are some small zones in the domain where the y^+ values are in the buffer layer, i.e. the range where neither the viscous stress nor the Reynolds stress dominates.

2.4.6. Discretisation and numerical methodology

The software Ansys Fluent, Release 2019 R3, is used to solve the mathematical model. The *SIMPLE* segregated algorithm is used for the pressure and velocity coupling. The *least squares cell-based* scheme is utilised for gradient computation, whereas *Second-Order Upwind* schemes are used for the convective terms in all the transport equations. Moreover, the *PRESTO!* scheme is considered to interpolate pressure values at the cell faces. It employs a staggered grid for the pressure values. Time discretisation is done using the so-called *First-Order implicit scheme*. Lastly, to address the volume fraction advection equations, we use the *Geo-Reconstruct* scheme. It is a variant of the PLIC technique (Tryggvason et al., 2011), which produces minimal numerical diffusion in the interface advection. For the description of these numerical schemes and their implementation in the used software package, we refer to Ansys, Inc. (2019). Some additional information on part of the used discretisation schemes can be found in Versteeg & Malalasekera (2007).

The numerical scheme for VOF advection allows to greatly reduce numerical diffusion of the interface, but it is an explicit scheme. Recall that, as described at the end of Section 2.3, volume fraction advection is done for a given velocity field after the normal vector of the interface is approximated. Since (2.29) is a hyperbolic equation (see e.g. Quarteroni, 2009), small time step sizes are required

Table 2.2: Computational grids, with mesh quality metrics and maximum specified time-step size used in the adaptive time-stepping method.

	# cells	Max. Skw.	Min. Orth.	Max. Δt [s]
Mesh 1	200900	0.82	0.22	$2.5{\cdot}10^{-4}$
Mesh 2	412682	0.82	0.22	$2.0{\cdot}10^{-4}$
Mesh 3	812178	0.82	0.21	$1.5{\cdot}10^{-4}$
Mesh 4	1670712	0.83	0.21	$1.0{\cdot}10^{-4}$

Table 2.3: Amount of tapped hot metal and slag in each run, in % of the total tapping volumetric flow rate and mass flow rate ($\dot{m}_{tap}$).

	% Volume		$\dot{m}_{tap}$ [kg/s]	
	Slag	Hot metal	Slag	Hot metal
Run A	0	100	0	133
Run B	50	50	25	67
Run C	70	30	35	40
Run A*	0	100	0	133

to comply with the *Courant-Fiedrichs-Lewy* (CFL) condition, which states a necessary condition for the numerical method stability. In particular, for a one-dimensional advection equation, and a given velocity v, it can be stated as follows (Laney, 1998, Ch. 12):

$$C = |v|\frac{\Delta t}{h} \leq 1,$$

where C is the *Courant number*, Δt is the time step size and h is the spatial discretisation parameter.

To reduce the computational effort, the *multiphase-specific* adaptive time stepping technique is used (see Ansys, Inc., 2019). It modifies the time step size based on a time scale calculated each time step by comparing a specified target global Courant number with that computed in the simulation. The global Courant number is defined using a combination among a flux-based and a velocity-based criterion, being the latter the most restrictive. It measures the ratio between the volume of the interface cells and the sum of the outgoing face fluxes. The starting time step size for all simulations is 10^{-5} s, with 10 fixed-size time steps being always performed. Then, the step is modified according to the computed time scale, with a maximum change ratio of 1.05 and a minimum of 0.4. We set up a target Global Courant Number of 0.5 for the computation of the time scale, and the maximum step size depends on the specific grid (see Table 2.2).

To assess whether the numerical solution has converged at each time step, we control the locally-scaled residuals corresponding to all the flow variables (Ansys, Inc., 2019), assuming that any time step has converged if all the residuals fall below 10^{-5}.

2.4.7. Analysed cases

We analyse three different states of the flow in the BF trough during a standard BF tapping that are representative of the stages during the tapping. First, *Run A* addresses the initial portion of the tapping, where only hot metal flows out from the taphole. Usually, this stage lasts for around 15-30 minutes, although the precise slag delay value widely depends on the BF conditions and other factors (see Section 1.2). It ends when the slag-iron interface within the BF hearth reaches the taphole level and slag also starts draining from the BF. *Run B* aims to assess the hydrodynamic state of the BF trough during this second stage. To this end, we set that the volumetric flow rate from the taphole is 50% slag and 50% hot metal, based on the observation the initial tapped amounts of slag and hot metal are similar (Shao & Saxén, 2012a). Typically, as described in Chapter 1, the total volumetric flow rate can rise slightly up to the time at which BF gas bursts out from the taphole and the tapping is ended by

plugging the orifice with BF clay. Nonetheless, we note that the taphole outflow conditions may vary significantly, as the taphole diameter may increase due to severe erosion, resulting in lower stream velocities. We neglect this phenomenon and maintain a constant outflow velocity of 6.29 m/s.

In *Run C*, we set slightly different conditions, considering a larger volumetric share of slag in the jet, of 70% slag and only 30% of hot metal. Moreover, we also address the particular case of the first tapping of the BF trough campaign. In this situation, the trough is empty and there are no fluids to mitigate the jet impact on the refractory. For this case, we consider the hot metal jet stream exiting the taphole and label it as *Run A**, provided that the same boundary conditions are considered and only the initial condition is changed from Run A. For each of these runs, we solve a time interval $(0, t_{end}]$, being $t_{end} = 150$ s, with the exception of Run A*, for which the end time is set as $t^*_{end} = 100$ s.

In Table 2.3, the volumetric flow rate (as % volume of slag and hot metal per unit of time of the total volume) and the corresponding mass flow rate for each run for the inlet condition are displayed. As mentioned above, when the flow is a combination of slag and hot metal, the interface among both phases in the taphole is assumed to be well-defined, with no mixing as considered in some previous studies (see e.g. Shao & Saxén, 2011). Therefore, we assume that the fluid phases reach the computational domain maintaining this stratification. Therefore, α_{slag} and α_{hm} are set on Γ_{inlet} by adjusting the values in the cells corresponding to the interface to match the desired mass flow rate in each case.

Below, we summarise the changes that are considered for the boundary conditions and initial conditions from those previously described in Sections 2.4.3 and 2.4.4.

- *Run A*. The volume fractions of slag and hot metal are set as $\alpha_{hm} = 1$ and $\alpha_{slag} = 0$ on Γ_{inlet}. The rest of the boundary conditions are as detailed in Section 2.4.3. The initial condition is set as described in Section 2.4.4.

- *Run B*. The volume fractions are set to match a 50% of slag and 50% of hot metal on Γ_{inlet}. The initial condition is set as the state of the computational domain Ω as computed at the end of the simulation of Run A, i.e. at $t = 150$ s.

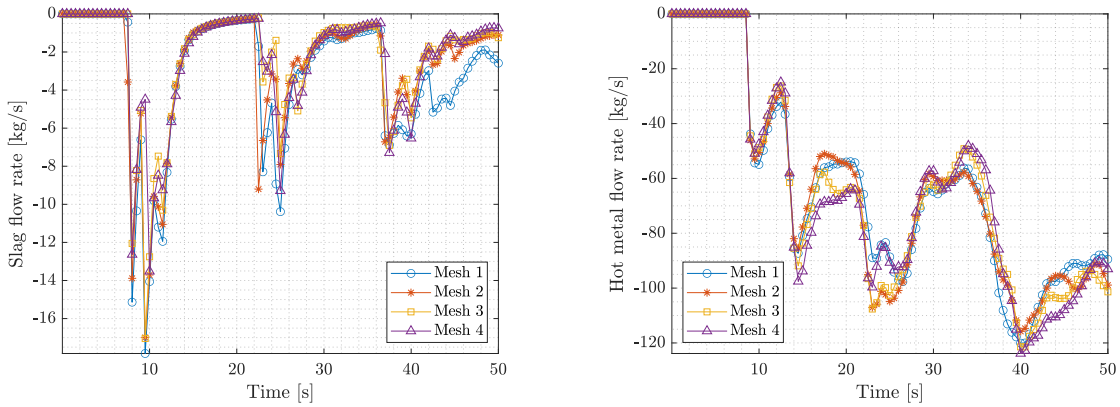
- *Run C*. The same initial condition as that used for Run B is considered. α_{slag} and α_{hm} are set to match a 70% of slag and 30% of hot metal on Γ_{inlet}.

- *Run A**: The conditions considered for Run A are used. Instead of the initial condition described for the volume fractions in Section 2.4.4, we set $\alpha_{slag} = \alpha_{hm} = 0$ in Ω.

2.5. Results and discussion

In this section, we discuss the main results that have been obtained after the solution of the mathematical model. First, in Section 2.5.1, the numerical results computed for Run A on four different computational grids are analysed, with the aim of assessing the dependency of the computed result on the discretisation parameter. Then, in Section 2.5.2 we discuss the numerical findings after solving Runs A, B and C with the conditions described in the previous section. Lastly, Section 2.5.3 is devoted to analyse the computed solution for *Run A**, where the trough is assumed to be empty as initial condition.

All the numerical results presented in this section have been obtained with the package Ansys Fluent, version 2019 R3 (Ansys, Inc., 2019). For the postprocessing of these results, the open-source software *Paraview* and the *Matplotlib* library in Python (Hunter, 2007) have been used, as well as the proprietary computing environment *MATLAB*. The simulations were run in parallel, using 48 cores in a PowerEdge R840 machine, part of the Mariscal computer cluster, hosted at the CESGA. The machine is equipped with 4 Intel Xeon Gold 6126 processors and 384 GB of RAM. For each 10 s of time in the simulations, approximately 4 days of computation were required.



(**a**) Slag. (**b**) Hot metal.

Figure 2.5: Outflow rates for the meshes considered in the grid sensitivity study.

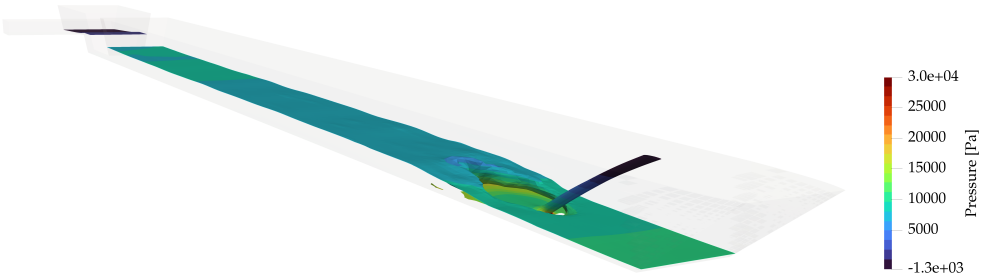
2.5.1. Grid validation

To address the grid dependency of the computed approximations of the solution, we study the differences between the results for the grids collected in Table 2.2, where the cell count is provided, as well as the maximum skewness and minimum orthogonal quality of each of the grids. Note that with the definition used by the software package, the best possible skewness and orthogonal quality are 0 and 1, respectively. In addition, the maximum step size that we imposed to the adaptive step size controller is also shown in Table 2.2. The boundary and initial conditions for this study are those described in Section 2.4.7 for Run A , i.e., only hot metal is assumed to be draining from the BF. For this study, the end time is set as $t^*_{end} = 100$ s.

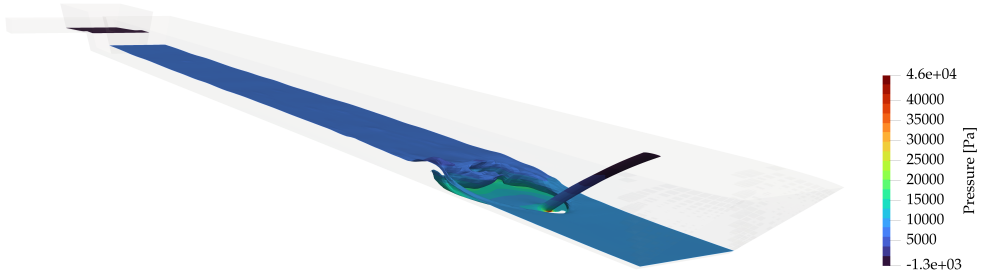
In preliminary numerical experiments, the methodology to obtain the numerical solution has been found to be very sensitive to the mesh quality. Specifically, meshes with an orthogonal quality below 0.1 lead to a divergence of the solver before reaching the time value $t = 1$ s. Notice from Figure 2.4 that most of the hexahedral cells in the mesh are very regular, and the only significantly distorted cells are those in the vicinity of the jet trajectory, where some degree of distortion was required to follow the expected jet path with the mesh.

In Figure 2.5 we compare the mass outflow rate of slag and hot metal for each of the grids during the time interval $(0, 50]$ s on Γ_{outlet}. Note that at the beginning of the simulation there is no outflow of slag nor hot metal. Then, as the jet impacts the pool of fluids within the trough, a small wave is formed, which travels from the impingement point along the trough. It reaches Γ_{outlet} in the slag runner at around $t = 7$ s and overflows the iron dam at roughly $t = 8.2$ s, leading to hot metal exiting the computational domain through the portion of Γ_{outlet} at the end of the trough, as evidenced by the slag and hot metal mass flow rates. The results depicted both in Figure 2.5a for slag and in Figure 2.5b for hot metal show good qualitative agreement among all considered meshes. However, the level of agreement deteriorates as time advances, particularly between Mesh 1 and the finer ones. Mesh 3 and Mesh 4 yield very similar results. Notice that, since we are considering the conditions for Run A (see Table 2.3), only hot metal is entering the computational domain through Γ_{inlet}. Therefore, a steady-state of the model requires the mass flow rate of slag in Figure 2.5a to be zero. Otherwise, the interfaces separating the phases cannot be stationary.

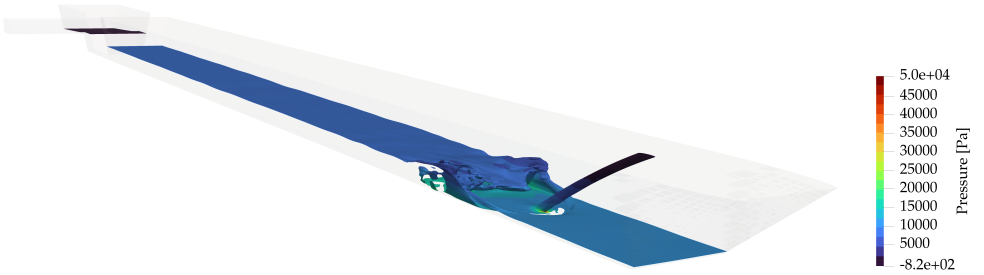
In Figure 2.6, the hot metal-air and slag-hot metal interfaces are depicted at $t = 25$ s for the four computational grids. The position of these interfaces is assumed to correspond to the contour $\alpha_{hm} = 0.5$. The interface is coloured by the pressure values and, while Meshes 2, 3 and 4 predict comparable pressure values, we remark that the structures of the flow become more intricate as the mesh is refined, with significant air and slag entrainment in the impact zone and complex vortex structures being formed. These lead to bubble formation, which can only be simulated with the finer meshes. However, we remind that an accurate prediction of these flow characteristics requires to include sur-



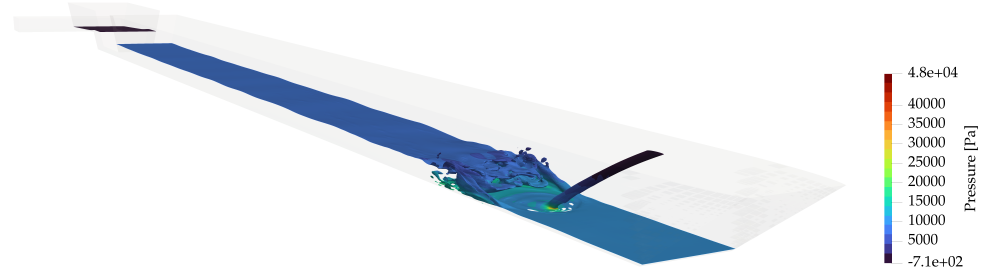
(**a**) Mesh 1.



(**b**) Mesh 2.



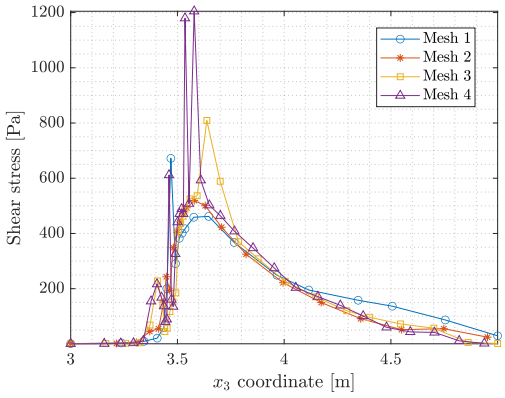
(**c**) Mesh 3.



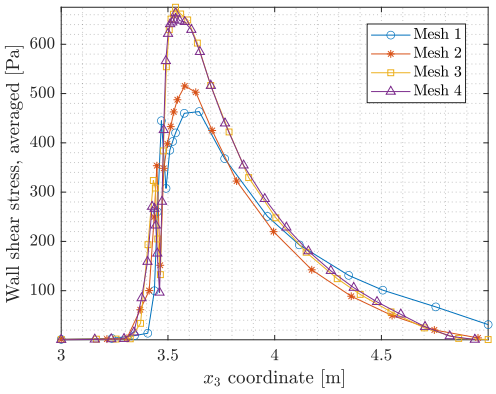
(**d**) Mesh 4.

Figure 2.6: Contour $\alpha_{hm} = 0.5$ at $t = 25$ s for the meshes considered in the grid sensitivity study, coloured by pressure values. The contour is interpreted as the slag-hot metal interface upstream of the skimmer and the hot-metal air free surface downstream of it.

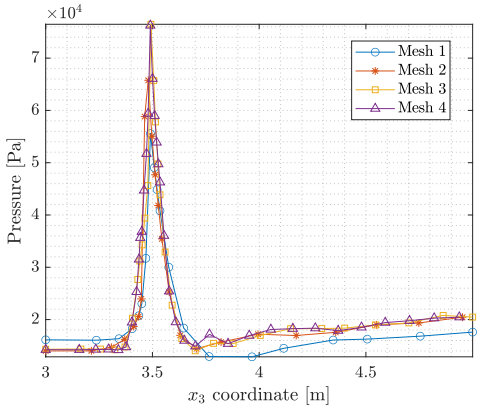
USC UNIVERSIDADE DE SANTIAGO DE COMPOSTELA



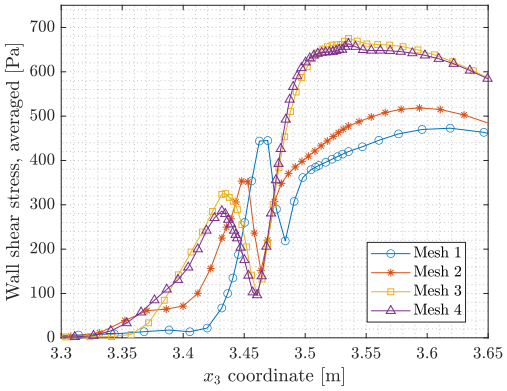
(**a**) Wall shear, $t = 100$s.



(**b**) Wall shear, averaged over $(75, 100]$ s.



(**c**) Pressure, $t = 100$ s.



(**d**) Wall shear close to the impingement point, averaged over $(75, 100]$ s.

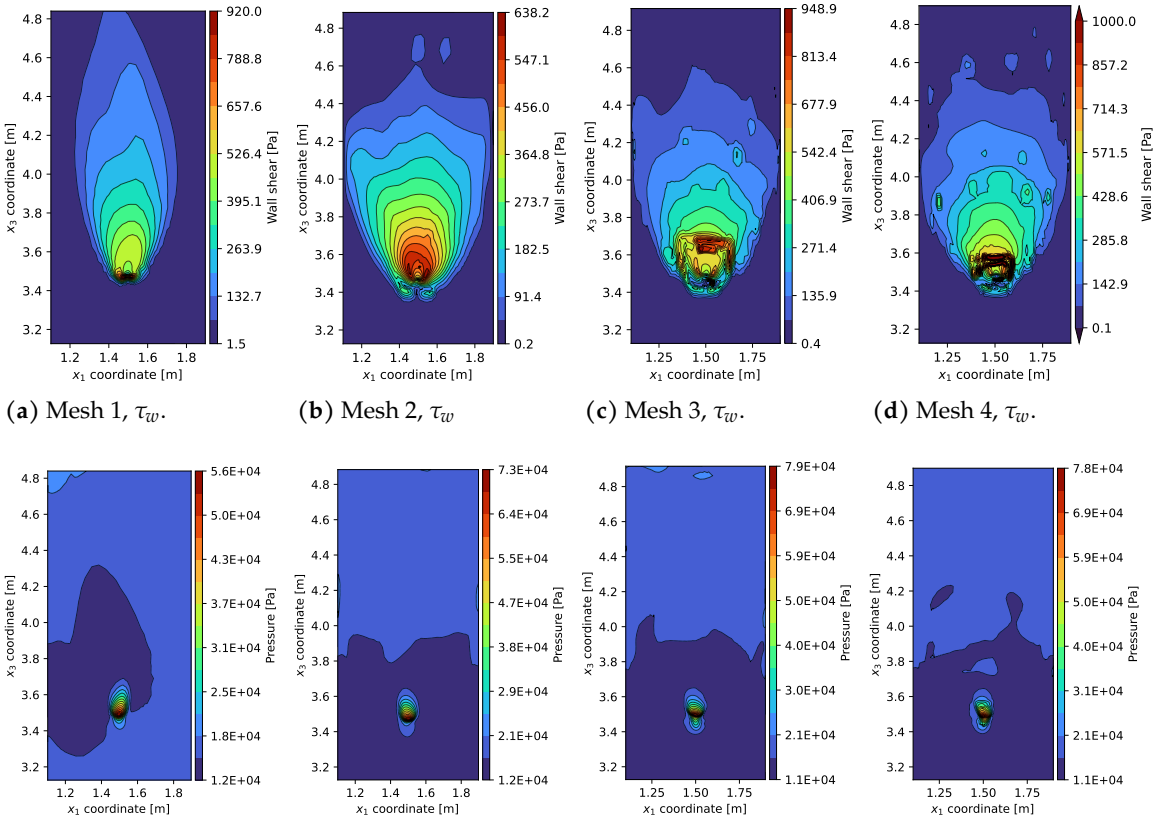
Figure 2.7: Wall shear and pressure on line crossing the jet impingement area.

face tension effects, which have been neglected (see Remark 2.4) and, arguably, the use of LES models to reliably simulate the larger turbulent eddies. All grids predict a phenomenon observed in the scale model studied by Begnis & Brandaleze (2006). Namely, the hot metal in the jet impingement zone is displaced, and the interface height is significantly lower at the flow stagnation region formed in the beginning of the trough when compared to that observed downstream of the impingement zone. As observed in other numerical studies, the interfaces between slag-iron and slag-air remain clear and horizontal away from the impact point (Kou et al., 2019).

As mentioned at the beginning of this chapter, it is of industrial interest to assess the wall shear stress and pressure profiles generated by the hot metal flow in the trough. In particular, the shear stress is closely related to the erosive phenomena, which play a significant role in refractory degradation. In Figure 2.7, the shear stress and pressure computed with each grid is plotted along the line given by the parametrisation $(x_3, h_B(x_3))$ with h_B being the bottom of the computational domain, defined in (2.32). It divides the part of Γ_{wall} highlighted in blue and labelled as jet impingement area in Figure 2.2 in two halves.

Remark 2.7. *The large differences in the instantaneous wall shear values depicted in Figure 2.7a, can be attributed to the observed changes in the volume fractions for the finest meshes, which can predict some degree of bubble formation and entrainment. As the wall shear stress directly depends on the viscosity of the fluid, bubbles have a significant effect in the computed values as they reach the bottom wall.*

Since we are fundamentally concerned with the main characteristics of the flow, we consider moving averages *in the subsequent manner. Let $\phi(\mathbf{x}, t)$ be the computed solution of an arbitrary flow variable. Then, we denote*



(**a**) Mesh 1, τ_w. (**b**) Mesh 2, τ_w (**c**) Mesh 3, τ_w. (**d**) Mesh 4, τ_w.

(**e**) Mesh 1, p. (**f**) Mesh 2, p. (**g**) Mesh 3, p. (**h**) Mesh 4, p.

Figure 2.8: Wall shear stress (τ_w) and pressure (p) on the wall at the jet impingement zone for the different grids considered in the grid validation analysis, $t = 100$ s.

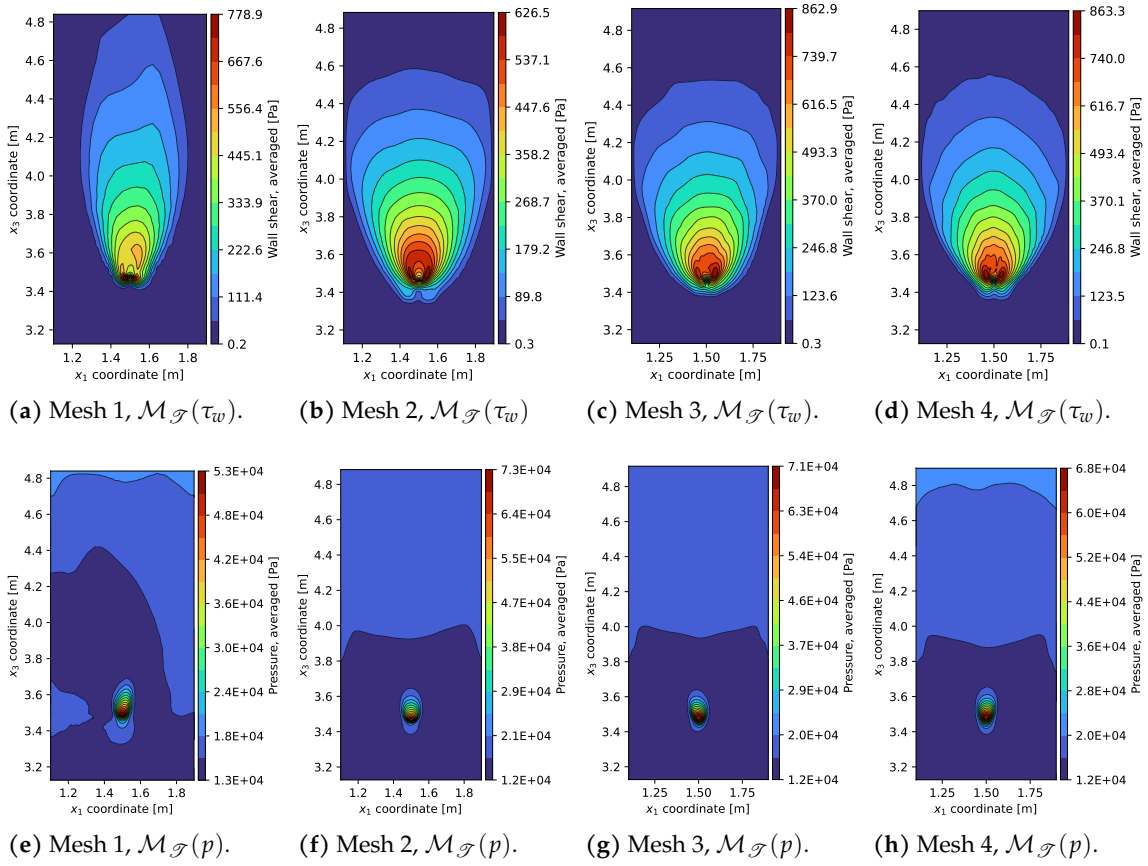
the averaged value of $\phi(\mathbf{x}, t)$ as $\mathcal{M}_{\mathscr{T}}(\phi)(\mathbf{x}, t)$, defined as:

$$\mathcal{M}_{\mathscr{T}}(\phi)(\mathbf{x}, t) = \frac{1}{\mathscr{T}} \int_{t-\mathscr{T}}^{t} \phi(\mathbf{x}, s)\, ds, \tag{2.35}$$

where $\mathscr{T}$ is a suitable time scale.

The interest in these new averaged values is that they allow to filter the large fluctuations observed in the volume fractions. We believe that may lead to meaningful estimations of the general characteristics of the flow. This procedure is applied regardless of whether the original flow value corresponds to a mean value in the RANS equations, such as the velocity or the pressure, as they are still affected by the volume fraction fluctuations due to bubble generation. To avoid confusing the reader, we shall usually refer to these variables as "averaged" and indicate the time interval during which the integration (2.35) is performed. Unless explicitly stated otherwise, we consider the averaging period $\mathscr{T} = 25$ s in all cases.

The averaged wall shear stress at $t = 100$ s for $\mathscr{T} = 25$ s is depicted in Figure 2.7b. The large shear stress oscillations shown previously in Figure 2.7a, attributed to entrained bubbles reaching Γ_{wall}, have been filtered by the averaging. In Figure 2.7d, the shear stress is displayed in close-up near the jet impact point. The plot resembles those experimentally measured for submerged jets in various conditions. Specifically, for a normally impinging circular jet, two symmetrical shear stress maximums are observed around a minimum, which corresponds to the impact point (Beltaos & Rajaratnam, 1974; Phares et al., 2000). In the plane hot metal jet numerical experiment conducted in Barral et al. (2021), the maximums were not symmetrical due to the oblique impact of the jet on the refractory wall, which is precisely the case in the reported results herein. Notice that while all meshes



(a) Mesh 1, $\mathcal{M}_{\mathscr{T}}(\tau_w)$. **(b)** Mesh 2, $\mathcal{M}_{\mathscr{T}}(\tau_w)$ **(c)** Mesh 3, $\mathcal{M}_{\mathscr{T}}(\tau_w)$. **(d)** Mesh 4, $\mathcal{M}_{\mathscr{T}}(\tau_w)$.

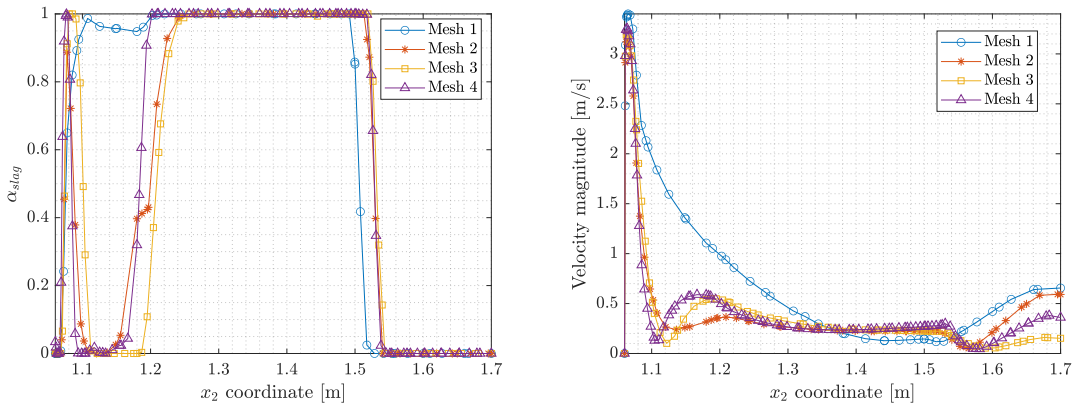
(e) Mesh 1, $\mathcal{M}_{\mathscr{T}}(p)$. **(f)** Mesh 2, $\mathcal{M}_{\mathscr{T}}(p)$. **(g)** Mesh 3, $\mathcal{M}_{\mathscr{T}}(p)$. **(h)** Mesh 4, $\mathcal{M}_{\mathscr{T}}(p)$.

Figure 2.9: Averaged wall shear stress ($\mathcal{M}_{\mathscr{T}}(\tau_w)$) and pressure ($\mathcal{M}_{\mathscr{T}}(p)$) on the wall at the jet impingement zone for the different grids considered in the grid validation analysis. The averaging is performed over $(75, 100]$ s.

seem to agree in the predicted impingement point, Mesh 1 and 2 yield substantially different maximum averaged stresses. On the other hand, pressure values are similar for all meshes, as displayed in Figure 2.7c.

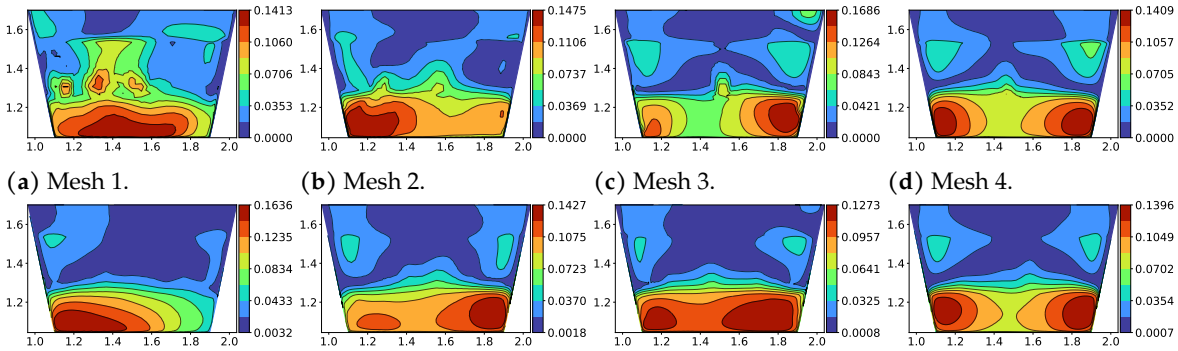
In Figure 2.8 the contours of wall shear stress and pressure at $t = 100$ s for the different grids are shown. The contours are displayed only in the part of Γ_{wall} that corresponds to the *jet impingement area* (see Figure 2.2). For a better comparison, in Mesh 4 we have adjusted the maximum depicted contour to be 1000 (the actual computed maximum shear stress is 1640 Pa). In agreement with the prior discussion, we find large differences between all meshes due to the finer meshes being able to capture more effects in air and slag bubble entrainment. The pressures, however, are very similar for all meshes. Instead, if the shear stress and pressure are averaged on the jet impingement area over the interval (75,100] s, the contours shown in Figure 2.9 are obtained. As discussed above for the plot over the line passing through the impact point, the averaging filters the unsteady and chaotic shear stress profiles and yields very similar results for Mesh 3 and Mesh 4.

In Figure 2.10, the values of α_{slag} and velocity magnitude computed at $t = 100$ s are depicted along a vertical line crossing Ω (i.e. along the direction $\mathbf{e}_2$) and passing through the point $\mathbf{x} = (1.5, 0, 4)$ m. As with the previously analysed results, it is observed that Mesh 1 yields very inaccurate predictions, while the remaining meshes show reasonable qualitative agreement. In Figure 2.10a, notice that Meshes 2, 3, and 4 predict a significant amount of entrained slag near the bottom of the computational domain flowing at a high speed value, around 3 m/s due to the impinging jet. To compare the velocity predictions among the considered grids, in Figure 2.11, the contours of the velocity magnitude are displayed on a cross-section of the trough corresponding to $x_3 = 7.35$ m and determined



(**a**) α_{slag}. (**b**) Velocity magnitude.

Figure 2.10: Computed solution for the different grids along the line $x_1 = 1.5$ m, $x_3 = 4$ m, $t = 100$ s.



(**a**) Mesh 1. (**b**) Mesh 2. (**c**) Mesh 3. (**d**) Mesh 4.

(**e**) Mesh 1. (**f**) Mesh 2. (**g**) Mesh 3. (**h**) Mesh 4.

Figure 2.11: Plane cross-section of the computational domain ($x_3 = 7.35$ m). Top: velocity magnitude contours at $t = 100$ s. Bottom: velocity magnitude, averaged over $(75, 100]$ s.

by the normal vector $\mathbf{n} = \mathbf{e}_3$. The contours in the top of the figure are instantaneous ones at $t = 100$ s, whereas those in the bottom are averaged values over $(75, 100]$ s. Notice that there are substantial differences between all meshes, including the more refined ones, although the qualitative characteristics of the velocity are similar between Mesh 3 and 4. Also, as this section is located 4 m away from the jet impingement point, we observe that the computed instantaneous values show much less significant fluctuations.

As opposed to other previous studies dealing with the numerical simulation of the trough, such as L. Wang et al. (2017); Kou et al. (2019), we have found no significant slag entrainment with hot metal. This difference can be attributed to the geometrical particularities of our trough configuration and jet impact point, since Kou et al. (2019) observed the former to have a substantial effect in the computed amount of entrained slag, finding less slag entrainment with deeper BF troughs. In particular, L. Wang et al. (2017) found a 100% separation efficiency of hot metal from slag when the iron dam and slag runner height difference was above 0.2 m. For the trough dimensions considered herein, this difference is precisely 0.2 m, as shown in Figure 1.4. Also, the different numerical approaches may play a substantial role in the analysis of separation. Since most of the entrainment is due to small droplets formed due to the intense shearing in the jet entry region (Ranjan et al., 2022), accurate simulation of this phenomenon may require very fine meshes and carefully considering surface tension effects. In any case, the settling velocity of the small droplets in the quiet zone that is generated downstream of the jet impact region can be estimated through Stokes' law (Cameron et al.,

Table 2.4: Initial and final median height of the interfaces, for Runs A,B and C.

	Run A		Run B		Run C	
	Initial [m]	Final [m]	Initial [m]	Final [m]	Initial [m]	Final [m]
Slag-air (h_{slag})	1.5	1.534	1.534	1.565	1.534	1.575
Hot metal-slag (h_{hm})	1.182	1.255	1.255	1.206	1.255	1.186

2019). Therefore, it is of interest to design BF troughs that maximise residence time of slag and hot metal, increasing the size of the quiet zone.

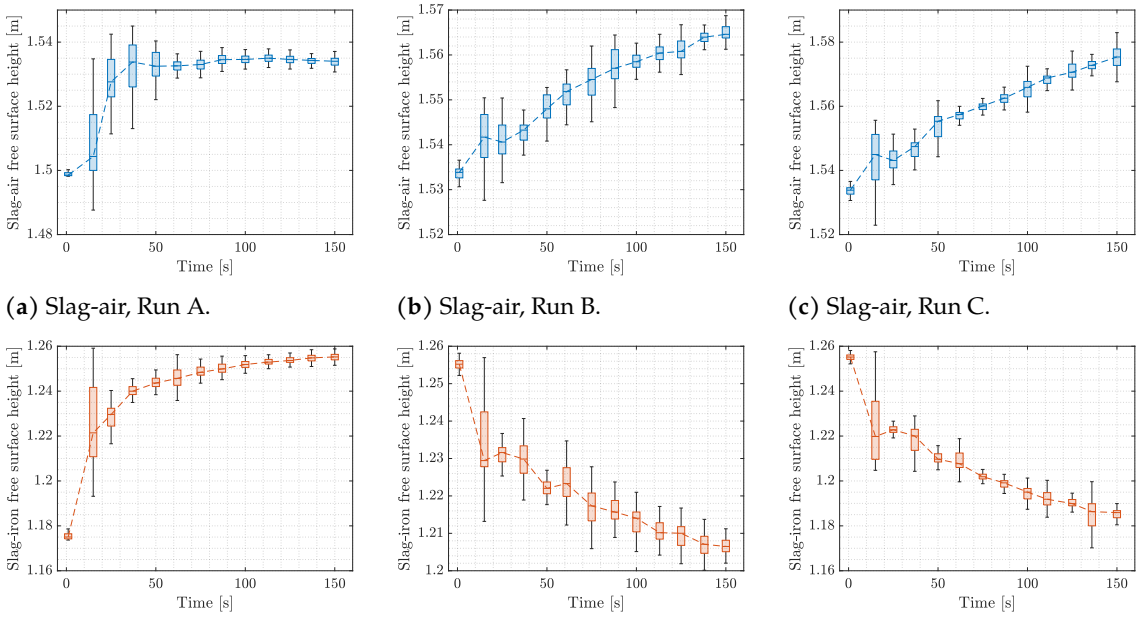
The presented results evidence a non-negligible degree of mesh dependency, even among the finer meshes (Mesh 3 and 4), especially if the instantaneous shear stress results or the velocities near the impingement point are compared. Far away from the impingement point, the velocity results are similar. If the computed fields are filtered in time, the fluctuations due to entrained bubbles are eliminated and small differences are observed for all the analysed flow variables between Mesh 3 and Mesh 4, including the wall shear in the jet impingement area. Therefore, we conclude that the latter mesh is sufficiently fine to guarantee a reasonable degree of accuracy for a prediction of general features of the flow. In the subsequent results, we solve the mathematical model for all the cases gathered in Table 2.3 using Mesh 4.

2.5.2. Runs A-C

In this section, the main characteristics of flow are studied, as well as the evolution of the interfaces separating the fluid phases and the shear stress due to the impinging jet for the taphole conditions described in Section 2.4.7 for a typical tapping cycle, i.e. Runs A, B, and C.

First, the evolution of the interfaces between the fluid phases is analysed. To compute the positions of the air-slag and slag-hot metal interfaces, we proceed as follows. Notice that in virtue of the discussion in Section 2.3, we may assume that the contour $\alpha_{slag} = 0.5$ indicates the position of these interfaces. Since we are interested in assessing the position of the part of these interfaces that is not affected by the strong circulations formed in the impingement point, after computing the coordinates of the points defining the contour, we only consider those points that satisfy $x_3 > 5$ m. Then, we assume that a point in such contour corresponds to the slag-hot metal interface if $\alpha_{hm} > \alpha_A$ for the corresponding interpolation of the volume fraction values. Naturally, if the previous condition is not satisfied, the point is assumed to belong to the air-slag interface. Separating the points in this manner, we repeat the procedure for several time values on Runs A, B and C, constructing the boxplots shown in Figure 2.12 by computing the corresponding statistics involving the x_2 coordinates of all points in the contour. The atypical values have not been included in the boxplots for clarity purposes.

In particular, we observe that in around only 50 s, both the slag and hot metal interfaces reach a quasi-steady position in Run A, with very low dispersion among all points composing the corresponding contours. During these first 50 seconds, the interface height rises, especially the one separating slag and hot metal. Notice that the initial thickness of hot metal is around 18 cm (the minimum value of h_B is 1 m) and at the end of Run A, it has grown to almost 26 cm, which is a 40% relative increase. In Runs B and C, representing conditions that involve combined flow of slag and hot metal in the taphole, we find that the dispersion in the computed heights of both interfaces is substantially larger, indicating that they are less plane. This is possibly a consequence of slag also flowing downstream in the BF trough, since in Run A the slag is mostly static in the whole computational domain. In Table 2.4, the median initial and final positions of the interfaces are summarised. In Figure 2.13, the $\alpha_{slag} = 0.5$ contour is displayed at $t = 150$ s for all runs, showing the global position of the slag-hot metal and slag-air interfaces. While the qualitative features observed in the figure are similar for all runs, we observe that the flow structures generated by the jet impact are apparently less complex when slag is being tapped. Also, note that the jet impact generates large bubbles of air which can be tracked with the VOF method. They resurface at a distance around 1-2 m away from the impact point, similar to that observed in He et al. (2002). Furthermore, in all conditions, the jet reaches the



(**a**) Slag-air, Run A. (**b**) Slag-air, Run B. (**c**) Slag-air, Run C.

(**d**) Slag-hot metal, Run A. (**e**) Slag-hot metal, Run B. (**f**) Slag-hot metal, Run C.

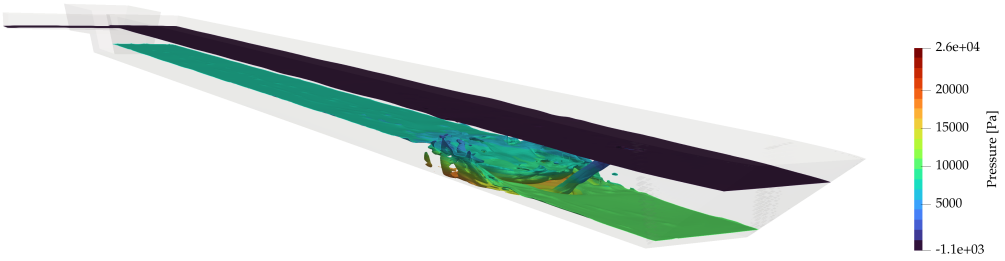
Figure 2.12: Evolution of the interface height for Runs A-C.

bottom wall maintaining a coherent structure, without significant spreading.

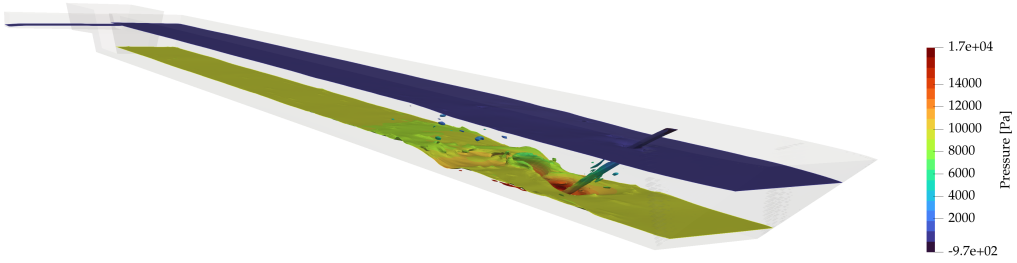
In Figure 2.14, the median height as a function of the longitudinal coordinate x_3 of all the interfaces is displayed for different time values for Runs A, B and C. The height values are obtained by inspecting the contours $\alpha_{slag} = 0.5$ and $\alpha_{hm} = 0.5$. To classify the points in each contour, first, the corresponding interface is identified as described above (e.g. whether the point belongs to the iron-air free surface or iron-slag interface). Then, the points are separated in subintervals according to their x_3 coordinate values. For all the contour values in each subinterval, the median value is plotted in Figures 2.14a-2.14d. The results in Figure 2.14a, which shows the interface location evolution for Run A, support the previously discussed findings. From the initial condition, note how the large kinetic energy unleashed by the jet impact first empties most of the hot metal upstream of the impingement point, as the slag-hot metal interface, shown at the left of the plot, is substantially higher at $t = 1$ s than in $t = 50$ s. However, it seems to recover height as time advances. The remaining interface positions show a very stable position, especially far away from the jet impingement area, with an almost completely flat profile for $x_3 > 5$ m. Also, we remark that the large inclination of the iron-slag free surface at the right of the plot is due to slope of the iron runner, which is of 3.5%. In Runs B and C, depicted in Figures 2.14b and 2.14c, the position of the hot metal-air interface, downstream of the skimmer, is much more stable in comparison. This is a direct consequence of the initial condition that was selected for these simulations, as the initial values for all flow variables were those computed at the end of Run A. Note that these numerical results are in qualitative agreement with the approximate positions of the interfaces separating oil, water and air in the scale model analysed in Begnis & Brandaleze (2006), who also reported flat profiles in the quiet region away from the impingement zone.

Lastly, in Figure 2.14d, the position of the interfaces is compared at the end time of the simulation for each run, i.e., at time $t = 150$ s. The results show again that during a standard tapping, while there is no significant variation of the slag-air free surface, the hot metal-slag free surface suffers non-negligible changes during the process, as discussed above. Specifically, we observe that the heights computed for most of the hot metal-slag interface are those already reported at the end time in the boxplots in Figure 2.12.

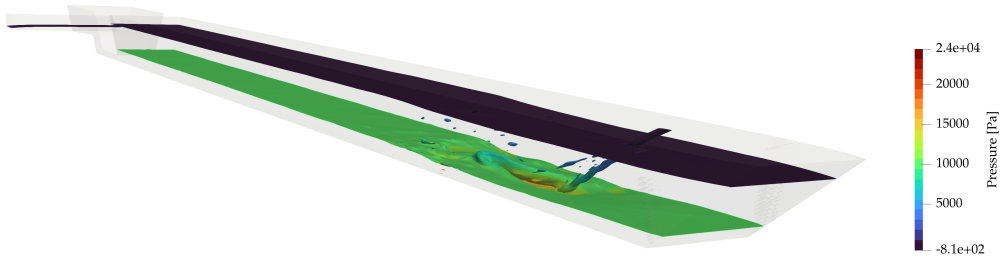
The fluctuations of the slag and hot metal level reported here have not been observed in the analysed literature. They are certainly difficult to measure, as the hot metal-slag interface is obviously



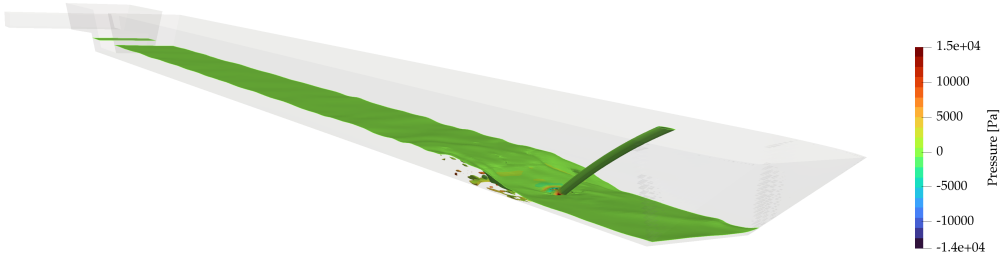
(**a**) Run A.



(**b**) Run B.



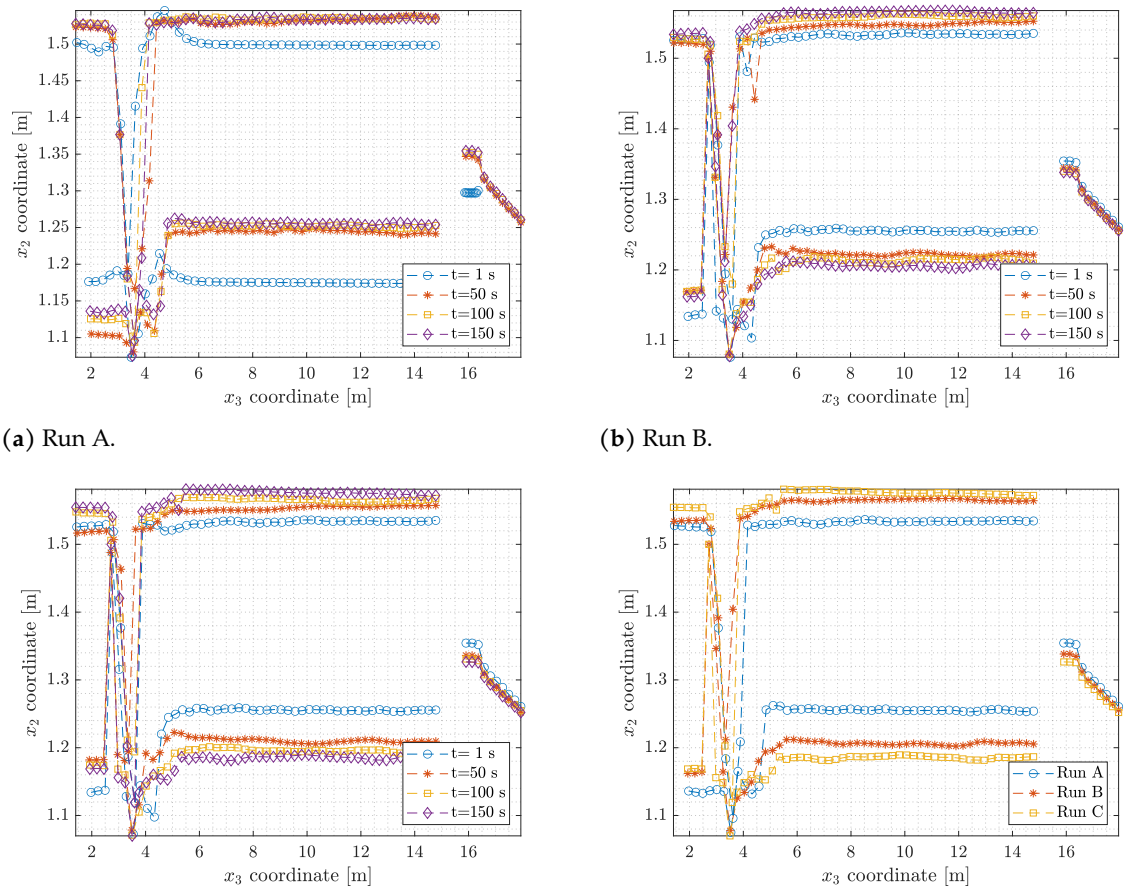
(**c**) Run C.



(**d**) Run A*.

Figure 2.13: Contour $\alpha_{slag} = 0.5$ at $t = 150$ s for Runs A-C and $\alpha_{hm} = 0.5$ at $t = 100$ s for Run A*, coloured by pressure values.

USC UNIVERSIDADE DE SANTIAGO DE COMPOSTELA



(**a**) Run A.

(**b**) Run B.

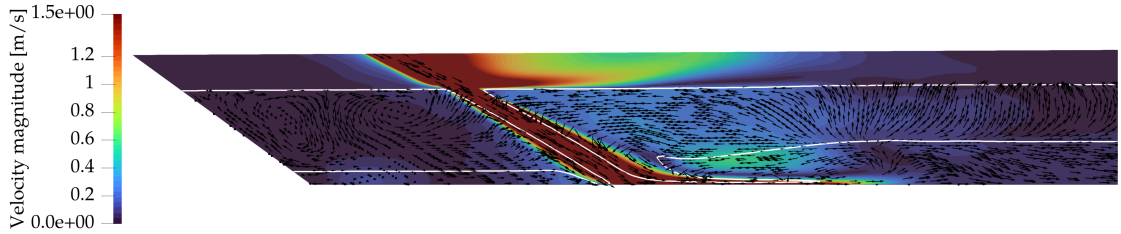
(**c**) Run C.

(**d**) At $t = 150$ s.

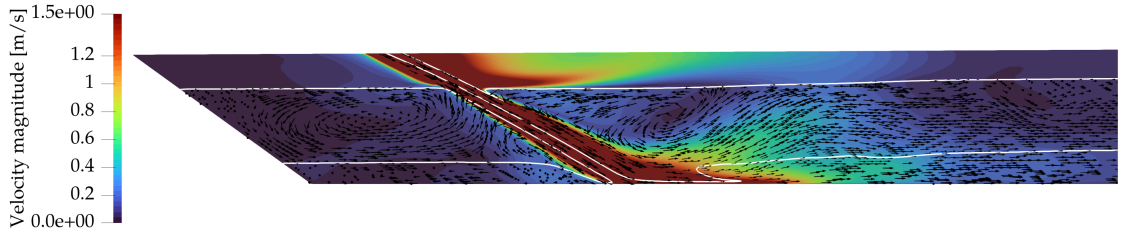
Figure 2.14: Median height of the interfaces at various time values for Runs A, B and C.

completely hidden by a thick slag layer in the trough. Noteworthy, they may have a substantial impact in BF trough operation. Towards the end of the tapping, the risk of slag going below the skimmer and contaminating the hot metal is increased, which is an important safety risk (Kumar et al., 2010). Furthermore, if the volume fraction of slag being drained from the BF increases, we expect the interface position to go further down. Also, the alternation between slag and hot metal in the same region of the wall can lead to an increase in the refractory wear rates (see Section 1.4).

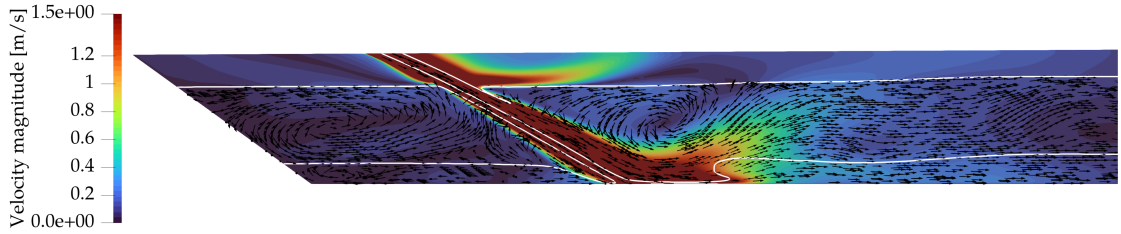
Concerning the flow structures in the trough, recirculation patterns and secondary structures that are strongly dependent on the taphole conditions are observed. In Figure 2.15, the velocity vectors on the plane $x_1 = 1.5$ m are shown for time $t = 150$ s in the zone where the iron and slag jet impinges the wall, for Runs A, B, and C. The vectors are only displayed on those points where $\alpha_{hm} > 0$ or $\alpha_{slag} > 0$. Moreover, note that the maximum velocity magnitude contour that is displayed does not correspond to the actual maximum, which is around 7 m/s for all runs. The contour $\alpha_{slag} = 0.5$ is also depicted as a white curve. We remark that all the displayed fields have been averaged over $(125, 150]$ s. When only hot metal is being tapped (Run A), two slag recirculations in the stagnation region upstream of the impingement point are generated, which merge in a single eddy as slag arrives at the trough from the BF (Runs B and C). In all cases, the slag downstream of the jet impact zone forms a backward-advancing current, which is stronger at the first stages of the tapping process. This phenomenon has been observed in several studies (see e.g. Luomala et al., 2001). In Run A, the iron near the slag is also circulating backwards, and we observe that while the global characteristics of the flow are essentially the same for Runs B and C, the differences induced by the slag arrival from the BF at the trough are



(**a**) Run A.



(**b**) Run B.



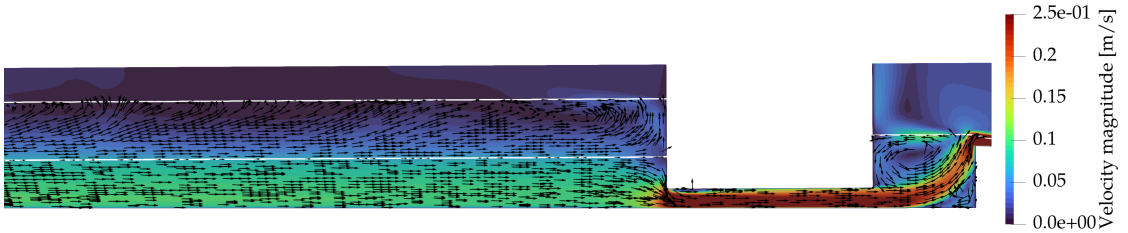
(**c**) Run C.

Figure 2.15: Jet impingement zone: velocity vectors on the plane $x_1 = 1.5$ m, with white contour lines corresponding to $\alpha_{slag} = 0.5$ and velocity magnitude contours. All the results correspond to averages over $(125, 150]$ s.

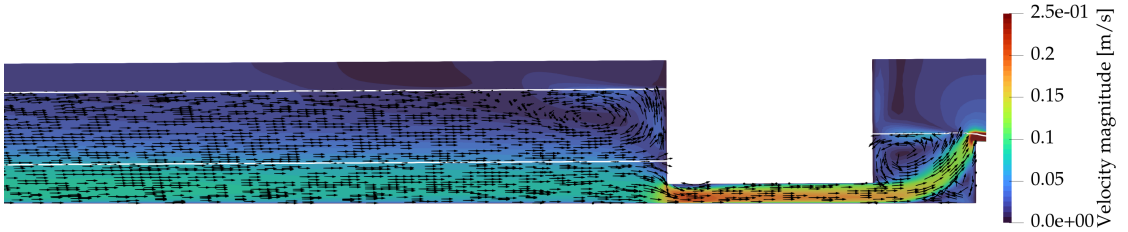
very significant.

Similar remarks apply to Figure 2.16, where the same contours and vectors are displayed at $t = 150$ s but in the final part of the BF trough, corresponding to the part where the slag runner goes sideways, the skimmer and the iron dam. Here, the contour $\alpha_{hm} = 0.5$ is shown in addition to the contour $\alpha_{slag} = 0.5$ as a white curve. Just before the iron dam, we notice that two hot metal circulations form around the main current similar to those observed in the physical scale model studied in Begnis & Brandaleze (2006). The flow underneath the skimmer is substantially stronger in Run A, as more hot metal is being drained from the BF. Before the skimmer, it is observed that the hot metal flow is plug-like, without any complicated recirculating structures. In contrast, a large circulation of slag forms as it reaches the skimmer wall and, in Run A, slag is going backwards in the free surface with the air, and is dragged with hot metal near the slag-iron interface.

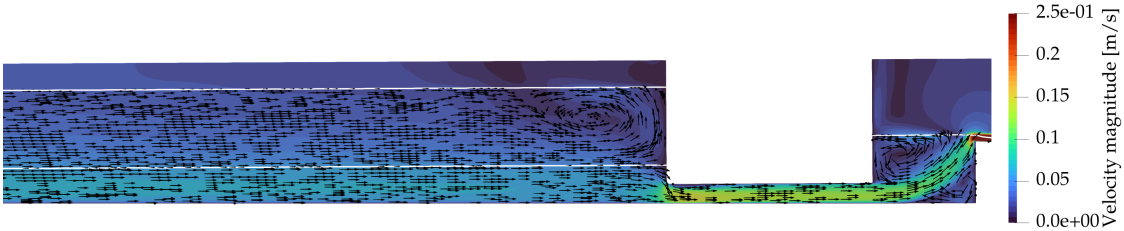
To further analyse the main flow features, in Figure 2.17, the velocity vectors are depicted on the plane $x_2 = 1.15$ m, with velocity magnitude contours. As in the previously discussed cases, we consider a maximum velocity contour of 1.5 m/s, and the results corresponds to the averaged variables over the interval $(125, 150]$ s. While in all runs the higher velocities are observed in the vicinity of the jet impingement region, the numerical findings for Run A show substantially different flow structures than those for Run B and C. Namely, we observe that in Run A, two symmetrical high-speed currents form near the working lining sidewalls, and two large recirculations of slag are generated downstream



(**a**) Run A.



(**b**) Run B.



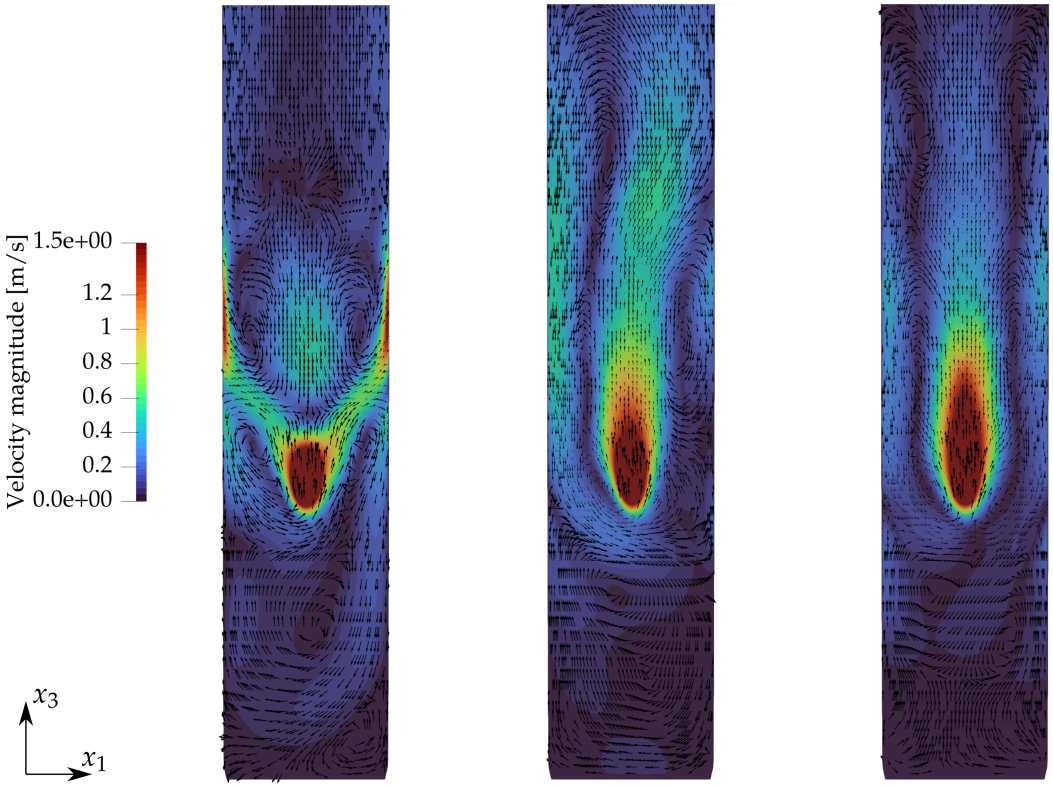
(**c**) Run C.

Figure 2.16: Skimmer and slag runner zone: velocity vectors on the plane $x_1 = 1.5$ m, with contour lines corresponding to $\alpha_{slag} = 0.5$ and $\alpha_{hm} = 0.5$, coloured by velocity magnitude contours. The results correspond to averages over $(125, 150]$ s.

of the jet. In contrast, in Runs B and C, the currents along the sidewalls near the jet are flowing backwards at much lower velocities. Two recirculations are also observed downstream of the jet, but flowing in the opposite direction as in Run A. Upstream of the jet entry zone, complicated vortices are observed with secondary eddies at low speeds. Similarly, in Figure 2.18, the velocity vectors are also shown but on the plane $x_2 = 1.5$ m instead. Since the displayed results are close to the slag-air interface, the predicted velocities are much lower and the jet shows essentially no spreading. In Runs B and C, slag is flowing backwards along the sidewalls, and in the latter case, the flow seems slightly more developed, with symmetrical circulations both downstream and upstream of the jet entry region.

The computed velocities clearly show that the flow structures in the trough are heavily-dependent on the slag and hot metal rates, even if volumetric flow rate is kept constant as it has been done in this study. This is especially true if slag and hot metal are being tapped simultaneously, resulting in quite different flow features compared to the typical flow conditions at the start of the tapping process, when only hot metal is being drained from the BF. Complicated flow structures, with return currents of both slag and hot metal are observed in all the analysed runs.

In Figure 2.19, the averaged v_3 contours are shown at times $t = 100$ s (top row) and $t = 150$ s (bottom row) on the cross-section $x_3 = 7.35$ m. Little time dependency is observed, and similar velocity profiles are found in slag and hot metal over time, after noting that the main differences occurring in



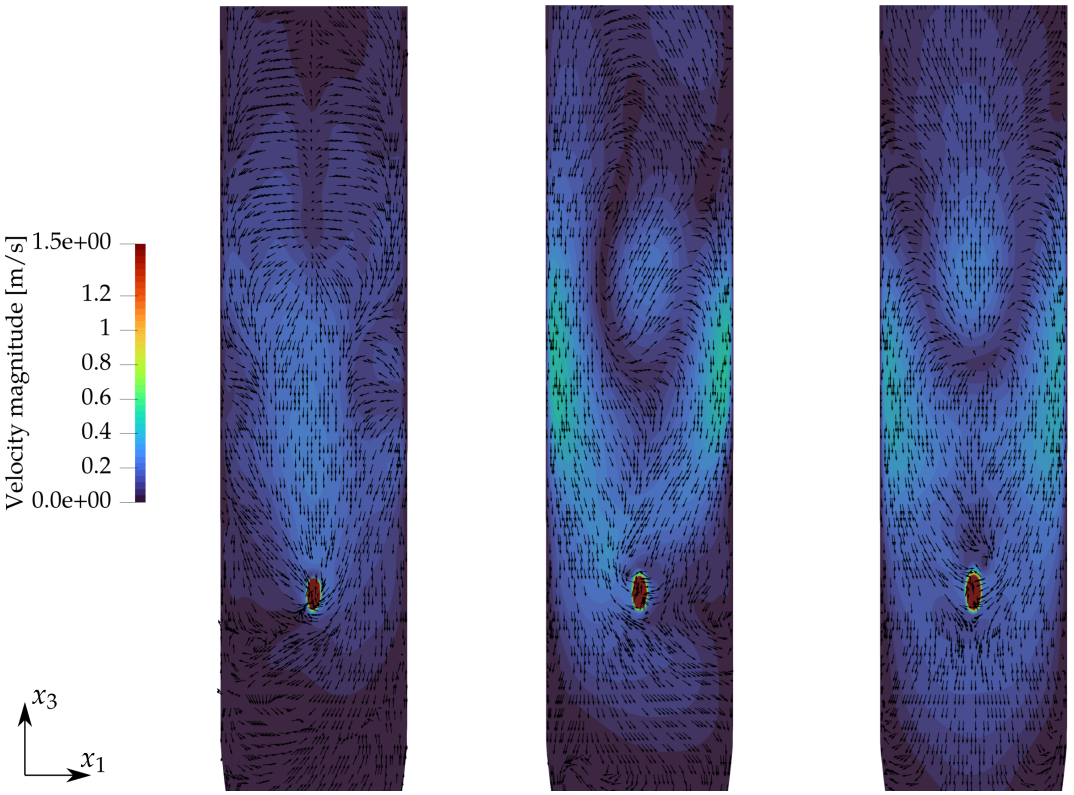
(**a**) Run A. (**b**) Run B. (**c**) Run C.

Figure 2.17: Jet impingement zone: velocity vectors on the plane $x_2 = 1.15$ m, with velocity magnitude contours. All the results correspond to averages over $(125, 150]$ s.

Run C are in the air portion of the cross-section. In Run A, in accordance with the previously discussed results, only hot metal flows downstream of the trough at a significant speed, and two backwards-advancing slag currents form in the walls. With the arrival of slag from the BF in Runs B and C, the slag flow develops, although small backwards slag currents still appear in the cross-section. These completely disappear towards the end of the tapping, as in Run C, and the flow in the slag is apparently fully developed. In contrast, the hot metal flow at this section is not completely developed. If the same averaged v_3 contours are analysed in Figure 2.20 on the $x_3 = 11$ m cross-section instead, the flow of hot metal and slag in Runs B and C seems to be a developed flow with no significant effects other than both fluid phases flowing downstream of the trough. Nevertheless, if only hot metal is being drained from the BF, the same complicated currents with slag advancing backwards are still observed.

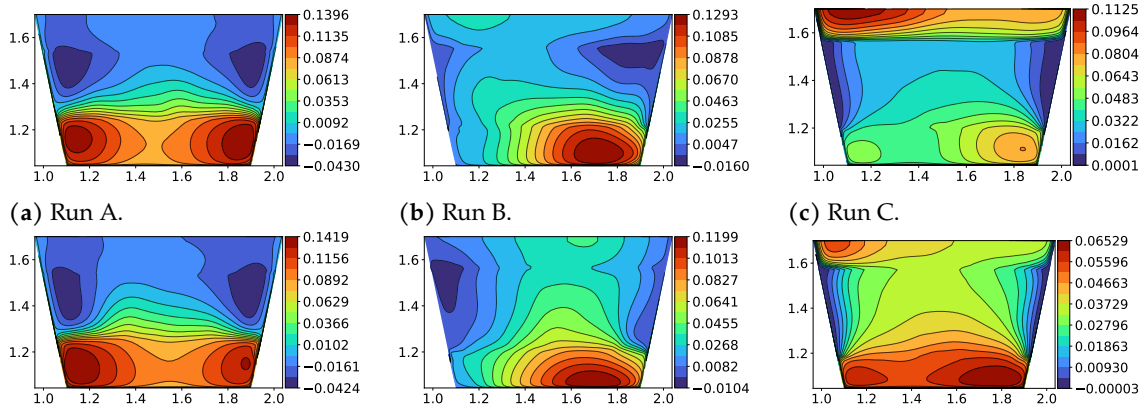
Regarding the influence of the tapping stage in the shear stress, in Figure 2.21 the corresponding contours of the averaged shear stress and pressure at $t = 150$ s are displayed. A substantial dependence of the shear stress on the composition of the jet is found, as the maximum stress values for Run A are above 40% higher than in Run C. Moreover, the zone with large stress values is more spread. The pressure contours also show a slightly different qualitative behaviour, as with slag tapping, a low pressure zone forms directly upstream of the impingement point. In addition, the pressure exerted by the jet impact on the trough is much larger in Run A. This is possibly a consequence of the high viscosity of slag, which prevents the jet from reaching the surface at larger speeds, as it slows down due to the high shear induced among the slag in the jet and that in the fluid pool. The velocity contours depicted in Figure 2.15 also illustrate this effect, as a much larger spread of the jet when it is composed by both slag and hot metal is observed.

In Figure 2.22, the averaged shear stress and pressure for all the runs is compared at times $t = 75$



(**a**) Run A. (**b**) Run B. (**c**) Run C.

Figure 2.18: Jet impingement zone: velocity vectors on the plane $x_2 = 1.5$ m, with velocity magnitude contours. All the results correspond to averages over $(125, 150]$ s.

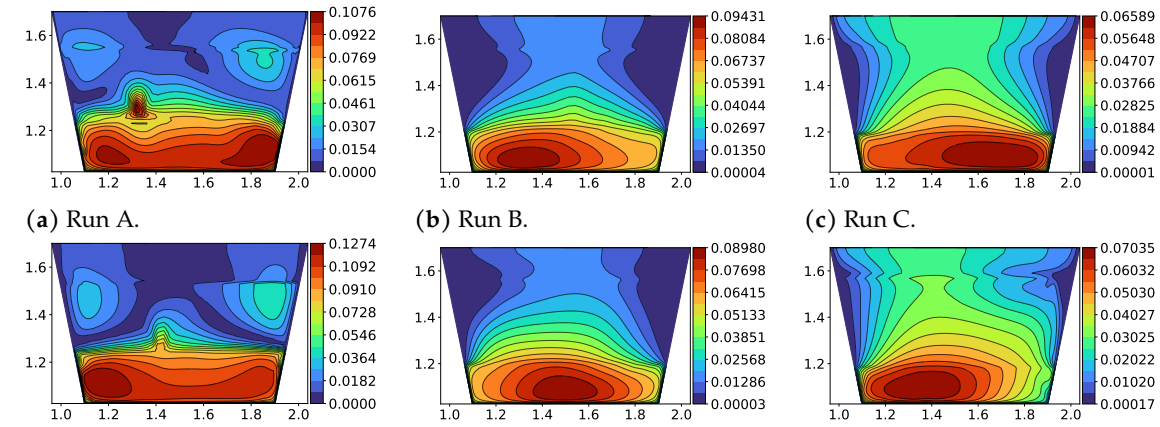


(**a**) Run A. (**b**) Run B. (**c**) Run C.

(**d**) Run A. (**e**) Run B. (**f**) Run C.

Figure 2.19: Plane cross-section at $x_3 = 7.35$ m. Top: v_3, averaged over $(75, 100]$ s. Bottom: v_3, averaged over $(125, 150]$ s.

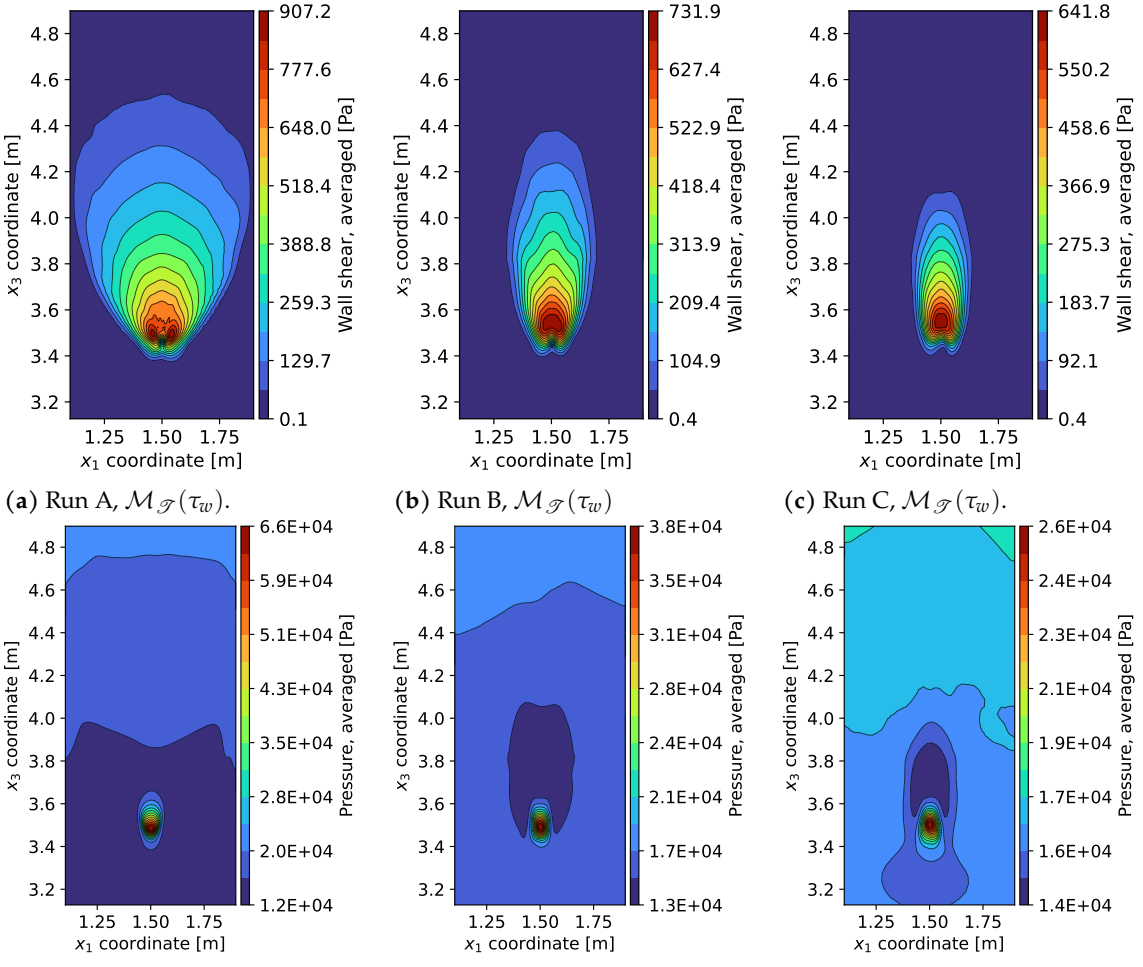
USC UNIVERSIDADE DE SANTIAGO DE COMPOSTELA



(**a**) Run A. (**b**) Run B. (**c**) Run C.

(**d**) Run A. (**e**) Run B. (**f**) Run C.

Figure 2.20: Plane cross-section at $x_3 = 11$ m. Top: v_3, averaged over $(75, 100]$ s. Bottom: v_3, averaged over $(125, 150]$ s.

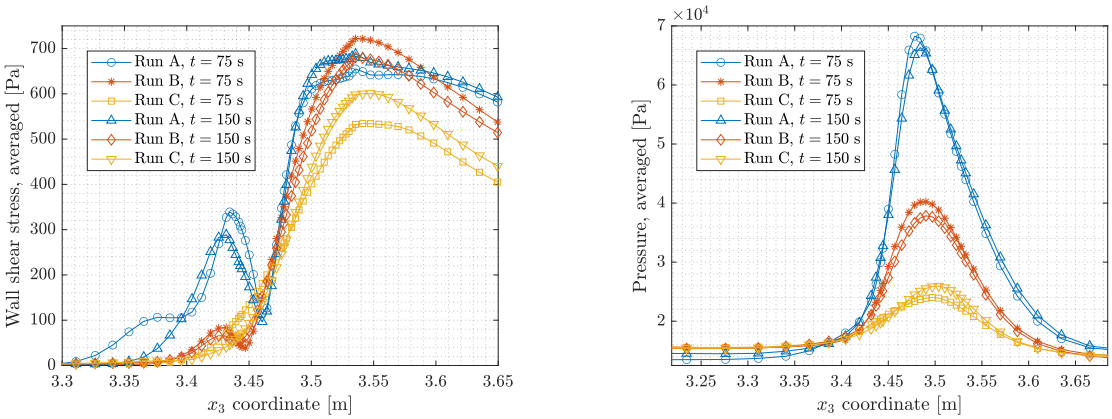


(**a**) Run A, $\mathcal{M}_{\mathscr{T}}(\tau_w)$. (**b**) Run B, $\mathcal{M}_{\mathscr{T}}(\tau_w)$ (**c**) Run C, $\mathcal{M}_{\mathscr{T}}(\tau_w)$.

(**d**) Run A, $\mathcal{M}_{\mathscr{T}}(p)$. (**e**) Run B, $\mathcal{M}_{\mathscr{T}}(p)$. (**f**) Run C, $\mathcal{M}_{\mathscr{T}}(p)$.

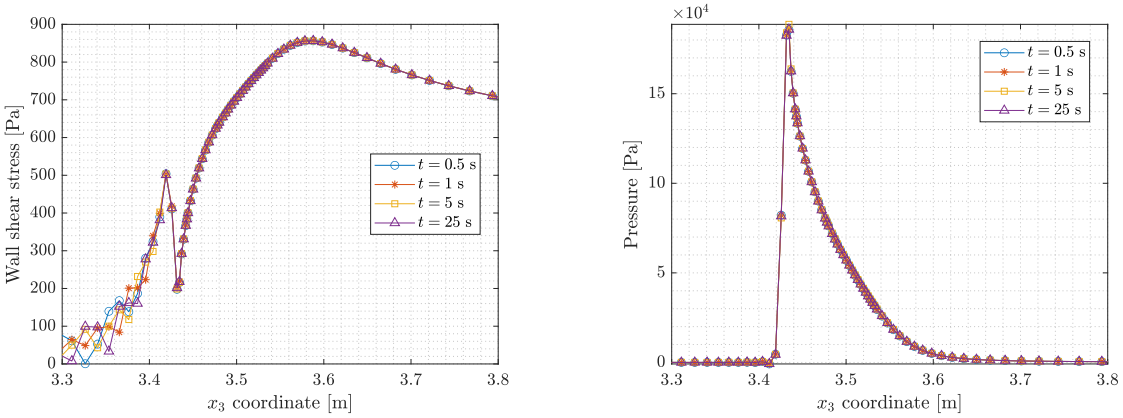
Figure 2.21: Averaged wall shear stress ($\mathcal{M}_{\mathscr{T}}(\tau_w)$) and pressure ($\mathcal{M}_{\mathscr{T}}(p)$) on the wall at the jet impingement zone at $t = 150$ s for Runs A-C. The averaging is performed over $(125, 150]$ s.

USC UNIVERSIDADE DE SANTIAGO DE COMPOSTELA



(**a**) Shear stress. (**b**) Pressure.

Figure 2.22: Averaged wall shear and pressure at line crossing the jet impingement area at different time values for Runs A-C. The averaging is performed for $\mathscr{T} = 25$ s.



(**a**) Shear stress. (**b**) Pressure.

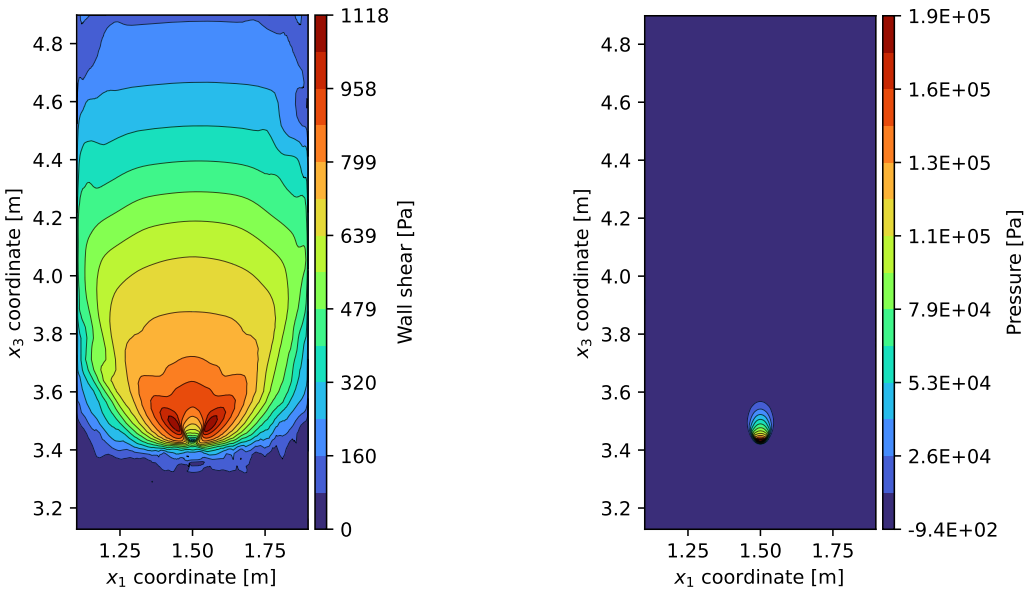
Figure 2.23: Run A*: Wall shear and pressure at line crossing the jet impingement area at various time values.

s and $t = 150$ s on the line dividing the jet impingement area. We find that both the shear stress and pressure are fairly stable during the simulation, with small variations over time in all cases. We note that at Run C, the structure with a local minimum of the shear stress in the impingement point is vanished, whereas in Run B, it is only marginally observed.

2.5.3. Run A*

In Run A*, we are mostly concerned with investigating the shear stress and pressure in the impact point. As there is no pool of fluids to mitigate the jet impact on the refractory, we expect higher values of the shear stress, especially during the first stages of the simulation. First, we note that, as depicted in figure 2.13d, a small hot metal layer is formed in the impingement point. Thus, in contrast with the prior cases, no significant air entrainment is predicted and the phenomena associated to trapped slag bubbles in the hot metal have also disappeared. Consequently, there is no need to filter the results to eliminate fluctuations in the volume fractions using the procedure detailed in Remark 2.7.

In Figure 2.23, the shear stress and pressure are depicted along the line crossing the jet impingement area for different time values. Again, as in Run A, a minimum of the shear stress curve in the stagnation point due to the jet impact on Γ_{wall} is observed, with non-symmetrical maximums around



(**a**) Shear stress.

(**b**) Pressure.

Figure 2.24: Run A*: Wall shear stress and pressure on the jet impingement area at $t = 25$ s.

it. The time dependency is essentially negligible and both the computed shear stress values and pressure are just slightly above those discussed in Section 2.5.2. This suggests that the role played by the pool of fluids in the impact mitigation is small. However, as showcased in Figure 2.24, if the shear stress and pressure contours are analysed in the complete impingement area, the shear stress values are substantially larger. The high-shearing zone spreads, and the maximum computed shear stress is approximately 23% larger in Run A* compared to Run A. This maximum value is very similar to that found in Barral et al. (2021) for a plane hot metal jet with a thin fluid pool, where also no significant time dependency of the results was observed. On the other hand, the computed pressure values are remarkably higher in Run A* if compared to those observed in Runs A-C. For instance, directly comparing the pressure curves in Figure 2.22b with those in Figure 2.23b we observe that the pressure is almost three times higher in Run A* when compared to Run A.

USC
UNIVERSIDADE DE SANTIAGO DE COMPOSTELA

USC
UNIVERSIDADE
DE SANTIAGO
DE COMPOSTELA

Chapter 3

Steady 3D thermo-hydrodynamic model

The scope of this chapter is to provide a mathematical model of the heat transfer in the BF trough that can yield predictions of the temperature field within the refractory linings. This could allow to find the position of the critical isotherms in the concrete refractories which, as discussed in Chapter 1, are strongly related to the refractory lining degradation. To simplify the model, a steady-state is assumed, neglecting any effect that the tapping process stops may have in the temperature. This effect is addressed in Chapter 5, where the heat transfer in a 2D cross-section of the BF trough during a campaign cycle is investigated.

Despite thermal effects being regarded as one of the triggers of refractory wear, very few works have dealt with heat transfer modelling in the specific setting of the BF trough. In the recent years, some authors have used CFD models to obtain temperature predictions in the trough. In particular, L. Wang et al. (2017) considered buoyancy-induced effects in the fluids, but heat transfer was addressed in a rather idealised setting, setting a constant wall temperature in the refractory hot face, and thereby excluding the solids from the model. Moreover, in Ge et al. (2020), the flow in the trough was studied, including the conjugate heat transfer with the working lining, but assuming a single-phase flow with mixture properties. A similar model was used in H. Yao et al. (2021), utilising hot metal instead, incorporating a linear thermoelastic problem to find the thermal stresses in the refractory.

None of the previous works attempted to describe the radiative heat transfer which, due to the high temperatures, is believed to be the dominant heat transfer mode in the trough. In the best of our knowledge, the only works in the open literature that have addressed this issue are Vázquez-Fernández et al. (2019) and our preliminary work Barral et al. (2019). The former solved the steady heat equation in a 2D cross-section of the trough, considering radiative heat exchange from the slag surface with the working lining, but neglecting the influence of the refractory cover. The latter also dealt with the steady-state temperature field but, instead, a 3D configuration was proposed, adding the cover as well as the forced air flow due to fume extraction. Moreover, in Vázquez-Fernández (2015), a previous version of the 2D model used in Vázquez-Fernández et al. (2019) was presented. On the other hand, Seoane (2016) considered a 3D model, but only on a small portion of the trough, applying a symmetry condition. The radiative heat exchange was also incorporated in a simplified setting, without including the refractory cover.

In this chapter, we aim to enhance the model and numerical methodology presented in Barral et al. (2019) in various aspects: first, instead of an analytical velocity profile for the slag and hot metal inlet velocity, we consider the output of the mathematical model solved in Chapter 2 to pose more realistic boundary conditions. Furthermore, we discard the assumption that the forced air flow due to the fume aspiration remains at a spatial constant density. Instead, we retain the density variations due to the temperature increase as it flows through the region below the cover. The numerical methodology is also improved, avoiding the need to compute a quasi-steady-state for a decoupled transient hydrodynamic problem. Lastly, we analyse the dependency of the results on the velocity of the forced circulation of air. Nonetheless, we maintain several assumptions, namely, we set as computational domain only the part of the runner where the flow of slag and hot metal is well-developed. Thus, we can assume that slag and hot metal are well separated by density difference, and use the solution computed in the previous chapter as an inlet boundary condition. Furthermore, the position of the interfaces with air, which was found to be essentially plane downstream of the impingement point, is fixed at the computed height at the end of Run C. In addition, the flow of hot metal and slag is assumed to be incompressible.

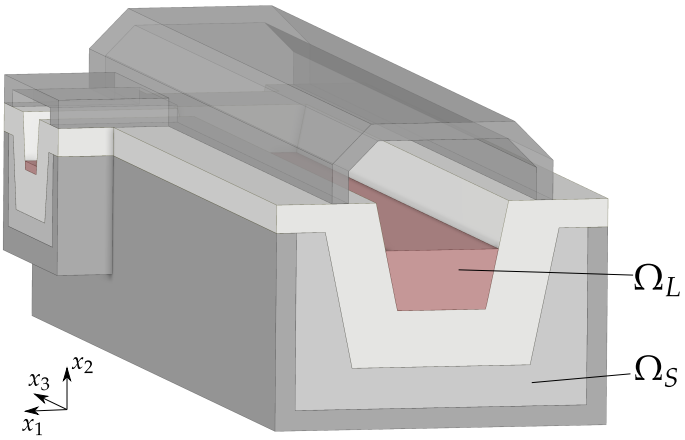


Figure 3.1: Solid (Ω_S) and slag/hot metal subdomains (Ω_L). The different layers (working, safety and insulation linings, as well as the cover) forming the solid part of the trough are highlighted in different colours.

The structure of the chapter is the following. In Section 3.1, the mathematical model is presented in detail, including a brief derivation of the general energy conservation equation, the description of the boundary conditions and the computational domain, as well as the technique used to address thermal radiation. Subsequently, Section 3.2 is devoted to introduce the numerical methodology and the grid that is used to solve the model. Lastly, in Section 3.3, we discuss the obtained numerical results, first presenting a grid validation study and then addressing the temperature in the BF trough for various values of the parameter v_{air}, which corresponds to the air velocity at the inlets.

3.1. Mathematical model

In this section, we introduce the mathematical model that is developed to address the steady-state of the temperature in the BF runner. As mentioned previously, we assume that the flow of hot metal and slag is incompressible and that the physical properties of both fluids remain at constant property values. In the previous chapter, it was observed that, downstream of the jet impingement point, the flow is well-developed with the slag-air and hot metal-air free surfaces remaining essentially plane. Hence, in this model, we fix the upper liquid position at a constant height value and avoid tracking the interface with air. However, the interface separating hot metal from slag is not fixed at any particular position and, instead, we utilise the VOF method (see Section 2.3) to find the location of such interface. On the other hand, turbulent effects remain of relevance. Thus, we use the SST $K-\omega$ RANS model to account for turbulence in the flow (see Section 2.2.2).

The outline of this section is the following. First, in Section 3.1.1, the computational domain is introduced. Then, for the sake of completeness, Section 3.1.2 briefly deals with the derivation of the energy conservation equation and the constitutive hypothesis that is considered in this chapter. In Section 3.1.3, the model that is used to account for the radiative heat exchange below the refractory cover is described. Subsequently, Section 3.1.4 is devoted to summarising the equations that are solved in each subdomain and how the involved variables are coupled. Lastly, Section 3.1.5 addresses the boundary conditions that are set to close the mathematical model.

Remark 3.1. *It was initially believed that after around 15 days, the temperature in the bulk of the solids remained roughly stationary given normal operation regime, with short stops among the tappings. In reality, as it is further analysed in Chapter 5, the stops between tappings are long enough in most campaign cycles to induce significant temperature oscillations. This prevents a true steady-state from being reached in the BF trough, even*

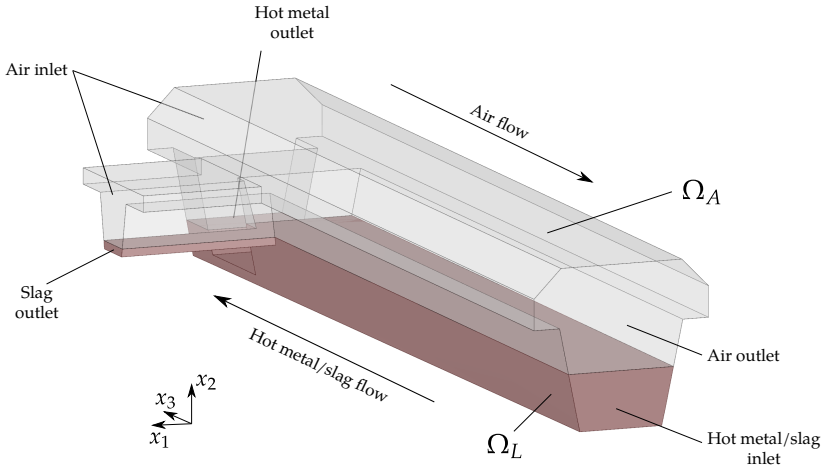


Figure 3.2: Fluid subdomain (Ω_F).

in those areas of the solids that are not directly in contact with slag and hot metal.

Despite this major drawback, the herein problem presented is still interesting, not only from a purely academic viewpoint, but also for the industry, as the steady-state is the worst-case scenario for the temperature field in a perfect condition trough (assuming that no wear has taken place). Therefore, assessing the temperature in the steady-state provides useful information regarding the position of the critical isotherms in that scenario. In addition, some numerical results from this problem are used to devise appropriate boundary conditions for a transient model, specifically designed to address the effect of the casting process stops in Chapter 5.

3.1.1. Computational domain

The computational domain Ω is split in a fluid subdomain, Ω_F, and a solid subdomain, Ω_S, such that $\overline{\Omega} = \overline{\Omega}_F \cup \overline{\Omega}_S$. In Ω_F we consider the part occupied by the air below the refractory cover, denoted as Ω_A; and the subdomain occupied by molten liquids, i.e., slag and hot metal, denoted as Ω_L. In Figure 3.1, the complete computational domain is depicted. The air subdomain has been hidden for clarity purposes.

As mentioned above, only the part of the trough where the flow can be assumed to be developed is considered as part of the computational domain. Specifically, we include only the part of the BF trough such that $x_3 > 7.35$ m, where we recall that x_3 represents the distance to the BF (see the drawings depicted in Figure 1.4). The part of the trough that is modelled in the computational domain is indicated by the discontinuous line in Figure 1.4a, comprising the last 7 m of the main trough before the iron dam. For consistency with the previous results, the origin of coordinates selected in the previous chapter is maintained (see Figure 2.4).

The solid subdomain, Ω_S, is constructed considering the different solid refractory layers introduced in Chapter 1. Nonetheless, we have not considered the steel casing as part of the computational domain. It is the structure over which the BF trough is built, formed by steel shells placed on thick beams, with a set of supporting steel ribs in the bottom. In addition, as depicted in Figure 1.3, lateral fins are incorporated to the casing, which enhance cooling with the air. Since to simulate each of these thin elements would prohibitively increase the computational complexity, modified heat transfer coefficients have been considered to account for their presence by weighting the increase in surface area (see Section 3.1.5).

To obtain the decomposition of Ω_F, depicted in Figure 3.2, the final result of the previous chapter for *Run C* is utilised, assuming that the computed positions of the free surfaces slag-air and hot metal-air at t_{end} correspond to a steady-state and thus, they remain at a constant height. Therefore, the height of the former is set as $h_{slag} = 1.57$ m, whereas the latter is set at $h^*_{hm} = 1.33$ m, thereby considering them as fixed planes in the model. As mentioned previously, the fluid subdomain Ω_F is split by these

planes in a part occupied by hot metal and slag, Ω_L, and another part occupied by air, Ω_A. Also, recall from the discussion above that hot metal and slag are still regarded as different immiscible phases of the flow, and the hot metal-slag interface position is found in Ω_L using the VOF method.

3.1.2. Energy conservation and equation of state

In this section, we provide a formal derivation of the standard energy conservation equation, which is incorporated to the conservation equations derived in Section 2.1. Then, we provide an expression for the equation of state that is used in the air subdomain, since the air circulating above the trough is considered a *weakly compressible* ideal gas. Lastly, some simplifying assumptions are introduced to obtain the corresponding form of the equation that holds in each subdomain. The discussion is not novel by any means and is introduced mainly for the sake of completeness, providing some additional information regarding the hypotheses required to obtain the mathematical model, stated in Section 3.1.4. Thus, its reading can be skipped.

Energy conservation equation

Recall from Section 2.1 that $\mathcal{B}$ denotes a body, i.e. a regular region in the Euclidean space, whereas $\mathcal{P}_t$ is the region occupied by an arbitrarily selected part $\mathcal{P} \subset \mathcal{B}$ at the time instant t. Set $(\boldsymbol{s}, \mathbf{b})$ as a system of forces and let (g, f) be a *system of heat* (Bermúdez, 2005), both defined on the trajectory of a motion X. The scalar field $g(\boldsymbol{\eta}, \mathbf{x}, t)$ denotes the *surface heat density*, with $\boldsymbol{\eta}$ being a unit vector. Moreover, $f(\mathbf{x}, t)$ is the heat per unit volume and time supplied by the environment. In the sequel, the procedure to obtain the energy equation is briefly sketched. For the sake of simplicity, we omit the dependency on the spatial point $\mathbf{x}$ and the time instant t of the involved fields when there is no risk of confusion.

The *First Principle of Thermodynamics* states that there exists a scalar field E_{tot}, called *specific total energy*, such that for every part $\mathcal{P}$ and time t, it holds that:

$$\frac{d}{dt}\int_{P_t} \rho E_{tot}\, dV = \int_{\partial P_t} \boldsymbol{s}(\mathbf{n}) \cdot \mathbf{v}\, dA + \int_{P_t} \mathbf{b} \cdot \mathbf{v}\, dV - \int_{\partial P_t} g(\mathbf{n})\, dA + \int_{P_t} f\, dV.$$

Furthermore, it can be shown that there exists a vector field $\mathbf{q}$, called *heat flux*, such that $g(\boldsymbol{\eta}, \mathbf{x}, t) = \mathbf{q}(\mathbf{x}, t) \cdot \boldsymbol{\eta}$ for each unit vector $\boldsymbol{\eta}$ (Bermúdez, 2005, Th. 1.4.3). Let e denote the *specific internal energy*, a scalar field defined as the total specific energy minus the kinetic energy, i.e.:

$$e = E_{tot} - \frac{|\mathbf{v}^2|}{2}.$$

Then, the subsequent local form of the energy conservation equation is satisfied:

$$\frac{\partial(\rho e)}{\partial t} + \operatorname{div}(\rho e \mathbf{v}) = \mathbf{T} : \mathbf{D}(\mathbf{v}) - \operatorname{div}(\mathbf{q}) + f, \tag{3.1}$$

where the colon denotes the double contraction of tensors, which for $\mathbf{A}$ and $\mathbf{B}$ being second-order tensors is simply defined as $\mathbf{A} : \mathbf{B} = A_{ij}B_{ij}$, considering the Einstein summation convention regarding repeated indices.

In flows with appreciable compressibility, the energy conservation equation (3.1) is often rearranged in terms of the *specific enthalpy*, $\mathcal{H}$, defined as

$$\mathcal{H} = e + \frac{p}{\rho}, \tag{3.2}$$

where we recall that p denotes the pressure of the fluid.

If the fluid is assumed to belong to the Newtonian class, substituting (3.2) in (3.1) and applying the constitutive law for the stress tensor (2.5), yields the subsequent conservation equation for the specific enthalpy:

$$\frac{\partial(\rho \mathcal{H})}{\partial t} + \operatorname{div}(\rho \mathcal{H} \mathbf{v}) = \mathbf{T}_v : \mathbf{D}(\mathbf{v}) + \left(\frac{\partial p}{\partial t} + \operatorname{grad}(p) \cdot \mathbf{v}\right) - \operatorname{div}(\mathbf{q}) + f, \tag{3.3}$$

USC UNIVERSIDADE DE SANTIAGO DE COMPOSTELA

where $\mathbf{T}_v$ is the viscous part of the stress tensor, introduced in (2.4).

Constitutive assumption

In addition to the constitutive assumption that provides a suitable expression for the stress tensor, additional assumptions are required for the heat flux $\mathbf{q}$. We assume that only heat conduction is relevant, as the fluids and solids involved in the mathematical model are either assumed transparent or opaque to thermal radiation (see Section 3.1.3). Then, the heat flux is usually modelled by assuming that the subsequent constitutive hypothesis, called *Fourier's law*, holds:

$$\mathbf{q} = -k \operatorname{grad}(T),$$

where T is a scalar field representing the *temperature*. If the material is isotropic, then it can be shown that k is also a scalar field, known as the *thermal conductivity* of the material (Gurtin, 1982).

Equation of state

The air that enters the computational domain through the defined inlets (see Figure 3.2) does so at ambient temperature, which we set as 293 K. After exposure to the high temperature surroundings below the refractory cover, it heats rapidly, leading to non-negligible density changes. In particular, we assume that all air physical properties are constant except for the density (see Table 1.1b). To model the density variations, we assume that air is an *ideal* or *perfect* gas, which satisfies the subsequent equation of state:

$$p = \rho R_g T, \tag{3.4}$$

where the *gas constant* R_g is such that $R_g = \mathcal{R}/M_w$, being M_w the molar mass and $\mathcal{R} = 8.3145$ J/(mol·K) the *universal gas constant*.

The specific enthalpy and heat of a perfect gas only depend on temperature and, in particular, since we assume that the specific heat is constant, i.e., that the gas is *calorically perfect*, it holds that (see e.g. Bermúdez, 2005):

$$\mathcal{H}(T) = \mathcal{H}_0 + \int_{T_0}^{T} c_p(s)\, ds = \mathcal{H}_0 + c_p(T - T_0), \tag{3.5}$$

where $\mathcal{H}_0$ is the *enthalpy of formation* and T_0 the *temperature of formation* or *reference temperature*. For simplicity, as they bear no influence in the computations, we consider the enthalpy of formation and the reference temperature as zero.

The pressure p can be decomposed in a spatially-constant part, p_{op}, and a fluctuation, called *gauge pressure*, $\widetilde{p}$:

$$p(\mathbf{x}, t) = \widetilde{p}(\mathbf{x}, t) + p_{op}(t). \tag{3.6}$$

The field p_{op} is often referred to as *operating pressure*. Since we are interested only in the steady-state, the temporal dependence of the operating pressure is also removed, rendering it as a constant. In particular, we consider it equal to the standard atmospheric pressure, i.e., $p_{op} = 101325$ Pa.

To assess the importance of pressure-related compressibility effects, the Mach number is used, defined for ideal gases as

$$Ma = \frac{\mathscr{V}}{\sqrt{\dfrac{c_p}{c_v} R_g \theta}}, \tag{3.7}$$

where c_v is the *specific heat at constant volume*, $\mathscr{V}$ is a characteristic velocity and θ denotes a characteristic temperature. The denominator in (3.7) is the speed of sound in the perfect gas, and the specific heat at constant volume of a perfect gas is related to that at constant pressure through Mayer's equation, i.e., $c_v = c_p - R_g$ (see e.g. Kundu et al., 2015).

In low-Mach number flows, the pressure changes due to the dynamic effects, included in the gauge pressure, $\widetilde{p}$, are much smaller than the operating pressure. In particular, for the air flow in the BF trough, we consider $\mathscr{V} = 10$ m/s and $\theta = 293$ K. Then, substituting with the values in Table 1.1b for

air in (3.7), using that $R_g = 296.9464\,\mathrm{J/(kg{\cdot}K)}$, we find that $Ma \approx 2.85e-2$. Therefore, since $Ma \ll 1$, after substitution of (3.6) in (3.4), the term due to $\widetilde{p}$ can be neglected, obtaining the following new equation of state:

$$\rho(T) = \frac{p_{op}}{\frac{\mathcal{R}}{M_w}T},$$

where the density of the fluid only depends on the local temperature value.

Note that compressible flows with $Ma \ll 1$ are often referred to as *weakly compressible*, since the hydrodynamical behaviour is that of an incompressible flow, and the density variations are mostly due to temperature changes.

Remark 3.2. *To avoid incurring in excessive round-off error, since in a flow with low-Mach number the operating pressure is much larger than the gauge pressure, it is customary to subtract the operating pressure from the momentum and energy conservation equations. Note that it does not affect the computed solution, which is defined up to a constant pressure value. Therefore, in those equations, after substituting with (3.6), only the term involving the gauge pressure is retained.*

Subsequently, we obtain specific forms of the energy conservation equation that arise from considering particular assumptions on each of the involved subdomains within Ω.

Energy conservation in Ω_A

In the air subdomain, we denote the corresponding specific enthalpy and temperature as $\mathcal{H}_A$ and T_A, respectively. In general, the subscript A denotes those variables and properties that correspond to air. Then, we assume that (3.3) holds in Ω_A:

$$\mathrm{div}(\rho_A \mathcal{H}_A \mathbf{v}_A) = \mathbf{T}_{v,A} : \mathbf{D}(\mathbf{v}_A) + \mathrm{grad}(p_A) \cdot \mathbf{v}_A + \mathrm{div}(k_A \mathrm{grad}(T_A)), \tag{3.8}$$

where the term involving the time derivative has been dropped in virtue of the steady-state assumption. Also, it has been set that the body heat is $f = 0$, provided that there are no heat sources in the problem.

Using dimensional analysis arguments, by obtaining the dimensionless analogue of (3.3), it can be shown that the following terms have the subsequent orders of magnitude (see e.g. Busto, 2018, and the references therein):

$$\mathbf{T}_v : \mathbf{D}(\mathbf{v}) \sim \frac{Ec}{Re}, \tag{3.9}$$

$$\frac{\partial p}{\partial t} + \mathrm{grad}(p) \cdot \mathbf{v} \sim Ec, \tag{3.10}$$

where the Reynolds number, Re, was introduced in (2.10) and Ec is the *Eckert number*, defined as:

$$Ec = \frac{\mathscr{V}^2}{c_p \Delta\theta},$$

with $\Delta\theta$ being the difference among the local flow temperature and the wall temperature.

The left hand sides of (3.9) and (3.10) are called the *viscous heating* and *pressure work* terms, respectively. For the BF trough system, it is reasonable to estimate a very large difference between the air flow and wall temperatures, reaching $\Delta\theta \sim 10^3$ K. Therefore, the Eckert number is very small, which implies that the pressure work term can be neglected. Furthermore, as the Reynolds number is also large, the viscous heating term is also negligible. Hence, (3.8) is rewritten as:

$$\mathrm{div}(\rho_A \mathcal{H}_A \mathbf{v}_A) - \mathrm{div}(k_A \mathrm{grad}(T_A)) = 0.$$

Furthermore, since the flow is turbulent, the enhanced diffusivity due to the turbulent eddies is modelled by incorporating the *turbulent thermal conductivity*, k_T, defined as

$$k_T = \frac{\mu_T c_p}{Pr_T}, \tag{3.11}$$

USC UNIVERSIDADE DE SANTIAGO DE COMPOSTELA

where $Pr_T = 0.85$ is the turbulent Prandtl number and μ_T is the eddy viscosity, computed using (2.16). Consequently, in Ω_A, we seek a temperature T_A such that

$$\operatorname{div}(\rho_A \mathcal{H}_A \mathbf{v}_A) - \operatorname{div}\big((k_A + k_{T,A})\operatorname{grad}(T_A)\big) = 0, \tag{3.12}$$

where $k_{T,A}$ is simply (3.11) considering the property values corresponding to air, gathered in Table 1.1b. Also, note that the specific enthalpy, velocity and temperature appearing in (3.12) should be regarded as the corresponding averaged fields, which we denote as the instantaneous values for simplicity (see Section 2.2). Lastly, note that the specific enthalpy $\mathcal{H}_A$ is directly related to the temperature through (3.5).

Remark 3.3. *In compressible flow with significant density variations, to obtain the suitable RANS equations requires to account for density and temperature fluctuations in addition to those involving velocity and pressure. If the standard Reynolds decomposition and averaging operator introduced in (2.11) and (2.12) are used to obtain the RANS equations, several additional terms arise that require closure assumptions. However, it is possible to avoid this complexity by using the so-called Favre averaging procedure, denoted as $\langle\cdot\rangle_F$. For an arbitrary flow variable ϕ, it yields a mass-averaged variable as follows:*

$$\langle\phi\rangle_F = \frac{\langle\rho\phi\rangle}{\langle\rho\rangle},$$

where $\langle\cdot\rangle$ is the conventional averaging operator, defined in (2.12).

The procedure decomposes the instantaneous flow variable ϕ into the mass-averaged part and the fluctuating part ϕ'':

$$\phi = \langle\phi\rangle_F + \phi''.$$

To obtain the averaged equations, the conventional Reynolds decomposition is considered for the density and pressure, whereas the Favre decomposition is considered for the remaining variables. Then, as shown in Wilcox (2006, Ch. 5), a system of equations analogous to that obtained for an incompressible flow is obtained, where the only difference is that the terms that require modelling involve now products of the new fluctuations. Therefore, in the air, the averaged fields that appear in the equations should be understood as Favre-averaged fields instead of standard Reynolds-averaged fields. However, from the computational standpoint, the equations that are solved are identical to those resulting from the standard Reynolds averaging.

Energy conservation in Ω_L

In the liquid subdomain, corresponding to hot metal and slag, to distinguish the corresponding fields from those of the air subdomain, we use the subscript L. The flow within this domain is assumed to be incompressible with constant property values. Furthermore, since the viscous heating term and pressure work terms are also negligible, from (3.3), we seek

$$\operatorname{div}(\widehat{\rho}\,\mathcal{H}_L \mathbf{v}_L) - \operatorname{div}(\widehat{k}\,\operatorname{grad}(T_L)) = 0. \tag{3.13}$$

Note that, since in Ω_L the position of the interface separating hot metal and slag is not known, we are using the VOF method to track it, as mentioned above. Therefore, in (3.13), the physical property values are taken as mixture properties (see Section 2.3), combining the constant values of hot metal and slag as follows:

$$\widehat{\rho} = \rho_{hm}\alpha_{hm} + \rho_{slag}(1 - \alpha_{hm}), \tag{3.14}$$

$$\widehat{k} = k_{hm}\alpha_{hm} + k_{slag}(1 - \alpha_{hm}), \tag{3.15}$$

where α_{hm} is the hot metal volume fraction and the constant values of the density of slag and hot metal, ρ_{slag} and ρ_{hm}, as well as those corresponding to the thermal conductivities, k_{slag} and k_{hm}, are taken from Table 1.1b.

The expression (3.5), which relates the temperature and specific enthalpy for an ideal gas, also holds for incompressible fluids. Hence, we obtain from (3.13) the subsequent equation, which only involves the temperature in Ω_L:

$$\widehat{\rho}\widehat{c}_p \mathrm{grad}(T_L) \cdot \mathbf{v}_L - \mathrm{div}(\widehat{k}\,\mathrm{grad}(T_L)) = 0, \tag{3.16}$$

where $\widehat{c}_p$ is defined in an analogous manner to (3.14)-(3.15). Note that (3.16) is the classical heat equation with a convection term due to the flow motion.

Also, since the flow is turbulent, we consider the corresponding equation involving Reynolds averaged variables and the turbulent thermal conductivity as above:

$$\widehat{\rho}\widehat{c}_p \mathrm{grad}(T_L) \cdot \mathbf{v}_L - \mathrm{div}\big((\widehat{k} + \widehat{k}_T)\mathrm{grad}(T_L)\big) = 0.$$

Here, the turbulent thermal conductivity is computed with the corresponding mixture properties, i.e.:

$$\widehat{k}_T = k_{T,hm}\alpha_{hm} + k_{T,slag}(1 - \alpha_{hm}),$$

where $k_{T,hm}$ and $k_{T,slag}$ are the conventional turbulent thermal conductivity (3.11) substituting with the property values of hot metal and slag, respectively.

Energy conservation in Ω_S

Lastly, in the solid subdomain, Ω_S, we consider a rigid solid and we only model heat transfer by conduction. In this case, T_S is the temperature in the solid, which satisfies that:

$$\mathrm{div}\big(k_S(\mathbf{x}, T_S(\mathbf{x}))\mathrm{grad}(T_S(\mathbf{x}))\big) = 0.$$

In the previous expression, we have kept the dependency on the spatial point $\mathbf{x}$ as well as that on temperature T_S, provided that piecewise constant conductivity values are considered. The constant values depend on the solid layer and take the values gathered in Table 1.1a. Also, the insulation lining thermal conductivity is temperature-dependant, using the function (1.1).

3.1.3. Radiation modelling

In Chapter 1, it has been discussed that, due to high temperatures that are reached, radiation heat transfer from the slag-air free surface to the exposed areas of the working lining and the cover plays a key role in heat transfer in the BF trough system. Thus, an appropriate model is required to account for it.

We assume that both slag and hot metal are *opaque* to radiation, as well as all the solids. Note that, in reality, slag is not opaque but semi-transparent. However, in all the situations portrayed in the previous chapter, the thickness of the slag layer in the trough has been shown to be above 30 cm, which is well-above the thickness required for a standard BF slag to be optically thick (Mills, 2011). Therefore, radiation can be assumed to only take place between the surfaces surrounding the air subdomain, Ω_A. It may be seen as a radiation cavity, where the radiative heat exchange occurs among the surfaces delimiting its boundaries. Here, we note that it is not a closed cavity (an *enclosure*), as the fictitious boundaries –the air inlets and outlets– require some special attention.

To account for radiation heat transfer, the *surface-to-surface model* (S2S) is used, also called *net radiation method* (Howell et al., 2015). It is a relatively simple model, but it is well suited to the nature of the problem. It was also used in similar settings, such as in Khodabandeh et al. (2017), where it was used to obtain the radiative flux inside an electric arc furnace. The S2S model describes radiation heat transfer among a set of M_i *grey*, *diffuse* and *opaque* surfaces defining an enclosure, with $i = 1, \ldots, N_S$, being N_S the total number of surfaces. The medium within the surfaces –air– is assumed to be a non-participating medium that is totally transparent to incident radiation. Each of these surfaces is

considered to be at a constant temperature T_i and, with these assumptions, the net radiation exchange between surfaces i and j may be obtained evaluating:

$$R_i = E_i + (1 - \varepsilon_i) \sum_{j=1}^{N_S} F_{ij} R_j, \tag{3.17}$$

where $E_i = \sigma \varepsilon_i T_i^4$ is the *emissive power* of surface i according to Stefan-Boltzmann's law, ε_i is the *emissivity*, R_i is the outgoing energy from surface i, known as *radiosity* and $\sigma = 5.67 \cdot 10^{-8}$ W/(m^2·K^4) is the Stefan-Boltzmann constant. In addition, F_{ij} is the *view factor* between the surfaces M_i and M_j, which is computed as follows

$$F_{ij} = \frac{1}{\text{meas}(M_i)} \int_{M_i} \int_{M_j} \frac{\cos\psi_i \cos\psi_j}{\pi r^2} \delta_{ij} \, dA_j dA_i.$$

In the previous expression, ψ_i is the plane angle between surface i normal vector and the vector pointing from i to j, whereas r denotes the distance among M_i and M_j. The Kronecker's delta, δ_{ij}, accounts for other surfaces blocking the view, in the sense that $\delta_{ij} = 0$ if there is an obstacle between M_i and M_j. Each view factor F_{ij} represents the fraction of radiation leaving i that is intercepted by surface j. Furthermore, meas(M_i) is the measure of M_i, i.e., its surface area.

If the temperature, T_i, and emissivity, ε_i, of each surface are known, then equations (3.17) for all $i \in \{1, \ldots, N_s\}$ can be regarded as a linear system of N_s equations and unknowns, whose solution yields the value of the radiosity of each surface, enabling to calculate the net heat flux due to radiation on M_i as follows

$$q_{rad,i} = R_i - \sum_{j=1}^{N_s} F_{ij} R_j.$$

Then, the function $\widetilde{q}_{rad}(\mathbf{x})$ is defined as $\widetilde{q}_{rad}(\mathbf{x}) = q_{rad,i}$ for $\mathbf{x} \in M_i$, $i = 1, \ldots, N_s$.

In order to ensure an accurate computation of the heat fluxes, the surfaces used in this method do not have to coincide with geometrical plane surfaces defining the cavity. Instead, the faces of the cells composing the mesh of the cavity boundary can be used as those surfaces to improve accuracy, being the emissivity in each face the one of the boundary to which they belong. The specific values of the emissivity are discussed in the subsequent section, with the rest of boundary conditions.

The coupling among the heat equation and the radiosity system takes place in the interfaces between the air subdomain, Ω_A, and the solid subdomain, Ω_S, as well as the hot metal and slag subdomain, Ω_L. At these parts of the domain, which are the inner refractory cover wall, part of the working lining and the free surfaces between slag, iron and air, we specify a suitable jump condition. In particular, we assume that the heat flux, $\mathbf{q}(\mathbf{x})$ is such that:

$$[\mathbf{q}]_{\partial\Omega_A^*}(\mathbf{x}) \cdot \mathbf{n}(\mathbf{x}) = \widetilde{q}_{rad}(\mathbf{x}) \tag{3.18}$$

where $\mathbf{n}$ is the unit normal vector pointing inward of the air subdomain and $\partial\Omega_A^* = \Sigma_{wall}^A \cup \Sigma_{free}$ (see Figure 3.3). Also, recall that the notation $[\cdot]$ denotes the jump of the involved field, defined in (2.26).

Remark 3.4. *Note that, in the previous discussion, the form of the equations to be solved has been given directly on the discrete setting, as we have written the linear system that results from the discretisation of the computational domain with a suitable grid. This framework is customarily introduced in the classical radiation heat transfer textbooks (e.g. Cengel, 2014) or general radiation textbooks (see e.g. Modest, 2013; Howell et al., 2015). Nonetheless, the system of equations arising from (3.17) is the discretisation emerging from an integral equation defined in the boundary of the radiating cavity. In Chapter 4, we describe in detail the rigorous definition of this problem, to which we refer as non-local radiation. In this chapter, for the sake of simplicity, we have adopted this framework, which is customarily followed in engineering literature.*

3.1.4. Model equations

In this section, we summarise the equations that are solved in each subdomain separately, recalling that we use the subscripts A, L and S to denote the corresponding variables for the air, hot metal/slag (liquid) and solid subdomains, respectively. Then, the coupling among the different solutions in each subdomain and the radiation model is described.

Air subdomain

In Ω_A, we solve the RANS equations under the steady-state assumption, considering a single-phase flow of air, modelling the forced air circulation below the refractory cover in the BF trough system. The flow is considered weakly compressible, with non-negligible density variations due to heating, assuming that air behaves as an ideal gas whose density does not depend on the local pressure field. The SST $K-\omega$ turbulence model (see Section 2.2.2) is used to model the effect of the turbulent fluctuations. The equations of the model are stated below.

Find $\mathbf{v}_A, p_A, K_A, \omega_A$ and T_A such that:

$$
\begin{aligned}
&\operatorname{div}(\rho_A \mathbf{v}_A) = 0, && \text{in } \Omega_A,\\
&\operatorname{div}(\rho_A \mathbf{v}_A \otimes \mathbf{v}_A) = -\operatorname{grad}(p_A) + \rho_A \mathbf{g}\\
&\qquad + \operatorname{div}\left((\mu_A + \mu_{T,A}) \left[2\mathbf{D}(\mathbf{v}_A) - \frac{2}{3}\operatorname{div}(\mathbf{v}_A)\mathbf{I} \right] - \frac{2}{3}\rho_A K_A \mathbf{I} \right), && \text{in } \Omega_A,\\
&\operatorname{div}(\rho_A \mathcal{H}_A \mathbf{v}_A) - \operatorname{div}\big((k_A + k_{T,A})\operatorname{grad}(T_A)\big) = 0, && \text{in } \Omega_A,\\
&\operatorname{div}(\rho_A K_A \mathbf{v}_A) = \operatorname{div}\left[\left(\mu_A + \frac{\mu_{T,A}}{\sigma_{K_A}} \right) \operatorname{grad}(K_A) \right] + G_{K_A} - Y_{K_A}, && \text{in } \Omega_A, \quad (3.19)\\
&\operatorname{div}(\rho_A \omega_A \mathbf{v}_A) = \operatorname{div}\left[\left(\mu_A + \frac{\mu_{T,A}}{\sigma_{\omega_A}} \right) \operatorname{grad}(\omega_A) \right] + G_{\omega_A} - Y_{\omega_A} + D_{\omega_A}, && \text{in } \Omega_A, \quad (3.20)\\
&\rho_A = \frac{p_{op}}{\frac{\mathcal{R}}{M_w} T_A}, && \text{in } \Omega_A,
\end{aligned}
$$

where the specific enthalpy is such that $\mathcal{H}_A = c_{p,A} T_A$. The eddy viscosity, $\mu_{T,A}$, is computed using expression (2.16) whereas the turbulent thermal conductivity, $k_{T,A}$, satisfies (3.11), considering air property values. Furthermore, the production, dissipation terms and cross-diffusion terms appearing in (3.19) and (3.20) follow the definitions given in Section 2.2.2, also considering the corresponding property values for air collected in Table 1.1b. The gravitational acceleration, $\mathbf{g}$, is defined as in the previous chapter, i.e., $\mathbf{g} = -9.81\mathbf{e}_2$.

Hot metal and slag subdomain

In Ω_L, similar equations to those considered in the air subdomain are solved, but considering a two-phase flow of hot metal and slag, and incorporating the volume fraction of hot metal, α_{hm}, with the corresponding transport equation to the model. Also, the variations of density due to temperature are neglected and the flow is assumed incompressible.

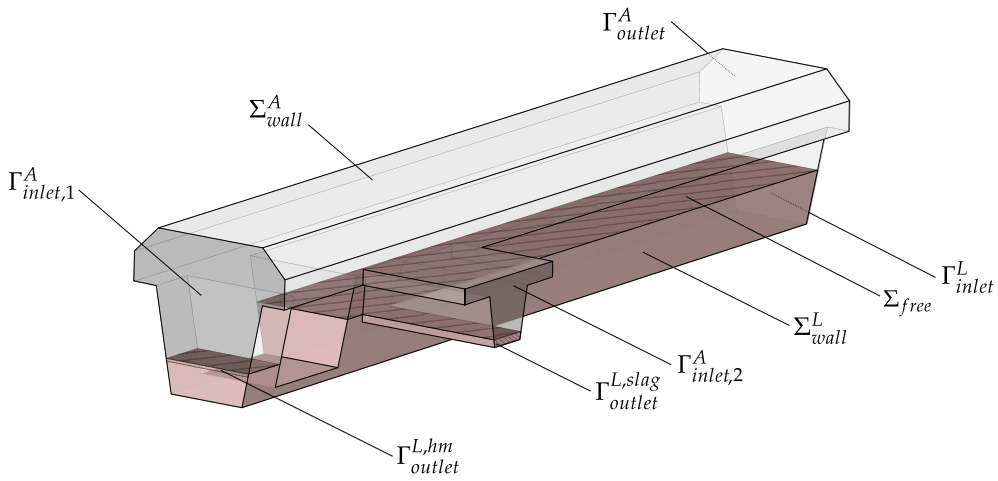


Figure 3.3: Interfaces and boundaries involving the fluid subdomain (Ω_F).

Find $\mathbf{v}_L$, p_L, K_L, ω_L, α_{hm} and T_L such that:

$$\begin{aligned}
&\operatorname{div}(\mathbf{v}_L) = 0, && \text{in } \Omega_L,\\
&\frac{\partial \alpha_{hm}}{\partial t} + \operatorname{div}(\alpha_{hm}\mathbf{v}_L) = 0, && \text{in } \Omega_L,\\
&\operatorname{div}(\widehat{\rho}\,\mathbf{v}_L \otimes \mathbf{v}_L) = -\operatorname{grad}(p_L) + \operatorname{div}\left((\widehat{\mu} + \widehat{\mu}_T)2\mathbf{D}(\mathbf{v}_L) - \frac{2}{3}\widehat{\rho}K_L\mathbf{I}\right) + \widehat{\rho}\mathbf{g}, && \text{in } \Omega_L,\\
&\widehat{\rho}\widehat{c}_p\operatorname{grad}(T_L)\cdot\mathbf{v}_L - \operatorname{div}\left(\widehat{k}\operatorname{grad}(T_L)\right), && \text{in } \Omega_L,\\
&\operatorname{div}(\widehat{\rho}K_L\mathbf{v}_L) = \operatorname{div}\left[\left(\widehat{\mu} + \frac{\widehat{\mu}_T}{\sigma_{K_L}}\right)\operatorname{grad}(K_L)\right] + G_{K_L} - Y_{K_L}, && \text{in } \Omega_L,\\
&\operatorname{div}(\widehat{\rho}\omega_L\mathbf{v}_L) = \operatorname{div}\left[\left(\widehat{\mu} + \frac{\widehat{\mu}_T}{\sigma_{\omega_L}}\right)\operatorname{grad}(\omega_L)\right] + G_{\omega_L} - Y_{\omega_L} + D_{\omega_L}, && \text{in } \Omega_L,
\end{aligned}$$

where we recall that the hat symbols denote mixture properties, computed as in (3.14)-(3.15), and bearing that the volume fractions of slag and hot metal satisfy that $\alpha_{slag} + \alpha_{hm} = 1$. The eddy viscosity is computed substituting with the corresponding mixture properties in (2.33).

Solid subdomain

In Ω_S, the heat equation is solved, as the only heat transfer phenomenon is modelled in the solids is heat conduction.

Find T_S such that:

$$\operatorname{div}\left(k_S(T_S)\operatorname{grad}(T_S)\right) = 0, \quad \text{in } \Omega_S,$$

where the thermal conductivity k_S also depends on the spatial coordinate, taking different values in each solid refractory layer.

Coupling

The coupling among the different solutions is done across the interfaces separating the subdomains, defining suitable jump conditions for the temperature and heat flux. These interfaces are either *fluid walls* or the plane surface separating the liquid and air subdomains. The latter is denoted as Σ_{free},

whereas the former is denoted as Σ_{wall}, with the superscripts L and A to distinguish the part of the interface involving liquid and air subdomains, respectively. These interfaces are shown in Figure 3.3, where only Ω_F is depicted for clarity purposes.

In principle, both temperature and heat flux should be assumed to be continuous on the interfaces. However, as detailed in Section 3.1.3, the heat flux on the radiating cavity boundary, $\partial\Omega_A^* = \Sigma_{free} \cup \Sigma_{wall}^A$ is allowed to be discontinuous due to the radiation contribution from the remainder of the cavity.

More precisely, on the interface separating the hot metal/slag and air subdomains, Σ_{free}, it holds that:

$$
\begin{aligned}
&[T]_{\Sigma_{free}} = T_A - T_L = 0,\\
&[\mathbf{q}]_{\Sigma_{free}} \cdot \mathbf{n} = (\mathbf{q}_A - \mathbf{q}_L) \cdot \mathbf{n} = (\widehat{k}\,\mathrm{grad}(T_L) - k_A \mathrm{grad}(T_A)) \cdot \mathbf{n} = \widetilde{q}_{rad},
\end{aligned}
$$

where $\mathbf{n}$ is the unit normal vector on Σ_{free}, and assumed to point from Ω_L towards Ω_A.

On the interface separating the air and solid subdomains, Σ_{wall}^A, we similarly set that:

$$
\begin{aligned}
&[T]_{\Sigma_{wall}^A} = T_A - T_S = 0,\\
&[\mathbf{q}]_{\Sigma_{wall}^A} \cdot \mathbf{n} = (\mathbf{q}_A - \mathbf{q}_S) \cdot \mathbf{n} = (k_S \mathrm{grad}(T_S) - k_A \mathrm{grad}(T_A)) \cdot \mathbf{n} = \widetilde{q}_{rad}.
\end{aligned}
$$

Here, the unit normal vector on Σ_{wall}^A is assumed to point from Ω_S towards Ω_A.

Lastly, on the interface that separates the hot metal/slag and solid subdomains, Σ_{wall}^L, we consider that the heat flux and temperature are continuous, i.e.:

$$
\begin{aligned}
&[T]_{\Sigma_{wall}^L} = T_L - T_S = 0,\\
&[\mathbf{q}]_{\Sigma_{wall}^L} \cdot \mathbf{n} = (\mathbf{q}_L - \mathbf{q}_S) \cdot \mathbf{n} = 0,
\end{aligned}
$$

where the normal vector points from Ω_S towards Ω_L.

3.1.5. Boundary conditions

In this section, we describe the boundary conditions that are used in the mathematical model. First, we address the so-called external boundaries of the computational domain, i.e., the parts of the solid refractory linings that are exposed to the surrounding air. These boundaries are denoted as $\Gamma_C^{n_c}$, $n_c \in \{1, 2, 3\}$, and are shown in Figure 3.4. They are the upper part of the trough, the lateral faces and the bottom of it. On them, free convection with the ambient air is assumed. Different heat transfer coefficients are used on each $\Gamma_C^{n_c}$. The computation of these heat transfer coefficients is presented in detail, using classical correlations for the Nusselt dimensionless number. Also, note that in Figure 3.4, the extent of Γ_{sym} is displayed, which corresponds to the part of the solid layers that are cut by the computational domain choice. On these parts of the boundary, since the precise details of the temperature field and heat flux are unknown, we assume symmetry conditions.

Subsequently, we address the boundary conditions that are imposed on the interfaces between the subdomains involved in the model. The boundary conditions set on the flow openings are also introduced, which correspond to the fictitious boundaries where fluid ingresses or exits the computational domain. We detail the conditions that are imposed at the corresponding inlets and outlets, also depicted in Figure 3.3. Recall that the subscripts A, L and S, when used in the involved variables, indicate that the corresponding field belongs to the air, hot metal/slag (liquid) and solid subdomain, respectively, since we are considering different systems of equations in each of them.

External boundaries

On the external boundaries of the trough, $\Gamma_C^{n_c}$, we set mixed radiation-convection boundary conditions:

$$
-k_S(T_S)\frac{\partial T_S}{\partial \mathbf{n}} = \widetilde{h}_{n_c}(T_S - T_{ext,c,n_c}) + \sigma\varepsilon_{n_c}(T_S^4 - T_{ext,r,n_c}^4).
$$

UNIVERSIDADE DE SANTIAGO DE COMPOSTELA

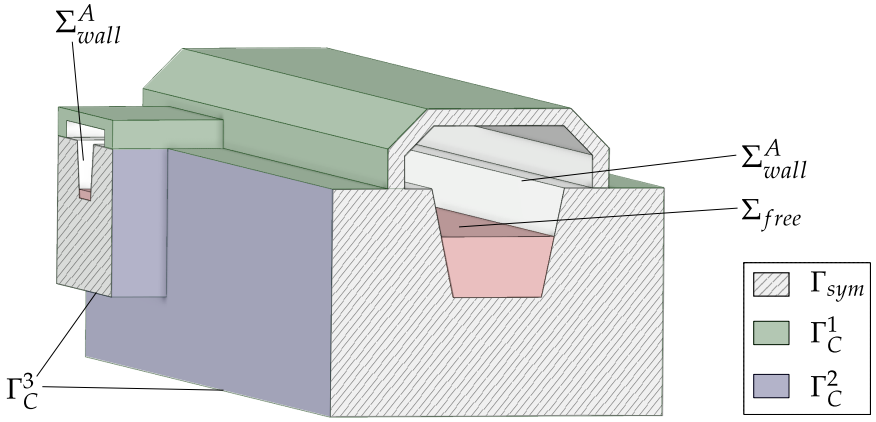


Figure 3.4: External and symmetry boundaries of the computational domain.

The ambient temperature for convection, T_{ext,c,n_c}, and that for radiation, T_{ext,r,n_c}, are considered equal to 293 K in all cases, i.e. $T_{ext,c,n_c} = T_{ext,r,n_c} = 293$ K. The values of the heat transfer coefficients, $\widetilde{h}_{n_c}$, are computed using standard correlations for vertical and horizontal flat plates assuming natural convection. Then, as discussed below, the values are enhanced by accounting for the increased surface area due to the presence of the steel casing, which is not included in the computational domain.

To obtain an estimation of the coefficients, based on some thermographies supplied by Arcelor-Mittal, we assume that they are at constant temperature of approximately $T_{surf} = 383$ K. Then, the so-called *film temperature* of the air within the boundary layer, T_f, (see e.g. Cengel, 2014) is such that

$$T_f = \frac{T_{surf} + T_{ext,c,n_c}}{2} = 338 \text{ K}.$$

Hence, in the correlations that are used subsequently, we consider the values in Table 3.1, corresponding to air at 350 K, extracted from Bergman et al. (2011, p. 995).

In the following, we discuss the computations that are carried out to obtain an estimation of the heat transfer coefficient on the external boundaries of the computational domain. On each part of the boundary, we set a suitable characteristic length, $\mathscr{L}_{n_c}$, and compute the Rayleigh dimensionless number:

$$Ra_{n_c} = \frac{\rho^2 c_p |\mathbf{g}| \beta (T_{surf} - T_{ext,c,n_c}) \mathscr{L}^3_{n_c}}{\mu k},$$

where the values of the physical properties take the values in Table 3.1 and $n_c \in \{1,2,3\}$. Also, β denotes the thermal expansion coefficient, which is approximated by $\beta = 1/T_f \approx 2.86 \cdot 10^{-3}$ 1/K.

Once the Rayleigh number is computed, taking into account the orientation of the boundary, the corresponding value is substituted in an adequate correlation for the Nusselt dimensionless number, Nu_{n_c}, specified below. Since this number is defined as:

$$Nu_{n_c} = \frac{h_{n_c} \mathscr{L}_{n_c}}{k}, \tag{3.21}$$

the heat transfer coefficients, h_{n_c}, $n_c \in \{1,2,3\}$, follow by manipulation of the previous expression.

On each boundary $\Gamma^{n_c}_C$, we obtain the corresponding h_{n_c} as follows:

Table 3.1: Air properties at 350 K. Source: Bergman et al. (2011).

ρ [kg/m^3]	μ [Pa · s]	c_p [J/(kg · K)]	k [W/(m · K)]
0.9950	$2.08 \cdot 10^{-5}$	$1.01 \cdot 10^3$	$3.00 \cdot 10^{-2}$

- If $n_c = 1$, $\Gamma_C^{n_c}$ corresponds to the external part of the refractory cover and the upper part of the trough. We consider a characteristic length based on the ratio of area with respect to the perimeter of the boundary, leading to $\mathscr{L}_{n_c} = 1.94$ m. The Rayleigh number is $Ra_{n_c} = 3.06 \cdot 10^{10}$. The correlation (9-23) in Cengel (2014, p. 468) for free convection on a flat plate facing upwards leads to:

$$Nu_{n_c} = 0.15 Ra_{n_c}^{\frac{1}{3}} = 469.17.$$

  Therefore, substitution in (3.21) yields that $h_{n_c} = 7.26$ W/(m$^2 \cdot$ K).

- If $n_c = 2$, $\Gamma_C^{n_c}$ is the lateral part of the trough. There, we consider a characteristic length $\mathscr{L}_{n_c} = 2$ m. The Rayleigh number is $Ra_{n_c} = 3.35 \cdot 10^{10}$. The correlation (9.26) in Bergman et al. (2011, p. 605) for free convection in the turbulent regime on a vertical flat plate is used, yielding:

$$Nu_{n_c} = \left(0.825 + \frac{0.387 Ra_{n_c}^{\frac{1}{6}}}{\left(1 + (0.492/Pr)^{\frac{9}{16}}\right)^{\frac{8}{27}}} \right)^2 = 369.57,$$

  where $Pr = \mu c_p / k$ is the Prandtl number. Thus, from (3.21), it follows that $h_{n_c} = 5.54$ W/(m$^2 \cdot$ K).

- Lastly, if $n_c = 3$, $\Gamma_C^{n_c}$ is the bottom boundary of the trough. In this case, we also consider a characteristic length based on the ratio of area with respect to the perimeter of the boundary, leading to $\mathscr{L}_{n_c} = 1.25$ m. The corresponding Rayleigh number is $Ra_{n_c} = 8.17 \cdot 10^9$ and, using correlation (9-24) in Cengel (2014), we obtain that

$$Nu_{n_c} = 0.27 Ra_{n_c}^{\frac{1}{4}} = 81.17.$$

  Hence, the corresponding heat transfer coefficient is $h_{n_c} = 1.95$ W/(m$^2 \cdot$ K).

Now, to account for the influence of the built-in fins and ribs on the steel casing in the cooling with the ambient air, we modify the computed coefficient to match the heat loss with the real surface area (considering the steel formwork with the incorporated fins and ribs), i.e., we compute the modified coefficient $\widetilde{h}_{n_c}$ using the subsequent expression:

$$\widetilde{h}_{n_c} = h_{n_c} A_{real} / A,$$

where h_{n_c} is the coefficient computed after substitution of the Nusselt number in (3.21), A_{real} is the surface area of the boundary considering the presence of fins and ribs and A the corresponding surface area assuming that the boundary is a flat plate.

In this manner, we obtain the results collected in Table 3.2. Since we are working with rough estimations, instead of the computed values in the table, we set as the corresponding heat transfer coefficients the rounded values of such numbers, i.e., $\widetilde{h}_2 = 8$ and $\widetilde{h}_3 = 4$ W/(m$^2 \cdot$ K). The same applies for the coefficient h_1, which is rounded as $\widetilde{h}_1 = 7$ W/(m$^2 \cdot$ K).

Table 3.2: Real surface area (including the steel casing), surface area in the computational domain, heat transfer coefficient obtained with a flat plate correlation and modified heat transfer coefficient for the external boundaries.

n_c	A_{real} [m^2]	A [m^2]	A_{real}/A [–]	h_{n_c} [W/(m$^2 \cdot$ K)]	$\widetilde{h}_{n_c}$ [W/(m$^2 \cdot$ K)]
2	54.03	38	1.42	5.54	7.87
3	61.98	28.5	2.17	1.95	4.23

USC UNIVERSIDADE SANTIAGO COMPOSTELA

Fluid walls

On the interface separating Ω_F from Ω_S, $\Sigma^L_{wall} \cup \Sigma^A_{wall}$, no-slip conditions should hold for the velocity field, as discussed in Section 2.2.3. Also, recall from the previous discussion that continuity of temperature and heat flux should be satisfied, except on Σ^A_{wall}, where the radiation contribution appears as a jump condition on the heat flux (3.18). The same applies to Σ_{free}. However, on this interface, instead of a no-slip condition, for the velocity of slag and hot metal ($\mathbf{v}_L$), we only require that $\mathbf{v}_L \cdot \mathbf{n} = 0$, i.e., a free-slip condition. For the air, we set that on Σ_{free} the velocity is $\mathbf{v}_A = \mathbf{0}$.

Remark 3.5. *In reality, it would be more accurate to set that the tangential velocities along Σ_{free} are continuous. However, this substantially increases the complexity of the model, as it couples the velocities between Ω_A and Ω_L. The condition that we set essentially means that the motion of hot metal and slag is unaffected by the air flow in the opposite direction, and since the slag velocity on the free surface (around 0.05 m/s) is much slower than the free stream air flow, it is reasonable to set $\mathbf{v}_A = \mathbf{0}$ for the air.*

Note that as it exists a boundary layer for the velocity field, the same applies to the temperature field. To appropriately compute the surface temperature on the walls, the *Reynolds analogy* is assumed to hold, which indicates that the processes of transport of momentum and heat are analogous. Then, it is possible to establish a relation with the expressions that hold for the dynamic boundary layer to find a wall law for the temperature (see e.g. Versteeg & Malalasekera, 2007). We skip the details concerning this issue, and refer the reader to Ansys, Inc. (2019) for the implementation of this approach in the software package that is subsequently used for the numerical simulation.

Regarding the radiation model, we recall that the radiation participating surfaces are the boundaries of the air subdomain, which are the internal cover wall, part of the working layer refractory, the slag free surface and the air inlets and outlets. We assume that the working lining refractory, the slag and the cover refractory have the same emissivity, $\varepsilon = 0.7$, which was supplied by ArcelorMittal.

Flow openings

At the flow openings corresponding to inlets, we impose a Dirichlet condition on the velocity and temperature. On the outlets, we set pressure-outlet boundary conditions, where the pressure values are imposed (see Section 2.4.3). In addition, since some of the inlets and outlets are also part of the cavity where radiation takes place, adequate values of the emissivity and boundary temperature need to be given. We briefly summarise those values below:

- On $\Gamma^A_{inlet,i}$, $i = \{1, 2\}$, which corresponds to the boundaries where the ambient air aspirated from the casthouse enters the computational domain, we set $T_A = 293$ K and $\mathbf{v}_A = v_{air}\mathbf{n}$, being $\mathbf{n}$ the normal vector in the inward-pointing direction and where v_{air} is the inlet air velocity, which is a parameter in the subsequent numerical studies. To provide values for the turbulent variables, standard values of the turbulent intensity, $I_T = 10\%$, and the viscosity ratio, $\mu/\mu_T = 5$, are considered.

  Concerning the radiation model, on $\Gamma^A_{inlet,2}$, we set $\varepsilon = 1$, which makes the surface behave as a black body emitting at $T = 293$ K. This means that all radiation going out through the boundary is expected to disperse around the casthouse, with incoming radiation emitted by bodies at ambient temperature. Moreover, on $\Gamma^A_{inlet,1}$, we impose that $\varepsilon = 0$. Therefore, it is modelled as a symmetry boundary for radiation, since all incoming radiation will be reflected in virtue of *Kirchhoff's law*, with no emission from the boundary.

- On Γ^L_{inlet}, the section of the pool of hot metal and slag where these fluids enter the computational domain, we set the averaged velocity computed at $t_{end} = 150$ s in Run C in Chapter 2, depicted in Figure 2.19 at the corresponding section of Γ^L_{inlet}. The volume fractions are also set appropriately. The temperature of the fluids is assumed to be $T_L = 1773$ K. The same standard values for the turbulence variables as on the air inlets are set.

- On Γ^{A}_{outlet}, the boundary condition is of pressure-outlet type. The gauge pressure is set as $p_A = 0$. Regarding the radiation model, the emissivity is set as $\varepsilon = 0$.

- On $\Gamma^{L,slag}_{outlet}$, corresponding to the boundary at the end of the slag trough, a pressure-outlet condition with the subsequent pressure value is set:

$$p_L(x_2) = (h_{slag} - x_2) \cdot (\rho_{slag} - \rho_{op})|\mathbf{g}|,$$

  where $\mathbf{g}$ is the gravitational acceleration vector and ρ_{op} is the operating density, which we consider equal to the air density at 293 K. Recall that x_2 is the vertical coordinate and that h_{slag} denotes the height of the slag-air free surface, which in this model is fixed at the value $h_{slag} = 1.575$ m.

- On $\Gamma^{L,hm}_{outlet}$, the small boundary at the end of the main trough where hot metal overflows the iron dam, a pressure-outlet condition with the subsequent pressure value is set:

$$p_L(x_2) = (h^*_{hm} - x_2)(\rho_{hm} - \rho_{op})|\mathbf{g}|,$$

  where we note that h^*_{hm} is the height of the iron-air interface at the end of the trough. Since its position is also fixed based on the results obtained in the previous chapter for Run C, it is set that $h^*_{hm} = 1.33$ m.

Remark 3.6. *The constant inlet temperature for hot metal and slag, i.e., $T_L = 1773$ on Γ^{L}_{inlet}, is a rough assumption. This value is set based on the estimated temperature of slag and hot metal within the BF hearth (see Chapter 1), which is also around 1773 K, although it is not constant and can slightly fluctuate. In reality, since Γ^{L}_{inlet} is located approximately 4 m downstream of the jet impingement point calculated in Chapter 2, the fluids may have cooled by the moment that they arrive at the boundary. However, most of the cooling should be restricted to the slag surface and, provided that we currently lack any estimation of the temperature in this free surface in the real trough setting, we take this value as a first approximation.*

Other boundaries

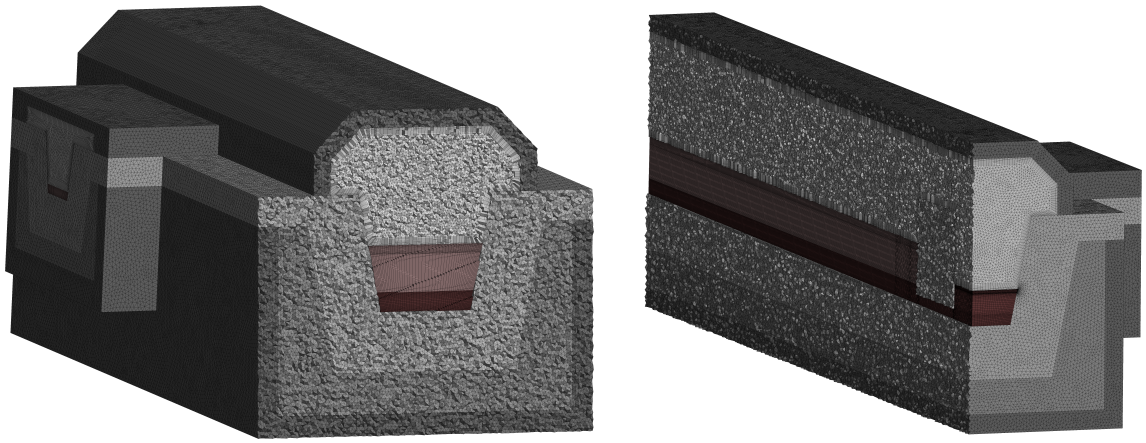
In the sections where the trough and the slag runner are cut, denoted as Γ_{sym} (see Figure 3.4) symmetry conditions on the temperature are considered, since the precise details of the temperature field are not known. Hence, we set that:

$$-k_S(T_S)\frac{\partial T_S}{\partial \mathbf{n}} = 0, \qquad \text{on } \Gamma_{sym}.$$

3.2. Numerical solution

The proposed mathematical model is solved using the package *Ansys Fluent*, Release 2021, R2. The considered numerical schemes are similar to those described in the previous chapter. Thus, we mainly discuss those that are different. Here, instead of the segregated SIMPLE algorithm to perform the pressure-velocity coupling, the coupled solver is used (see Ansys, Inc., 2021). On the other hand, since the only interface that we are explicitly tracking is that among hot metal-slag, which we expect to be plane and near the initial value set as initial seed for the computation, the so-called *Compressive* scheme is deemed adequate. It is an implementation of the well-known CICSAM scheme (Tryggvason et al., 2011). For the temperature, a *Second-order upwind* scheme is used, whereas the remaining numerical schemes are the same.

Note that, while no initial condition is required for this model, initial values are chosen appropriately to obtain a faster convergence to the solution. We assume that the interface separating hot metal and slag is located initially at the position found at the end of Run C in the previous chapter. This gives the initial value for the volume fractions. For the remaining flow variables, we set $\mathbf{v} = \mathbf{0}$ m/s, $K = 0$ m^2/s^2, $\omega = 1$ s^{-1} and $T = 500$ K, in all the subdomains were they are defined. The pressure



(**a**) Transversal cut.

(**b**) Longitudinal cut.

Figure 3.5: Mesh 4 of the computational domain.

field in hot metal and slag, p_L, is initialised using the hydrostatic value computed using the heights of the free surfaces and the constant density of each phase.

To assess the convergence of the simulation, we monitor the globally scaled residuals of the velocity, turbulence variables, volume fraction and energy equation. The convergence criteria is that all fall below 10^{-4}. In addition, we monitor the mass imbalance in Ω_L and the average value of the temperature in the inner face of the cover, exposed to incoming radiation from the slag free surface, ensuring that both are small when the previous criteria is satisfied. The simulations were run in parallel, using 48 cores in a PowerEdge R840 machine, equipped with 4 Intel Xeon Gold 6126 processors. For the finest grid considered, convergence to the steady-state was reached in around 24 hours.

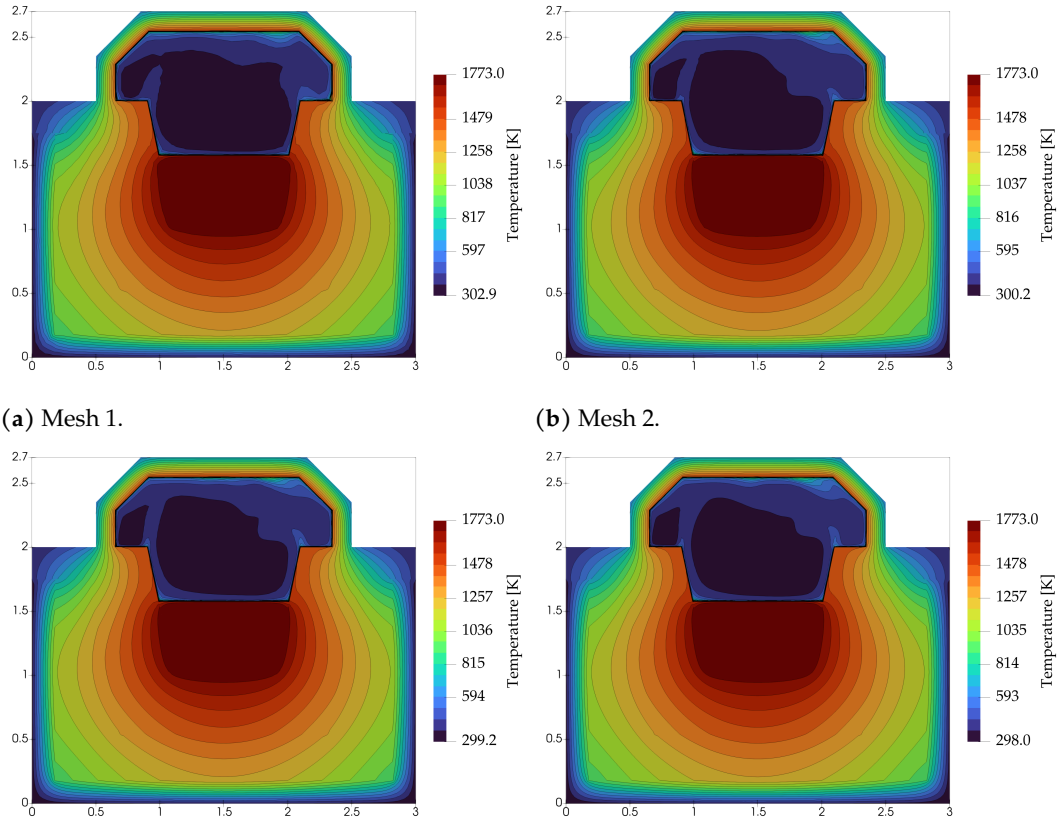
3.2.1. Mesh

A grid of the computational domain is constructed, depicted in Figure 3.5. Non-conformal mesh interfaces among Ω_S, Ω_A and Ω_L are used. They allow to construct a mesh that is adequately refined in those areas where higher resolution is needed, and coarser where the gradients are not as steep. Instead, if a conformal mesh was used, the fine elements in the hot metal and slag subdomain, Ω_L, would propagate into the solid material layers, where an accurate solution can be obtained with much coarser mesh sizes. In addition, it is easier to obtain a better quality mesh with the non-conformal interfaces, which is essential to guarantee the stability of the computations.

Through refinement of the first constructed mesh, four different grids are built. The solution of the mathematical model is carried out in Section 3.3.1 in these different grids to assess their influence on the computed solution. In Table 3.3, we report the number of cells in each mesh, as well as the maximum skewness and minimum orthogonal quality. Recall from Section 2.5.1 that with the definition in the software package, 0 is the worst possible orthogonal quality and 1 the worst skewness.

Table 3.3: Computational grids chosen for the mesh sensitivity study, with mesh quality metrics.

	# cells	Max. Skw.	Min. Orth.
Mesh 1	1566798	0.79	0.21
Mesh 2	5507604	0.72	0.28
Mesh 3	10753399	0.74	0.27
Mesh 4	20697071	0.72	0.26



(**a**) Mesh 1. (**b**) Mesh 2.

(**c**) Mesh 3. (**d**) Mesh 4.

Figure 3.6: Temperature contours in the cross-section $x_3 = 8$ m for the different meshes considered in the grid sensitivity study ($v_{air} = 2$ m/s).

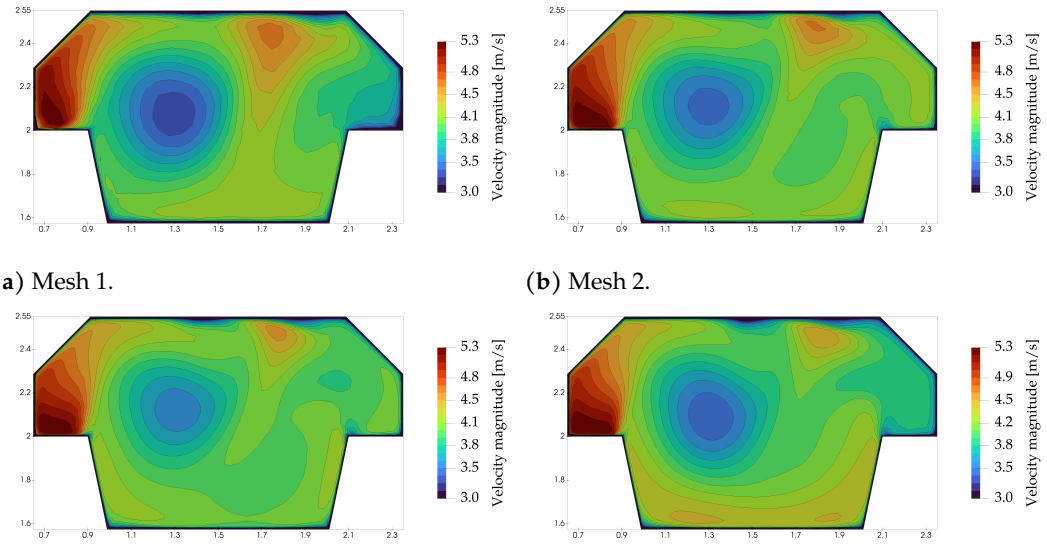
3.3. Results and discussion

In the sequel, we showcase and discuss the main results obtained after solving the 3D steady thermal model of the BF trough. First, Section 3.3.1 deals with the grid sensitivity study. Then, in Section 3.3.2, we discuss in detail the results computed for a value of the air velocity parameter $v_{air} = 2$ m/s. Subsequently, Section 3.3.3 is devoted to address the dependency of the computed results on the air velocity. Lastly, in Section 3.3.4, we discuss the validation of the model with measurements made with thermocouples embedded in the BF trough.

3.3.1. Grid validation

To investigate the dependency of the computed results on the discretisation parameter, we compute the solution on the grids collected in Table 3.3, considering that the inlet air velocity is $v_{air} = 2$ m/s.

In Figure 3.6, the temperature contours on the cross-section $x_3 = 8$ m are depicted for all the considered grids. Notice that the part corresponding to hot metal and slag is at an almost homogeneous temperature of 1773 K, and the apparent differences between the meshes are minimal. Slight variations are found in the air subdomain with the finer meshes. To better assess these differences, in Figure 3.7, the velocity magnitude is plotted on the same cross-section, only considering the air subdomain, Ω_A. In contrast with the previously displayed contours, while the main structures of the flow are qualitatively similar, some degree of mesh dependency is observed, with the velocity over the slag free surface being somewhat larger in Mesh 4.



(**a**) Mesh 1.

(**b**) Mesh 2.

(**c**) Mesh 3.

(**d**) Mesh 4.

Figure 3.7: Velocity magnitude contours in the cross-section $x_3 = 8$ m of the air subdomain (Ω_A), for the different meshes considered in the grid sensitivity study ($v_{air} = 2$ m/s).

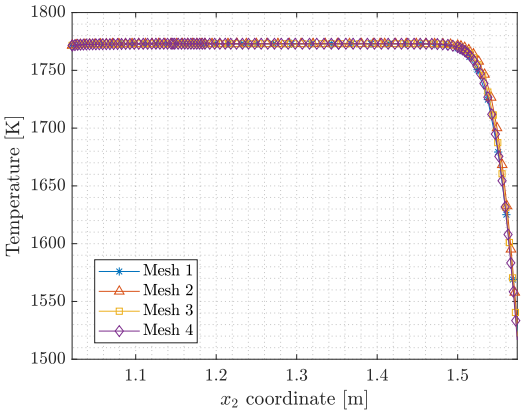
In Figure 3.8, to better quantify the differences among the computational grids, the solution is plot along a vertical line crossing the whole of Ω. In particular, the line has a constant $x_1 = 1.5$ m and $x_3 = 11$ m. Notice that Figures 3.8a and 3.8b only show the part of the line intersecting Ω_L. The agreement among all meshes for the temperature in this subdomain is very good. Also, we remark that the model predicts significant slag cooling near the slag-air free surface ($x_2 = 1.575$ m), which is around 200 K cooler than the bulk of the slag and hot metal. Regarding the computed velocity magnitudes, although some differences are observed, the qualitative features of the predictions are very similar. If the complete line is considered, we find that the temperature in the solids is essentially the same, even for the coarsest mesh.

Although the results evidence some degree of mesh dependency, especially in velocities computed in Ω_A, provided that the main interest of the proposed model is to obtain an accurate prediction of the steady temperature field in the main trough, Mesh 4 is considered sufficiently fine, as the observed differences in the temperature predictions are minimal in all cases. Thus, the subsequently presented results are obtained using Mesh 4.

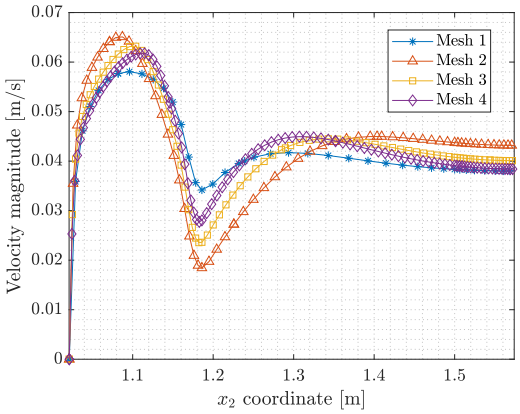
3.3.2. Main results

In this section, we discuss additional numerical results obtained after solving the model considering an inlet air velocity of $v_{air} = 2$ m/s and Mesh 4. In Figure 3.9, the velocity magnitude is depicted on the longitudinal plane $x_1 = 1.5$ m, which splits the main trough in two halves. Different scales for the air velocity ($\mathbf{v}_A$) and the slag/hot metal velocity ($\mathbf{v}_L$) are shown, given that they have different orders of magnitude. In addition, the streamlines of $\mathbf{v}_A$ are depicted. First, we note that the steady-state velocity contours in Ω_L are qualitatively similar to those computed in the previous chapter, where the influence of the jet impact on the liquid pool was assessed. Also, we remark that even though the air inlet velocity is very low, at some points of the domain fairly higher speeds are reached, around 8 m/s as the flow curves above the skimmer. The air streamlines evidence a quite complicated flow, with a rather large amount of swirling around the trough, which possibly results in enhanced heat removal by forced convection.

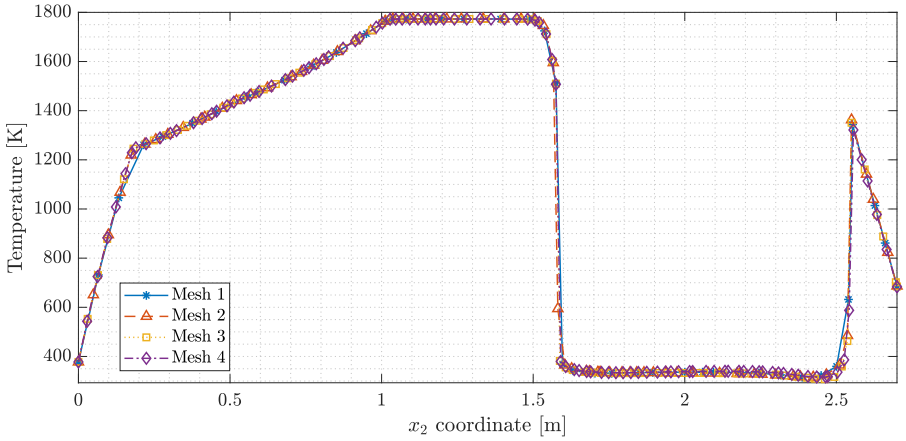
In Figure 3.10a the temperature contours in the external part are shown, hiding the air subdomain for clarity purposes. It is observed that the lateral part and the bottom are close to ambient temper-



(**a**) Temperature in Ω_L.



(**b**) Velocity magnitude in Ω_L.



(**c**) Temperature on the whole of Ω.

Figure 3.8: Temperature and velocity magnitude along the line $x_1 = 1.5$ m and $x_3 = 11$ m on selected parts of the computational domain, grid sensitivity study ($v_{air} = 2$ m/s).

ature, whereas the refractory cover shows a significantly larger temperature. Moreover, in Figure 3.10b, the position of the critical isotherms is depicted (see Section 1.4.2). While the 1473 and 1523 K isotherms are well inside the working lining, the 1423 K isotherm reaches the back-up safety lining in the bottom part, and is also quite close in the laterals. Note that these numerical results assume tacitly that the trough remains in perfect condition, i.e., that no significant wear has occurred. Nonetheless, as discussed in Chapter 1, *post-mortem* analysis of the wear profiles reveals significant material erosion (see e.g. Rüther & Lüngen, 1989; Begnis & Brandaleze, 2006). This implies that, if the steady-state assumption is realistic and the trough suffers some degree of damage, these isotherms may easily reach the safety lining, indicating increased risk of damage spreading away from the working lining and complete trough breakage.

Moreover, Figure 3.11 depicts the temperature along a longitudinal cut of Ω for $x_1 = 1.5$ m, showcasing that the high temperatures found in the cover are due to radiation, since air remains at comparatively low temperature values. In addition, it is evident that most of Ω_L remains at an almost homogeneous temperature, with the exception of a thin layer below Σ_{free}. This is better displayed in Figures 3.12a and 3.12b, where the temperature on two cross-sections of Ω_L is shown ($x_3 = 8$ m and $x_3 = 11$ m). Also, Figures 3.12c and 3.12d depict the velocity magnitude in the same cross-sections, showing that similar flow features to those obtained in Chapter 2 in this part of the trough are computed with the steady model.

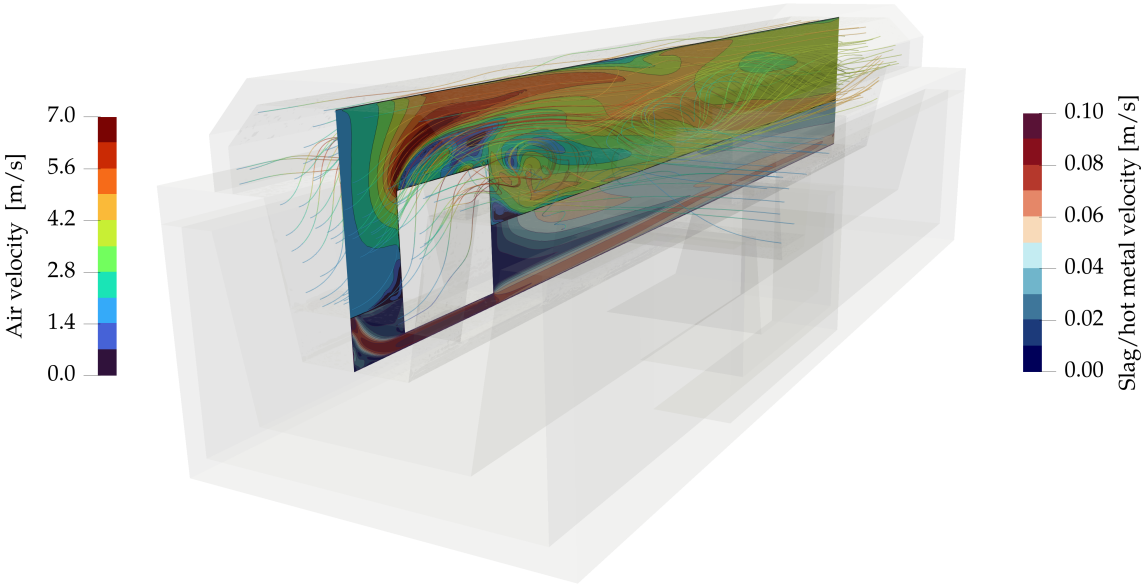
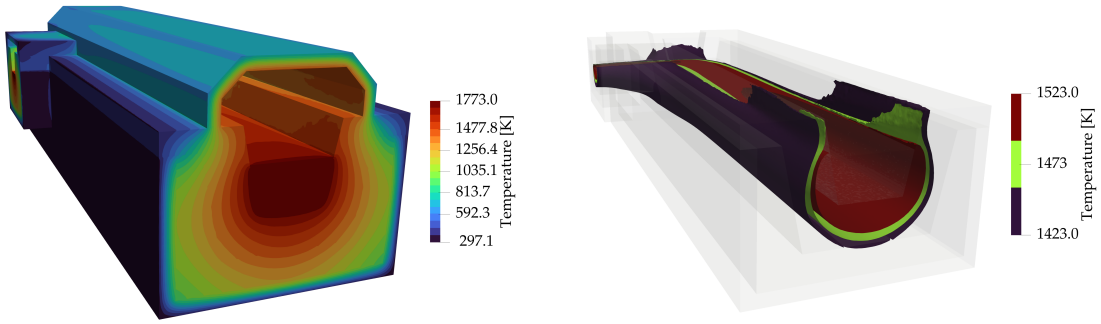


Figure 3.9: Velocity magnitude contours with separate scales in Ω_A and Ω_L. The streamlines of the air flow are also depicted, coloured by velocity magnitude, $v_{air} = 2$ m/s.



(**a**) Temperature contours.

(**b**) Critical isotherms.

Figure 3.10: Temperature contours and critical isotherms in the solid subdomain (Ω_S) and hot metal/slag subdomain (Ω_L), $v_{air} = 2$ m/s.

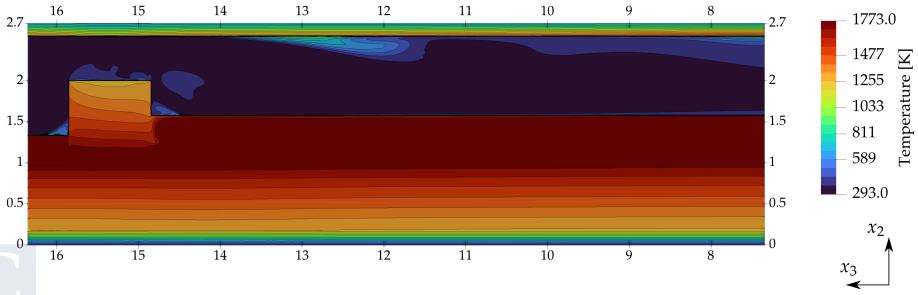
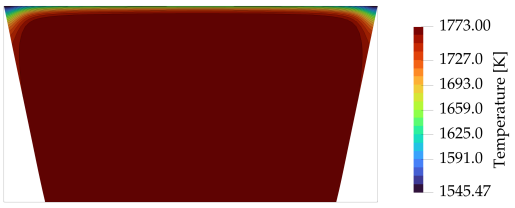
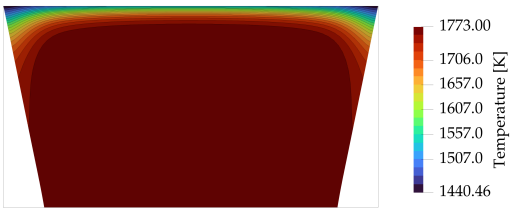


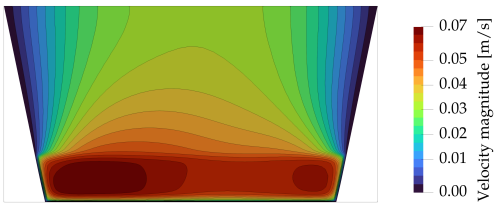
Figure 3.11: Temperature contours in the plane $x_1 = 1.5$ m, $v_{air} = 2$ m/s.



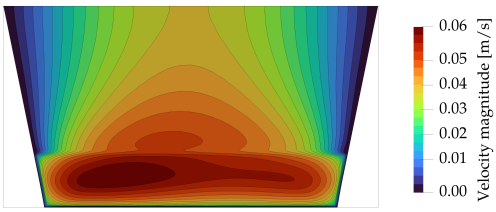
(**a**) Temperature, $x_3 = 8$ m.



(**b**) Temperature, $x_3 = 11$ m



(**c**) Velocity magnitude, $x_3 = 8$ m.



(**d**) Velocity magnitude, $x_3 = 11$ m.

Figure 3.12: Temperature and velocity magnitude contours in the cross-sections $x_3 = 8$ m and $x_3 = 11$ m of the hot metal and slag subdomain (Ω_L).

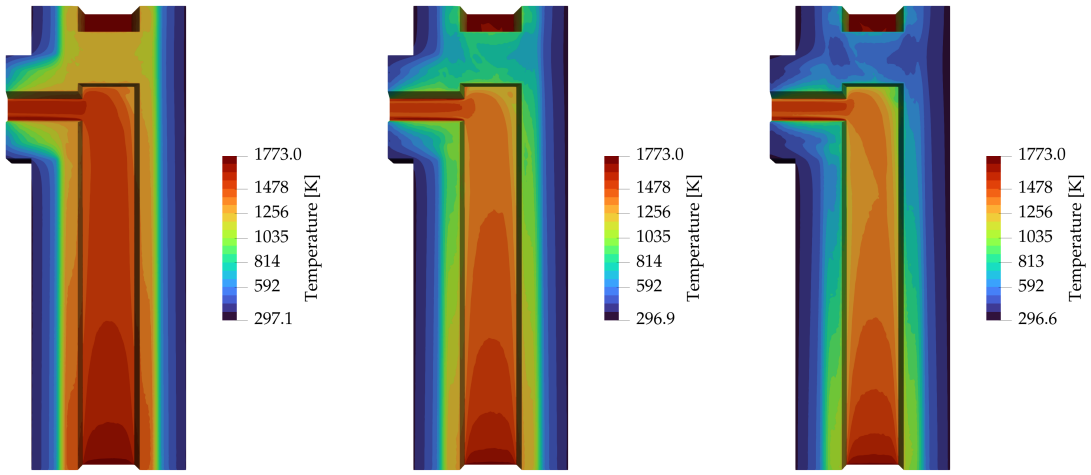
The temperature contours in the computational domain, seen from above and hiding the air subdomain and the cover, are shown in Figure 3.13a. Thus, the temperature on Σ_{free} is shown, composed of the slag-air and hot metal-air (after the skimmer) free surfaces, as well as the upper part of the working lining. It is noteworthy that the slag temperature sharply decreases from the inlet value as it flows downstream, because of the heat lost due to radiation emission and convection with the air. However, hot metal remains hot as it comes out of the skimmer. This is consistent with plant data, where it is observed that hot metal does not significantly cool during its voyage along the BF trough.

3.3.3. Sensitivity to the air velocity

The air velocity on the inlet boundaries is uncertain. As described in Chapter 1, the aspiration is performed next to the taphole and it has the main purpose of collecting the various pollutant fumes that are generated during the BF tapping (Cameron et al., 2019). However, the precise specifications of the fume aspiration device are unknown. Hence, since we were unable to quantify the amount of aspirated air nor its velocity, we cannot provide an educated guess of a realistic v_{air} parameter value. This motivates our wish to study the dependency of the computed temperatures on the air velocity. In addition, we compare the average air temperature on the outlet boundary, Γ^A_{outlet}, with experimental temperature measurements in the air aspiration.

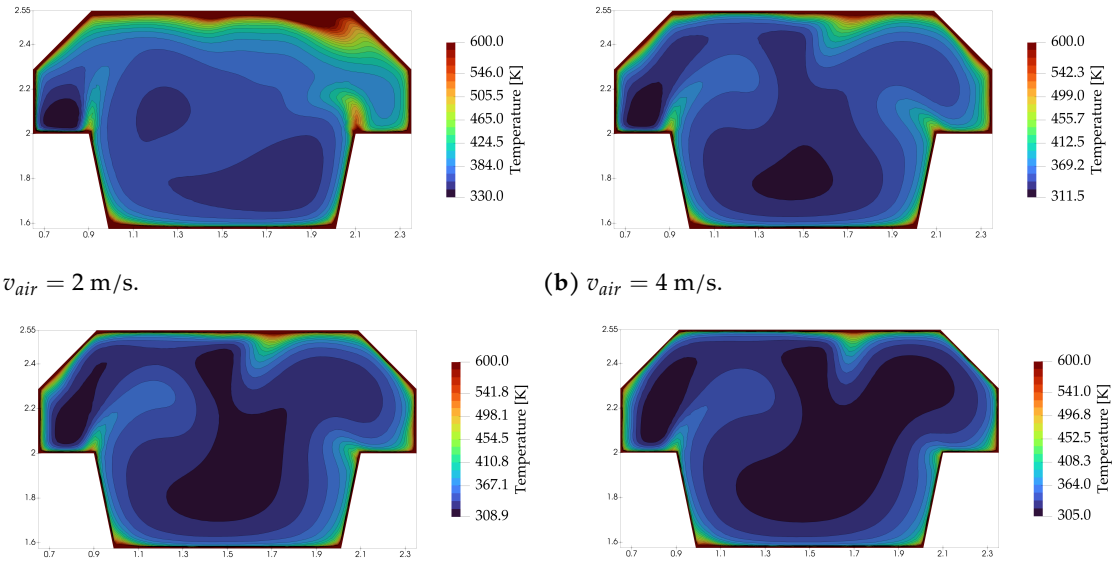
The mathematical model is solved, considering Mesh 4 and changing the inlet air velocity v_{air} within the range from 2 m/s to 10 m/s. In Figure 3.13, the temperature contours on Σ_{free} and the working lining are displayed for three different air velocities. Notice that, despite radiation being the dominant heat transfer mechanism due to the high temperatures, the forced convection with air has clearly a non-negligible effect, and it is responsible for a significant amount of heat loss in the exposed refractories. For higher v_{air} values, the temperatures on Σ_{free} are slightly lower, and fall below the liquidus temperature of typical BF slags ($CaO–MgO–Al_2O_3–SiO_2$), which is around 1600 K (L. Wang et al., 2012). In some regions, the temperatures reach values close the solidus temperature, around 1300 K. Therefore, slag solidification near the slag-air interface should be taken into account in further studies.

Moreover, in Figure 3.14, the temperature contours in the $x_3 = 8$ m cross-section in the air subdomain are displayed, for various v_{air} values. It is clear that with higher inlet air velocity values, the effect of buoyancy-induced circulations becomes weaker and the bulk of the flow remains at a



(**a**) $v_{air} = 2$ m/s. (**b**) $v_{air} = 6$ m/s. (**c**) $v_{air} = 10$ m/s.

Figure 3.13: Temperature contours in the working lining and Σ_{free}, seen from above and hiding the air subdomain and the refractory cover, for various v_{air} values.



(**a**) $v_{air} = 2$ m/s. (**b**) $v_{air} = 4$ m/s.

(**c**) $v_{air} = 8$ m/s. (**d**) $v_{air} = 10$ m/s.

Figure 3.14: Temperature contours in the cross-section $x_3 = 8$ m of the air subdomain (Ω_A), for various v_{air} values.

USC UNIVERSIDADE DE SANTIAGO DE COMPOSTELA

temperature closer to the ambient one. However, even for the larger air velocities, e.g., $v_{air} = 10$ m/s, the minimum temperature is 12 K above the ambient, and large areas of the cross-section show temperatures above 360 K.

In Table 3.4, the average radiative heat flux, q_{rad}, total heat flux, q, and temperature, T, are shown for each considered value of the air velocity. For a more comprehensive comparison, instead of reporting the results only for Σ^A_{wall}, we have split this interface considering separately its intersection with the refractory cover, denoted as Σ_{cover}, and its intersection with the working lining, Σ_{work}. Recall that the normal vector in these surfaces is considered as pointing towards the air subdomain, which explains the negative values in the reported q_{rad} and q fluxes, as they are defined as the projections in the normal direction to the interfaces. For instance, the heat flux values in Σ_{free} are positive as the slag-air free surface is releasing heat into the rest of the cavity. It is a remarkable finding that, with increasing air velocities, the radiative heat flux on Σ_{free} also increases since, as displayed in Figure 3.13, the temperature of the interface is lower. This is most likely a consequence of the enhanced convection being more effective in reducing the temperature on Σ^A_{wall}, which results in increased radiative heat flux from the slag free surface, as the temperature difference among these two boundaries becomes larger despite the temperature drop observed in Σ_{free}. Naturally, as the outgoing radiative heat flux from the slag-air interface rises, the remainder of the cavity receives an increased amount of radiation and, hence, the computed q_{rad} has a larger absolute value.

The simulation of the air motion is the most complicated part of the model. Therefore, one of the interests of the study presented herein is that the numerical results can be used to provide suitable estimations of the heat transfer coefficient on the radiation cavity. Recall that in the grid validation study presented above, the main grid-dependencies were found in the numerical results concerning the air flow. With an adequate heat transfer coefficient on $\Sigma_{free} \cup \Sigma^A_{wall}$, say h_R, the air part can be removed, leading to much faster computations. Note that the notation with the subscript R owes to the heat transfer coefficient being that on the radiating cavity in the trough. To obtain an approximation of h_R, we use that the convection contribution to the heat flux is precisely the difference among q and q_{rad} in Table 3.4. Thus, we estimate the heat transfer coefficient as:

$$h = \frac{q - q_{rad}}{T_{surf} - T_0}, \tag{3.22}$$

where T_0 is the free stream temperature and T_{surf} is the average surface temperature. In this case, we consider $T_0 = 293$ K, the ambient temperature on the air inlets. Substituting with the computed values in Table 3.4, the heat transfer coefficients reported in Table 3.5 can be obtained. An estimation of h_R over the whole interface $\Sigma_{free} \cup \Sigma^A_{wall}$ follows from weighting each heat transfer coefficient by the surface area of each part. In particular, we note that the corresponding surface areas are $A_{\Sigma_{free}} = 8.8$ m^2, $A_{\Sigma_{cover}} = 24.18$ m^2 and $A_{\Sigma_{work}} = 15.55$ m^2, leading to the h_R calculated values also gathered in Table 3.5.

3.3.4. Comparison with experimental measurements

In Figure 3.15, a boxplot depicting the evolution of the measured temperature at the air aspiration is shown, considering a dataset comprising the first 78 tappings in one taphole of the BF trough. Note

Table 3.4: Average radiative heat flux (q_{rad}) [W/m^2], average total heat flux (q) [W/m^2] and temperature (T) [K] on several parts of the radiation cavity, for various inlet air velocity values (v_{air}).

	Σ_{free}			Σ_{cover}			Σ_{work}		
v_{air}	q_{rad}	q	T	q_{rad}	q	T	q_{rad}	q	T
2 m/s	$8.15{\cdot}10^4$	$9.35{\cdot}10^4$	$1.54{\cdot}10^3$	$-1.97{\cdot}10^4$	$-1.17{\cdot}10^4$	$1.31{\cdot}10^3$	$-1.20{\cdot}10^4$	$-5.41{\cdot}10^2$	$1.32{\cdot}10^3$
4 m/s	$8.97{\cdot}10^4$	$1.07{\cdot}10^5$	$1.49{\cdot}10^3$	$-2.15{\cdot}10^4$	$-1.00{\cdot}10^4$	$1.19{\cdot}10^3$	$-1.47{\cdot}10^4$	$9.67{\cdot}10^1$	$1.20{\cdot}10^3$
6 m/s	$9.68{\cdot}10^4$	$1.19{\cdot}10^5$	$1.45{\cdot}10^3$	$-2.29{\cdot}10^4$	$-8.43{\cdot}10^3$	$1.07{\cdot}10^3$	$-1.67{\cdot}10^4$	$5.98{\cdot}10^2$	$1.09{\cdot}10^3$
8 m/s	$1.04{\cdot}10^5$	$1.32{\cdot}10^5$	$1.42{\cdot}10^3$	$-2.43{\cdot}10^4$	$-7.24{\cdot}10^3$	$9.80{\cdot}10^2$	$-1.86{\cdot}10^4$	$9.44{\cdot}10^2$	$9.96{\cdot}10^2$
10 m/s	$1.06{\cdot}10^5$	$1.38{\cdot}10^5$	$1.40{\cdot}10^3$	$-2.48{\cdot}10^4$	$-6.10{\cdot}10^3$	$8.90{\cdot}10^2$	$-1.93{\cdot}10^4$	$1.34{\cdot}10^3$	$9.08{\cdot}10^2$

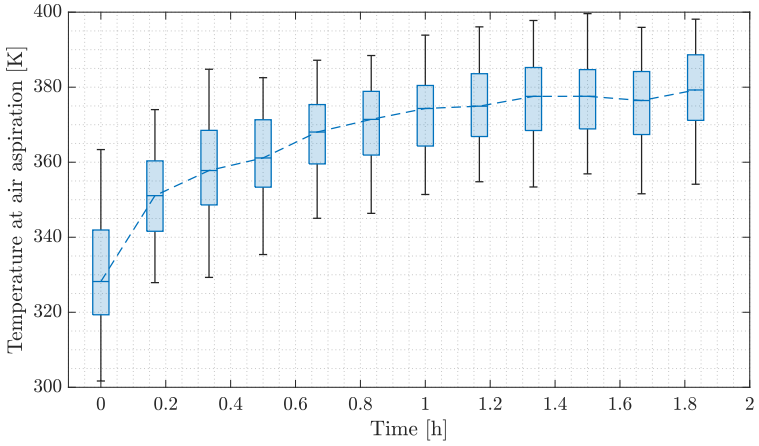


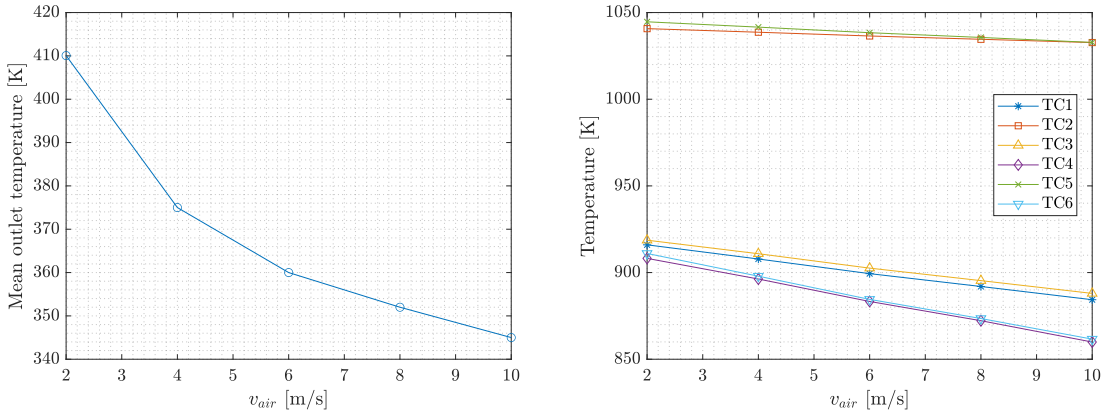
Figure 3.15: Air aspiration temperature measurements during the first tappings of a campaign cycle.

that, while there is a significant dispersion of the measurements, a general trend is clearly observed, which shows that the temperature increases rapidly until stabilising after about 0.8 h of tapping. The median quasi-steady temperature during a tapping (after 1 h, approximately) is around 375 K. Moreover, in Figure 3.16a, the average computed temperature on Γ^A_{outlet} is displayed for the different v_{air} values. Since this boundary is located where the air aspiration is performed, 7.35 m away from the taphole, the air circulating along the trough should be hotter than on the outlet considered in the present computational domain. Therefore, it is unlikely that any value of v_{air} below 6 m/s is realistic, and values within the range $v_{air} \in [8, 10]$ m/s are probably more representative of the real BF setting that is being addressed in this manuscript.

Moreover, to validate the model, ArcelorMittal Spain has provided a temperature experimental measurement obtained with 6 thermocouples (TC). The temperature snapshot is taken during the tapping process of the BF in standard operation. The devices are embedded in the insulation lining, located approximately in groups of three at two different cross-sections with constant x_3 coordinate; two of them on each lateral of the trough and the remaining one in the bottom. Thus, they are well-protected from any slag or hot metal infiltration that could reach the safety lining. Viewed from the BF, TC1 and TC4 are located in the left lateral side, TC2 and TC5 in the bottom, whereas TC3 and TC6 are in the right lateral side. The first set of TC is located at $x_3 = 8$ m, whereas the second set on $x_3 = 12$ m. The locations of these devices are the same in each cross-section and are stated in Section 5.4. Since the thermocouples are composed of a 20×20 cm^2 plate, to compare the temperature measurement with the numerical approximation, we find the average temperature by integrating on the corresponding surface. For the lateral thermocouples, the plate is aligned vertically, while for those in the bottom of the trough, the plate is oriented horizontally. The comparison among the measurement and the numerical temperature, as well as the corresponding errors, are collected in Table 3.6, for $v_{air} = 8$ m/s. An apparently good level of agreement is found among the computations

Table 3.5: Heat transfer coefficients on the parts of the radiation cavity [W/(m^2·K)], computed through (3.22), and heat transfer coefficient (h_R), for various v_{air} values.

v_{air}	h_{free}	h_{cover}	h_{work}	h_R
2 m/s	9.62	7.84	11.06	9.20
4 m/s	14.44	12.76	16.21	14.17
6 m/s	19.17	18.57	21.76	19.70
8 m/s	24.71	24.78	27.87	25.76
10 m/s	29.35	31.30	33.62	31.69



(**a**) On Γ^A_{outlet}.

(**b**) On the surfaces corresponding to the thermocouple locations.

Figure 3.16: Average temperature on air outlet (Γ^A_{outlet}) and on the surfaces corresponding to the thermocouple positions, with respect to v_{air}.

and the measurements, with a mean relative error below 2.5%.

In Figure 3.16b, the computed average temperature on the surfaces corresponding to the thermocouple locations are shown for different v_{air} values. In accordance with the prior discussion, for higher air velocities, lower temperatures are computed at the TC locations. However, there are some TCs that are more affected by the enhanced forced convection, as evidenced by the different slopes that are observed in the figure. In particular, TC4-TC6, which correspond to those thermocouples located closer to the slag runner, show larger sensitivity to the air velocity. Also, the lateral thermocouples are more influenced by the increasing air velocity, whereas the bottom ones show little impact.

Remark 3.7. *The good agreement observed in Table 3.6 is not very significant and could be slightly misleading. The temperature snapshot used to validate the model is the same considered in the previous work (Barral et al., 2019), and was supplied by ArcelorMittal as representative of the quasi steady-state readings during the trough campaign cycle. Nonetheless, in reality, a careful analysis of transient thermocouple measurements, provided afterwards by the company, revealed that long stops prevent the trough from fully reaching the steady-state, with significant oscillations in the observed temperatures due to the discontinuous tapping process. Also, the reader may notice that the temperature measurements represented in Chapter 5 are substantially lower to those reported here in all thermocouples. This is because the measurements presented therein were supplied by the company later, and correspond to a different trough of the same BF, but with almost identical geometrical parameters. This large difference can be explained by slight deviations in the positioning of the thermocouples: the low thermal conductivity within the insulation lining means that small deviations from the indicated position can lead to large differences in the temperature measurement, as shown in Section 5.4.*

Table 3.6: Thermocouple (TC) temperature measurements, numerical temperature values, absolute error and relative error, $v_{air} = 8$ m/s

	Measurement [K]	Numerical [K]	Absolute error [K]	Relative error [−]
TC 1	942	891.97	50.03	$5.31{\cdot}10^{-2}$
TC 2	1043	1034.58	8.42	$8.07{\cdot}10^{-3}$
TC 3	899	895.35	3.65	$4.06{\cdot}10^{-3}$
TC 4	849	872.20	23.23	$2.74{\cdot}10^{-2}$
TC 5	1028	1035.64	7.65	$7.44{\cdot}10^{-3}$
TC 6	917	873.49	43.51	$4.74{\cdot}10^{-2}$

Chapter 4

Non-local radiation model

This chapter is dedicated to the study of a transient heat diffusion problem with a non-local radiation boundary. The model will be used in the subsequent chapter to assess the thermal response of the main trough cross-section during its complete campaign cycle. From a mathematical standpoint, the works of Tiihonen (1997a,b) established the mathematical framework for the so-called *non-local radiation* problems, which involve the solution of integral equations on the boundary of the radiation cavity with a non-participating, transparent medium. It can be seen that it is a generalisation of a technique known as *net-radiation method*, *view factor method* or *surface-to-surface radiation*, described in radiation and heat transfer books (see e.g. Bergman et al., 2011; Modest, 2013), and used in Chapter 3 to obtain the steady temperature in the BF trough. The framework can be extended also to semitransparent mediums (Laitinen & Tiihonen, 2001), and a summary of mathematical results concerning the heat diffusion and non-local radiation coupled problem can be found in Druet (2009), with an extension to less regular source terms. Non-local radiation problems have been used in several similar applications, such as Bermúdez et al. (2011).

In Section 4.1, a brief overview of the integro-differential equation that models general thermal radiation is given. Then, in Section 4.2, a formal derivation of the non-local radiation model is carried out. To this end, we start from the radiative heat transfer equation and assume that the radiation heat transfer takes place in a non-participant cavity, surrounded by an opaque domain. Since the boundary of the cavity is assumed to be diffuse and grey, the problem can be reduced to an integral equation of the second kind, defined only on the boundary. Although, as mentioned above, this is a well-studied problem, the formal derivation from the general radiation equations was not done in the bibliography, to the best of our knowledge. Instead, a heat balance on the boundary was proposed from which the integral equation follows by intuitive arguments. This procedure, even though it leads to the same equation, obscures the assumptions required for the model to make sense.

In Section 4.3, the formulation of the radiation problem in a plane setting is derived from the 3D model. Subsequently, Section 4.4 focuses on the issue of the numerical solution of the model, presenting a numerical algorithm which uses a fixed-point method to iteratively solve the transient heat equation and the integral equation on the boundary. The time discretisation is performed using ESDIRK methods (Kværnø, 2004), which allow to readily modify the step size to keep the discretisation error within specified bounds.

To verify the numerical algorithm and its implementation, we devote Section 4.5 to pose and solve a manufactured solution test for a plane non-local radiation problem, coupled with heat conduction. Hence, an analytical solution for the set of governing equations is obtained, determining suitable initial and boundary conditions. This method is often known as method of manufactured solutions (MMS) (Roache, 2001; Roy, 2005). When only heat diffusion is present, the derivation of the analytical solution is straightforward. However, for more complicated physics, such derivation can only be performed under very particular assumptions. In the case of coupled heat diffusion and non-local radiation, the main difficulty is dealing with the integral operator. For 3D geometries, if the domain is chosen as a spherical cavity, the derivation of the test greatly simplifies, as shown in Bermúdez

USC UNIVERSIDADE DE SANTIAGO DE COMPOSTELA

This chapter reproduces contents from the following article:

- Barral, P., Pérez-Pérez, L.J., & Quintela, P. (2022). *Transient thermal response with nonlocal radiation of a blast furnace main trough*. Applied Mathematical Modelling. 105, 197 – 225. doi:10.1016/j.apm.2021.12.029

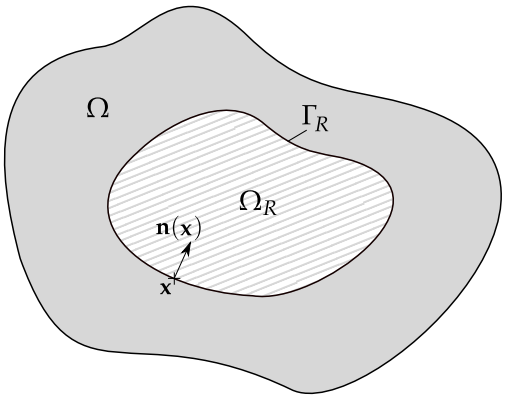


Figure 4.1: Sketch of a 2D section of the problem domain.

et al. (2011). On the other hand, for the 2D case, such derivation is substantially more intricate. In Blackwell et al. (2009), a procedure to obtain an analytical solution for the radiosity integral equation on a circular cavity was proposed. This methodology was also applied in Silva III & Carnes (2016) to obtain a test including steady heat diffusion within an annulus surrounding the cavity. Nonetheless, the proposed analytical test has the shortcoming of not being smooth. This approach is extended to provide a strategy that allows to derive the analytical solution by solving a Cauchy problem defined on the circumference, which leads to a smooth temperature field. Lastly, in Section 4.6, the manufactured solution test is solved using different time discretisation schemes, validating the numerical methodology and analysing the observed numerical errors.

4.1. General thermal radiation

Let $\Omega \subset \mathbb{R}^3$ be a domain with a smooth enough boundary. Let us assume that Ω surrounds a cavity Ω_R, depicted in Figure 4.1. Furthermore, assume that Ω is totally opaque to radiation, meaning that thermal radiation is only relevant within the open set Ω_R. Let Γ_R be the part of the boundary of Ω that is in contact with Ω_R, i.e., $\Gamma_R = \partial\Omega \cap \overline{\Omega}_R$. Furthermore, for the sake of simplicity, we assume that $\mathbb{R}^3 \setminus \Gamma_R$ is a non-connected set. This statement is usually formulated by saying that Ω is an *enclosure*, since all radiation originated inside Ω_R and emitted from its boundary returns to Ω. Note that it holds that $\partial\Omega_R = \Gamma_R$.

In the sequel, we briefly address the modelling of general radiative heat transport inside Ω_R and the boundary condition that corresponds to the boundary of the cavity. To do so, we derive the corresponding equations in a formal manner, assuming that the involved fields have sufficient regularity for the manipulations to be valid.

4.1.1. Radiative heat transfer equation

Thermal radiation is electromagnetic radiation comprising mainly wavelengths ranging from 10^{-7} m to 10^{-3} m (Modest, 2013). It is customarily defined in terms of the unknown *spectral intensity*, i. The spectral intensity is defined as the radiative energy flux at a specific wavelength $\lambda \in (0, \infty)$ per unit time, per projected normal unit area in the propagation direction $\mathbf{s}$, and in a unit solid angle. Hence, it depends on the point $\mathbf{x} \in \Omega_R$, the direction $\mathbf{s} \in S^2$, being S^2 the unit sphere, the wavelength λ, and also on the time t. Then, we set the spectral intensity as a function $i : \Omega_R \times (0, \infty) \times S^2 \times (0, t_{end}] \to \mathbb{R}$, where $(0, t_{end}]$ is the time interval. As well as any other spectral variable related to electromagnetic waves, notice that i could have been equivalently defined in terms of the frequency, wavenumber or angular frequency instead of the wavelength (see e.g. Howell et al., 2015). It is described by the

Radiative Transfer Equation (RTE):

$$\frac{1}{c}\frac{\partial i}{\partial t} + \mathbf{s}\cdot \operatorname{grad}_{\mathbf{x}}(i) = -ai + ai_b - \varsigma i + \frac{\varsigma}{4\pi}\int_{S^2} \phi(\hat{\mathbf{s}},\mathbf{s}) i(\mathbf{x},\lambda,\hat{\mathbf{s}},t)\, dA_{\hat{\mathbf{s}}}, \tag{4.1}$$

for $(\mathbf{x},\lambda,\mathbf{s},t) \in \Omega_R \times (0,\infty) \times S^2 \times (0,t_{end}]$. In the equation above, c denotes the speed of light in the medium, a and ς are the absorption and scattering coefficients, respectively, and i_b is the spectral intensity of a black body. The function $\phi : S^2 \times S^2 \to \mathbb{R}$ is the scattering phase function; which describes the probability that a ray coming from one direction may be scattered into a certain other direction. Finally, $dA_{\hat{\mathbf{s}}}$ denotes the surface area element (on the unit sphere S^2, in this particular case); the subscript specifies that integration should be understood with respect to the $\hat{\mathbf{s}}$ variable. Note that in (4.1), outside of the integral, we have omitted the explicit dependency of the spectral intensity on the specific point $(\mathbf{x},\lambda,\mathbf{s},t)$ to avoid excessively cumbersome notation.

The terms in the right hand side of expression (4.1) refer to the contributions due to absorption, emission, the loss due to scattering and the gain due to scattering from direction $\mathbf{s}$, respectively. For more details on the formal derivation of this equation, we refer to Modest (2013, Ch. 10).

Remark 4.1. *Usually, the term containing temporal derivative in expression (4.1) is dropped even in mathematical models that have some sort of time-dependency. This is due to the huge difference when comparing the speed of propagation of light to the other processes that may be present in the problem, such as heat conduction or convection. In practice, this implies that equilibrium in radiative heat transfer is reached much faster, instantly in comparison. Since this is true for the application in the BF trough, the time derivative is neglected and, for ease of notation, we also omit explicitly stating the dependence on time in the radiation related quantities. Nonetheless, it should be noted that the radiated energy still depends on time as, for instance, the temperature on the boundary of the cavity may change with time.*

We assume that the medium is *grey*, i.e., that the scattering coefficient, ς, and the absorption coefficient, a, are independent of the wavelength. In such case, (4.1) can be recast in terms of the *total intensity*, $I : \Omega_R \times S^2 \to \mathbb{R}$, which for a fixed $(\mathbf{x},\mathbf{s}) \in \Omega_R \times S^2$ is defined as:

$$I(\mathbf{x},\mathbf{s}) = \int_0^\infty i(\mathbf{x},\lambda,\mathbf{s})\, d\lambda. \tag{4.2}$$

The *total radiation intensity of a black body*, I_b, is defined as (see Remark 4.2 below)

$$I_b(\mathbf{x}) = \int_0^\infty i_b(\mathbf{x},\lambda)\, d\lambda = \frac{\sigma T^4(\mathbf{x})}{\pi}, \tag{4.3}$$

where we recall that $\sigma = 5.67{\cdot}10^{-8}$ W/(m$^2{\cdot}$ K^4) is the Stefan-Boltzmann constant.

Moreover, the total intensity leads to the definition of the *radiative heat flux*, defined as the radiation contribution in all directions (Modest, 2013, p. 292):

$$\mathbf{q}_{rad}(\mathbf{x}) = \int_{S^2} I(\mathbf{x},\mathbf{s})\mathbf{s}\, dA_{\mathbf{s}}. \tag{4.4}$$

Integrating (4.1) over all wavelengths and using (4.2), we obtain the subsequent equation involving the total radiation intensity (Ferrín, 1999):

$$\mathbf{s}\cdot \operatorname{grad}_{\mathbf{x}}(I) = -aI + aI_b - \varsigma I + \frac{\varsigma}{4\pi}\int_{S^2} \phi(\hat{\mathbf{s}},\mathbf{s}) I(\mathbf{x},\hat{\mathbf{s}}) dA_{\hat{\mathbf{s}}}, \tag{4.5}$$

where, in virtue of Remark 4.1, the time dependency has been neglected.

Remark 4.2. *An alternative radiation variable is the spectral emissive power, $E_\lambda : \Omega_R \times (0,\infty) \to \mathbb{R}$. It measures the amount of radiative energy that is emitted in all directions for a given wavelength. The total emissive power, E, is defined by integrating over all wavelengths, analogously as (4.2):*

$$E(\mathbf{x}) = \int_0^\infty E_\lambda(\mathbf{x},\lambda)\, d\lambda.$$

USC UNIVERSIDADE DE SANTIAGO DE COMPOSTELA

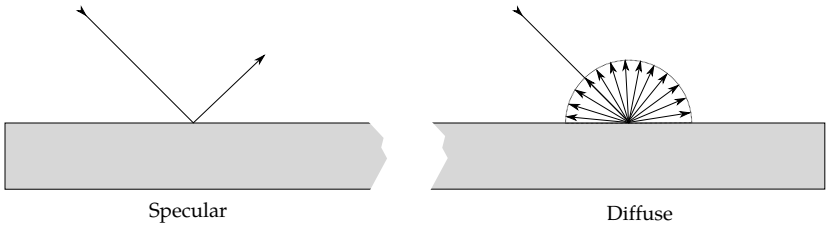


Figure 4.2: Schematic of specular and diffuse reflection on an opaque surface.

The total and spectral emissive power of a black body are denoted as E_b and $E_{b\lambda}$. In particular, E_b is described by the Stefan-Boltzmann law, which asserts that (see e.g. Bergman et al., 2011):

$$E_b(\mathbf{x}) = n^2 \sigma T^4(\mathbf{x}),$$

where n is the refractive index of the medium, defined such that for vacuum it holds that $n = 1$. Since for most gases, $n \approx 1$ (Modest, 2013, p. 3), we shall assume that $n = 1$. In addition, it can be proved that the spectral intensity of a black body, i_b, is independent of direction and it is related to the spectral emissive power of a black body through the subsequent expression (Modest, 2013, p. 15):

$$E_{b\lambda}(\mathbf{x}, \lambda) = \pi i_b(\mathbf{x}, \lambda).$$

4.1.2. Boundary condition

The boundary of the enclosure, Γ_R, is assumed to be opaque. We identify it with a radiating surface, and we usually refer to it simply as a *surface*. Given that Γ_R is opaque, incident radiation is either absorbed or reflected. Although, in general, reflection may depend on wavelength and the specific incidence direction, here we restrict to the case of *grey* and *diffuse surfaces*, i.e., the reflection does not depend on wavelength nor direction. It should be noted that real surfaces are actually specular, at least to some degree (see Figure 4.2). Nevertheless, the surface roughness leads to the diffuse assumption being a reasonable approximation in many practical cases.

As any other body at a temperature above absolute zero, the surface radiates energy. It is customary to assume that the emitted radiation from a diffusely reflecting surface does not depend on direction either. Consequently, for $\mathbf{x} \in \Gamma_R$ we find that

$$I(\mathbf{x}, \mathbf{s}) = I(\mathbf{x}), \qquad \text{if } \mathbf{s} \cdot \mathbf{n}(\mathbf{x}) > 0,$$

where $\mathbf{n}(\mathbf{x})$ denotes the inward-pointing unit normal vector of Ω_R at $\mathbf{x} \in \Gamma_R$, as depicted in Figure 4.1. At any $\mathbf{x} \in \Gamma_R$, we can distinguish among *incoming* radiation, i.e., the energy that arrives at the surface that has been radiated from the rest of Ω_R and its boundary, and *outgoing* radiation. The latter is the sum of the emitted and reflected radiation at that particular point on Γ_R. The normal vector is used to identify those directions in S^2 that correspond to either incoming or outgoing radiation. Specifically, at each $\mathbf{x} \in \Gamma_R$, S^2 is split in the incoming directions, denoted as $S^2_-(\mathbf{x})$, and the outgoing directions, $S^2_+(\mathbf{x})$, which are defined as

$$S^2_-(\mathbf{x}) = \{\mathbf{s} \in S^2 : \ \mathbf{s} \cdot \mathbf{n}(\mathbf{x}) < 0\}.$$

$$S^2_+(\mathbf{x}) = \{\mathbf{s} \in S^2 : \ \mathbf{s} \cdot \mathbf{n}(\mathbf{x}) > 0\},$$

Then, as the *outgoing radiation* is the sum of the reflected and emitted radiation, using that $I(\mathbf{x}, \mathbf{s})$ is the same for any $\mathbf{s} \in S^2_+(\mathbf{x})$ since the surface is diffuse, it holds that (Modest, 2013)

$$I(\mathbf{x}, \mathbf{s}) = I(\mathbf{x}) = \varepsilon(\mathbf{x}) I_b(\mathbf{x}) + (1 - \vartheta(\mathbf{x})) \frac{G(\mathbf{x})}{\pi}, \qquad \text{on } \Gamma_R \times S^2_+(\mathbf{x}), \tag{4.6}$$

USC UNIVERSIDADE DE SANTIAGO DE COMPOSTELA

where ε denotes the *emissivity*, ϑ denotes the *absorptivity* and the unknown $G : \Gamma_R \to \mathbb{R}$ is the *total irradiation*. It is defined as the total incoming radiative energy to the surface, in $\mathrm{W/m^2}$. Hence, at a given point $\mathbf{x} \in \Gamma_R$, it can be found by integrating the total intensity, I, over all incoming directions (see e.g. Bergman et al., 2011):

$$G(\mathbf{x}) = \int_{S^2_-(\mathbf{x})} I(\mathbf{x}, \mathbf{s}) |\mathbf{s} \cdot \mathbf{n}(\mathbf{x})| \, dA_{\mathbf{s}}. \tag{4.7}$$

Similarly, the *radiosity*, $R : \Gamma_R \to \mathbb{R}$, which corresponds to the outgoing radiative energy from the surface, is defined as the subsequent expression:

$$R(\mathbf{x}) = \int_{S^2_+(\mathbf{x})} I(\mathbf{x}, \mathbf{s}) \mathbf{s} \cdot \mathbf{n}(\mathbf{x}) \, dA_{\mathbf{s}}. \tag{4.8}$$

Equivalently, the radiosity can be regarded as the rate at which radiation leaves a surface due to emission and reflection in all directions, per unit surface area (Cengel, 2014).

The emissivity is a physical property of the surface. It measures the fraction of emitted energy by the surface relative to that emitted by a black body. On the other hand, the absorptivity refers to the fraction of the total incident radiation that is absorbed by the surface. In general, both depend on either wavelength or direction, as well as on the temperature of the surface. Since we assume that the surface is diffuse and grey, the only dependence left is that on temperature, which for the sake of simplicity we neglect as well, as it has no impact in the subsequent discussion. Using the definition of the emissivity, for any $\mathbf{x} \in \Gamma_R$, we obtain that the emissive power (see e.g. Bergman et al., 2011) is

$$E(\mathbf{x}) = \varepsilon(\mathbf{x}) \sigma T^4(\mathbf{x}). \tag{4.9}$$

Absorptivity and emissivity are related through *Kirchhoff's Law*:

$$\vartheta(\mathbf{x}) = \varepsilon(\mathbf{x}). \tag{4.10}$$

Therefore, for $\mathbf{x} \in \Gamma_R$, substituting (4.3), (4.7) and (4.10) in (4.6), for any outgoing direction it follows that:

$$\pi I(\mathbf{x}) = (1 - \varepsilon(\mathbf{x})) \int_{S^2_-(\mathbf{x})} I(\mathbf{x}, \mathbf{s}) |\mathbf{s} \cdot \mathbf{n}(\mathbf{x})| \, dA_{\mathbf{s}} + \varepsilon(\mathbf{x}) \sigma T^4(\mathbf{x}), \tag{4.11}$$

which is the standard boundary condition for the total radiative intensity for diffuse and grey radiation. Note that, if the absorptivity is $\vartheta = 1$ on Γ_R, then $\varepsilon = 1$ by Kirchhoff's law and (4.11) simply becomes $I(\mathbf{x}) = I_b(\mathbf{x})$ for all $\mathbf{x} \in \Gamma_R$.

Remark 4.3. *For any $\mathbf{x} \in \Gamma_R$, if $\mathbf{s} \in S^2_+(\mathbf{x})$, total radiation intensity does not depend on direction, as we assume that the reflection and emission are diffuse on the opaque surface forming the boundary Γ_R. Therefore, from (4.8) it holds that*

$$R(\mathbf{x}) = \int_{S^2_+(\mathbf{x})} I(\mathbf{x}, \mathbf{s}) \mathbf{s} \cdot \mathbf{n}(\mathbf{x}) \, dA_{\mathbf{s}} = I(\mathbf{x}) \int_{S^2_+(\mathbf{x})} \mathbf{s} \cdot \mathbf{n}(\mathbf{x}) \, dA_{\mathbf{s}} = \pi I(\mathbf{x}), \tag{4.12}$$

which coincides with the left hand side of (4.11).

4.2. Non-local radiation problem

In the previous section, we established that, for a radiation cavity Ω_R where the medium is participating and radiation is grey, the total radiation intensity satisfies equation (4.5). Moreover, at the boundary of the cavity, the intensity in the outgoing directions ($\mathbf{s} \in S^2_+(\mathbf{x})$) is such that the boundary condition (4.11) holds. In the subsequent discussion, we further simplify the equation (4.11) assuming that Ω_R is a non-participant and transparent medium; thus, it does not emit, absorb or scatter radiation. In such setting, (4.5) transforms in an integral equation defined on the boundary Γ_R, where the unknowns are the radiosity R and the surface temperature T.

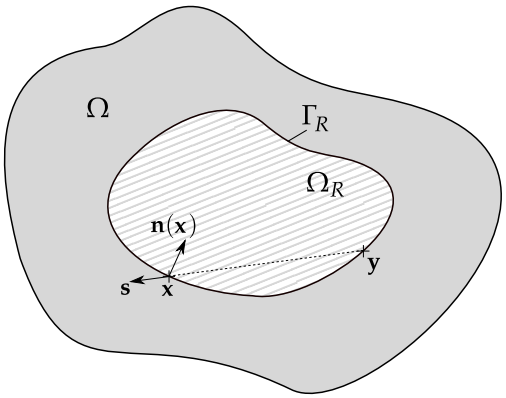


Figure 4.3: Cross-section of the problem setting, displaying the relation between the points $\mathbf{y}, \mathbf{x}$ and the unit vector $\mathbf{s}$.

4.2.1. Derivation of the integral kernel

Assuming that the medium in Ω_R is non-participant, it holds that $a = 0$ and $\varsigma = 0$ (see Modest, 2013, p. 27). Therefore, (4.5) simply becomes

$$\operatorname{grad}_{\mathbf{x}}\big(I(\mathbf{x},\mathbf{s})\big)\cdot\mathbf{s} = 0, \qquad (\mathbf{x},\mathbf{s}) \in \Omega_R \times S^2. \tag{4.13}$$

Consequently, the total intensity is constant along the paths determined by straight lines. Set a fixed $\mathbf{x} \in \Omega_R$. Then, for any $\mathbf{y} \in \Omega_R$, let $\mathbf{s} \in S^2$ such that $\mathbf{s} = (\mathbf{x}-\mathbf{y})/|\mathbf{x}-\mathbf{y}|$. From (4.13), it follows that

$$I(\mathbf{x},\mathbf{s}) = I(\mathbf{y},\mathbf{s}). \tag{4.14}$$

To account for non-convex cavities where the points on the boundary do not necessarily see each other due to the presence of obstacles blocking the view, we introduce the so-called *blocking* or *visibility factor* $\Theta : \Gamma_R \times \Gamma_R \to \{0,1\}$:

$$\Theta(\mathbf{x},\mathbf{y}) = \begin{cases} 1, & \text{if } \overline{\mathbf{xy}} \subset \Omega_R, \\ 0, & \text{if } \overline{\mathbf{xy}} \not\subset \Omega_R, \end{cases} \tag{4.15}$$

where $\overline{\mathbf{xy}}$ is the straight line segment going from $\mathbf{x}$ to $\mathbf{y}$:

$$\overline{\mathbf{xy}} := \{\mathbf{x} + \hat{\lambda}(\mathbf{y}-\mathbf{x}) : \hat{\lambda} \in (0,1)\}. \tag{4.16}$$

Notice that $\Theta(\mathbf{x},\mathbf{x}) = 0$ by definition, since $\overline{\mathbf{xx}} = \{\mathbf{x}\}$ and $\mathbf{x} \notin \Omega_R$.

Using $\Theta(\mathbf{x},\mathbf{y})$, set $\mathbf{x} \in \Gamma_R$ fixed and let $\widetilde{\Gamma}_{R,\mathbf{x}}$ be the portion of Γ_R that is *visible* from $\mathbf{x}$, i.e.

$$\widetilde{\Gamma}_{R,\mathbf{x}} = \{\mathbf{y} \in \Gamma_R : \Theta(\mathbf{x},\mathbf{y}) = 1\}.$$

Consider the function $\varphi : \widetilde{\Gamma}_{R,\mathbf{x}} \to S^2_-(\mathbf{x})$, defined as

$$\varphi(\mathbf{y}) = \frac{\mathbf{x}-\mathbf{y}}{|\mathbf{x}-\mathbf{y}|}.$$

Notice that it is a differentiable mapping. Since Ω is an enclosure, then it is also surjective and, provided that $\widetilde{\Gamma}_{R,\mathbf{x}}$ is only the part of Γ_R that is visible from $\mathbf{x}$, it is injective. This function is often known as *central projection*. In particular, the differential of φ at $\mathbf{y} \in \widetilde{\Gamma}_{R,\mathbf{x}}$, denoted as $D\varphi_{\mathbf{y}}$, which maps any vector $\mathbf{v}$ in the tangent plane of the boundary at the point $\mathbf{y}$ to the tangent plane of S^2 at $\varphi(\mathbf{y})$, is such that (see Montiel & Ros, 2009, p. 54):

$$D\varphi_{\mathbf{y}}(\mathbf{v}) = -\frac{\mathbf{v}}{|\mathbf{x}-\mathbf{y}|} + \frac{(\mathbf{x}-\mathbf{y})\otimes(\mathbf{x}-\mathbf{y})}{|\mathbf{x}-\mathbf{y}|^3}\mathbf{v}. \tag{4.17}$$

USC UNIVERSIDADE DE SANTIAGO DE COMPOSTELA

Consider the set $\mathcal{N}_{\mathbf{x}} = \{\mathbf{y} \in \widetilde{\Gamma}_{R,\mathbf{x}} : \mathbf{n}(\mathbf{y}) \cdot (\mathbf{x} - \mathbf{y}) = 0\}$. We assume that this subset of $\widetilde{\Gamma}_{R,\mathbf{x}}$ is of zero measure. Note that $\ker D\varphi_{\mathbf{y}} = \{\eta(\mathbf{x} - \mathbf{y}), \eta \in \mathbb{R}\}$ and let $\mathbf{z} \in \widetilde{\Gamma}_{R,\mathbf{x}}$ such that $\mathbf{x} - \mathbf{z}$ belongs to the tangent plane to $\widetilde{\Gamma}_{R,\mathbf{x}}$ at $\mathbf{z}$. Then, it holds that $\mathbf{z} \in \mathcal{N}_{\mathbf{x}}$, and we can conclude that in the region $\mathcal{R}_1$, defined as $\mathcal{R}_1 = \widetilde{\Gamma}_{R,\mathbf{x}} \setminus \mathcal{N}_{\mathbf{x}}$, the kernel of the differential becomes the zero vector, i.e. $\ker D\varphi_{\mathbf{y}} = \{\mathbf{0}\}$, for any $\mathbf{y} \in \mathcal{R}_1$. Accordingly, $\varphi : \mathcal{R}_1 \to \varphi(\mathcal{R}_1)$ is a diffeomorphism. Let us denote by $\mathcal{R}_2 = \varphi(\mathcal{R}_1)$. Then, by Theorem 5.14 in Montiel & Ros (2009), if $h : \mathcal{R}_2 \to \mathbb{R}$ is an integrable function, it holds that

$$\int_{\mathcal{R}_2} h(\mathbf{s})\, dA_{\mathbf{s}} = \int_{\mathcal{R}_1} h(\varphi(\mathbf{y}))|\text{Jac }\varphi|(\mathbf{y})\, dA_{\mathbf{y}}, \tag{4.18}$$

where the $|Jac\ \varphi|$ denotes the *absolute value of the Jacobian*, and is defined as

$$|\text{Jac }\varphi|(\mathbf{y}) = |D\varphi_{\mathbf{y}}(\mathbf{v}_1) \times D\varphi_{\mathbf{y}}(\mathbf{v}_2)|,$$

being $\{\mathbf{v}_1, \mathbf{v}_2\}$ an orthonormal basis of the tangent plane of $\widetilde{\Gamma}_{R,\mathbf{x}}$ at $\mathbf{y}$.

Assume that the basis $\{\mathbf{v}_1, \mathbf{v}_2\}$ is such that it gives the orientation of the inward-pointing unit normal vector of Ω_R. Therefore, at each $\mathbf{y} \in \widetilde{\Gamma}_{R,\mathbf{x}}$, $\mathbf{v}_1 \times \mathbf{v}_2 = \mathbf{n}(\mathbf{y})$. Let $\mathbf{P}_{\mathbf{y}} = (\mathbf{x} - \mathbf{y}) \otimes (\mathbf{x} - \mathbf{y})$ and notice that $\mathbf{P}_{\mathbf{y}} \in Sym$, i.e., it is a symmetric linear mapping on $\mathbb{R}^3$. Using (4.17), it follows that, for the previous basis:

$$\begin{aligned}|\text{Jac }\varphi|(\mathbf{y}) &= \left|\frac{1}{|\mathbf{x}-\mathbf{y}|^2}(\mathbf{v}_1 \times \mathbf{v}_2) - \frac{1}{|\mathbf{x}-\mathbf{y}|^4}(\mathbf{v}_1 \times \mathbf{P}_{\mathbf{y}}\mathbf{v}_2) - \frac{1}{|\mathbf{x}-\mathbf{y}|^4}(\mathbf{P}_{\mathbf{y}}\mathbf{v}_1 \times \mathbf{v}_2)\right| \\ &= \left|\frac{1}{|\mathbf{x}-\mathbf{y}|^2}\mathbf{n}(\mathbf{y}) - \frac{1}{|\mathbf{x}-\mathbf{y}|^4}\left(\text{Tr}(\mathbf{P}_{\mathbf{y}})\mathbf{v}_1 \times \mathbf{v}_2 - \mathbf{P}_{\mathbf{y}}(\mathbf{v}_1 \times \mathbf{v}_2)\right)\right|,\end{aligned} \tag{4.19}$$

where it has been used that $\mathbf{P}_{\mathbf{y}}\mathbf{v}_1$ and $\mathbf{P}_{\mathbf{y}}\mathbf{v}_2$ are collinear vectors as well as the identity $\mathbf{Ma} \times \mathbf{b} + \mathbf{a} \times \mathbf{Mb} = \text{Tr}(\mathbf{M})\mathbf{a} \times \mathbf{b} - \mathbf{M}(\mathbf{a} \times \mathbf{b})$, which holds for any $\mathbf{M} \in Sym$ and $\mathbf{a}, \mathbf{b} \in \mathbb{R}^3$.

From (4.19), noting that $\text{Tr}(\mathbf{P}_{\mathbf{y}}) = |\mathbf{x} - \mathbf{y}|^2$ and since $\mathbf{v}_1 \times \mathbf{v}_2 = \mathbf{n}(\mathbf{y})$, the definition of $\mathbf{P}_{\mathbf{y}}$ directly leads to

$$|\text{Jac }\varphi|(\mathbf{y}) = \left|\frac{(\mathbf{x}-\mathbf{y}) \otimes (\mathbf{x}-\mathbf{y})}{|\mathbf{x}-\mathbf{y}|^4}\mathbf{n}(\mathbf{y})\right| = \left|\frac{\mathbf{n}(\mathbf{y}) \cdot (\mathbf{x}-\mathbf{y})}{|\mathbf{x}-\mathbf{y}|^4}(\mathbf{x}-\mathbf{y})\right| = \frac{\mathbf{n}(\mathbf{y}) \cdot (\mathbf{x}-\mathbf{y})}{|\mathbf{x}-\mathbf{y}|^3}, \tag{4.20}$$

where in the last equality, it has been used that $\mathbf{n}(\mathbf{y})$ is the inward-pointing unit normal vector, and hence $\mathbf{n}(\mathbf{y}) \cdot (\mathbf{x} - \mathbf{y}) > 0$ (see Figure 4.3).

Let us assume that the set $\varphi(\mathcal{R}_1) \setminus S^2_-(\mathbf{x})$ is of measure zero. Thus, substituting (4.20) in (4.18) and using that $\mathcal{R}_1 \setminus \widetilde{\Gamma}_{R,\mathbf{x}}$ is also of null measure:

$$\begin{aligned}\int_{S^2_-(\mathbf{x})} h(\mathbf{s})\, dA_{\mathbf{s}} &= \int_{\varphi(\mathcal{R}_1)} h(\mathbf{s})\, dA_{\mathbf{s}} = \int_{\mathcal{R}_1} h(\varphi(\mathbf{y}))|\text{Jac }\varphi|(\mathbf{y})\, dA_{\mathbf{y}} = \int_{\widetilde{\Gamma}_{R,\mathbf{x}}} h(\varphi(\mathbf{y}))|\text{Jac }\varphi|(\mathbf{y})\, dA_{\mathbf{y}} \\ &= \int_{\widetilde{\Gamma}_{R,\mathbf{x}}} h(\varphi(\mathbf{y}))\frac{\mathbf{n}(\mathbf{y}) \cdot (\mathbf{x}-\mathbf{y})}{|\mathbf{x}-\mathbf{y}|^3}\, dA_{\mathbf{y}}.\end{aligned}$$

Now, assume that $I(\mathbf{x}, \mathbf{s})$ is an integrable function in $S^2_-(\mathbf{x})$ and set $h(\mathbf{s}) = I(\mathbf{x}, \mathbf{s})|\mathbf{s} \cdot \mathbf{n}(\mathbf{x})|$. Substituting in the previous expression and noticing that the point $\mathbf{x}$ is fixed, we find that:

$$\int_{S^2_-(\mathbf{x})} I(\mathbf{x}, \mathbf{s})|\mathbf{s} \cdot \mathbf{n}(\mathbf{x})|\, dA_{\mathbf{s}} = \int_{\widetilde{\Gamma}_{R,\mathbf{x}}} I\left(\mathbf{x}, \frac{\mathbf{x}-\mathbf{y}}{|\mathbf{x}-\mathbf{y}|}\right)\frac{\mathbf{n}(\mathbf{x}) \cdot (\mathbf{y}-\mathbf{x})\mathbf{n}(\mathbf{y}) \cdot (\mathbf{x}-\mathbf{y})}{|\mathbf{x}-\mathbf{y}|^4}\, dA_{\mathbf{y}}, \tag{4.21}$$

where it has been used that $\mathbf{n}(\mathbf{x}) \cdot (\mathbf{x} - \mathbf{y}) < 0$.

Provided that $\mathbf{s} = (\mathbf{x} - \mathbf{y})/|\mathbf{x} - \mathbf{y}|$ is an outgoing direction for any $\mathbf{y} \in \widetilde{\Gamma}_{R,\mathbf{x}}$, from (4.12) and (4.14) it follows that

$$I(\mathbf{x}, \mathbf{s}) = I(\mathbf{y}, \mathbf{s}) = I(\mathbf{y}) = \frac{R(\mathbf{y})}{\pi}.$$

USC UNIVERSIDADE DE SANTIAGO DE COMPOSTELA

Therefore, substituting in (4.21) and including the visibility factor $\Theta(\mathbf{x},\mathbf{y})$ to transform the integral over the subset of the boundary composed of the visible points from $\mathbf{x}$, $\widetilde{\Gamma}_{R,\mathbf{x}}$, into an integral on the whole of Γ_R, we obtain that

$$\int_{S^2_-(\mathbf{x})} I(\mathbf{x},\mathbf{s})|\mathbf{s}\cdot\mathbf{n}(\mathbf{x})|\,dA_{\mathbf{s}} = \int_{\Gamma_R} W(\mathbf{x},\mathbf{y})R(\mathbf{y})dA_{\mathbf{y}}, \tag{4.22}$$

where $W(\mathbf{x},\mathbf{y}) : \Gamma_R \times \Gamma_R \to \mathbb{R}$ is the following integral kernel:

$$W(\mathbf{x},\mathbf{y}) = \frac{\mathbf{n}(\mathbf{x})\cdot(\mathbf{y}-\mathbf{x})\mathbf{n}(\mathbf{y})\cdot(\mathbf{x}-\mathbf{y})}{\pi|\mathbf{y}-\mathbf{x}|^4}\Theta(\mathbf{x},\mathbf{y}). \tag{4.23}$$

The kernel (4.23) is sometimes known as the *view factor* or *Gebhart factor*. Also, in radiation or heat transfer textbooks, note that the term view factor is often reserved for the result of integrating the kernel on finite surface areas and $W(\mathbf{x},\mathbf{y})$ is introduced as a *differential view factor*.

4.2.2. Non-local radiation integral equation

Recall the boundary condition for the total intensity (4.11). Considering it in (4.12) and using (4.22), we obtain that the radiosity for any $\mathbf{x} \in \Gamma_R$ is such that

$$R(\mathbf{x}) = (1-\varepsilon(\mathbf{x}))\int_{\Gamma_R} W(\mathbf{x},\mathbf{y})R(\mathbf{y})\,dA_{\mathbf{y}} + \varepsilon(\mathbf{x})\sigma T^4(\mathbf{x}). \tag{4.24}$$

Notice that in (4.24) the dependence on direction, $\mathbf{s}$, has completely disappeared and, as the medium is non-participating and transparent, the radiosity at any point on Γ_R is directly related to the temperature at $\mathbf{x}$ and the radiosity at the remainder of the boundary. Hence, to obtain the heat flux due to radiation on Γ_R, it suffices to solve (4.24) instead of the RTE for the total intensity (4.5) in $\Omega_R \times S^2$.

We denote equation (4.24) as the *integral equation for non-local radiation*. It is a Fredholm integral equation of the second kind. To simplify the writing, the integral operator $\widetilde{\mathcal{K}}$ is introduced, given explicitly by

$$\widetilde{\mathcal{K}}(R)(\mathbf{x}) = \int_{\Gamma_R} W(\mathbf{x},\mathbf{y})R(\mathbf{y})\,dA_{\mathbf{y}}, \qquad \mathbf{x}\in\Gamma_R. \tag{4.25}$$

With the assumptions that we have imposed on the radiation, we remark that this operator directly relates the incoming radiation at a given point (irradiation) to the outgoing radiation from the remainder of the cavity Γ_R. Indeed, taking into account (4.7) and (4.22):

$$G(\mathbf{x}) = \widetilde{\mathcal{K}}(R)(\mathbf{x}). \tag{4.26}$$

Using the operator $\widetilde{\mathcal{K}}$, we rewrite the integral equation (4.24) as

$$(\mathcal{I} - (1-\varepsilon(\mathbf{x}))\widetilde{\mathcal{K}})(R)(\mathbf{x}) = \varepsilon(\mathbf{x})\sigma T^4(\mathbf{x}), \tag{4.27}$$

where $\mathcal{I}$ is the identity operator.

With the defined operators, we can establish the net heat flux at Γ_R due to radiation, q_{rad}, as the difference between the outgoing radiation and the incoming radiation. Using (4.7), (4.8) and (4.26) and considering the radiative heat flux, $\mathbf{q}_{rad}$, defined in (4.4):

$$q_{rad}(\mathbf{x}) = \mathbf{q}_{rad}(\mathbf{x})\cdot\mathbf{n}(\mathbf{x}) = R(\mathbf{x}) - G(\mathbf{x}) = \widetilde{\mathcal{Q}}(R)(\mathbf{x}),$$

where we define the operator $\widetilde{\mathcal{Q}}$ as

$$\widetilde{\mathcal{Q}} = \mathcal{I} - \widetilde{\mathcal{K}}. \tag{4.28}$$

Remark 4.4. *The main properties of the integral operator (4.25) were studied in Tiihonen (1997b). In particular, it can be shown that if Γ_R is piecewise $\mathcal{C}^{1,\delta}$ and Lipschitz, with a zero-measure set of non-smooth points, then the operator $\widetilde{\mathcal{K}}$ is weakly singular and maps $L^p(\Gamma_R)$ into itself compactly for any $p \in [1,\infty]$. Moreover, if the emissivity satisfies*

$$0 < \varepsilon_0 \le \varepsilon(\mathbf{x}) \le 1,$$

the operator $\mathcal{I} - (1-\varepsilon)\widetilde{\mathcal{K}}$ is invertible. In such case, (4.27) has a unique solution when the right hand side is in $L^p(\Omega)$, for $p \in [1,\infty]$.

USC

4.2.3. Model problem of coupled conduction and non-local radiation

The solution of the integral equation (4.27) requires knowledge of the temperature on Γ_R. We assume that conduction is negligible in the cavity Ω_R. Then, to obtain the temperature on the domain Ω, we solve the transient heat equation:

$$\rho c_p \frac{\partial T}{\partial t}(\mathbf{x},t) - \operatorname{div}\big(k \operatorname{grad}(T(\mathbf{x},t))\big) = f(\mathbf{x},t), \qquad \text{in } \Omega \times (0, t_{end}],$$

where k, c_p and ρ denote the thermal conductivity, specific heat and density, respectively. In this chapter, we assume that these properties are constant in Ω. The right hand side, f, represents a heat source.

In addition, on the radiating boundary, we solve the integral equation derived in Section 4.2 for each $t \in (0, t_{end}]$:

$$(\mathcal{I} - (1-\varepsilon(\mathbf{x})\widetilde{\mathcal{K}})(R(t))(\mathbf{x}) = \varepsilon(\mathbf{x})\sigma T^4(\mathbf{x},t),$$

where we have explicitly stated the dependency of all relevant fields on $(\mathbf{x},t)$ to avoid confusion. Moreover, for the sake of simplicity, we assume that the emissivity is constant on Γ_R.

The model must be completed with suitable boundary conditions. On Γ_R, a Neumann condition is set. The heat flux on this boundary is assumed to be equal to the contribution from radiation plus an additional function g, i.e.:

$$-k\frac{\partial T}{\partial \mathbf{n}}(\mathbf{x},t) = q_{rad}(\mathbf{x},t) + g(\mathbf{x},t), \qquad \text{on } \Gamma_R \times (0, t_{end}]. \tag{4.29}$$

Notice that this expression couples the integral equation (4.27) with the heat equation.

Set $\Gamma_D = \partial\Omega \setminus \Gamma_R$. On Γ_D, we impose a Dirichlet boundary condition, i.e. we assume that the temperature is known and equal to a given function T_D:

$$T(\mathbf{x},t) = T_D(\mathbf{x},t), \qquad \text{on } \Gamma_D \times (0, t_{end}]. \tag{4.30}$$

To complete the model, we set the initial temperature equal to a given function, i.e., that $T(\mathbf{x},0) = T_0(\mathbf{x})$ in Ω. Thus, the problem is formulated as follows.

Problem $(\mathcal{P}_R)$. Find $T(\mathbf{x},t)$ and $R(\mathbf{x},t)$ such that:

$$\begin{aligned}
&\rho c_p \frac{\partial T}{\partial t}(\mathbf{x},t) - \operatorname{div}\big(k \operatorname{grad}(T(\mathbf{x},t))\big) = f(\mathbf{x},t), && \text{in } \Omega \times (0, t_{end}],\\
&(\mathcal{I} - (1-\varepsilon(\mathbf{x})\widetilde{\mathcal{K}})(R(t))(\mathbf{x}) = \varepsilon(\mathbf{x})\sigma T^4(\mathbf{x},t), && \text{on } \Gamma_R \times (0, t_{end}],\\
&T(\mathbf{x},0) = T_0(\mathbf{x}), && \text{in } \Omega,\\
&T(\mathbf{x},t) = T_D(\mathbf{x},t), && \text{on } \Gamma_D \times (0, t_{end}],\\
&-k\frac{\partial T}{\partial \mathbf{n}}(\mathbf{x},t) = q_{rad}(\mathbf{x}) + g(\mathbf{x},t), && \text{on } \Gamma_R \times (0, t_{end}],\\
&q_{rad}(\mathbf{x},t) = \widetilde{\mathcal{Q}}(R)(\mathbf{x},t) && \text{on } \Gamma_R \times (0, t_{end}].
\end{aligned}$$

In summary, the thermal radiation problem in the enclosure Ω_R surrounded by a domain Ω can be posed as a non-local radiation problem, where only an integral equation on $\Gamma_R = \partial\Omega_R$ needs to be solved to characterise radiative heat transfer. Recall that, to obtain $(\mathcal{P}_R)$ from the general radiative heat transfer equation, we have assumed that:

(H.1) Ω_R is a non-participating and transparent medium: $\varsigma = a = 0$.

(H.2) The refractive index of Ω_R is $n = 1$.

(H.3) The surface defined by the boundary of Ω_R, Γ_R, is diffuse and grey.

(H.4) Heat conduction in Ω_R is negligible.

4.3. Plane problem

In the subsequent sections, we focus on a plane coupled non-local radiation and heat conduction problem. While it is true that most applications are inherently 3-dimensional, in some situations a plane problem might be a reasonable approximation. In the case of the BF trough, where practically the entire structure is covered by a refractory cover or hood (see Figure 1.4), a radiation cavity is formed. Its cross-section is almost the same for about 12 m, with low temperature gradients in the longitudinal direction. In such setting, a plane problem could yield sufficiently accurate temperature predictions in a cross-section, allowing for large reductions in computational complexity.

This kind of problem has not been given much attention. For instance, the integral kernel for 2D problems is stated in Tiihonen (1997b, p. 49), but no attempt to derive the plane setting or the hypotheses that should hold in order to obtain adequate approximations is made. On the other hand, in classic thermal radiation textbooks such as Modest (2013, p. 136) or Howell et al. (2015, p. 155), the derivation of the so-called *differential view factors* for a 2D problem, which can be related to the integral kernel that define the integral equations, is presented as an intuitive example, not in a rigorous framework.

In this section, starting from the integral kernel (4.23) corresponding to a 3D domain and the model problem described in Section 4.2.3, under suitable assumptions on the data and the computational domain, we derive the corresponding 2D problem, posed in a cross-section of the 3D domain. For the sake of simplicity, we shall assume that the cavity Ω_R is convex, which means that for any $\mathbf{x}, \mathbf{y} \in \Gamma_R$ such that $\mathbf{x} \neq \mathbf{y}$, the segment $\overline{\mathbf{xy}}$, defined in (4.16), belongs to Ω_R. Hence, it holds that $\Theta(\mathbf{x}, \mathbf{y}) = 1$.

4.3.1. Cylindrical domain

Set $L > 0$ and let Ω be a (hollow) *cylindrical domain*, defined as follows:

$$\Omega = \{(x_1, x_2, x_3) \in \mathbb{R}^3 : (x_1, x_2) \in \varpi, |x_3| < L\}, \tag{4.31}$$

where $\varpi \subset \mathbb{R}^2$. In Figure 4.4, a schematic of a cylindrical domain is depicted. In addition, we assume that the boundary $\partial\Omega$ can be decomposed as $\partial\Omega = \Gamma_D \cup \Gamma^{\pm} \cup \Gamma_R$, such that the pairwise intersections result in zero-measure sets. With $\Gamma^{\pm}$ we denote the set

$$\Gamma^{\pm} = \{(x_1, x_2, x_3) \in \mathbb{R}^3 : x_3 = \pm L\}.$$

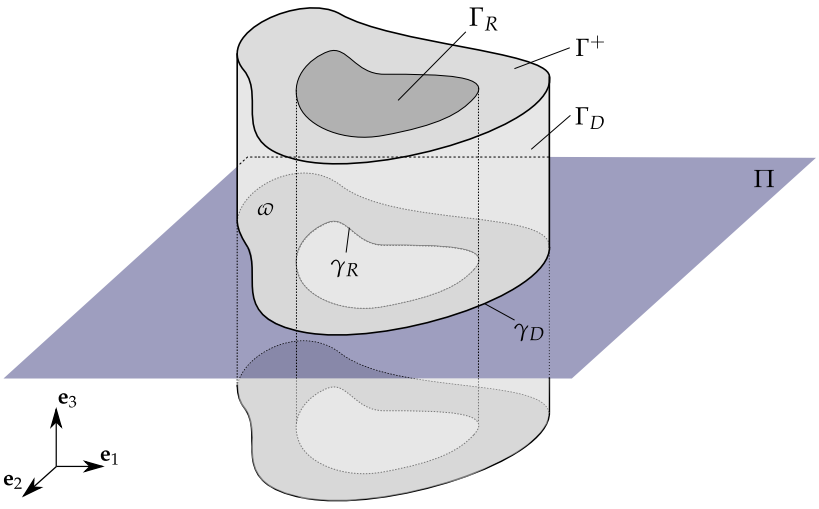


Figure 4.4: Schematic of a cylindrical domain.

We assume that the parts of the boundary corresponding to Γ_R and Γ_D can be written as

$$\begin{aligned}\Gamma_D &= \gamma_D \times (-L, L),\\ \Gamma_R &= \gamma_R \times (-L, L),\end{aligned} \tag{4.32}$$

where γ_R and γ_D are plane curves.

On Γ_R and Γ_D, we keep the conditions (4.29) and (4.30), respectively, whereas on $\Gamma^{\pm}$, we specify that the heat flux is zero, i.e.:

$$-k\frac{\partial T}{\partial \mathbf{n}}(\mathbf{x}, t) = 0, \qquad \text{on } \Gamma^{\pm} \times (0, t_{end}]. \tag{4.33}$$

In the cylindrical domain (4.31), we consider Problem $(\mathcal{P}_R)$, adding the condition (4.33). Moreover, we assume that the data does not depend on the x_3 coordinate (see Figure 4.4). Gathering all these observations, the following problem is deduced.

Problem $(\widehat{\mathcal{P}}^*_{PR})$. Find $T(\mathbf{x}, t)$ and $R(\mathbf{x}, t)$ such that:

$$\begin{aligned}
&\rho c_p \frac{\partial T}{\partial t}(\mathbf{x}, t) - \operatorname{div}\big(k \operatorname{grad}(T(\mathbf{x}, t))\big) = f(x_1, x_2, t), && \text{in } \Omega \times (0, t_{end}],\\
&(\mathcal{I} - (1 - \varepsilon(x_1, x_2))\widetilde{\mathcal{K}})(R(t))(\mathbf{x}) = \varepsilon(x_1, x_2)\sigma T^4(\mathbf{x}, t), && \text{on } \Gamma_R \times (0, t_{end}],\\
&T(\mathbf{x}, 0) = T_0(x_1, x_2), && \text{in } \Omega,\\
&T(\mathbf{x}, t) = T_D(x_1, x_2, t), && \text{on } \Gamma_D \times (0, t_{end}],\\
&-k\frac{\partial T}{\partial \mathbf{n}}(\mathbf{x}, t) = 0, && \text{on } \Gamma^{\pm} \times (0, t_{end}],\\
&-k\frac{\partial T}{\partial \mathbf{n}}(\mathbf{x}, t) = q_{rad}(\mathbf{x}, t) + g(x_1, x_2, t), && \text{on } \Gamma_R \times (0, t_{end}],\\
&q_{rad}(\mathbf{x}, t) = \widetilde{\mathcal{Q}}(R(t))(\mathbf{x}), && \text{on } \Gamma_R \times (0, t_{end}].
\end{aligned}$$

When $\Gamma_R = \emptyset$, it is well-known that the solution to Problem $(\widehat{\mathcal{P}}^*_{PR})$ can be obtained by solving a plane problem in ω, as the solution $T(\mathbf{x}, t)$ does not depend on the coordinate x_3. The case when the radiation boundary is present is slightly more complicated. Specifically, the difficulty lies on addressing that, given an arbitrary $\mathbf{x} \in \omega$, the integral kernel (4.23) still depends on any $\mathbf{y} \in \Gamma_R$.

In the following discussion, we establish the framework to obtain the solution to $(\widehat{\mathcal{P}}^*_{PR})$ by solving a plane problem on the cross-section $\omega \subset \mathbb{R}^2$, considering that $\Gamma_R \neq \emptyset$. In particular, we derive an expression of the integral kernel that only needs to be integrated over γ_R, instead of the complete Γ_R. For the sake of simplicity, during most of the subsequent section, we drop the dependence on time of the involved fields in the writing, as it does not affect the discussion.

4.3.2. Plane integral kernel

Set Ω satisfying (4.31) and, as in the previous section, with a sufficiently regular boundary. In particular, it suffices that it is a $\mathcal{C}^1$ domain. Furthermore, let $L \to \infty$. In that case, we say that Ω is an *infinitely long cylindrical domain*, defined as

$$\Omega = \{(x_1, x_2, x_3) : (x_1, x_2) \in \omega, x_3 \in \mathbb{R}\}. \tag{4.34}$$

Notice that, in this particular setting, we have that $\Gamma^{\pm} = \emptyset$.

We recall the definition of the integral operator $\widetilde{\mathcal{K}}$ in (4.25), which appears at the non-local radiation boundary condition. In the specific case of Ω being defined by (4.34), and bearing the assumption that Γ_R is given by (4.32), we note that Γ_R can be regarded as a special case of a *ruled surface*, with

$\Gamma_R = \gamma_R \times \mathbb{R}$. Since Ω is of class $\mathcal{C}^1$, then Γ_R can be partitioned in n_S sets Γ_R^i such that $\bigcup_{i=1}^{n_S} \Gamma_R^i = \Gamma_R$. For any $i = 1, \dots, n_S$, there exists an orthogonal matrix A_i, an open set $V_i \subset \mathbb{R}^2$ and a mapping $h_i \in \mathcal{C}^1(V_i)$ such that (Roubíček, 2013):

$$\Gamma_R^i = \{A_i \psi,\ \psi \in \mathbb{R}^3 : (\psi_1, \psi_3) \in V_i \text{ and } \psi_2 = h_i(\psi_1, \psi_3)\}.$$

Since $\Gamma_R = \gamma_R \times \mathbb{R}$, the functions h_i do not depend on the coordinate ψ_3. Thereby, a parametrisation of each Γ_R^i can be given by

$$\mathbb{X}^i(c, s) = (\alpha_1^i(c), \alpha_2^i(c), s), \qquad c \in \widetilde{V}_i,\ s \in \mathbb{R},$$

where $\boldsymbol{\alpha}^i(c) = \widetilde{A}_i(c,\ h_i(c))^T$ is a plane curve, $\widetilde{V}_i$ being the projection of the open set V_i along the first coordinate and $\widetilde{A}_i$ is an orthogonal matrix of order two.

Since the covering of Γ_R is not disjoint, we generate a partition of unity associated to such covering to address integration on Γ_R. In particular, let $\mathcal{N} : \Gamma_R \to \mathbb{N}$ be a function which assigns to each $\mathbf{y} \in \Gamma_R$ the number of sets Γ_R^i to which it belongs, i.e. $1 \leq \mathcal{N}(\mathbf{y}) \leq n_S$. Then, set the subsequent mappings

$$\chi_i(\mathbf{y}) = \begin{cases} 0, & \text{if } \mathbf{y} \notin V_i, \\ \dfrac{1}{\mathcal{N}(\mathbf{y})}, & \text{if } \mathbf{y} \in V_i. \end{cases}$$

Notice that, for any $\mathbf{y} \in \Gamma_R^i$, $\sum_{i=1}^{n_S} \chi_i(\mathbf{y}) = 1$.

Then, the integral over Γ_R appearing in (4.25) can be rewritten using the parametrisations given by $\mathbb{X}^i$ and the partition of unity:

$$\int_{\Gamma_R} W(\mathbf{x}, \mathbf{y}) R(\mathbf{y}) dA_{\mathbf{y}} = \sum_{i=1}^{n_S} \int_{\widetilde{V}_i} \int_{-\infty}^{\infty} \chi_i(\mathbb{X}^i(c,s)) W(\mathbf{x}, \mathbb{X}^i(c,s)) R(\mathbb{X}^i(c,s)) |\mathbb{X}_c^i(c,s) \times \mathbb{X}_s^i(c,s)|\, ds dc, \tag{4.35}$$

where $\mathbb{X}_c^i$ and $\mathbb{X}_s^i$ denote the partial derivatives with respect to the variables c and s, respectively.

Let $R^* : \gamma_R \times (0, t_{end}] \to \mathbb{R}$, be the plane analogue of the radiosity, defined as:

$$R^*(\mathbf{x}^*, t) = R(x_1, x_2, 0, t),$$

for any $t \in (0, t_{end}]$ and $\mathbf{x}^* \in \gamma_R$ such that $(x_1^*, x_2^*) = (x_1, x_2)$.

Since none of the data of the problem does depend on coordinate x_3, it is reasonable to assume that solution to Problem $(\widehat{\mathcal{P}}_{PR}^*)$, i.e., the temperature $T(\mathbf{x}, t)$ and the radiosity $R(\mathbf{x}, t)$, do not depend on coordinate x_3 either. Then, for any $\mathbf{y} \in \Gamma_R$, it holds that $R^*(\mathbf{y}^*) = R(\mathbf{y})$, where we have dropped the time dependency again for the sake of simplicity. Moreover, it follows that $R^*(\mathbf{y}^*) = R^*(\boldsymbol{\alpha}^i(c))$, for some $i \in \{1, \dots, n_S\}$ and $c \in \widetilde{V}_i$.

Let $\mathbf{x}^*$ be a fixed point in γ_R and set $\mathbf{x} \in \Gamma_R$ such that $\mathbf{x} = (x_1^*, x_2^*, 0)$. Using that $\mathbb{X}^i$ only depends on $\boldsymbol{\alpha}^i$,

$$|\mathbb{X}_c^i(c,s) \times \mathbb{X}_s^i(c,s)| = |(\boldsymbol{\alpha}^i)'(c)|,$$

and applying *Fubini's Theorem*, from (4.35), we obtain that

$$\begin{aligned} \int_{\Gamma_R} W(\mathbf{x}, \mathbf{y}) R(\mathbf{y}) dA_{\mathbf{y}} &= \sum_{i=1}^{n_S} \int_{\widetilde{V}_i} \chi_i(\boldsymbol{\alpha}^i(c)) R^*(\boldsymbol{\alpha}^i(c)) |(\boldsymbol{\alpha}^i)'(c)| \left(\int_{-\infty}^{\infty} W(\mathbf{x}, \mathbb{X}^i(c,s)) ds \right) dc \\ &= \sum_{i=1}^{n_S} \int_{\widetilde{V}_i} \chi_i(\boldsymbol{\alpha}^i(c)) R^*(\boldsymbol{\alpha}^i(c)) w(\mathbf{x}^*, \boldsymbol{\alpha}^i(c)) |(\boldsymbol{\alpha}^i)'(c)|\, dc \\ &= \sum_{i=1}^{n_S} \int_{\boldsymbol{\alpha}^i} \chi_i(\mathbf{y}^*) w(\mathbf{x}^*, \mathbf{y}^*) R^*(\mathbf{y}^*) ds_{\mathbf{y}^*} = \int_{\gamma_R} w(\mathbf{x}^*, \mathbf{y}^*) R^*(\mathbf{y}^*)\, ds_{\mathbf{y}^*}, \end{aligned}$$

USC UNIVERSIDADE DE SANTIAGO DE COMPOSTELA

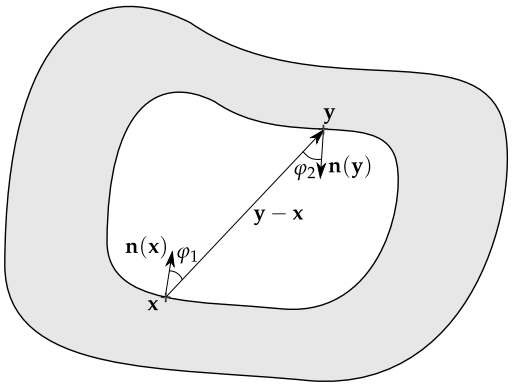


Figure 4.5: Sketch depicting the angles used in the derivation of the plane integral kernel.

where $w(\mathbf{x}^*, \mathbf{y}^*) : \gamma_R \times \gamma_R \to \mathbb{R}$ is the *plane integral kernel* for non-local radiation, defined as follows:

$$w(\mathbf{x}^*, \mathbf{y}^*) = \int_{-\infty}^{\infty} W(\mathbf{x}, (y_1^*, y_2^*, y_3))\, dy_3. \tag{4.36}$$

It is clear that we can pose the integral operator $\widetilde{\mathcal{K}}$ in a plane setting, where only integration along the curve γ_R is required. We shall denote this operator by $\mathcal{K}$, defined as:

$$\mathcal{K}(R^*)(\mathbf{x}^*) = \int_{\gamma_R} w(\mathbf{x}^*, \mathbf{y}^*) R^*(\mathbf{y}^*)\, ds_{\mathbf{y}^*}. \tag{4.37}$$

In the discussion below, we focus on deriving an analytical expression for $w(\mathbf{x}^*, \mathbf{y}^*)$ from (4.36). Recall that $\mathbf{x}^* \in \gamma_R$ is fixed and $\mathbf{x} = (x_1^*, x_2^*, 0)$. For any $\mathbf{y} \in \Gamma_R$, let φ_1, φ_2 denote the angles subtended by the vectors $\mathbf{y} - \mathbf{x}$ and $\mathbf{n}(\mathbf{x})$, $\mathbf{n}(\mathbf{y})$, as displayed in Figure 4.5. Substituting in (4.23), it follows that

$$W(\mathbf{x}, \mathbf{y}) = \frac{\cos\ \varphi_1 \cos \varphi_2}{\pi |\mathbf{x} - \mathbf{y}|^2}. \tag{4.38}$$

Now, given the assumptions on Ω and Γ_R discussed above, $\mathbf{x}$ and $\mathbf{y}$ must belong to Γ_R^i and Γ_R^j, for some $i, j \in \{1, \ldots, n_S\}$. Let Π denote the plane $x_3 = 0$, and note that its intersection with Γ_R^i and Γ_R^j is equal to the curves $\boldsymbol{\alpha}^i$ and $\boldsymbol{\alpha}^j$, respectively (see Figure 4.4). Naturally, $\mathbf{x} \in \Pi$ but, in general, $\mathbf{y} \notin \Pi$. Let $\mathbf{y}_\Pi$ be the orthogonal projection of $\mathbf{y}$ on the plane Π, i.e., $\mathbf{y}_\Pi = (y_1, y_2, 0)$, displayed in Figure 4.6.

If $\mathbb{X}(c, s)$ is a parametrisation of an orientable surface, recall that a normal vector at a point $\mathbf{x} = \mathbb{X}(c, s)$ can be computed from:

$$\mathbf{n}(\mathbf{x}) = \frac{\mathbb{X}_c(c, s) \times \mathbb{X}_s(c, s)}{|\mathbb{X}_c(c, s) \times \mathbb{X}_s(c, s)|}.$$

We assume that the parametrisations $\mathbb{X}^i$ of Γ_R^i are oriented such that this computation yields the outward-pointing (from Ω) unit normal vector. Hence, it is straightforward to conclude that the normal vector on any Γ_R^i only depends on the plane curves that generate the surfaces. Furthermore, it belongs to the plane Π. Hence, for the points $\mathbf{x}, \mathbf{y} \in \Gamma_R$, we can write that

$$\begin{aligned} \mathbf{n}(\mathbf{x}) &= (n_{x1}, n_{x2}, 0), \\ \mathbf{n}(\mathbf{y}) &= (n_{y1}, n_{y2}, 0). \end{aligned}$$

Note that $\mathbf{n}(\mathbf{y}_\Pi) = \mathbf{n}(\mathbf{y})$. Let β_1, β_2 be the plane angles in Π between the vectors $\mathbf{y}_\Pi - \mathbf{x}$ and $\mathbf{n}(\mathbf{x})$, $\mathbf{n}(\mathbf{y})$, respectively, as depicted in Figure 4.6. It holds that

$$\begin{aligned} \cos \varphi_1 &= \frac{\mathbf{n}(\mathbf{x}) \cdot (\mathbf{y} - \mathbf{x})}{|\mathbf{y} - \mathbf{x}|} = \frac{n_{x1}(y_1 - x_1) + n_{x2}(y_2 - x_2)}{|\mathbf{y} - \mathbf{x}|} \\ &= \frac{\mathbf{n}(\mathbf{x}) \cdot (\mathbf{y}_\Pi - \mathbf{x})}{|\mathbf{y} - \mathbf{x}|} = \frac{|\mathbf{y}_\Pi - \mathbf{x}|}{|\mathbf{y} - \mathbf{x}|} \cos \beta_1. \end{aligned} \tag{4.39}$$

USC UNIVERSIDADE DE SANTIAGO DE COMPOSTELA

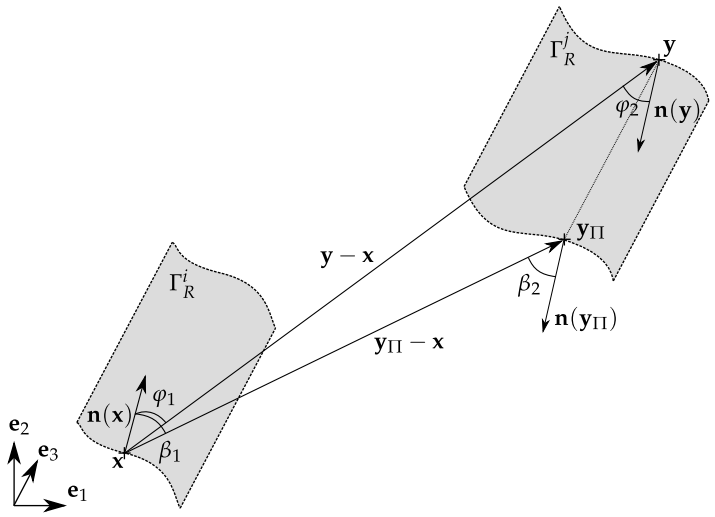


Figure 4.6: Set-up for the plane integral kernel derivation.

Analogously, it is satisfied that

$$\cos\varphi_2 = \frac{|\mathbf{y}_\Pi - \mathbf{x}|}{|\mathbf{y}-\mathbf{x}|}\cos\beta_2. \tag{4.40}$$

In addition, it holds that the modulus of the vector $\mathbf{y}-\mathbf{x}$ is such that (see Figure 4.6)

$$|\mathbf{y}-\mathbf{x}| = (|\mathbf{y}_\Pi - \mathbf{x}|^2 + y_3^2)^{\frac{1}{2}}. \tag{4.41}$$

Consequently, substituting (4.39), (4.40) and (4.41) in (4.38):

$$W(\mathbf{x},\mathbf{y}) = \frac{\cos\beta_1\cos\beta_2|\mathbf{y}_\Pi-\mathbf{x}|^2}{\pi(|\mathbf{y}_\Pi-\mathbf{x}|^2+y_3^2)^2}.$$

Then, given $\mathbf{x}^*, \mathbf{y}^* \in \gamma_R$, using the previous expression, the plane integral kernel can be directly computed from the definition (4.36) as follows, letting $\mathbf{y} = (y_1^*, y_2^*, y_3)$ and recalling that $\mathbf{x} = (x_1^*, x_2^*, 0)$:

$$\begin{aligned} w(\mathbf{x}^*,\mathbf{y}^*) &= \int_{-\infty}^{\infty} W(\mathbf{x},(y_1^*,y_2^*,y_3))\,dy_3 = \int_{-\infty}^{\infty}\frac{\cos\beta_1\cos\beta_2|\mathbf{y}_\Pi-\mathbf{x}|^2}{\pi(|\mathbf{y}_\Pi-\mathbf{x}|^2+y_3^2)^2}dy_3 \\ &= \frac{\cos\beta_1\cos\beta_2|\mathbf{y}_\Pi-\mathbf{x}|^2}{\pi}\int_{-\infty}^{\infty}\frac{1}{(|\mathbf{y}_\Pi-\mathbf{x}|^2+y_3^2)^2}dy_3 \\ &= \frac{\cos\beta_1\cos\beta_2|\mathbf{y}_\Pi-\mathbf{x}|^2}{\pi}\lim_{\epsilon\to\infty}\left[\operatorname{atan}\left(\frac{y_3}{|\mathbf{y}_\Pi-\mathbf{x}|}\right)\left(\frac{1}{2|\mathbf{y}_\Pi-\mathbf{x}|^3}+\frac{y_3}{2|\mathbf{y}_\Pi-\mathbf{x}|^2(|\mathbf{y}_\Pi-\mathbf{x}|^2+y_3^2)}\right)\right]_{-\epsilon}^{\epsilon} \\ &= \frac{\cos\beta_1\cos\beta_2|\mathbf{y}_\Pi-\mathbf{x}|^2}{2|\mathbf{y}_\Pi-\mathbf{x}|^3} = \frac{\cos\beta_1\cos\beta_2|\mathbf{y}^*-\mathbf{x}^*|^2}{2|\mathbf{y}^*-\mathbf{x}^*|^3} = \frac{\mathbf{n}(\mathbf{x}^*)\cdot(\mathbf{y}^*-\mathbf{x}^*)\mathbf{n}(\mathbf{y}^*)\cdot(\mathbf{x}^*-\mathbf{y}^*)}{2|\mathbf{y}^*-\mathbf{x}^*|^3}. \end{aligned}$$

In the last equality, the definition of the angles β_1 and β_2 has been used to obtain an expression of the integral kernel that only depends on the points on γ_R. For the sake of simplicity, in the rest of this part of the manuscript, as we deal with plane problems, we drop the starred versions of the points in the plane to simplify the notation and understand that $\mathbf{x},\mathbf{y}\in\gamma_R$. Then, the plane integral kernel is simply written as:

$$w(\mathbf{x},\mathbf{y}) = \frac{\mathbf{n}(\mathbf{x})\cdot(\mathbf{y}-\mathbf{x})\mathbf{n}(\mathbf{y})\cdot(\mathbf{x}-\mathbf{y})}{2|\mathbf{y}-\mathbf{x}|^3}\Theta(\mathbf{x},\mathbf{y}), \tag{4.42}$$

USC UNIVERSIDADE DE SANTIAGO DE COMPOSTELA

where we have also included the visibility factor $\Theta(\mathbf{x},\mathbf{y})$, which in general non-convex cavities is required to account for obstacles blocking the view. The derivation herein presented assumed that the cavity was convex for simplicity purposes, but can be generalised to the non-convex case.

Using (4.42) and the previous remark, the integral operator (4.37) is such that

$$\mathcal{K}(R)(\mathbf{x}) = \int_{\gamma_R} w(\mathbf{x},\mathbf{y}) R(\mathbf{y})\, ds_{\mathbf{y}}, \tag{4.43}$$

where R is defined on γ_R.

Analogously, we define the plane counterpart of the operator $\widetilde{\mathcal{Q}}$, defined in (4.28), as:

$$\mathcal{Q} = \mathcal{I} - \mathcal{K}. \tag{4.44}$$

In summary, we have established that Problem $(\mathcal{P}_R)$, involving a non-local radiation boundary Γ_R in an infinitely long cylindrical domain Ω, can be solved as the following plane problem if the data does not depend on the x_3 coordinate.

Problem $(\mathcal{P}_{PR})$. Find $T(\mathbf{x},t)$ and $R(\mathbf{x},t)$ such that:

$$\begin{aligned}
&\rho c_p \frac{\partial T}{\partial t}(\mathbf{x},t) - \operatorname{div}\big(k \operatorname{grad}(T(\mathbf{x},t))\big) = f(\mathbf{x},t), && \text{in } \varpi \times (0,t_{end}], \\
&(\mathcal{I} - (1-\varepsilon(\mathbf{x}))\mathcal{K})(R(t))(\mathbf{x}) = \varepsilon(\mathbf{x})\sigma T^4(\mathbf{x},t), && \text{on } \gamma_R \times (0,t_{end}], \\
&T(\mathbf{x},0) = T_0(\mathbf{x}), && \text{in } \varpi, \\
&T(\mathbf{x},t) = T_D(\mathbf{x},t), && \text{on } \gamma_D \times (0,t_{end}], \\
&-k\frac{\partial T}{\partial \mathbf{n}}(\mathbf{x},t) = q_{rad}(\mathbf{x},t) + g(\mathbf{x},t), && \text{on } \gamma_R \times (0,t_{end}], \\
&q_{rad}(\mathbf{x},t) = \mathcal{Q}(R(t))(\mathbf{x}), && \text{on } \gamma_R \times (0,t_{end}],
\end{aligned} \tag{4.45}$$

where $\mathcal{K}$ and $\mathcal{Q}$ are the integral operators defined in (4.43) and (4.44). Furthermore, note that $\mathbf{x} = (x_1, x_2)$.

Remark 4.5. *For a finitely-long cylindrical domain such as (4.31), a similar setting can be used to deduce a plane problem involving the non-local radiation condition. Note that for this case $\Gamma^{\pm} \neq \emptyset$ and that the boundary condition on this boundary has to be zero heat flux. However, as opposed to the case without non-local radiation ($\Gamma_R = \emptyset$), where the solution of the plane problem in ϖ is equivalent to the solution in Ω, this does not hold when non-local radiation is present. The issue is that we cannot extend the domain for $x_3 > L$ to compute the kernel for plane problems. Furthermore, Ω_R is not an enclosure.*

Let $L^2(\varpi)$ denote the Lebesgue space of square-integrable functions in ϖ. Moreover, let $H^1(\varpi)$ be the Sobolev space of functions in $L^2(\varpi)$ such that their distributional derivative is also in $L^2(\varpi)$ and let $H^1_{0,\gamma_D}(\varpi)$ be the subspace of $H^1(\varpi)$ formed by those elements with zero trace on γ_D. Hereafter, we assume that the data are smooth enough for the following operations to make sense.

For each $t \in (0,t_{end}]$, we multiply (4.45) by a test function $v = v(\mathbf{x})$. Then, we integrate in the corresponding domain, apply a Green's formula, and use the boundary conditions, leading to the following variational formulation of $(\mathcal{P}_{PR})$.

Problem $(\mathcal{VP}_{PR})$. For each $t \in (0,t_{end}]$, find $T(t) \in H^1(\varpi)$ and $R(t) \in L^2(\gamma_R)$ such that $\dfrac{\partial T(t)}{\partial t} \in L^2(\varpi)$, $T(t) = T_D(t)$ on γ_D, and satisfying:

$$\int_{\varpi} \rho c_p \frac{\partial T(t)}{\partial t} v\, dA + \int_{\varpi} k \operatorname{grad}(T(t)) \cdot \operatorname{grad}(v)\, dA = \int_{\varpi} f(t) v\, dA - \int_{\gamma_R} (\mathcal{Q}(R(t)) + g(t)) v\, ds \tag{4.46}$$

for all $v \in H^1_{0,\gamma_D}(\varpi)$, and such that:

$$(\mathcal{I} - (1-\varepsilon)\mathcal{K})(R(t)) = \varepsilon\sigma T^4(t), \qquad \text{on } \gamma_R, \tag{4.47}$$

for $t \in (0,t_{end}]$ with $T(0) = T_0$.

USC UNIVERSIDADE DE SANTIAGO DE COMPOSTELA

4.4. Numerical solution

Let τ_h be a triangulation of the domain ω, constructed such that $\overline{\omega} = \cup_{K\in\tau_h} K$. To discretise Problem $(\mathcal{VP}_{PR})$ a method of lines is used: first, the spatial semi-discretisation is obtained, which leads to a system of ODEs, as described in Section 4.4.1. Then, in Section 4.4.2, the time-discretisation is carried out. Section 4.4.3 deals with automatic adaptation of the time step size using the embedded error estimator in the time-stepping method. The complete algorithm that we use to solve the coupled problem is introduced in Section 4.4.4.

4.4.1. Spatial discretisation

In the following, we first discuss the discretisation of the variational form of the heat equation (4.46), appearing in $(\mathcal{VP}_{PR})$, and assuming a known radiosity $R_h(t)$. Subsequently, the discretisation of the integral equation is addressed.

Heat equation

Let $t \in (0, t_{end}]$ and V_h be the finite-dimension space of continuous functions whose restrictions to the triangles forming the triangulation τ_h are polynomials of degree 1. We set $N_h = \dim V_h$ and denote as V_h^0 the subspace of V_h composed of the functions with zero trace on γ_D. Substituting with $T_h \in V_h$ and R_h in (4.46) and (4.47), we obtain the discrete formulation of the problem. Furthermore, let $\{w_j\}_{j=1}^{N_h}$ be a basis of V_h. Since $T_h(t) \in V_h$, we decompose it as

$$T_h(t) = \sum_{j=1}^{N_h} \xi_j(t) w_j, \tag{4.48}$$

where the coefficients ξ_j are the new unknowns of the problem. Let $\overline{\xi}$ be the corresponding vector of unknowns, i.e. $\overline{\xi}(t) = (\xi_1(t), \xi_2(t), \ldots, \xi_{N_h}(t))^T$. Replacing T_h with (4.48) in the discrete formulation and taking into account that it is enough to consider w_i as test functions, we obtain the system of ODEs

$$\overline{M}\frac{d\overline{\xi}}{dt}(t) = \overline{b}(t, \overline{\xi}(t)), \tag{4.49}$$

where the function $\overline{b} : \mathbb{R} \times \mathbb{R}^{N_h} \to \mathbb{R}^{N_h}$ and the mass matrix $\overline{M}$ are the following:

$$\begin{aligned} b_i(t, \overline{\xi}(t)) &= -\sum_{j=1}^{N_h} \xi_j(t) \int_\omega k \,\mathrm{grad}(w_j) \cdot \mathrm{grad}(w_i)\, dA + \int_\omega f(t) w_i \, dA \\ &\quad - \int_{\gamma_R} (\mathcal{Q}(R_h(t)) + g(t)) w_i \, ds, \\ M_{ij} &= \int_\omega \rho c_p w_j w_i \, dA, \qquad 1 \le i, j \le N_h. \end{aligned}$$

Note that, to set the essential condition, i.e., that $T_h = T_D$ on γ_D for each $t \in (0, t_{end}]$, the standard method of directly modifying the arising linear system matrix and right hand side is applied (see e.g. Quarteroni, 2009).

Radiosity integral equation

To compute the radiosity, we solve the integral equation (4.47), where the temperature at the right hand side is computed by solving (4.49). To deal with the coupling of radiosity with temperature, in Subsection 4.4.4 we propose a fixed-point algorithm. In the following discussion, we assume that the temperature is known (so we avoid writing the radiosity time dependency too) and we focus only on the discretisation of the integral equation.

Let $\tau_h^{\mathcal{G}}$ be the mesh on γ_R induced by the edges ζ_j of the τ_h elements that belong to this boundary. Moreover, let $N_h^{\mathcal{G}}$ be the number of segments in $\tau_h^{\mathcal{G}}$ and $V_h^{\mathcal{G}}$ be the space formed by piecewise constant functions at each element of this γ_R mesh, generated by the subsequent basis functions

$$z_j(\mathbf{x}) := \begin{cases} 1, & \text{if } \mathbf{x} \in \zeta_j, \\ 0, & \text{otherwise,} \end{cases}$$

where $1 \leq j \leq N_h^{\mathcal{G}}$. We look for a discretised radiosity $R_h \in V_h^{\mathcal{G}}$, so we can express it in terms of the basis:

$$R_h(\mathbf{x}) = \sum_{j=1}^{N_h^{\mathcal{G}}} \eta_j z_j(\mathbf{x}), \tag{4.50}$$

where the coefficients η_j are the unknowns.

Let $\mathbf{x}_i$, with $1 \leq i \leq N_h^{\mathcal{G}}$, be the collocation points, which are selected as the midpoints of the segments $\zeta_i \in \tau_h^{\mathcal{G}}$. For the ith collocation point, we substitute it in (4.47), where the operator $\mathcal{K}$ is given by (4.43), and consider the discretisation of the radiosity (4.50), obtaining

$$\eta_i - (1-\varepsilon) \sum_{j=1}^{N_h^{\mathcal{G}}} \eta_j \int_{\gamma_R} w(\mathbf{x}_i, \mathbf{y}) z_j(\mathbf{y}) ds_{\mathbf{y}} = \varepsilon \sigma T_h^4(\mathbf{x}_i),$$

for $1 \leq i \leq N_h^{\mathcal{G}}$ and where the discretised temperature T_h is assumed to be known. Note that, for simplicity, we are considering the emissivity as a constant, as in the later sections we shall also use a constant value. Gathering all the equations, the radiosity R_h can be obtained as the solution of the linear system

$$(\overline{I} - \overline{K})\overline{\eta} = \overline{l}, \tag{4.51}$$

where $\overline{I}$ denotes the identity matrix, $\overline{\eta} = (\eta_1, \ldots, \eta_{N_h^{\mathcal{G}}})^T$ is the vector of unknowns and

$$\begin{aligned} K_{ij} &= (1-\varepsilon) \int_{\gamma_R} w(\mathbf{x}_i, \mathbf{y}) z_j(\mathbf{y}) ds_{\mathbf{y}}, & 1 \leq i, j \leq N_h^{\mathcal{G}}, \\ l_i &= \varepsilon \sigma T_h^4(\mathbf{x}_i), & 1 \leq i \leq N_h^{\mathcal{G}}. \end{aligned} \tag{4.52}$$

Let us remark that the computation of the integrals appearing in (4.52) requires the evaluation of the kernel (4.42). In our setting, this reduces to the computation of line integrals, which we evaluate by direct integration using Gaussian quadrature. Since there are some parts of the cavity that may block the view between certain points, we perform an evaluation of (4.15) on an edge to edge basis, i.e. we set $\Theta(\mathbf{x}_i, \mathbf{y}) = 0$ for $\mathbf{y} \in \zeta_j$ if $\Theta(\mathbf{x}_i, \mathbf{x}_j) = 0$. For more complex geometries, such as 3D enclosures with many obstructions, specifically designed methods, such as the hemicube algorithm, are more suitable for the computation of said integrals (see e.g. Kramer et al., 2015).

4.4.2. Time discretisation

Assuming a known radiosity, (4.49) is a system of N_h ODEs in time. For its numerical solution, standard methods for initial value problems can be used. However, in the application discussed in the subsequent chapter to the BF trough, the use time step size adaptivity and high-order schemes in time to discretise the problem are advantageous to keep the discretisation error within reasonable bounds while reducing the computational cost. Therefore, a Runge-Kutta (RK) method with an embedded method of different order are used to obtain an error estimate, which allows to automatically adapt the time step size. The family of ESDIRK methods, proposed in Kværnø (2004), has the advantage of including a computationally inexpensive local error estimator, which allows to modify the step size accordingly.

In general, if the solution $\overline{\xi}^n$ at time t^n is assumed to be known, the discretisation of system (4.49) employing an s-stage RK method can be written as (Jørgensen et al., 2018):

$$t_l^{n+1} = t^n + c_l \Delta t^n, \tag{4.53}$$

$$\overline{M}\overline{\mathcal{X}}_l^{n+1} = \overline{M}\overline{\xi}^n + \Delta t^n \sum_{p=1}^{s} a_{lp}\overline{b}(t_p^{n+1}, \overline{\mathcal{X}}_p^{n+1}), \tag{4.54}$$

$$\overline{M}\overline{\xi}^{n+1} = \overline{M}\overline{\xi}^n + \Delta t^n \sum_{p=1}^{s} d_p\overline{b}(t_p^{n+1}, \overline{\mathcal{X}}_p^{n+1}), \tag{4.55}$$

where $l = 1, \ldots, s, s > 1$ is the number of stages of the scheme, and a_{lp}, c_l and d_p are the coefficients of the RK method. In (4.53)-(4.55) we denote with t_p^{n+1} and $\overline{\mathcal{X}}_p^{n+1}$ the RK internal time nodes and stages, whereas $\Delta t^n = t^{n+1} - t^n$ denotes the time step size. Moreover, $\overline{\xi}^{n+1}$ is the numerical approximation computed by the method at time t^{n+1}. The embedded RK method yields a different approximation, denoted as $\overline{\xi}^{*,n+1}$:

$$\overline{M}\overline{\xi}^{*,n+1} = \overline{M}\overline{\xi}^n + \Delta t^n \sum_{p=1}^{s} d_p^*\overline{b}(t_p^{n+1}, \overline{\mathcal{X}}_p^{n+1}).$$

The higher order method provides an estimator of the local truncation error $\overline{e}^{n+1}$ for the lower order one:

$$\overline{e}^{n+1} = \overline{\xi}^n - \overline{\xi}^{*,n+1}.$$

In particular, we consider an ESDIRK method, which are a subclass of Singly Diagonally Implicit Runge-Kutta (SDIRK) methods, semi-implicit RK methods with a Butcher tableau having equal diagonal entries, i.e. $a_{ll} = \widehat{\gamma}$ for $l > 1$, and $a_{ij} = 0$ for $i < j$. For more details, we refer to Wanner & Hairer (1996). ESDIRK methods have, in addition, an explicit first stage. Thus, they satisfy that $c_1 = 0$ as well as $a_{11} = 0$, and the first stage is equal to the approximation in the previous time step ($\overline{\mathcal{X}}_1^{n+1} = \overline{\xi}^n$). The RK pair can be designed so that it is *stiffly accurate*. This means that $a_{sp} = d_p$ for $p = 1, \ldots, s$. Therefore, the last stage coincides with the approximation corresponding to the next time step, i.e. $\overline{\xi}^{n+1} = \overline{\mathcal{X}}_s^{n+1}$. Specifically, we use the ESDIRK 3/2 scheme (Kværnø, 2004). The corresponding RK pair is such that both the advancing and embedded methods are stiffly accurate and A-stable (Wanner & Hairer, 1996; Jørgensen et al., 2018). The scheme has 4 stages ($s = 4$) and is characterised by the following Butcher tableau:

$$\begin{array}{c|cccc} 0 & 0 & & & \\ c_2 & a_{21} & \widehat{\gamma} & & \\ 1 & d_1^* & d_2^* & \widehat{\gamma} & \\ 1 & d_1 & d_2 & d_3 & \widehat{\gamma} \\ \hline & d_1 & d_2 & d_3 & \widehat{\gamma} \\ & d_1^* & d_2^* & \widehat{\gamma} & \end{array} = \begin{array}{c|ccc} 0 & 0 & & \\ 2\widehat{\gamma} & \widehat{\gamma} & \widehat{\gamma} & \\ 1 & \frac{-4\widehat{\gamma}^2+6\widehat{\gamma}-1}{4\widehat{\gamma}} & \frac{-2\widehat{\gamma}+1}{4\widehat{\gamma}} & \widehat{\gamma} \\ 1 & \frac{6\widehat{\gamma}-1}{12\widehat{\gamma}} & \frac{-1}{12\widehat{\gamma}(2\widehat{\gamma}-1)} & \frac{-6\widehat{\gamma}^2+6\widehat{\gamma}-1}{3(2\widehat{\gamma}-1)} \quad \widehat{\gamma} \\ \hline & \frac{6\widehat{\gamma}-1}{12\widehat{\gamma}} & \frac{-1}{12\widehat{\gamma}(2\widehat{\gamma}-1)} & \frac{-6\widehat{\gamma}^2+6\widehat{\gamma}-1}{3(2\widehat{\gamma}-1)} \quad \widehat{\gamma} \\ & \frac{-4\widehat{\gamma}^2+6\widehat{\gamma}-1}{4\widehat{\gamma}} & \frac{-2\widehat{\gamma}+1}{4\widehat{\gamma}} & \widehat{\gamma} \end{array} \tag{4.56}$$

The methods are of order 3 and 2. If local extrapolation is used to advance each time step, the highest order one is selected as the advancing method to avoid losing accuracy. In such case, the method is denoted as ESDIRK 3/2a and the $\widehat{\gamma}$ value in (4.56) must be chosen as $\widehat{\gamma} = 0.4358665215$ to obtain the desired stability properties (Kværnø, 2004). Independently of which method is selected as the advancing one, the error estimator simply becomes

$$\overline{e}^{n+1} = \overline{\mathcal{X}}_s^{n+1} - \overline{\mathcal{X}}_{s-1}^{n+1},$$

in virtue of both methods in the pair being stiffly accurate.

USC UNIVERSIDADE DE SANTIAGO

4.4.3. Adaptive time stepping

The integration error can be adjusted using the error estimator available from the embedded RK method. In particular, we define the following norm of the local error estimate at time step n:

$$r^{n+1} = \frac{1}{\sqrt{N_h}} \left(\sum_{j=1}^{N_h} \left(\frac{e_j^{n+1}}{atol + rtol|\xi_j^{n+1}|} \right)^2 \right)^{\frac{1}{2}}, \tag{4.57}$$

where $atol$ and $rtol$ are the specified absolute and relative tolerances.

The goal of the adaptive technique is to maximise Δt^{n+1} so that (4.57) satisfies $r^{n+1} \approx 1$. With this purpose, the following elementary controller (Wanner & Hairer, 1996) can be used:

$$\Delta t^{n+1} = \left(\frac{1}{r^{n+1}} \right)^{\frac{1}{p^*}} \Delta t^n,$$

p^* being the order of the embedded method. For the ESDIRK 3/2 RK pair, we have $p^* = 3$. In Söderlind (2003), linear digital control theory was used to propose several step size controllers that produce smoother step size sequences. In particular, we consider the so-called H211b controller:

$$\Delta t^{n+1} = \left(\frac{1}{r^{n+1}} \right)^{\frac{1}{bp^*}} \left(\frac{1}{r^n} \right)^{\frac{1}{bp^*}} \left(\frac{\Delta t^n}{\Delta t^{n-1}} \right)^{-\frac{1}{b}} \Delta t^n, \tag{4.58}$$

where the parameter b is such that $b \in (1, \infty)$. The value $b = 4$ is selected. Alternatively, the controller can be written in terms of the step size ratio c^n, defined as

$$c^n = \frac{\Delta t^{n+1}}{\Delta t^n}. \tag{4.59}$$

Then, (4.58) becomes

$$c^n = \left(\frac{1}{r^{n+1}} \right)^{\frac{1}{bp^*}} \left(\frac{1}{r^n} \right)^{\frac{1}{bp^*}} \left(c^{n-1} \right)^{-\frac{1}{b}}.$$

To avoid too large step size changes, we use the smooth limiter suggested in Söderlind & Wang (2006) to compute a limited step size ratio:

$$\hat{c}^n = 1 + \kappa \, \text{atan}((c^n - 1)/\kappa), \tag{4.60}$$

where κ is a customizable parameter. We choose $\kappa = 2$, which effectively limits the step size increase to a factor around 4. The step size is controlled using the limited ratio $\hat{c}^n$, as $\Delta t^{n+1} = \hat{c}^n \Delta t^n$.

At the first step size, the elementary controller is used with an initial step size. Then, the H211b controller is employed until the end time value corresponding to the problem is reached, using the smooth limiter (4.60) to modify the step size. The step rejection criterion is based on the estimated error and the limited step size ratio. Whenever the controller yields a major step size reduction, the step is rejected and recomputed (Söderlind & Wang, 2006). Specifically, we choose a minimum ratio equal to 0.9, such that if $\hat{c}^n < 0.9$, the step is rejected and the numerical approximation at time step $n + 1$ is recomputed using the suggested step size by the controller.

4.4.4. Algorithm

A fixed point-type algorithm that solves iteratively the coupling between the heat equation in the domain and the radiosity integral equation on the radiation boundary is proposed. Before the procedure begins, the computational mesh is loaded and the matrix representing the integral operator $\mathcal{K}$, defined in (4.43), is computed. A flow chart of the algorithm, which consists of several embedded loops, is provided in Figure 4.7. The outer loop is the time-stepping loop whereas the inner loop is

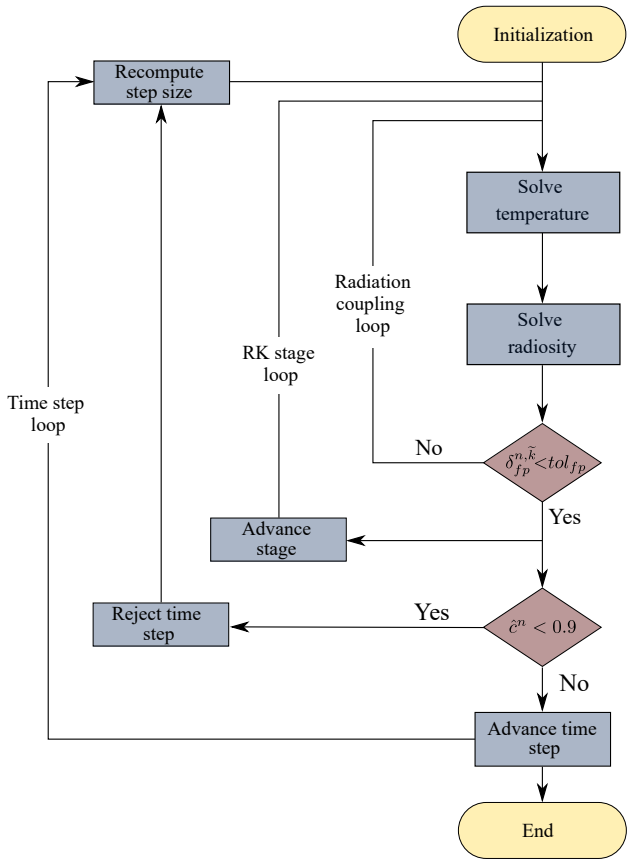


Figure 4.7: Flow diagram of the algorithm.

used to compute the radiosity and temperature at a given stage of the RK method. Specifically, at time t^n, we assume that the discretised temperature T_h^n and radiosity R_h^n are known, and denote as $R_{h,l}^{n+1}$ the numerical approximation of the radiosity at the RK internal time node t_l^{n+1}, corresponding to the lth stage. Then, to compute $\overline{\mathcal{X}}_l^{n+1}$ and $R_{h,l}^{n+1}$, we proceed with the radiation coupling loop, as described in Algorithm 4.1.

Once the last stage is computed, $\overline{\mathcal{X}}_s^{n+1}$, the local error estimator provided by the RK pair is used to test if the time step size is adequate, which involves computing the norm (4.57) and rejecting the step when necessary. If the step is accepted, we set T_h^{n+1} using that $\overline{\xi}^{n+1} = \overline{\mathcal{X}}_s^{n+1}$. Then, either if the step is rejected or accepted, a new time step size is computed using the H211b controller (4.59), as described in Subsection 4.4.3. If N_{fp}^{max} iterations are computed without achieving convergence for any RK stage, the step is rejected and T_h^{n+1} and R_h^{n+1} are recomputed reducing the step size by a factor of two.

4.5. Derivation of a 2D coupled manufactured solution test

The aim of this section is, for a given temperature field, to find the corresponding radiosity such that the pair, for suitable data, is the solution to the coupled transient heat conduction in a 2D domain with a non-local radiation boundary, i.e., the solution to Problem $(\mathcal{P}_{PR})$. In 3D cavities, the derivation of this type of manufactured solution test can be done considering a spherical surface as the radiation cavity, which has the advantage of simplifying the integral kernel, becoming constant (Bermúdez et al., 2011). In the 2D case, it is possible to consider a circumference as cavity, which also leads to an integral kernel that is much easier to manipulate analytically than the general expression. Nev-

Algorithm 4.1 Fixed point algorithm to obtain $\overline{\mathcal{X}}_l^{n+1}$ and $R_{h,l}^{n+1}$

1. Initialisation: for $s \geq l \geq 1$ and $n \geq 0$, set $\overline{\mathcal{X}}_l^{n+1,0} = \overline{\mathcal{X}}_{l-1}^{n+1}$ and $R_{h,l}^{n+1,0} = R_{h,l-1}^{n+1}$.

2. Iteration $\widetilde{k}+1$: for $\widetilde{k} \geq 0$, use $\overline{\mathcal{X}}_l^{n+1,\widetilde{k}}$ and $R_{h,l}^{n+1,\widetilde{k}}$ to obtain

   a) $\overline{\mathcal{X}}_l^{n+1,*}$ as solution of the heat equation, using $R_{h,l}^{n+1,\widetilde{k}}$ to compute the radiative heat flux on $\widehat{\gamma}_R$.

   b) $R_{h,l}^{n+1,*}$ as solution to the radiosity integral equation (4.51) using $\overline{\mathcal{X}}_l^{n+1,*}$ as data.

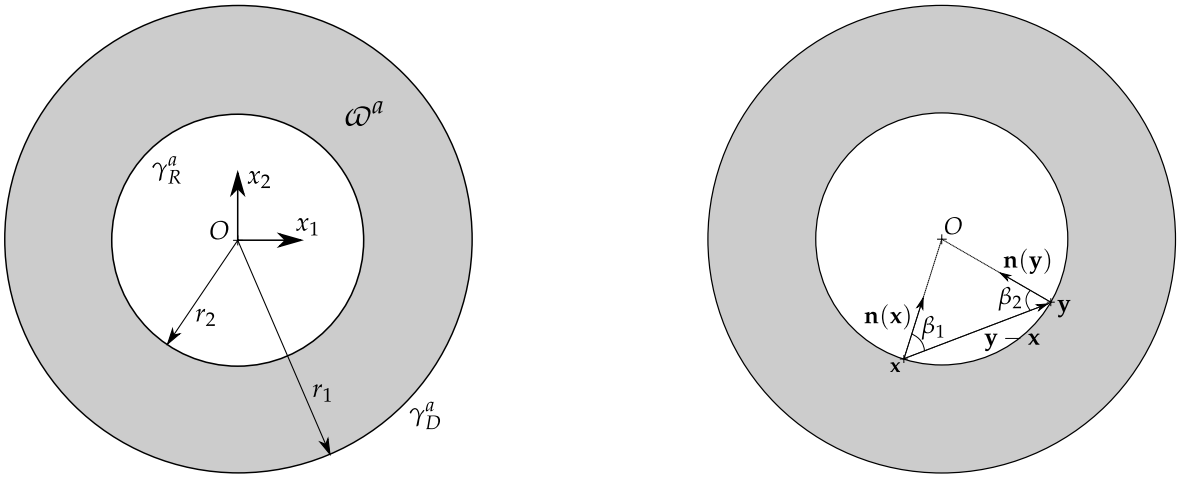
   c) Compute the residuals $\delta_{fp,l}^{n,\widetilde{k}}(\overline{\mathcal{X}})$ and $\delta_{fp,l}^{n,\widetilde{k}}(R_h)$, defined as

$$\delta_{fp,l}^{n,\widetilde{k}}(\overline{\mathcal{X}}) = \frac{\|\overline{\mathcal{X}}_l^{n+1,*} - \overline{\mathcal{X}}_l^{n+1,\widetilde{k}}\|_2}{\|\overline{\mathcal{X}}_l^{n+1,\widetilde{k}}\|_2},$$
$$\delta_{fp,l}^{n,\widetilde{k}}(R_h) = \frac{\|R_{h,l}^{n+1,*} - R_{h,l}^{n+1,\widetilde{k}}\|_2}{\|R_{h,l}^{n+1,\widetilde{k}}\|_2}.$$

   If both fall below a given threshold tol_{fp}, the algorithm converges.

   d) Else, compute $\overline{\mathcal{X}}_l^{n+1,\widetilde{k}+1}$ and $R_{h,l}^{n+1,\widetilde{k}+1}$ applying a relaxation step with parameter v_{fp}

$$\overline{\mathcal{X}}_l^{n+1,\widetilde{k}+1} = (1 - v_{fp})\overline{\mathcal{X}}_l^{n+1,\widetilde{k}} + v_{fp}\overline{\mathcal{X}}_l^{n+1,*},$$
$$R_{h,l}^{n+1,\widetilde{k}+1} = (1 - v_{fp})R_{h,l}^{n+1,\widetilde{k}} + v_{fp}R_{h,l}^{n+1,*}.$$



(**a**) Boundaries.

(**b**) Relation between the β_1 and β_2 angles on γ_R^a.

Figure 4.8: Manufactured solution test domain.

USC UNIVERSIDADE DE SANTIAGO DE COMPOSTELA

ertheless, the kernel is not constant, significantly increasing the difficulty of the test derivation. In Blackwell et al. (2009), a manufactured solution test was proposed for this setting, without including the heat equation in the domain surrounding the radiation cavity. In Silva III & Carnes (2016), the same procedure was applied to obtain a test including the coupled steady heat conduction in the surroundings. However, the insertion of a cut line in the domain was required to mitigate the effects of a singularity in the temperature gradient.

Here, we define a slightly different methodology to obtain a manufactured solution test which overcomes this limitation and incorporates dependence on time. To this end, a simpler approach to obtain the corresponding radiosity to a given temperature is proposed, which relies on the periodicity of the data on the circumference. In Section 4.5.1, a derivation of the simplified expression of the non-local radiation integral kernel on the circumference is presented. This expression is used in Section 4.5.2 to propose a Cauchy problem, whose solution for a given temperature yields a radiosity that satisfies the original integral equation on the cavity. Also, the derivation of the manufactured test proposed in Blackwell et al. (2009) is analysed in Section 4.5.3. Lastly, in Section 4.5.4, from a set temperature field, the corresponding radiosity is found by solving the Cauchy problem, resulting in a new manufactured solution test. Specifically, we look for a temperature that solves the following problem, which is analogous to $(\mathcal{P}_{PR})$, but adding the superscript a to clarify that the data is specifically arranged to yield an academic problem with a known solution.

Problem $(\mathcal{P}^a_{PR})$. Find $T^a(\mathbf{x},t)$ and $R^a(\mathbf{x},t)$ such that:

$$
\begin{aligned}
&\rho^a c_p^a \frac{\partial T^a}{\partial t}(\mathbf{x},t) - \operatorname{div}\big(k^a \operatorname{grad}(T^a(\mathbf{x},t))\big) = f^a(\mathbf{x},t), && \text{in } \varpi^a \times (0, t^a_{end}],\\
&(\mathcal{I} - (1-\varepsilon^a)\mathcal{K})(R^a(t))(\mathbf{x}) = \varepsilon^a \sigma^a (T^a)^4(\mathbf{x},t), && \text{on } \gamma^a_R \times (0, t^a_{end}],\\
&T^a(\mathbf{x},0) = T^a_0(\mathbf{x}), && \text{in } \varpi^a,\\
&T^a(\mathbf{x},t) = T^a_D(\mathbf{x},t), && \text{on } \gamma^a_D \times (0, t^a_{end}],\\
&-k^a \frac{\partial T^a}{\partial \mathbf{n}}(\mathbf{x},t) = q^a_{rad}(\mathbf{x},t) + g^a(\mathbf{x},t), && \text{on } \gamma^a_R \times (0, t^a_{end}],\\
&q^a_{rad}(\mathbf{x},t) = \mathcal{Q}(R^a(t))(\mathbf{x}), && \text{on } \gamma_R \times (0, t^a_{end}],
\end{aligned}
\tag{4.61}
$$

The computational domain ϖ^a, sketched in Figure 4.8a, is selected as the annular region bounded by two circumferences of radius $r_1 = 1$ m and $r_2 = 2$ m. As in Problem $(\mathcal{P}_{PR})$, on γ^a_R, corresponding to the inner circumference, a non-local radiation boundary condition is applied. On the exterior circumference, labelled as γ^a_D, a Dirichlet boundary condition is set. Moreover, we consider a constant emissivity ε^a on γ^a_R.

4.5.1. Simplified integral kernel

We recall the expression (4.42), which defines the integral kernel of the operator $\mathcal{K}$ in the 2D setting:

$$
w(\mathbf{x},\mathbf{y}) = \frac{\mathbf{n}(\mathbf{x})\cdot(\mathbf{y}-\mathbf{x})\mathbf{n}(\mathbf{y})\cdot(\mathbf{x}-\mathbf{y})}{2|\mathbf{y}-\mathbf{x}|^3}\Theta(\mathbf{x},\mathbf{y}). \tag{4.62}
$$

In the case of the cavity bounded by γ^a_R, the visibility factor is $\Theta(\mathbf{x},\mathbf{y}) = 1$ for any $\mathbf{x},\mathbf{y} \in \gamma^a_R$, since the cavity is convex. To derive the expression of the simplified kernel on the circumference, denoted as w^a, we follow an approach that substantially simplifies the procedure that was proposed in Blackwell et al. (2009). Notice that any diameter perpendicular to a chord of the circumference divides it into two equal parts, the relation $2r_1\cos\beta_2 = 2r_1\cos\beta_1 = |\mathbf{y}-\mathbf{x}|$ holds for any $\mathbf{x},\mathbf{y} \in \gamma^a_R$, being β_1 and β_2 the angles depicted in Figure 4.8b. Using this property, (4.62) is expressed as follows:

$$
w^a(\mathbf{x},\mathbf{y}) = \frac{\cos^2\beta_1}{2|\mathbf{x}-\mathbf{y}|} = \frac{|\mathbf{y}-\mathbf{x}|}{8}, \tag{4.63}
$$

USC UNIVERSIDADE DE SANTIAGO DE COMPOSTELA

since the inner radius is $r_1 = 1$. Using a polar coordinate system and that $r = r_1 = 1$, we establish that

$$\begin{aligned} x_1 &= \cos\theta, \quad y_1 = \cos\psi, \\ x_2 &= \sin\theta, \quad y_2 = \sin\psi, \end{aligned}$$

for some $\theta, \psi \in [0, 2\pi)$. Furthermore, it is satisfied that

$$|\mathbf{y} - \mathbf{x}| = \sqrt{2 - 2(\cos\psi\cos\theta + \sin\psi\sin\theta)}.$$

Then, (4.63) can be expressed for $\mathbf{x}, \mathbf{y} \in \gamma_R$ as follows:

$$w^a(\mathbf{x}, \mathbf{y}) = \widehat{w}^a(\theta, \psi) = \frac{1}{8}\sqrt{2 - 2(\cos\psi\cos\theta + \sin\psi\sin\theta)}. \tag{4.64}$$

Using trigonometric identities, (4.64) transforms into

$$\widehat{w}^a(\theta, \psi) = \frac{1}{4}\left|\sin\frac{\psi - \theta}{2}\right|.$$

Lastly, considering that $\theta, \psi \in [0, 2\pi)$, we obtain the following expression for the integral kernel, valid for γ_R^a being the unit circumference:

$$\widehat{w}^a(\theta, \psi) = \begin{cases} \dfrac{1}{4}\sin\dfrac{\psi - \theta}{2}, & \text{if } \theta \le \psi < 2\pi, \\ -\dfrac{1}{4}\sin\dfrac{\psi - \theta}{2}, & \text{if } 0 \le \psi < \theta. \end{cases} \tag{4.65}$$

Remark 4.6. *As stated in Blackwell et al. (2009), a necessary condition for the radiation kernel to be well-defined when the non-local radiation boundary γ_R is an enclosure is that, for any $\mathbf{x} \in \gamma_R$, it holds that*

$$\int_{\gamma_R} w(\mathbf{x}, \mathbf{y}) ds_y = 1.$$

From (4.65), this can be easily verified for the proposed test. Indeed, for each $\mathbf{x} \in \gamma_R^a$

$$\int_{\gamma_R^a} w^a(\mathbf{x}, \mathbf{y}) ds_y = \int_0^{2\pi} \widehat{w}^a(\theta, \psi) d\psi = 1.$$

4.5.2. Cauchy problem for non-local radiation

In the subsequent discussion, to simplify the writing, dependence on time is omitted. On the radiation boundary, we recall that the radiosity R^a is the solution to (4.61). On γ_R^a, using the simplified integral kernel (4.65), the radiosity equation (4.61) becomes

$$\widehat{R}^a(\theta) = \widehat{E}^a(\theta) - \frac{1 - \varepsilon^a}{4}\int_0^\theta \sin\frac{\psi - \theta}{2}\widehat{R}(\psi)d\psi + \frac{1 - \varepsilon^a}{4}\int_\theta^{2\pi} \sin\frac{\psi - \theta}{2}\widehat{R}(\psi)d\psi, \tag{4.66}$$

where we recall that the emissive power for a grey surface is defined as (4.9).

Following the strategy detailed in Blackwell et al. (2009), the integral equation (4.66) can be transformed into an ordinary differential equation. The procedure detailed below is analogous, with the only change that our parametrisation of the inner circumference, γ_R^a, uses $\theta \in [0, 2\pi)$ instead of $[-\pi, \pi)$. With this purpose, we take the first and second order derivatives with respect to θ in (4.66), apply Leibniz's rule, and deduce that:

$$\widehat{R}^{a\prime\prime}(\theta) + \frac{\varepsilon^a}{4}\widehat{R}^a(\theta) = \widehat{E}^{a\prime\prime}(\theta) + \frac{\widehat{E}^a(\theta)}{4}. \tag{4.67}$$

USC UNIVERSIDADE DE SANTIAGO DE COMPOSTELA

If it holds that $\widehat{E}^a$ is an emissive power such that it is periodic with periodic derivative in $[0, 2\pi)$, i.e.:

$$\widehat{E}^a(0) = \widehat{E}^a(2\pi), \qquad \widehat{E}^{a\prime}(0) = \widehat{E}^{a\prime}(2\pi), \tag{4.68}$$

then, substituting in (4.66), it follows that

$$\widehat{R}^a(0) = \widehat{R}^a(2\pi), \qquad \widehat{R}^{a\prime}(0) = \widehat{R}^{a\prime}(2\pi). \tag{4.69}$$

Therefore, for an emissive power such that it satisfies conditions (4.68), to obtain a unique solution of equation (4.67), we can require that the radiosity also satisfies the same periodicity conditions in the interval $[0, 2\pi)$.

Remark 4.7. *Assume that ε^a is constant on γ_R^a and that $T^a(\mathbf{x}, t)$ is a classic solution to Problem $(\mathcal{P}_{PR}^a)$, in the sense that $T^a \in \mathcal{C}^{2,1}(\overline{\varpi}^a \times [0, t_{end}^a])$. Then, the temperature T^a written in polar coordinates satisfies*

$$\widehat{T}^a(r, 0) = \widehat{T}^a(r, 2\pi), \qquad \frac{\partial \widehat{T}^a}{\partial \theta}(r, 0) = \frac{\partial \widehat{T}^a}{\partial \theta}(r, 2\pi),$$

for $r_1 \leq r \leq r_2$. Moreover, considering $\widehat{E}^a(\theta) = \varepsilon^a \sigma^a (\widehat{T}^a(r_1, \theta))^4$, the derivative of the emissive power with respect to θ is such that

$$\widehat{E}^{a\prime}(\theta) = 4\varepsilon^a \sigma^a (\widehat{T}^a(r_1, \theta))^3 \frac{\partial \widehat{T}^a}{\partial \theta}(r_1, \theta).$$

Hence, conditions (4.68) follow. Therefore, if the data is smooth enough, it is natural to require conditions (4.69) to be satisfied to obtain a manufactured solution test defined in ϖ^a being the annular region depicted in Figure 4.8a.

In summary, to find the corresponding radiosity for a given temperature on γ_R^a, it suffices to solve the following Cauchy problem:

$$\begin{cases} \widehat{R}^{a\prime\prime}(\theta) + \dfrac{\varepsilon^a}{4} \widehat{R}^a(\theta) = \widehat{E}^{a\prime\prime}(\theta) + \dfrac{\widehat{E}^a(\theta)}{4}, \\ \widehat{R}^a(0) = \widehat{R}^a(2\pi), \\ \widehat{R}^{a\prime}(0) = \widehat{R}^{a\prime}(2\pi), \end{cases} \tag{4.70}$$

where the emissive power, $\widehat{E}^a$, is such that (4.68) holds.

4.5.3. Test by Blackwell et al.

In this section, we describe the steps followed in Blackwell et al. (2009) to obtain a manufactured solution test. To do so, we maintain our parametrisation of the circumference, using the interval $[0, 2\pi)$, which leads to slightly different computations to those appearing in the aforementioned reference, which resorts to the interval $[-\pi, \pi)$ instead. The purpose of the discussion is to highlight the main shortcomings of this approach and the differences with our proposed methodology.

Instead of requiring that the corresponding radiosity satisfies the periodicity conditions derived above, a temperature field that leads to a homogeneous differential equation is set, i.e., a temperature such that the right hand side in (4.67) becomes zero. Let us assume that $\varepsilon^a \in (0, 1)$. If $\varepsilon^a = 1$, the material is a black body and there is no need to compute reflected radiation.

Specifically, we consider the following temperature field

$$\widehat{T}^a(\theta) = \left(\sin \frac{\theta}{2}\right)^{\frac{1}{4}}. \tag{4.71}$$

USC UNIVERSIDADE DE SANTIAGO DE COMPOSTELA

Thereafter, we proceed to derive the radiosity field corresponding to the temperature (4.71). In particular, the emissive power is such that

$$\widehat{E}^a(\theta) = \varepsilon^a \sigma^a \sin\frac{\theta}{2}, \tag{4.72}$$

Then, the ODE in (4.70) is solved, assuming that the solution $\widehat{R}^a(\theta)$ is periodic in $[0, 2\pi]$, but without imposing the condition on the derivative. Thus, we find that

$$\widehat{R}^a(\theta) = C_1 \sin\frac{\sqrt{\varepsilon^a}\theta}{2} + \frac{C_1 \sin\sqrt{\varepsilon^a}\pi}{1-\cos\sqrt{\varepsilon^a}\pi}\cos\frac{\sqrt{\varepsilon^a}\theta}{2}. \tag{4.73}$$

Remark 4.8. *In Blackwell et al. (2009), instead of (4.71), the proposed temperature field is*

$$\widehat{T}^a(\theta) = \left(\cos\frac{\theta}{2}\right)^{\frac{1}{4}}, \tag{4.74}$$

which clearly results in an emissive power that leads to a null RHS in (4.67), and thus leads to a homogeneous ODE. However, such solution would not be valid in the setting proposed here due to the difference in the parametrisations of the boundary γ_R^a, as substituting in (4.74) it follows that $\widehat{T}(0) \neq \widehat{T}(2\pi)$.

To find a unique radiosity field, Blackwell et al. (2009) used that the radiosity must also satisfy the integral equation (4.66) on a point inside the interval $[0, 2\pi)$. For instance, choosing $\theta = \pi$ and matching (4.66) with (4.73) leads to

$$\begin{aligned}
\widehat{R}^a(\pi) &= \widehat{E}^a(\pi) - \frac{1-\varepsilon^a}{4}\int_0^\pi \sin\frac{\psi-\pi}{2}\widehat{R}^a(\psi)d\psi + \frac{1-\varepsilon^a}{4}\int_\pi^{2\pi}\sin\frac{\psi-\pi}{2}\widehat{R}^a(\psi)d\psi. \\
&= \widehat{E}^a(\pi) - \frac{1-\varepsilon^a}{4}\left[C_1\int_0^\pi \sin\frac{\psi-\pi}{2}\sin\frac{\sqrt{\varepsilon^a}\psi}{2}d\psi + \frac{C_1\sin\sqrt{\varepsilon^a}\pi}{1-\cos\sqrt{\varepsilon^a}\pi}\int_0^\pi \sin\frac{\psi-\pi}{2}\cos\frac{\sqrt{\varepsilon^a}\pi}{2}d\psi\right] \\
&\quad + \frac{1-\varepsilon^a}{4}\left[C_1\int_\pi^{2\pi} \sin\frac{\psi-\pi}{2}\sin\frac{\sqrt{\varepsilon^a}\psi}{2}d\psi + \frac{C_1\sin\sqrt{\varepsilon^a}\pi}{1-\cos\sqrt{\varepsilon^a}\pi}\int_\pi^{2\pi} \sin\frac{\psi-\pi}{2}\cos\frac{\sqrt{\varepsilon^a}\psi}{2}d\psi\right].
\end{aligned}$$

Solving for C_1 in the previous expression after computing the corresponding integrals, we find that $C_1 = \sqrt{\varepsilon^a}$. Consequently, the desired radiosity is

$$\widehat{R}^a(\theta) = \sqrt{\varepsilon^a}\sin\frac{\sqrt{\varepsilon^a}\theta}{2} + \frac{\sqrt{\varepsilon^a}\sin\sqrt{\varepsilon^a}\pi}{1-\cos\sqrt{\varepsilon^a}\pi}\cos\frac{\sqrt{\varepsilon^a}\theta}{2}. \tag{4.75}$$

To simplify the previous expression, the subsequent trigonometric identity is used

$$\frac{\sin\sqrt{\varepsilon^a}\pi}{1-\cos\sqrt{\varepsilon^a}\pi} = \cot\frac{\sqrt{\varepsilon^a}\pi}{2}.$$

After substitution in (4.75) and grouping terms, we obtain that

$$\widehat{R}^a(\theta) = \frac{\sqrt{\varepsilon^a}}{\sin\frac{\pi\sqrt{\varepsilon^a}}{2}}\cos\left(\frac{\sqrt{\varepsilon^a}}{2}(\theta-\pi)\right). \tag{4.76}$$

Remark 4.9. *The radiosity found in (4.76) is equivalent to the one derived in Blackwell et al. (2009), which as mentioned in Remark 4.8, uses a different temperature field due to the choice of the interval $[-\pi, \pi)$. Indeed, let $\widetilde{\theta} \in [-\pi, \pi)$ and set the following translation*

$$u(\widetilde{\theta}) = \widetilde{\theta} + \pi,$$

USC UNIVERSIDADE DE SANTIAGO DE COMPOSTELA

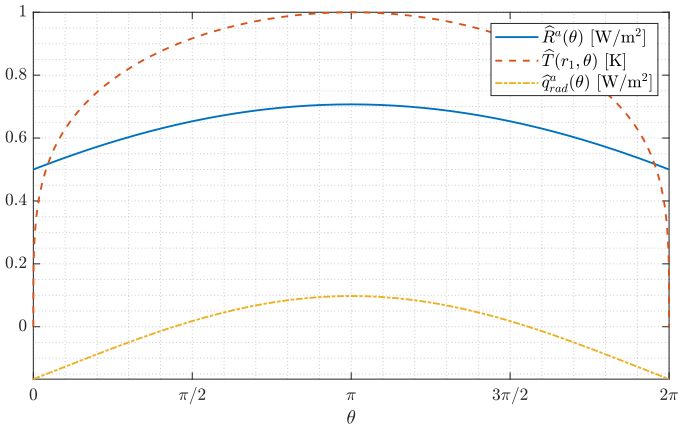


Figure 4.9: Radiosity, temperature and heat flux due to radiation on γ_R^a, test by Blackwell et al.

it follows that, from the computed radiosity (4.76)*:*

$$\widehat{R}^a(u(\widetilde{\theta})) = \frac{\sqrt{\varepsilon^a}}{\sin\dfrac{\pi\sqrt{\varepsilon^a}}{2}}\cos\frac{\sqrt{\varepsilon^a}}{2}\widetilde{\theta},$$

which coincides with the function obtained in the aforementioned reference.

Once the radiosity is computed, the irradiation on γ_R^a, G^a, can be obtained by substitution in expression (4.26). Then, the radiative heat flux can be found by subtracting the irradiation to the radiosity:

$$\widehat{q}^a_{rad}(\theta) = \mathcal{Q}(\widehat{R}^a)(\theta) = \widehat{R}^a(\theta) - \widehat{G}^a(\theta).$$

In Figure 4.9, the radiosity, temperature and heat flux due to radiation on γ_R^a are shown, considering an emissivity value $\varepsilon^a = 0.25$.

Remark 4.10. *As a direct consequence of having considered a temperature field that results in the emissive power* (4.72)*, which does not satisfy the hypothesis on the derivative in* (4.68)*, the obtained radiosity has a non-periodic derivative as well. This is not problematic for the purposes of Blackwell et al.* (2009)*, since their aim is to obtain a manufactured solution test only for the integral equation on γ_R^a. However, for our intents, which also seek to use the test for coupled heat conduction on the annulus surrounding the cavity, this approach has a shortcoming. Namely, as it becomes evident from the temperature plot in Figure 4.9, the gradient of* (4.71) *is singular along $\theta = 0$.*

This subtle issue complicates extending the test to incorporate heat conduction in the domain surrounding the cavity, as noted in Silva III & Carnes (2016)*. There, to mitigate the singularity effects, which also results in the corresponding source term being singular (obtained by substitution of the temperature in the heat equation), a cut line along the ray corresponding to the θ value where the singularity is located was introduced in the domain. Setting an artificial Dirichlet condition on the cut line led to a successful numerical solution of the test.*

In any case, it should be noted that the usual procedure when using manufactured solution tests to verify numerical implementations (see e.g. Roache, 2001) involves measuring if the theoretical convergence rates are achieved as the discretisation parameter is refined. Nonetheless, the classical results on a priori error estimation require that the solution is sufficiently regular. For instance, if we consider a discretisation using a first-order Lagrange finite element of the heat equation such as that described in Section 4.4.1 for the model problem then, to guarantee the order 1 convergence rate in the $H^1(\varpi^a)$ norm, the exact solution must belong to $H^2(\varpi^a)$ (see Quarteroni, 2009, Th. 4.6). Unfortunately, this is not the case for the temperature (4.71)*.*

4.5.4. New manufactured solution test

Subsequently, we provide a test that is suitable for our setting, avoiding the introduction of artefacts such as a cut line inside the domain. To derive it, we use a temperature field which leads to an emissive power satisfying periodicity conditions (4.68). This results in the ODE (4.67) being non homogeneous. Consequently, significantly more involved computations when compared to those presented above are required to obtain the closed form of the analytic solutions. In the following discussion, we will skip most of them, which were done with the help of the *Symbolic Math Toolbox* available in MATLAB (MuPAD).

We start by proposing the subsequent temperature field:

$$T^a(\mathbf{x},t) = A(t)x_1x_2, \tag{4.77}$$

where $A(t)$ only depends on the time t. Since the inner radius is $r = r_1 = 1$, the restriction of (4.77) to γ_R^a rewritten in polar coordinates becomes

$$\widehat{T}^a(\theta,t) = A(t)\cos\theta\sin\theta.$$

Moreover, the corresponding emissive power is such that

$$\widehat{E}^a(\theta,t) = A^4(t)\varepsilon^a\sigma^a\cos^4\theta\sin^4\theta.$$

For this emissive power, the Cauchy problem (4.70) can be directly solved to obtain its unique solution at each time t, obtaining that:

$$\widehat{R}^a(\theta,t) = \frac{3A^4(t)\sigma^a}{64(64-\varepsilon^a)(\varepsilon^a-256)}\Big(84(\varepsilon^a)^2\sin^2(2\theta) - 85(\varepsilon^a)^2\sin^2(4\theta) - 21504\varepsilon^a\sin^2(2\theta) + 5440\varepsilon^a\sin^2(4\theta) + 8192\varepsilon^a - 8192\Big).$$

The heat flux due to radiation, q^a_{rad}, can be computed using the integral operator $\mathcal{Q}(\widehat{R}^a)$, which results in the following expression:

$$\mathcal{Q}(\widehat{R}^a)(\theta,t) = \frac{4A^4(t)\varepsilon^a\sigma^a}{(64-\varepsilon^a)(\varepsilon^a-256)}\left(128\cos(4\theta) - 32\cos^2(8\theta) + \frac{\varepsilon^a}{2}\cos(4\theta) - \frac{\varepsilon^a}{2}\cos(8\theta)\right).$$

We choose an emissivity value $\varepsilon^a = 0.25$, for which the radiosity and the heat flux simplify to:

$$\widehat{R}^a(\theta,t) = A^4(t)\sigma^a\frac{7225\cos^2(4\theta) - 14322\cos(4\theta) + 39865}{1855040},$$

$$\mathcal{Q}(\widehat{R}^a)(\theta,t) = 2A^4(t)\sigma^a\frac{170\cos^2(4\theta) - 341\cos(4\theta) - 85}{86955}.$$

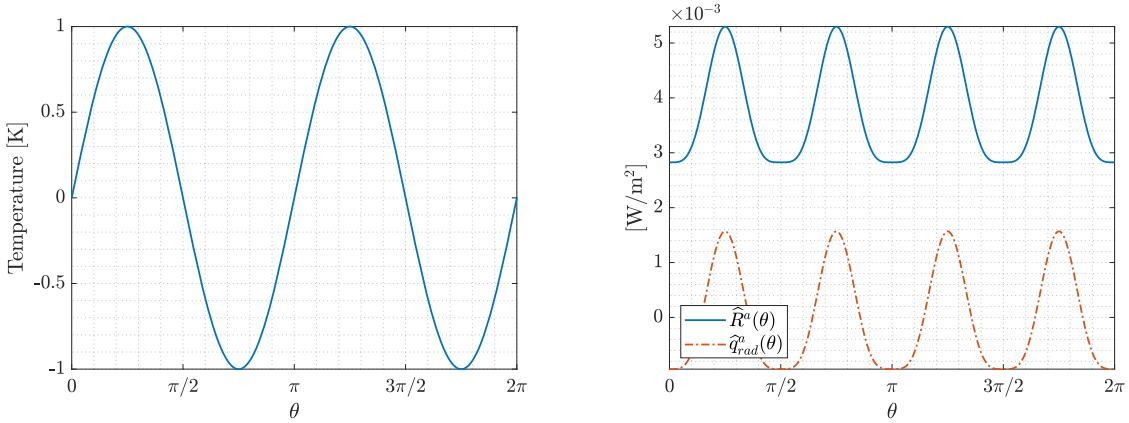
In Figure 4.10, the radiosity, temperature and radiative heat flux on γ_R^a are shown, for $A(t) = 2$ and considering $\sigma^a = 1/100\ \mathrm{W/(m^2{\cdot}K^4)}$. To pose the manufactured solution test, the radiosity and radiation heat flux are rewritten in cartesian coordinates. With this purpose, noting that $\cos(4\theta) = 8\cos^4\theta - 8\cos^2\theta + 1$ we obtain that

$$R^a(\mathbf{x},t) = A^4(t)\sigma^a\frac{462400x_1^8 - 924800x_1^6 + 463424x_1^4 - 1024x_1^2 + 32768}{1855040}, \tag{4.78}$$

$$\mathcal{Q}(R^a)(\mathbf{x},t) = 2A^4(t)\sigma^a\frac{10880x_1^8 - 21760x_1^6 + 10872x_1^4 + 8x_1^2 - 256}{86955}.$$

USC UNIVERSIDADE DE SANTIAGO

It remains to compute the data f^a and g^a for the test. First, we set a constant thermal conductivity,



(**a**) Temperature.

(**b**) Radiosity and radiative heat flux.

Figure 4.10: Radiosity, temperature and heat flux due to radiation on γ_R^a for the new manufactured solution test, considering $A(t) = 2$, $\sigma^a = 1/100$ W/(m^2·K^4) and $\varepsilon^a = 0.25$.

density, and specific heat such that $c_p^a = \rho^a = k^a = 1$. Therefore, the source term becomes

$$f^a = \rho^a c_p^a \frac{\partial T^a}{\partial t} - \operatorname{div}(k^a \operatorname{grad}(T^a)) = A'(t) x_1 x_2. \tag{4.79}$$

On the other hand, on γ_R^a, it must be satisfied that

$$-k^a \frac{\partial T^a}{\partial \mathbf{n}} = g^a + q_{rad}^a.$$

Therefore, observing that the outward pointing normal vector on γ_R^a is written as $\mathbf{n}(\mathbf{x}) = -(x_1, x_2)$, the Neumann data g^a can be directly computed:

$$\begin{aligned} g^a(\mathbf{x}, t) &= -k^a \operatorname{grad}(T^a) \cdot \mathbf{n} - q_{rad}^a = -k^a \operatorname{grad}(T^a) \cdot \mathbf{n} - \mathcal{Q}(R^a) \\ &= 2A(t) x_1 x_2 - 2A^4(t) \sigma^a \frac{10880 x_1^8 - 21760 x_1^6 + 10872 x_1^4 + 8 x_1^2 - 256}{86955}. \end{aligned} \tag{4.80}$$

4.6. Numerical experiments with the manufactured solution test

In this section, the manufactured solution test derived in Section 4.5.4 is solved, using the discretisation and numerical algorithm described in Section 4.4. In addition, different time discretisation schemes are considered to compare their behaviour. First, in Section 4.6.1, the numerical approximations computed with an implicit Euler and the ESDIRK 3/2a are addressed for a fixed step size. Then, in Section 4.6.2, the adaptive time stepping technique described in Section 4.4.3 is considered, using the H211b adaptive step size controller to modify the step size according to various fixed tolerance values.

Let T_{exact} be the temperature field (4.77) which, in virtue of the discussion in the previous section, is the exact solution to Problem $(\mathcal{P}_{PR}^a)$ if we assume that $\rho^a = c_p^a = k^a = 1$, $\varepsilon^a = \frac{1}{4}$, and consider suitable data f^a and g^a. Thereafter, we set the following time dependent term in (4.77):

$$A(t) = 2 \sin\left(\frac{\pi t}{2}\right).$$

USC

The corresponding radiosity R_{exact} can be obtained by substitution in (4.78). Similarly, the expressions for the source term f^a and the heat flux g^a must satisfy (4.79) and (4.80), respectively. The proposed

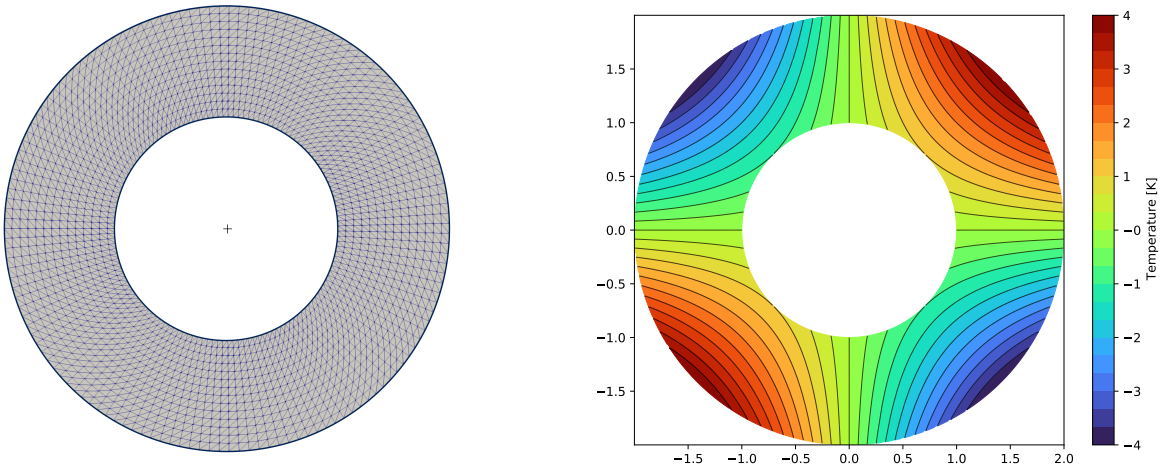


Figure 4.11: Mesh 5 (left) and T_{exact} at $t = 5$ s (right).

Table 4.1: Maximum element size, minimum element size, number of elements in the triangulation of ϖ^a and number of edge elements in the mesh of γ_R^a.

	h_{max}	h_{min}	$\#\tau_h^a$	$\#\tau_h^{\mathcal{G},a}$
Mesh 1	$6.99{\cdot}10^{-1}$	$5.95{\cdot}10^{-1}$	88	22
Mesh 2	$3.69{\cdot}10^{-1}$	$2.94{\cdot}10^{-1}$	344	43
Mesh 3	$1.79{\cdot}10^{-1}$	$1.33{\cdot}10^{-1}$	1566	87
Mesh 4	$9.08{\cdot}10^{-2}$	$6.68{\cdot}10^{-2}$	6288	173
Mesh 5	$4.59{\cdot}10^{-2}$	$3.33{\cdot}10^{-2}$	24912	346
Mesh 6	$2.30{\cdot}10^{-2}$	$1.65{\cdot}10^{-2}$	100886	691
Mesh 7	$1.14{\cdot}10^{-2}$	$8.22{\cdot}10^{-3}$	403544	1382
Mesh 8	$5.58{\cdot}10^{-3}$	$4.03{\cdot}10^{-3}$	1678336	2816

temperature is set as the Dirichlet condition $T_D^a = T_{exact}|_{\gamma_D^a}$ on $\gamma_D^a \times (0, t_{end}^a]$ and the initial condition is $T_0^a(\mathbf{x}) = 0$ in ϖ^a.

To solve $(\mathcal{P}_{PR}^a)$, we use eight different grids, with the total number of elements and number of elements on the radiation boundary γ_R^a reported in Table 4.1. Provided that the meshes are not fully uniform, the maximum element size h_{max} and the minimum element size h_{min} of each mesh are also provided in the table. In Figure 4.11, Mesh 5 is displayed, as well as the temperature contours at $t = 5$ s of the exact solution.

The problem is solved until reaching $t_{end}^a = 10$ s, setting that $\sigma^a = 10^{-2}$ W/(m^2·K^4). In Algorithm 4.1, the parameter values $v_{fp} = 1$ and $tol_{fp} = 10^{-8}$ are selected. To compare the approximate solution and the analytical one, the temperature relative error in the $L^2(0, t_{end}^a; L^2(\varpi^a))$ and $L^2(0, t_{end}^a; H^1(\varpi^a))$ norms are computed, considering the following approximations, extracted from Bermúdez et al. (2013):

$$e_{h,L^2}^{\Delta t}(T_h) := \left(\frac{\sum_{n=0}^{N_t^a-1} \Delta t^n \| T_{exact}(t^{n+1}) - T_h^{n+1} \|_{L^2(\varpi^a)}^2}{\sum_{n=0}^{N_t^a-1} \Delta t^n \| T_{exact}(t^{n+1}) \|_{L^2(\varpi^a)}^2} \right)^{\frac{1}{2}}, \tag{4.81}$$

$$e_{h,H^1}^{\Delta t}(T_h) := \left(\frac{\sum_{n=0}^{N_t^a-1} \Delta t^n || T_{exact}(t^{n+1}) - T_h^{n+1} ||_{H^1(\varpi^a)}^2}{\sum_{n=0}^{N_t^a-1} \Delta t^n || T_{exact}(t^{n+1}) ||_{H^1(\varpi^a)}^2} \right)^{\frac{1}{2}},$$

USC UNIVERSIDADE DE SANTIAGO DE COMPOSTELA

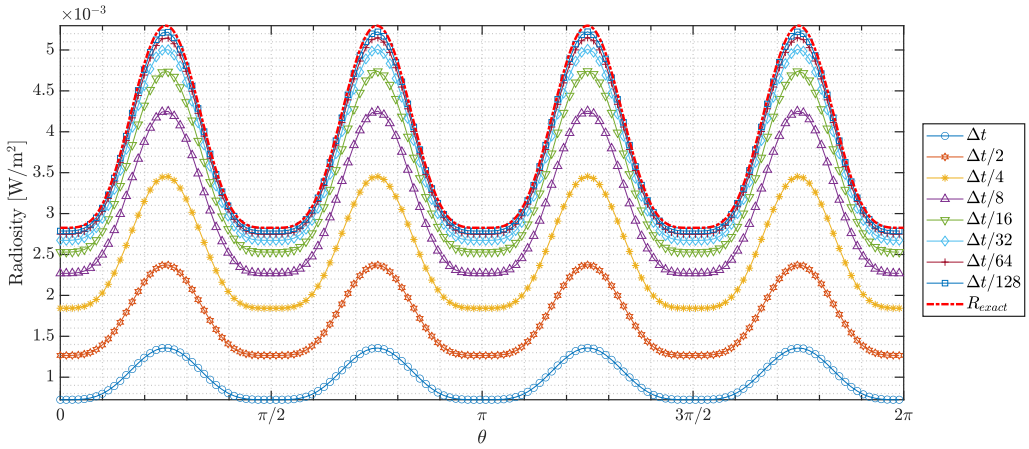


Figure 4.12: Approximated radiosity for Problem $(\mathcal{P}^a_{PR})$, with implicit Euler and different step size values at $t = 5$ s with Mesh 5.

where N_t^a denotes the number of time steps. Similarly, to analyse the error approximating the radiosity, we define the relative error norm $e^{\Delta t}_{h,L^2}(R_h)$ by considering R_{exact} instead of T_{exact} in (4.81), as well as the $L^2(\gamma_R^a)$ norm instead of the $L^2(\varpi^a)$ norm:

$$e^{\Delta t}_{h,L^2}(R_h) := \left(\frac{\sum_{n=0}^{N_t^a-1} \Delta t^n ||R_{exact}(t^{n+1}) - R_h^{n+1}||^2_{L^2(\gamma_R^a)}}{\sum_{n=0}^{N_t^a-1} \Delta t^n ||R_{exact}(t^{n+1})||^2_{L^2(\gamma_R^a)}} \right)^{\frac{1}{2}}.$$

The model is solved numerically using the open-source computing platform FEniCS (Alnæs et al., 2015). Its components automatically generate efficient low-level code to assemble the corresponding linear system from a symbolic representation of the weak formulation in the UFL language (Logg et al., 2012).

4.6.1. Fixed step size

Instead of the time discretisation proposed in Subsection 4.4.2 using an adaptive time stepping technique, firstly we consider a fixed step size to solve Problem $(\mathcal{P}^a_{PR})$. To this end, we compare the performance of an implicit Euler scheme and the ESDIRK 3/2a. In comparison, the former is much easier to implement and is fairly inexpensive numerically, which motivates its use in various industrial problems on different fields (Bermúdez et al., 2017) and also on similar applications (Bermúdez et al., 2006) due to its unconditional stability. Furthermore, the formal order in time of the Euler scheme is one, which matches the expected order of convergence of the radiosity approximation in space. In both cases, the reference value $\Delta t = 1$ s is set, which is successively divided by a factor of two to analyse the convergence in the considered error norms as the mesh and the step size are refined.

Concerning the use of the implicit Euler scheme, in Figure 4.12, the numerical approximations for the radiosity are compared with the exact solution for the different step sizes, also at time $t = 5$ s. Except for the smallest ones, we remark that the errors are very large. In Table 4.2, the computed relative errors are gathered; the rows at the top correspond to $e^{\Delta t}_{h,L^2}(T_h)$, whereas those in the middle and the bottom correspond to $e^{\Delta t}_{h,H^1}(T_h)$ and $e^{\Delta t}_{h,L^2}(R_h)$, respectively. Inspecting the entries within boxes in the tables, we observe the expected formal asymptotic behaviour as both the time step and mesh size are refined, i.e., $O(h^2 + \Delta t)$, $O(h + \Delta t)$ convergences in the $L^2(0, t^a_{end}; L^2(\omega^a))$, $H^1(0, t^a_{end}; H^1(\omega^a))$ norms for the temperature, and $O(h + \Delta t)$ convergence for the radiosity in the $L^2(0, t^a_{end}; L^2(\gamma_R^a))$ norm. It is also worth noticing that the relative error due to the time discretisation is too large to

Table 4.2: Implicit Euler scheme: $e^{\Delta t}_{h,L^2}(T_h)$ (top), $e^{\Delta t}_{h,H^1}(T_h)$ (middle) and $e^{\Delta t}_{h,L^2}(R_h)$ (bottom) relative errors.

	Mesh 1	Mesh 2	Mesh 3	Mesh 4	Mesh 5	Mesh 6	Mesh 7	Mesh 8
Δt	$9.35E{-2}$	$1.12E{-1}$	$1.18E{-1}$	$1.19E{-1}$	$1.20E{-1}$	$1.20E{-1}$	$1.20E{-1}$	$1.20E{-1}$
$\Delta t/2$	$4.68E{-2}$	$5.97E{-2}$	$6.44E{-2}$	$6.53E{-2}$	$6.56E{-2}$	$6.56E{-2}$	$6.57E{-2}$	$6.57E{-2}$
$\Delta t/4$	$2.44E{-2}$	$2.96E{-2}$	$3.34E{-2}$	$3.41E{-2}$	$3.43E{-2}$	$3.44E{-2}$	$3.44E{-2}$	$3.44E{-2}$
$\Delta t/8$	$1.95E{-2}$	$1.39E{-2}$	$1.67E{-2}$	$1.74E{-2}$	$1.76E{-2}$	$1.76E{-2}$	$1.76E{-2}$	$1.76E{-2}$
$\Delta t/16$	$2.10E{-2}$	$6.91E{-3}$	$8.15E{-3}$	$8.70E{-3}$	$8.86E{-3}$	$8.90E{-3}$	$8.91E{-3}$	$8.91E{-3}$
$\Delta t/32$	$2.28E{-2}$	$5.27E{-3}$	$3.86E{-3}$	$4.29E{-3}$	$4.43E{-3}$	$4.47E{-3}$	$4.48E{-3}$	$4.48E{-3}$
$\Delta t/64$	$2.39E{-2}$	$5.63E{-3}$	$1.88E{-3}$	$2.07E{-3}$	$2.20E{-3}$	$2.24E{-3}$	$2.24E{-3}$	$2.25E{-3}$
$\Delta t/128$	$2.44E{-2}$	$6.10E{-3}$	$1.25E{-3}$	$9.75E{-4}$	$1.08E{-3}$	$1.11E{-3}$	$1.12E{-3}$	$1.12E{-3}$
Δt	$1.95E{-1}$	$1.74E{-1}$	$1.69E{-1}$	$1.68E{-1}$	$1.67E{-1}$	$1.67E{-1}$	$1.67E{-1}$	$1.67E{-1}$
$\Delta t/2$	$1.51E{-1}$	$1.09E{-1}$	$9.56E{-2}$	$9.25E{-2}$	$9.16E{-2}$	$9.14E{-2}$	$9.14E{-2}$	$9.14E{-2}$
$\Delta t/4$	$1.34E{-1}$	$7.95E{-2}$	$5.63E{-2}$	$5.01E{-2}$	$4.83E{-2}$	$4.79E{-2}$	$4.78E{-2}$	$4.78E{-2}$
$\Delta t/8$	$1.30E{-1}$	$6.90E{-2}$	$3.89E{-2}$	$2.88E{-2}$	$2.56E{-2}$	$2.47E{-2}$	$2.45E{-2}$	$2.44E{-2}$
$\Delta t/16$	$1.29E{-1}$	$6.61E{-2}$	$3.29E{-2}$	$1.97E{-2}$	$1.45E{-2}$	$1.29E{-2}$	$1.25E{-2}$	$1.24E{-2}$
$\Delta t/32$	$1.29E{-1}$	$6.53E{-2}$	$3.12E{-2}$	$1.66E{-2}$	$9.87E{-3}$	$7.28E{-3}$	$6.49E{-3}$	$6.27E{-3}$
$\Delta t/64$	$1.29E{-1}$	$6.52E{-2}$	$3.07E{-2}$	$1.57E{-2}$	$8.29E{-3}$	$4.93E{-3}$	$3.65E{-3}$	$3.25E{-3}$
$\Delta t/128$	$1.29E{-1}$	$6.51E{-2}$	$3.06E{-2}$	$1.54E{-2}$	$7.84E{-3}$	$4.13E{-3}$	$2.46E{-3}$	$1.82E{-3}$
Δt	$6.92E{-1}$	$7.34E{-1}$	$7.50E{-1}$	$7.53E{-1}$	$7.54E{-1}$	$7.54E{-1}$	$7.54E{-1}$	$7.54E{-1}$
$\Delta t/2$	$4.84E{-1}$	$5.32E{-1}$	$5.51E{-1}$	$5.55E{-1}$	$5.56E{-1}$	$5.57E{-1}$	$5.57E{-1}$	$5.57E{-1}$
$\Delta t/4$	$2.78E{-1}$	$3.24E{-1}$	$3.45E{-1}$	$3.50E{-1}$	$3.51E{-1}$	$3.51E{-1}$	$3.51E{-1}$	$3.51E{-1}$
$\Delta t/8$	$1.43E{-1}$	$1.73E{-1}$	$1.93E{-1}$	$1.97E{-1}$	$1.98E{-1}$	$1.99E{-1}$	$1.99E{-1}$	$1.99E{-1}$
$\Delta t/16$	$9.40E{-2}$	$8.63E{-2}$	$1.01E{-1}$	$1.05E{-1}$	$1.06E{-1}$	$1.06E{-1}$	$1.06E{-1}$	$1.06E{-1}$
$\Delta t/32$	$9.74E{-2}$	$4.97E{-2}$	$5.26E{-2}$	$5.40E{-2}$	$5.45E{-2}$	$5.47E{-2}$	$5.47E{-2}$	$5.47E{-2}$
$\Delta t/64$	$1.09E{-1}$	$4.42E{-2}$	$3.01E{-2}$	$2.81E{-2}$	$2.79E{-2}$	$2.78E{-2}$	$2.78E{-2}$	$2.78E{-2}$
$\Delta t/128$	$1.16E{-1}$	$4.73E{-2}$	$2.26E{-2}$	$1.63E{-2}$	$1.46E{-2}$	$1.42E{-2}$	$1.40E{-2}$	$1.40E{-2}$

see the optimal convergence rates as the mesh size is refined, given a constant Δt. For instance, in Table 4.2, considering the row $\Delta t/128$ corresponding to $e^{\Delta t}_{h,L^2}(T_h)$ (top of the table), we observe that the error is reducing with rate $O(h^2)$, which is the expected rate for $P1$ finite elements in the $L^2(\omega^a)$ norm. The behaviour continues up until reaching Mesh 3, where the convergence in space stagnates. This is also the case in the row at the bottom of the table, corresponding to the error approximating the radiosity. When the mesh is sufficiently fine, such as Mesh 4, successively considering refined step sizes yields an order one convergence rate of the $e^{\Delta t}_{h,L^2}(T_h)$ relative error.

Instead, if the ESDIRK 3/2a method is used to solve the manufactured solution test $(\mathcal{P}^a_{PR})$ with the same reference step size, the accuracy of the computed solution improves significantly. In Figure 4.13, the numerical approximation for the radiosity with this method is displayed, for the different mesh sizes and $\Delta t/128$. From Mesh 3 to Mesh 8, the approximation essentially overlaps the exact solution, in contrast with the results shown in Figure 4.12 for the implicit Euler scheme. In Table 4.3, the $e^{\Delta t}_{h,L^2}(T_h)$, $e^{\Delta t}_{h,H^1}(T_h)$ and $e^{\Delta t}_{h,L^2}(R_h)$ relative errors are shown. Specifically, considering $e^{\Delta t}_{h,L^2}(T_h)$ (top of the table), we observe that for the coarsest meshes, reducing the time step size yields no decrease of the error, as the space discretisation error dominates. On the other hand, for the finest meshes, a fast decay of the error is observed. Comparing the results in Table 4.2 with those in Table 4.3, we observe that the RK scheme yields a significant error reduction on the temperature approximation, which reaches up to three orders of magnitude for the $\Delta t/128$ step size and Mesh 8, in the $e^{\Delta t}_{h,L^2}(T_h)$ norm. Concerning the relative error $e^{\Delta t}_{h,H^1}(T_h)$, as evidenced by the results shown in the middle of Table 4.3, the space discretisation error dominates in all the considered cases. For Mesh 3 and the coarser meshes, reducing the time step produces no effect at all.

In Figure 4.14a, a log-log scale plot of the $e^{\Delta t}_{h,L^2}(T_h)$ relative error considering Mesh 8 is shown. In the case of using the implicit Euler scheme, the expected theoretical rate $O(\Delta t)$ is clearly observed

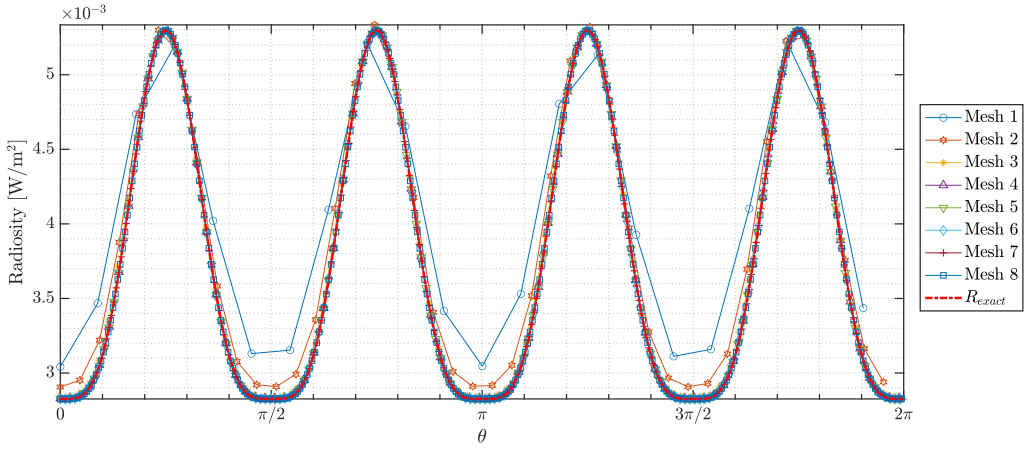
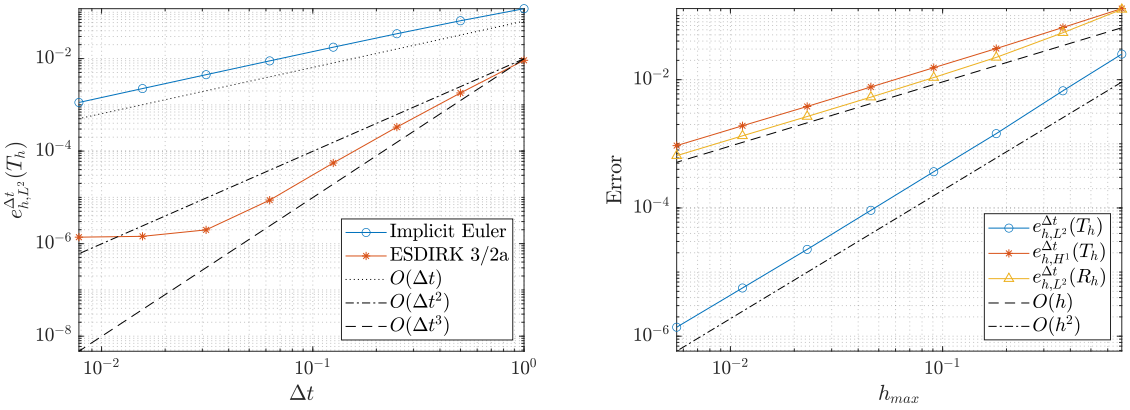


Figure 4.13: Approximated radiosity with ESDIRK 3/2a and different meshes at $t = 5$ s, $\Delta t/128$.

Table 4.3: ESDIRK 3/2a: $e^{\Delta t}_{h,L^2}(T_h)$ (top), $e^{\Delta t}_{h,H^1}(T_h)$ (middle) and $e^{\Delta t}_{h,L^2}(R_h)$ (bottom) relative errors.

	Mesh 1	Mesh 2	Mesh 3	Mesh 4	Mesh 5	Mesh 6	Mesh 7	Mesh 8
Δt	2.32E−2	8.93E−3	8.75E−3	9.05E−3	9.15E−3	9.17E−3	9.18E−3	9.18E−3
$\Delta t/2$	2.47E−2	6.54E−3	2.07E−3	1.77E−3	1.79E−3	1.80E−3	1.80E−3	1.80E−3
$\Delta t/4$	2.50E−2	6.66E−3	1.43E−3	4.57E−4	3.30E−4	3.28E−4	3.30E−4	3.30E−4
$\Delta t/8$	2.50E−2	6.70E−3	1.44E−3	3.65E−4	1.01E−4	5.74E−5	5.51E−5	5.53E−5
$\Delta t/16$	2.50E−2	6.71E−3	1.44E−3	3.66E−4	9.13E−5	2.33E−5	9.78E−6	8.55E−6
$\Delta t/32$	2.50E−2	6.71E−3	1.44E−3	3.67E−4	9.17E−5	2.25E−5	5.66E−6	1.76E−6
$\Delta t/64$	2.50E−2	6.71E−3	1.44E−3	3.67E−4	9.18E−5	2.26E−5	5.63E−6	1.36E−6
$\Delta t/128$	2.50E−2	6.71E−3	1.44E−3	3.67E−4	9.18E−5	2.26E−5	5.64E−6	1.36E−6
Δt	1.29E−1	6.64E−2	3.31E−2	2.00E−2	1.49E−2	1.33E−2	1.29E−2	1.28E−2
$\Delta t/2$	1.29E−1	6.52E−2	3.07E−2	1.56E−2	8.11E−3	4.61E−3	3.20E−3	2.74E−3
$\Delta t/4$	1.29E−1	6.51E−2	3.06E−2	1.54E−2	7.70E−3	3.85E−3	1.97E−3	1.06E−3
$\Delta t/8$	1.29E−1	6.51E−2	3.06E−2	1.54E−2	7.69E−3	3.82E−3	1.91E−3	9.41E−4
$\Delta t/16$	1.29E−1	6.51E−2	3.06E−2	1.54E−2	7.69E−3	3.82E−3	1.91E−3	9.37E−4
$\Delta t/32$	1.29E−1	6.51E−2	3.06E−2	1.54E−2	7.69E−3	3.82E−3	1.91E−3	9.37E−4
$\Delta t/64$	1.29E−1	6.51E−2	3.06E−2	1.54E−2	7.69E−3	3.82E−3	1.91E−3	9.37E−4
$\Delta t/128$	1.29E−1	6.51E−2	3.06E−2	1.54E−2	7.69E−3	3.82E−3	1.91E−3	9.37E−4
Δt	9.19E−2	7.82E−2	9.20E−2	9.50E−2	9.59E−2	9.61E−2	9.61E−2	9.62E−2
$\Delta t/2$	1.17E−1	4.82E−2	2.39E−2	1.79E−2	1.63E−2	1.59E−2	1.58E−2	1.58E−2
$\Delta t/4$	1.24E−1	5.29E−2	2.18E−2	1.08E−2	5.79E−3	3.67E−3	2.91E−3	2.68E−3
$\Delta t/8$	1.25E−1	5.38E−2	2.22E−2	1.08E−2	5.33E−3	2.68E−3	1.38E−3	7.60E−4
$\Delta t/16$	1.25E−1	5.40E−2	2.23E−2	1.08E−2	5.34E−3	2.66E−3	1.33E−3	6.56E−4
$\Delta t/32$	1.25E−1	5.40E−2	2.23E−2	1.08E−2	5.34E−3	2.67E−3	1.33E−3	6.54E−4
$\Delta t/64$	1.25E−1	5.40E−2	2.23E−2	1.08E−2	5.34E−3	2.67E−3	1.33E−3	6.54E−4
$\Delta t/128$	1.25E−1	5.40E−2	2.23E−2	1.08E−2	5.34E−3	2.67E−3	1.33E−3	6.54E−4

USC UNIVERSIDADE DE SANTIAGO DE COMPOSTELA



(a) $e^{\Delta t}_{h,L^2}(T_h)$ with various step sizes, using implicit Euler and ESDIRK 3/2a methods, Mesh 8

(b) $e^{\Delta t}_{h,L^2}(T_h)$, $e^{\Delta t}_{h,H^1}(T_h)$ and $e^{\Delta t}_{h,L^2}(R_h)$ for $\Delta t/32$ using ESDIRK 3/2a scheme for different mesh sizes.

Figure 4.14: Relative errors in log-log scale.

whereas the ESDIRK 3/2a results in a convergence rate between $O(\Delta t^3)$ and $O(\Delta t^2)$. Specifically, the estimated convergence rate using the RK scheme, computed by linear regression of the first 5 points, is 2.51. For the smallest step sizes, convergence rapidly deteriorates and stagnates around 10^{-6}. This behaviour owes to the space discretisation error becoming dominant, since the $O(h^2)$ rate in space does not allow it to fall below such value for the considered mesh sizes, as shown by the column corresponding to Mesh 6 in Table 4.3, or in Figure 4.14b, where the expected convergence rates in space are collected. Hence, the error can only be further reduced by considering a finer mesh.

4.6.2. Adaptive step size

As described in Subsection 4.4.3, when using the ESDIRK 3/2a scheme instead of considering a constant step size, the local error estimator provided by the method can be used to adapt the time step size. Hence, we choose a fixed tolerance value $tol = 2 \cdot 10^{-3}$ and consider $atol = rtol = tol$ as the parameters in the error norm (4.57). This tolerance value is successively reduced to solve Problem $(\mathcal{P}^a_{PR})$. In Figure 4.15, the computed step size values are displayed with respect to time for Mesh 8. The rejected steps are represented as squares. For all tolerance values, it is observed that the first step, supplied to the H211b controller as the reference value $\Delta t = 1$ s, is always rejected and adapted to a smaller step size.

In Table 4.4, the maximum step size, the number of accepted and rejected steps as well as the acceptance rate computed by the controller are displayed. The number of steps increases with decreasing tolerance. Conversely, the number of rejected steps does not show a clear increasing trend. Hence, the acceptance rate is approximately constant for the larger tolerance values and starts to increase from $tol/4$ onwards. In Table 4.5, the relative errors computed for the different tolerance values and meshes are shown. For the coarser meshes, the committed $e^{\Delta t}_{h,L^2}(T_h)$ error in the space discretisation dominates, and $O(h^2)$ order is observed as the mesh is refined for a constant tolerance, up until Mesh 5. The convergence rate is slightly below order 1 with respect to the tolerance, $O(tol)$, as evidenced in Figure 4.16, where the $e^{\Delta t}_{h,L^2}(T_h)$ relative error corresponding to Mesh 8 is plotted for all the tolerance values. The slope of the error is approximately equal to 0.93. As in the previous discussion when using the ESDIRK 3/2a scheme without adapting the step size, the space discretisation error is dominant in the $e^{\Delta t}_{h,H^1}(T_h)$ relative error, and the theoretical convergence rate is observed as the mesh is refined. Similar remarks apply to $e^{\Delta t}_{h,L^2}(R_h)$, for the different tolerance values.

The computed results for the proposed manufactured solution test show that the numerical algorithm performs within expectations. When the mesh size and the step size are both suitable, the

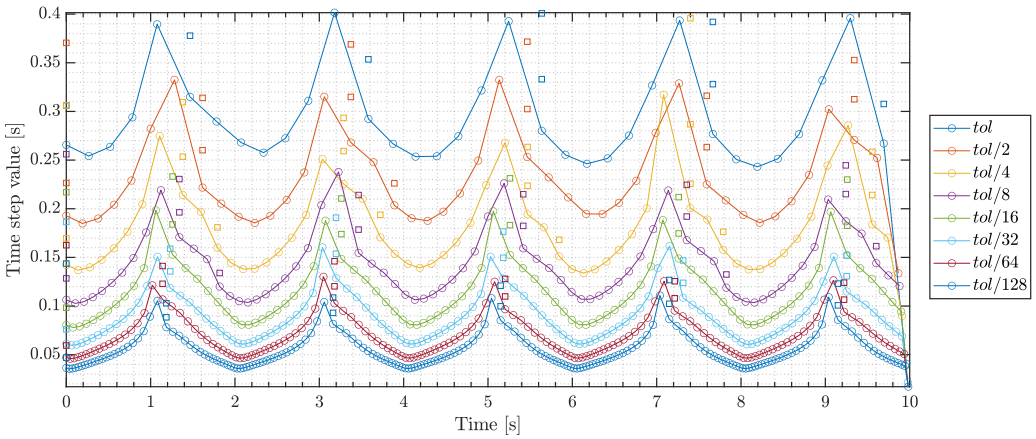


Figure 4.15: Computed step size values for the different tolerance values in Mesh 8. The coloured square symbols (□) represent the rejected steps for each tolerance.

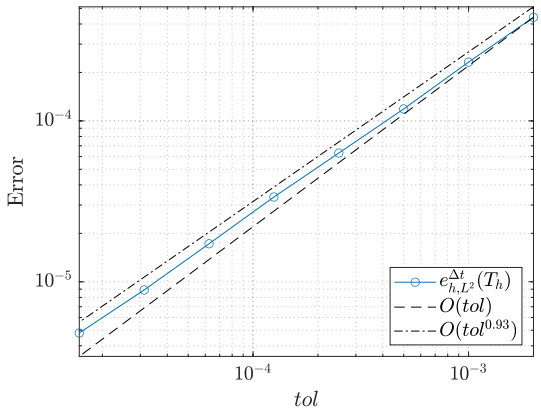


Figure 4.16: $e^{\Delta t}_{h,L^2}(T_h)$ with Mesh 8 for various tolerance values, using ESDIRK 3/2a with H211b controller.

Table 4.4: Maximum step size, number of accepted steps and rejected steps and acceptance rate using the H211b controller.

	Max. step size [s]	Accepted steps	Rejected steps	Acceptance rate
tol	$4.01{\cdot}10^{-1}$	35	12	$7.45{\cdot}10^{-1}$
$tol/2$	$3.32{\cdot}10^{-1}$	44	14	$7.59{\cdot}10^{-1}$
$tol/4$	$3.17{\cdot}10^{-1}$	57	18	$7.60{\cdot}10^{-1}$
$tol/8$	$2.38{\cdot}10^{-1}$	72	16	$8.18{\cdot}10^{-1}$
$tol/16$	$1.98{\cdot}10^{-1}$	91	13	$8.75{\cdot}10^{-1}$
$tol/32$	$1.62{\cdot}10^{-1}$	117	13	$9.00{\cdot}10^{-1}$
$tol/64$	$1.30{\cdot}10^{-1}$	150	13	$9.20{\cdot}10^{-1}$
$tol/128$	$1.11{\cdot}10^{-1}$	191	13	$9.36{\cdot}10^{-1}$

USC DE SANTIAGO DE COMPOSTELA

Table 4.5: ESDIRK 3/2a with H211b controller for adaptive step size.: $e^{\Delta t}_{h,L^2}(T_h)$ (top), $e^{\Delta t}_{h,H^1}(T_h)$ (middle) and $e^{\Delta t}_{h,L^2}(R_h)$ (bottom) relative errors.

	Mesh 1	Mesh 2	Mesh 3	Mesh 4	Mesh 5	Mesh 6	Mesh 7	Mesh 8
tol	$2.50E{-2}$	$6.70E{-3}$	$1.48E{-3}$	$5.56E{-4}$	$4.45E{-4}$	$4.40E{-4}$	$4.40E{-4}$	$4.40E{-4}$
$tol/2$	$2.51E{-2}$	$6.71E{-3}$	$1.46E{-3}$	$4.30E{-4}$	$2.50E{-4}$	$2.36E{-4}$	$2.36E{-4}$	$2.32E{-4}$
$tol/4$	$2.50E{-2}$	$6.70E{-3}$	$1.44E{-3}$	$3.80E{-4}$	$1.45E{-4}$	$1.18E{-4}$	$1.18E{-4}$	$1.19E{-4}$
$tol/8$	$2.50E{-2}$	$6.70E{-3}$	$1.44E{-3}$	$3.68E{-4}$	$1.07E{-4}$	$6.34E{-5}$	$6.05E{-5}$	$6.31E{-5}$
$tol/16$	$2.50E{-2}$	$6.69E{-3}$	$1.44E{-3}$	$3.66E{-4}$	$9.58E{-5}$	$3.94E{-5}$	$3.38E{-5}$	$3.36E{-5}$
$tol/32$	$2.50E{-2}$	$6.69E{-3}$	$1.44E{-3}$	$3.65E{-4}$	$9.18E{-5}$	$2.72E{-5}$	$1.79E{-5}$	$1.72E{-5}$
$tol/64$	$2.50E{-2}$	$6.69E{-3}$	$1.44E{-3}$	$3.65E{-4}$	$9.11E{-5}$	$2.34E{-5}$	$1.01E{-5}$	$8.89E{-6}$
$tol/128$	$2.50E{-2}$	$6.69E{-3}$	$1.44E{-3}$	$3.66E{-4}$	$9.12E{-5}$	$2.24E{-5}$	$6.91E{-6}$	$4.81E{-6}$
tol	$1.29E{-1}$	$6.52E{-2}$	$3.06E{-2}$	$1.54E{-2}$	$7.72E{-3}$	$3.88E{-3}$	$2.02E{-3}$	$1.15E{-3}$
$tol/2$	$1.29E{-1}$	$6.51E{-2}$	$3.06E{-2}$	$1.54E{-2}$	$7.70E{-3}$	$3.84E{-3}$	$1.95E{-3}$	$1.00E{-3}$
$tol/4$	$1.29E{-1}$	$6.51E{-2}$	$3.06E{-2}$	$1.54E{-2}$	$7.69E{-3}$	$3.83E{-3}$	$1.92E{-3}$	$9.56E{-4}$
$tol/8$	$1.29E{-1}$	$6.51E{-2}$	$3.06E{-2}$	$1.54E{-2}$	$7.69E{-3}$	$3.82E{-3}$	$1.91E{-3}$	$9.43E{-4}$
$tol/16$	$1.29E{-1}$	$6.51E{-2}$	$3.06E{-2}$	$1.54E{-2}$	$7.69E{-3}$	$3.82E{-3}$	$1.91E{-3}$	$9.39E{-4}$
$tol/32$	$1.29E{-1}$	$6.51E{-2}$	$3.06E{-2}$	$1.54E{-2}$	$7.69E{-3}$	$3.82E{-3}$	$1.91E{-3}$	$9.38E{-4}$
$tol/64$	$1.29E{-1}$	$6.51E{-2}$	$3.06E{-2}$	$1.54E{-2}$	$7.69E{-3}$	$3.82E{-3}$	$1.91E{-3}$	$9.37E{-4}$
$tol/128$	$1.29E{-1}$	$6.51E{-2}$	$3.06E{-2}$	$1.54E{-2}$	$7.69E{-3}$	$3.82E{-3}$	$1.91E{-3}$	$9.37E{-4}$
tol	$1.23E{-1}$	$5.26E{-2}$	$2.17E{-2}$	$1.08E{-2}$	$5.99E{-3}$	$4.03E{-3}$	$3.36E{-3}$	$3.17E{-3}$
$tol/2$	$1.24E{-1}$	$5.33E{-2}$	$2.19E{-2}$	$1.07E{-2}$	$5.47E{-3}$	$3.07E{-3}$	$2.08E{-3}$	$1.73E{-3}$
$tol/4$	$1.24E{-1}$	$5.36E{-2}$	$2.21E{-2}$	$1.07E{-2}$	$5.35E{-3}$	$2.77E{-3}$	$1.56E{-3}$	$1.06E{-3}$
$tol/8$	$1.24E{-1}$	$5.38E{-2}$	$2.22E{-2}$	$1.07E{-2}$	$5.33E{-3}$	$2.69E{-3}$	$1.40E{-3}$	$7.97E{-4}$
$tol/16$	$1.25E{-1}$	$5.39E{-2}$	$2.22E{-2}$	$1.08E{-2}$	$5.33E{-3}$	$2.67E{-3}$	$1.35E{-3}$	$6.99E{-4}$
$tol/32$	$1.25E{-1}$	$5.40E{-2}$	$2.22E{-2}$	$1.08E{-2}$	$5.33E{-3}$	$2.66E{-3}$	$1.34E{-3}$	$6.68E{-4}$
$tol/64$	$1.25E{-1}$	$5.39E{-2}$	$2.23E{-2}$	$1.08E{-2}$	$5.33E{-3}$	$2.66E{-3}$	$1.33E{-3}$	$6.58E{-4}$
$tol/128$	$1.25E{-1}$	$5.39E{-2}$	$2.23E{-2}$	$1.08E{-2}$	$5.34E{-3}$	$2.66E{-3}$	$1.33E{-3}$	$6.55E{-4}$

theoretical convergence rates are reached. Nonetheless, it is observed that for a smooth problem such as the presented one, with small radiative heat fluxes, the computed errors for the implicit Euler scheme are very large, even for the smallest step sizes. The ESDIRK 3/2a scheme enables to greatly reduce the time discretisation error. However, this comes at the cost of increasing the computational time by a factor of three approximately, as three stage solutions have to be computed at each time step. Since the method has an embedded computationally inexpensive error estimator, the step size may be readily adapted using an error controller. In such case, for the H211b controller, we obtain comparable errors if the same number of steps are used, meaning that no significant gain is achieved.

In particular, the time discretisation error is too large to observe an $O(h^2)$ rate as the mesh is refined and, for instance, the $e^{\Delta t}_{h,L^2}(T_h)$ relative error for Mesh 8 and $\Delta t/128$ is three orders of magnitude larger using the implicit Euler than the ESDIRK 3/2a. Nevertheless, for the problem in the main trough that is addressed in the subsequent chapter, the advantage of using an adaptive step size is much more clear, since for a fixed tolerance value, the difference between the minimum and maximum step sizes computed by the controller becomes substantially larger. In the proposed manufactured solution test, as the temperature variations are relatively smooth and periodic in time, the maximum step sizes computed by the H211b are at most twice the smallest step size for each tolerance value.

USC UNIVERSIDADE DE SANTIAGO DE COMPOSTELA

USC
UNIVERSIDADE
DE SANTIAGO
DE COMPOSTELA

Chapter 5

Transient 2D thermal model of the BF trough campaign cycle

The purpose of this chapter is to study the influence of the casting process stops on the temperature in the main trough. Usually, these stops are kept short. However, various factors can lead to longer stops occurring. In such case, the bulk of the solids may cool down significantly, resulting in large temperature oscillations and enhanced risk of spalling of the infiltrated refractory layers, as discussed in Section 1.4.2. Special attention is devoted to the evolution of the position of the temperature critical isotherms in the refractories.

The non-local radiation model and the numerical methodology presented in Chapter 4 are used to model the heating in a BF trough cross-section during its campaign cycle. Two different submodels are solved in sequence: one for those times when the BF is not being cast and a different one for times corresponding to BF tappings. Real BF operation data is used to determine the sequence of problems to be solved, comprising more than 300 BF tappings and the corresponding stops, which span for around two months of duration. The numerical results are compared with experimental measurements obtained with thermocouples embedded in the trough. Provided that there is a substantial degree of uncertainty regarding their placement, a minimisation problem is posed and solved to obtain a correction from their reported positions within feasible regions.

This chapter is structured as follows. In Section 5.1, we describe the mathematical model for the transient behaviour of the temperature in a 2D cross-section of the BF trough. Then, in Section 5.2, some details concerning the discretisation and numerical algorithm that is used to solve the problem are described. In Section 5.3, we present the computed numerical results, using data from two different BF trough campaign cycles. Lastly, in Section 5.4, a methodology to adjust the position of the thermocouples within their feasible regions is proposed.

5.1. Mathematical model

As it has been mentioned in the previous chapters, the BF tapping process is not fully continuous, as each cast lasts for about 90 minutes. At the end of each tapping, the taphole is plugged and is drilled again whenever the liquid level within the furnace is sufficiently high (see Section 1.2). Since the trough that we model corresponds to a BF with three tapholes, usually the tappings are done alternatively in two of them, while the third taphole or the corresponding runner system is being repaired. We define a *unit cycle* as a single cast and the subsequent stop. Recall that, due to severe degradation, the trough is relined after several unit cycles are completed to prevent damage on the safety and insulation linings. This set of cycles that the trough withstands before it is repaired is denoted as *campaign cycle*.

This chapter reproduces contents from the following articles:

- Barral, P., Pérez-Pérez L.J., & Quintela, P. (2022). *Numerical simulation of the transient heat transfer in a blast furnace main trough during its complete campaign cycle*. International Journal of Thermal Sciences. 173, 107349. doi:10.1016/j.ijthermalsci.2021.107349
- Barral, P., Pérez-Pérez, L.J., & Quintela, P. (2022). *Transient thermal response with nonlocal radiation of a blast furnace main trough*. Applied Mathematical Modelling. 105, 197 – 225. doi:10.1016/j.apm.2021.12.029

USC UNIVERSIDADE DE SANTIAGO DE COMPOSTELA

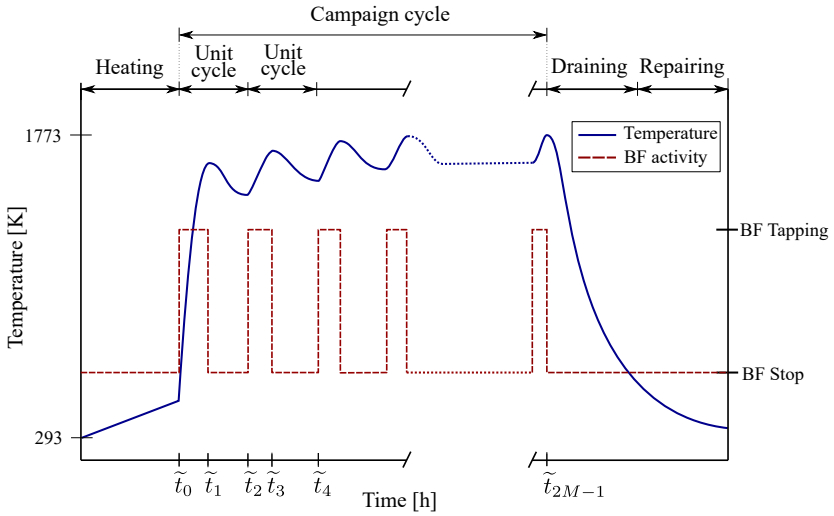


Figure 5.1: Temperature schematic at the contact area with fluids of the working lining during a campaign cycle.

Between campaign cycles, the fluids in the trough are drained and reparations are performed. Then, the refractory linings are heated, and a new campaign cycle begins. In Figure 5.1, a schematic of the temperature values on the working lining contact area with hot metal and slag is depicted during a campaign cycle. The time values $\widetilde{t}_c$, with $c = 0, \ldots, 2M-1$, indicate the times at which tappings are started and ended, M being the total number of tappings or unit cycles. Standard campaign cycles last up to 2 months.

In addition, we define as runner *lifetime cycle* the set of campaign cycles and the drains and repairs between them. When it ends, the main trough is completely rebuilt. Typically, runner lifetime cycles are much longer than campaign cycles and can reach several years of duration. In Figure 5.2, temperature measurements within the insulation lining are depicted during campaign cycles, comprising a complete runner lifetime cycle. If the unit cycle stops are kept short, experimental measurements show that the temperature in the bulk of the solids composing the runner reaches a quasi steady-state. However, in real unit cycles trough downtime may be far from such situation. This explains the large temperature swings that are observed for some campaigns. These larger oscillations correspond to longer stops that can last for up to several days.

To evaluate the outage-related cooling that occurs under real operating conditions and its influence on the refractory materials, we aim to obtain the temperature field corresponding to a full campaign cycle of a main trough. Therefore, a time interval of around two months of operation needs to be solved. Since it would be extremely difficult to solve a detailed 3D model including the fluid flow for such time scales, a number of simplifications are introduced. Hence, we consider only the 2D cross-section corresponding to the middle part of the main trough, situated before the slag runner at $x_3 = 8$ m, where the coordinate x_3 denotes the distance to the BF as in Chapters 2 and 3.

5.1.1. Tapping cycles

Let $\mathcal{T} = (t_0, t_{end}]$ denote the time interval during which we aim to study the evolution of the temperature in the BF trough. According to the above discussion, it corresponds to a complete campaign cycle. This period can be split in two subsets, $\mathcal{T}_{stop}$ and $\mathcal{T}_{cast}$, which are the time interval during which there is no fluid discharge from the BF hearth, and the total cast time interval, respectively. Consequently, we have that

$$\mathcal{T} = (t_0, t_{end}] = \mathcal{T}_{stop} \cup \mathcal{T}_{cast}.$$

The sets $\mathcal{T}_{cast}$ and $\mathcal{T}_{stop}$ may be subdivided in many smaller time subintervals, which correspond to the BF tappings (or casts) and stops during each unit cycle, respectively. For instance, if we consider

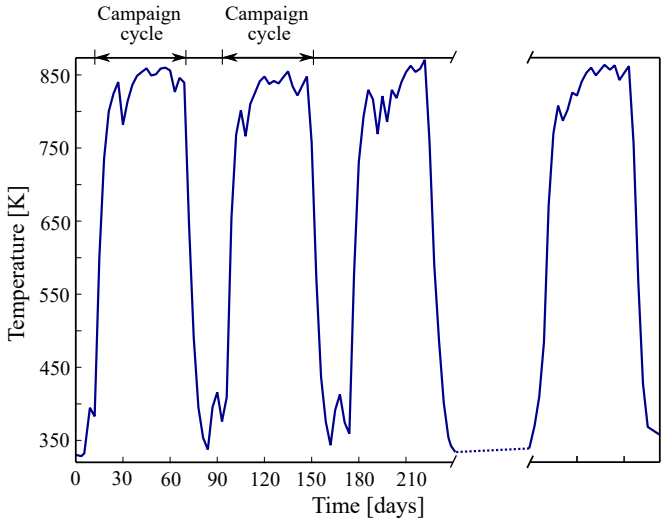


Figure 5.2: Temperature measurements in the insulation lining during a runner lifetime cycle.

a campaign cycle composed of M tappings, we find:

$$\mathcal{T}_{cast} = \bigcup_{m=0}^{M-1} (\tilde{t}_{2m}, \tilde{t}_{2m+1}] = \bigcup_{m=0}^{M-1} \mathcal{T}_{cast}^{m}, \tag{5.1}$$

$$\mathcal{T}_{stop} = \bigcup_{m=0}^{M-2} (\tilde{t}_{2m+1}, \tilde{t}_{2m+2}] = \bigcup_{m=0}^{M-2} \mathcal{T}_{stop}^{m}, \tag{5.2}$$

where we assume that $\tilde{t}_{2M-1} = t_{end}$.

At a given time $t \in \mathcal{T}$, we solve a different thermal model depending on whether the BF is stopped or tapping, i.e., if t belongs to $\mathcal{T}_{stop}^{m}$ or $\mathcal{T}_{cast}^{m}$ for some m. We denote the corresponding problems as $(\mathcal{P}_{stop})^m$ and $(\mathcal{P}_{cast})^m$, respectively. These problems are solved sequentially, meaning that Problem $(\mathcal{P}_{cast})^m$ has as initial condition the final temperature value computed in $(\mathcal{P}_{stop})^{m-1}$, for $m = 1, \dots M-1$. For $m = 0$, which corresponds to the first cast, an initial state for the temperature in the trough is supplied as initial condition. The specific procedure to obtain the initial temperature is discussed in Section 5.1.5. The same applies to $(\mathcal{P}_{stop})^m$, which uses as initial value the final temperature in $(\mathcal{P}_{cast})^m$, for $m = 0, 1, \dots, M-2$.

To generate the splitting among $\mathcal{T}_{cast}$ and $\mathcal{T}_{stop}$ following (5.1) and (5.2), the time values $\tilde{t}_c$ are required, with $c = 0, \dots, 2M-1$. To find them, real operation data of a BF is used, supplied by ArcelorMittal Spain. The data are composed of values ranging from 0 to 1, which are equal to the fraction of each hour that the BF was discharging material through the taphole. Assuming that there is only one cast start or stop during each hour, a function which is 1 for $t \in \mathcal{T}_{cast}$ and 0 if $t \in \mathcal{T}_{stop}$ is constructed, similar to the BF activity curve displayed in Figure 5.1. The function determines the values $\tilde{t}_c$. For instance, for the set of values gathered in Table 5.1, we reconstruct the function shown in Figure 5.3. In particular, for this simple example, we find that there are two casts. The first one starts and ends at $\tilde{t}_0 = 0$ h and $\tilde{t}_1 = 1.5$ h, respectively. The second cast starts at $\tilde{t}_2 = 3.9$ h and ends at $\tilde{t}_3 = 5.4$ h.

Table 5.1: Example of BF activity values.

Register index [h]	1	2	3	4	5	6	7
Value	1.0	0.5	0.0	0.1	1.0	0.4	0.0

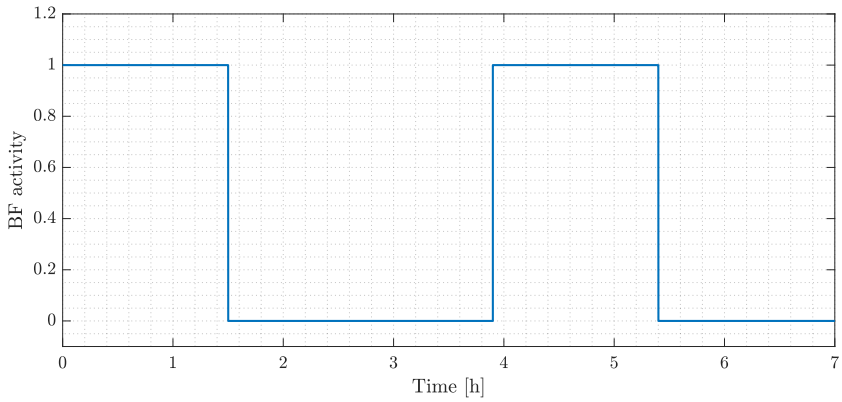
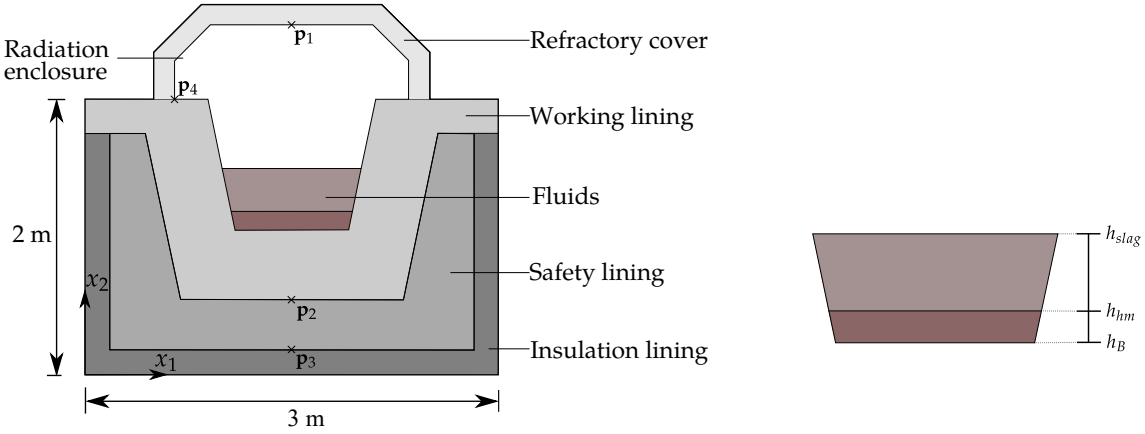


Figure 5.3: Signal indicating whether the BF is tapping or stopped.



(**a**) Complete computational domain.

(**b**) Detail of the fluid subdomain

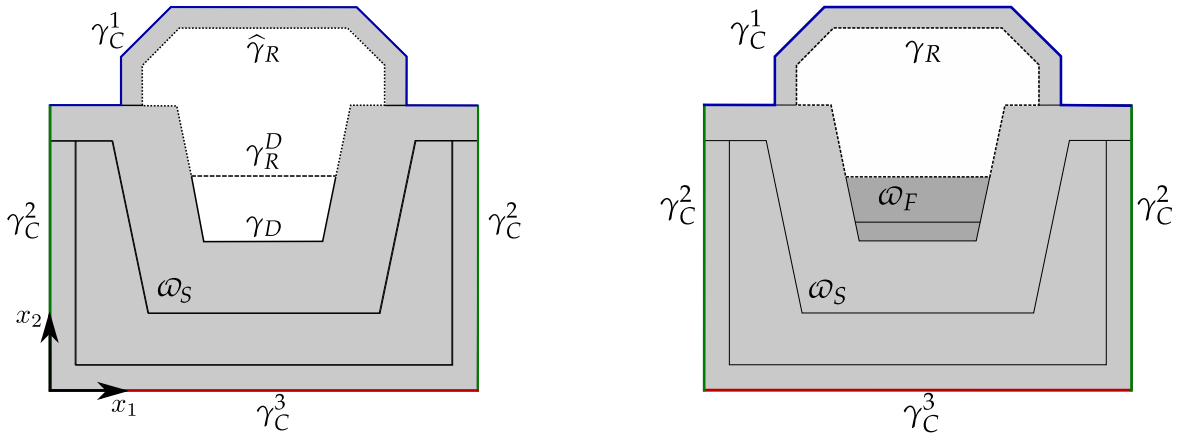
Figure 5.4: Cross-section of the main trough.

5.1.2. Computational domain

The computational domain is selected as the cross-section depicted in Figure 5.4. We consider a fluid subdomain, ω_F, which comprises the area occupied by the slag and hot metal pool, and a solid subdomain, ω_S, which corresponds to the solid refractory materials. As in Chapter 3, the steel casing is not included in the computational domain, as it incorporates several fins and ribs, which are not compatible with a 2D thermal model. Nevertheless, their effect is considered by appropriately enhancing the heat losses through the boundaries (see Section 3.1.5).

During each cast, the fluid region is excluded from the computational domain. Instead, the thermal behaviour of the fluids computed in Barral et al. (2019) is used to deduce a time-dependent Dirichlet temperature profile, under the assumption that the fluids quickly reach a temperature steady-state. The model addressed therein is similar to that described in Chapter 3. The profile also depends on the initial temperature, and is explained in detail in Section 5.1.4. Thus, the domain for the Problem $(\mathcal{P}_{cast})^m$ is reduced to the solid subdomain, i.e. $\omega_{cast} = \omega_S$ for all m, as depicted in Figure 5.5a.

Recall that during the unit cycle stops, the main trough holds the remaining liquids from preceding casts, which allows to preserve heat and help slag-hot metal slag separation in subsequent casts. The trough is drained only to perform emergency reparations or at the end of each campaign cycle. Thus, since in the problem corresponding to unit cycle stops, $(\mathcal{P}_{stop})^m$, the scope is to assess the cooling of the main trough, the complete cross-section is considered, including the fluids that are retained in the runner during the stops. Hence, for $0 \leq m \leq M-2$, the domain of Problem $(\mathcal{P}_{stop})^m$ is



(**a**) Domain ω_{cast}.

(**b**) Domain ω_{stop}.

Figure 5.5: Boundaries of the computational domain.

$\omega_{stop} = \omega_F \cup \omega_S \cup \mathring{\gamma}_D$, as displayed in Figure 5.5b. The boundary γ_D is defined as $\gamma_D = \overline{\omega}_F \cap \overline{\omega}_S$. For the sake of simplicity, we denote by $\omega(t)$ the computational domain at time $t \in \mathcal{T}$:

$$\omega(t) = \begin{cases} \omega_{stop}, & \text{if } t \in \mathcal{T}_{stop}, \\ \omega_{cast}, & \text{if } t \in \mathcal{T}_{cast}. \end{cases}$$

Also, we note that the numerical results shown in Chapter 2 indicate that the slag-air and hot metal-air interfaces are almost completely plane away from the jet impact point. However, they are not steady during the campaign cycle, as the slag level slightly increases during the tapping process as the amount of slag being drained from the BF increases. On the other hand, the height of the hot metal-slag interface rises swiftly at the beginning of the tapping from the initial equilibrium position, as only molten iron is being drained from the BF. Then, once slag is also tapped simultaneously, the hot metal height level decreases back to a position close to the initial one. In particular, the differences gathered in Table 2.4 were computed in the various considered conditions. The height increase of the slag-air interface is small in comparison to the dimensions of the trough cross-section, and thereby it is unlikely that it has a very significant influence in heat transfer. Nevertheless, it should be noted that the hot metal level oscillations are large, especially if the relative initial and final depth of the hot metal bath in the trough are analysed for Run A, resulting in an increase above 50%. Since the proposed model does not solve the fluids during the tappings, these liquid level variations are neglected to further simplify the model, provided that the aim of this chapter is to address the influence of the stops between consecutive casts in the heat transfer towards the solid refractory layers.

Hence, we assume that both the slag-air and hot metal-air interfaces remain at a constant height during the campaign cycle. The corresponding heights are calculated assuming that the fluids are at rest during the unit cycle stops, following the procedure detailed in Section 2.4.4. Using this approach, considering the coordinate axes and origin depicted in Figure 5.4a, we find that the slag upper surface is located at $x_2 = 1.5$ m and the hot metal surface is at $x_2 = 1.18$ m. Therefore, we set that $h_{hm} = 1.18$ m and $h_{slag} = 1.5$ m in Figure 5.4b, which shows how the fluid subdomain, ω_F, is divided in two regions, one occupied by slag and the other by hot metal. Moreover, we recall that the bottom of the fluid subdomain is denoted as h_B, which for the considered trough follows expression (2.32). At the corresponding distance from the BF for the selected cross-section, $x_3 = 8$ m, the height of the bottom is $h_B = 1.04$ m.

5.1.3. Model equations

To model the evolution of the temperature in the trough cross-section, both for the cast and stop problems, we use the transient heat equation:

$$\rho c_p \frac{\partial T}{\partial t} - \operatorname{div}(k(T)\operatorname{grad}(T)) = 0, \tag{5.3}$$

for $t \in \mathcal{T}$ and $\mathbf{x} \in \varpi(t)$, with $\mathbf{x} = (x_1, x_2)$. Recall that the thermal conductivity, the specific heat, and the density are denoted as k, c_p and ρ, respectively, and take the values gathered in Table 1.1a, depending on whether the specific point lies within each specific material.

On the boundary γ_R, which corresponds to the radiation cavity (see Figure 5.4a), the non-local radiation model described in Chapter 4 is used to model the radiation heat exchange. Under the assumption that the radiation cavity constitutes an opaque, diffuse and grey surface, whereas the air within is a transparent medium to radiation, the radiosity on γ_R, R, satisfies for $t \in \mathcal{T}$ that

$$(\mathcal{I} - (1 - \varepsilon_R(\mathbf{x}))\mathcal{K})(R(t))(\mathbf{x}) = \varepsilon_R(\mathbf{x})\sigma T^4(\mathbf{x}, t), \tag{5.4}$$

where $\mathcal{I}$ is the identity operator and ε_R is the emissivity, considered constant with value $\varepsilon_R = 0.7$. Moreover, σ is the Stefan-Boltzmann constant and $\mathcal{K}$ denotes the integral operator defined in (4.43). The coupling between the radiosity and the heat equation is done through the radiative heat flux, q_{rad}, which appears as a term in the boundary condition on γ_R for the temperature. It is calculated using the integral operator $\mathcal{Q}$, introduced in (4.44):

$$q_{rad}(\mathbf{x}, t) = \mathcal{Q}(R(t))(\mathbf{x}) := (\mathcal{I} - \mathcal{K})(R(t))(\mathbf{x}).$$

In general applications, the hypotheses that are assumed to describe thermal radiation using (5.4) are far from realistic, as discussed in Chapter 4. The non-local radiation model is derived from the RTE assuming that a number of rather idealistic conditions hold, which include that the medium within the radiation cavity is totally transparent to radiation, while the solid refractories, slag and hot metal are opaque to radiation. It should be noted that some fumes produced during the BF tapping process are not completely transparent to radiation. However, since the air suction is performed next to the taphole, the forced air circulation below the cover flows countercurrent to slag and hot metal, with air being suctioned mainly from the opposite side of the refractory cover. Thus, the air composition in the computational domain can be expected to be similar to that of the casthouse environment air.

5.1.4. Boundary conditions

The boundaries of the domains are decomposed as displayed in Figure 5.5 for ϖ_{cast} and ϖ_{stop}. We start by describing the boundary conditions used for the cast problems in detail. Subsequently, the modifications introduced for the stop problems are briefly summarised.

Cast problems

In the following discussion, we detail the boundary conditions considered for each $(\mathcal{P}_{cast})^m$. The boundary of its domain is independent of m and is given by

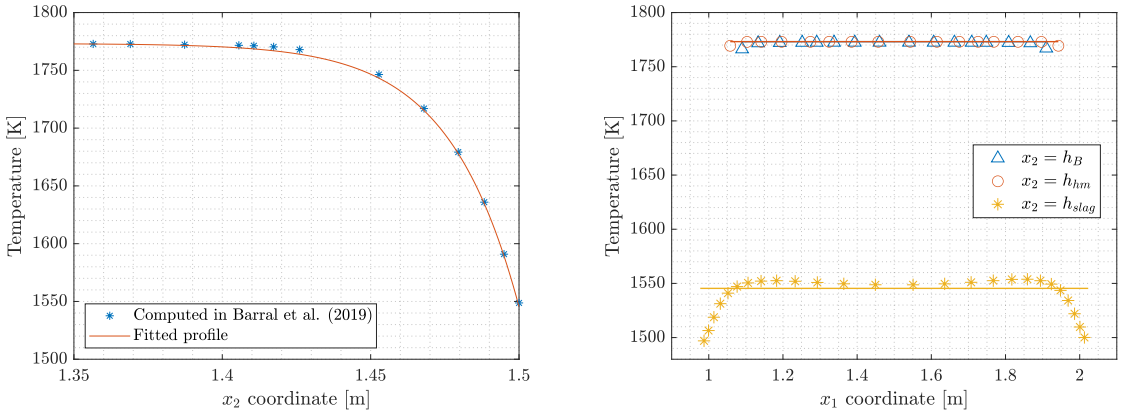
$$\gamma_{cast} = \bigcup_{n_c=1}^{3} \gamma_C^{n_c} \cup \gamma_D \cup \widehat{\gamma}_R,$$

as depicted in Figure 5.5a.

The boundary γ_D corresponds to the interface between the solids and fluids. On it, a Dirichlet condition using a known temperature is set:

$$T(\mathbf{x}, t) = T^m_{D,cast}(\mathbf{x}, t), \tag{5.5}$$

USC UNIVERSIDADE DE SANTIAGO DE COMPOSTELA



(**a**) Along the vertical slag centreline.

(**b**) Along horizontal lines.

Figure 5.6: Computed temperatures in the fluids (from Barral et al., 2019) and proposed fitted temperature profile $T_{F,cast}$ (solid lines) at different locations.

for all $\mathbf{x} \in \gamma_D$ and $t \in \mathcal{T}_{cast}$. In (5.5), the temperature $T^m_{D,cast}$ is calculated as indicated below.

At the beginning of the tapping, the temperature in the fluids rises quickly due to the hot metal and slag coming from the BF hearth at a very high temperature. From the results in Chapter 2, the residence time of hot metal and slag can be estimated to be around 180 s and 400 s, respectively. Since each tapping lasts for approximately 90 minutes, the flow develops rapidly and the temperature can be expected to reach a quasi steady-state in the fluids. In Barral et al. (2019), the steady-state temperature of the main trough was computed using a 3D thermo-hydrodynamic model, using a similar methodology to that proposed in Chapter 3. At the vertical centreline crossing the fluids in the fluid subdomain ω_F (i.e. for $x_3 = 8$ m and $x_1 = 1.5$ m), the temperature depicted in Figure 5.6a was obtained. Recall that h_B, h_{hm} and h_{slag} denote the positions at which the bottom of the trough, as well as the hot metal-slag and slag-air interfaces are located, respectively. Only the closest part to the slag-air free surface is shown, as for lower heights the temperature is almost homogeneous. To approximate the computed temperatures in Barral et al. (2019), we propose the following fitting function, also displayed in Figure 5.6a:

$$T_{F,cast}(x_2) = -1.52e - 9x_2^{63.46} + 1773, \tag{5.6}$$

being $h_B \leq x_2 \leq h_{slag}$, where $h_B = 1.04$ m and $h_{slag} = 1.5$ m.

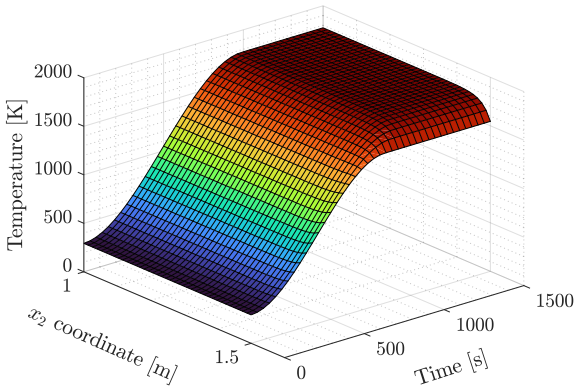
To model the temperature rise in the fluids during the tappings, we assume that the approximated steady profile $T_{F,cast}$ is reached swiftly. Moreover, we neglect any variations along the x_1 coordinate, which were found to be much smaller in magnitude when compared to variations in the x_2 coordinate, as depicted in Figure 5.6b, where the temperature along horizontal lines crossing the fluids at different height values are plotted. Specifically, we consider that the temperature in ω_F is such that

$$T^m_{D,cast}(\mathbf{x}, t) = \begin{cases} T^{m-1}_{stop}(\mathbf{x}, \tilde{t}_{2m}) - \dfrac{3\lambda^2_{steady}(t - \tilde{t}_{2m})^2}{\Delta T^m(\mathbf{x})} - \dfrac{2\lambda^3_{steady}(t - \tilde{t}_{2m})^3}{(\Delta T^m(\mathbf{x}))^2}, & \text{if } t \leq t^m_{steady}(\mathbf{x}), \\ T_{F,cast}(x_2), & \text{otherwise,} \end{cases} \tag{5.7}$$

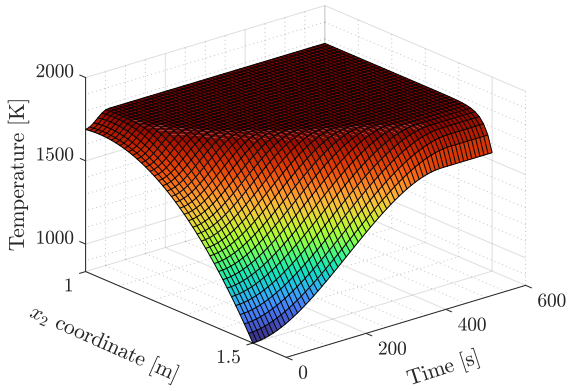
where $\tilde{t}_{2m}$ denotes the time value corresponding to the end of the preceding stop, and $T^{m-1}_{stop}(\mathbf{x}, \tilde{t}_{2m})$ is the computed temperature for $(\mathcal{P}_{stop})^{m-1}$ at its end time. Moreover, $\Delta T^m(\mathbf{x})$ denotes the difference among the steady temperature and the initial temperature at point $\mathbf{x}$, i.e.:

$$\Delta T^m(\mathbf{x}) = T^{m-1}_{stop}(\mathbf{x}, \tilde{t}_{2m}) - T_{F,cast}(x_2).$$

USC UNIVERSIDADE DE SANTIAGO DE COMPOSTELA



(**a**) $T_0 = 293$ K.



(**b**) For a typical initial temperature during the trough campaign cycle.

Figure 5.7: Temperature profile $T^m_{D,cast}$.

If $m = 0$, corresponding to the first unit cycle of the trough campaign, in (5.7) we consider $T^{m-1}_{stop} = T_0$, where T_0 is the initial temperature value, discussed in Section 5.1.5. Furthermore, the time needed to reach the stationary temperature is

$$t^m_{steady}(\mathbf{x}) = \tilde{t}_{2m} + \frac{T_{F,cast}(x_2) - T^{m-1}_{stop}(\mathbf{x}, \tilde{t}_{2m})}{\lambda_{steady}}. \tag{5.8}$$

The parameter λ_{steady} is assumed to take the value $\lambda_{steady} = 3/2$ K/s in (5.7) and (5.8). This choice guarantees that in the most extreme scenario ($T^{m-1}_{stop} \approx 293$ K), the stationary temperature is reached in approximately 15 minutes, as depicted in Figure 5.7a. For a regular casting regime, the stops are not long enough for the fluids to cool significantly, and the steady-state is reached much faster, as depicted in Figure 5.7b using a typical value for the initial temperature $T^{m-1}_{stop}(\mathbf{x}, \tilde{t}_{2m})$, extracted from the numerical results discussed in Section 5.3.

The profile is constructed such that it is continuous in $\mathcal{T}^m_{cast}$ and strictly increasing in $(\widetilde{t}_{2m}, t^m_{steady})$, with zero time derivative at the endpoints of the latter interval. Note that the temperature profile (5.7) implicitly assumes that slag is completely molten. Nevertheless, the temperature findings in Barral et al. (2019) and also on Chapter 3 suggest that partial solidification of slag near the free surface with air could occur, which would likely result in a higher temperature gradient than that shown in Figure 5.7.

Subsequently, we summarise the boundary conditions that are applied for the cast problems:

- On the external boundaries $\gamma^{n_c}_C$, $1 \leq n_c \leq 3$, mixed convection-radiation boundary conditions are considered:
$$-k(T)\frac{\partial T}{\partial \mathbf{n}} = h_{n_c}(T - T_{ext,c,n_c}) + \sigma\varepsilon_{n_c}(T^4 - T^4_{ext,r,n_c}), \tag{5.9}$$
for all $t \in \mathcal{T}_{cast}$. The values for the heat transfer coefficients, h_{n_c}, are displayed in Table 5.2. They are obtained through the procedure described in Section 3.1.5, whereas h_R was selected based on computational estimations similar to those conducted in 3.3.3, assessing the influence of the forced air flow below the refractory cover. The convection and radiation ambient temperatures as well as the emissivity are considered equal on the three boundaries ($T_{ext,r,n_c} = T_{ext,c,n_c} = 293$ K and $\varepsilon_{n_c} = 0.7$).
- On $\gamma_D = \overline{\omega}_F \cap \overline{\omega}_S$, which is the interface between the fluids and solids, we set the previously discussed Dirichlet condition, using expression (5.7):
$$T^m_{cast}(\mathbf{x}, t) = T^m_{D,cast}(\mathbf{x}, t),$$

USC UNIVERSIDADE DE SANTIAGO DE COMPOSTELA

for all $\mathbf{x} \in \gamma_D$ and $t \in \mathcal{T}^m_{cast}$.

- On $\widehat{\gamma}_R = \gamma_R \cap \overline{\omega}_S$, a convection contribution due to the forced air flow below the cover is added to the radiation heat flux q_{rad}, obtained by solving (5.4):

$$-k\frac{\partial T}{\partial \mathbf{n}} = h_R(T - T_{ext,c,R}) + q_{rad}, \tag{5.10}$$

for all $t \in \mathcal{T}_{cast}$ and where the temperature of the surroundings is $T_{ext,c,R} = 293$ K. The heat transfer coefficient, h_R, is equal to the value indicated in Table 5.2. Note that even though the radiation contribution is only applied on the part of the radiation cavity that belongs to the boundary of ω_{cast}, the integral equation (5.4) is solved on the complete cavity γ_R, as the radiosity on the slag upper surface, γ^D_R, is unknown even if the temperature satisfies (5.7). Therefore, for $(\mathcal{P}_{cast})^m$, (5.4) is solved for all $t \in \mathcal{T}^m_{cast}$ assuming that $T_{|\gamma^D_R} = T^m_{D,cast}$.

Stop problems

For $\mathcal{P}^m_{stop}$, their domain, ω_{stop}, and therefore their boundary, γ_{stop}, are also independent of m. In this case, it holds that

$$\gamma_{stop} = \bigcup_{n_c=1}^{3} \gamma_C^{n_c} \cup \gamma_R,$$

as displayed in Figure 5.5b.

On the external part of the trough, the boundary conditions are the same for the cast and the stop problems. Thus, for $(\mathcal{P}_{stop})^m$, on $\gamma_C^{n_c}$, with $1 \leq n_c \leq 3$, we set (5.9) for all $t \in \mathcal{T}_{stop}$. In this case, there is no Dirichlet condition on γ_D, as the fluids are included in the computational domain. However, note that the radiation cavity boundary is slightly different for the stop problems when compared to the cast problems, as depicted in Figure 5.5, where the boundary becomes γ_R instead of $\widehat{\gamma}_R$. Recall from above that during the stops the temperature on the fluids is not known and the heat equation is also solved in ω_F.

5.1.5. Initial condition

The reparations between campaign cycles last for around 20 days, as illustrated by Figure 5.2. During this period, the cover is removed, and the refractory layers cool down as reparations are performed. Also, after being rebuilt, the working lining is heated before the first BF tapping to prevent damage from the initial thermal shock. The temperature state after this process, which corresponds to the initial temperature at the start of a campaign cycle, is unknown. Nevertheless, an approximated temperature field must be supplied as initial condition at $t = \tilde{t}_0$ for the proposed model. As it is detailed in Section 5.4, the measurements obtained with three thermocouples located in the selected cross-section of the trough are available. They show that there is a significant amount of residual heat in the trough at the start of the campaign cycles, with the bottom being at a higher temperature than the laterals. To obtain the required initial condition, a possibility would be to consider an averaged homogeneous value using the three thermocouple measurements in the two campaign cycles for which we

Table 5.2: Heat transfer coefficients.

	h [W/(m^2·K)]
h_R	35
h_1	7
h_2	8
h_3	4

USC UNIVERSIDADE DE SANTIAGO DE COMPOSTELA

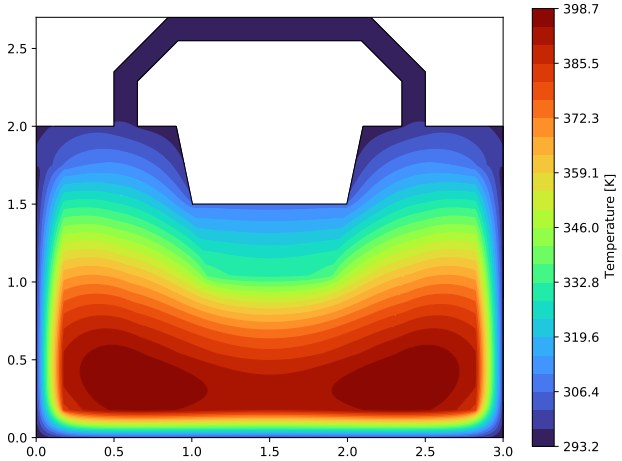


Figure 5.8: Temperature contours of the initial temperature T_0.

have data, equal to 322 K. However, given that the temperature in the safety lining could be substantially larger than in the insulation lining, where the thermocouples are placed, it is unlikely that this procedure yields an accurate guess of the initial temperature. Hence, to find a more realistic initial temperature we propose the following procedure:

(1) A steady-state problem corresponding to $(\mathcal{P}_{cast})^m$ is solved to obtain the steady-state temperature in the solids. This involves solving the heat equation (5.3) in ω_{cast}, assuming a steady-state as well as $T^m_{cast} = T_{F,cast}$ on γ_D, and satisfying boundary conditions (5.9) and (5.10).

(2) A Problem $(\mathcal{P}_{stop})^m$ using the steady-state temperature computed in the previous step as initial condition is solved, until reaching a time value $t = 20$ days.

Following these steps, we obtain the temperature field depicted in Figure 5.8. The temperature distribution in the cross-section shows that the residual heat is concentrated in the area close to the bottom of the trough, as predicted by the thermocouple measurements. However, it is observed that the temperatures within the safety lining are substantially higher than those in the insulation lining, where the thermocouples are located. The obtained temperature is denoted as T_0 and is used as initial condition for the first cast, i.e., Problem $\mathcal{P}^0_{cast}$. Moreover, since the rest of the problems in the sequence that are solved also require an initial condition, let us remember that, for this purpose, the final temperature calculated as solution to the previous problem in the sequence is set as the initial condition.

5.1.6. Strong formulation

A summary of the complete formulation of the two problems that are sequentially solved is provided below, including the heat equation, the radiation integral equation and the corresponding boundary conditions that were discussed previously:

Problem $(\mathcal{P}_{cast})^m$. Find $T^m_{cast}(\mathbf{x},t)$ and $R^m_{cast}(\mathbf{x},t)$ such that:

$$\rho c_p \frac{\partial T^m_{cast}}{\partial t} - \operatorname{div}\big(k(T^m_{cast})\operatorname{grad}(T^m_{cast})\big) = 0, \qquad \text{in } \varpi_{cast}\times\mathcal{T}^m_{cast}, \tag{5.11}$$

$$T^m_{cast}(\widetilde{t}_{2m}) = \begin{cases} T_0, & \text{if } m=0,\\ T^{m-1}_{stop}(\widetilde{t}_{2m}), & \text{if } m\geq 1,\end{cases} \qquad \text{in } \varpi_{cast}, \tag{5.12}$$

$$T^m_{cast} = T^m_{D,cast}, \qquad \text{on } \gamma_D\times\mathcal{T}^m_{cast}, \tag{5.13}$$

$$-k(T^m_{cast})\frac{\partial T^m_{cast}}{\partial \mathbf{n}} = h_{n_c}(T^m_{cast}-T_{ext,c,n_c}) + \sigma\varepsilon_{n_c}((T^m_{cast})^4 - T^4_{ext,r,n_c}), \qquad \text{on } \gamma_C^{n_c}\times\mathcal{T}^m_{cast},$$

$$-k\frac{\partial T^m_{cast}}{\partial \mathbf{n}} = h_R(T^m_{cast}-T_{ext,c,R}) + q_{rad}, \qquad \text{on } \widehat{\gamma}_R\times\mathcal{T}^m_{cast},$$

$$q_{rad} = \mathcal{Q}(R^m_{cast}), \qquad \text{on } \gamma_R\times\mathcal{T}^m_{cast},$$

$$(\mathcal{I}-(1-\varepsilon_R)\mathcal{K})(R^m_{cast}) = \varepsilon_R\sigma(T^m_{cast})^4, \qquad \text{on } \gamma_R\times\mathcal{T}^m_{cast},$$

where $1\leq n_c\leq 3$ and $0\leq m\leq M-1$.

In (5.12), at the first cast of the main trough campaign cycle, the initial condition, T_0, is that already described in Section 5.1.5. In (5.13), the temperature $T^m_{D,cast}$ is given by (5.7).

Problem $(\mathcal{P}_{stop})^m$. Find $T^m_{stop}(\mathbf{x},t)$ and $R^m_{stop}(\mathbf{x},t)$ such that:

$$\rho c_p \frac{\partial T^m_{stop}}{\partial t} - \operatorname{div}\big(k(T^m_{stop})\operatorname{grad}(T^m_{stop})\big) = 0, \qquad \text{in } \varpi_{stop}\times\mathcal{T}^m_{stop}, \tag{5.14}$$

$$T^m_{stop}(\widetilde{t}_{2m+1}) = T^{*,m}_{cast}(\widetilde{t}_{2m+1}), \qquad \text{in } \varpi_{stop},$$

$$-k(T^m_{stop})\frac{\partial T^m_{stop}}{\partial \mathbf{n}} = h_{n_c}(T^m_{stop}-T_{ext,c,n_c}) + \sigma\varepsilon_{n_c}((T^m_{cast})^4 - T^4_{ext,r,n_c}), \qquad \text{on } \gamma_C^{n_c}\times\mathcal{T}^m_{cast},$$

$$-k\frac{\partial T^m_{stop}}{\partial \mathbf{n}} = h_R(T^m_{stop}-T_{ext,c,R}) + q_{rad}, \qquad \text{on } \gamma_R\times\mathcal{T}^m_{stop},$$

$$q_{rad} = \mathcal{Q}(R^m_{stop}), \qquad \text{on } \gamma_R\times\mathcal{T}^m_{stop},$$

$$(\mathcal{I}-(1-\varepsilon_R)\mathcal{K})(R^m_{stop}) = \varepsilon_R\sigma(T^m_{stop})^4, \qquad \text{on } \gamma_R\times\mathcal{T}^m_{stop},$$

where $1\leq n_c\leq 3$ and $0\leq m\leq M-2$. Moreover, with $T^{*,m}_{cast}$, we denote an extension of the computed temperature for the cast problem using (5.7):

$$T^{*,m}_{cast}(\mathbf{x},\widetilde{t}_{2m+1}) = \begin{cases} T^m_{cast}(\mathbf{x},\widetilde{t}_{2m+1}), & \text{if } \mathbf{x}\in\varpi_{cast},\\ T^m_{D,cast}(\mathbf{x},\widetilde{t}_{2m+1}), & \text{otherwise.}\end{cases} \tag{5.15}$$

5.1.7. Variational formulation

To obtain a variational formulation of the previous problems, we multiply equations (5.11) and (5.14) for each $t\in\mathcal{T}^m_{cast}$ or $t\in\mathcal{T}^m_{stop}$, respectively, by a test function $v=v(\mathbf{x})$. Then, we integrate in the corresponding domains, apply a Green's formula, and use the boundary conditions considered for each problem. As result, we obtain the following variational formulations of both $(\mathcal{P}_{cast})^m$ and $(\mathcal{P}_{stop})^m$, respectively.

USC UNIVERSIDADE DE SANTIAGO DE COMPOSTELA

Problem $(\mathcal{VP}_{cast})^m$. For each $t \in \mathcal{T}^m_{cast}$, find $T^m_{cast}(t) \in H^1(\varpi_{cast})$ and $R^m_{cast}(t) \in L^2(\gamma_R)$, such that $\dfrac{\partial T^m_{cast}(t)}{\partial t} \in L^2(\varpi_{cast})$, $T^m_{cast}(t) = T^m_{D,cast}(t)$ on γ_D and

$$\begin{aligned}\int_{\varpi_{cast}} \rho c_p \frac{\partial T^m_{cast}(t)}{\partial t} v \, dA + \int_{\varpi_{cast}} k(T^m_{cast}(t))\mathrm{grad}(T^m_{cast}(t)) \cdot \mathrm{grad}(v) \, dA + \int_{\widehat{\gamma}_R} h_R T^m_{cast}(t) v \, ds \\ + \sum_{n_c=1}^{3} \int_{\gamma_C^{n_c}} \left(h_{n_c} T^m_{cast}(t) + \sigma \varepsilon_{n_c} (T^m_{cast}(t))^4 \right) v \, ds \\ = \sum_{n_c=1}^{3} \int_{\gamma_C^{n_c}} \left(h_{n_c} T_{ext,c,n_c} + \sigma \varepsilon_{n_c} T^4_{ext,r,n_c} \right) v \, ds + \int_{\widehat{\gamma}_R} (h_R T_{ext,R} - \mathcal{Q}(R^m_{cast}(t))) v \, ds,\end{aligned}$$

for all $v \in H^1_{0,\gamma_D}(\varpi_{cast})$, and satisfying:

$$(\mathcal{I} - (1-\varepsilon_R)\mathcal{K})(R^m_{cast}(t)) = \varepsilon_R \sigma (T^m_{cast}(t))^4, \qquad \text{on } \gamma_R,$$

for $t \in \mathcal{T}^m_{cast}$. Furthermore, $T^m_{cast}(\tilde{t}_{2m}) = T^{m-1}_{stop}(\tilde{t}_{2m})$ for $1 \le m \le M-1$. If $m = 0$, then $T^0_{cast}(0) = T_0$.

Problem $(\mathcal{VP}_{stop})^m$. For each $t \in \mathcal{T}^m_{stop}$, find $T^m_{stop}(t) \in H^1(\varpi_{stop})$ and $R^m_{stop}(t) \in L^2(\varpi_{stop})$, such that $\dfrac{\partial T^m_{stop}(t)}{\partial t} \in L^2(\varpi_{stop})$ and

$$\begin{aligned}\int_{\varpi_{stop}} \rho c_p \frac{\partial T^m_{stop}(t)}{\partial t} v \, dA + \int_{\varpi_{stop}} k(T^m_{stop}(t))\mathrm{grad}(T^m_{stop}(t)) \cdot \mathrm{grad}(v) \, dA + \int_{\gamma_R} h_R T^m_{stop}(t) v \, ds \\ + \sum_{n_c=1}^{3} \int_{\gamma_C^{n_c}} \left(h_{n_c} T^m_{stop}(t) + \sigma \varepsilon_{n_c} (T^m_{stop}(t))^4 \right) v \, ds \\ = \sum_{n_c=1}^{3} \int_{\gamma_C^{n_c}} \left(h_{n_c} T_{ext,c,n_c} + \sigma \varepsilon_{n_c} T^4_{ext,r,n_c} \right) v \, ds + \int_{\gamma_R} (h_R T_{ext,R} - \mathcal{Q}(R^m_{stop}(t))) v \, ds,\end{aligned} \tag{5.16}$$

for all $v \in H^1(\varpi_{stop})$, and satisfying:

$$(\mathcal{I} - (1-\varepsilon_R)\mathcal{K})(R^m_{stop}(t)) = \varepsilon_R \sigma (T^m_{stop}(t))^4, \qquad \text{on } \gamma_R,$$

for $t \in \mathcal{T}^m_{stop}$ and $0 \le m \le M-2$. In addition, $T^m_{stop}(\tilde{t}_{2m+1}) = T^{*,m}_{cast}(\tilde{t}_{2m+1})$ (see (5.15)).

5.2. Numerical solution

Let τ_h be a triangulation of the domain ϖ_{stop}, built such that $\overline{\varpi}_{stop} = \cup_{K \in \tau_h} K$, and conforming to the different materials in the BF main trough. The triangulation used for the domain ϖ_{cast} is a subset of τ_h. From the variational formulations detailed previously, we perform a similar discretisation to that described in Section 4.4 for the plane non-local radiation problem, i.e. a method of lines is used to obtain the spatial semi-discretisation, whereas the radiosity integral equation is discretised using a collocation method.

The time discretisation is completely analogous to that addressed in Section 4.4.2, thereby we skip giving any further details. Nonetheless, note that the aim is to solve a problem with very large time scales (in the order of months) with mostly gentle temperature changes, but also involving short periods of sharp temperature change in time, especially at the beginning of each cast. Therefore, the use of the adaptive time stepping technique described therein is essential to control the committed error while reducing the computational cost.

This section is structured as follows. In Section 5.2.1, the novelties in the spatial semi-discretisation with respect to that presented in Section 4.4.1 are briefly discussed. Then, in Section 5.2.2, a Newton method is proposed to deal with the non-linearities appearing in the thermal conductivity and

boundary conditions. Lastly, in Section 5.2.3, the complete algorithm that we use to solve the coupled problem is discussed. Throughout the discussion, we assume that the discretised radiosity, $R_h(t)$, is known. The particularities of this discretisation are also skipped, as we use the same collocation method as that described in Section 4.4.1.

5.2.1. Spatial discretisation

In virtue of the mesh of the domain ϖ_{cast} being a submesh of the domain ϖ_{stop}, we start by discussing the discretisation of the variational form of the heat equation appearing in Problem $(\mathcal{VP}_{stop})^m$. Afterwards, the changes that concern problem $(\mathcal{VP}_{cast})^m$ are briefly detailed.

Stop problem

Let $t \in \mathcal{T}_{stop}$ and V_h be the finite-dimension space of continuous functions whose restrictions to the triangles forming the triangulation τ_h are polynomials of degree 1, i.e.:

$$V_h = \{v_h \in C^0(\overline{\varpi}_{stop}) : v_h|_K \in \mathbb{P}_1(K),\ \forall K \in \tau_h\}.$$

We consider a Galerkin approximation and let $N_h = \dim V_h$. Then, the weak formulation (5.16) holds for any $v_h \in V_h$ since $V_h \subset H^1(\varpi_{stop})$. Therefore, for $t \in \mathcal{T}_{stop}$ we seek $T_h(t) \in V_h$ such that $\frac{\partial T_h(t)}{\partial t} \in L^2(\varpi_{stop})$ and satisfying:

$$\begin{aligned}
&\int_{\varpi_{stop}} \rho c_p \frac{\partial T_h(t)}{\partial t} v_h \, dA + \int_{\varpi_{stop}} k(T_h(t))\mathrm{grad}(T_h(t)) \cdot \mathrm{grad}(v_h) \, dA + \int_{\gamma_R} h_R T_h(t) v_h \, ds \\
&\qquad + \sum_{n_c=1}^{3} \int_{\gamma_C^{n_c}} \left(h_{n_c} T_h(t) + \sigma \varepsilon_{n_c} (T_h(t))^4 \right) v_h \, ds \qquad (5.17) \\
&\quad = \sum_{n_c=1}^{3} \int_{\gamma_C^{n_c}} \left(h_{n_c} T_{ext,c,n_c} + \sigma \varepsilon_{n_c} T_{ext,r,n_c}^4 \right) v_h \, ds + \int_{\gamma_R} (h_R T_{ext,R} - \mathcal{Q}(R_h)) v_h \, ds.
\end{aligned}$$

The discretised radiosity, R_h, is obtained by solving the coupled integral equation, as detailed in Section 4.4.1.

Let $\{w_j\}$ be a basis of V_h. Since $T_h(t) \in V_h$, we decompose it as in (4.48). Recall that the coefficients ξ_j denote the unknowns of the problem. Now, replacing (4.48) in (5.17) and taking into account that it is enough to consider as test functions the basis functions, w_i, it follows that

$$\begin{aligned}
&\sum_{j=1}^{N_h} \frac{d\xi_j(t)}{dt} \int_{\varpi_{stop}} \rho c_p w_j w_i \, dA + \sum_{j=1}^{N_h} \xi_j(t) \int_{\varpi_{stop}} k \left(\textstyle\sum_{d=1}^{N_h} \xi_d(t) w_d \right) \mathrm{grad}(w_j) \cdot \mathrm{grad}(w_i) \, dA \\
&\qquad + \sum_{j=1}^{N_h} \xi_j(t) \left[\int_{\gamma_R} h_R w_j w_i \, ds + \sum_{n_c=1}^{3} \int_{\gamma_C^{n_c}} h_{n_c} w_j w_i \, ds \right] \\
&\qquad + \sum_{n_c=1}^{3} \int_{\gamma_C^{n_c}} \sigma \varepsilon_{n_c} \left(\textstyle\sum_{d=1}^{N_h} \xi_d(t) w_d \right)^4 w_i \, ds \qquad (5.18) \\
&\quad = \sum_{n_c=1}^{3} \int_{\gamma_C^{n_c}} \left(h_{n_c} T_{ext,c,n_c} + \sigma \varepsilon_{n_c} T_{ext,r,n_c}^4 \right) w_i \, ds + \int_{\gamma_R} (h_R T_{ext,R} - \mathcal{Q}(R_h)) w_i \, ds,
\end{aligned}$$

for $i = 1, 2, \ldots, N_h$.

Set $\overline{\xi}(t) = (\xi_1(t), \xi_2(t), \ldots, \xi_{N_h}(t))^T$ as the vector of unknowns. Moreover, let $\overline{b} : \mathbb{R} \times \mathbb{R}^{N_h} \to \mathbb{R}^{N_h}$

and $\overline{M}$ be such that:

$$\begin{aligned} b_i(t,\overline{\xi}(t)) = &\sum_{n_c=1}^{3}\int_{\gamma_C^{n_c}}\left(h_{n_c}T_{ext,c,n_c}+\sigma\varepsilon_{n_c}T_{ext,r,n_c}^4\right)w_i\,ds+\int_{\gamma_R}(h_RT_{ext,R}-\mathcal{Q}(R_h))w_i\,ds\\ &-\sum_{j=1}^{N_h}\xi_j(t)\int_{\omega_{stop}}k\left(\textstyle\sum_{d=1}^{N_h}\xi_d(t)w_d\right)\mathrm{grad}(w_j)\cdot\mathrm{grad}(w_i)\,dA\\ &-\sum_{j=1}^{N_h}\xi_j(t)\left[\int_{\gamma_R}h_Rw_jw_i\,ds+\sum_{n_c=1}^{3}\int_{\gamma_C^{n_c}}h_{n_c}w_jw_i\,ds\right]\\ &-\sum_{n_c=1}^{3}\int_{\gamma_C^{n_c}}\sigma\varepsilon_{n_c}(\textstyle\sum_{d=1}^{N_h}\xi_d(t)w_d)^4w_i\,ds, \qquad 1\le i\le N_h, \end{aligned} \tag{5.19}$$

$$M_{ij}=\int_{\omega_{stop}}\rho c_pw_jw_i\,dA, \qquad 1\le i,j\le N_h.$$

Hence, (5.18) can be written as the following system of ODEs

$$\overline{M}\frac{d\overline{\xi}}{dt}(t)=\overline{b}(t,\overline{\xi}(t)), \tag{5.20}$$

where we remark that $\overline{b}$ is non-linear, as evidenced by (5.19).

Cast problem

An analogous system of ODEs to (5.20) can be obtained for Problem $(\mathcal{VP}_{cast})^m$ considering the computational domain ω_{cast} instead of ω_{stop} and the following subspace of V_h:

$$V_h^0=\{v_h\in V_h:\mathrm{supp}(v_h)\cap\omega_{cast}\neq\emptyset \text{ and } v_h|_{\gamma_D}=0\}.$$

Also, recall that the integrals on γ_R are considered on $\widehat{\gamma}_R$ instead, and N_h is replaced by $N_h^0=\dim V_h^0$.

In both cases, the nonlinear system of ODEs is discretised in time using the ESDIRK 3/2a RK method as discussed in Section 4.4.2. The step size is automatically adapted with the H211b controller described in Section 4.4.3.

5.2.2. Newton method

To obtain the solution at each time step t^{n+1}, we apply the Runge-Kutta (RK) method introduced in Section (4.4.2). Recall that the method has a first explicit stage with Butcher tableau (4.56). Hence, it holds that the first stage, $\overline{\mathcal{X}}_1^{n+1}$, is such that it coincides with the discretised temperature at the previous time step, i.e., $\overline{\mathcal{X}}_1^{n+1}=\overline{\xi}^n$. Thus, (4.54) needs to be solved for $l=2,\dots,s$. Since the function $\overline{b}$, defined in (5.19), is non-linear, a Newton method is used to obtain the internal stage values. With this purpose, we define the following function at stage l:

$$\overline{g}_l^n(\overline{y})=\overline{M}\overline{y}-\overline{M}\overline{\xi}^n-\Delta t^n\left(\sum_{p=1}^{l-1}a_{lp}\overline{b}(t_p^{n+1},\overline{\mathcal{X}}_p^{n+1})+a_{ll}\overline{b}(t_l^{n+1},\overline{y})\right),$$

where $\overline{y}\in\mathbb{R}^{N_h}$ and $l=2,\dots,s$. Finding a root of $\overline{g}_l^n$ is equivalent to finding the solution $\overline{\mathcal{X}}_l^{n+1}$ for the lth stage in (4.54) at time step $n+1$. Therefore, we propose the following Newton algorithm to find the root. Starting from a given initial iteration $\overline{y}^0$, and being $\overline{y}^{k^*}$ known for $k^*\ge 0$, we compute

$$J\overline{g}_l^n(\overline{y}^{k^*})\overline{y}^{k^*+1}=-\overline{g}_l^n(\overline{y}^{k^*})+J\overline{g}_l^n(\overline{y}^{k^*})\overline{y}^{k^*}, \qquad k^*=0,\dots,N_{newton}^{max},$$

USC UNIVERSIDADE DE SANTIAGO DE COMPOSTELA

where N_{newton}^{max} is the maximum number of iterations, and $J\overline{g}_l^n$ denotes the Jacobian matrix of $\overline{g}_l^n$, which has the following components (for the stop problems):

$$\begin{aligned}\frac{\partial g_{l,i}^n}{\partial y_j}(\overline{y}) = &\int_{\omega_{stop}} \rho c_p w_j w_i \, dA + \Delta t^n a_{ll}\Bigg[\int_{\omega_{stop}} k(\textstyle\sum_{d=1}^{N_h} y_d w_d)\mathrm{grad}(w_j)\cdot\mathrm{grad}(w_i)\, dA \\ &+ \int_{\omega_{stop}} y_j \left(k'(\textstyle\sum_{d=1}^{N_h} y_d w_d) w_j (w_j)\cdot\mathrm{grad}(w_i)\right) dA \\ &+ \int_{\gamma_R} h_R w_j w_i \, ds + \sum_{n_c=1}^{3}\int_{\gamma_C^{n_c}} h_{n_c} w_j w_i \, ds \\ &+ 4\sum_{n_c=1}^{3}\int_{\gamma_C^{n_c}} \sigma\varepsilon_{n_c}\left(\textstyle\sum_{d=1}^{N_h} y_d w_d\right)^3 w_j w_i \, ds\Bigg], \qquad 2\le l\le s, 1\le i,j\le N_h.\end{aligned} \tag{5.21}$$

In (5.21), k' is the derivative of the thermal conductivity. Since $a_{ll} = \widehat{\gamma}$, we note that the Jacobian matrix does not depend on the internal stage l, i.e., at the nth time step, (5.21) is identical for any l such that $2 \le l \le s$.

Note that the proposed algorithm is actually a pseudo-Newton algorithm, in the sense that we assume a known R_h at each Newton iteration (see (5.19)). As the radiosity depends on the temperature, the $\mathcal{Q}(R_h)$ term appearing in the functional $\overline{g}_l^n$ should also depend on the unknown $\overline{y}$.

5.2.3. Algorithm

To couple the radiosity integral equation with the heat equation, the segregated approach described in Section 4.4.4 is used, which involves a fixed point algorithm for each RK stage. It consists of three embedded loops; an inner one to compute the radiosity and temperature at a given stage and time step, another for the time stepping and an outer loop to advance throughout the sequence of cast and stop problems. It follows the flow chart depicted in Figure 5.9. Recall that the fixed point algorithm control is based on the relative incremental residual for both the temperature and radiosity, which must fall below a given threshold. In addition, the step size controller, introduced in Section 4.4.3, rejects and recomputes the current time step if the change ratio $\hat{c}^n$ is below a given value of 0.9. Also, if the end time of the corresponding problem is reached, then the step size is adjusted accordingly and, if that step is finally accepted, the algorithm advances to the subsequent cast or stop problem. The same parameters for the H211b step size controller to those reported in the previous chapter are considered. The only difference with the description provided in Section 4.4.3 is that a maximum step size $\Delta t = 300$ s is set during the cast problems to improve the stability of the algorithm.

5.3. Results

In this section, the obtained results after solving the previously described mathematical model are shown and discussed. The model is solved using the open-source finite element computing platform FEniCS. First, to ensure that the considered mesh of the computational domain is suitable, Section 5.3.1 is devoted to compare the obtained solution for different mesh sizes. In addition, the sensitivity of the solution with respect to the tolerance parameter selected in the H211b controller (4.58) to automatically adapt the time step size is analysed. Subsequently, in Section 5.3.2, the obtained results for the selected tolerance and mesh size are discussed, considering a single BF tapping, first of standard duration and afterwards assuming a 15-day long continuous cast. Finally, in Section 5.3.3, the simulation of two complete campaign cycles of the trough is addressed, solving a sequence of $(\mathcal{VP}_{cast})^m$ and $(\mathcal{VP}_{stop})^m$ problems, constructed using real BF operation data.

5.3.1. Sensitivity test

To address the dependency of the solution to Problem $(\mathcal{VP}_{cast})^m$ on the space discretisation parameter, h, we consider the meshes gathered in Table 5.3, where the total number of triangles in the mesh

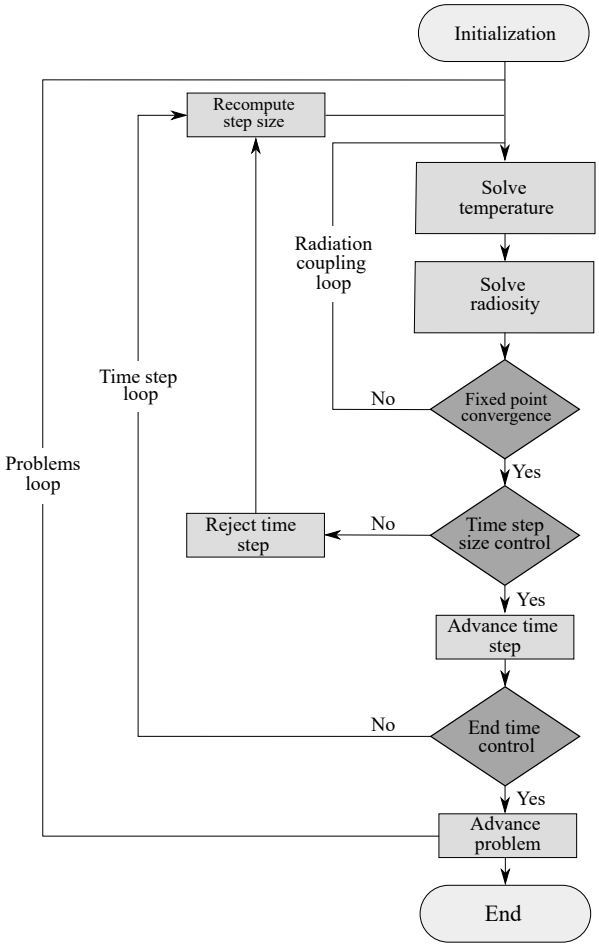


Figure 5.9: Flow diagram of the algorithm.

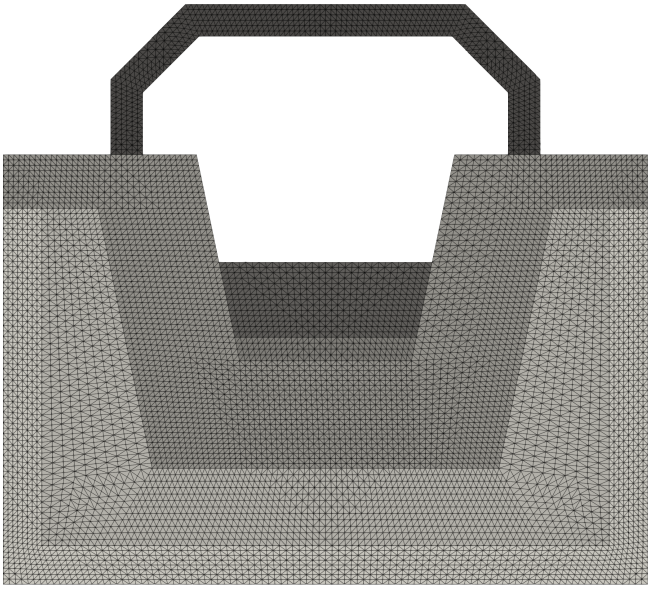
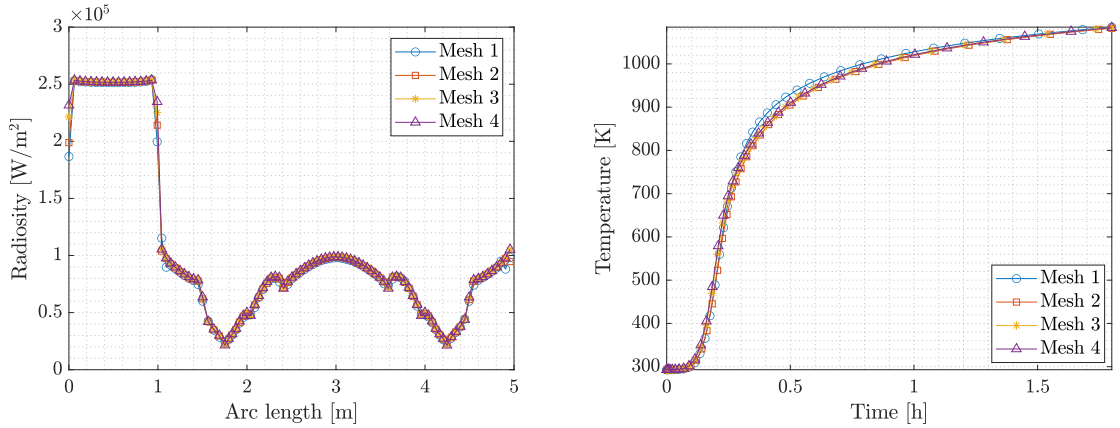


Figure 5.10: Triangulation of the domain ϖ_{stop}, Mesh 2.

Table 5.3: Meshes used for the mesh sensitivity test, maximum element size, minimum element size, number of triangle elements in the grid of the domain and number of edge elements on the non-local radiation boundary.

	h_{max}	h_{min}	$\#\tau_h$	$\#\tau_h^{\mathcal{G}}$
Mesh 1	$1.14{\cdot}10^{-1}$	$5.37{\cdot}10^{-2}$	3802	100
Mesh 2	$6.34{\cdot}10^{-2}$	$2.69{\cdot}10^{-2}$	15208	200
Mesh 3	$3.17{\cdot}10^{-2}$	$1.34{\cdot}10^{-2}$	60832	400
Mesh 4	$1.58{\cdot}10^{-2}$	$6.73{\cdot}10^{-3}$	243328	800



(**a**) Radiosity on γ_R at $t = t_{end}$.

(**b**) Temperature on $\mathbf{x} = (1.5, 2.5)$ m over time.

Figure 5.11: Computed numerical solution for the considered mesh sizes.

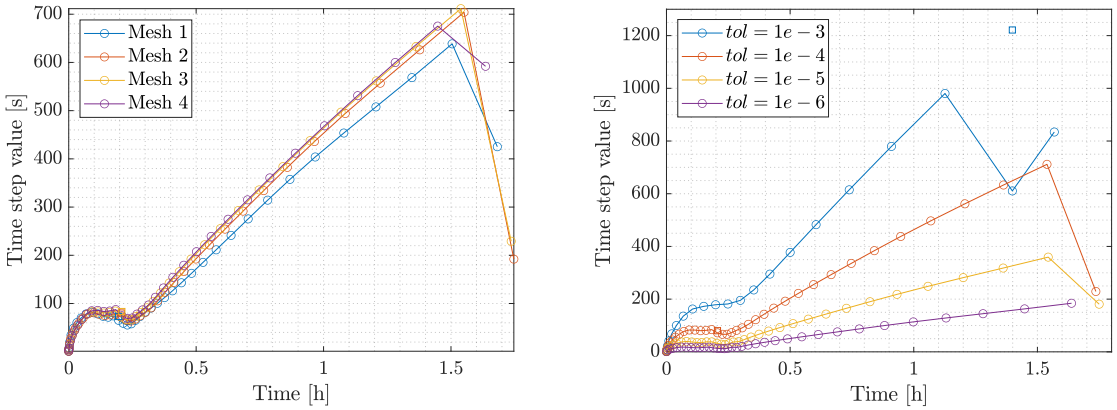
and the number of edge elements in the non-local radiation boundary γ_R mesh are presented, as well as the minimum element size h_{min} and the maximum element size h_{max}. The reported number of elements corresponds to the restriction of the triangulation, τ_h, to the subdomain ω_{cast}. In Figure 5.10, the triangulation corresponding to Mesh 2 is shown.

A single BF tapping is considered to address the mesh sensitivity. Consequently, Problem $(\mathcal{VP}_{cast})^m$ for $m = 0$ is solved. A fixed tolerance value for the step size controller $tol = atol = rtol = 10^{-4}$ is considered, with a starting step size $\Delta t = 1$ s. Moreover, in the remainder of this section, we set $v_{fp} = 0.8$ and $tol_{fp} = 10^{-4}$ in Algorithm 4.1. Also, instead of the initial condition described in Section 5.1.5, we simply consider $T_0 = 293$ K. In Figure 5.11a, the radiosity on γ_R is displayed as a function of arc length on the boundary at $t = t_{end} = 1.8$ h, for all mesh sizes. The starting point of the curve corresponds to the left corner of the slag surface ($\mathbf{x} = (1.041, 1.5)$ m) with γ_R parametrised anticlockwise. Meshes 2, 3 and 4 produce almost identical results, whereas the computed radiosity with Mesh 1 shows small differences in comparison with the remaining meshes. In Figure 5.11b, the computed temperature at point $\mathbf{x} = (1.5, 2.5)$ m, located in the inner part of the middle of the cover, is displayed over time. For Mesh 1, the computed temperature is above the remaining mesh sizes, whereas Mesh 2 is slightly below the results for Meshes 3 and 4.

In Figure 5.12a, the accepted step size values computed by the controller are plotted for the considered grids. The rejected steps are also shown, depicted as squares. For all mesh sizes, the same general trend is observed, as the step size rapidly grows until reaching around 100 s. At this point, the temperature on the slag surface, γ_R^D, has increased enough for the radiative heat fluxes to become relevant. Thus, the step size is adjusted accordingly by decreasing its size. Then, once the radiosity on the non-local radiation boundary stabilises, the step sizes swiftly rise back, increasing until reaching the end time t_{end}. Provided that the same tolerance value is selected for all meshes, the differences among the computed step sizes are small. In Table 5.4, the maximum step size, the number of ac-

Table 5.4: Maximum step size, number of accepted steps, number of rejected steps and acceptance rate using the H211b controller with $tol = 10^{-4}$ for the different mesh sizes, grid sensitivity test.

	Max. step size [s]	Accepted steps	Rejected steps	Acceptance rate
Mesh 1	$5.39{\cdot}10^{2}$	39	1	$9.75{\cdot}10^{-1}$
Mesh 2	$7.04{\cdot}10^{2}$	38	0	1.00
Mesh 3	$7.11{\cdot}10^{2}$	37	1	$9.74{\cdot}10^{-1}$
Mesh 4	$6.75{\cdot}10^{2}$	36	1	$9.73{\cdot}10^{-1}$



(**a**) For the different meshes, with $tol = 10^{-4}$.

(**b**) For the various tolerance values, Mesh 3.

Figure 5.12: Step size values.

cepted and rejected steps as well as the acceptance rate of steps are collected, showing similar results for the considered meshes.

In view of the presented results, Mesh 3 is considered fine enough to obtain an accurate approximation of the solution for the proposed problem. Hereinafter, in all the displayed results, Mesh 3 is used to solve the problem. For this mesh size, if different tolerance values for the controller are selected, a similar trend for the time step size values is observed, as displayed in Figure 5.12b. For tolerances $tol = 10^{-5}$ and $tol = 10^{-6}$, the parameter tol_{fp} in Algorithm 4.1 is adjusted so that the tolerance of the fixed point algorithm is as restrictive as that of the step size controller, i.e., $tol_{fp} = tol$. In Table 5.5, the maximum step size, the number of accepted and rejected steps as well as the acceptance rate computed by the controller are gathered for the selected tolerance values. The maximum step sizes are two orders of magnitude above the initial step size.

For the selected tolerance values, both the computed temperature and radiosity are very similar. However, the choice of the tolerance significantly affects the performance of the fixed point algorithm. To illustrate this dependence, in Figure 5.13, the number of iterations computed to solve the second RK stage at each step is represented. The trends are similar, showing that the lower the tolerance, the lower the number of iterations required to converge, as the computed time step sizes are smaller. Furthermore, as the time step size increases, convergence of the algorithm can be compromised, as evidenced by the reported iteration count for $tol = 10^{-3}$ towards the end time of the problem, which rises quickly and eventually shows an unconverged stage solution near $t = 1.4$ h, corresponding to the rejected step depicted in Figure 5.12b for that tolerance. This behaviour can also appear in the rest of the considered tolerances for larger values of the end time t_{end}, as the computed step sizes may also become too large for the fixed point algorithm to converge. In view of the presented results, $tol = 10^{-4}$ is considered enough to obtain a sufficiently accurate approximation of the solution to the proposed problem.

Table 5.5: Maximum step size, number of accepted steps, number of rejected steps and acceptance rate using the H211b controller for various tolerance values.

tol	Max. step size [s]	Accepted steps	Rejected steps	Acceptance rate
10^{-3}	$9.80{\cdot}10^{2}$	22	1	$9.56{\cdot}10^{-1}$
10^{-4}	$7.12{\cdot}10^{2}$	37	1	$9.74{\cdot}10^{-1}$
10^{-5}	$3.82{\cdot}10^{2}$	69	0	1.00
10^{-6}	$1.97{\cdot}10^{2}$	140	0	1.00

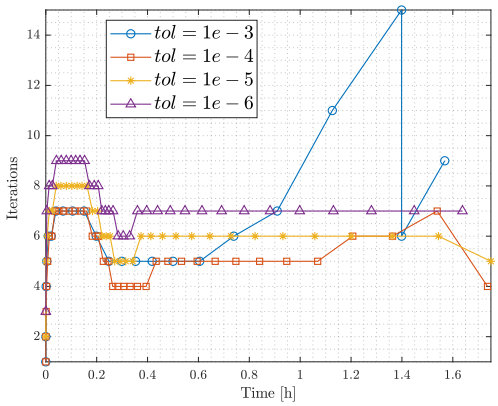


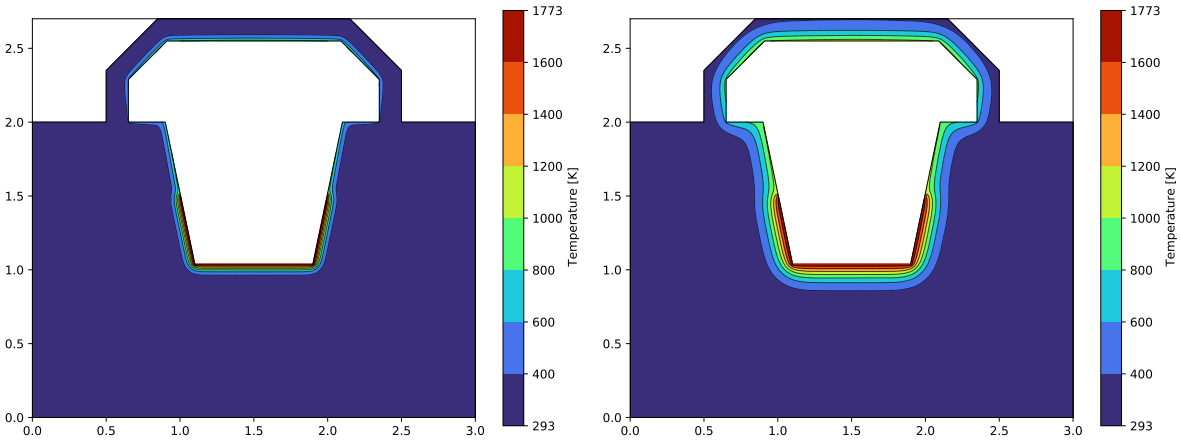
Figure 5.13: Number of computed fixed point algorithm iterations for the second RK stage at each time step, different tolerance values.

5.3.2. Single BF tapping

Using Mesh 3 and a tolerance parameter $tol = 10^{-4}$ such that $atol = rtol = tol$ in the norm of the local error estimator (4.57), Problem $(\mathcal{VP}_{cast})^m$ for $m = 0$ is solved, i.e., a single BF tapping is addressed. Again, the homogeneous initial condition $T_0 = 293$ K that was used in the previous section is set. First, we consider a time interval $\mathcal{T}^0_{cast} = (t_0, t_{end}] = (0, 1.8]$ h. For these values and a starting step size $\Delta t^0 = 1$ s, as it was shown in Table 5.4, only 37 time steps are required to solve the problem. However, as displayed in Figure 5.12a, at the start of the tapping, small steps are needed to maintain the error estimator below the specified bounds, evidencing the convenience of using an adaptive step size controller for this problem.

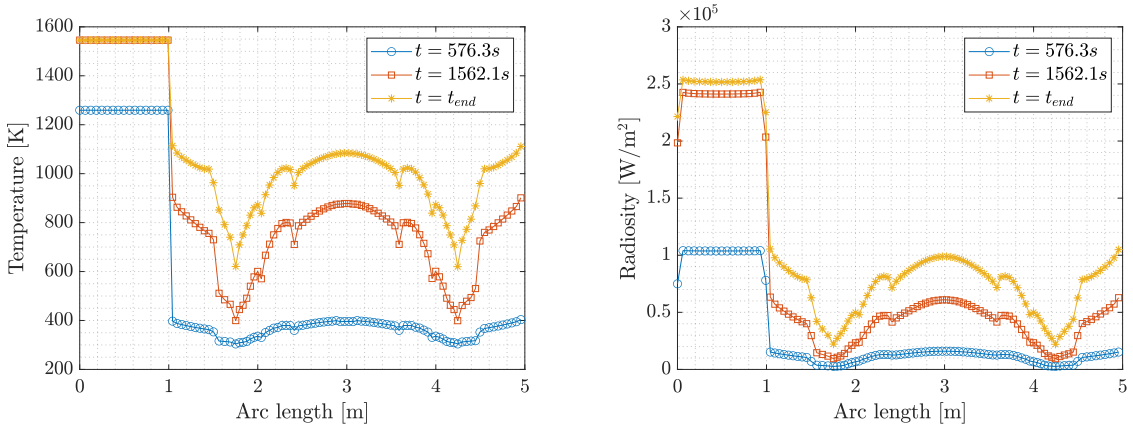
In Figures 5.14a and 5.14b the temperature contours at $t = 1562.1$ s and $t = t_{end}$ are depicted, respectively. High temperature values are observed only in the closest parts to the fluids, which heat rapidly following the profile determined by (5.7). Most of the trough is unaffected due to its large thermal inertia, still remaining at the initial temperature $T_0 = 293$ K. However, those parts of the working lining and the refractory cover that are exposed to radiation emission from the slag-air surface heat quickly. In particular, temperature reaches up to 1100 K in the middle of the cover. To better showcase the evolution of the temperature on the radiation enclosure, in Figure 5.15a, the temperature on γ_R is shown for different time values, as a function of arc length. The hottest part of the cavity corresponds to the slag surface, where the temperature rises swiftly. Therefore, radiosity increases, which leads to a quick temperature build-up in the remainder of γ_R. In Figure 5.15b, the radiosity on γ_R is displayed for the same time values. As in Figure 5.11a, the highest radiosity value is observed at the slag surface, which drives heat transfer towards the rest of the radiation cavity.

In addition, we solve $(\mathcal{VP}_{cast})^0$ considering a continuous cast lasting 15 days, i.e., $\mathcal{T}^0_{cast} = (0, 15]$ days. For this particular situation, a steady-state of the temperature in the cross-section of the trough is almost reached. In Figure 5.16a, the temperature contours in such situation are depicted. Figure 5.16b shows the critical isotherms (1423, 1473 K and 1523 K). Recall that these isotherms indicate the



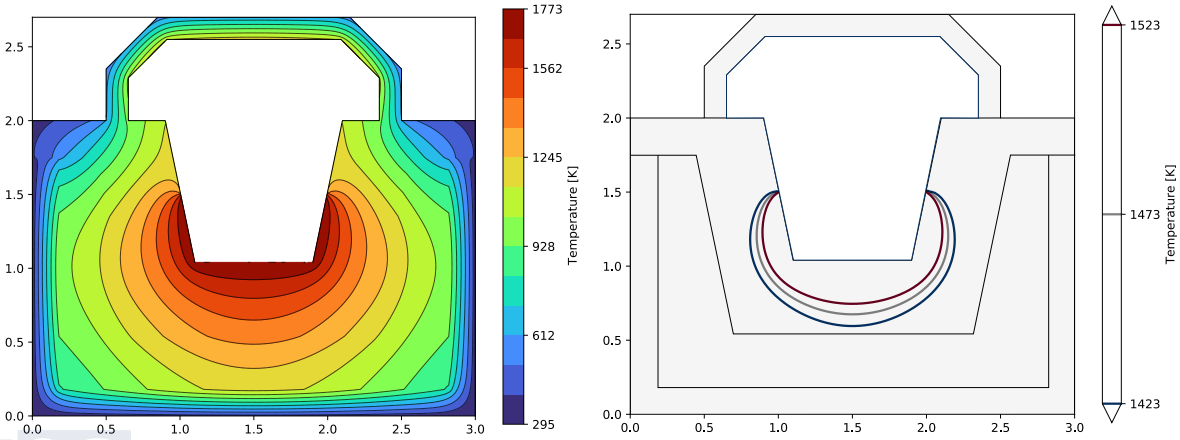
(**a**) $t = 1562.1$ s. (**b**) $t = t_{end} = 1.8$ h.

Figure 5.14: Temperature contours at various time values, single tapping.



(**a**) Temperature (**b**) Radiosity.

Figure 5.15: Temperature and radiosity on γ_R at various time values, single tapping.



(**a**) Temperature contours at $t = t_{end}$. (**b**) Temperature isotherms at $t = t_{end}$.

Figure 5.16: Continuous cast with $t_{end} = 15$ days.

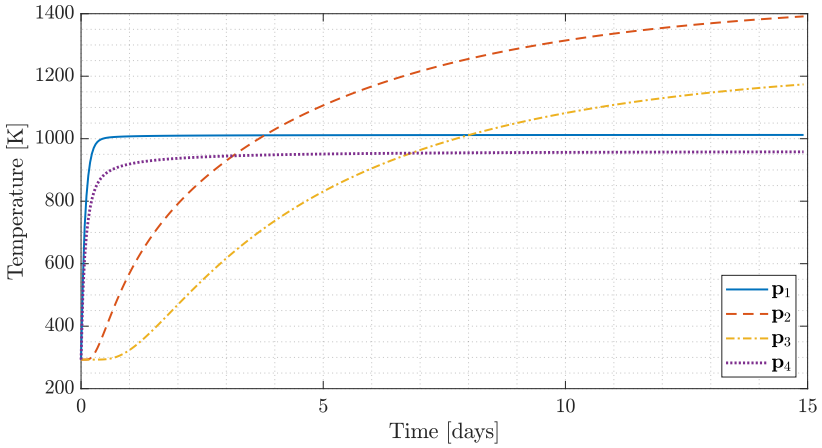


Figure 5.17: Computed temperature over time, at selected points in ϖ_{cast}, $t_{end} = 15$ days (Continuous cast).

onset of chemical composition changes in the refractories and are related to an increase in the degree of wear (see Section 1.4.2). For instance, the 1423 K isotherm corresponds to the solidus temperature of the eutectic mixture Fe-C, the main components of hot metal. Maintaining this isotherm within the working lining ensures that any infiltrated hot metal in the safety lining solidifies, forming a protective layer and reducing the possibility of a major trough breakage (Kumar et al., 2010).

The 1423 K isotherm lies close to the safety lining in the bottom of the trough after 15 days of continuous cast, indicating risk of hot metal infiltration within the safety lining. Also, as already was suggested by Figures 5.15a and 5.15b, the temperature and radiosity on γ_R stabilise much quicker than the temperature in the remaining of the trough. This is clearly shown in Figure 5.17, where the evolution in time of the temperature computed at several points in the domain is depicted. Specifically, the temperature at points $\mathbf{p}_1 = (1.5, 2.55)$, $\mathbf{p}_2 = (1.5, 0.54)$ and $\mathbf{p}_3 = (1.5, 0.18)$ m is shown. These points are located along the vertical symmetry line of the domain at the middle of the cover, the boundary among the working and safety linings, and the boundary between the safety and insulation linings, respectively (see Figure 5.4a). The temperature at point $\mathbf{p}_4 = (0.65, 2)$ m is also displayed, which has the particularity of not being directly exposed to incoming radiation from the slag surface. This results in a slower temperature increase when compared to the parts that are exposed, such as $\mathbf{p}_1$, where the temperature computed at $t = 1.8$ h was already very close to the steady-state temperature. However, at $t_{end} = 15$ days, the temperature on the insulation and safety linings is still not completely stable. In particular, a delay of almost a day for the temperature build-up to start is observed in the insulation lining, as evidenced by the depicted evolution of the temperature at $\mathbf{p}_3$.

We remark that the proposed setting with $t_{end} = 15$ days is far from realistic, since the BF draining process is not continuous. The effect of the process stops to control the liquid level in the BF hearth has a substantial impact in the temperature within the BF trough, as it is discussed in the subsequent section.

5.3.3. Simulation of two campaign cycles

The problem described in Section 5.1, composed of a sequence of cast and stop problems, is solved. This sequence is determined by data comprising two different campaign cycles to assess whether the BF is being cast, as described in Section 5.1.1. A summary of the main characteristics of the considered campaign cycles is displayed in Table 5.6. The two solved cycles are consecutive, with the trough downtime between them removed.

In Figure 5.18, the time step size computed by the adaptive controller is plotted against the time value for the two considered campaign cycles, from $t = 10$ days to $t = 20$ days. The step size rises quickly from the start size at each cast or stop problem, which is $\Delta t^0 = 1$ s. Often, this first step

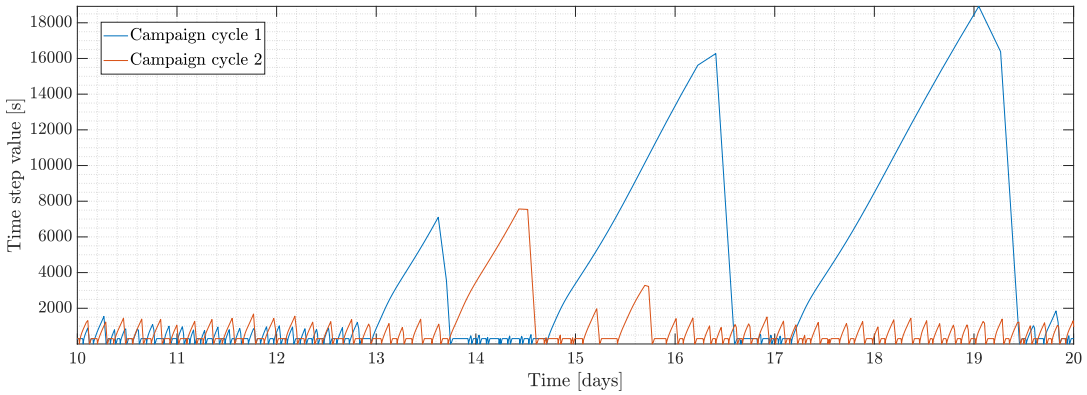


Figure 5.18: Time step values computed by the H211b controller during the two campaign cycles.

is rejected and recomputed with a smaller value. Furthermore, the presence of long stops during the campaign cycles is evident, as they allow for much larger step sizes without increasing the error beyond the selected tolerance value. In Table 5.7, the maximum step size, the number of accepted and rejected steps, and the acceptance rate are gathered for the two campaign cycles that are solved. The acceptance rate is above 0.98 in both cases, while the maximum step size in each campaign is determined by the length of the longest stop during the BF activity recorded during the campaign, which lasts for longer than two days, as shown in Figure 5.18.

In Figure 5.19a, the computed temperature field $T^0_{cast,h}$, solution to Problem $(\mathcal{VP}_{cast})^0$, after the first cast of the BF in Campaign cycle 1 is displayed, i.e. at time $\widetilde{t}_1$. Even though during each $(\mathcal{VP}_{cast})^m$ only the domain $\varpi_{cast} = \varpi_S$ is solved, the fluids are also included in the shown contour plots as their temperature is assumed to be known and equal to (5.7). High temperatures are observed only in the zone that is close to the liquids, as most of the solid is still unaffected, showing similar temperature values to those of the initial condition (see Figure 5.8). In contrast, the parts of the working lining that are affected by the radiation from the slag surface show significant heating, as well as the refractory cover, reaching temperatures around 1100 K.

To showcase the effect of the short stops in the runner activity, the temperature after the subsequent stop following the first tapping, $T^0_{stop,h}(\cdot, \widetilde{t}_2)$ is depicted in Figure 5.19b. Approximately half an hour has passed since the end of the preceding cast, and most of the cooling takes place in the fluids. On the other hand, the cover and the working lining still remain at a high temperature.

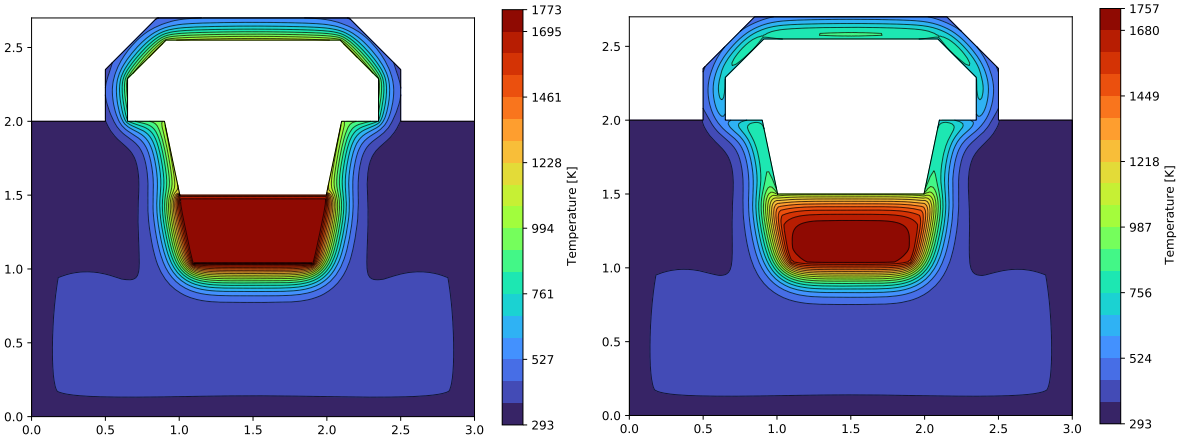
In Figure 5.19c, the temperature contours after approximately 10 days of casts and stops are shown. Specifically, the contours correspond to $T^{76}_{cast,h}(\cdot, \widetilde{t}_{153})$. The temperature field is substantially different to that displayed in Figures 5.19a and 5.19b, as the bulk of the solids displays a much higher temper-

Table 5.6: Start date, end date and total number of casts (M) for each solved campaign cycle.

	Start date	End date	Number of casts
Campaign cycle 1	28/05/2018	28/07/2018	347
Campaign cycle 2	21/08/2018	18/10/2018	325

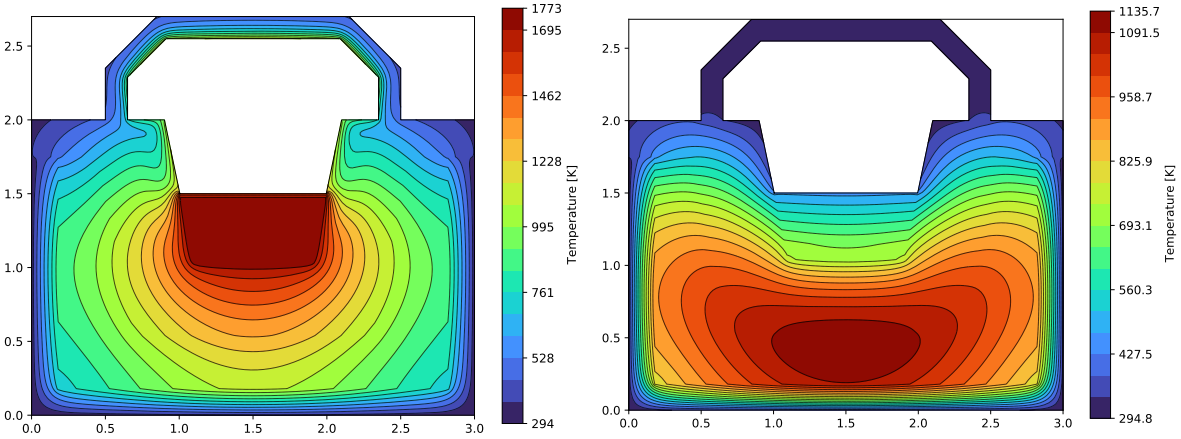
Table 5.7: Maximum step size, number of accepted steps, number of rejected steps and acceptance rate using the H211b controller for the considered campaign cycles.

	Max. step size [s]	Accepted steps	Rejected steps	Acceptance rate
Campaign 1	$1.89{\cdot}10^4$	21509	408	$9.81{\cdot}10^{-1}$
Campaign 2	$9.05{\cdot}10^3$	21171	411	$9.81{\cdot}10^{-1}$



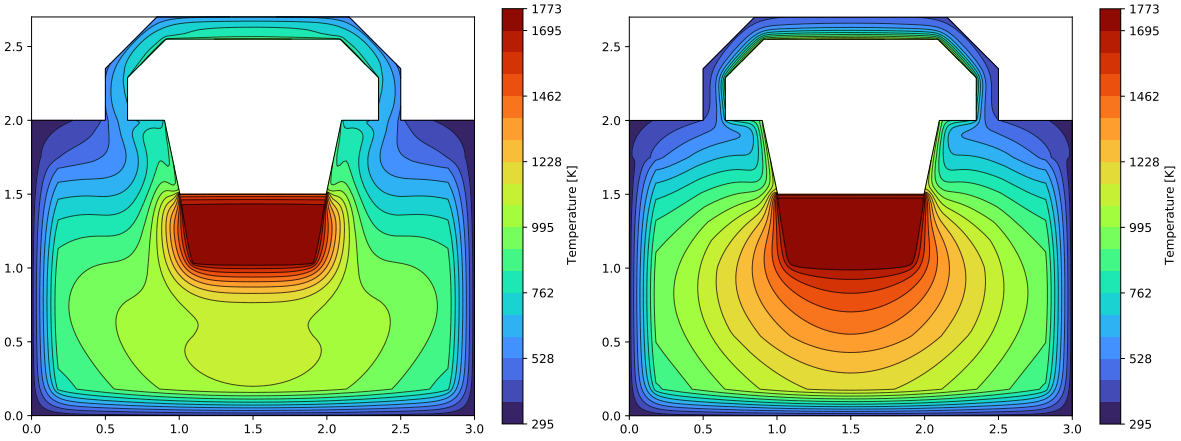
(a) $T^{0}_{cast,h}(\cdot, \widetilde{t}_1)$, $\widetilde{t}_1 = 0.16$ days.

(b) $T^{0}_{stop,h}(\cdot, \widetilde{t}_2)$, $\widetilde{t}_2 = 0.18$ days.



(c) $T^{76}_{cast,h}(\cdot, \widetilde{t}_{153})$, $\widetilde{t}_{153} = 10.33$ days.

(d) $T^{104}_{stop,h}(\cdot, \widetilde{t}_{209})$, $\widetilde{t}_{209} = 16.60$ days.

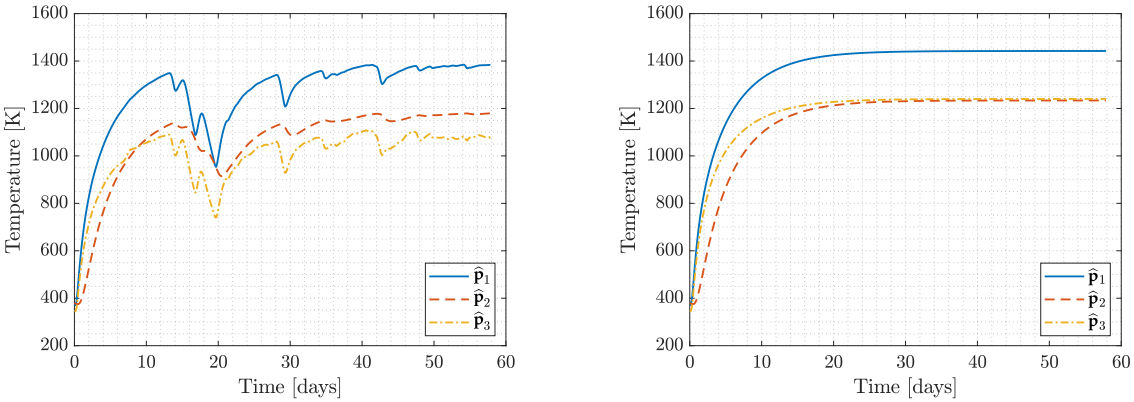


(e) $T^{106}_{cast,h}(\cdot, t)$, $t = 16.87$ days.

(f) $T^{323}_{cast,h}(\cdot, t_{end})$, $t_{end} = 57.84$ days.

Figure 5.19: Temperature contours at various time values during Campaign cycle 1.

USC UNIVERSIDADE DE SANTIAGO DE COMPOSTELA



(**a**) Campaign cycle 1.

(**b**) Continuous cast.

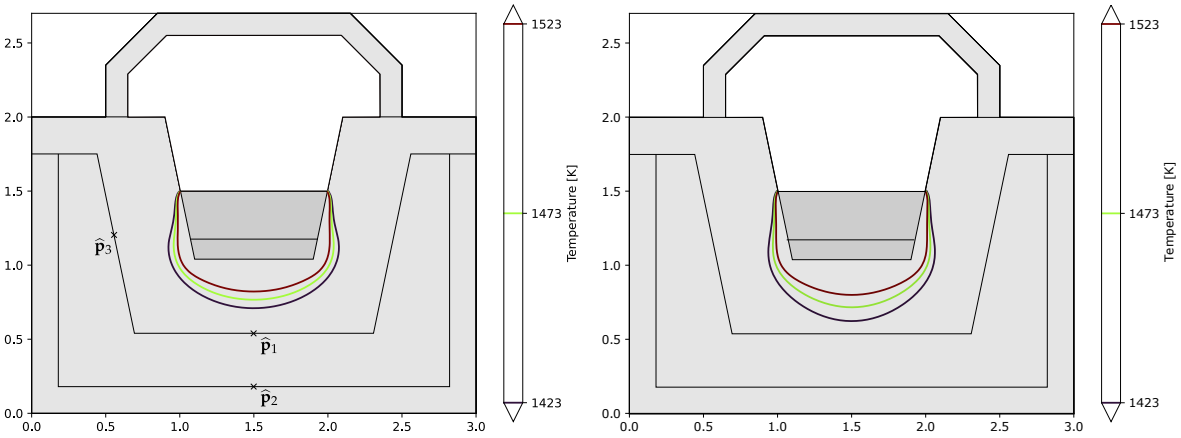
Figure 5.20: Temperature evolution at selected points, Campaing cycle 1.

ature. Towards the end of the campaign, the temperature is similar, as depicted in Figure 5.19f for $t = 57.84$ days. However, the temperature field is far from a steady-state, as demonstrated by the temperature contours shown in Figure 5.19d. This temperature snapshot corresponds to a time value after a long stop, which lasted for around 2.2 days. The cover and the upper part of the working lining and fluids has substantially cooled down. Nonetheless, due to the large thermal inertia of the trough, the bulk of the solids remains above 1000 K. After a couple of casts, the temperatures rapidly rise, as depicted in Figure 5.19e, around six minutes after the start of the cast.

To better assess the influence of the casting process stops in the predicted temperature in the bulk of the solids, in Figure 5.20 we analyse the evolution of the temperature at points $\widehat{\mathbf{p}}_1 = (1.5, 0.54)$ m, $\widehat{\mathbf{p}}_2 = (1.5, 0.18)$ m and $\widehat{\mathbf{p}}_3 = (0.56, 1.2)$ m (see Figure 5.21a), using the BF activity to model the stops as described for Campaign cycle 1 in Figure 5.20a. Moreover, in Figure 5.20b, the temperature evolution at those points is displayed, but considering the results for the 15 day-continuous cast problem addressed in Section 5.3.2 instead. The main observed differences are due to some prolonged stops, which last long enough for the refractories to evidence a considerable degree of cooling. Also, note that at neither of the defined points the true steady-state is reached during the whole campaign cycle when compared to the continuous cast, where a steady-state is reached for all points around $t = 20$ days. At points $\widehat{\mathbf{p}}_1$ and $\widehat{\mathbf{p}}_2$, a difference around 50 K is observed at $t = t_{end}$, while at point $\widehat{\mathbf{p}}_3$, located between the working and safety linings at a lateral of the trough, the difference reaches 160 K. Naturally, the differences become larger the closer to the fluids. They are especially significant in the cover, where even the shortest stops lead to substantially large temperature drops. These results show that the effect of the long stops in the temperature field is clearly non-negligible. Hence, the assumption of a quasi steady-state being reached in the solids that has been made in previous studies may not be fully realistic.

Figure 5.21 shows the critical isotherms at different time values. Both at $t = 10.33$ days and $t = 57.84$ days, during the first campaign cycle, they remain at a similar position and are well-inside the working lining. During long stop periods, the temperature of the solids goes below these critical values, as depicted in Figure 5.19d. Nonetheless, it is noteworthy that the 1423 K isotherm lies close to the safety lining in the bottom of the trough, especially towards the end of the campaign.

Concerning the radiosity, in Figure 5.22, its value on the radiation boundary, γ_R, is represented as a function of the curve arc length for the time values displayed in Figure 5.19. The boundary is travelled anti-clockwise, starting from the point $\mathbf{x} = (1.041, 1.5)$ m. During BF tappings, the radiosity reaches high values quickly. These values are qualitatively very similar in all cases. However, throughout stops, it decreases sharply, especially on the slag surface. If the stop is long, such as the one happening at $t = 16.60$ days, the radiosity value becomes very low. For that time value, its maximum on γ_R is 2356 W/m^2, two orders of magnitude below the maximum values predicted during the tappings.



(a) $T^{76}_{cast,h}(\cdot, \widetilde{t}_{153})$, $\widetilde{t}_{153} = 10.33$ days. **(b)** $T^{323}_{cast,h}(\cdot, t_{end})$, $t_{end} = 57.84$ days.

Figure 5.21: Critical isotherms, Campaign cycle 1.

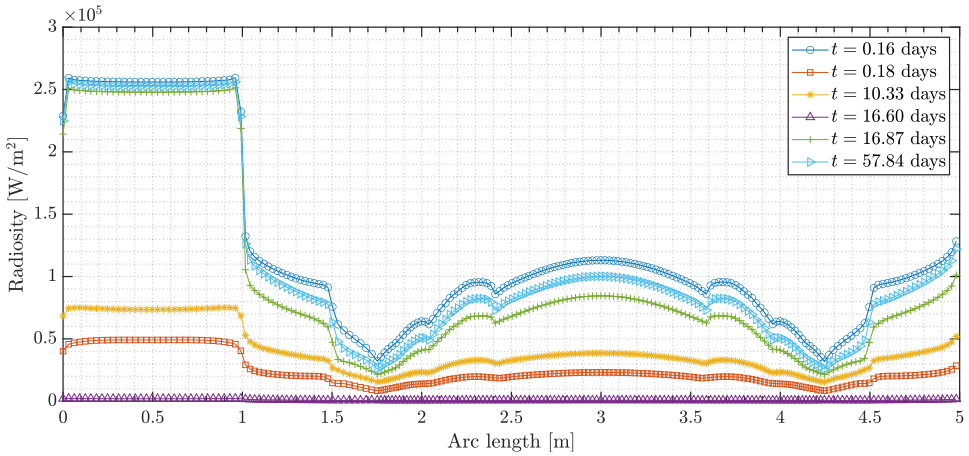
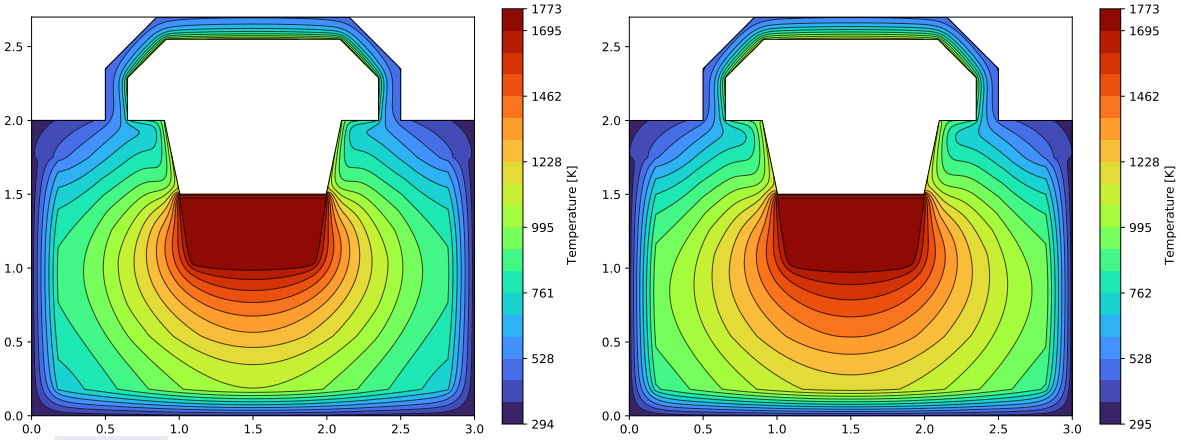


Figure 5.22: Computed radiosity on γ_R for various time values for Campaign cycle 1.



(a) $T^{62}_{cast,h}(\cdot, \widetilde{t}_{124})$, $\widetilde{t}_{124} = 10.01$ days. **(b)** $T^{323}_{cast,h}(\cdot, t_{end})$, $t_{end} = 55.44$ days.

Figure 5.23: Temperature contours at various time values during Campaign cycle 2.

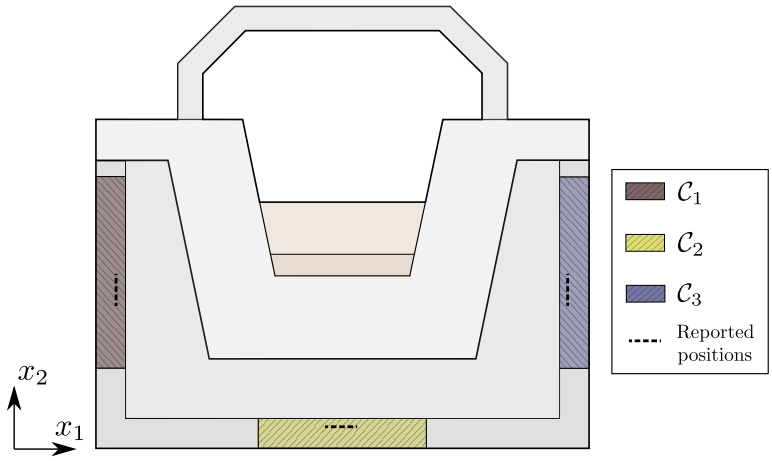


Figure 5.24: Feasible region for the thermocouples location in the BF runner cross-section.

The observed behaviour of the temperatures for Campaign cycle 2 is very similar to that described for the first cycle, as evidenced by the temperature contours shown in Figures 5.23a and 5.23b, after approximately 10 days and at the end time, respectively.

5.4. Assessment of thermocouple positions

Temperature measurements made with thermocouples installed in the main trough for the two campaign cycles used in Section 5.3.3 are available. The devices consist of a thin 20×20 cm^2 metal plate, placed within the insulation lining. As described in Section 3.3.4, due to the low thermal conductivity, large thermal gradients appear in the insulation material. Consequently, small deviations from the reported position may lead to big differences in the obtained measurements. Furthermore, the reported position is not entirely accurate, as the thermocouples are installed during the main trough construction process. Hence, the raw measurements seem are likely to be unsuitable for the model validation.

In this section, a minimisation problem to obtain a corrected position for the thermocouples is presented. First, in Section 5.4.1, the problem is motivated after comparing the measurements made by the devices with the computed temperatures at their reported locations. Then, in Section 5.4.2, the corresponding minimisation problems to obtain a corrected position are presented. In Section 5.4.3, a hybrid gradient descent and simulated annealing algorithm (GRSA) is introduced. Lastly, in Section 5.4.4, the GRSA is applied to the BF main trough problem to obtain a corrected position for the thermocouples.

5.4.1. Motivation

In the cross-section corresponding to $\varpi(t)$, there are three installed thermocouples, one in the bottom and two in both lateral sides. The plate composing the devices is aligned horizontally for the bottom thermocouple and vertically for the lateral thermocouples. In Figure 5.24, their reported positions are depicted. As described previously, the devices are embedded within the insulation lining. We denote as TC1, TC2 and TC3 the lateral left, bottom and lateral right thermocouples, respectively.

In Figure 5.25, the computed temperature and the corresponding thermocouple temperature measurement are shown over time during Campaign cycle 1. Even if the agreement between the numerical and experimental curves is very poor, the computed temperatures show similar qualitative behaviour. In particular, the large oscillations are located at the same time values. This suggests that the strategy to model the BF activity, separating casts from stops is adequate, since the effect of the longer stops is captured by the model. For instance, both the measurements and the computed

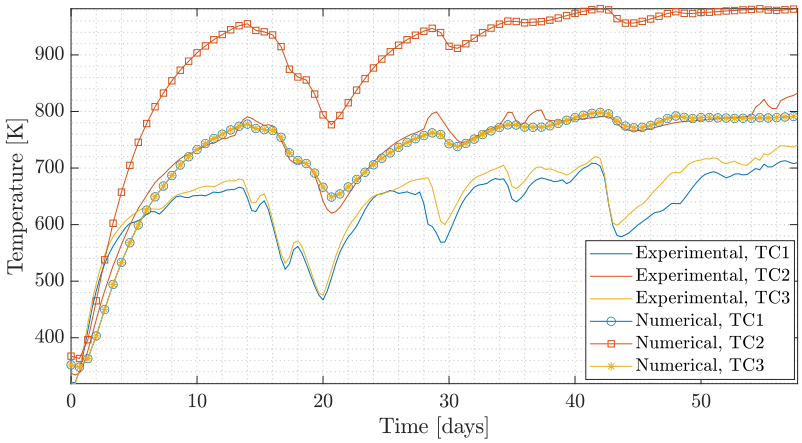


Figure 5.25: Temperature over time at the reported thermocouple locations, Campaign cycle 1.

temperatures show the effect of the long stop around $t = 16.60$ days. We note that the computed temperature at the reported positions of the lateral thermocouples (TC1 and TC3) is identical in virtue of the domain and boundary conditions being symmetric. As discussed above, the thermocouple reported position is not accurate and small deviations in their placement may explain the large differences in the obtained measurements, owing to the low thermal conductivity within the insulation lining.

5.4.2. Minimisation problem

To compare the numerical results with the experimental measurements we propose a procedure that allows to find a correction for the given position of the thermocouples minimising the difference among the measurement and the computed numerical approximation. Specifically, we aim to find a minimum of a suitable functional defined in a feasible region for each thermocouple. To this end, the feasible regions portrayed in Figure 5.24 are introduced:

$$\begin{aligned}\mathcal{C}_1 &:= [0, 0.18] \times [0.5, 1.65],\\ \mathcal{C}_2 &:= [1.1, 1.9] \times [0, 0.18],\\ \mathcal{C}_3 &:= [2.82, 3.0] \times [0.5, 1.65].\end{aligned}$$

The originally reported positions of the centre point of each thermocouple's plate, also depicted in Figure 5.24, are the following:

$$\begin{aligned}\mathbf{x}_1^0 &= (0.13, 0.965),\\ \mathbf{x}_2^0 &= (1.50, 0.13),\\ \mathbf{x}_3^0 &= (2.82, 0.965).\end{aligned}$$

Given that the measurement at each thermocouple corresponds to the temperature in its thin metal plate, the numerically computed temperature is integrated along a line of length $L = 20$ cm whose midpoint is considered as the thermocouple position $\mathbf{x}_d$, with $d \in \{1, 2, 3\}$. Hence, we propose to solve the following global optimisation problem:

Find $\mathbf{x}_d$ such that:

$$J_d(\mathbf{x}_d) = \min_{\mathbf{x} \in \mathcal{C}_d} J_d(\mathbf{x}), \tag{5.22}$$

USC UNIVERSIDADE DE SANTIAGO DE COMPOSTELA

where $\mathcal{C}_d$ denotes the feasible region for the dth thermocouple and J_d is the following functional:

$$J_d(\mathbf{x}) = \left[\frac{1}{t_{end} - \widetilde{t}_0}\int_{\widetilde{t}_0}^{t_{end}} \left(\left(\frac{1}{L}\int_{x_2-\frac{L}{2}}^{x_2+\frac{L}{2}} T_h((x_1,s),t)\,ds - T_{d,exp}(t)\right)W(t)\right)^2 dt\right]^{\frac{1}{2}}, \tag{5.23}$$

for $d \in \{1,3\}$ and

$$J_d(\mathbf{x}) = \left[\frac{1}{t_{end} - \widetilde{t}_0}\int_{\widetilde{t}_0}^{t_{end}} \left(\left(\frac{1}{L}\int_{x_1-\frac{L}{2}}^{x_1+\frac{L}{2}} T_h((s,x_2),t)\,ds - T_{d,exp}(t)\right)W(t)\right)^2 dt\right]^{\frac{1}{2}}, \tag{5.24}$$

for $d = 2$. In (5.23) and (5.24), T_h is the computed numerical approximation of the temperature, obtained solving problems $(\mathcal{VP}_{stop})^m$ for $0 \leq m \leq M-2$ and $(\mathcal{VP}_{cast})^m$ for $0 \leq m \leq M-1$, and defined for $t \in \mathcal{T}$:

$$T_h(t) = \begin{cases} T^m_{cast,h}, & \text{if } t \in \mathcal{T}^m_{cast}, \\ T^m_{stop,h}, & \text{if } t \in \mathcal{T}^m_{stop}. \end{cases}$$

Moreover, $T_{d,exp}(t)$ denotes the time-dependent temperature measurement at the dth thermocouple. The function $W(t)$ is a weight defined as follows:

$$W(t) = \frac{t_{end} - t}{t_{end}}.$$

Its role is to compensate for the model not being an accurate representation of reality in the latter stages of the campaign cycle, since the working lining suffers heavy damage as the cycle advances. Provided that refractory degradation is not included in the model, the weight increases the relevance of the difference between the numerically computed temperature and the measurement during the beginning of the campaign cycle, decreasing the importance of said difference towards its end.

Note that the J_d functional in (5.23) and (5.24) is defined as the difference between the experimental measurement and the mean numerically computed temperature at each thermocouple plate, multiplied by the weight as mentioned above, and averaged over the total time span of the campaign cycle.

5.4.3. Hybrid GRSA algorithm

Functionals (5.23) and (5.24) are, in general, non-convex and may have several local minima. Therefore, an adequate technique to solve constrained global optimisation problems is required. To solve the presented problem, we use a hybrid gradient descent and simulated annealing method (GRSA), proposed in Yiu et al. (2004). Even though the simulated annealing is theoretically effective in locating the global minimum of a non-convex function, since convergence to the minimum can be proved (Ingber, 1993), the convergence rate is very slow. Therefore, the GRSA incorporates a gradient descent algorithm to obtain a local minimum using as initial guess a point provided by the simulated annealing algorithm, which performs a global search in the feasible set, thus avoiding getting trapped in local minima and speeding up the convergence of the simulated annealing approach.

In Y.-J. Wang & Zhang (2007), an enhancement of the GRSA method was proposed, called the GRFSA method. It involves the transformation of the objective function using tunnelling. The GRFSA algorithm was found to improve the convergence rates, especially in large scale problems, where the number of functional evaluations can be significantly reduced. However, in modestly sized problems, such as the one proposed here, the performance of both methods is similar. Therefore, we resort to the GRSA algorithm. To simplify the notation, in this subsection, the subscript d of each thermocouple is omitted.

Let $J(\mathbf{x})$ be a differentiable functional, defined in a convex region $\mathcal{C} \subset \mathbb{R}^N$. To seek the global minima of J, we follow Algorithm 5.1. The parameters used for the hybrid algorithm, simulated annealing and gradient descent are summarised in Table 5.8. The local search, as discussed previously, features a gradient descent (GR) algorithm. We use a *backtracking line search* to find the step size at

Algorithm 5.1 Hybrid GRSA algorithm

1. Initialisation: provide an initial guess $\widetilde{\mathbf{x}}$ in $\mathcal{C}$.
2. Local search: the gradient descent algorithm (GR) with $\mathbf{y}^0 = \widetilde{\mathbf{x}}$ as initial guess is used to obtain a point $\mathbf{x}^0$.
3. Hybrid iteration $p+1$: for $N_{hyb}^{max} \geq p \geq 0$, perform:
   a) Global search: execute the simulated annealing algorithm with $\mathbf{z}^{0,0} = \mathbf{x}^p$ as initial guess until a point $\mathbf{x}^{p+1,*}$ is obtained.
   b) Local search: using $\mathbf{y}^0 = \mathbf{x}^{p+1,*}$ as initial guess, a gradient descent algorithm is used to obtain a point $\mathbf{x}^{p+1}$.
4. Convergence test: step 3 continues until N_{hyb}^{conv} consecutive hybrid iterations show no further progress in the solution, i.e., if $|J(\mathbf{x}^{\widetilde{p}+1}) - J(\mathbf{x}^{\widetilde{p}})| < tol_{hyb}$ for $p - N_{hyb}^{conv} + 1 \leq \widetilde{p} \leq p$, then the algorithm is stopped.

Algorithm 5.2 Projected gradient descent (GR)

1. Initialisation: provide $\mathbf{y}^0$ in $\mathcal{C}$.
2. Gradient descent iteration $p+1$: for $p \geq 0$, using $\mathbf{y}^0$ as initial guess, we perform
   a) Obtain the descent direction $\mathbf{d}(\mathbf{y}^p) = -\text{grad}\big(J(\mathbf{y}^p)\big)/|\text{grad}\big(J(\mathbf{y}^p)\big)|$.
   b) Compute the step length ν_p using the computed descent direction and a backtracking line search algorithm, starting with $\nu_p = 1$:
      (b1) If $\mathbf{y}^p + \nu_p \mathbf{d}(\mathbf{y}^p) \notin \mathcal{C}$, then repeat setting $\nu_p = \beta_b \nu_p$, with $\beta_b \in (0,1)$. Else, proceed to the next step.
      (b2) If $J(\mathbf{y}^p + \nu_p \mathbf{d}(\mathbf{y}^p)) > J(\mathbf{y}^p) + \alpha_b \,\text{grad}\big(J(\mathbf{y}^p)\big) \cdot \mathbf{d}(\mathbf{y}^p)$, where $\alpha_b \in (0, 0.5)$, set $\nu_p = \beta_b \nu_p$ and repeat this step. Else, proceed to next iteration in step 2.
3. Convergence test: step 2 continues until $|J(\mathbf{y}^{p+1}) - J(\mathbf{y}^p)| < tol_{gr}$ or the maximum number of iterations N_{gr} is reached.

Table 5.8: Parameter values for GRSA algorithm.

Simulated annealing		*Gradient descent*	
N_c	150	tol_{gr}	$1e-6$
N_{pert}	250	N_{gr}	100
α_c	0.9	α_b	0.25
tol_{sa}	0.5	β_b	0.5
C^0	0.7	*Hybrid algorithm*	
		N_{hyb}^{conv}	3
		N_{hyb}^{max}	30
		tol_{hyb}	$tol_{gr}/100$

USC UNIVERSIDADE DE SANTIAGO DE COMPOSTELA

Algorithm 5.3 Simulated annealing (SA)

1. Initialisation: provide $\mathbf{z}^{0,0}$ in $\mathcal{C}$ and C^0.
2. Simulated annealing cooling iteration $p+1$: for $N_c \geq p \geq 0$, using $\mathbf{z}^{p,0}$ as initial guess, we perform:
   a) Perturbation iteration $j+1$: for $N_{pert} \geq j \geq 0$, perform the following steps:
   (a1) Sample a random $b \in \{1,2,3\}$.
   - If b is 1, then generate a random $i \in \{1,\dots,N\}$. Sample a perturbation Δz_i such that $\Delta\mathbf{z} = (0,\dots,\Delta z_i,\dots,0)$ and $\mathbf{z}^{p,j} + \Delta\mathbf{z} \in \mathcal{C}$.
   - Else if b is 2, then generate a random $m \in \{1,\dots,N\}$ and a set of indexes $I \subset \{1,\dots,N\}$ such that its cardinal is m. Then sample a perturbation $\Delta\mathbf{z}$ such that $\mathbf{z}^{p,j} + \Delta\mathbf{z} \in \mathcal{C}$, with $\Delta z_i = 0$ for $i \notin I$.
   - Else, generate a random $\Delta\mathbf{z}$ such that $\mathbf{z}^{p,j} + \Delta\mathbf{z} \in \mathcal{C}$.

   (a2) Let $\mathbf{z}^* = \mathbf{z}^{p,j} + \Delta\mathbf{z}$.
   - If $J(\mathbf{z}^*) < J(\mathbf{z}^{0,0})$ and $\left|\frac{J(\mathbf{z}^*)-J(\mathbf{z}^{0,0})}{J(\mathbf{z}^{0,0})}\right| < tol_{sa}$, then set $\mathbf{z}^{p+1,j+1} = \mathbf{z}^*$ and stop the algorithm.
   - Else if $J(\mathbf{z}^*) < J(\mathbf{z}^{p,j})$ then set $\mathbf{z}^{p,j+1} = \mathbf{z}^*$ and start a new perturbation in step (a).
   - Else, generate a random number $r \in [0,1]$. If $r < C^p \exp\left(-\frac{J(\mathbf{z}^*)-J(\mathbf{z}^{p,j})}{C^p}\right)$ then set $\mathbf{z}^{p,j+1} = \mathbf{z}^*$. Else, set $\mathbf{z}^{p,j+1} = \mathbf{z}^{p,j}$. Start a new perturbation in step (a).

   b) After N_{pert} are executed, set $\mathbf{z}^{p+1,0} = \mathbf{z}^{p,j+1}$, update $C^{p+1} = \alpha_c C^p$ and start a new cooling iteration.

each iteration (Boyd & Vandenberghe, 2004). The algorithm follows the steps stated in Algorithm 5.2. We note that since the feasible set $\mathcal{C}$ is assumed to be convex, the backtracking search is guaranteed to find a point inside the feasible region by successively multiplying by β_b in step (b1), as $\beta_b \in (0,1)$.

The simulated annealing method, stated in Algorithm 5.3, is mainly used to provide descent points to the gradient descent algorithm. A flow chart is provided in Figure 5.26. It is similar to the one proposed for the global search in Yiu et al. (2004). Within it, all N_c cooling iterations and N_{pert} perturbations are completed unless a point with a sufficiently better value than the initial guess is found in step (a2). Occasionally, points with a worse functional value will be accepted in step (a2). This prevents the algorithm from getting stuck in local minima. The probability of accepting a worse functional value at iteration p depends on the corresponding *cooling parameter* C^p, which decreases as the iteration count advances. The cooling parameter is frequently known as *temperature* in the specialised bibliography. This designation is avoided herein due to the risk of confusion with the temperature in the trough.

Test examples

In this subsection, the implementation of the GRSA algorithm is tested with two different benchmark tests, extracted from the literature.

Easom function. It is a non-convex function which has several local minima, with a global minimum value of -1 at $\mathbf{x} = (x_1, x_2) = (\pi, \pi)$. The function is defined as follows:

$$J(x_1, x_2) = -\cos(x_1)\cos(x_2)\exp(-(x_1-\pi)^2 - (x_2-\pi)^2).$$

USC UNIVERSIDADE DE SANTIAGO DE COMPOSTELA

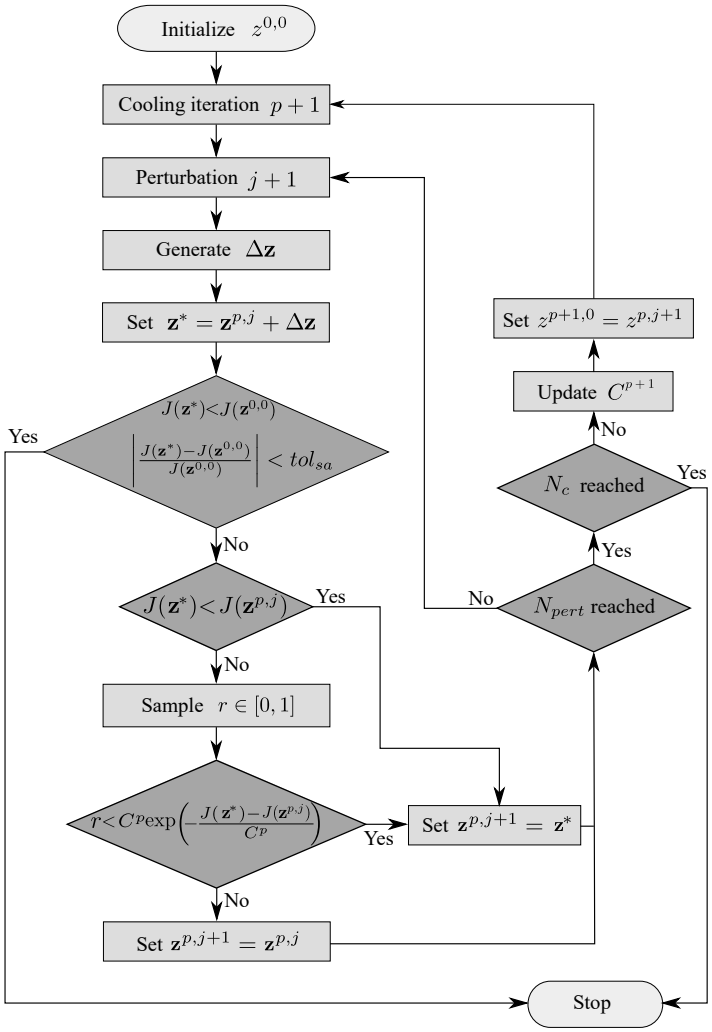
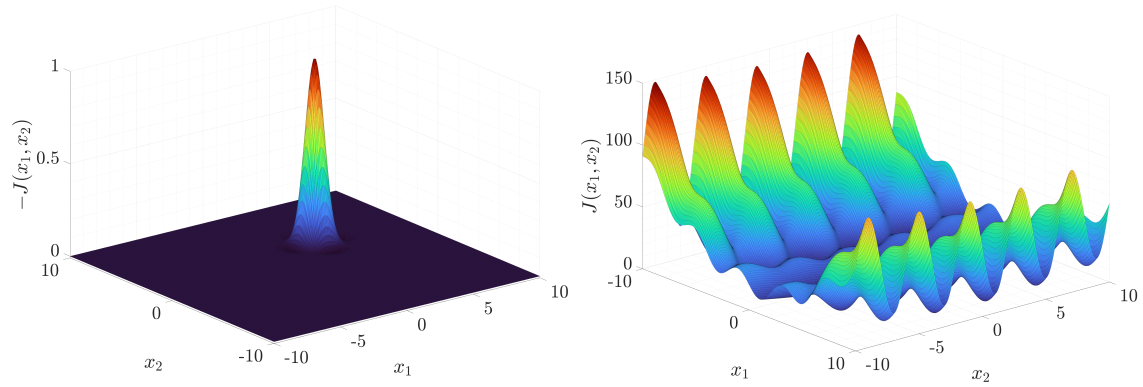


Figure 5.26: Flow chart of the simulated annealing (SA) algorithm.



(**a**) Easom function. (**b**) Levy function, $N = 2$.

Figure 5.27: Test functions for the optimisation algorithm.

The surface that it generates is displayed in Figure 5.27a, for a feasible region $\mathcal{C}$ selected as the square $[-L, L]^2$, with $L = 10$. Note that for clarity purposes $-J(x_1, x_2)$ is depicted. The main difficulty in finding the global minimum of the Easom function is that the search space becomes increasingly wide compared to the region where the function decays below zero as L grows larger.

In Du & Swamy (2016), a classic simulated annealing method was used to solve the minimisation problem for the Easom function, updating the cooling parameter C^p following an exponential schedule, as in Algorithm 5.3. For the therein stated algorithm to be successful, the search space had to be restricted to $[-10, 10]^2$, corresponding to $L = 10$, and the initial state vector $\mathbf{x}$ had to be randomly sampled inside the region $[-0.5, 0.5]^2$. Otherwise, the simulated annealing approach failed to find the global minimum.

Here, the GRSA algorithm is used to solve the problem, using a random $\mathbf{x}^0 \in \mathcal{C}$ as initial seed. The parameters shown in Table 5.8 are used for the method considering different values for the feasible region $[-L, L]^2$. The main results for a total of 50 runs for each L are summarised in Table 5.9a. Thus, the reported minimum value, number of functional evaluations and time are computed as the average values over the 50 runs. Moreover, the success rate is defined as the fraction of the runs that have computed a minimum value F such that $|F - J(\mathbf{x}_{min})| < 10^{-3}$, where $J(\mathbf{x}_{min})$ is the actual value of the global minimum, in this case $J(\mathbf{x}_{min}) = -1$. The computation times indicated in the table are obtained in a PC equipped with an *AMD Ryzen 9 5900X* processor using a single thread.

The results show that the hybrid algorithm is able to obtain the global minimum in all the considered cases, except for one of the runs for $L = 500$, where the search region becomes too large for the method to reliably converge to the global minimum. Nonetheless, if the parameters in Table 5.8 are slightly tuned, then the algorithm is also able to find the global minimum for all the test runs.

Levy function. The N-dimensional Levy function, introduced in Levy & Montalvo (1985), is defined by the following expression:

$$J(\mathbf{x}) = \frac{\pi}{N}\left(10\sin^2(\pi y_1) + (y_N - 1)^2 + \sum_{i=1}^{N-1}\left[(y_i - 1)^2(1 + 10\sin^2(\pi y_{i+1}))\right]\right),$$

where $y_i = 1 + 0.25(x_i - 1)$.

For any $N \geq 1$, the function has a global minimum at $x_i = 1$ for $1 \leq i \leq N$, with value $J(\mathbf{x}) = 0$. As depicted in Figure 5.27b for $N = 2$, it has many local minima. The Levy function was also used in Yiu et al. (2004) to test the GRSA algorithm, showing a good performance for different N values.

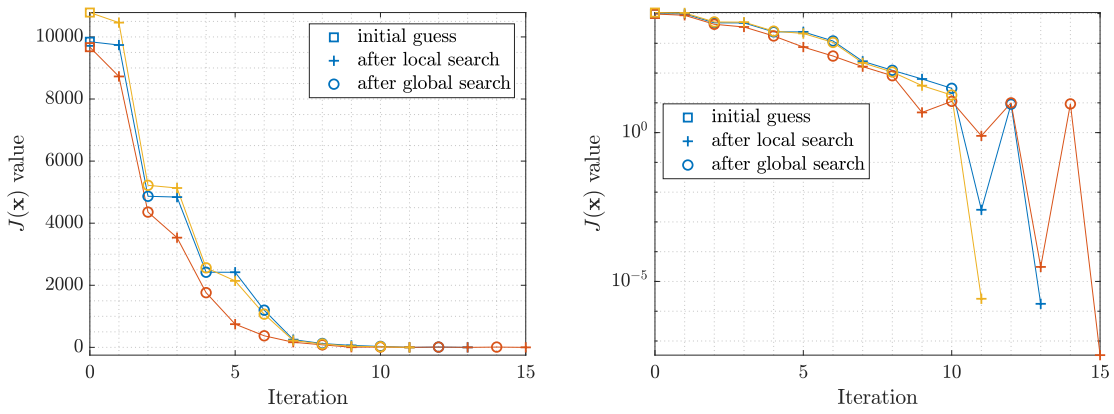
Table 5.9: Success rate, global minimum value, number of functional evaluations and computational time for the GRSA algorithm on the test examples. Reported values are computed averaging for 50 runs.

(**a**) Easom function, varying the size of the feasible region L.

L	Success rate	Min. value	# J evaluations	Time [s]
10	1.0	-1.0	$3.35{\cdot}10^{3}$	$2.18{\cdot}10^{-2}$
50	1.0	-1.0	$4.50{\cdot}10^{3}$	$3.07{\cdot}10^{-2}$
100	1.0	-1.0	$1.02{\cdot}10^{4}$	$6.78{\cdot}10^{-2}$
500	0.88	-0.88	$9.95{\cdot}10^{4}$	$6.59{\cdot}10^{-1}$

(**b**) Levy function, varying the dimension N.

N	Success rate	Min. value	# J evaluations	Time [s]
10	1.0	$3.59{\cdot}10^{-7}$	$1.73{\cdot}10^{4}$	$3.87{\cdot}10^{-1}$
50	1.0	$2.18{\cdot}10^{-7}$	$2.14{\cdot}10^{4}$	$1.94{\cdot}10^{0}$
100	1.0	$1.34{\cdot}10^{-8}$	$2.68{\cdot}10^{4}$	$4.61{\cdot}10^{0}$
500	1.0	$4.49{\cdot}10^{-7}$	$6.80{\cdot}10^{4}$	$5.60{\cdot}10^{1}$
1000	1.0	$5.47{\cdot}10^{-7}$	$1.04{\cdot}10^{5}$	$1.70{\cdot}10^{2}$



(**a**) Linear scale.

(**b**) Semi-logarithmic scale.

Figure 5.28: Convergence histories of three runs for the Levy function with $N = 1000$.

For the proposed algorithm, using the parameters shown in Table 5.8 and considering $x_i \in [-10, 10]$, we obtain the results displayed in Table 5.9b for a varying dimension N. In all the proposed cases, the GRSA is able to find the global minimum, although the computational time and functional evaluations grow quickly as N becomes larger. In Figure 5.28, the convergence histories of three runs for $N = 1000$ are plotted, showing the J value after each local and global search. As evidenced by the semi-log graph, the last iterations of the simulated annealing accept points with worse functional values, which allow to avoid getting trapped in local minima and find the global minimum.

5.4.4. Application to the BF main trough problem validation

To obtain a correction for the thermocouple position, the hybrid GRSA algorithm, described in Section 5.4.2, is used to solve the minimisation problem (5.22), considering the numerical approximation T_h obtained as the solution for the BF activity corresponding to Campaign cycle 1.

Using the originally reported positions as initial guess, i.e., $\tilde{\mathbf{x}} = \mathbf{x}_d^0$, the GRSA algorithm yields a corrected location for the thermocouple's plate centre point, denoted as $\mathbf{x}_{d,1}^*$. The plate corrected and reported positions are shown in Figure 5.29. It is observed that the thermocouple in the bottom of the trough remains almost in the same position, whereas both lateral ones are moved upwards and are placed between the safety and insulation linings. In Table 5.10, the reported and corrected thermocouple positions using the data corresponding to Campaign cycle 1, as well as the functional values at both points are displayed for $d \in \{1, 2, 3\}$. As evidenced by the results, the functional value decreases significantly at the corrected positions. It is noteworthy that in the case of the bottom thermocouple (TC2), the corrected position is only 4 cm away from the originally reported one, but the functional value is over 10 times less. This shows that even minor deviations in the thermocouple placements may have a high impact on the temperature readings due to the large thermal gradients. Thus, to achieve an effective and reliable use of the thermocouples, it is critical to be thorough in their placement.

At the corrected positions, good levels of agreement among the numerically computed temperatures and the measurements are observed during Campaign cycle 1, as displayed in Figure 5.30a. However, the agreement deteriorates as time advances and, towards the end of the cycle, the curves are substantially different. As wear or material damage are not included in the model, to obtain the numerical results we are implicitly assuming that the main trough remains in perfect condition during the whole campaign. As it has been mentioned throughout the previous chapters, this is not the case in reality. Precisely, the increasing disagreement among the measurements and numerical results is an indication of the suffered wear, as the model and material properties are representative of the reality only during the first stages of the campaigns. Note that the bottom thermocouple (TC2) is

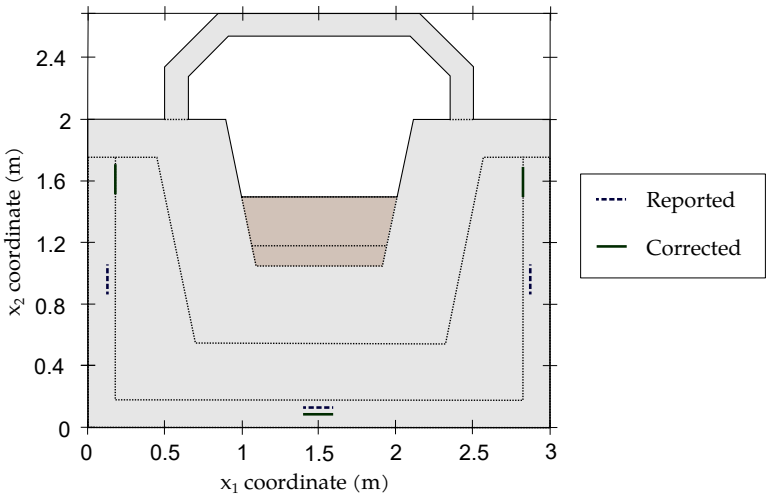


Figure 5.29: Thermocouple reported positions and corrected positions after a hybrid GRSA algorithm run using numerical solution for Campaign cycle 1.

still yielding similar temperatures to the model towards the end of the campaign cycle. This suggests that wear and loss of properties are much more severe at the laterals of the trough, which is consistent with what has been reported in the literature, as wear rates in pooling troughs are found to be more pronounced in the laterals, especially near the slag-hot metal interface in the jet impingement region (Cameron et al., 2019; Ranjan et al., 2022).

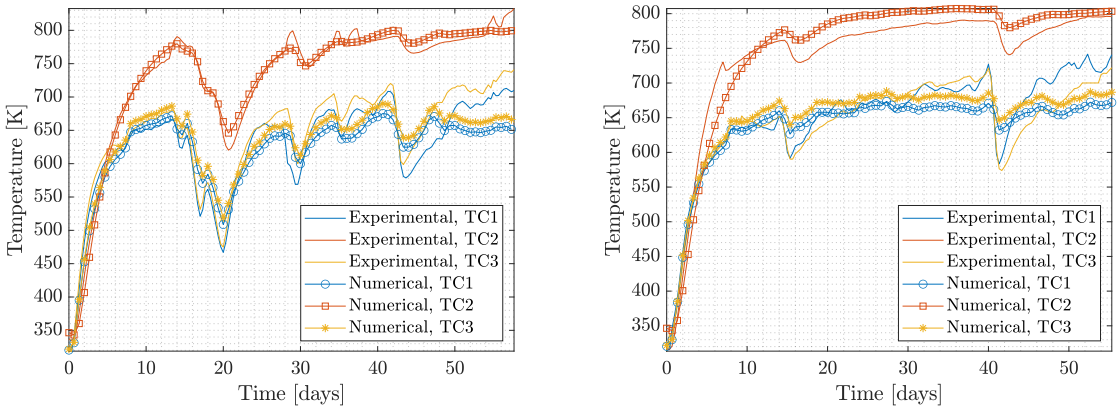
The temperature measurements and the numerically computed temperatures at the corrected thermocouple positions are shown in Figure 5.30b for Campaign cycle 2. The temperature measurements during Campaign 2 show a smoother behaviour if compared to Campaign 1, as the stops are kept shorter during the former. The numerical results and the measurements for Campaign 2 also show good levels of agreement that worsen as time advances.

To assess the validity of the proposed methodology, the results should not vary significantly if Campaign cycle 2 is used to obtain the corrected thermocouple locations. With this purpose, we take as initial guess the locations obtained as the result of the minimisation problem for Campaign cycle 1. Thus, (5.22) is solved, but considering instead the numerical approximation to the temperature using the BF activity corresponding to Campaign cycle 2, as well as the thermocouple measurements during this cycle.

In Table 5.11, the obtained results after running the hybrid GRSA algorithm using the results obtained for Campaign cycle 2 are displayed. The corrected position for Campaign cycle 1 is used as initial seed, i.e., we consider $\mathbf{x}_{d,2}^0 = \mathbf{x}_{d,1}^*$. At the bottom thermocouple (TC2) and the left lateral (TC1), negligible improvements in the functional value are computed, which lead to very small thermocouple displacements from the obtained positions for Campaign cycle 1. For the right lateral thermocouple (TC3), a slight improvement for the functional value is found if the thermocouple is moved slightly over 1 cm upwards.

Table 5.10: Originally reported thermocouple positions $\mathbf{x}_d^0$, corrected positions $\mathbf{x}_{d,1}^*$ and functional value at both locations for the three thermocouples, Campaign cycle 1.

	TC1	TC2	TC3
$\mathbf{x}_d^0$	$(0.130, 0.965)$	$(1.500, 0.130)$	$(2.870, 0.965)$
$\mathbf{x}_{d,1}^*$	$(0.180, 1.613)$	$(1.500, 0.087)$	$(2.820, 1.596)$
$J_d(\mathbf{x}_d^0)$	59.87	83.77	54.90
$J_d(\mathbf{x}_{d,1}^*)$	13.02	7.24	14.19



(**a**) Campaign cycle 1.

(**b**) Campaign cycle 2.

Figure 5.30: Temperature over time at the corrected thermocouple locations.

Table 5.11: Originally found (for Campaign cycle 1) thermocouple positions $\mathbf{x}^*_{d,1}$, corrected positions $\mathbf{x}^*_{d,2}$ and functional value at both locations for the three thermocouples using the results for Campaign cycle 2.

	TC1	TC2	TC3
$\mathbf{x}^*_{d,1}$	$(0.180, 1.613)$	$(1.500, 0.087)$	$(2.820, 1.596)$
$\mathbf{x}^*_{d,2}$	$(0.180, 1.612)$	$(1.500, 0.086)$	$(2.820, 1.610)$
$J_d(\mathbf{x}^*_{d,1})$	8.35	17.62	11.98
$J_d(\mathbf{x}^*_{d,2})$	8.33	17.59	9.84

It should be noted that the discrepancies between the measurements and the numerical predictions can be only partially attributed to the unknown measurement locations. The presented methodology is only completely valid when the model is an accurate representation of the reality. As mentioned previously and shown by the obtained results, this may not be the case during the latter stages of the campaign cycles, when refractory wear increases. In addition, various simplifying assumptions that have been considered may negatively affect the accuracy of the proposed model. Namely, the 2D hypothesis, the disregard of any flow during BF stops or the assumption that the temperature profile (5.6) is an accurate representation of the temperature of the fluids during the BF casts, are likely to be somewhat idealistic and possibly need careful revision. In order to assess the extent of the impact of these simplifying assumptions, better temperature monitoring and careful positioning of the thermocouples in the trough are required.

USC UNIVERSIDADE DE SANTIAGO DE COMPOSTELA

USC
UNIVERSIDADE
DE SANTIAGO
DE COMPOSTELA

Conclusions and perspectives

In this part of the manuscript, a hierarchy of mathematical models has been introduced. Their numerical solutions yield insights on the hydrodynamics and thermal response of the BF trough, which are closely related to refractory wear. Some of the existing knowledge gaps in the literature on the phenomena related to the BF trough have been addressed. Namely, a careful analysis of the evolution of the fluid interfaces during the BF tapping process, the characterisation of the shear stress for various tapping conditions, and the evaluation of the heat transfer in the trough have been carried out.

The numerical techniques were thoroughly tested, assessing grid resolution dependency and verifying the own-developed code with a manufactured solution test. In addition, comparisons with experimental measurements have been made when available. A critical comparison of the numerical results with the existing research in the field was also done.

The foremost conclusions drawn from the studies carried out in this part of the manuscript are summarised below, excluding Chapter 1 due to its introductory purpose.

Ch. 2. The goal of this chapter was to develop a transient 3D CFD model of the flow in the BF trough. The proposed model is similar to those appearing in some recent studies, but uses a slightly more advanced turbulence model and incorporates the three-phase flow. Also, some complexities such as the interface position evolution or the influence of the slag fraction in the tapping stream were analysed. The results show that the shear stress curves are similar to those appearing in experimental and numerical studies concerning submerged impinging jets on planar surfaces, with a minimum in-between two maxima. The flow structures and the shear stress are observed to depend on the slag fraction that is being tapped. Qualitatively similar flow patterns to those reported in previous studies have been found. Furthermore, the liquid levels are observed evolve rapidly to a steady-state during each tapping, with significant bath thickness changes depending on the slag fraction. It is believed that these interface position changes can lead to increased wear, as the slag-hot metal line location is predicted to vary significantly during each BF tapping.

Ch. 3. The scope of this chapter was to address the 3D heat transfer in the trough under a steady-state assumption. To this end, the results from the CFD model solved in Chapter 2 are used to set suitable inlet conditions for the model, which considers only the middle and end parts of the BF trough. The influence of the forced air current below the refractory cover and the radiative heat transfer due to emission from the high temperature slag-air free surface is investigated. Despite the high temperatures in the trough, forced convection was observed to have a significant impact on the temperature. The position of the critical isotherms was analysed in the solid refractories. In particular, the isotherm corresponding to the Fe-C eutectic point (1423 K), is close to the safety lining, indicating a large risk of hot metal penetration. The computed temperature near the slag-air interface suggests that slag solidification may be significant.

Ch. 4. The purpose of this chapter was to derive the non-local radiation model in the 2D setting from the general RTE, propose a suitable numerical procedure for the solution of the coupled conduction and radiation problem, and verify the implementation of the method. A segregated algorithm for the solution of problem was presented. To assess the performance and correctness of the numerical implementation, a new technique for the derivation of a manufactured solution test is provided. A benchmark case was introduced and its analytical solution was given. For this case, the performance of the ESDIRK 3/2a scheme was

USC UNIVERSIDADE DE SANTIAGO DE COMPOSTELA

compared to that of an implicit Euler method, considering both an adaptive step size and a constant step size. The provided algorithm was found to perform well in adequately approximating the radiosity, which is a critical factor in the temperature build-up in the BF trough, and also retains a good approximation of the temperature over long time scales.

Ch. 5. A mathematical model of the heat transfer in a BF main trough cross-section was proposed during a complete campaign cycle. To account for the radiation heat transfer, the non-local model and numerical procedure addressed in Chapter 4 were used. BF operation data comprising two different campaigns of the main trough were incorporated to investigate the effect of the tapping cycles in the temperature field. The results show that the effect of long stops during the process is non-negligible, which implies that steady-state assumptions in the bulk of the solids are not fully realistic. Despite the simplifying assumptions that were made, the computed temperatures show qualitative agreement with the measurements. Nevertheless, as there is a substantial degree of uncertainty concerning the position of the thermocouples, a technique to find a corrected position inside a feasible region was used. In particular, the GRSA algorithm was employed to find the position for each thermocouple by minimising a cost functional. At the found corrected positions, much better levels of agreement were reached among the measurements and the computed temperatures. Provided that the model does not account for wear or material deterioration, the discrepancies among the computed temperature values and the measurements, which grow towards the end of the campaigns, suggest severe damage and loss of properties in the working lining. The results also indicate that most of the wear is located in the lateral sections of the runner, as the observed temperature differences are much larger for the lateral thermocouples, in agreement with the existing literature concerning the wear of refractory materials in the BF trough.

Future research

There are many open questions that are interesting, both from academic and industrial standpoints. In general, while the herein presented contributions can offer some valuable information on the various and complicated phenomena in the BF trough, direct characterisation of refractory wear remains an open challenge. Most of the proposed models could be improved with better data for the physical properties, as many property values have been considered constant due to the lack of reliable experimental data. A publication regarding the main results concerning Chapters 2 and 3 is currently in preparation.

Some possible lines of future research related to the specific results presented in each chapter are summarised subsequently.

Ch. 2. Further research should be carried out considering longer end time of the simulations, and addressing different taphole diameters and velocities. The use of LES or hybrid approaches, such as *Detached eddy simulation* (DES), could be considered to model turbulence instead of the SST $K-\omega$ model. In addition, the influence of a dispersed taphole flow could be analysed. Better geometrical configurations for the BF trough can be proposed based on the numerical results, aiming to minimise the region of the wall exposed to both slag and hot metal, reducing shear stress, and increasing residence time to ensure good slag-metal separation.

Ch. 3. The influence of the inlet condition on the computed temperature should be studied, both concerning supplied velocities and temperature. In particular, a more realistic temperature profile needs to be supplied to the model. Moreover, since slag is predicted to be below liquidus temperature in a significant part of the air-slag free surface, solidification should be incorporated in further studies. Better temperature monitoring is required to validate the model, especially in the refractory cover and the external part of the steel shell. The effect of the small gaps between the pieces forming the refractory should be also addressed.

USC UNIVERSIDADE DE SANTIAGO DE COMPOSTELA

Ch. 4. Alternative approaches for the radiosity and temperature coupling should be investigated, such as considering the inverse integral operator or the fully coupled problem instead. Some of the assumptions that were required to derive the non-local radiation equation could be proved. Also, the convergence of the segregated algorithm to the solution, which has been observed to depend on the relaxation parameter v_{fp}, should be studied.

Ch. 5. Further research should be conducted to experimentally validate the model, as the discrepancies between the measurements and the temperature predictions can only be partially attributed to the uncertainties regarding the thermocouple placement. More detailed experimental measurements of the material properties should be carried out to address their temperature dependency, which can be readily incorporated to the model. Furthermore, the mathematical model should also be improved by introducing the phase change that may take place in the fluids during the stops, especially during those that are prolonged. Using better thermocouple monitoring, both concerning the number of devices and the reliability of their placement, an inverse heat transfer model could be developed, which would allow using the computed deviation of the numerical solution from the experimental measurements to assess the wear profile in the working lining. In addition, it could be interesting to prove the existence and uniqueness of solution of the problem, which remains open due to the presence of several non-linearities that have not been addressed in the literature.

USC
UNIVERSIDADE
DE SANTIAGO
DE COMPOSTELA

USC
UNIVERSIDADE
DE SANTIAGO
DE COMPOSTELA

Part II

Equivalent material for the ceramic cup masonry

USC
UNIVERSIDADE
DE SANTIAGO
DE COMPOSTELA

USC
UNIVERSIDADE
DE SANTIAGO
DE COMPOSTELA

Contents

Introduction **165**

6. Preliminaries. Some results related to linear elasticity **167**
6.1. Basic notation . . . 167
6.2. Linear elasticity . . . 168
6.3. Pure Neumann boundary condition . . . 173

7. Mathematical homogenisation. A classical result in linear elasticity **189**
7.1. Basic terminology . . . 189
7.2. Homogenisation in linear elasticity . . . 190
7.3. Numerical solution of the auxiliary problems . . . 192

8. Stress basic tests **195**
8.1. Introduction . . . 195
8.2. Statement of the stress basic tests . . . 197
8.3. Numerical experiments . . . 198

9. Displacement basic tests **213**
9.1. Symmetry results . . . 213
9.2. Basic tests . . . 218
9.3. Equivalence with the corrector problems . . . 223
9.4. Numerical experiments . . . 228

Conclusions and perspectives **241**

USC
UNIVERSIDADE DE SANTIAGO DE COMPOSTELA

USC
UNIVERSIDADE
DE SANTIAGO
DE COMPOSTELA

Introduction

The Blast Furnace (BF) is the most crucial part of the integrated steel production. During its operation, it has to withstand harsh operation conditions, which include erosive phenomena and chemical corrosion caused by hot metal and slag, enhanced by the high temperature environment. At the end of their useful life, which lasts for 12 to 15 years, the furnace must be relined and rebuilt (Cameron et al., 2019). The relining process is very costly, so it is in the industrial interest to extend the life of BF campaigns. Generally, the main factor limiting the life of the furnace is the wear and tear on the hearth wall (Zhao et al., 2007).

Provided that the temperature inside the BF reaches values above 2000°C, they are built using specific refractory materials, which are able to withstand the extreme conditions of the furnace. Although the particular design of each BF may vary, the general characteristics are shared among all BFs. Some designs incorporate an additional protection layer, known as the *ceramic cup*. It is a masonry composed of corundum refractory bricks bonded by castable joints, placed as the innermost layer of the hearth wall, only separated from the hot metal and slag by a thin castable protective lining. The ceramic cup is regarded as an important part of hearth lining, as it offers good penetration resistance to hot metal (Li et al., 2015), as well as good chemical stability at high temperatures (S. Yao et al., 2020). Outwards in the wall, an additional layer, constructed with large carbon blocks, separates the ceramic cup from the environment, increasing insulation.

Extreme heat and access difficulty pose a challenge to experimentation, which motivates the industrial interest in the assessment of the thermo-mechanical behaviour of the refractory materials composing the BF wall by means of numerical simulation. For the ceramic cup simulation, this would require considering both the castable joints and the bricks as different materials. Due to the number of bricks and the size of the joints (see Figure 1), this is computationally unfeasible. However, there are many methodologies in the literature related to homogenisation techniques for masonry constructions made up of bricks, with and without mortar, for linear and non-linear behaviour laws (e.g. Gasser et al., 2004; Lourenço et al., 2006; T. Nguyen et al., 2009; Mathieu et al., 2012). These methodologies allow to greatly reduce the computational complexity by modelling the masonry as a homogeneous material. A recent and comprehensive review of the state of the art concerning different modelling strategies for the numerical simulation of masonry structures can be found in D'Altri et al. (2020).

Provided that the heterogeneous masonry with bricks and joints can be generated by periodic repetition of a reference unit cell, under the assumption that the wall response is linear elastic, tools from the classical theory of periodic homogenisation can be used to compute the constant effective coefficients characterising the homogenised material (see e.g. Cioranescu & Donato, 1999). To obtain these coefficients, the solutions to some auxiliary problems have to be computed, which are defined in the periodicity cell, and require imposing a periodic boundary condition on all faces of the cell, as well as restricting the mean displacement. These constraints are not always straightforward to implement, especially when dealing with the commercial software packages frequently used for engineering purposes.

In this part of the manuscript, two fast and easy-to-use methodologies are proposed, mitigating these difficulties. They are inspired by uniaxial compression and shear tests, used to characterise the elastic behaviour of materials experimentally. With this purpose, a general anisotropic linear elasticity problem with different involved materials is proposed. To obtain the corresponding equivalent homogeneous material, we first introduce a technique termed *stress basic tests* (S-BT), which is based on solving six problems that generate independent stress states in the reference period. These problems are linear elasticity problems with pure Neumann boundary conditions. Since they are ill-posed problems, the uniqueness of solution is achieved introducing a Lagrange multiplier, considering a



Figure 1: Ceramic cup reconstruction, showing the taphole zone of the hearth wall. Source: ArcelorMittal.

similar formulation to that proposed in Bochev & Lehoucq (2011).

Nevertheless, due to some shortcomings of the S-BT technique, we subsequently introduce a slightly different methodology, called *displacement basic tests* (D-BT). It replaces the Neumann boundary conditions with Dirichlet conditions, imposed only on selected components of the displacement. Assuming that the reference cell has some symmetries and that the involved materials are orthotropic, this sort of numerical tests yield the same homogenised material as solving the auxiliary periodic problems associated with the mathematical homogenisation theory. The D-BT allows the elimination of the periodicity conditions and the zero-mean constraint that are required to solve these problems. Thus, numerical techniques that are well-understood and available in many commercial packages and open-source code libraries can be directly applied to efficiently solve the D-BT.

This part of the manuscript is structured as follows. In Chapter 6, the classical theory of linear elasticity is recalled and some results concerning the pure traction elasticity problem are addressed. To obtain a well-posed formulation of the problem, a Lagrange multiplier is introduced, and a suitable preconditioning technique to solve the arising linear system is presented. Its numerical performance is analysed in comparison with two other popular solution strategies using a couple of manufactured solution tests. Subsequently, Chapter 7 briefly introduces the terminology and concepts regarding the theory of periodic homogenisation, as well as a classical result regarding the homogenisation of the linear elasticity system, extracted from Cioranescu & Donato (1999). In Chapter 8, the S-BT technique is described. Various numerical experiments are carried out with different periodicity cells. Lastly, in Chapter 9, the D-BT methodology is addressed. A mathematical proof regarding the equivalence of this technique with periodic homogenisation is presented. Some additional numerical experiments are conducted to illustrate the technique with different reference cells. The homogenisation of the ceramic cup masonry is carried out.

USC UNIVERSIDADE DE SANTIAGO DE COMPOSTELA

Chapter 6

Preliminaries. Some results related to linear elasticity

This chapter is devoted to recall some central concepts from the theory of linear elasticity, mainly following Gurtin (1982) and Ciarlet (1988). The existence and uniqueness of solution of the pure Neumann linear elasticity system is also addressed. To obtain a well-posed formulation of this system, we propose a methodology that uses a Lagrange multiplier, similar to that discussed by Bochev & Lehoucq (2011). The numerical performance of this methodology is compared to other widespread solution strategies using a couple of manufactured solution tests.

The outline of this chapter is as follows. We start by introducing the main terminology and notation that is used in this part of the manuscript. Subsequently, in Section 6.2, the classical constitutive law in anisotropic linear elasticity is recalled. A model problem that shall appear for various choices of computational domain and data is presented. Lastly, Section 6.3 is dedicated to the study of the pure Neumann problem and the methodology that we propose to obtain a numerical approximation of a solution to the problem.

6.1. Basic notation

We assume that Ω is a domain in $\mathbb{R}^3$, i.e., a subset of $\mathbb{R}^3$ which is open, bounded, connected and with a Lipschitz continuous boundary. $\mathbf{L}^2(\Omega)$ and $\mathbf{H}^1(\Omega)$ denote the spaces of vector-valued functions $\mathbf{v}$ whose components v_i belong to $L^2(\Omega)$ and $H^1(\Omega)$, respectively. They are endowed with the standard norms:

$$\|\mathbf{v}\|_{\mathbf{L}^2(\Omega)} = \left(\sum_{i=1}^{3} \|v_i\|^2_{L^2(\Omega)} \right)^{\frac{1}{2}}, \tag{6.1}$$

$$\|\mathbf{v}\|_{\mathbf{H}^1(\Omega)} = \left(\sum_{i=1}^{3} \|v_i\|^2_{H^1(\Omega)} \right)^{\frac{1}{2}} = \left(\sum_{i=1}^{3} \|v_i\|^2_{L^2(\Omega)} + \sum_{i,j=1}^{3} \left\| \frac{\partial v_i}{\partial x_j} \right\|^2_{L^2(\Omega)} \right)^{\frac{1}{2}}. \tag{6.2}$$

The boldface notation is also adopted to denote the spaces of tensor-valued functions. The corresponding norms in those spaces are defined in a completely analogous manner to (6.1) and (6.2).

For any $f \in L^1(\Omega)$, we denote as $\mathcal{M}_\Omega(f)$ the *mean value* of f in Ω, defined as:

$$\mathcal{M}_\Omega(f) := \frac{1}{\text{meas}(\Omega)} \int_\Omega f \, dV, \tag{6.3}$$

where $\text{meas}(\Omega)$ denotes the measure of the set Ω. In the case of vector-valued or tensor-valued functions, (6.3) is interpreted as the mean value of each component. For instance, if $\mathbf{f}$ takes values in $\mathbb{R}^3$, then $\mathcal{M}_\Omega(\mathbf{f}) = \mathbf{0}$ means that $\mathcal{M}_\Omega(f_i) = 0$ for all $i \in I_3$.

Let I_N denote the set of natural indices from 1 to $N \in \mathbb{N}$:

$$I_N = \{1, 2, \ldots, N\}.$$

USC UNIVERSIDADE DE SANTIAGO DE COMPOSTELA

Using these sets of indices, we introduce the *index transformation* $\gamma : I_3 \times I_3 \to I_6$, which is defined as follows:

$$\gamma(i,j) = \begin{cases} i, & \text{if } i = j, \\ 9 - i - j, & \text{if } i \neq j. \end{cases} \tag{6.4}$$

Notation. *In the sequel, the Einstein summation convention for repeated Latin subscripts is adopted. Moreover, unless otherwise stated, we shall assume that the Latin indices i, j, r, s take arbitrary values in the set $I_3 = \{1, 2, 3\}$. The double contraction of tensors, denoted with a colon, is defined for $\mathbf{A}$ and $\mathbf{B}$ being second order tensors as*

$$\mathbf{A} : \mathbf{B} = A_{ij} B_{ij},$$

whereas for $\mathbb{A}$ being a fourth order tensor, it satisfies that

$$(\mathbb{A} : \mathbf{B})_{ij} = A_{ijrs} B_{rs}.$$

6.2. Linear elasticity

In this section, we address some problems in solid mechanics, which studies how a solid body moves and deforms under the action of forces. Specifically, the scope is restricted to *elastic bodies*, i.e., those materials that return to their rest shape once the applied forces are removed. Rigorously, an elastic body is a material body whose constitutive class is characterised by a response function that depends only on the deformation gradient (see Gurtin, 1982). In particular, we focus in the linear case, where the gradient of the displacement $\mathbf{u} = (u_1, u_2, u_3)^T$ is assumed to be small.

6.2.1. Constitutive law

Let us set the domain Ω as the reference configuration of a linear elastic material and let $\mathbf{x}$ be a generic material point in Ω. Set *Lin* as the set of second order tensors. The linear operator $\mathbb{C}(\mathbf{x}) \in \mathcal{L}(Lin, Lin)$ denotes the fourth order *elasticity tensor*, with $\mathcal{L}(Lin, Lin)$ being the set of continuous linear mappings among the set of second order tensors. The classical constitutive law for linear elasticity, relating the stress and strain associated to the displacement field, can be expressed as

$$\boldsymbol{\sigma}(\mathbf{u}) = \mathbb{C} : \boldsymbol{\varepsilon}(\mathbf{u}), \tag{6.5}$$

where $\boldsymbol{\sigma}(\mathbf{u})$ denotes the *stress tensor* and $\boldsymbol{\varepsilon}(\mathbf{u})$ stands for the *linearised strain tensor*, defined as

$$\boldsymbol{\varepsilon}(\mathbf{u}) = \frac{1}{2}\left(\nabla \mathbf{u} + \nabla \mathbf{u}^T\right).$$

An admissible elasticity tensor satisfies several symmetries (see e.g. Bower, 2009). This constraint, as well as some other hypotheses that are required to ensure the well-posedness of the linear elasticity problem that is introduced below, are collected in the subsequent class of fourth order tensors.

Definition 6.1. *Let $\alpha, \beta \in \mathbb{R}$ such that $\alpha, \beta > 0$. $\mathcal{M}(\alpha, \beta, \mathcal{O})$ denotes the set of fourth order tensors $\mathbb{A} = (A_{ijrs})$ defined in the open set $\mathcal{O}$ such that*

(i) $A_{ijrs} \in L^\infty(\mathcal{O})$.

(ii) $A_{ijrs}(\mathbf{x}) = A_{jirs}(\mathbf{x}) = A_{rsij}(\mathbf{x})$, *a.e. in* $\mathcal{O}$.

(iii) $A_{ijrs}(\mathbf{x}) M_{ij} M_{rs} \geq \alpha M_{ij} M_{ij}$, *a.e. in* $\mathcal{O}$ *for every symmetric matrix* $\mathbf{M} = (M_{ij})$.

(iv) $|\mathbb{A} : \mathbf{M}| \leq \beta |\mathbf{M}|$, *for any matrix* $\mathbf{M}$.

USC UNIVERSIDADE DE SANTIAGO DE COMPOSTELA

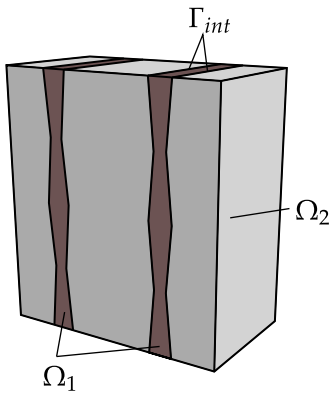


Figure 6.1: Reference configuration Ω composed of two disjoint subdomains Ω_1 and Ω_2.

In the previous definition, we use $|\cdot|$ to denote the following standard norm in the space of square matrices of dimension 3:

$$|\mathbf{M}| = (\mathbf{M} : \mathbf{M})^{\frac{1}{2}}.$$

From now on, for any elasticity tensor $\mathbb{C}$, we assume that there exist $\alpha, \beta > 0$ such that $\mathbb{C} \in \mathcal{M}(\alpha, \beta, \Omega)$. Equivalently, in virtue of the symmetries of the elasticity tensor (see (ii) in Definition 6.1), it can be shown that it is completely defined by 21 independent components (see Bower, 2009). Therefore, using that both the stress and strain tensors are symmetric, the constitutive law (6.5) can be rewritten using *Voigt notation*:

$$\{\boldsymbol{\sigma}\}(\mathbf{u}) = [\mathbf{C}]\{\boldsymbol{\varepsilon}\}(\mathbf{u}), \tag{6.6}$$

where

$$\{\boldsymbol{\sigma}\} = \left(\sigma_{11}, \sigma_{22}, \sigma_{33}, \sigma_{23}, \sigma_{13}, \sigma_{12}\right)^T,$$

$$\{\boldsymbol{\varepsilon}\} = \left(\varepsilon_{11}, \varepsilon_{22}, \varepsilon_{33}, 2\varepsilon_{23}, 2\varepsilon_{13}, 2\varepsilon_{12}\right)^T,$$

$$[\mathbf{C}] = \begin{pmatrix} c_{11} & c_{12} & c_{13} & c_{14} & c_{15} & c_{16} \\ c_{12} & c_{22} & c_{23} & c_{24} & c_{25} & c_{26} \\ c_{13} & c_{23} & c_{33} & c_{34} & c_{35} & c_{36} \\ c_{14} & c_{24} & c_{34} & c_{44} & c_{45} & c_{46} \\ c_{15} & c_{25} & c_{35} & c_{45} & c_{55} & c_{56} \\ c_{16} & c_{26} & c_{36} & c_{46} & c_{56} & c_{66} \end{pmatrix}.$$

The matrix $[\mathbf{C}]$ is known as *stiffness matrix*. Note that, in order to avoid confusion, the components of the stiffness matrix have been written in lower-case, as opposed to those of the elasticity tensor. For convenience, we shall frequently resort to the constitutive law expressed in Voigt notation.

In some applications, it is of interest to rewrite (6.6) as

$$\{\boldsymbol{\varepsilon}\}(\mathbf{u}) = [\mathbf{S}]\{\boldsymbol{\sigma}\}(\mathbf{u}), \tag{6.7}$$

where $[\mathbf{S}] = [\mathbf{C}]^{-1}$ is the *compliance matrix*.

Using the index transformation (6.4), it holds that for $i, j, r, s \in I_3$, the components of the elasticity tensor are related to those of the stiffness matrix as simply $C_{ijrs} = c_{pq}$, where $p = \gamma(i, j)$ and $q = \gamma(r, s)$.

In the ensuing chapters, the body occupying the domain Ω will usually correspond to a piecewise-constant heterogeneous material, being the composition of two or more homogeneous linear elastic materials. In the case of two materials, we consider that the first one occupies a subdomain Ω_1, whereas the second occupies a subdomain Ω_2, such that $\Omega_1 \cap \Omega_2 = \emptyset$ and $\overline{\Omega} = \overline{\Omega}_1 \cup \overline{\Omega}_2$, as depicted in Figure 6.1. Let the components of the stiffness matrices of both materials be denoted by the

constants c^1_{pq} and c^2_{pq}, $p, q \in I_6$. Hence, the entries of the stiffness matrix are such that

$$c_{pq}(\mathbf{x}) = \begin{cases} c^1_{pq}, & \text{if } \mathbf{x} \in \Omega_1, \\ c^2_{pq}, & \text{if } \mathbf{x} \in \Omega_2. \end{cases} \tag{6.8}$$

An important subclass of linear elastic materials are *isotropic materials*, i.e., those linear elastic materials whose properties are the same in all directions. An equivalent way of stating this fact is to say that any plane in the material is a plane of symmetry. In these materials, only two independent coefficients are required to completely characterise the material response (Gurtin, 1982), and the constitutive law (6.5) simplifies to:

$$\boldsymbol{\sigma}(\mathbf{u}) = \lambda \mathrm{tr}(\boldsymbol{\varepsilon}(\mathbf{u}))\mathbf{I} + 2\mu\boldsymbol{\varepsilon}(\mathbf{u}), \tag{6.9}$$

where λ, μ denote the *Lamé parameters* and $\mathbf{I}$ is the identity matrix. The second Lamé parameter μ is frequently known as the *shear modulus*.

As it is customary in engineering, instead of providing the corresponding Lamé parameters to characterise an isotropic elastic material, we shall frequently state its Young's modulus, E, and its Poisson's ratio, ν. The corresponding Lamé parameters are obtained by substitution in the following expressions:

$$\lambda = \frac{E\nu}{(1-2\nu)(1+\nu)}, \qquad \mu = \frac{E}{2(1+\nu)}.$$

In Chapter 9, to obtain a mathematically rigorous alternative to the basic tests presented in Chapter 8, it will be assumed that the material belongs to another class of linear elastic materials that are not isotropic, but have some specific symmetries: *orthotropic* materials. An orthotropic material has three perpendicular symmetry planes at each point in Ω. If these planes are aligned with the coordinate planes, the stiffness matrix defining the behaviour law (6.6) may be written as (see e.g. Ting, 1996):

$$[\mathbf{C}] = \begin{pmatrix} c_{11} & c_{12} & c_{13} & 0 & 0 & 0 \\ c_{12} & c_{22} & c_{23} & 0 & 0 & 0 \\ c_{13} & c_{23} & c_{33} & 0 & 0 & 0 \\ 0 & 0 & 0 & c_{44} & 0 & 0 \\ 0 & 0 & 0 & 0 & c_{55} & 0 \\ 0 & 0 & 0 & 0 & 0 & c_{66} \end{pmatrix},$$

where the material is characterised by only 9 independent coefficients. For an orthotropic material, if the constitutive relationship is expressed using the inverse form (6.7), then the coefficients of the compliance matrix can be defined in terms of the generalised Poisson's ratios, ν_{ij}, Young's modulus, E_i and shear modulus μ_{ij}:

$$[\mathbf{S}] = \begin{pmatrix} 1/E_1 & -\nu_{12}/E_1 & -\nu_{13}/E_1 & 0 & 0 & 0 \\ -\nu_{21}/E_2 & 1/E_2 & -\nu_{23}/E_2 & 0 & 0 & 0 \\ -\nu_{31}/E_3 & -\nu_{32}/E_3 & 1/E_3 & 0 & 0 & 0 \\ 0 & 0 & 0 & 1/\mu_{23} & 0 & 0 \\ 0 & 0 & 0 & 0 & 1/\mu_{13} & 0 \\ 0 & 0 & 0 & 0 & 0 & 1/\mu_{12} \end{pmatrix}. \tag{6.10}$$

These generalised coefficients have an analogous interpretation as the usual Young's modulus, shear modulus and Poisson's ratio. For instance, the Poisson's ratio ν_{12} determines the expansion in the direction $\mathbf{e}_2$ when a uniaxial compression load is applied in the direction $\mathbf{e}_1$ (see Bower, 2009). Note that since the compliance matrix is also symmetric, it holds that $\nu_{ij}/E_i = \nu_{ji}/E_j$.

6.2.2. Infinitesimal rigid motions

In linearised elasticity, an important class of displacements is formed by those displacements that do not induce any deformation of the body occupying the domain Ω, which are known as *infinitesimal*

rigid motions or *displacements*. Since we will seek a displacement field in $\mathbf{H}^1(\Omega)$, we define the space of infinitesimal rigid motions, denoted as $\mathcal{Z}(\Omega)$, as the subsequent closed subspace of $\mathbf{H}^1(\Omega)$:

$$\mathcal{Z}(\Omega) := \{\mathbf{v} \in \mathbf{H}^1(\Omega) : \boldsymbol{\varepsilon}(\mathbf{v}) = \mathbf{0} \text{ in } \Omega\}. \tag{6.11}$$

The lemma that is stated below provides an equivalent characterisation of the space of infinitesimal rigid displacements, yielding that in the particular case of a three-dimensional body, $\mathcal{Z}(\Omega)$ is a finite-dimensional subspace of $\mathbf{H}^1(\Omega)$, with dimension equal to six.

Lemma 6.1. *The space of infinitesimal rigid motions of Ω, $\mathcal{Z}(\Omega)$, can be equivalently defined as*

$$\mathcal{Z}(\Omega) = \{\mathbf{v} \in \mathbf{H}^1(\Omega) : \mathbf{v}(\mathbf{x}) = \mathbf{a} + \mathbf{b} \times \mathbf{x},\ \mathbf{a}, \mathbf{b} \in \mathbb{R}^3\}.$$

Proof. Let $\mathbf{v} \in \mathbf{H}^1(\Omega)$ such that $\mathbf{v} \in \mathcal{Z}(\Omega)$. Hence, $\boldsymbol{\varepsilon}(\mathbf{v}) = \mathbf{0}$ in Ω. The subsequent identity holds for $i, j, r \in I_3$:

$$\frac{\partial^2 v_i}{\partial x_j \partial x_r} = \frac{\partial}{\partial x_j}\varepsilon_{ir}(\mathbf{v}) + \frac{\partial}{\partial x_r}\varepsilon_{ij}(\mathbf{v}) - \frac{\partial}{\partial x_i}\varepsilon_{jr}(\mathbf{v}), \qquad \text{in } D'(\Omega),$$

where $D'(\Omega)$ denotes the dual space of $D(\Omega)$, the space formed by the infinitely differentiable functions defined in Ω with compact support contained in Ω.

Since $\varepsilon_{ij}(\mathbf{v}) = 0$, it follows that

$$\frac{\partial^2 v_i}{\partial x_j \partial x_r} = 0, \qquad \text{in } D'(\Omega).$$

In virtue of a classical result (Schwartz, 1966, p. 60), provided that Ω is connected, v_i is either constant or a polynomial of degree 1 in x_j:

$$v_i = a_i + b_{ij} x_j, \tag{6.12}$$

where $\mathbf{a} = (a_i) \in \mathbb{R}^3$ and $\mathbf{B} = (b_{ij}) \in Lin$.

Since $\varepsilon_{ij}(\mathbf{v}) = 0$, then $b_{ii} = 0$ and $b_{ij} = -b_{ij}$. Therefore, $\mathbf{B}$ belongs to Skw, the set of all skew second-order tensors.

Equation (6.12) may be equivalently stated as $v_i = a_i + (\mathbf{b} \times \mathbf{x})_i$, where the vector $\mathbf{b} \in \mathbb{R}^3$ is defined as $\mathbf{b} = (-b_{23}, b_{13}, -b_{12})^T$. Hence, the desired result directly follows since, conversely, any $\mathbf{v}$ such that $\mathbf{v} = \mathbf{a} + \mathbf{b} \times \mathbf{x}$ for $\mathbf{a}, \mathbf{b} \in \mathbb{R}^3$ clearly satisfies that $\boldsymbol{\varepsilon}(\mathbf{v}) = \mathbf{0}$. □

The first part of the previous proof shows that $\mathcal{Z}(\Omega)$ can be also defined as (see Ciarlet, 2010, Th. 2.2):

$$\mathcal{Z}(\Omega) = \{\mathbf{v} \in \mathbf{H}^1(\Omega) : \mathbf{v}(\mathbf{x}) = \mathbf{B}\mathbf{x} + \mathbf{a},\ \text{a.e. on } \mathbf{x} \in \Omega, \mathbf{B} \in Skw, \mathbf{a} \in \mathbb{R}^3\}. \tag{6.13}$$

Remark 6.1. *A basis for $\mathcal{Z}(\Omega)$, $\{\boldsymbol{\xi}^p\}$, with $p \in I_6$, may be given in terms of the following set*

$$\{\mathbf{e}_1, \mathbf{e}_2, \mathbf{e}_3, \mathbf{e}_1 \times \mathbf{x}, \mathbf{e}_2 \times \mathbf{x}, \mathbf{e}_3 \times \mathbf{x}\}. \tag{6.14}$$

Note that this basis is neither orthogonal nor unitary with respect to the standard $\mathbf{L}^2(\Omega)$ inner product.

The subsequent classical and well-known Korn's inequality, which we state below for the sake of completeness, allows to obtain the existence and uniqueness of linear elasticity variational problems when defined in suitable spaces that have been purged of infinitesimal rigid motions.

Theorem 6.1. *Let V be a closed subspace of $\mathbf{H}^1(\Omega)$ such that $V \cap \mathcal{Z}(\Omega) = \{\mathbf{0}\}$. Then, there exists $C > 0$ such that*

$$\|\mathbf{v}\|_{\mathbf{H}^1(\Omega)} \leq C \|\boldsymbol{\varepsilon}(\mathbf{v})\|_{\mathbf{L}^2(\Omega)}, \qquad \forall \mathbf{v} \in V.$$

USC UNIVERSIDADE DE SANTIAGO

Proof. See Oleïnik et al. (1992, Th. 2.5). □

6.2.3. Model problem

In this section, we introduce a model problem in linear elasticity that we shall use for several different choices of the computational domain, boundary conditions and data. A weak formulation of the problem, suitable for the numerical approximation of its solution using a standard finite element method is obtained. Lastly, the existence and uniqueness of solution to such problem is briefly discussed.

Let us assume that the domain Ω is such that its boundary, $\partial\Omega$, can be partitioned in two disjoint closed sets Γ_D and Γ_N, with $\text{meas}(\Gamma_D) > 0$. Let $\mathbf{f}$ denote the density of applied body forces in Ω and let $\mathbf{g}$ be the density of applied surface forces on Γ_N.

Assuming that the material body is linear elastic and that it is in static equilibrium with the applied forces, using the classic axioms of continuum mechanics it can be derived that the momentum conservation equation in the reference configuration Ω simply becomes (Ciarlet, 1988)

$$-\text{Div}(\boldsymbol{\sigma}(\mathbf{u})) = \mathbf{f}, \qquad \text{in } \Omega,$$

where the stress tensor $\boldsymbol{\sigma}$ follows the constitutive relation (6.5). Moreover, provided that the density of applied forces on Γ_N is $\mathbf{g}$, it must hold that

$$\boldsymbol{\sigma}(\mathbf{u})\mathbf{n} = \mathbf{g}, \qquad \text{on } \Gamma_N,$$

where $\mathbf{n}$ is the outward-pointing unit normal vector.

As discussed previously, the body may be the composition of two or more elastic materials with different properties. In the particular setting of two materials occupying subdomains Ω_1 and Ω_2, such that $\overline{\Omega} = \overline{\Omega}_1 \cup \overline{\Omega}_2$, the interface Γ_{int} corresponds to the set $\Gamma_{int} = \partial\Omega_1 \cap \partial\Omega_2$, as depicted in Figure 6.1. On Γ_{int}, the materials are assumed to be perfectly bonded to each other. This implies that the displacement is continuous and that the principle of action-reaction holds, i.e., that:

$$\begin{cases} \boldsymbol{\sigma}^1(\mathbf{u}^1)\mathbf{n}^1 = -\boldsymbol{\sigma}^2(\mathbf{u}^2)\mathbf{n}^2, \\ \mathbf{u}^1 = \mathbf{u}^2, \end{cases} \quad \text{on } \Gamma_{int}, \tag{6.15}$$

where the superscripts denote the restrictions of the involved fields to the subdomains Ω_1 and Ω_2. Also, note that $\mathbf{n}_1 = -\mathbf{n}_2$. For the sake of simplicity, in the rest of the manuscript, conditions (6.15) are implicitly assumed to hold without explicitly stating so.

To complete the problem formulation, a Dirichlet boundary condition is set on Γ_D. In particular, we impose that the displacement $\mathbf{u}$ is such that $\mathbf{u} = \mathbf{u}_D$ on Γ_D. We assume that there is a *lifting* of this data $R_{\mathbf{u}} \in \mathbf{H}^1(\Omega)$ such that $R_{\mathbf{u}}\big|_{\Gamma_D} = \mathbf{u}_D$. Putting all these observations together, the subsequent model problem for the linearised elasticity system is obtained:

Problem $(\mathcal{P})$. Find $\mathbf{u}$ such that:

$$-\text{Div}(\boldsymbol{\sigma}(\mathbf{u})) = \mathbf{f}, \qquad \text{in } \Omega, \tag{6.16}$$

$$\boldsymbol{\sigma}(\mathbf{u}) = \mathbb{C} : \boldsymbol{\varepsilon}(\mathbf{u}), \qquad \text{in } \Omega, \tag{6.17}$$

$$\mathbf{u} = \mathbf{u}_D, \qquad \text{on } \Gamma_D,$$

$$\boldsymbol{\sigma}(\mathbf{u})\mathbf{n} = \mathbf{g}, \qquad \text{on } \Gamma_N. \tag{6.18}$$

If the density of volume forces $\mathbf{f}$ and the density of applied forces $\mathbf{g}$ are such that $\mathbf{f} \in \mathbf{L}^2(\Omega)$ and $\mathbf{g} \in \mathbf{L}^2(\Gamma_N)$, a weak formulation of Problem $(\mathcal{P})$ is obtained by multiplying equation (6.16) by a test function $\mathbf{v} \in \mathbf{H}^1_{0,\Gamma_D}(\Omega)$ and integrating in Ω. Note that $\mathbf{H}^1_{0,\Gamma_D}(\Omega)$ denotes the subspace of $\mathbf{H}^1(\Omega)$ formed by those functions with zero trace on Γ_D, i.e., $\mathbf{H}^1_{0,\Gamma_D}(\Omega) = \{\mathbf{v} \in \mathbf{H}^1(\Omega) \mid \mathbf{v} = \mathbf{0} \text{ on } \Gamma_D\}$. Then, application of the Gauss Theorem leads to

$$\int_\Omega \boldsymbol{\sigma}(\mathbf{u}) : \nabla\mathbf{v}\, dV - \int_{\partial\Omega} \boldsymbol{\sigma}(\mathbf{u})\mathbf{n} \cdot \mathbf{v}\, dA = \int_\Omega \mathbf{f} \cdot \mathbf{v}\, dV, \qquad \forall \mathbf{v} \in \mathbf{H}^1_{0,\Gamma_D}(\Omega). \tag{6.19}$$

USC UNIVERSIDADE DE SANTIAGO DE COMPOSTELA

Furthermore, note that

$$\nabla\mathbf{v} = \frac{1}{2}(\nabla\mathbf{v} + \nabla\mathbf{v}^T) + \frac{1}{2}(\nabla\mathbf{v} - \nabla\mathbf{v}^T) = \boldsymbol{\varepsilon}(\mathbf{v}) + \boldsymbol{\omega}(\mathbf{v}),$$

where $\boldsymbol{\omega}(\mathbf{v}) := 1/2(\nabla\mathbf{v} - \nabla\mathbf{v}^T)$ is known as the *rotational tensor* associated to $\mathbf{v}$. By definition, $\boldsymbol{\omega}(\mathbf{v}) \in Skw$. Then, provided that $\boldsymbol{\varepsilon}(\mathbf{v})$ is symmetric and that the inner product of a symmetric and a skew-symmetric tensor is zero, it follows that

$$\boldsymbol{\sigma}(\mathbf{u}) : \nabla\mathbf{v} = \boldsymbol{\sigma}(\mathbf{u}) : (\boldsymbol{\varepsilon}(\mathbf{v}) + \boldsymbol{\omega}(\mathbf{v})) = \boldsymbol{\sigma}(\mathbf{u}) : \boldsymbol{\varepsilon}(\mathbf{v}).$$

Hence, from (6.19), using the constitutive law (6.17) and the boundary condition (6.18), we find the following variational formulation.

Problem $(\mathcal{VP})$. Find $\mathbf{u} \in \mathbf{H}^1(\Omega)$ such that $\mathbf{u} = \mathbf{u}_D$ on Γ_D and

$$a(\mathbf{u}, \mathbf{v}) = l(\mathbf{v}), \qquad \forall \mathbf{v} \in \mathbf{H}^1_{0,\Gamma_D}(\Omega),$$

where the bilinear form $a(\cdot,\cdot)$ and the functional $l(\mathbf{v})$ are defined as follows

$$a(\mathbf{u}, \mathbf{v}) = \int_\Omega (\mathbb{C} : \boldsymbol{\varepsilon}(\mathbf{u})) : \boldsymbol{\varepsilon}(\mathbf{v})\, dV, \tag{6.20}$$

$$l(\mathbf{v}) = \int_\Omega \mathbf{f} \cdot \mathbf{v}\, dV + \int_{\Gamma_N} \mathbf{g} \cdot \mathbf{v}\, dA. \tag{6.21}$$

Remark 6.2. *The bilinear form (6.20) is symmetric. Indeed, since $\mathbb{C} \in \mathcal{M}(\alpha, \beta, \Omega)$ for some $\alpha, \beta > 0$, it holds that*

$$(\mathbb{C} : \boldsymbol{\varepsilon}(\mathbf{u})) : \boldsymbol{\varepsilon}(\mathbf{v}) = C_{ijrs}\varepsilon_{rs}(\mathbf{u})\varepsilon_{ij}(\mathbf{v}) = \varepsilon_{rs}(\mathbf{u})C_{rsij}\varepsilon_{ij}(\mathbf{v}) = \boldsymbol{\varepsilon}(\mathbf{u}) : (\mathbb{C} : \boldsymbol{\varepsilon}(\mathbf{v})),$$

and hence $a(\mathbf{u}, \mathbf{v}) = a(\mathbf{v}, \mathbf{u})$.

Given the assumptions on the data, it is a well-known fact that Problem $(\mathcal{VP})$ has a unique solution. Considering the lifting of the boundary data $R_\mathbf{u} \in \mathbf{H}^1(\Omega)$, an auxiliary variational equation is obtained to find $\mathbf{u}^0 = \mathbf{u} - R_\mathbf{u} \in \mathbf{H}^1_{0,\Gamma_D}(\Omega)$. This equation has a unique solution in virtue of the Lax-Milgram Theorem, as the resulting bilinear form is coercive as a consequence of Theorem 6.1.

6.3. Pure Neumann boundary condition

In this section, we address the special case when $\Gamma_D = \emptyset$ in Problem $(\mathcal{P})$. Then, $\Gamma_N = \partial\Omega$ and the boundary condition imposed to the problem is a pure Neumann one. This specific situation is often referred to as the *pure traction* linear elasticity problem and, as it is subsequently discussed, it turns out to be an ill-posed problem. Specifically, the problem only has a solution if the applied forces satisfy a *compatibility condition* and, if it has a solution, it has infinitely many.

First, we pose the strong and weak formulations of the pure Neumann problem, which are analogous to those for Problem $(\mathcal{P})$. Then, following a similar framework to that detailed in Brenner & Scott (2008) for a planar isotropic setting, we focus on the issue of existence and uniqueness of solution, finding a suitable function space where the problem is well-posed. Subsequently, a methodology to constrain the problem to seek the solution in such space is introduced, using a Lagrange multiplier. To this end, we loosely follow the approach presented in Bochev & Lehoucq (2011). Lastly, other methodologies to solve the pure Neumann problem are discussed and their numerical performance is compared to that of the proposed approach using a couple of manufactured solution tests.

The methodology presented in this section will be further applied to deal with the so-called *basic tests* that are proposed in Chapter 8, where various problems that are introduced to obtain a homogenised equivalent material have a pure Neumann boundary condition.

6.3.1. Existence and uniqueness of solution

From the model problem $(\mathcal{P})$, we obtain the pure Neumann elasticity problem by setting $\Gamma_D = \emptyset$. The corresponding variational formulation is obtained following an analogous procedure, considering a test function $\mathbf{v} \in \mathbf{H}^1(\Omega)$.

Problem $(\mathcal{P}_{PN})$. Find $\mathbf{u}$ such that:

$$-\operatorname{Div}(\boldsymbol{\sigma}(\mathbf{u})) = \mathbf{f}, \qquad \text{in } \Omega, \tag{6.22}$$

$$\boldsymbol{\sigma}(\mathbf{u}) = \mathbb{C} : \boldsymbol{\varepsilon}(\mathbf{u}), \qquad \text{in } \Omega,$$

$$\boldsymbol{\sigma}(\mathbf{u})\mathbf{n} = \mathbf{g}, \qquad \text{on } \partial\Omega. \tag{6.23}$$

Problem $(\mathcal{VP}_{PN})$. Find $\mathbf{u} \in \mathbf{H}^1(\Omega)$ such that:

$$a(\mathbf{u}, \mathbf{v}) = l(\mathbf{v}), \qquad \forall \mathbf{v} \in \mathbf{H}^1(\Omega), \tag{6.24}$$

where $a(\cdot,\cdot)$ is the bilinear form defined in (6.20) and $l(\cdot)$ is the subsequent linear functional:

$$l(\mathbf{v}) = \int_\Omega \mathbf{f} \cdot \mathbf{v}\, dV + \int_{\partial\Omega} \mathbf{g} \cdot \mathbf{v}\, dA. \tag{6.25}$$

As mentioned above, Problem $(\mathcal{P}_{PN})$ as well as its weak counterpart $(\mathcal{VP}_{PN})$ are clearly ill-posed: if $\mathbf{u}$ is a displacement field such that it is a solution to $(\mathcal{VP}_{PN})$, then $\mathbf{u} + \mathbf{z}$ is also a solution for any $\mathbf{z} \in \mathcal{Z}(\Omega)$, where $\mathcal{Z}(\Omega)$ is the space of infinitesimal rigid displacements of Ω, defined in (6.11). Therefore, if the problem has a solution, such solution is not unique.

To obtain a space where the problem has a unique solution, we introduce the space $\mathcal{W}(\Omega)$, defined as the following closed subspace of $\mathbf{H}^1(\Omega)$:

$$\mathcal{W}(\Omega) := \left\{ \mathbf{v} \in \mathbf{H}^1(\Omega) : \int_\Omega \mathbf{v}\, dV = \mathbf{0}, \int_\Omega \boldsymbol{\omega}(\mathbf{v})\, dV = \mathbf{0} \right\},$$

where we recall that $\boldsymbol{\omega}(\mathbf{v}) = \frac{1}{2}(\nabla\mathbf{v} - \nabla\mathbf{v}^T)$.

As shown by the subsequent result, any function in $\mathbf{H}^1(\Omega)$ can be decomposed as the sum of an infinitesimal rigid displacement and an element of $\mathcal{W}(\Omega)$.

Lemma 6.2. *Let $\mathbf{v} \in \mathbf{H}^1(\Omega)$. Then, there exists $(\mathbf{w}, \mathbf{z}) \in \mathcal{W}(\Omega) \times \mathcal{Z}(\Omega)$ such that*

$$\mathbf{v} = \mathbf{w} + \mathbf{z}.$$

Proof. Assume that $\mathbf{v} \in \mathbf{H}^1(\Omega)$ and consider the tensor field $\boldsymbol{\omega}(\mathbf{v}) \in \mathbf{L}^2(\Omega)$. Let $\mathbf{a} \in \mathbb{R}^3$ and $\mathbf{B} \in \mathit{Lin}$ such that

$$\mathbf{B} = \mathcal{M}_\Omega(\boldsymbol{\omega}(\mathbf{v})), \qquad \mathbf{a} = \mathcal{M}_\Omega(\mathbf{v} - \mathbf{B}\mathbf{x}).$$

Clearly, it holds that $\mathbf{B} \in \mathit{Skw}$. Recall that $\mathcal{Z}(\Omega)$ can be defined as (6.13) and set $\mathbf{z} \in \mathcal{Z}(\Omega)$ such that $\mathbf{z} = \mathbf{B}\mathbf{x} + \mathbf{a}$. Moreover, let $\mathbf{w} \in \mathbf{H}^1(\Omega)$ be defined as $\mathbf{w} = \mathbf{v} - \mathbf{z}$. Then, since $\boldsymbol{\omega}(\mathbf{z}) = \mathbf{B}$, it follows that

$$\int_\Omega \mathbf{w}\, dV = \int_\Omega \mathbf{v} - (\mathbf{B}\mathbf{x} + \mathbf{a})\, dV = \mathbf{0},$$

$$\int_\Omega \boldsymbol{\omega}(\mathbf{w})\, dV = \int_\Omega \boldsymbol{\omega}(\mathbf{v})\, dV - \int_\Omega \boldsymbol{\omega}(\mathbf{z})\, dV = \mathbf{0}.$$

Consequently, $\mathbf{w} \in \mathcal{W}(\Omega)$ and $\mathbf{v} = \mathbf{w} + \mathbf{z}$, with $\mathbf{z} \in \mathcal{Z}(\Omega)$.

□

Remark 6.3. *Bearing the definition of the rotational tensor $\omega(\mathbf{v})$, it is established that the space $\mathcal{W}(\Omega)$ can be equivalently characterised as*

$$\mathcal{W}(\Omega) := \left\{ \mathbf{v} \in \mathbf{H}^1(\Omega) : \int_\Omega \mathbf{v}\, dV = \mathbf{0}, \int_\Omega \mathit{curl}\, \mathbf{v}\, dV = \mathbf{0} \right\}.$$

As a consequence of Lemma 6.2, given that $\mathcal{W}(\Omega) \cap \mathcal{Z}(\Omega) = \{\mathbf{0}\}$, we may assert that $\mathbf{H}^1(\Omega) = \mathcal{W}(\Omega) \oplus \mathcal{Z}(\Omega)$. Note that this is only to be understood in the algebraic sense, since these subspaces are not orthogonal.

The following result, analogous to that presented in Brenner & Scott (2008, p. 319) for a planar and isotropic setting, allows to establish the existence and uniqueness of solution to Problem $(\mathcal{VP}_{PN})$ in the space $\mathcal{W}(\Omega)$. In addition, it shows that the problem is *solvable* (i.e., there is a solution, not necessarily unique) if and only if the data $\mathbf{f}$ and $\mathbf{g}$ satisfy a certain compatibility condition.

Theorem 6.2. *Let* $\mathbf{f} \in \mathbf{L}^2(\Omega)$, $\mathbf{g} \in \mathbf{L}^2(\partial\Omega)$ *and set* $\mathbb{C} \in \mathcal{M}(\alpha, \beta, \Omega)$ *for some* $\alpha, \beta > 0$. *Then, Problem* $(\mathcal{VP}_{PN})$ *is solvable if and only if the following compatibility condition holds*

$$l(\mathbf{z}) = \int_\Omega \mathbf{f} \cdot \mathbf{z}\, dV + \int_{\partial\Omega} \mathbf{g} \cdot \mathbf{z}\, dA = 0, \qquad \forall \mathbf{z} \in \mathcal{Z}(\Omega). \tag{6.26}$$

Furthermore, if the problem is solvable, the solution is unique in the space $\mathcal{W}(\Omega)$.

Proof. Let us assume that the problem is solvable and let $\mathbf{u} \in \mathbf{H}^1(\Omega)$ be a solution. Then, for any test function $\mathbf{z} \in \mathcal{Z}(\Omega)$, given that $\boldsymbol{\varepsilon}(\mathbf{z}) = \mathbf{0}$, it follows that

$$a(\mathbf{u}, \mathbf{z}) = 0.$$

Therefore, from (6.24) we conclude that if a solution exists, then

$$l(\mathbf{z}) = \int_\Omega \mathbf{f} \cdot \mathbf{z}\, dV + \int_{\partial\Omega} \mathbf{g} \cdot \mathbf{z}\, dA = 0, \qquad \forall \mathbf{z} \in \mathcal{Z}(\Omega),$$

and the compatibility condition (6.26) holds.

Reciprocally, assume that the data $\mathbf{f}$ and $\mathbf{g}$ are such that the compatibility condition (6.26) is satisfied. Then, consider the variational problem restricted to the space $\mathcal{W}(\Omega)$. In such setting, in virtue of Theorem 6.1 it holds that the bilinear form $a(\mathbf{u}, \mathbf{v})$ is $\mathcal{W}(\Omega)$-coercive.

Furthermore, since $\mathbf{f} \in \mathbf{L}^2(\Omega)$ and $\mathbf{g} \in \mathbf{L}^2(\partial\Omega)$, then the linear functional $l(\cdot)$ is continuous in $\mathbf{H}^1(\Omega)$. In addition, since the elasticity tensor $\mathbb{C}$ belongs to $\mathcal{M}(\alpha, \beta, \Omega)$, then the continuity of the bilinear form $a(\cdot, \cdot)$ follows directly from (iv) in Definition 6.1. Thus, the Lax Milgram theorem ensures that there exists a unique $\widetilde{\mathbf{u}} \in \mathcal{W}(\Omega)$ such that

$$a(\widetilde{\mathbf{u}}, \mathbf{w}) = l(\mathbf{w}), \qquad \forall \mathbf{w} \in \mathcal{W}(\Omega).$$

On the other hand, it holds that

$$a(\widetilde{\mathbf{u}}, \mathbf{z}) = l(\mathbf{z}) = 0, \qquad \forall \mathbf{z} \in \mathcal{Z}(\Omega),$$

provided that $\boldsymbol{\varepsilon}(\mathbf{z}) = \mathbf{0}$ and the compatibility condition holds.

Since by Lemma 6.2, any $\mathbf{v} \in \mathbf{H}^1(\Omega)$ can be presented as $\mathbf{v} = \mathbf{w} + \mathbf{z}$, with $\mathbf{w} \in \mathcal{W}(\Omega), \mathbf{z} \in \mathcal{Z}(\Omega)$, it follows that

$$a(\widetilde{\mathbf{u}}, \mathbf{v}) = l(\mathbf{v}).$$

Thereby, $\widetilde{\mathbf{u}}$ is a solution to Problem $(\mathcal{VP}_{PN})$. □

Let $\mathbf{H}^1(\Omega)/\mathcal{Z}(\Omega)$ denote the quotient space formed by the equivalence classes $[\mathbf{v}]$ of functions in $\mathbf{H}^1(\Omega)$ with respect to the relation

$$\mathbf{v}_1 \simeq \mathbf{v}_2 \iff \mathbf{v}_1 - \mathbf{v}_2 \in \mathcal{Z}(\Omega), \qquad \mathbf{v}_1, \mathbf{v}_2 \in \mathbf{H}^1(\Omega).$$

The space $\mathbf{H}^1(\Omega)/\mathcal{Z}(\Omega)$ is endowed with the norm

$$\|[\mathbf{v}]\|_{\mathbf{H}^1(\Omega)/\mathcal{Z}(\Omega)} = \inf_{\mathbf{z} \in \mathcal{Z}(\Omega)} \|\mathbf{v} - \mathbf{z}\|_{\mathbf{H}^1(\Omega)}.$$

In $\mathbf{H}^1(\Omega)/\mathcal{Z}(\Omega)$, the following result holds as a consequence of Theorem 6.2.

Corollary 6.1. *Let the hypotheses of Theorem 6.2 hold. Then, if Problem* $(\mathcal{VP}_{PN})$ *is solvable, its solution is unique in the quotient space* $\mathbf{H}^1(\Omega)/\mathcal{Z}(\Omega)$.

Proof. From Theorem 6.2, if Problem $(\mathcal{VP}_{PN})$ has a solution, it is unique in $\mathcal{W}(\Omega)$. Let $\mathbf{u} \in \mathcal{W}(\Omega)$ be that solution. Hence $\widetilde{\mathbf{u}} = \mathbf{u} + \mathbf{z}, \mathbf{z} \in \mathcal{Z}(\Omega)$ is also a solution in $\mathbf{H}^1(\Omega)$. Consequently, $[\mathbf{u}]$ is a solution in $\mathbf{H}^1(\Omega)/\mathcal{Z}(\Omega)$.

Lastly, if there were two different solutions $[\mathbf{v}_1]$, $[\mathbf{v}_2]$ in $\mathbf{H}^1(\Omega)/\mathcal{Z}(\Omega)$, then $[\mathbf{v}_1 - \mathbf{v}_2] \neq [\mathbf{0}]$ and there exist $\mathbf{w}_1 \neq \mathbf{w}_2$ in $\mathcal{W}(\Omega)$ such that $\mathbf{v}_1 = \mathbf{w}_1 + \mathbf{z}$, $\mathbf{v}_2 = \mathbf{w}_2 + \mathbf{z}$. Thus, both $\mathbf{w}_1$ and $\mathbf{w}_2$ satisfy (6.24) in $\mathcal{W}(\Omega)$, which is a contradiction with the fact that the solution is unique in $\mathcal{W}(\Omega)$. □

Remark 6.4. *Since $\mathcal{Z}(\Omega)$ is a closed subspace of $\mathbf{H}^1(\Omega)$, the mapping $\varphi(\mathbf{v}) = [\mathbf{v}]$, defined in the orthogonal complement of the space of infinitesimal rigid motions, $\mathcal{Z}(\Omega)^\perp$, is an isometric isomorphism between $\mathcal{Z}^\perp(\Omega)$ and $\mathbf{H}^1(\Omega)/\mathcal{Z}(\Omega)$. Hence, the solution is unique in this space as well, in virtue of Corollary 6.1.*

The compatibility condition (6.26) is established with respect to the space $\mathcal{Z}(\Omega)$. Equivalently, we may consider this condition, but written in terms of the data themselves, considering $\mathbf{f} \in \mathbf{L}^2(\Omega)$ and $\mathbf{g} \in \mathbf{L}^2(\partial\Omega)$ such that:

$$\int_\Omega f_i \, dV + \int_{\partial\Omega} g_i \, dA = 0, \tag{6.27}$$

$$\int_\Omega (\mathbf{f} \times \mathbf{x})_i \, dV + \int_{\partial\Omega} (\mathbf{g} \times \mathbf{x})_i \, dA = 0, \tag{6.28}$$

that is, the resulting of the applied forces and momentum should be both null. Whenever both (6.27) and (6.28) are satisfied, it directly follows that the compatibility condition (6.26) holds taking into account the basis of $\mathcal{Z}(\Omega)$ defined in (6.14). The converse is also true.

As established in this result and in accordance with the prior discussion, we remark that the solution of $(\mathcal{VP}_{PN})$ in $\mathbf{H}^1(\Omega)$ is not unique even if the compatibility condition (6.26) is satisfied. However, this solution is unique whenever $\mathbf{u}$ lies in the subspace $\mathcal{W}(\Omega)$ or within the quotient space $\mathbf{H}^1(\Omega)/\mathcal{Z}(\Omega)$. Thus, in order to have a well-posed formulation, we seek a solution of the subsequent problem.

Problem $(\mathcal{VP}_{PN})_{\mathcal{W}}$. Find $\mathbf{u} \in \mathcal{W}(\Omega)$ such that:

$$a(\mathbf{u}, \mathbf{v}) = l(\mathbf{v}), \qquad \forall \mathbf{v} \in \mathbf{H}^1(\Omega),$$

where $a(\cdot,\cdot)$ and $l(\cdot)$ are the bilinear form and linear functional defined in (6.20) and (6.25), respectively, with the data $\mathbf{f}$ and $\mathbf{g}$ in $l(\cdot)$ satisfying the compatibility conditions (6.27) and (6.28).

6.3.2. Saddle point formulation

The variational problem $(\mathcal{VP}_{PN})_{\mathcal{W}}$ is not suitable for its numerical discretisation using a standard finite element method. Specifically, note that the usual families of finite dimension function spaces used to obtain a discrete formulation of the problem, such as the globally continuous piecewise polynomials, are not embedded in the space in which the solution of the problem is unique, $\mathcal{W}(\Omega)$. Thus, it is not straightforward to obtain an internal approximation of such space.

In this section, in order to weakly impose the constraint that the solution belongs to $\mathcal{W}(\Omega)$, a framework that poses Problem $(\mathcal{VP}_{PN})_{\mathcal{W}}$ as a saddle point problem with unique solution is developed. With this purpose, a Lagrange multiplier is used. The approach is similar to that discussed in Bochev & Lehoucq (2011), where the same functional was used to set the constraint on the solution to a linear elasticity problem with a pure Neumann boundary. A similar procedure was also detailed in Kuchta et al. (2019), where instead of $\mathcal{W}(\Omega)$, the Lagrange multiplier was used to seek a solution in the orthogonal complement $\mathcal{Z}(\Omega)^\perp$.

Provided that the bilinear form (6.20) is symmetric (see Remark 6.2), Problem $(\mathcal{VP}_{PN})_{\mathcal{W}}$ is equivalent to the subsequent minimisation problem (see e.g. Quarteroni, 2009):

Problem $(\mathcal{MP}_{PN})_{\mathcal{W}}$. Find $\mathbf{u} \in \mathcal{W}(\Omega)$ such that:

$$J(\mathbf{u}) = \inf_{\mathbf{v} \in \mathcal{W}(\Omega)} J(\mathbf{v}), \tag{6.29}$$

where the functional $J \in V'$ is defined as

$$J(\mathbf{v}) = \frac{1}{2} a(\mathbf{v}, \mathbf{v}) - l(\mathbf{v}),$$

being V' the dual of the space $V = \mathbf{H}^1(\Omega)$. Given that the solution to Problem $(\mathcal{VP}_{PN})_{\mathcal{W}}$ is unique in $\mathcal{W}(\Omega)$, (6.29) has a unique minimiser.

USC

Since we seek a solution in the space $\mathcal{W}(\Omega)$, instead of directly defining the problem in this space, we consider the minimisation problem (6.29) with the constraint that the solution must belong to $\mathcal{W}(\Omega)$. With this purpose, the space $Q = \mathbb{R}^6$ is introduced, endowed with standard euclidean norm $\|\cdot\|_Q$. We define the linear operator $\mathcal{B} : V \to Q'$:

$$\mathcal{B}\mathbf{v} = \left(\int_\Omega v_1 \, dV, \int_\Omega v_2 \, dV, \int_\Omega v_3 \, dV, \int_\Omega (\text{curl } \mathbf{v})_1 \, dV, \int_\Omega (\text{curl } \mathbf{v})_2 \, dV, \int_\Omega (\text{curl } \mathbf{v})_3 \, dV \right). \tag{6.30}$$

Remark 6.5. *Note that, in virtue of Remark 6.3,* $\ker(\mathcal{B}) = \mathcal{W}(\Omega)$. *Also, recall the basis of* $\mathcal{Z}(\Omega)$ *introduced in (6.14). Hence, for any* $\mathbf{z} \in \mathcal{Z}(\Omega)$, *we write that*

$$\mathbf{z} = \sum_{p=1}^{6} \kappa_p \boldsymbol{\xi}^p,$$

where $\boldsymbol{\xi}^p$ *denote the vector fields composing (6.14) and* $\kappa_p \in \mathbb{R}$ *the coefficients with respect to the basis, with* $p \in I_6$.

Set $\mathbf{q} \in Q$. *Then, we can explicitly establish the unique* $\mathbf{z} \in \mathcal{Z}(\Omega)$ *such that* $\mathcal{B}\mathbf{z} = \mathbf{q}$ *in terms of the basis functions* $\{\boldsymbol{\xi}^p\}$. *Indeed, let* $\mathbf{p}^c$ *denote the centroid or geometric centre of the domain* Ω*:*

$$\mathbf{p}^c = \frac{1}{meas(\Omega)} \int_\Omega \mathbf{x} \, dV.$$

Choosing the following values of the coefficients κ_p, *it holds that* $\mathcal{B}\mathbf{z} = \mathbf{q}$*:*

$$\kappa_i = \frac{1}{meas(\Omega)} \begin{cases} q_i + \dfrac{1}{2}(\mathbf{p}^c \times \widetilde{\mathbf{q}})_i, & \text{if } 1 \leq i \leq 3, \\ \dfrac{1}{2} q_i, & \text{if } 4 \leq i \leq 6, \end{cases} \tag{6.31}$$

where $\widetilde{\mathbf{q}} = (q_4, q_5, q_6)^T$.

Using the operator defined in (6.30), the following constrained minimisation problem is set.

Problem $(\mathcal{MP}_{PN})_{\mathcal{C}}$. Find $\mathbf{u} \in V$ such that:

$$J(\mathbf{u}) = \inf_{\mathbf{v} \in V} J(\mathbf{v}),$$
$$\text{s.t. } \mathcal{B}\mathbf{u} = \mathbf{0}.$$

6.3.3. Existence and uniqueness of solution to the saddle point problem

The operator $\mathcal{B}$ induces the bilinear form $b(\cdot, \cdot) : V \times Q \to \mathbb{R}$, defined as follows

$$b(\mathbf{v}, \mathbf{q}) = \langle \mathcal{B}\mathbf{v}, \mathbf{q} \rangle_{Q',Q} = \mathcal{B}\mathbf{v} \cdot \mathbf{q}. \tag{6.32}$$

From (6.32), we obtain the subsequent saddle point problem, where $\mathbf{q}$ plays the role of a Lagrange multiplier to impose the constraint that $\mathbf{u}$ belongs to $\mathcal{W}(\Omega)$.

Problem $(\mathcal{LP}_{PN})$. Find $(\mathbf{u}, \mathbf{p}) \in V \times Q$ such that:

$$a(\mathbf{u}, \mathbf{v}) + b(\mathbf{v}, \mathbf{p}) = l(\mathbf{v}), \qquad \forall \mathbf{v} \in V, \tag{6.33}$$
$$b(\mathbf{u}, \mathbf{q}) = 0, \qquad \forall \mathbf{q} \in Q. \tag{6.34}$$

We now discuss the existence and uniqueness of solution to Problem $(\mathcal{LP}_{PN})$. Two auxiliary estimates that are used in the sequel to establish the result are introduced. The first one concerns the continuity of the operator $\mathcal{B}$, whereas the second involves a bound in the $\mathbf{L}^2(\Omega)$ norm of the divergence.

Lemma 6.3. *Let $V = \mathbf{H}^1(\Omega)$ and $Q = \mathbb{R}^6$. The linear operator $\mathcal{B} : V \to Q'$, defined in (6.30), is continuous.*

Proof. Set $\mathbf{v} \in V$. Identifying the spaces Q' and Q, we consider $\mathbf{q} \in Q$ such that $\mathbf{q} = \mathcal{B}\mathbf{v}$ and apply the Cauchy-Schwarz inequality to obtain

$$\begin{aligned} \|\mathcal{B}\mathbf{v}\|_{Q'}^2 = \|\mathbf{q}\|_Q^2 = \sum_{i=1}^{6} \mathbf{q}_i^2 = \sum_{i=1}^{3} \left(\int_\Omega v_i \, dV \right)^2 + \sum_{j=1}^{3} \left(\int_\Omega (\text{curl } \mathbf{v})_j \, dV \right)^2 \\ \leq \text{meas}(\Omega) \left(\sum_{i=1}^{3} \|v_i\|_{L^2(\Omega)}^2 + \sum_{j=1}^{3} \|(\text{curl } \mathbf{v})_j\|_{L^2(\Omega)}^2 \right). \end{aligned} \tag{6.35}$$

Note that

$$\sum_{j=1}^{3} \|(\text{curl } \mathbf{v})_j\| L^2(\Omega)^2 \leq \sum_{i,j=1}^{3} \left\| \frac{\partial v_i}{\partial x_j} \right\|_{L^2(\Omega)}^2 = \|\nabla \mathbf{v}\|_{\mathbf{L}^2(\Omega)}^2. \tag{6.36}$$

Then, from (6.35) and (6.36) it follows that

$$\|\mathcal{B}\mathbf{v}\|_{Q'}^2 \leq \text{meas}(\Omega) \left(\|\mathbf{v}\|_{\mathbf{L}^2(\Omega)}^2 + \|\nabla \mathbf{v}\|_{\mathbf{L}^2(\Omega)}^2 \right) = \text{meas}(\Omega) \|\mathbf{v}\|_{\mathbf{H}^1(\Omega)}^2.$$

□

Lemma 6.4. *Let $\mathbf{u} \in V$. Then, the following inequality holds:*

$$\|Div \, \mathbf{u}\|_{L^2(\Omega)} \leq \sqrt{3} \|\nabla \mathbf{u}\|_{\mathbf{L}^2(\Omega)}.$$

Proof. Set $x \in \mathbb{R}$ and $f(x) = |x|^2$, which is clearly a convex function. Then, applying Jensen's inequality (see e.g. Rudin, 2006) it holds that

$$\left| \sum_{i=1}^{3} x_i \right|^2 \leq 3 \left(\sum_{i=1}^{3} |x_i|^2 \right). \tag{6.37}$$

With the choice $x_i = \|\frac{\partial u_i}{\partial x_i}\|_{L^2(\Omega)}$ in (6.37), it follows that

$$\|\text{Div } \mathbf{u}\|_{L^2(\Omega)} = \left\| \sum_{i=1}^{3} \frac{\partial u_i}{\partial x_i} \right\|_{L^2(\Omega)} \leq \sqrt{3} \left(\sum_{i=1}^{3} \left\| \frac{\partial u_i}{\partial x_i} \right\|_{L^2(\Omega)}^2 \right)^{\frac{1}{2}} \leq \sqrt{3} \|\nabla \mathbf{u}\|_{\mathbf{L}^2(\Omega)}.$$

□

To establish the well-posedness of Problem $(\mathcal{LP}_{PN})$ we use the following classical result from Brezzi (1974), which shows the existence and uniqueness of solution to a general saddle point problem fitting the same framework, provided that the data and function spaces involved satisfy some conditions. For the sake of completeness, we state the theorem below without proof.

Theorem 6.3. *Set V and Q as Hilbert spaces and $a(\cdot,\cdot)$ as well as $b(\cdot,\cdot)$ as bilinear continuous forms defined in $V \times V$ and $V \times Q$, respectively. Then, if $f \in V'$ and $g \in Q'$, the saddle point problem*

$$\begin{aligned} a(u,v) + b(v,p) &= \langle f, v \rangle_{V',V}, \qquad \forall v \in V, \\ b(u,q) &= \langle g, q \rangle_{Q',Q}, \qquad \forall q \in Q, \end{aligned}$$

has a unique solution $(u,p) \in V \times Q$ if $a(\cdot,\cdot)$ is coercive in the kernel of $b(\cdot,\cdot)$, i.e., there exists $\alpha^* > 0$ such that

$$a(v,v) \geq \alpha^* \|v\|_V^2, \tag{6.38}$$

for all $v \in V$ such that $b(v,q) = 0 \; \forall q \in Q$ and, in addition, the so-called inf-sup *condition is satisfied*

$$\sup_{v \in V, v \neq 0} \frac{b(v,q)}{\|v\|_V} \geq \beta^* \|q\|_Q, \qquad \forall q \in Q, \tag{6.39}$$

for some $\beta^* > 0$.

USC UNIVERSIDADE DE SANTIAGO

The condition (6.39) is frequently known as *Brezzi condition* or *LBB condition* (Ladyzhenskaya, Babuška and Brezzi). The next result proves that Problem $(\mathcal{LP}_{PN})$ satisfies these conditions and, therefore, has a unique solution.

Theorem 6.4. *Let* $\mathbf{f}$ *and* $\mathbf{g}$ *be such that the functional* $l(\mathbf{v})$*, defined in* (6.21)*, belongs to* V'*. Then, there exists a unique solution* $(\mathbf{u}, \mathbf{p}) \in V \times Q$ *to Problem* $(\mathcal{LP}_{PN})$*.*

Proof. We establish that the conditions of the aforementioned classical result are satisfied. In particular, note that the bilinear form $a(\cdot,\cdot)$ in Problem $(\mathcal{LP}_{PN})$ is the same as that of Problem $(\mathcal{P}_{PN})$. Hence, as discussed in the proof of Theorem 6.2, it is continuous since there are $\alpha, \beta > 0$ such that $\mathbb{C} \in \mathcal{M}(\alpha, \beta, \Omega)$. Moreover, since $\mathcal{B}$ is a continuous operator by Lemma 6.3, the bilinear form $b(\mathbf{v}, \mathbf{q})$ is continuous as well. Indeed,

$$|b(\mathbf{v},\mathbf{q})| = |\langle \mathcal{B}\mathbf{v}, \mathbf{q}\rangle_{Q',Q}| = |\mathcal{B}\mathbf{v}\cdot\mathbf{q}| \leq \|\mathcal{B}\mathbf{v}\|_{Q'}\|\mathbf{q}\|_Q \leq \mathrm{meas}(\Omega)^{\frac{1}{2}}\|\mathbf{v}\|_V\|\mathbf{q}\|_Q.$$

In addition, the application of Theorem 6.1 allows to conclude that the bilinear form $a(\cdot,\cdot)$ is $\mathcal{W}(\Omega)$-coercive (see also Theorem 6.2).

Lastly, it remains to prove that the inf-sup condition (6.39) holds. To this end, we first give a bound in terms of the norm of the space V for the elements of the basis of $\mathcal{Z}(\Omega)$, defined in (6.14). In the case of the first three elements of the basis ($p \in I_3$), it is straightforward that

$$\|\boldsymbol{\xi}^p\|_V = \left(\sum_{i=1}^{3}\|\xi_i^p\|^2_{L^2(\Omega)} + \sum_{i,j=1}^{3}\left\|\frac{\partial \xi_i^p}{\partial x_j}\right\|^2_{L^2(\Omega)}\right)^{1/2} \leq \mathrm{meas}(\Omega)^{1/2}.$$

On the other hand, for $p = I_6 \setminus I_3$, we first note that

$$\boldsymbol{\xi}^4 = (0, -x_3, x_2),\ \boldsymbol{\xi}^5 = (x_3, 0, -x_1),\ \boldsymbol{\xi}^6 = (-x_2, x_1, 0).$$

Hence, for this elements of the basis it holds that $|\boldsymbol{\xi}^p| < |\mathbf{x}|$. Furthermore, since Ω is a domain in $\mathbb{R}^3$, it holds that there exists $R > 0$ such that $\Omega \subset B(\mathbf{0}, R)$, being $B(\mathbf{0}, R)$ the ball centred in the origin of coordinates and radius R. Hence, $|\mathbf{x}| < R$ and thus

$$\|\boldsymbol{\xi}^p\|_{\mathbf{H}^1(\Omega)} \leq \left(\int_\Omega |\mathbf{x}|^2\, dV + 2\mathrm{meas}(\Omega)\right)^{1/2} = ((2+R^2)\mathrm{meas}(\Omega))^{1/2} = C(\Omega).$$

Clearly, since $C(\Omega) > \mathrm{meas}(\Omega)^{1/2}$, it can be established that, for any $p \in I_6$

$$\|\boldsymbol{\xi}^p\|_V \leq C(\Omega). \tag{6.40}$$

Therefore, the V norm bound on all the elements of the basis of $\mathcal{Z}(\Omega)$ is a constant that depends only on the domain Ω.

Set $\mathbf{q} \in Q$. Then, as discussed in Remark 6.5, there is $\mathbf{z} \in \mathcal{Z}(\Omega)$ such that $\mathcal{B}\mathbf{z} = \mathbf{q}$, being κ_p, $p \in I_6$, the coordinates of $\mathbf{z}$ with respect to the basis of $\mathcal{Z}(\Omega)$. Then, using (6.40) and the values of κ_p (6.31), it follows that

$$\begin{aligned}\|\mathbf{z}\|_V &= \left\|\sum_{p=1}^{6}\kappa_p\boldsymbol{\xi}^p\right\|_V \leq \sum_{p=1}^{6}|\kappa_p|\|\boldsymbol{\xi}^p\|_V \leq C(\Omega)\sum_{p=1}^{6}|\kappa_p| \\ &\leq \frac{C(\Omega)}{\mathrm{meas}(\Omega)}\left(1 + \frac{|p_1^c| + |p_2^c| + |p_3^c|}{2}\right)\sum_{p=1}^{6}|q_p| = C_2(\Omega)\|\mathbf{q}\|_1 \leq \frac{1}{\beta}\|\mathbf{q}\|_Q,\end{aligned} \tag{6.41}$$

where it has been also used that the $\|\cdot\|_1$ and $\|\cdot\|_2$ norms are equivalent.

Consequently, since $\mathcal{Z}(\Omega) \subset V$, it holds that

$$\sup_{\mathbf{v}\in V, \mathbf{v}\neq\mathbf{0}}\frac{b(\mathbf{v},\mathbf{q})}{\|\mathbf{v}\|_V} \geq \frac{b(\mathbf{z},\mathbf{q})}{\|\mathbf{z}\|_V} = \frac{\mathbf{q}\cdot\mathbf{q}}{\|\mathbf{z}\|_V} \geq \beta\|\mathbf{q}\|_Q.$$

USC UNIVERSIDADE DE SANTIAGO DE COMPOSTELA

□

Remark 6.6. *As established in Theorem 6.4, the existence and uniqueness of solution for the saddle point problem arising when considering a Lagrange multiplier does not depend on any compatibility conditions for the data. This means that, for given data* $\mathbf{f}$ *and* $\mathbf{g}$ *that do not satisfy* (6.27) *and* (6.28)*, the problem is still solvable, as opposed to Problem* $(\mathcal{VP}_{PN})$.

The following corollary clearly establishes the relation between the solutions to $(\mathcal{VP}_{PN})_{\mathcal{W}}$ and the saddle point formulation $(\mathcal{LP}_{PN})$.

Corollary 6.2. *Assume that the hypotheses of Theorem 6.2 hold. If* $\mathbf{u}$ *is the solution to* $(\mathcal{VP}_{PN})_{\mathcal{W}}$*, then* $(\mathbf{u}, \mathbf{0})$ *is the unique solution to* $(\mathcal{LP}_{PN})$*. The converse also holds.*

Proof. Set $\mathbf{u} \in \mathcal{W}(\Omega)$ be the unique solution to Problem $(\mathcal{VP}_{PN})_{\mathcal{W}}$. We can analyse under what conditions on the multiplier $\mathbf{p}$, $(\mathbf{u},\mathbf{p})$ is the solution to $(\mathcal{LP}_{PN})$. Since $\ker \mathcal{B} = \mathcal{W}(\Omega)$, then (6.34) holds for any test function $\mathbf{q} \in Q$. In addition, let $\mathbf{v} \in V$ and note that for $\mathbf{p} = \mathbf{0}$, $b(\mathbf{v}, \mathbf{p}) = 0$. Hence, since $\mathbf{u}$ is the unique solution to (6.24), (6.33) is satisfied for all $\mathbf{v} \in V$.

Conversely, set $(\mathbf{u}, \mathbf{p})$ as the unique solution to Problem $(\mathcal{LP}_{PN})$ in $V \times Q$. Let an arbitrary $\mathbf{v} \in V$ and set the decomposition $\mathbf{v} = \mathbf{w} + \mathbf{z}$, with $\mathbf{w} \in \mathcal{W}(\Omega)$ and $\mathbf{z} \in \mathcal{Z}(\Omega)$. Then, since $a(\mathbf{u}, \mathbf{z}) = 0$ for any $\mathbf{z} \in \mathcal{Z}(\Omega)$ and $b(\mathbf{w}, \mathbf{p}) = 0$ for any $\mathbf{w} \in \mathcal{W}(\Omega)$, from (6.33) it follows that

$$a(\mathbf{u}, \mathbf{w}) + b(\mathbf{z}, \mathbf{p}) = l(\mathbf{w}) + l(\mathbf{z}), \tag{6.42}$$

for any $(\mathbf{w}, \mathbf{z}) \in \mathcal{W}(\Omega) \times \mathcal{Z}(\Omega)$ such that $\mathbf{w} + \mathbf{z} = \mathbf{v}$. Therefore, it must hold that $b(\mathbf{z}, \mathbf{p}) = l(\mathbf{z})$. Note that (6.34) implies that $\mathbf{u} \in \mathcal{W}(\Omega)$ and, hence, if the data is compatible, since $l(\mathbf{z}) = 0$, then $\mathbf{p} = \mathbf{0}$ and it directly follows from (6.42) that $\mathbf{u}$ is the unique solution to Problem $(\mathcal{VP}_{PN})_{\mathcal{W}}$. □

Using that both V and Q are Hilbert spaces, the saddle point problem $(\mathcal{LP}_{PN})$ may be recast as an operator equation by defining the linear operator $\mathcal{A} : V \to V'$ and the adjoint operator of $\mathcal{B}$, $\mathcal{B}^T : Q \to V'$ in the following way:

$$\begin{aligned} a(\mathbf{u}, \mathbf{v}) &= \langle \mathcal{A}\mathbf{u}, \mathbf{v} \rangle_{V',V}, \\ b(\mathbf{v}, \mathbf{q}) &= \langle \mathcal{B}\mathbf{v}, \mathbf{q} \rangle_{Q',Q} = \langle \mathcal{B}^T\mathbf{q}, \mathbf{v} \rangle_{V',V}, \end{aligned}$$

for any $\mathbf{u}, \mathbf{v} \in V$ and $\mathbf{q} \in Q$.

Then, solving $(\mathcal{LP}_{PN})$ is equivalent to finding $(\mathbf{u}, \mathbf{p}) \in V \times Q$ such that

$$\begin{aligned} \mathcal{A}\mathbf{u} + \mathcal{B}^T\mathbf{p} &= l, && \text{in } V', \\ \mathcal{B}\mathbf{u} &= \mathbf{0}, && \text{in } Q'. \end{aligned}$$

6.3.4. Numerical solution

When seeking a numerical approximation of the solution to Problem $(\mathcal{LP}_{PN})$, for instance, using a finite element method, it is usual to consider an internal approximation of the spaces $V \times Q$, say, by $V_h \times Q_h$, where V_h and Q_h are of finite dimension such that $V_h \subset V$ and $Q_h \subset Q$. It is a well-known issue that the conditions required to establish the existence and uniqueness of solution are not necessarily preserved in the discrete spaces. Usually, the most troublesome one is the LBB condition (6.39), which frequently requires the use of a specific pair of finite elements. Nonetheless, in the framework of the pure traction problem, the existence and uniqueness of the corresponding discrete problem is readily established. To this end, we consider the discrete problem analogue of $(\mathcal{LP}_{PN})$.

Problem $(\mathcal{LP}_{PN})_h$. Find $(\mathbf{u}_h, \mathbf{p}_h) \in V_h \times Q_h$ such that:

$$\begin{aligned} a(\mathbf{u}_h, \mathbf{v}_h) + b(\mathbf{v}_h, \mathbf{p}_h) &= l(\mathbf{v}_h), && \forall \mathbf{v}_h \in V_h, \\ b(\mathbf{u}_h, \mathbf{q}_h) &= 0, && \forall \mathbf{q}_h \in Q_h. \end{aligned}$$

Specifically, we choose V_h as the continuous functions whose restrictions to the elements forming the mesh of Ω are polynomials of degree 1. Set $N_h = \dim V_h$ and note that $\mathcal{Z}(\Omega) \subset V_h$. In such case, the subsequent result holds.

Theorem 6.5. *Let $Q_h = Q$ and V_h be the finite-dimensional spaces defined above. Then, Problem $(\mathcal{LP}_{PN})_h$ has a unique solution $(\mathbf{u}_h, \mathbf{p}_h) \in V_h \times Q_h$.*

Proof. We establish the conditions for the classical result considered in the proof of Theorem 6.4. Note that since V_h is of finite dimension and a subspace of V, then V_h is closed and hence also a Hilbert space. The continuity of the bilinear forms $a(\cdot,\cdot)$ and $b(\cdot,\cdot)$ directly follows from the continuity in $V \times V$ and $V \times Q$. Moreover, the restriction of $\mathcal{B}$ to V_h is still continuous and, since $Q_h = Q$, then condition (6.38) holds. Lastly, we check that the inf-sup condition (6.39) is satisfied. Indeed, since $\mathbf{z} \in V_h$ and using (6.41)

$$\sup_{\mathbf{v}_h \in V_h, \mathbf{v}_h \neq \mathbf{0}} \frac{b(\mathbf{v}_h, \mathbf{q}_h)}{\|\mathbf{v}_h\|_{V_h}} \geq \frac{b(\mathbf{z}, \mathbf{q})}{\|\mathbf{z}\|_{V_h}} = \frac{\mathbf{q} \cdot \mathbf{q}}{\|\mathbf{z}\|_{V_h}} \geq \beta^* \|\mathbf{q}\|_{Q_h}.$$

□

6.3.5. Other solution strategies

In addition to the technique using a Lagrange multiplier detailed above, a solution of the singular problem $(\mathcal{P}_{PN})$ can be numerically approximated using other strategies. In this section, we describe a couple of widely used alternatives.

One simple and somewhat common strategy to solve singular problems such as the linear elasticity with a pure Neumann boundary condition is to artificially constrain the candidate solution by specifying its value in a set degrees of freedom (see e.g. Bochev & Lehoucq, 2005). In the particular case of Problem $(\mathcal{P}_{PN})$ discretised using Lagrange finite elements of order 1, this amounts to set the displacement $\mathbf{u}$ at least at three non-collinear nodes in the computational mesh. At a continuous level, the procedure effectively ensures that there is a Dirichlet boundary Γ_D such that $\partial\Omega = \Gamma_D \cup \Gamma_N$ and $\text{meas}(\Gamma_D) > 0$.

Then, the problem essentially becomes an instance of Problem $(\mathcal{VP})$ which, as previously discussed, is well-posed without any additional modifications. The idea is to select a set of nodes sufficiently far away from where the surface and volume loading are acting in order to avoid creating large artefacts in the solution.

Remark 6.7. *When using this approach to solve Problem $(\mathcal{P}_{PN})$, the solved problem changes. Certainly, the obtained solution is not a solution of the original problem with pure Neumann boundary unless the prescribed displacement coincides with one of the solutions of the pure traction problem.*

Also, even if the Dirichlet condition actually corresponds to the exact solution of the problem, this approach may lead to very poorly conditioned system matrices, which heavily deteriorates convergence rates when using iterative solvers. In some cases, non-convergent numerically approximations appear, as reported in Kuchta et al. (2019).

In particular, during the 139 European Study Group with Industry, this technique was used to solve the pure Neumann basic tests that will be introduced in Chapter 8 to obtain a homogenised material (see Barral et al., 2018). The results were unsatisfactory, as the artificial Dirichlet conditions led to some non-symmetric entries in the stiffness matrix of the computed homogeneous material.

Other popular and numerically inexpensive technique to deal with singular problems such as Problem $(\mathcal{P}_{PN})$ is to use a Krylov method to solve the underlying linear system of equations after the corresponding weak formulation is discretised. Krylov subspace methods are a class of iterative solvers that generalise very popular methods such as the conjugate gradient method. Other notable examples of Krylov solvers are the Minimal Residual Method (MinRes) and the Generalised Minimal Residual Method (GMRES).

Consider a linear system of equations with a symmetric matrix $\mathbf{A}$ whose dimension is $N_h \times N_h$:

$$\mathbf{A}\mathbf{x} = \mathbf{b}, \tag{6.43}$$

where the right hand side $\mathbf{b}$ is also given. Krylov methods construct the so-called *Krylov subspace* K_j at each iteration j:

$$K_j(\mathbf{A}, \mathbf{r}_0) = \text{span}\{\mathbf{r}_0, \mathbf{A}\mathbf{r}_0, \ldots, \mathbf{A}^{j-1}\mathbf{r}_0\},$$

USC DE COMPOSTELA

where $\mathbf{x}_0$ is the initial guess and $\mathbf{r}_0$ denotes the residual vector at the first iteration, defined as $\mathbf{r}_0 = \mathbf{b} - \mathbf{A}\mathbf{x}_0$.

The successive approximations $\mathbf{x}_j$ to the solution of system (6.43) are sought in the corresponding subspace for each iteration. The procedure to find $\mathbf{x}_j \in K_j$ depends on the specific solver. For instance, in Krylov solvers of the Ritz-Galerkin class, such as the conjugate gradient method, the approximated solution is constructed by enforcing that the residual satisfies $\mathbf{r}_j \perp K_j(\mathbf{A}, \mathbf{r}_0)$ (see Van der Vorst, 2003).

Assume that the linear system comes from a direct discretisation of Problem $(\mathcal{VP}_{PN})$. Hence, the resulting system matrix is singular, i.e. $\det(\mathbf{A}) = 0$. Thus, the system is solvable if and only if the right hand side is compatible, which in the discrete setting means that $\mathbf{b} \in \operatorname{Im} \mathbf{A}$, where we identify $\mathbf{A}$ with the linear transformation that it induces. This is the discrete analogue of the compatibility condition, noting that it essentially means that $\mathbf{b}$ must not have components in the nullspace of $\mathbf{A}$. Clearly, the system admits infinitely many solutions, since given a solution $\mathbf{x}$, $\mathbf{x} + \mathbf{v}$ with $\mathbf{v} \in \operatorname{Ker} \mathbf{A}$ is also a solution.

If a Krylov method is used to solve the system with compatible right hand side, a zero initial guess ($\mathbf{x}_0 = \mathbf{0}$) may be chosen. As the Krylov subspaces are constructed only with $\mathbf{A}$ and $\mathbf{b}$, we have that $\mathbf{x}_j \in K_j(\mathbf{A}, \mathbf{b})$ necessarily implies that $\mathbf{x}_j \in \operatorname{Im} \mathbf{A}$. In the particular setting of the pure traction problem, noting that $\operatorname{Ker} \mathbf{A} \simeq \mathcal{Z}(\Omega)$, any approximation of the solution constructed in this manner satisfies that $\mathbf{x}_j \in \mathcal{Z}(\Omega)^\perp$. Hence, the method converges to the unique solution of the problem in $\mathcal{Z}(\Omega)^\perp$. For a detailed description of these techniques, we refer to Saad (2003).

6.3.6. Preconditioning of the saddle point system

The sparse linear systems resulting from the discretisation of Problem $(\mathcal{LP}_{PN})$ can be solved with direct methods. However, in most applications when solving problems of this kind, the number of unknowns rapidly grows with successively refined meshes, making iterative solvers much more efficient. It is a well-known fact that the rate of convergence of iterative methods is bounded by the condition number of the system matrix (Golub & Van Loan, 2013). The aim of preconditioning is to improve this condition number, and thus it becomes an essential tool in order to successfully apply iterative methods. In this section, we briefly describe the strategy that is employed to solve $(\mathcal{LP}_{PN})$ with an iterative method.

Efficient preconditioning of saddle point problems is not straightforward. The construction of mesh and parameter-independent preconditioners is heavily problem-reliant. For the specific setting of the pure traction problem, in Kuchta et al. (2019), a couple of block-diagonal preconditioners were developed for a saddle point formulation similar to the one presented above. In particular, to ensure that the preconditioner is independent of the discretisation parameter h, an $\mathbf{L}^2(\Omega)$-orthonormal basis of the space $\mathcal{Z}(\Omega)$ is shown to be required.

For our purposes, it will suffice with a slightly simpler preconditioner, but constructed in a similar manner. Consider a system of the form (6.43), and assume that it corresponds to the discretisation of $(\mathcal{LP}_{PN})$. Instead of said system, we solve:

$$\mathbf{PAx} = \mathbf{Pb}, \tag{6.44}$$

where the preconditioner $\mathbf{P}$ is the discretisation of the operator $\mathcal{P} : V' \times Q' \to V \times Q$, defined as follows:

$$\mathcal{P} = \begin{pmatrix} \mathcal{K} + \mathcal{M} & \\ & \mathcal{I}_Q \end{pmatrix}^{-1}.$$

In the previous expression, the operators $\mathcal{K} : V \to V'$, $\mathcal{M} : V \to V'$ and $\mathcal{I}_Q : Q' \to Q$ are such that

$$\begin{aligned} \langle \mathcal{K}\mathbf{u}, \mathbf{v} \rangle_{V',V} &= (c^* \nabla \mathbf{u}, \nabla \mathbf{v})_{\mathbf{L}^2(\Omega)}, \\ \langle \mathcal{M}\mathbf{u}, \mathbf{v} \rangle_{V',V} &= (c^* \mathbf{u}, \mathbf{v})_{\mathbf{L}^2(\Omega)}, \\ \langle \mathcal{I}_Q \mathbf{p}, \mathbf{q} \rangle_{Q',Q} &= \mathbf{p} \cdot \mathbf{q}, \end{aligned}$$

USC UNIVERSIDADE DE SANTIAGO DE COMPOSTELA

with $(\cdot,\cdot)_{\mathbf{L}^2(\Omega)}$ denoting the standard scalar product in $\mathbf{L}^2(\Omega)$ and $c^* \in L^\infty(\Omega)$ being equal to the maximum component of the elasticity tensor $\mathbb{C}$ in those points where it is defined, i.e.:

$$c^*(\mathbf{x}) = \max_{i,j,k,l \in I_3} C_{ijkl}(\mathbf{x}), \tag{6.45}$$

for almost any $\mathbf{x} \in \Omega$.

Remark 6.8. *In (6.45), c^* can be equivalently defined as the maximum of the stiffness matrix $[\mathbf{C}]$. In the applications addressed in the subsequent chapters, the stiffness matrix is piecewise-constant, with entries c_{pq}, $p, q \in I_6$ such as in (6.8) (see also Figure 6.1). Therefore, if both materials are also isotropic, from the constitutive law (6.9) it can be established that*

$$c^*(\mathbf{x}) = \begin{cases} 2\mu^1 + \lambda^1, & \mathbf{x} \in \Omega^1, \\ 2\mu^2 + \lambda^2, & \mathbf{x} \in \Omega^2, \end{cases}$$

where μ^1, λ^1 denote the Lamé parameters of the material occupying subdomain Ω^1 and μ^2, λ^2 denote the Lamé parameters of the material occupying subdomain Ω^2.

To solve system (6.44), note that $\mathbf{P}$ is not explicitly computed and, instead, the action of the preconditioner on the approximate solution is obtained using an algebraic multigrid (AMG) V-cycle (Trottenberg et al., 2000). Specifically, the matrix corresponding to the discretisation of the block $(\mathcal{K} + \mathcal{M})$ is supplied to a *fieldsplit* object in the PETSc library (Balay et al., 2022). It is set to call the *hypre* library (Falgout & Yang, 2002) to obtain the preconditioner action, using the *BoomerAMG* implementation of the AMG method. The system is then solved with a MinRes solver as implemented in PETSc. The remaining settings were kept at their default values, with the exception of the solver tolerances.

6.3.7. Numerical experiments

This section is devoted to address the performance of the different solution strategies described in Section 6.3.5 for the pure Neumann linear elasticity problem. With this purpose, they are compared with the approach presented in the previous section, which solves the system arising from the discretisation of Problem $(\mathcal{LP}_{PN})$. A couple of numerical tests with manufactured solution are constructed and solved with the introduced strategies.

For the sake of simplicity, in both tests an isotropic homogeneous material is considered. From a given manufactured solution, the corresponding stress is directly obtained from the constitutive equation (6.9). Then, the resulting densities of volume and surface forces ($\mathbf{f}$ and $\mathbf{g}$, respectively) are obtained by computing the divergence of the stress and by evaluating the boundary conditions. To analyse the error in the numerical approximation of the stress induced by the displacement, the von Mises norm of the stress tensor is computed, which is defined as:

$$\sigma_{VM} = \frac{1}{2}\sqrt{(\sigma_{11} - \sigma_{22})^2 + (\sigma_{22} - \sigma_{33})^2 + (\sigma_{33} - \sigma_{11})^2 + 6(\sigma_{23}^2 + \sigma_{31}^2 + \sigma_{12}^2)}.$$

Below, the two manufactured solution tests are presented. It can be verified that the manufactured displacements are such that $\mathbf{u}_{ex}$ belongs to the space $\mathcal{W}(\Omega)$ and the data satisfies the compatibility conditions (6.27) and (6.28).

Test 1. Set $\Omega = (0,2)^3$ and let the exact solution be

USC UNIVERSIDADE DE SANTIAGO DE COMPOSTELA

$$\mathbf{u}_{ex} = \begin{pmatrix} -x_1 + x_2 + x_3 - 1 \\ x_1 - x_2 + x_3 - 1 \\ x_1 + x_2 - x_3 - 1 \end{pmatrix}.$$

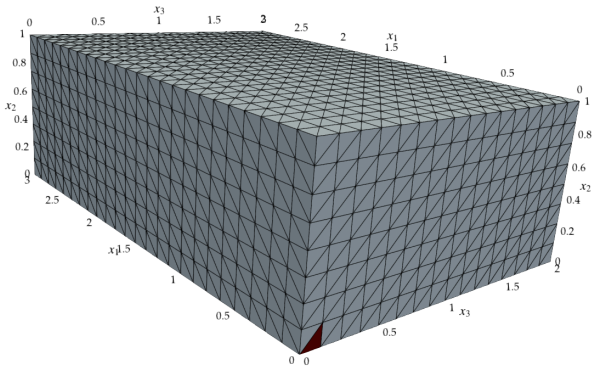


Figure 6.2: Element face highlighted in red corresponding to the Dirichlet boundary for the *pinning* approach, for the computational domain considered in Test 2.

The stress tensor induced by the displacement is such that

$$\boldsymbol{\sigma}(\mathbf{u}_{ex}) = \begin{pmatrix} -3\lambda - 2\mu & 2\mu & 2\mu \\ 2\mu & -3\lambda - 2\mu & 2\mu \\ 2\mu & 2\mu & -3\lambda - 2\mu \end{pmatrix},$$

and the corresponding von Mises stress norm is $\sigma_{VM}(\mathbf{u}_{ex}) = 6\mu$. The density of applied surface forces $\mathbf{g}$ and the density of volume forces $\mathbf{f}$ directly follow from substitution in (6.22) and (6.23), respectively:

$$\mathbf{f} = \mathbf{0},$$
$$\mathbf{g} = \begin{cases} \pm\big(-3\lambda - 2\mu, 2\mu, 2\mu\big)^T, & \text{on } \Gamma_1^{\pm}, \\ \pm\big(2\mu, -3\lambda - 2\mu, 2\mu\big)^T, & \text{on } \Gamma_2^{\pm}, \\ \pm\big(2\mu, 2\mu, -3\lambda - 2\mu\big)^T, & \text{on } \Gamma_3^{\pm}. \end{cases}$$

For the presented numerical results, we consider $\lambda = 1$ and $\mu = 2$.

Test 2. The domain $\Omega = (0,3) \times (0,1) \times (0,2)$ is set. The subsequent displacement field is proposed

$$\mathbf{u}_{ex} = \begin{pmatrix} 0 \\ \sin(2\pi x_2) \\ \cos(2\pi x_3) \end{pmatrix}.$$

The stress tensor is found analogously to Test 1:

$$\boldsymbol{\sigma}(\mathbf{u}_{ex}) = 2\lambda\pi(\cos(2\pi x_2) - \sin(2\pi x_3))\mathbf{I} + 4\mu\pi \begin{pmatrix} 0 & 0 & 0 \\ 0 & \cos(2\pi x_2) & 0 \\ 0 & 0 & -\sin(2\pi x_3) \end{pmatrix}.$$

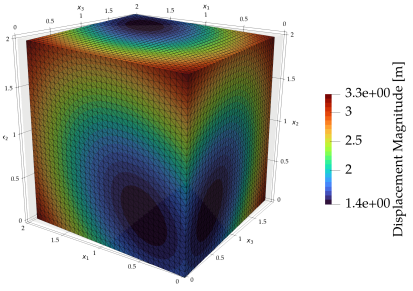
The von Mises stress norm is such that

$$\sigma_{VM}(\mathbf{u}_{ex}) = 4\mu\pi\big(\cos(2\pi x_2)\sin(2\pi x_3) + \cos^2(2\pi x_2) + \sin^2(2\pi x_3)\big)^{\frac{1}{2}}.$$

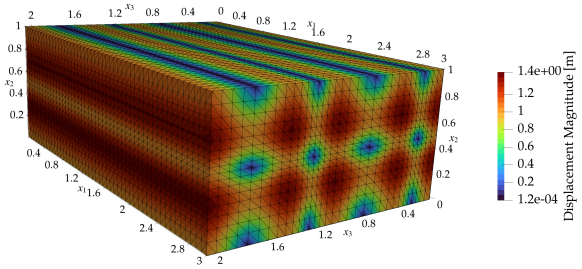
Moreover, the density of applied surface forces $\mathbf{g}$ and of volume forces $\mathbf{f}$ directly follow applying (6.22) and (6.23), respectively:

$$\mathbf{f} = \big(0, \pi^2\sin(2\pi x_2)(4\lambda + 8\mu), 4\pi^2\cos(2\pi x_3)(4\lambda + 8\mu)\big)^T,$$
$$\mathbf{g} = \begin{cases} \pm\mathbf{e}_1 2\pi\lambda\big(\cos(2\pi x_2) - \sin(2\pi x_3)\big), & \text{on } \Gamma_1^{\pm}, \\ \pm\mathbf{e}_2\big(2\pi\lambda(\cos(2\pi x_2) - \sin(2\pi x_3)) + 4\mu\pi\cos(2\pi x_2)\big), & \text{on } \Gamma_2^{\pm}, \\ \pm\mathbf{e}_3\big(2\pi\lambda(\cos(2\pi x_2) - \sin(2\pi x_3)) + 4\mu\pi\sin(2\pi x_3)\big), & \text{on } \Gamma_3^{\pm}. \end{cases}$$

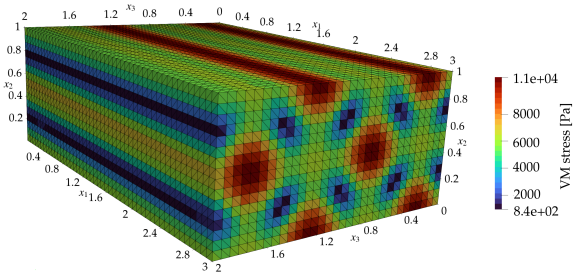
USC UNIVERSIDADE DE SANTIAGO DE COMPOSTELA



(**a**) Test 1, displacement.



(**b**) Test 2, displacement.



(**c**) Test 2, VM stress.

Figure 6.3: Computed solutions using Lagrange multipliers (SPP).

Further simplification of the expression for $\mathbf{g}$ can be achieved by evaluating the values of x_2, x_3 on $\Gamma_2^{\pm}$ and $\Gamma_3^{\pm}$,respectively. For the presented numerical results concerning this test, we consider $\lambda = 100$ and $\mu = 500$.

As mentioned above, we approximate the solution of these tests following the approaches that we summarise below:

1. **Saddle point formulation (SPP)**. Instead of directly solving the ill-posed $(\mathcal{VP}_{PN})$, a Lagrange multiplier is incorporated and the well-posed formulation $(\mathcal{LP}_{PN})$ is solved instead. The block-diagonal preconditioner detailed in Section 6.3.6 with a MinRes iterative method is used to solve the discretised problem.

2. **Krylov solver with nullspace basis (CG)**. Since the data is compatible, $(\mathcal{VP}_{PN})$ is discretised without further modifications. A basis of $\mathcal{Z}(\Omega)$ is supplied to a Conjugate Gradient (CG) solver. The hypre *BoomerAMG* preconditioner is used for preconditioning the system, with the same settings considered in the block-diagonal preconditioner for the saddle point formulation.

3. **Artificially constraining the displacement (Pinning)**. To obtain a well-posed problem from $(\mathcal{VP}_{PN})$, the displacement is set to be equal to the exact solution on all degrees of freedom belonging to an element face next to the corner $\mathbf{x}_{min} = (0, 0, 0)$, as depicted in Figure 6.2. The problem is then solved with a CG method, also using AMG as a preconditioner.

In all three cases, the relative and absolute tolerances of the solver are set to 10^{-8} for the preconditioned residual norm. For both test problems, if the nullspace basis was not supplied to the solver in the CG approach, the solver did not converge, despite using $\mathbf{x}_0 = \mathbf{0}$ as initial guess.

Continuous Lagrange finite elements of order one are used to discretise the presented examples. To obtain the corresponding algebraic systems for the three approaches we employ the open-source library FEniCS (Logg et al., 2012; Alnæs et al., 2015). The constructed meshes are formed by uniform tetrahedra with a discretisation parameter h. The asymptotic converge rates are analysed computing the committed error in various norms. Namely, we report the relative error in the $\mathbf{L}^2(\Omega)$ and $\mathbf{H}^1(\Omega)$

Table 6.1: Errors for the saddle point formulation (top), supplying a nullspace basis to a CG solver (middle) and artificially constraining the displacement on the degrees of freedom corresponding to an element face (bottom).

(**a**) Test 1.

h	# dofs	# iterations	$e_{h,\mathbf{L}^2(\Omega)}(\mathbf{u})$	$e_{h,\mathbf{H}^1(\Omega)}(\mathbf{u})$	$e_{h,L^2(\Omega)}(\sigma_{VM})$
0.25	2187	32	$1.7091E{-8}$	$3.1381E{-8}$	$9.1888E{-9}$
0.125	14739	34	$2.5021E{-8}$	$4.8376E{-8}$	$9.9131E{-9}$
0.0625	107811	36	$1.4930E{-8}$	$4.5345E{-8}$	$8.8070E{-9}$
0.03125	823875	37	$1.5490E{-8}$	$5.0373E{-8}$	$9.0899E{-9}$
0.015625	6440067	40	$1.4965E{-8}$	$4.6293E{-8}$	$8.6959E{-9}$
0.25	2187	8	$8.9809E{-10}$	$1.9090E{-9}$	$4.5289E{-10}$
0.125	14739	8	$6.1184E{-9}$	$1.2974E{-8}$	$3.1474E{-9}$
0.0625	107811	9	$1.8332E{-9}$	$4.2276E{-9}$	$9.8765E{-10}$
0.03125	823875	9	$4.9908E{-9}$	$1.2603E{-8}$	$2.8655E{-9}$
0.015625	6440067	10	$2.5340E{-9}$	$5.8230E{-9}$	$1.3801E{-9}$
0.25	2187	17	$6.5440E{-9}$	$9.5525E{-9}$	$2.0472E{-9}$
0.125	14739	22	$2.3319E{-9}$	$2.0079E{-9}$	$3.7481E{-10}$
0.0625	107811	26	$9.3248E{-9}$	$6.0402E{-9}$	$8.4998E{-10}$
0.03125	823875	31	$1.4959E{-7}$	$9.5552E{-8}$	$1.5408E{-10}$
0.015625	6440067	28	$2.0437E{-3}$	$1.3238E{-3}$	$2.2005E{-7}$

(**b**) Test 2.

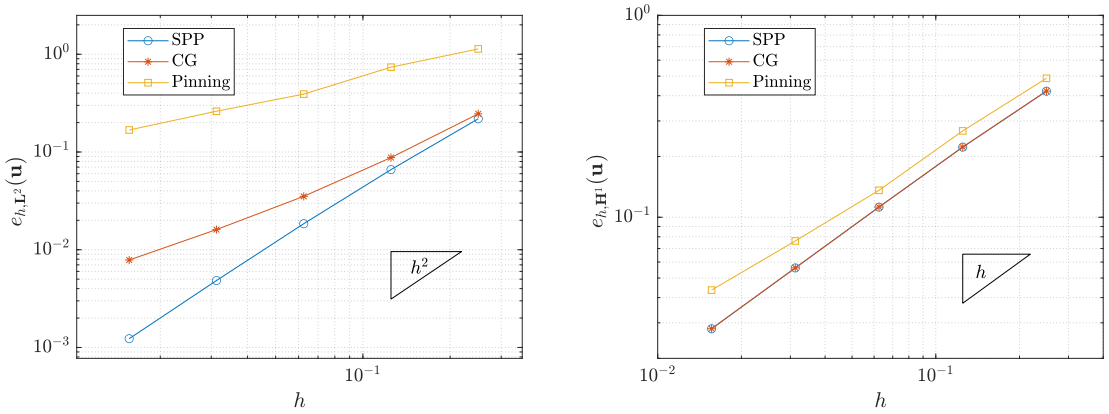
h	# dofs	# iterations	$e_{h,\mathbf{L}^2(\Omega)}(\mathbf{u})$	$e_{h,\mathbf{H}^1(\Omega)}(\mathbf{u})$	$e_{h,L^2(\Omega)}(\sigma_{VM})$
0.25	2187	48	$2.1883E{-1}$	$4.2126E{-1}$	$3.2651E{-1}$
0.125	14739	49	$6.6023E{-2}$	$2.2253E{-1}$	$1.6020E{-1}$
0.0625	107811	49	$1.8456E{-2}$	$1.1228E{-1}$	$7.7581E{-2}$
0.03125	823875	47	$4.8388E{-3}$	$5.6094E{-2}$	$3.8253E{-2}$
0.015625	6440067	47	$1.2294E{-3}$	$2.8019E{-2}$	$1.9029E{-2}$
0.25	2187	11	$2.4588E{-1}$	$4.2164E{-1}$	$3.2651E{-1}$
0.125	14739	11	$8.7695E{-2}$	$2.2273E{-1}$	$1.6020E{-1}$
0.0625	107811	12	$3.5173E{-2}$	$1.1238E{-1}$	$7.7581E{-2}$
0.03125	823875	13	$1.6076E{-2}$	$5.6147E{-2}$	$3.8253E{-2}$
0.015625	6440067	14	$7.8460E{-3}$	$2.8045E{-2}$	$1.9029E{-2}$
0.25	2187	21	$1.1343E0$	$4.8806E{-1}$	$3.2672E{-1}$
0.125	14739	26	$7.3722E{-1}$	$2.6772E{-1}$	$1.6022E{-1}$
0.0625	107811	30	$3.9128E{-1}$	$1.3602E{-1}$	$7.7582E{-2}$
0.03125	823875	35	$2.6111E{-1}$	$7.6309E{-2}$	$3.8253E{-2}$
0.015625	6440067	43	$1.6804E{-1}$	$4.3585E{-2}$	$1.9029E{-2}$

norms of the displacement, which are respectively defined as:

$$e_{h,\mathbf{L}^2}(\mathbf{u}) = \frac{\|\mathbf{u}_h - \mathbf{u}_{ex}\|_{\mathbf{L}^2(\Omega)}}{\|\mathbf{u}_{ex}\|_{\mathbf{L}^2(\Omega)}}, \qquad e_{h,\mathbf{H}^1}(\mathbf{u}) = \frac{\|\mathbf{u}_h - \mathbf{u}_{ex}\|_{\mathbf{H}^1(\Omega)}}{\|\mathbf{u}_{ex}\|_{\mathbf{H}^1(\Omega)}},$$

The relative error committed in the approximation of the von Mises stress norm, $e_{h,\mathbf{L}^2}(\sigma_{VM})$, defined in a completely analogous manner, is also computed.

In Figures 6.3a and 6.3b, the contours of the computed displacements for Test 1 and Test 2 using the saddle point formulation are displayed. Also, the von Mises stress norm corresponding to Test 2 is depicted in Figure 6.3c. In Table 6.1a, the iteration count and errors in the approximation of the displacement and the VM stress norm are gathered for Test 1. The results concerning the saddle point formulation are at the top, those related to using the CG solver with the nullspace basis are in the middle and the pinning results are at the bottom. Since the space V_h is formed by the continuous



(a) $\mathbf{L}^2(\Omega)$ norm. **(b)** $\mathbf{H}^1(\Omega)$ norm.

Figure 6.4: Test 2. Relative error approximating the displacements.

functions whose restrictions to the tetrahedra in the mesh are first degree polynomials, $\mathbf{u}_{ex} \in V_h$. Hence, the exact solution is recovered numerically, up to the accuracy determined by the tolerance of the iterative method used to solve the algebraic systems. This holds for all the considered cases, with the exception of the finest mesh ($h = 0.015625$) used for the pinning approach, for which this property is lost and the errors increase sharply in comparison to the coarser meshes. The iteration counts rise by around 20% from the coarsest to the finest mesh (SPP and CG), whereas for pinning, the iteration count increases substantially upon reaching the point where the solver is unable to recover the exact solution numerically. The von Mises stress norm, which is constant, is also recovered exactly up to the tolerance of the iterative solvers.

In Table 6.1b, the same errors are collected for Test 2, as well as the iteration count for the three methodologies. Concerning the displacement, since $\mathbf{u}_{ex}$ belongs to $\mathcal{C}^\infty(\Omega)$, we expect $O(h)$ convergence in the $\mathbf{H}^1(\Omega)$ norm and $O(h^2)$ convergence in the $\mathbf{L}^2(\Omega)$ norm (see e.g. Quarteroni, 2009). As depicted in Figure 6.4, this optimal asymptotic behaviour clearly observed for the saddle point formulation. For the Krylov solver with nullspace basis (CG), the theoretical convergence rate is observed in the $\mathbf{H}^1(\Omega)$ norm. Nonetheless, the asymptotic convergence rates in the $\mathbf{L}^2(\Omega)$ norm are deteriorated, and the order 2 is not observed. With pinning, the errors are substantially larger and the slope is just around 0.5 for the $\mathbf{L}^2(\Omega)$ norm. Concerning the stress, all numerical methodologies yield the same errors. The iteration count for SPP with the devised preconditioning methodology is clearly bounded, whereas it slightly increases with successively refined meshes supplying the nullspace basis to a CG solver. On the other hand, the iteration count when pinning is employed in Test 2 rises significantly.

Judging from the results, it appears that the most appealing methodology is to simply supply the nullspace basis to the CG solver since, for the two numerical tests, virtually the same errors are obtained in the stronger norm ($\mathbf{H}^1(\Omega)$) in comparison to the saddle point formulation, requiring less computational effort. In particular, we have found the computational cost to be roughly twice as much for SPP than for the CG approach. Nevertheless, it is necessary to have compatible data for the problem to use it, as opposed to the saddle point formulation. Pinning can be useful in some situations, but even with knowledge of the exact solution, deteriorated convergence rates are observed and possibly unbounded iteration counts.

USC UNIVERSIDADE DE SANTIAGO DE COMPOSTELA

USC
UNIVERSIDADE
DE SANTIAGO
DE COMPOSTELA

Chapter 7

Mathematical homogenisation. A classical result in linear elasticity

The goal of homogenisation is to describe the macroscopic, or effective, response of a medium that has an intricate microstructure by obtaining a homogeneous material whose global characteristics are a good approximation of those of the heterogeneous one. The classical version of the theory, which is the one that is presented below, assumes a *periodic medium*. Several notions allow to obtain the description of the medium as the parameter ϵ, defined as the ratio between the size of the period and the sample of the medium goes to zero, such as the two-scale convergence (Allaire, 1992) or the periodic unfolding method (Cioranescu et al., 2018). Moreover, there are several frameworks in homogenisation that can be applied to any type of disordered media, such as the $G-$ or $H-$ convergence (see e.g. Allaire, 2012).

In this chapter, for the sake of completeness, the main features of the mathematical theory of homogenisation are introduced. With this purpose, the notation and presentation from Cioranescu & Donato (1999) is followed. It is structured as follows. In Section 7.1, the basic terminology in periodic homogenisation is presented. Subsequently, in 7.2 a classical result concerning the asymptotic behaviour of the linear elastic system in a periodic medium is stated, also extracted from the aforementioned reference. Lastly, Section 7.3 is devoted to introduce a numerical methodology to obtain an approximation of the corrector functions for the linear elasticity system.

7.1. Basic terminology

Let $Y \subset \mathbb{R}^3$ denote the following open set, known as the *reference period* or *unit periodicity cell*:

$$Y = (0, L_1) \times (0, L_2) \times (0, L_3), \tag{7.1}$$

where $L_i > 0$ for all $i \in \{1, 2, 3\}$. Its boundary, ∂Y, is partitioned in the following six subsets:

$$\Gamma_i^+ := \{\mathbf{y} \in \overline{Y} : y_i = L_i\},$$
$$\Gamma_i^- := \{\mathbf{y} \in \overline{Y} : y_i = 0\}.$$

We shall denote as $\Gamma_i^\pm$ the union of the opposite pairs of faces Γ_i^+ and Γ_i^-, i.e. $\Gamma_i^\pm = \Gamma_i^+ \cup \Gamma_i^-$. In relation with the set Y, we introduce the subsequent notion of periodicity.

Definition 7.1. *Let h be a scalar function defined a.e. on $\mathbb{R}^3$ and Y given by (7.1). Then, h is called* Y-periodic *if for any $k \in \mathbb{Z}$, $i \in \{1, 2, 3\}$ and almost any $\mathbf{x} \in \mathbb{R}^3$:*

$$h(\mathbf{x} + kL_i\mathbf{e}_i) = h(\mathbf{x}),$$

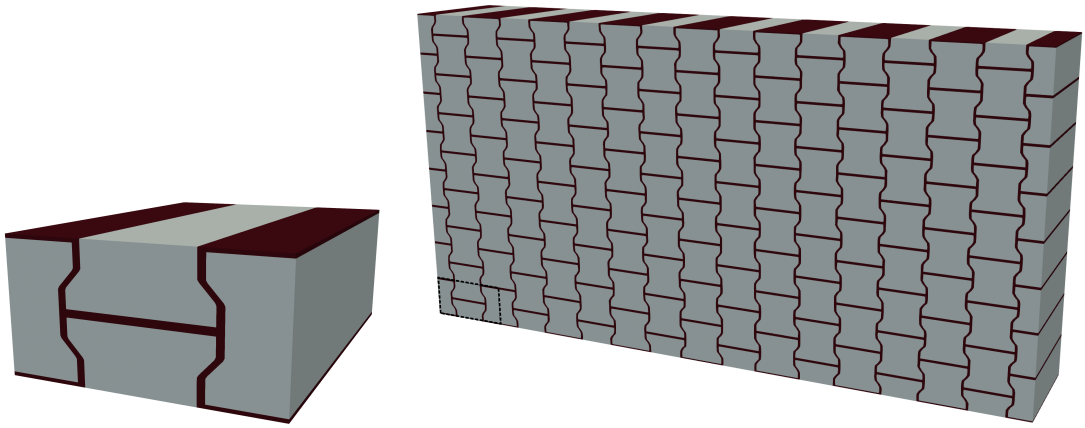
where $\{\mathbf{e}_1, \mathbf{e}_2, \mathbf{e}_3\}$ is the canonical basis of $\mathbb{R}^3$.

Definition 7.2. *Let f be a scalar function defined for almost every $\mathbf{y} \in Y$. Its extension by periodicity to the whole $\mathbb{R}^3$, $f^\#$, is defined as*

$$f^\#(\mathbf{x}) = f^\#(\mathbf{y} + k_i L_i \mathbf{e}_i) = f(\mathbf{y}) \quad \text{a.e. in } \mathbb{R}^3, \tag{7.2}$$

where $k_i = [x_i / L_i]$ and y_i is its remainder, being $[z]$ the integer part of any real number z.

USC UNIVERSIDADE DE SANTIAGO



(**a**) Reference cell (Y). (**b**) Masonry wall (Ω).

Figure 7.1: Masonry wall obtained repeating a representative element.

In the case of vector-valued and tensor-valued functions, we say that they are Y-periodic and define their extension by applying Definition 7.1 and 7.2 to their components, respectively.

For functions that belong to the function space $\mathbf{H}^1(Y)$ we introduce appropriate subspaces that preserve the notion of periodicity described in Definition 7.1. First, the space $C^\infty_{per}(Y)$ is defined as the subset of $C^\infty(\mathbb{R}^3)$ of Y-periodic functions. Then, we denote as $H^1_{per}(Y)$ the closure of $C^\infty_{per}(Y)$ in the H^1-norm. Its vector-valued counterpart is denoted as $\mathbf{H}^1_{per}(Y)$.

Remark 7.1. *The space $H^1_{per}(Y)$ can be equivalently defined as the space composed of those functions $u \in H^1(Y)$ such that u has identical traces on the opposite faces of the reference period Y (see e.g. Höpker, 2016).*

In addition, we introduce the following subspace of $\mathbf{H}^1_{per}(Y)$, formed by those elements that have zero mean value:

$$\mathbf{W}_{per}(Y) = \{\mathbf{v} \in \mathbf{H}^1_{per}(Y) \mid \mathcal{M}_Y(\mathbf{v}) = \mathbf{0}\}. \tag{7.3}$$

7.2. Homogenisation in linear elasticity

Let Ω be a domain of $\mathbb{R}^3$. We assume that it is constructed by the assembly of several periodically repeating reference cells Y, as illustrated in Figure 7.1. The size of the heterogeneities, in this example, the size of the joints separating the bricks, is characterised by the size of the reference cell, and is assumed to be small in comparison to that of the complete domain. Mathematically, this is defined through a small parameter $\epsilon > 0$, which represents this periodic structure and, by definition, the scale of the reference elements composing Ω is taken to be ϵY.

The underlying idea in homogenisation is to observe that letting $\epsilon \to 0$ we reduce and make the heterogeneities less significant, effectively meaning that the composition of the materials becomes homogeneous.

In the specific framework of linear elasticity, we set $\mathbb{C}$, the fourth order elasticity tensor, such that it is Y-periodic and $\mathbb{C} \in \mathcal{M}(\alpha, \beta, Y)$ for some $\alpha, \beta > 0$. Let ϵ be a positive real number. We define

$$\begin{aligned} C^\epsilon_{ijrs}(\mathbf{x}) &= C_{ijrs}\left(\frac{\mathbf{x}}{\epsilon}\right), \\ \mathbb{C}^\epsilon(\mathbf{x}) &= \mathbb{C}\left(\frac{\mathbf{x}}{\epsilon}\right) = (C^\epsilon_{ijrs}(\mathbf{x})), \end{aligned} \tag{7.4}$$

a.e. on $\mathbf{x} \in \mathbb{R}^3$ and with $i, j, r, s \in I_3$. Note that with these definitions, $\mathbb{C}^\epsilon \in \mathcal{M}(\alpha, \beta, \Omega)$.

USC DE SANTIAGO DE COMPOSTELA

We present below a variant of the model problem $(\mathcal{P})$ where the elasticity tensor depends on the periodicity parameter ϵ.

Problem $(\mathcal{P}^\epsilon)$. Find $\mathbf{u}^\epsilon$ such that:

$$\begin{aligned} -\operatorname{Div}(\boldsymbol{\sigma}^\epsilon(\mathbf{u}^\epsilon)) &= \mathbf{f}, && \text{in } \Omega, \\ \boldsymbol{\sigma}^\epsilon(\mathbf{u}^\epsilon) &= \mathbb{C}^\epsilon : \boldsymbol{\varepsilon}(\mathbf{u}^\epsilon), && \text{in } \Omega, \\ \mathbf{u}^\epsilon &= \mathbf{0}, && \text{on } \Gamma_D, \\ \boldsymbol{\sigma}^\epsilon(\mathbf{u}^\epsilon)\mathbf{n} &= \mathbf{g}, && \text{on } \Gamma_N. \end{aligned}$$

If $\mathbf{f} \in \mathbf{H}^1_{0,\Gamma_D}(\Omega)'$ and $\mathbf{g} \in \mathbf{H}^{-\frac{1}{2}}(\Gamma_N)$, the following weak formulation of $\mathcal{P}^\epsilon$ is obtained.

Problem $(\mathcal{VP}^\epsilon)$. Find $\mathbf{u}^\epsilon \in \mathbf{H}^1_{0,\Gamma_D}(\Omega)$ such that:

$$\int_\Omega \boldsymbol{\sigma}^\epsilon(\mathbf{u}^\epsilon) : \boldsymbol{\varepsilon}(\mathbf{v})\, dV = \langle \mathbf{f}, \mathbf{v} \rangle_{\mathbf{H}^1_{0,\Gamma_D}(\Omega)', \mathbf{H}^1_{0,\Gamma_D}(\Omega)} + \langle \mathbf{g}, \mathbf{v} \rangle_{\mathbf{H}^{-\frac{1}{2}}(\Gamma_N), \mathbf{H}^{\frac{1}{2}}(\Gamma_N)} \quad \forall \mathbf{v} \in \mathbf{H}^1_{0,\Gamma_D}(\Omega). \tag{7.5}$$

Under the previous assumptions, it can be shown that (7.5) has a unique solution (see Cioranescu & Donato, 1999, Th. 10.6).

7.2.1. Auxiliary periodic problems

The following auxiliary periodic problems on the reference unit cell Y are defined, whose solutions are known as the *corrector functions* for the linearised elasticity system $(\mathcal{P}^\epsilon)$, $\boldsymbol{\mathcal{X}}^{lk}$, for $l, k \in I_3$.

Problem $(\mathcal{P}_C)^{lk}$. Find $\boldsymbol{\mathcal{X}}^{lk}$ such that:

$$\begin{aligned} -\operatorname{Div}(\boldsymbol{\sigma}(\boldsymbol{\mathcal{X}}^{lk} - \mathbf{p}^{lk})) &= \mathbf{0}, && \text{in } Y, \\ \boldsymbol{\sigma}(\boldsymbol{\mathcal{X}}^{lk}) &= \mathbb{C} : \boldsymbol{\varepsilon}(\boldsymbol{\mathcal{X}}^{lk}), && \text{in } Y, \\ \boldsymbol{\mathcal{X}}^{lk}\ & Y-\text{periodic}, \\ \mathcal{M}_Y(\boldsymbol{\mathcal{X}}^{lk}) &= \mathbf{0}, \end{aligned}$$

where

$$\mathbf{p}^{lk} = y_k \mathbf{e}_l.$$

The following second-order tensor is introduced:

$$\mathbf{E}^{ij} = \frac{1}{2}(\mathbf{e}_i \otimes \mathbf{e}_j + \mathbf{e}_j \otimes \mathbf{e}_i). \tag{7.6}$$

Recalling the definition of the space $\mathbf{W}_{per}(Y)$ (7.3), we obtain the following weak formulation of Problem $(\mathcal{P}_C)^{lk}$.

Problem $(\mathcal{VP}_C)^{lk}$. Find $\boldsymbol{\mathcal{X}}^{lk} \in \mathbf{W}_{per}(Y)$ such that:

$$\int_Y \boldsymbol{\sigma}(\boldsymbol{\mathcal{X}}^{lk}) : \boldsymbol{\varepsilon}(\mathbf{v})\, dV = \int_Y \boldsymbol{\sigma}(\mathbf{p}^{lk}) : \boldsymbol{\varepsilon}(\mathbf{v})\, dV, \quad \forall \mathbf{v} \in \mathbf{W}_{per}(Y), \tag{7.7}$$

which has a unique solution for $l, k \in I_3$ (see Cioranescu & Donato, 1999, Prop. 10.10).

7.2.2. Homogenisation result

The behaviour of the weak solution $\mathbf{u}^\epsilon$ to Problem $(\mathcal{VP}^\epsilon)$ as $\epsilon \to 0$ is determined by the following result, extracted from Cioranescu & Donato (1999, Th. 10.11).

USC DE SANTIAGO DE COMPOSTELA

Theorem 7.1. *Let* $\mathbf{f} \in \mathbf{H}^1_{0,\Gamma_D}(\Omega)'$, $\mathbf{g} \in \mathbf{H}^{-\frac{1}{2}}(\Gamma_N)$ *and* $\mathbb{C}^\epsilon$ *defined in* (7.4), *with* $\mathbb{C} \in \mathcal{M}(\alpha, \beta, Y)$ *for some* $\alpha, \beta > 0$. *Set* $\mathbf{u}^\epsilon \in \mathbf{H}^1_{0,\Gamma_D}(\Omega)$ *as the solution of Problem* $(\mathcal{VP}^\epsilon)$. *Then:*

(i) $\mathbf{u}^\epsilon \rightharpoonup \mathbf{u}^0$ *weakly in* $\mathbf{H}^1_{0,\Gamma_D}(\Omega)$.

(ii) $\mathbb{C}^\epsilon : \varepsilon(\mathbf{u}^\epsilon) \rightharpoonup \mathbb{C}^0 : \varepsilon(\mathbf{u}^0)$ *weakly in* $\mathbf{L}^2(\Omega)$,

being the displacement field $\mathbf{u}^0$ *the unique solution in* $\mathbf{H}^1_{0,\Gamma_D}(\Omega)$ *of the homogenised system*

Problem $(\mathcal{P}^0)$. *Find* $\mathbf{u}^0$ *such that:*

$$\begin{aligned} -Div(\boldsymbol{\sigma}^0(\mathbf{u}^0)) &= \mathbf{f}, && \text{in } \Omega, \\ \boldsymbol{\sigma}^0(\mathbf{u}^0) &= \mathbb{C}^0 : \varepsilon(\mathbf{u}^0), && \text{in } \Omega, \\ \mathbf{u}^0 &= \mathbf{0}, && \text{on } \Gamma_D, \\ \boldsymbol{\sigma}^0(\mathbf{u}^0)\mathbf{n} &= \mathbf{g}, && \text{on } \Gamma_N. \end{aligned}$$

The homogenised tensor $\mathbb{C}^0$ *is constant, and its elements are given by*

$$C^0_{ijlk} = \mathcal{M}_Y(C_{ijrs}\varepsilon_{rs}(\mathbf{w}^{lk})), \tag{7.8}$$

where

$$\mathbf{w}^{lk} = -\boldsymbol{\mathcal{X}}^{lk} + \mathbf{p}^{lk}, \tag{7.9}$$

for any $l, k \in I_3$.

It can be shown that there exist $\alpha^0, \beta^0 > 0$ such that the homogenised material tensor, obtained in (7.8), satisfies that $\mathbb{C}^0 \in \mathcal{M}(\alpha^0, \beta^0, \Omega)$. Therefore, it has the classic symmetries of an elasticity tensor and preserves the coercivity of the original tensor.

7.3. Numerical solution of the auxiliary problems

In this section, we briefly address the numerical methodology that is followed to numerically obtain an approximation of the corrector functions for the linear elasticity system, i.e., to solve the auxiliary periodic problems $(\mathcal{VP}_C)^{lk}$. In Chapters 8 and 9, two alternative methodologies to obtain a characterisation of the effective coefficients of the homogenised material are presented. These methodologies turn out to be more amenable than the corrector problems to obtain a numerical solution, but have some specific drawbacks. To analyse their performance, several arrangements of composites and mechanical properties of the components are tested, comparing the results to those obtained by considering the correctors.

To numerically solve $(\mathcal{VP}_C)^{lk}$, instead of seeking an internal approximation of the space $\mathbf{W}_{per}(Y)$, the solution is sought in $\mathbf{H}^1_{per}(Y)$ and the zero mean value constraint is weakly imposed by introducing a Lagrange multiplier. To this end, a similar procedure to that detailed for the pure Neumann linear elasticity problem in Section 6.3.3 is followed. Specifically, let $b_C(\cdot,\cdot)$ denote the following bilinear form in $\mathbf{H}^1_{per}(Y) \times \widetilde{Q}$:

$$b_C(\mathbf{u}, \mathbf{q}) = \int_Y \mathbf{u} \cdot \mathbf{q} \; dV, \tag{7.10}$$

where $\widetilde{Q} = \mathbb{R}^3$. To enforce the constraint, we note that it suffices to ensure that each corrector function $\boldsymbol{\mathcal{X}}^{lk}$ is such that

$$b_C(\boldsymbol{\mathcal{X}}^{lk}, \mathbf{q}) = 0, \; \forall \mathbf{q} \in \widetilde{Q}.$$

Moreover, let $l^{lk}_C(\cdot)$ denote the linear functional in $\mathbf{H}^1_{per}(Y)$ that corresponds to the right hand side of each auxiliary periodic problem, i.e.:

$$l^{lk}_C(\mathbf{v}) = \int_Y \boldsymbol{\sigma}(\mathbf{p}^{lk}) : \varepsilon(\mathbf{v}) \, dV. \tag{7.11}$$

USC UNIVERSIDADE DE SANTIAGO DE COMPOSTELA

Using (7.10) and (7.11), the corresponding saddle point formulation reads as follows.

Problem $(\mathcal{LP}_C)^{lk}$. Find $(\boldsymbol{\mathcal{X}}^{lk}, \widetilde{\mathbf{p}}) \in \mathbf{H}^1_{per}(Y) \times \widetilde{Q}$ such that:

$$\begin{aligned} &a(\boldsymbol{\mathcal{X}}^{lk}, \mathbf{v}) + b_C(\mathbf{v}, \widetilde{\mathbf{p}}) = l_C^{lk}(\mathbf{v}), && \forall \mathbf{v} \in \mathbf{H}^1_{per}(Y), \\ &b_C(\boldsymbol{\mathcal{X}}^{lk}, \mathbf{q}) = 0, && \forall \mathbf{q} \in \widetilde{Q}. \end{aligned}$$

To numerically approximate the solution to $(\mathcal{LP}_C)^{lk}$, V_h is considered as the space of continuous functions whose restrictions to the elements forming the mesh of Y are polynomials of degree 1. To guarantee the periodicity of the solution, we shall assume that the mesh is constructed so that the nodes on each face have a corresponding node on the opposite face. Then, we denote as $V_{h,per}$ the subspace of V_h where the degrees of freedom on these opposite faces are set to have equal value. Seeking the approximation to $\boldsymbol{\mathcal{X}}^{lk}$ in this subspace, we obtain the subsequent discrete counterpart to Problem $(\mathcal{LP}_C)^{lk}$.

Problem $(\mathcal{LP}_C)^{lk}_h$. Find $(\boldsymbol{\mathcal{X}}^{lk}_h, \widetilde{\mathbf{p}}) \in V_{h,per} \times \widetilde{Q}$ such that:

$$\begin{aligned} &a(\boldsymbol{\mathcal{X}}^{lk}_h, \mathbf{v}_h) + b_C(\mathbf{v}_h, \widetilde{\mathbf{p}}) = l_C^{lk}(\mathbf{v}_h), && \forall \mathbf{v}_h \in V_{h,per}, \\ &b_C(\boldsymbol{\mathcal{X}}^{lk}_h, \mathbf{q}) = 0, && \forall \mathbf{q} \in \widetilde{Q}. \end{aligned}$$

Note that to obtain a numerical solution of the previous problem is not entirely straightforward. First, the introduction of the multiplier to enforce the zero-mean constraint difficults the use of iterative methods to solve the corresponding algebraic system. Furthermore, although the periodicity conditions can be imposed readily when the mesh is such that the points in the opposite faces of the domain coincide, for complex reference cells it is not always feasible to design such meshes. In particular, for arbitrary meshes that are unstructured, more complicated techniques are necessary to impose periodicity (see V.-D. Nguyen et al., 2012). In Chapters 8 and 9, two sets of problems whose solution also can be used to obtain a characterisation of the homogenised material are introduced. They are also defined in the reference cell Y, but eliminate the need of the periodicity constraint.

USC UNIVERSIDADE DE SANTIAGO DE COMPOSTELA

USC
UNIVERSIDADE
DE SANTIAGO
DE COMPOSTELA

Chapter 8

Stress basic tests

This chapter is devoted to the discussion of a simple technique that allows to obtain the coefficients of a homogeneous material whose linear elastic mechanical response is similar to that of a heterogeneous material. To this end, we compute the numerical solution of a set of basic tests inspired by how experimental uniaxial compression and shear tests are conducted. The mathematical model of these basic tests corresponds to pure traction linear elasticity problems, i.e., linear elasticity problems with pure Neumann boundary conditions. Since this type of boundary condition specifies the stresses, we refer to this technique as stress basic tests (S-BT). As discussed in Section 6.3, the pure traction linear elasticity problem is not well-posed. Therefore, to obtain the homogenised equivalent material, we apply a formulation with a Lagrange multiplier with the described preconditioning strategy.

The outline of this chapter is as follows. In Section 8.1 we introduce the main idea of the methodology. Subsequently, in Section 8.2, the specific linear elasticity problems that are solved are stated. Section 8.3 is devoted to address the performance of the methodology with some practical examples inspired by real applications. Lastly, some drawbacks of this methodology are discussed.

8.1. Introduction

Set Y as the *reference unit cell*, defined in (7.1) and, for a fixed $\epsilon > 0$, consider the linear elasticity system $(\mathcal{P}^\epsilon)$. Instead of solving the periodic auxiliary problems to obtain the corrector functions, in this chapter, a conceptually simple approach is presented.

Using that the geometrical symmetry is satisfied in all directions of the material, we assume that a good characterisation of the mechanical response of the reference cell can be extrapolated to the entire structure. If ϵ is sufficiently small, under suitable circumstances that shall be specified in the sequel, the approximation obtained with this method can be reasonably accurate.

Specifically, to obtain an approximation of the response of the heterogeneous material without having to take into account the particularities of its microstructure, we shall consider a homogeneous constant stiffness matrix, denoted as $[\overline{\mathbf{C}}]$. The entries of this matrix are obtained through the solution of six basic tests defined in the cell Y, subjecting this reference period to uniform stress conditions. They are defined such that independent stress states are generated at the unit cell. In particular, three uniaxial compression tests and three shear tests are posed.

To this end, it suffices to compute 21 components of $[\overline{\mathbf{C}}]$, provided that it should be a symmetric matrix. Nevertheless, we propose to compute all 36 of them in order to check this assertion. With this purpose, we pose a system composed of 36 equations that arise from solving 6 problems. Given the displacement field solution to the mth basic test, $\mathbf{u}^m$, with $m \in I_6$, we compute the mean stress and strain, which for simplicity we denote as $\{\overline{\boldsymbol{\sigma}}\}^m$ and $\{\overline{\boldsymbol{\varepsilon}}\}^m$, respectively:

$$\{\overline{\boldsymbol{\sigma}}\}^m := \mathcal{M}_Y(\{\boldsymbol{\sigma}\}(\mathbf{u}^m)), \tag{8.1}$$

$$\{\overline{\boldsymbol{\varepsilon}}\}^m := \mathcal{M}_Y(\{\boldsymbol{\varepsilon}\}(\mathbf{u}^m)). \tag{8.2}$$

We shall assume that the matrix $[\overline{\mathbf{C}}] = (\bar{c}_{pq})$, $p, q \in I_6$, relates the mean stress (8.1) to the mean strain (8.2) through the usual constitutive law for linear elasticity, i.e., for a fixed $m \in I_6$, it holds that

$$[\overline{\mathbf{C}}]\{\overline{\boldsymbol{\varepsilon}}\}^m = \{\overline{\boldsymbol{\sigma}}\}^m. \tag{8.3}$$

USC UNIVERSIDADE DE SANTIAGO DE COMPOSTELA

The previous expression gives 6 equations for the mth basic test. Therefore, from the 6 tests we obtain the desired 36 equations. These will uniquely determine the matrix $[\overline{\mathbf{C}}]$ if the average stress and strain tensors are linearly independent for the designed tests. Equivalently, the system defined in (8.3) can be recast in matrix form. To this end, using the solutions to the basic tests, we define the matrix $\boldsymbol{\mathcal{E}} = (\mathcal{E}_{mp})$, where

$$\mathcal{E}_{mp} = (\mathcal{M}_Y(\{\boldsymbol{\varepsilon}\}_p(\mathbf{u}^m))) = (\{\overline{\boldsymbol{\varepsilon}}\}_p^m), \tag{8.4}$$

with $m, p \in I_6$. Note that the mth row of $\mathcal{E}$ coincides with the deformation vector of the mth basic test.

A block matrix $\widetilde{\boldsymbol{\mathcal{E}}}$, of dimension 36×36, is assembled by placing six diagonal blocks equal to the matrix $\boldsymbol{\mathcal{E}}$ and zeros elsewhere:

$$\widetilde{\boldsymbol{\mathcal{E}}} = \begin{pmatrix} \boldsymbol{\mathcal{E}} & & & \\ & \boldsymbol{\mathcal{E}} & & \\ & & \ddots & \\ & & & \boldsymbol{\mathcal{E}} \end{pmatrix}, \tag{8.5}$$

i.e., for $n, t \in I_{36}$, then the components of $\widetilde{\boldsymbol{\mathcal{E}}}$ are

$$\widetilde{\mathcal{E}}_{nt} = \mathcal{M}_Y(\{\boldsymbol{\varepsilon}\}_{(t)_6}(\mathbf{u}^{(n)_6}))\delta_{\lceil n \rceil_6 \lceil t \rceil_6} = \{\overline{\boldsymbol{\varepsilon}}\}_{(t)_6}^{(n)_6}\delta_{\lceil n \rceil_6 \lceil t \rceil_6},$$

where for any $z, N \in \mathbb{N}$, the function $(z)_N$ is defined as the remainder of the integer division of $z-1$ by N plus one:

$$(z)_N = z - N\left[\frac{z-1}{N}\right].$$

In addition, let $\lceil z \rceil_N$ denote the ceiling function of the division of $z-1$ by N, i.e.:

$$\lceil z \rceil_N = \left[\frac{z-1}{N}\right] + 1.$$

For the sake of simplicity, in the following we shall omit the subscript and denote $(z) = (z)_6$ and $\lceil z \rceil = \lceil z \rceil_6$.

Let $\mathbf{b} \in \mathbb{R}^{36}$ denote the vector whose components are defined as

$$b_n = \mathcal{M}_Y(\{\boldsymbol{\sigma}\}_{\lceil n \rceil}(\mathbf{u}^{(n)})) = \{\overline{\boldsymbol{\sigma}}\}_{\lceil n \rceil}^{(n)},$$

for any $n \in I_{36}$. For instance, for $n = 7$:

$$b_7 = \mathcal{M}_Y(\{\boldsymbol{\sigma}\}_2(\mathbf{u}^1)) = \mathcal{M}_Y(\sigma_{22}(\mathbf{u}^1)).$$

Set $\overline{\mathbf{c}} \in \mathbb{R}^{36}$ as the arrangement of the unknown stiffness matrix as a vector. Specifically, its nth component, with $n \in I_{36}$, is

$$\overline{c}_n = \overline{c}_{pq},$$

where $p = \lceil n \rceil$ and $q = (n)$.

Therefore, to obtain the stiffness matrix corresponding to the homogeneous equivalent material $[\overline{\mathbf{C}}]$, we solve the system of equations (8.3), which in matrix form reads as

$$\widetilde{\boldsymbol{\mathcal{E}}}\overline{\mathbf{c}} = \mathbf{b}. \tag{8.6}$$

In this form, it follows that the system has a unique solution if the mean strains computed from the basic tests are linearly independent, i.e., the rows of the matrix $\mathcal{E}$ are independent. In the subsequent section, we state the problems that we aim to solve to compute $[\overline{\mathbf{C}}]$.

8.2. Statement of the stress basic tests

The displacement $\mathbf{u}^m$, $m \in I_6$, is obtained as the solution of the following linear elasticity problem, defined in the reference cell Y and considering a pure Neumann boundary condition.

Problem $(\mathcal{P}_{PN})^m$. Find $\mathbf{u}^m$ such that:

$$\begin{aligned} -\operatorname{Div}(\boldsymbol{\sigma}(\mathbf{u}^m)) &= \mathbf{0}, \quad \text{in } Y, \\ \boldsymbol{\sigma}(\mathbf{u}^m) &= \mathbb{C} : \boldsymbol{\varepsilon}(\mathbf{u}^m), \quad \text{in } Y, \\ \boldsymbol{\sigma}(\mathbf{u}^m)\mathbf{n} &= \boldsymbol{\Sigma}^m \mathbf{n}, \quad \text{on } \partial Y, \end{aligned} \tag{8.7}$$

where $\boldsymbol{\Sigma}^m$ is a constant second order tensor such that $\boldsymbol{\Sigma}^m \in Sym$.

The corresponding weak formulation, obtained analogously as that of Problem $(\mathcal{VP}_{PN})$, reads as follows.

Problem $(\mathcal{VP}_{PN})^m$. Find $\mathbf{u}^m \in \mathbf{H}^1(Y)$ such that:

$$a(\mathbf{u}^m, \mathbf{v}) = l^m(\mathbf{v}), \qquad \forall \mathbf{v} \in \mathbf{H}^1(Y),$$

where the bilinear form $a(\mathbf{u}, \mathbf{v})$ is defined similarly as (6.20), but in the reference cell Y instead, and $l^m(\mathbf{v})$ corresponds to definition (6.21) on the reference cell Y with $\mathbf{f} = \mathbf{0}$ and $\mathbf{g} = \boldsymbol{\Sigma}^m \mathbf{n}$:

$$\begin{aligned} a(\mathbf{u}, \mathbf{v}) &= \int_Y (\mathbb{C} : \boldsymbol{\varepsilon}(\mathbf{u})) : \boldsymbol{\varepsilon}(\mathbf{v}) \, dV, \\ l^m(\mathbf{v}) &= \int_{\partial Y} \boldsymbol{\Sigma}^m \mathbf{n} \cdot \mathbf{v} \, dA. \end{aligned} \tag{8.8}$$

To obtain six independent stress states in the reference cell Y, the stress condition on the boundary, $\boldsymbol{\Sigma}^m$, is defined as follows. Let $m \in I_6$, then for $l, k \in I_3$ such that $\gamma(l,k) = m$, we introduce

$$\boldsymbol{\Sigma}^m = \boldsymbol{\Sigma}^{lk} := 2\widetilde{\eta}\mathbf{E}^{lk} - \widetilde{\eta}\operatorname{Tr}(\mathbf{E}^{lk})(\mathbf{e}_l \otimes \mathbf{e}_k), \tag{8.9}$$

where the second order tensor $\mathbf{E}^{lk}$ is defined in (7.6) and $\widetilde{\eta} \in \mathbb{R}$ is a parameter.

Remark 8.1. *Set $\widetilde{\eta} = 1$ in (8.9). It is straightforward to notice that if $m \leq 3$, provided that $\gamma(l,k) = m$ then $l = k = m$ and*

$$\Sigma_{ij}^{mm} = \begin{cases} 1, & \text{if } i = j = m, \\ 0, & \text{otherwise.} \end{cases}$$

Therefore, for instance, if $m = 1$, then it holds that

$$\boldsymbol{\Sigma}^1 = \boldsymbol{\Sigma}^{11} = \begin{pmatrix} 1 & 0 & 0 \\ 0 & 0 & 0 \\ 0 & 0 & 0 \end{pmatrix}.$$

Hence, this test corresponds to a uniaxial stress state in the coordinate axis $\mathbf{e}_m$. The boundary condition on ∂Y (8.7) simply becomes

$$\boldsymbol{\sigma}(\mathbf{u}^m)\mathbf{n} = \begin{cases} \pm\mathbf{e}_m, & \text{on } \Gamma_m^{\pm}, \\ \mathbf{0}, & \text{otherwise.} \end{cases}$$

On the other hand, if $m > 3$, then $l \neq k$ and (8.9) simplifies to $\boldsymbol{\Sigma}^m = 2\mathbf{E}^{lk}$. For instance, if $m = 4$, then $l = 2$ and $k = 3$ (or $l = 3$ and $k = 2$) and thus

$$\Sigma^4 = \Sigma^{23} = \begin{pmatrix} 0 & 0 & 0 \\ 0 & 0 & 1 \\ 0 & 1 & 0 \end{pmatrix}.$$

Therefore, in this case, the Neumann condition (8.7) reads as

$$\boldsymbol{\sigma}(\mathbf{u}^4)\mathbf{n} = \begin{cases} \pm\mathbf{e}_2, & \text{a.e. on } \Gamma_3^{\pm}, \\ \pm\mathbf{e}_3, & \text{a.e. on } \Gamma_2^{\pm}, \\ \mathbf{0}, & \text{on } \partial Y \setminus (\Gamma_2^{\pm} \cup \Gamma_3^{\pm}). \end{cases}$$

So, the test corresponds to a simple shearing in the orthogonal directions $\mathbf{e}_2$ and $\mathbf{e}_3$.

USC UNIVERSIDADE DE SANTIAGO

8.3. Numerical experiments

This section deals with the analysis of the performance of the stress basic test methodology (S-BT) for some example compositions of materials. With this purpose, we select three different reference cells Y and compute the corresponding equivalent material stiffness matrix $[\overline{\mathbf{C}}]$ by solving the system of equations (8.6) after obtaining the numerical approximations to the solution to Problem $(\mathcal{P}_{PN})^m$, $m \in I_6$. We denote the approximation of such matrix as $[\overline{\mathbf{C}}_h]$.

Several configurations of the domain Ω are constructed by assembling periodically repeating cells. In this domain, the mechanical response predicted by the equivalent material is tested numerically against the heterogeneous material to assess whether it yields a reasonable approximation of the displacements and stresses. In addition, we also consider the homogenised material that is obtained by solving the auxiliary periodic problems using the saddle point formulation $(\mathcal{LP}_C)^{lk}_h$, introduced in Chapter 7. Some naïve choices of the equivalent material effective properties, such as a rule of mixtures, are also considered for comparison.

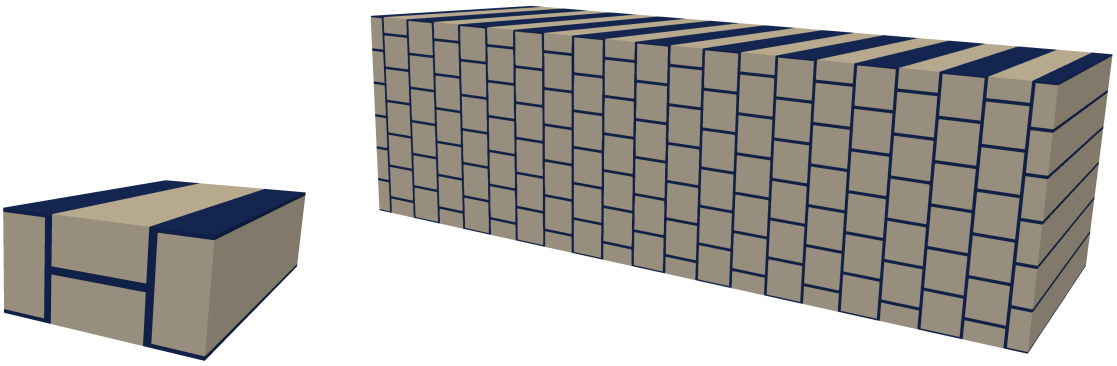
Note that the choice of the cell is not unique and multiple options are possible for each configuration. Certainly, it is computationally advantageous to consider the smallest possible Y such that it periodically repeats over the domain Ω. Nevertheless, as it will be discussed in Section 8.3.4, the equivalent material stiffness matrix obtained with the S-BT methodology is not independent of the reference cell choice and, in some cases, the effective material predictions improve significantly with larger reference cells. This undesirable behaviour, among other shortcomings of the strategy that will be discussed below, motivate the introduction of a new set of basic tests in Chapter 9 which are mathematically rigorous.

The preliminary analysis discussed in this section will be further completed by more numerical results presented at the end of Chapter 9. To construct all the depicted meshes of unit cells and assemblies of these for the numerical experiments, taking advantage of the simple configurations that are considered, an automated tool in *Python* was developed to directly construct the geometries and meshes. To this end, several components available in the FEniCS library are used (see e.g. Alnæs et al., 2015). The cell geometries are automatically built from specific parameters, such as the thickness of the mortar joints or the width of the bricks.

In all the cases analysed in this section, the heterogeneous compositions of materials correspond to layouts of two different homogeneous isotropic linear elastic materials. Therefore, their mechanical response is determined by the values of the Young's modulus, E, and the Poisson's ratio, ν. For the sake of simplicity, and since the main motivation of this work is to address the characterisation of the masonry of bricks and joints in the BF ceramic cup, we shall refer in all the considered cases as "brick" to the most predominant material in the heterogeneous configuration and as "mortar" to the less predominant one. We remark that the scope of the presented methodology is not restricted to the characterisation of masonries and can be suitable for various classes of composite materials. In Table 8.1, we gather the properties of the materials considered in the three discussed cases. The selected values for Cell A come from the preliminary work Barral et al. (2018), whereas those proposed for Cell B and Cell C are chosen carefully to better showcase the behaviour of the stress basic tests to obtain the homogenised material. In all the computations presented in this Section, the parameter $\widetilde{\eta}$ in (8.9) takes the value $\widetilde{\eta} = 1000$.

Table 8.1: Material properties for the numerical experiments with the square brick and mortar masonry (Cell A), the hexagonal brick layout with mortar joints (Cell B) and the layered composite (Cell C).

	Cell A		Cell B		Cell C	
	E [Pa]	ν [–]	E [Pa]	ν[–]	E [Pa]	ν [–]
Brick	$7{\cdot}10^9$	0.2	$1{\cdot}10^9$	0.08	$1{\cdot}10^7$	0.25
Mortar	$7{\cdot}10^7$	0.2	$1{\cdot}10^7$	0.2	$1{\cdot}10^9$	0.1



(**a**) Reference cell (Y). (**b**) Masonry wall (Ω).

Figure 8.1: Square brick and mortar masonry (Cell A).

8.3.1. Test problems

A couple of simple problems are presented to compare the mechanical response of the heterogeneous assembly of unit cells and the computed homogenised equivalent materials. For all the proposed reference cells Y, the domain Ω is constructed by periodically repeating the cell in the canonical basis directions, generating a composite material that has a heterogeneous microstructure. Since Y is assumed to be prismatic with dimensions L_i, $i \in I_3$, as introduced in (7.1), the boundaries of Ω are partitioned in six subsets in an analogous manner to those of Y, i.e.:

$$\Gamma_i^+ := \{\mathbf{x} \in \overline{\Omega} : x_i = x_{i,max}\},$$
$$\Gamma_i^- := \{\mathbf{x} \in \overline{\Omega} : x_i = x_{i,min}\},$$

where $x_{i,min}$ and $x_{i,max}$ denote the minimum and maximum value of the corresponding coordinate in $\overline{\Omega}$, respectively. Note that, by construction $x_{i,min} = k_{min} L_i$ and $x_{i,max} = k_{max} L_i$ for some $k_{min}, k_{max} \in \mathbb{Z}$, for all $i \in I_3$.

Below, we briefly describe the data and boundary conditions used for each test problem in this section.

Problem 1. The general elasticity problem $(\mathcal{P})$ is considered, with $\Gamma_D = \Gamma_1^{\pm}$. Hence, $\Gamma_N = \partial\Omega \setminus \Gamma_D$. The density of body and surface forces are respectively set as:

$$\mathbf{f} = (0, 100, 0)^T \text{ N/m}^3,$$
$$\mathbf{g} = \mathbf{0} \text{ Pa}.$$

For the second problem that is proposed, instead of directly using problem $(\mathcal{P})$ for different data, we consider a slight variant of it where symmetry conditions are imposed. This allows to avoid the generation of high stresses in the corners where the zero displacement condition is specified. Namely, we solve the problem below.

Problem 2. Find $\mathbf{u}$ such that:

$$\begin{aligned}
-\operatorname{Div}(\boldsymbol{\sigma}(\mathbf{u})) &= \mathbf{f}, && \text{in } \Omega,\\
\boldsymbol{\sigma}(\mathbf{u}) &= \mathbb{C} : \boldsymbol{\varepsilon}(\mathbf{u}), && \text{in } \Omega,\\
\mathbf{u} \cdot \mathbf{n} &= 0, \\
\boldsymbol{\sigma}_t &= \mathbf{0}, && \text{on } \Gamma_S,\\
\boldsymbol{\sigma}(\mathbf{u})\mathbf{n} &= \mathbf{g}, && \text{on } \Gamma_N.
\end{aligned}$$

USC UNIVERSIDADE DE SANTIAGO DE COMPOSTELA

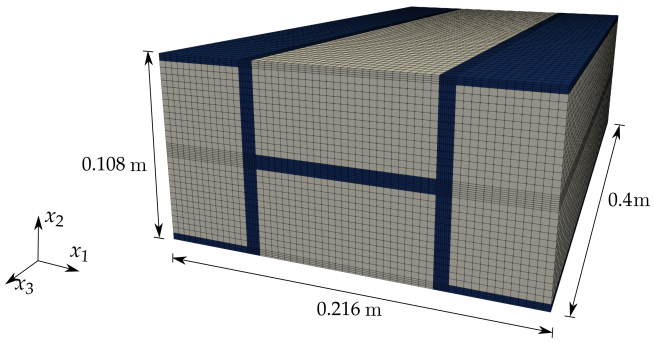


Figure 8.2: Square brick and mortar reference cell, Mesh 4.

In particular, we set $\Gamma_S = \Gamma_1^- \cup \Gamma_2^+ \cup \Gamma_3^+$ and $\Gamma_N = \partial\Omega \setminus \Gamma_S$. The density of body forces is such that $\mathbf{f} = \mathbf{0}$ and the density of surface forces is

$$\mathbf{g} = \begin{cases} -1500\mathbf{e}_1, & \text{on } \Gamma_1^+, \\ 1000\sin(2\pi x_1/x_{1,max})(\mathbf{e}_1 + \mathbf{e}_3), & \text{on } \Gamma_2^-, \\ \mathbf{0}, & \text{on } \Gamma_3^-. \end{cases}$$

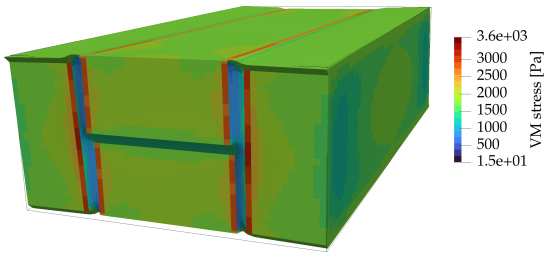
8.3.2. Cell A. Square brick and mortar masonry

The first configuration that we test for the heterogeneous material corresponds to a masonry of bricks and joints. It mimics the dimensions and layout of the ceramic cup of the BF, but considering square bricks instead of the more involved pattern that is used in reality. The proposed reference cell Y and an example of masonry is shown in Figure 8.1. As mentioned previously, it is similar to that analysed in the preliminary work Barral et al. (2018). In this work, the basic tests were designed with an analogous viewpoint, i.e., to propose a set of numerical tests that replicate how experimentation is performed to compute the effective parameters of a material. Nevertheless, the arising pure Neumann linear elasticity problems were numerically solved by prescribing an artificial zero displacement boundary condition in a selected element face (pinning), as described in Section 6.3.5, which yielded unsatisfactory results.

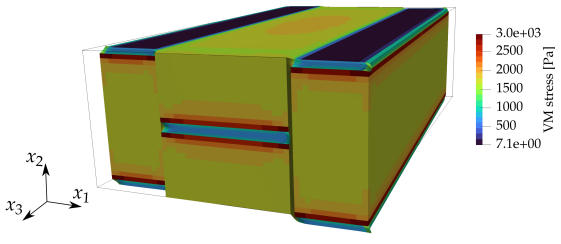
The dimensions of the Cell A are displayed in Figure 8.2. Specifically, we consider that the bricks have a width and height of 0.1 m (x_1 and x_2 directions) and are 0.4 m long (x_3 direction). For this reference cell, we first present a mesh convergence study. The aim is to investigate the possible dependency of the computed stiffness matrix of the homogenised material on the selected discretisation parameter h to approximate the solution of Problem $(\mathcal{P}_{PN})^m$, for $m \in I_6$. With this purpose, taking advantage of the simple geometry of the cell, symmetric hexahedral meshes of the domain are constructed choosing different values for h. Provided that the meshes are not fully uniform, as they are slightly more fine in the mortar joints, the maximum element size, h_{max}, as well as the minimum el-

Table 8.2: Number of vertices in the mesh (N_h), maximum element size (h_{max}) and minimum element size (h_{min}) for the square masonry (Cell A).

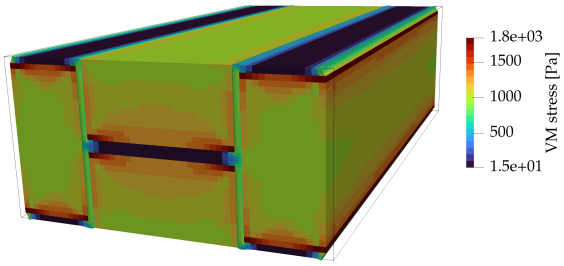
	N_h	h_{max}	h_{min}
Mesh 1	15283	$1.91{\cdot}10^{-3}$	$9.78{\cdot}10^{-4}$
Mesh 2	39975	$1.45{\cdot}10^{-3}$	$4.96{\cdot}10^{-4}$
Mesh 3	85701	$1.16{\cdot}10^{-3}$	$3.31{\cdot}10^{-4}$
Mesh 4	180987	$8.98{\cdot}10^{-4}$	$2.49{\cdot}10^{-4}$
Mesh 5	474397	$6.04{\cdot}10^{-4}$	$1.99{\cdot}10^{-4}$
Mesh 6	1195525	$4.13{\cdot}10^{-4}$	$1.66{\cdot}10^{-4}$



(**a**) Shear test on the plane with normal vector $\mathbf{e}_1$ ($m = 4$).



(**b**) Shear test on the plane with normal vector $\mathbf{e}_2$, ($m = 5$).



(**c**) Uniaxial compression test on the axis $\mathbf{e}_1$, ($m = 1$).

Figure 8.3: Von Mises stress norm on the deformed configuration of Y for the approximation of the solution to the basic tests $(\mathcal{P}_{PN})^m$, $m = 1, 4, 5$; Mesh 4.

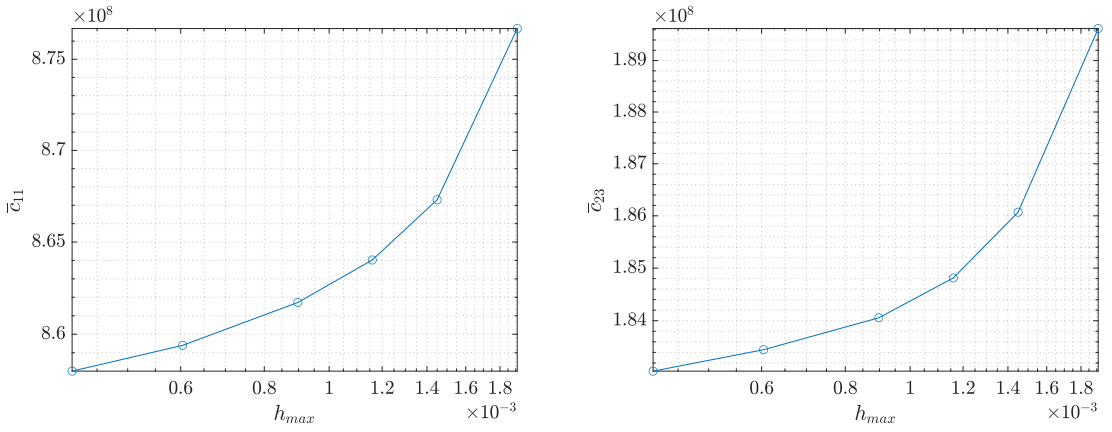
ement size, h_{min}, are reported in Table 8.2, altogether with the number of vertices in each mesh. In Figure 8.2, Mesh 4 is shown.

For each mesh, the complete set of basic tests $(\mathcal{P}_{PN})^m$ is solved. In Figure 8.3, the von Mises stress norm is displayed on the deformed configuration for the basic tests corresponding to $m = \{1, 4, 5\}$ for Mesh 4. We recall that these tests induce a uniaxial stress state along the direction $\mathbf{e}_1$ and a shear stress state in the planes with normal vectors $\mathbf{e}_1$ and $\mathbf{e}_2$, respectively. Then, the equivalent material stiffness matrix $[\overline{\mathbf{C}}_h]$ is computed by solving the system of equations (8.6). Note that the basic tests are solved in the saddle point formulation discussed in Section 6.3.2 for the general elasticity problem with a pure Neumann boundary. For the coarser meshes, a direct method can be used to solve the arising linear system from the discretisation of the problem. Specifically, for Mesh 4, we compute the following stiffness matrix:

$$[\overline{\mathbf{C}}_h] = \begin{pmatrix} \mathbf{8.62{\cdot}10^8} & \mathbf{7.41{\cdot}10^7} & \mathbf{1.77{\cdot}10^8} & -3.55{\cdot}10^{-7} & -7.71{\cdot}10^{-7} & -8.67{\cdot}10^{-8} \\ \mathbf{7.41{\cdot}10^7} & \mathbf{9.01{\cdot}10^8} & \mathbf{1.84{\cdot}10^8} & 9.55{\cdot}10^{-6} & -1.51{\cdot}10^{-6} & 5.44{\cdot}10^{-6} \\ \mathbf{1.77{\cdot}10^8} & \mathbf{1.84{\cdot}10^8} & \mathbf{5.11{\cdot}10^9} & -2.25{\cdot}10^{-6} & 3.56{\cdot}10^{-6} & 8.81{\cdot}10^{-7} \\ -2.20{\cdot}10^{-7} & 2.21{\cdot}10^{-7} & -1.90{\cdot}10^{-6} & \mathbf{3.73{\cdot}10^8} & 2.98{\cdot}10^{-6} & -1.53{\cdot}10^{-6} \\ -8.56{\cdot}10^{-8} & 1.75{\cdot}10^{-7} & -4.89{\cdot}10^{-6} & 1.13{\cdot}10^{-6} & \mathbf{3.33{\cdot}10^8} & -1.09{\cdot}10^{-7} \\ 4.14{\cdot}10^{-6} & -4.81{\cdot}10^{-7} & 1.40{\cdot}10^{-6} & -4.42{\cdot}10^{-6} & -1.42{\cdot}10^{-6} & \mathbf{2.05{\cdot}10^8} \end{pmatrix} \tag{8.10}$$

Hence, the methodology described in this chapter predicts that the mechanical response of the layout of bricks and mortar joints displayed in Figure 8.1, which both behave as isotropic elastic materials, can be characterised as an anisotropic homogeneous elastic material with the coefficients gathered in (8.10). Note that most of the entries in the computed stiffness matrix are zeros to machine precision when compared to the order of the larger coefficients in the matrix. Therefore, the stiffness matrix of the homogenised material corresponds to an orthotropic material with its symmetry planes aligned with the coordinate planes.

USC
DE SANTIAGO
DE COMPOSTELA



(a) $\bar{c}_{11}$. **(b)** $\bar{c}_{23}$.

Figure 8.4: Computed coefficients of the stiffness matrix $\overline{\mathbf{C}}_h$ with respect to the maximum element size h_{max}.

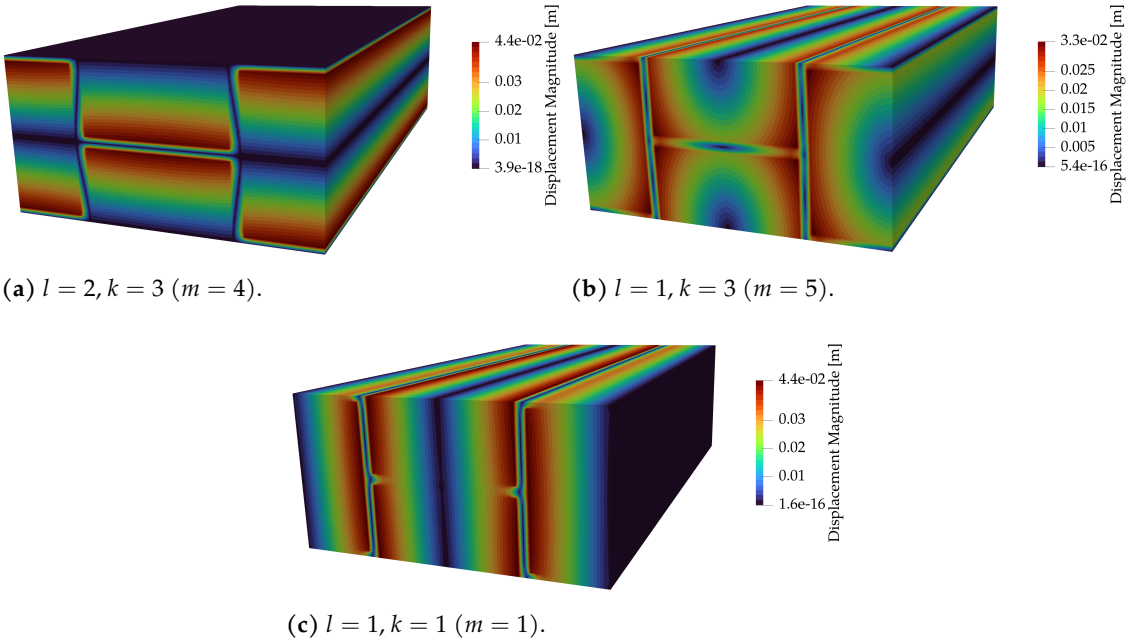
From Mesh 5 onwards, a MinRes iterative solver with the block preconditioning strategy detailed in Section 6.3.6 is used instead, as the computational resources required for an efficient direct solve of the algebraic systems become unfeasible. For the selected absolute and relative tolerance values of 10^{-9}, the computed solutions show no significant differences. Nevertheless, after obtaining the equivalent homogeneous stiffness matrix, the accuracy in the computation of those coefficients that were machine-precision zeros is substantially deteriorated in comparison to the direct solver. To compare the stiffness matrix obtained using an iterative solver with that previously obtained, the solution for Mesh 4 is computed again in this manner, obtaining the subsequent coefficients:

$$[\overline{\mathbf{C}}_h] = \begin{pmatrix} \mathbf{8.62{\cdot}10^8} & \mathbf{7.41{\cdot}10^7} & \mathbf{1.77{\cdot}10^8} & 2.14{\cdot}10^3 & 1.57{\cdot}10^2 & -2.34{\cdot}10^2 \\ \mathbf{7.41{\cdot}10^7} & \mathbf{9.01{\cdot}10^8} & \mathbf{1.84{\cdot}10^8} & 1.81{\cdot}10^3 & 5.47{\cdot}10^2 & -9.80{\cdot}10^1 \\ \mathbf{1.77{\cdot}10^8} & \mathbf{1.84{\cdot}10^8} & \mathbf{5.11{\cdot}10^9} & 8.38{\cdot}10^2 & 7.46{\cdot}10^1 & -7.50{\cdot}10^1 \\ -6.92{\cdot}10^2 & 9.26{\cdot}10^2 & 1.50{\cdot}10^3 & \mathbf{3.73{\cdot}10^8} & 2.96{\cdot}10^0 & -4.83{\cdot}10^2 \\ -3.18{\cdot}10^2 & -3.51{\cdot}10^2 & 1.98{\cdot}10^2 & -1.14{\cdot}10^3 & \mathbf{3.33{\cdot}10^8} & -1.66{\cdot}10^1 \\ 6.85{\cdot}10^3 & -2.80{\cdot}10^3 & 1.79{\cdot}10^3 & -1.60{\cdot}10^3 & -2.60{\cdot}10^1 & \mathbf{2.05{\cdot}10^8} \end{pmatrix}$$

Note that the leading order coefficients computed with the iterative and direct solvers are the same. The differences in the smaller coefficients can be attributed to increased numerical errors in the integration of the stress and strain to obtain the equations of the system (8.6) due to the iterative solver. By adjusting the tolerance values to a lower threshold, the magnitude of the smaller entries can be controlled, although it is of little practical interest, since the calculated values for the 10^{-9} tolerance are sufficient to evidence that they are zero in comparison to those of leading order. Hence, for the iterative solver concerning the S-BT approach, this tolerance value is set unless otherwise specified.

In Figure 8.4, the coefficients $\bar{c}_{11}$ and $\bar{c}_{23}$ of the stiffness matrix are depicted for the different maximum element sizes, h_{max}, of the considered meshes of Y. Although for the finest meshes there is still a slight dependency of the computed values on the discretisation parameter, it is essentially negligible from Mesh 4 onwards, with h_{max} below $9 \cdot 10^{-4}$ (see Table 5.3).

For the selected reference cell, in addition to compute $[\overline{\mathbf{C}}]$, we solve $(\mathcal{LP}_C)_h^{lk}$ to obtain an approximation of the corrector functions of the linear elasticity system, introduced in Section 7.3, for comparison of the S-BT with the rigorous mathematical approach. In Figure 8.5, the computed approximations to $\boldsymbol{\mathcal{X}}^{23}$, $\boldsymbol{\mathcal{X}}^{13}$ and $\boldsymbol{\mathcal{X}}^{11}$ are displayed. Then, the components of the homogenised elasticity tensor, $\mathbb{C}^0$, corresponding to the limit problem $(\mathcal{P}^0)$, are obtained following (7.8). Specifically, the corresponding



(a) $l = 2, k = 3$ $(m = 4)$.

(b) $l = 1, k = 3$ $(m = 5)$.

(c) $l = 1, k = 1$ $(m = 1)$.

Figure 8.5: Modulus of the computed approximation of $\boldsymbol{\mathcal{X}}^{lk}$, Mesh 4.

arrangement of the elasticity tensor for Mesh 4 as a stiffness matrix is the following:

$$[\mathbf{C}_h^0] = \begin{pmatrix} \mathbf{8.91{\cdot}10^8} & \mathbf{6.05{\cdot}10^7} & \mathbf{1.90{\cdot}10^8} & -2.08{\cdot}10^{-7} & -5.79{\cdot}10^{-7} & 8.83{\cdot}10^{-7} \\ \mathbf{6.05{\cdot}10^7} & \mathbf{9.40{\cdot}10^8} & \mathbf{2.00{\cdot}10^8} & -8.16{\cdot}10^{-7} & -4.64{\cdot}10^{-7} & -1.64{\cdot}10^{-6} \\ \mathbf{1.90{\cdot}10^8} & \mathbf{2.00{\cdot}10^8} & \mathbf{6.09{\cdot}10^9} & -8.70{\cdot}10^{-7} & -1.27{\cdot}10^{-6} & -1.59{\cdot}10^{-7} \\ -7.66{\cdot}10^{-8} & -7.67{\cdot}10^{-7} & -1.08{\cdot}10^{-7} & \mathbf{3.99{\cdot}10^8} & -1.42{\cdot}10^{-6} & -5.37{\cdot}10^{-7} \\ -9.06{\cdot}10^{-7} & -8.12{\cdot}10^{-8} & 2.26{\cdot}10^{-7} & -1.35{\cdot}10^{-8} & \mathbf{3.41{\cdot}10^8} & -6.89{\cdot}10^{-7} \\ 1.96{\cdot}10^{-7} & 5.57{\cdot}10^{-7} & 1.51{\cdot}10^{-7} & -5.21{\cdot}10^{-8} & -5.09{\cdot}10^{-7} & \mathbf{2.32{\cdot}10^8} \end{pmatrix}$$

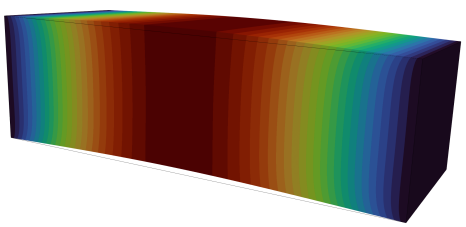
There are significant differences in the entries of $[\mathbf{C}_h^0]$ and $[\overline{\mathbf{C}}_h]$. For ease of comparison, in Table 8.3, the nine relevant coefficients of matrices $[\mathbf{C}_h^0]$ (Correctors) and $[\overline{\mathbf{C}}_h]$ (S-BT) are gathered. While most of them remain with similar values, c_{12} and c_{33} show a relative difference which goes slightly above 20%.

For this cell, taking into account that the corresponding volume fractions of brick and mortar are $\alpha_b = 0.857$ and $\alpha_m = 0.143$, a crude estimation of the elastic coefficients of the homogenised masonry can be made considering a *rule of mixtures*. It involves assuming that the equivalent material is homogeneous isotropic with Young's modulus $\widehat{E}$ and Poisson's ratio $\widehat{\nu}$ computed through a volume averaging, i.e.:

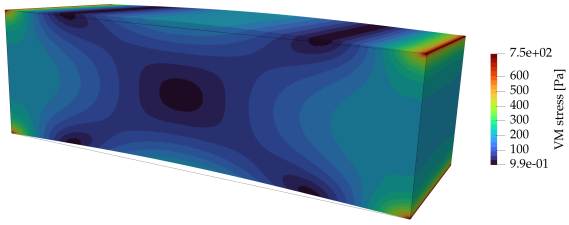
$$\widehat{E} = \alpha_m E_m + \alpha_b E_b,$$
$$\widehat{\nu} = \alpha_m \nu_m + \alpha_b \nu_b.$$

For the specific volume fractions and properties for this cell, it follows that $\widehat{E} = 6.01{\cdot}10^9$ Pa and $\widehat{\nu} = \nu_b = \nu_m = 0.2$. The corresponding entries that characterise the mixture material stiffness matrix are also included in Table 8.3. Note that the differences with the previous approaches are huge, which will potentially lead to large deviations of the displacement and stress predictions if a rule of mixtures is used to characterise the homogenised material behaviour.

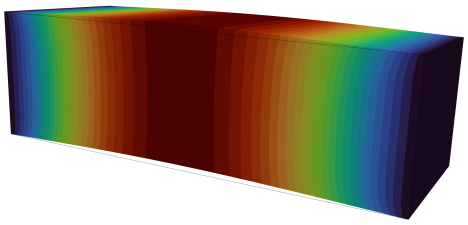
A domain Ω is constructed joining several cells Y by periodical extension. The considered domain is composed of a total of 120 cells, with a number of repetitions $\mathbf{k}^p = (10, 6, 2)$, where each component k_i^p indicates the number of cells that are considered in the direction $\mathbf{e}_i$. In this domain, we solve



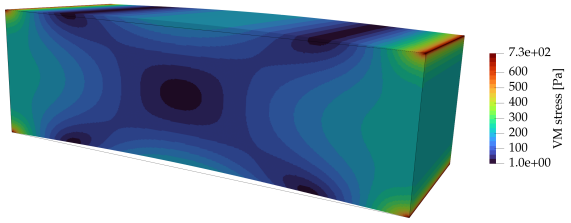
(**a**) Displacement, basic tests.



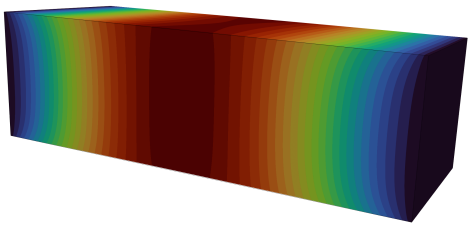
(**b**) VM stress, basic tests.



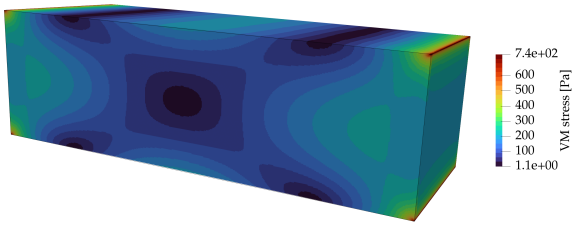
(**c**) Displacement, correctors.



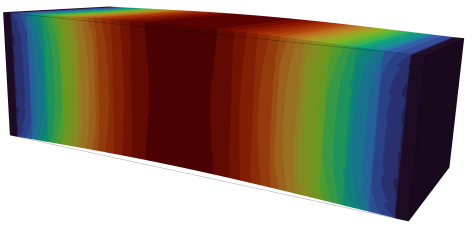
(**d**) VM stress, correctors.



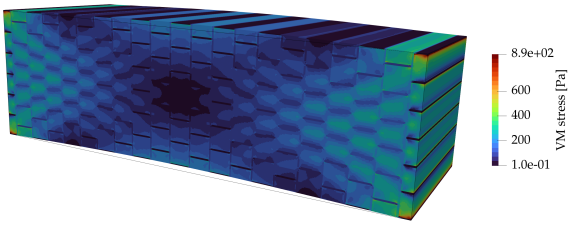
(**e**) Displacement, mixture.



(**f**) VM stress, mixture.



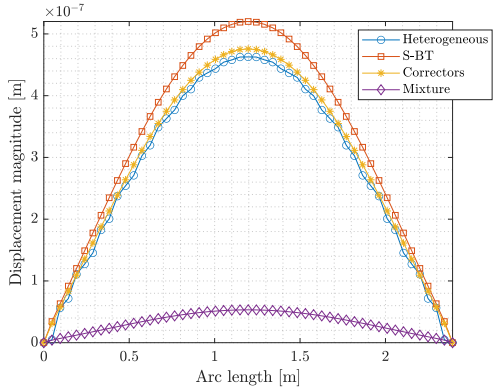
(**g**) Displacement, heterogeneous.



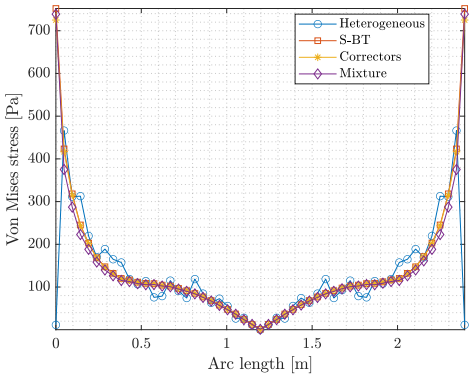
(**h**) VM stress, heterogeneous.

Figure 8.6: Contours of the numerical solution of Problem 1, Cell A, considering the homogenised material predicted by the S-BT, the correctors, a rule of mixtures, and the real heterogeneus material. The results are displayed on the deformed configuration.

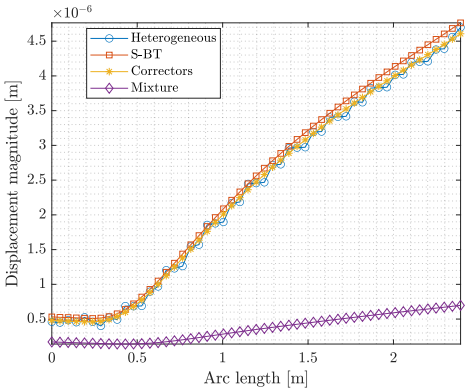
USC
UNIVERSIDADE
DE SANTIAGO
DE COMPOSTELA



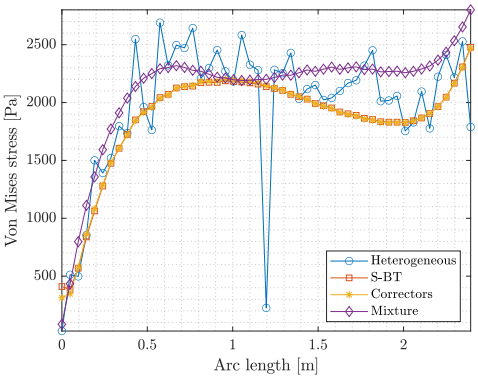
(**a**) Displacement, Problem 1.



(**b**) VM stress, Problem 1.

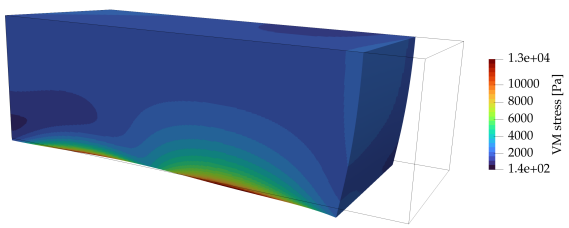


(**c**) Displacement, Problem 2.

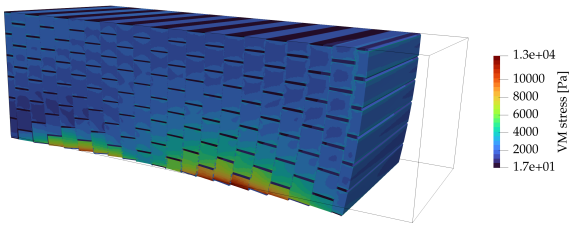


(**d**) VM stress, Problem 2.

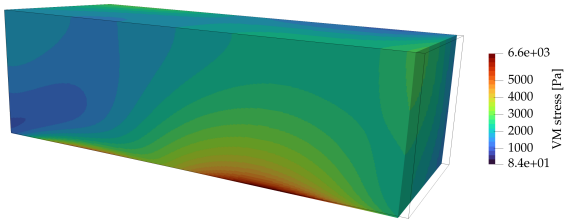
Figure 8.7: Solution for Cell A, along the line $[\mathbf{x}_{min}, \mathbf{x}_{max}]$.



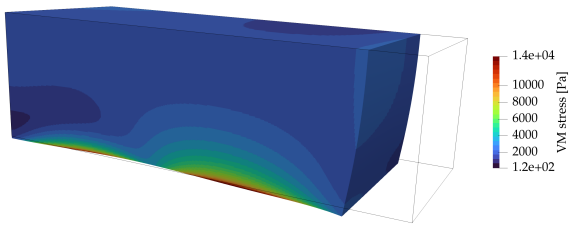
(**a**) VM stress, basic tests.



(**b**) VM stress, heterogeneous.



(**c**) VM stress, mixture.



(**d**) VM stress, correctors.

Figure 8.8: Contours of the von Mises stress in Problem 2, Cell A, considering different approaches to characterise the equivalent material and the heterogeneous material.

Table 8.3: Cell A. Comparison of the coefficients of the constant stiffness matrix for the equivalent materials: stress basic tests (S-BT), solving the auxiliary periodic problems (Correctors) and rule of mixtures.

	c_{11}	c_{22}	c_{33}	c_{23}	c_{13}	c_{12}	c_{44}	c_{55}	c_{66}
S-BT	$8.62{\cdot}10^8$	$9.01{\cdot}10^8$	$5.11{\cdot}10^9$	$1.84{\cdot}10^8$	$1.77{\cdot}10^8$	$7.41{\cdot}10^7$	$3.73{\cdot}10^8$	$3.33{\cdot}10^8$	$2.05{\cdot}10^8$
Correctors	$8.91{\cdot}10^8$	$9.40{\cdot}10^8$	$6.09{\cdot}10^9$	$2.00{\cdot}10^8$	$1.90{\cdot}10^8$	$6.05{\cdot}10^7$	$3.99{\cdot}10^8$	$3.41{\cdot}10^8$	$2.32{\cdot}10^8$
Mixture	$6.68{\cdot}10^9$	$6.68{\cdot}10^9$	$6.68{\cdot}10^9$	$1.67{\cdot}10^9$	$1.67{\cdot}10^9$	$1.67{\cdot}10^9$	$2.50{\cdot}10^9$	$2.50{\cdot}10^9$	$2.50{\cdot}10^9$

the problems detailed in Section 8.3.1, considering the homogenised materials with the computed stiffness matrix that corresponds to the prediction given by the solution of the stress basic tests ($[\mathbf{C}] = [\overline{\mathbf{C}}_h]$), the correctors ($[\mathbf{C}] = [\mathbf{C}_h^0]$), and considering the rule of mixtures. For comparison, we also solve the heterogeneous material, i.e., we consider that the stiffness matrix depends on the point $\mathbf{x}$ according to the specific layout of joints and bricks.

In Figure 8.6, the displacement and the von Mises stress norm are depicted after solving Problem 1, considering the homogenised material predicted by the stress basic tests and the correctors, and the real heterogeneous material. It is noteworthy that both the qualitative VM stress norm and displacement are similar. In particular, the results from the two different homogenised alternatives are qualitatively identical. However, the local effects in the stress due to the corners in the bricks of the heterogeneous material are not predicted by any of the equivalent materials. To better analyse the differences in the computed solution, in Figures 8.7a and 8.7b, the displacements and VM stress are shown on a line crossing the domain from corner to corner, as a function of the arc length. The line is defined with a starting point $\mathbf{x}_{min}$ and with end point $\mathbf{x}_{max}$. The line defined in this manner captures all the relevant phenomena for the posed problems, including the sharp stress variations in the heterogeneous material due to the presence of the mortar joints and the high stresses produced in the corners of the domain due to the zero displacement conditions used in Problem 1. From the displayed results, it is clear that the displacement prediction by the mixture rule is very inaccurate. In contrast, both the homogeneous material yielded by the basic tests and the homogeneous material corresponding to the correctors lead to a very similar computed displacement. The VM stresses follow a similar trend in all the considered cases.

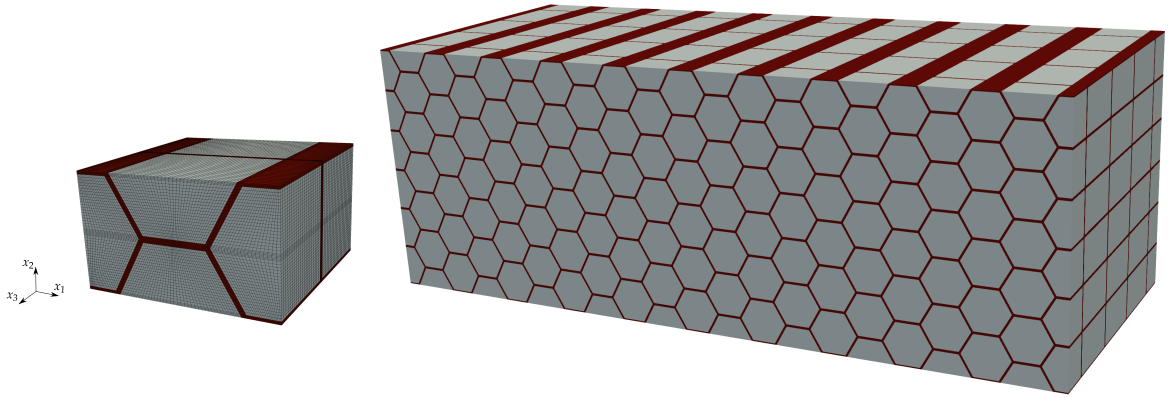
Considering Problem 2, analogous results are observed. In order to further clarify the issue on the local effects on the stress, in Figure 8.8 the computed VM stress norm is shown for the homogenised material and the heterogeneous one. Again, it is clear that there are multiple maximums in the stress that correspond to the corners of the bricks that are only captured if the microstructure is solved, i.e., a full heterogeneous material is considered. Nonetheless, as evidenced by the results displayed in Figures 8.7b and 8.7d, the global behaviour of the stress is well reproduced, even for a small assembly of cells such as the one considered in this case.

8.3.3. Cell B. Hexagonal brick layout with mortar joints

The second configuration that we analyse is similar to that presented in the previous section. Instead of a square layout of bricks and mortar joints, a hexagonal pattern formed by bricks whose cross-sections are regular hexagons is considered, as shown in Figure 8.9. The corresponding unit cell for this case (Cell B) is selected analogously as the previous one.

For this cell, the side of the hexagonal bricks is 0.1 m. The length of the brick ($\mathbf{e}_3$ direction) is equal to 0.2 m. All the mortar joints have a thickness of 0.008 m. We note that, in contrast with Cell A, in this case there are also joints in the $\mathbf{e}_3$ direction. In particular, the volume fractions of brick and mortar in Cell B are $\alpha_b = 0.874$ and $\alpha_m = 0.126$. Therefore, bearing the material properties gathered in Table 8.1, the Young's modulus and Poisson's ratio according to the rule of mixtures for this arrangement of materials are $\widehat{E} = 8.75{\cdot}10^8$ Pa and $\widehat{\nu} = 0.095$, respectively.

To solve the basic tests and the auxiliary periodic problems, a discretisation parameter similar to that of the previous study is considered. After solving the linear system arising from the discretisation



(**a**) Reference cell (Y). (**b**) Masonry wall (Ω).

Figure 8.9: Hexagonal brick layout with mortar joints (Cell B).

of the stress basic tests with a direct solver, the subsequent stiffness matrix is obtained:

$$[\overline{\mathbf{C}}_h] = \begin{pmatrix} \mathbf{1.50{\cdot}10^8} & \mathbf{3.09{\cdot}10^7} & \mathbf{8.65{\cdot}10^6} & 3.58{\cdot}10^{-9} & -1.66{\cdot}10^{-8} & 1.86{\cdot}10^{-7} \\ \mathbf{3.09{\cdot}10^7} & \mathbf{1.42{\cdot}10^8} & \mathbf{8.92{\cdot}10^6} & 1.11{\cdot}10^{-7} & 6.95{\cdot}10^{-8} & -7.55{\cdot}10^{-8} \\ \mathbf{8.65{\cdot}10^6} & \mathbf{8.92{\cdot}10^6} & \mathbf{2.32{\cdot}10^8} & 2.97{\cdot}10^{-7} & 3.38{\cdot}10^{-7} & 1.50{\cdot}10^{-7} \\ 2.03{\cdot}10^{-8} & -3.44{\cdot}10^{-8} & -9.34{\cdot}10^{-8} & \mathbf{4.51{\cdot}10^7} & -1.12{\cdot}10^{-7} & 7.07{\cdot}10^{-8} \\ 3.90{\cdot}10^{-7} & 1.03{\cdot}10^{-7} & 2.64{\cdot}10^{-7} & 3.18{\cdot}10^{-7} & \mathbf{4.69{\cdot}10^7} & 6.11{\cdot}10^{-7} \\ 6.98{\cdot}10^{-8} & 9.36{\cdot}10^{-8} & 1.05{\cdot}10^{-7} & -1.05{\cdot}10^{-8} & -1.05{\cdot}10^{-7} & \mathbf{5.56{\cdot}10^7} \end{pmatrix}$$

In addition, solving the periodic auxiliary problems to obtain an approximation of the correctors and computing the homogenised elasticity tensor (7.8), it follows that

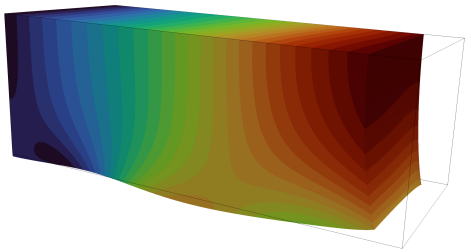
$$[\mathbf{C}_h^0] = \begin{pmatrix} \mathbf{1.59{\cdot}10^8} & \mathbf{2.93{\cdot}10^7} & \mathbf{7.07{\cdot}10^6} & -3.95{\cdot}10^{-8} & 7.34{\cdot}10^{-8} & 2.97{\cdot}10^{-8} \\ \mathbf{2.93{\cdot}10^7} & \mathbf{1.47{\cdot}10^8} & \mathbf{6.84{\cdot}10^6} & -1.65{\cdot}10^{-7} & -4.98{\cdot}10^{-9} & -6.21{\cdot}10^{-9} \\ \mathbf{7.07{\cdot}10^6} & \mathbf{6.84{\cdot}10^6} & \mathbf{2.45{\cdot}10^8} & 3.06{\cdot}10^{-8} & -1.66{\cdot}10^{-7} & -6.13{\cdot}10^{-9} \\ -1.10{\cdot}10^{-8} & 1.35{\cdot}10^{-7} & -2.07{\cdot}10^{-7} & \mathbf{4.57{\cdot}10^7} & 1.38{\cdot}10^{-7} & -2.55{\cdot}10^{-8} \\ -6.09{\cdot}10^{-8} & 5.70{\cdot}10^{-9} & 1.77{\cdot}10^{-7} & 2.32{\cdot}10^{-8} & \mathbf{4.77{\cdot}10^7} & -8.14{\cdot}10^{-8} \\ 1.77{\cdot}10^{-8} & 1.76{\cdot}10^{-8} & -8.14{\cdot}10^{-9} & 7.30{\cdot}10^{-8} & -1.49{\cdot}10^{-7} & \mathbf{6.40{\cdot}10^7} \end{pmatrix}$$

As in the described situation for Cell A, both approaches yield substantially different leading-order coefficients in the stiffness matrix of the equivalent material. The differences among both matrices reach up to 20% relative difference in some of the coefficients, as displayed in Table 8.4.

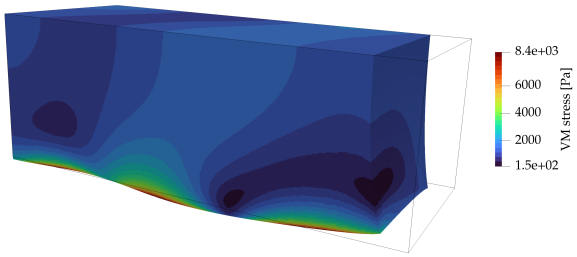
The domain Ω is built joining several cells Y by periodical extension, considering a repetition pattern $\mathbf{k}^p = (10, 6, 3)$. In Figure 8.10, the contours of the computed displacements and von Mises stress norm after solving Problem 1 are displayed, considering the equivalent material obtained through the stress basic tests and the heterogeneous one. Once again, the qualitative global behaviour of both the displacements and stresses is well-captured by the equivalent material. In Figure 8.11, the results

Table 8.4: Cell B.Comparison of the coefficients of the constant stiffness matrix for the equivalent materials: stress basic tests (S-BT), solving the auxiliary periodic problems (Correctors) and rule of mixtures.

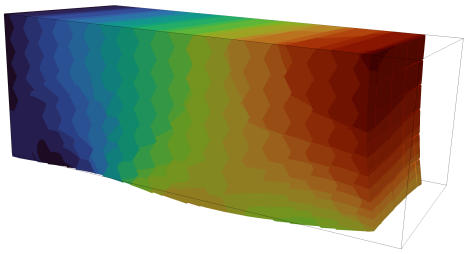
	c_{11}	c_{22}	c_{33}	c_{23}	c_{13}	c_{12}	c_{44}	c_{55}	c_{66}
S-BT	$1.50{\cdot}10^8$	$1.42{\cdot}10^8$	$2.32{\cdot}10^8$	$8.92{\cdot}10^6$	$8.65{\cdot}10^6$	$3.09{\cdot}10^7$	$4.51{\cdot}10^7$	$4.69{\cdot}10^7$	$5.56{\cdot}10^7$
Correctors	$1.59{\cdot}10^8$	$1.47{\cdot}10^8$	$2.45{\cdot}10^8$	$6.84{\cdot}10^6$	$7.07{\cdot}10^6$	$2.93{\cdot}10^7$	$4.57{\cdot}10^7$	$4.77{\cdot}10^7$	$6.40{\cdot}10^7$
Mixture	$8.93{\cdot}10^8$	$8.93{\cdot}10^8$	$8.93{\cdot}10^8$	$9.37{\cdot}10^7$	$9.37{\cdot}10^7$	$9.37{\cdot}10^7$	$4.00{\cdot}10^8$	$4.00{\cdot}10^8$	$4.00{\cdot}10^8$



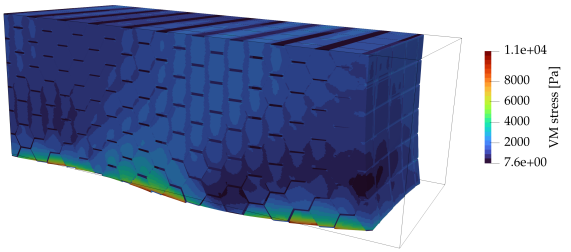
(**a**) Displacement, basic tests.



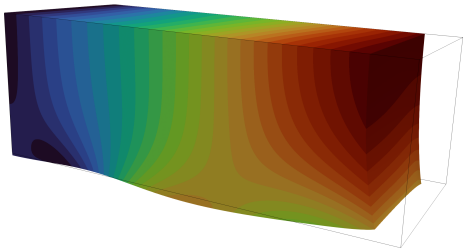
(**b**) VM stress, basic tests.



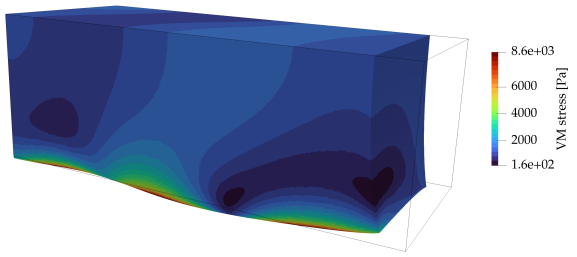
(**c**) Displacement, heterogeneous.



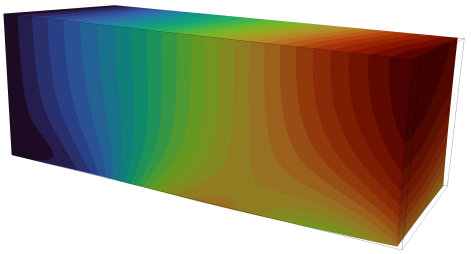
(**d**) VM stress, heterogeneous.



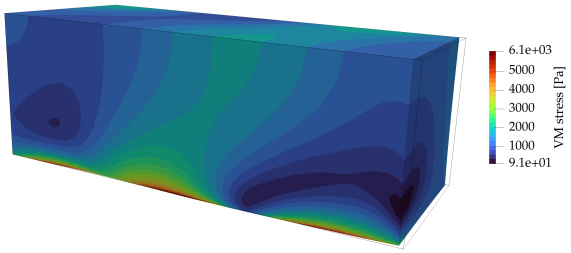
(**e**) Displacement, correctors.



(**f**) VM stress, correctors.



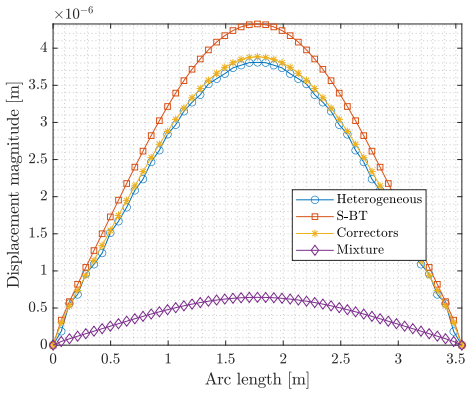
(**g**) Displacement, mixture.



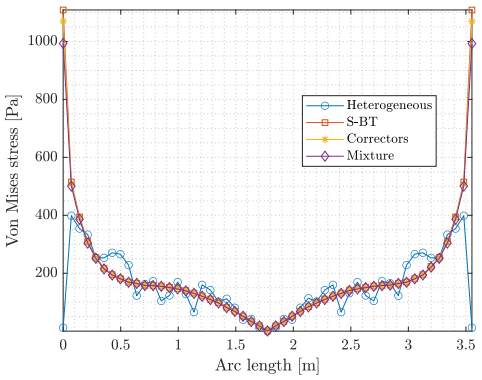
(**h**) VM stress, mixture.

Figure 8.10: Contours of the numerical solution to Problem 1, Cell B, considering the homogenised material predicted by the S-BT, correctors and mixture rule, and the heterogeneous material. The results are displayed on the deformed configuration.

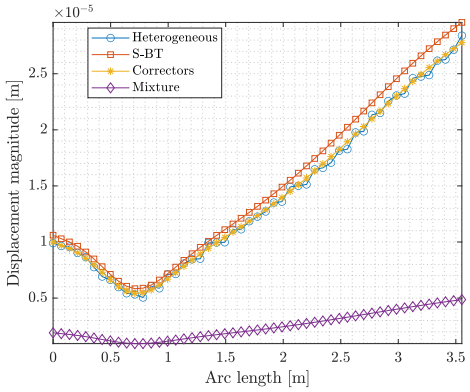
USC
UNIVERSIDADE
DE SANTIAGO
DE COMPOSTELA



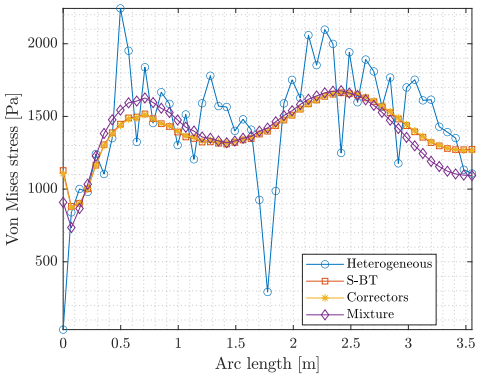
(**a**) Displacement, Problem 1.



(**b**) VM stress, Problem 1.



(**c**) Displacement, Problem 2.



(**d**) VM stress, Problem 2.

Figure 8.11: Numerical solution for Cell B, along the line $[\mathbf{x}_{min}, \mathbf{x}_{max}]$.

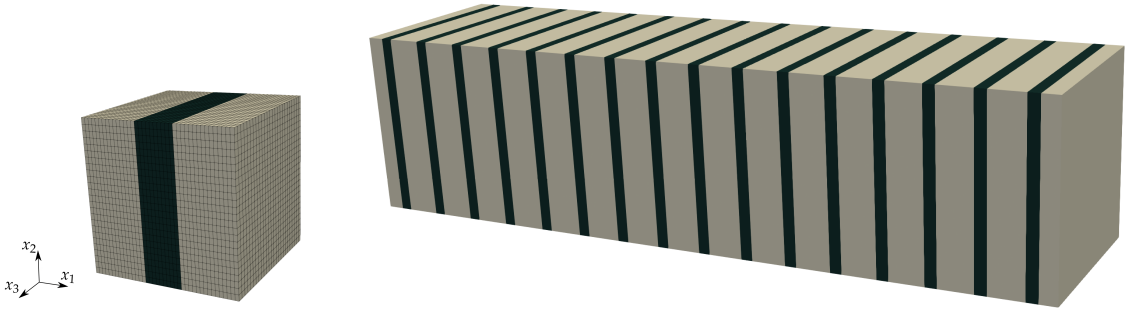
along the line $[\mathbf{x}_{min}, \mathbf{x}_{max}]$ are shown, both for Problem 1 and Problem 2, depicting a similar behaviour as in Cell A, i.e., that both the equivalent material computed with the correctors and the basic tests yield reasonable qualitative predictions of the displacements and stresses. However, the predictions with the correctors remain more accurate.

8.3.4. Cell C. Layered composite

The last configuration that is discussed in this section corresponds to a much simpler layout. It features a composite of two different isotropic materials that are placed forming different layers, as shown in Figure 8.12b. Nonetheless, this case illustrates a specific application where the S-BT approach fails to deliver an accurate characterisation of the homogenised material, as opposed to directly solving the auxiliary periodic problems.

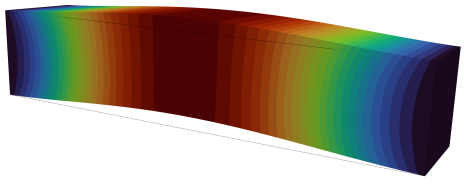
The dimensions of the layers are 0.15 m for the thicker ones and 0.05 m for the narrower ones, in the $\mathbf{e}_1$ direction. The reference cell that is selected to analyse this case is displayed in Figure 8.12. It corresponds to a cube, i.e. $Y = (0, 0.2)^3$. For this composite material, instead of solving $(\mathcal{VP}_{PN})^m$ in Y, the dependency of the selected reference cell is studied. With this purpose, the S-BT methodology is applied to unit cells of different size constructed by periodically repeating Y in the canonical basis directions.

Note that, as opposed to the previously presented cases, in Cell C the stiffer material corresponds to the least prominent one (depicted in green in Figure 8.12b). The specific property values are shown in Table 8.1. As mentioned at the end of the introduction of this section, we still refer to them as brick and mortar, respectively. In this case, the volume fractions are simply $\alpha_b = 0.75$ and $\alpha_m = 0.25$. Thus,

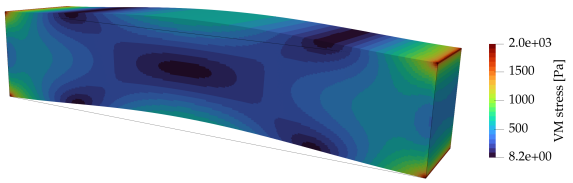


(**a**) Reference cell (Y). (**b**) Assembly of reference cells (Ω).

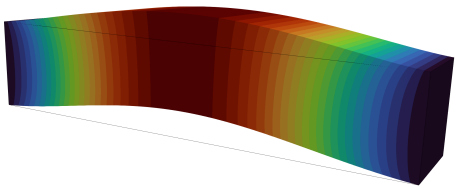
Figure 8.12: Layered composite (Cell C).



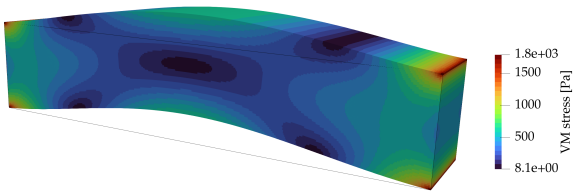
(**a**) Displacement, S-BT.



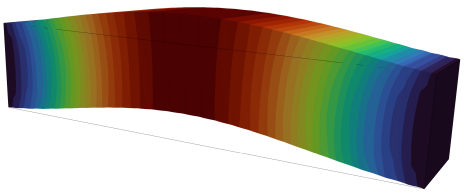
(**b**) VM stress, S-BT.



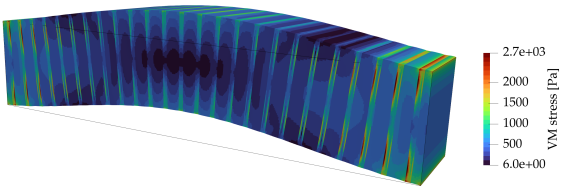
(**c**) Displacement, correctors.



(**d**) VM stress, correctors.



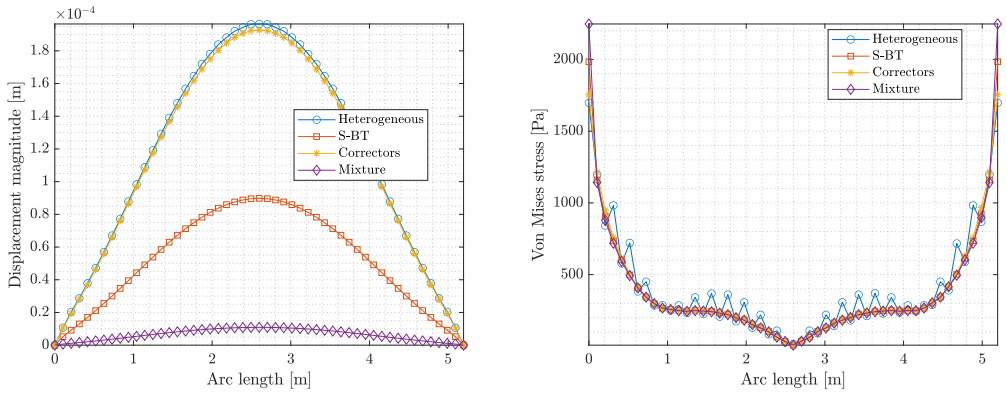
(**e**) Displacement, heterogeneous.



(**f**) VM stress, heterogeneous.

Figure 8.13: Numerical solution of Problem 1, Cell C, considering the homogenised material predicted by S-BT (1,1,1), the correctors, and the heterogeneous material. The results are displayed on the deformed configuration.

USC UNIVERSIDADE DE SANTIAGO DE COMPOSTELA



(**a**) Displacement. (**b**) VM stress.

Figure 8.14: Solution for Cell C and Problem 1 along the line $[\mathbf{x}_{min}, \mathbf{x}_{max}]$.

applying the rule of mixtures we find that $\widehat{E} = 2.58{\cdot}10^8$ and $\widehat{\nu} = 0.2125$.

In Table 8.5, the stiffness matrix coefficients computed by solving the basic tests and the auxiliary periodic problems are depicted. For S-BT, recall that the numbers inside the parentheses indicate the number of cells Y that are assembled in each direction to solve the basic tests. For instance, S-BT $(4,8,8)$ means that Problems $(\mathcal{VP}_{PN})^m$, $m \in I_6$, are solved in a reference cell constructed by joining periodical repetitions of $Y = (0,0.2)^3$ 4 times in the $\mathbf{e}_1$ direction, 8 times in the $\mathbf{e}_2$ direction and 8 times in the $\mathbf{e}_3$ direction. As it could be expected from the composite material with the specific arrangement shown in Figure 8.12, both the correctors and the S-BT return that the homogenised material is *transversely isotropic*. However, the values of some of the computed coefficients are remarkably different for these approaches. Namely, for the (1,1,1) arrangement in S-BT, the computed value of c_{44} is more than one order of magnitude below the one calculated with the correctors. This behaviour is observed for several coefficients, in particular, those that govern the mechanical response in the isotropy plane of the material (the plane with normal vector $\mathbf{e}_1$). When larger reference cells are constructed to solve S-BT, better predictions of the coefficients are produced, which seem to slowly converge to the values computed with the correctors as larger cells are considered.

As a direct consequence of this bad behaviour of the S-BT methodology for this particular cell arrangement, the displacement predictions when compared to those of the correctors are very inaccurate. For a layout of reference cells considering a repetition pattern $\mathbf{k}^p = (15,5,5)$, the solution to Problem 1 is displayed in Figure 8.13, considering the equivalent material given by the (S-BT) with the standard reference cell, the correctors and the real heterogeneous material. Also, in Figure 8.14, the displacement magnitude and the VM stress norm are shown along the line $[\mathbf{x}_{min}, \mathbf{x}_{max}]$.

Despite the simplicity of the method and the straightforward underlying physical intuition, as this last example demonstrates, the S-BT methodology is not fully reliable. Nonetheless, it should be noted that for most applications where the size of the heterogeneities of the material is small relative to the size of the cell, the predictions remain reasonably accurate. In any case, the homogenised material

Table 8.5: Cell C. Comparison of the coefficients of the constant stiffness matrix for the equivalent materials: stress basic tests (S-BT), solving the auxiliary periodic problems (Correctors) and rule of mixtures. For S-BT, the number of cells assembled in each direction to solve the basic tests are indicated.

	c_{11}	c_{22}	c_{33}	c_{23}	c_{13}	c_{12}	c_{44}	c_{55}	c_{66}
S-BT (1,1,1)	$1.59{\cdot}10^7$	$2.30{\cdot}10^7$	$2.30{\cdot}10^7$	$5.75{\cdot}10^6$	$5.27{\cdot}10^6$	$5.27{\cdot}10^6$	$8.91{\cdot}10^6$	$5.32{\cdot}10^6$	$5.32{\cdot}10^6$
S-BT (2,2,2)	$1.59{\cdot}10^7$	$3.65{\cdot}10^7$	$3.65{\cdot}10^7$	$5.83{\cdot}10^6$	$5.23{\cdot}10^6$	$5.23{\cdot}10^6$	$1.42{\cdot}10^7$	$5.32{\cdot}10^6$	$5.32{\cdot}10^6$
S-BT (4,4,4)	$1.59{\cdot}10^7$	$6.36{\cdot}10^7$	$6.36{\cdot}10^7$	$6.35{\cdot}10^6$	$5.14{\cdot}10^6$	$5.14{\cdot}10^6$	$2.39{\cdot}10^7$	$5.32{\cdot}10^6$	$5.32{\cdot}10^6$
S-BT (4,8,8)	$1.59{\cdot}10^7$	$1.02{\cdot}10^8$	$1.02{\cdot}10^8$	$8.10{\cdot}10^6$	$5.01{\cdot}10^6$	$5.01{\cdot}10^6$	$3.87{\cdot}10^7$	$5.32{\cdot}10^6$	$5.32{\cdot}10^6$
Correctors	$1.59{\cdot}10^7$	$2.62{\cdot}10^8$	$2.62{\cdot}10^8$	$2.85{\cdot}10^7$	$4.43{\cdot}10^6$	$4.43{\cdot}10^6$	$1.17{\cdot}10^8$	$5.32{\cdot}10^6$	$5.32{\cdot}10^6$
Mixture	$2.91{\cdot}10^8$	$2.91{\cdot}10^8$	$2.91{\cdot}10^8$	$7.85{\cdot}10^7$	$7.85{\cdot}10^7$	$7.85{\cdot}10^7$	$1.06{\cdot}10^8$	$1.06{\cdot}10^8$	$1.06{\cdot}10^8$

yielded by the corrector problems is indeed more reliable and accurate, both in the displacements and stresses for all the analysed cases. In the next chapter, the S-BT is adapted to produce a new set of basic tests that will not require the imposition of difficult constraints such as the periodicity or the zero mean value that are needed for the auxiliary periodic problems, but having the property of being mathematically rigorous and reliable for engineering predictions.

USC
UNIVERSIDADE
DE SANTIAGO
DE COMPOSTELA

Chapter 9

Displacement basic tests

In this chapter, an alternative technique to the one presented in Chapter 8 to obtain the homogeneous elastic material corresponding to a material with a periodic heterogeneous microstructure is discussed. Instead of the pure traction linear elasticity problems considered previously for the stress basic tests (S-BT), the problems in the reference cell Y can be solved imposing Dirichlet conditions set only on some selected components of the displacement. We refer to these problems as displacement basic tests (D-BT).

Under suitable geometric symmetry assumptions, it can be shown that the solutions of these new basic tests are related to those of the corrector problems discussed in Chapter 7. Thus, they can be used to obtain a homogeneous material whose elasticity tensor corresponds to that of the limit problem in Theorem 7.1, but removing constraints such as the zero-mean and the periodicity. This results in problems that are more amenable for their numerical solution.

This chapter is structured as follows. In Section 9.1, some auxiliary results that are required to prove specific symmetries of the solutions to the D-BT are introduced. Subsequently, in Section 9.2, the statement of the displacement basic tests is presented. Then, Section 9.3 deals with the connection between the solutions of these basic tests and the auxiliary periodic problems of the linear elasticity system. A result that allows to easily compute the stiffness matrix of the homogenised material from the basic test solutions is proven. Lastly, Section 9.4 presents several numerical experiments with different compositions of materials as reference cell. The industrial case that motivated this part of the manuscript, the homogenisation of the ceramic cup of the BF, is addressed.

9.1. Symmetry results

This section is devoted to the introduction of the main assumption and tools that are required to mathematically justify the proposed homogenisation technique. In addition, a couple of auxiliary results are presented to establish the Y-periodicity of the solution of two different linearised elasticity problems under homogeneous Dirichlet boundary conditions. The first one restricts the normal displacements on the faces delimiting the boundary of Y, whereas the second one involves the tangential displacements.

The subsequent notion regarding the reflections with respect to (w.r.t.) the midplanes of the reference period Y is introduced. Owing to (7.1), these planes coincide with the planes defined by $y_i = L_i/2$.

Definition 9.1. *The reflection w.r.t. the plane $y_1 = L_1/2$ is defined as the following linear mapping*

$$\phi^1(y_1, y_2, y_3) = (L_1 - y_1, y_2, y_3), \tag{9.1}$$

for all $\mathbf{y} \in Y$. The reflections corresponding to the remaining coordinate planes are defined analogously.

Note that any reflection ϕ^i is an isometry. In particular, the determinant of its Jacobian matrix is one and $\phi^i(Y) = Y$. Furthermore, its inverse coincides with itself. Using the reflections ϕ^i, the *even* and *odd* functions w.r.t. the coordinate planes are introduced as follows.

Definition 9.2. *Let f be a scalar function defined a.e. in Y. f is even w.r.t. the plane $y_i = L_i/2$ if $f(\mathbf{y}) = f(\phi^i(\mathbf{y}))$ for almost every $\mathbf{y} \in Y$, where $\phi^i(\mathbf{y})$ is the linear mapping defined as the reflection w.r.t. such plane. Similarly, f is odd w.r.t. the plane $y_i = L_i/2$ if $f(\mathbf{y}) = -f(\phi^i(\mathbf{y}))$ for almost every $\mathbf{y} \in Y$.*

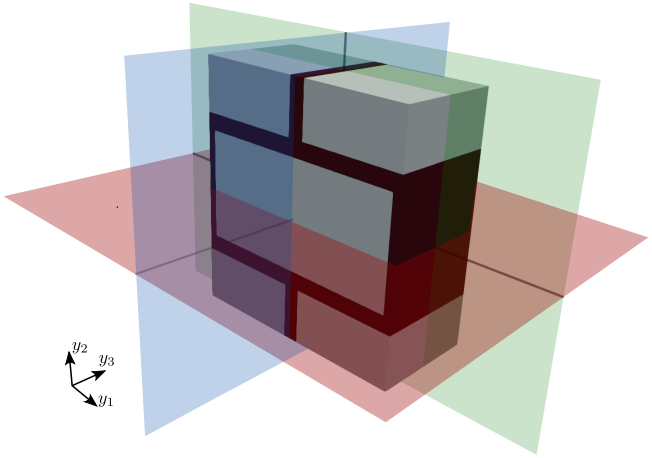


Figure 9.1: Reference cell Y satisfying the symmetry hypotheses (H.2).

For shorthand, in the following discussion, given a generic scalar function f defined a.e. in Y we shall simply indicate that f is even (resp. odd) w.r.t. $y_i, i \in I_3$, meaning that it is even (resp. odd) w.r.t. $y_i = L_i/2$. When applied to vector-valued or tensor-valued functions, Definition 9.2 is interpreted in the sense that all components of such function satisfy the condition of being even or odd w.r.t. the plane.

We shall assume that the mechanical response of the body occupying the domain Y is characterised by the constitutive law (6.5). Furthermore, we assume the following additional hypotheses on the elasticity tensor $\mathbb{C}$:

(H.1) There exist $\alpha, \beta > 0$ such that $\mathbb{C} \in \mathcal{M}(\alpha, \beta, Y)$.

(H.2) $\mathbb{C}$ is even with respect to the planes $y_i = L_i/2, i \in I_3$.

(H.3) $\mathbb{C}$ corresponds to an orthotropic material a.e. in Y, with the symmetry planes of the orthotropic material aligned with the coordinate planes.

Remark 9.1. *Hypothesis (H.3) above means that the material must have at least the three symmetry planes that characterise orthotropic elastic materials. Naturally, the subsequent results hold for any elastic material that has those symmetry planes plus any additional symmetry, such as cubic, transversely isotropic or isotropic materials.*

A physical setting for Y being occupied by a heterogeneous material satisfying hypotheses (H.1)-(H.3) is shown in Figure 9.1, where the two different homogeneous materials composing the cell are coloured differently and satisfy all the required symmetries.

9.1.1. Weak auxiliary problem

Let $\mathbf{L} \in Lin$ such that $\mathbf{L} \in \mathbf{L}^2(Y)$. Then, we define the following auxiliary weak problem in a general functional space V which will be specified later. In particular, we shall choose V as two suitable closed subspaces of $\mathbf{H}^1(Y)$.

Problem $(\mathcal{VP}_A)$. Find $\mathbf{u} \in V$ such that:

$$a(\mathbf{u}, \mathbf{v}) = l(\mathbf{v}), \qquad \forall \mathbf{v} \in V,$$

where $a(\mathbf{u}, \mathbf{v})$ is defined in (8.8) and

$$a(\mathbf{u}, \mathbf{v}) = \int_Y \boldsymbol{\sigma}(\mathbf{u}) : \boldsymbol{\varepsilon}(\mathbf{v})\, dV, \tag{9.2}$$

$$l(\mathbf{v}) = \int_Y \mathbf{L} : \nabla \mathbf{v}\, dV. \tag{9.3}$$

USC UNIVERSIDADE DE SANTIAGO DE COMPOSTELA

9.1.2. Normal displacements

First, we consider the space V in $(\mathcal{VP}_A)$ as the following closed subspace of $\mathbf{H}^1(Y)$:

$$\mathcal{N} := \{\mathbf{v} \in \mathbf{H}^1(Y) |\ \mathbf{v}\cdot\mathbf{n} = 0 \text{ on } \partial Y\}, \tag{9.4}$$

endowed with the standard norm in $\mathbf{H}^1(Y)$. As shown by the following result, the only infinitesimal rigid motion in this space is the trivial one.

Lemma 9.1. *Let $\mathbf{v} \in \mathcal{N} \cap \mathcal{Z}(Y)$, with $\mathcal{Z}(Y)$ being the space of infinitesimal rigid motions of Y, defined in (6.11). Then $\mathbf{v} \equiv \mathbf{0}$.*

Proof. Set $\mathbf{v} \in \mathcal{Z}(Y)$ such that $\mathbf{v} \in \mathcal{N}$. In particular, there are $\mathbf{a}, \mathbf{b} \in \mathbb{R}^3$ such that $\mathbf{v}$ satisfies (6.12). Also, on ∂Y, $\mathbf{v}\cdot\mathbf{n} = 0$. Since the faces forming ∂Y are aligned with the coordinate axes, for each i, $v_i = 0$ on Γ_i^-. Provided that $a_i \neq b_{ij}y_j$ for all $y_j \in \Gamma_i^-$, $j \neq i$, then $a_i, b_{ij} = 0$ and thus $\mathbf{v} \equiv \mathbf{0}$. □

Proposition 9.1. *Let Y be the unit cell (7.1), $\mathbf{L} \in$ Lin such that $\mathbf{L} \in \mathbf{L}^2(Y)$ and $\mathbb{C} \in \mathcal{M}(\alpha, \beta, Y)$ for some $\alpha, \beta > 0$. Then, Problem $(\mathcal{VP}_A)$ has a unique solution in $V = \mathcal{N}$.*

Proof. The bilinear form (9.2) is continuous given property (iv) in Definition 6.1. Furthermore, since $\mathbf{L} \in \mathbf{L}^2(Y)$, the continuity of the functional (9.3) is easily established. Lastly, using Lemma 9.1, the coercivity of the bilinear form follows directly from Theorem 6.1 for $V = \mathcal{N}$, since using (iii) in Definition 6.1, we obtain

$$a(\mathbf{u},\mathbf{u}) = \int_Y C_{ijrs}\varepsilon_{rs}(\mathbf{u})\varepsilon_{ij}(\mathbf{u})dV \geq \alpha \sum_{i,j=1}^{3} \int_Y \varepsilon_{ij}^2(\mathbf{u})\, dV \geq \frac{\alpha}{C}\|\mathbf{u}\|^2_{\mathbf{H}^1(Y)}, \qquad \forall \mathbf{u} \in \mathcal{N}.$$

Hence, the Lax-Milgram Theorem ensures that there is a unique solution to Problem $(\mathcal{VP}_A)$ in $\mathcal{N}$. □

In addition, if the elasticity tensor $\mathbb{C}$ satisfies Hypotheses (H.2) and (H.3), under specific symmetry properties of the data $\mathbf{L}$, the particularities of the definition of the subspace $\mathcal{N}$ enable to prove a result regarding the periodicity of the unique solution to the problem. To this end, we first define the following subspace of $\mathcal{N}$, composed of those functions having specific symmetries with respect to the coordinate planes:

$$\mathcal{N}_S = \{\mathbf{v} \in \mathcal{N} : v_i \text{ is odd w.r.t. } y_i \text{ and even w.r.t. } y_j, j \neq i\}.$$

The space $\mathcal{N}_S$ can be characterised as shown by the result below.

Lemma 9.2. *Let $\mathbf{u} \in \mathcal{N}_S$. It holds that*

(i) $\mathcal{M}_Y(\mathbf{u}) = \mathbf{0}$,

(ii) $\mathcal{M}_Y(\varepsilon(\mathbf{u})) = \mathbf{0}$.

Furthermore, the trace of $\mathbf{u}$ coincides on the opposite faces of Y and the extension $\mathbf{u}^\#$ of $\mathbf{u}$ belongs to $\mathbf{W}_{per}(Y)$.

Proof. Set $\mathbf{u} \in \mathcal{N}_S$. Let $i = 1$, $Y' = (0, L_2) \times (0, L_3)$ and $\mathbf{y}' = (y_2, y_3)$ be a generic point within Y'. Then, using the change of variable $\mathbf{y} = \phi^1(\widehat{\mathbf{y}})$ and recalling the properties of the reflection ϕ^1, it holds that

$$\begin{aligned}
\mathcal{M}_Y(u_1) &= \frac{1}{\text{meas}(Y)} \int_{Y'} \int_0^{L_1} u_1(y_1, \mathbf{y}')\, dy_1 d\mathbf{y}' \\
&= \frac{1}{\text{meas}(Y)} \left(\int_{Y'} \int_0^{L_1/2} u_1(y_1, \mathbf{y}')\, dy_1 d\mathbf{y}' + \int_{Y'} \int_{L_1/2}^{L_1} u_1(y_1, \mathbf{y}')\, dy_1 d\mathbf{y}' \right) \\
&= \frac{1}{\text{meas}(Y)} \left(\int_{Y'} \int_0^{L_1/2} u_1(y_1, \mathbf{y}')\, dy_1 d\mathbf{y}' + \int_{Y'} \int_0^{L_1/2} u_1(\phi^1(\widehat{y}_1, \widehat{\mathbf{y}}'))\, d\widehat{y}_1 d\widehat{\mathbf{y}}' \right) \\
&= \frac{1}{\text{meas}(Y)} \left(\int_{Y'} \int_0^{L_1/2} u_1(y_1, \mathbf{y}')\, dy_1 d\mathbf{y}' - \int_{Y'} \int_0^{L_1/2} u_1(\widehat{y}_1, \widehat{\mathbf{y}}')\, d\widehat{y}_1 d\widehat{\mathbf{y}}' \right) = 0,
\end{aligned}$$

USC UNIVERSIDADE DE SANTIAGO DE COMPOSTELA

since $\mathbf{u} \in \mathcal{N}_S$ implies that u_1 is odd w.r.t. y_1. Considering the reflections w.r.t. the remaining components of $\mathbf{u}$, the proof for them is completely analogous.

Note that $\mathbf{u} \in \mathcal{N}$ implies that $u_i|_{\Gamma_i^+} = u_i|_{\Gamma_i^-} = 0$. Since w.r.t. y_i, $\mathbf{u}$ is even on the remaining components, then $\mathbf{u}$ has the same trace on the opposite faces of Y. Its extension $\mathbf{u}^\#$, defined for each component as (7.2), belongs to $\mathbf{H}^1_{per}(Y)$. Furthermore, since $\mathcal{M}_Y(\mathbf{u}) = \mathbf{0}$, then it directly follows that $\mathbf{u}^\# \in \mathbf{W}_{per}(Y)$.

Lastly, it remains to see that (ii) holds. If $l \neq k$ and setting $d \in I_3$ such that $d \neq l$ and $d \neq k$, a straightforward application of Fubini's Theorem leads to

$$\begin{aligned}\mathcal{M}_Y(\varepsilon_{lk}(\mathbf{u})) &= \frac{1}{2\text{meas}(Y)} \int_0^{L_d}\int_0^{L_l}\int_0^{L_k} \frac{\partial u_l}{\partial y_k} + \frac{\partial u_k}{\partial y_l}\, dy_k dy_l dy_d \\ &= \frac{1}{2\text{meas}(Y)} \left(\int_0^{L_d}\int_0^{L_l}\int_0^{L_k} \frac{\partial u_l}{\partial y_k}\, dy_k dy_l dy_d + \int_0^{L_d}\int_0^{L_k}\int_0^{L_l} \frac{\partial u_k}{\partial y_l}\, dy_l dy_k dy_d \right) = 0.\end{aligned}$$

A similar computation allows to obtain the result for the case $l = k$. □

Remark 9.2. *Lemma 9.2 allows to identify $\mathcal{N}_S$ with a subspace of $\mathbf{W}_{per}(Y)$, as any $\mathbf{u} \in \mathcal{N}_S$ can be identified with its extension to the whole $\mathbb{R}^3$, $\mathbf{u}^\#$, which belongs to $\mathbf{W}_{per}(Y)$.*

Proposition 9.2. *Let Y, $\mathbf{L}$ and $\mathbb{C}$ satisfy the hypotheses of Proposition 9.1. Furthermore, assume that $\mathbb{C}$ satisfies Hypotheses (H.2) and (H.3) and $\mathbf{L}$ is such that for $i, j \in I_3$:*

(i) L_{ii} is even w.r.t. y_r, $r \in I_3$.

(ii) L_{ij} for $i \neq j$ is odd w.r.t. y_i, y_j and even w.r.t. y_d, with $d \in I_3 \setminus \{i, j\}$.

Then, the unique solution $\mathbf{u}$ of $(\mathcal{VP}_A)$ in $\mathcal{N}$ is such that $\mathbf{u} \in \mathcal{N}_S$.

Proof. Set $\mathbf{u}$ as the unique solution of $(\mathcal{VP}_A)$ in $\mathcal{N}$. Let ϕ^1 denote the reflection with respect to the plane $y_1 = L_1/2$, defined in (9.1). Then, let $\widehat{\mathbf{u}}(\mathbf{y}) = (-u_1, u_2, u_3)^T(\phi^1(\mathbf{y}))$, for almost all $\mathbf{y} \in Y$. A straightforward application of the chain rule leads to

$$\{\varepsilon(\widehat{\mathbf{u}})\}(\mathbf{y}) = \big(\varepsilon_{11}(\mathbf{u}), \varepsilon_{22}(\mathbf{u}), \varepsilon_{33}(\mathbf{u}), 2\varepsilon_{23}(\mathbf{u}), -2\varepsilon_{13}(\mathbf{u}), -2\varepsilon_{12}(\mathbf{u})\big)^T(\phi^1(\mathbf{y})). \tag{9.5}$$

Set an arbitrary test function $\mathbf{v} \in \mathcal{N}$. Set $\widehat{\mathbf{v}}(\mathbf{y}) = (-v_1, v_2, v_3)^T(\phi^1(\mathbf{y}))$ for almost all $\mathbf{y} \in Y$. Since $\phi^1(Y) = Y$, then $\widehat{\mathbf{v}} \in \mathbf{H}^1(Y)$. Furthermore, given that $\widehat{\mathbf{v}} \cdot \mathbf{n} = 0$ on ∂Y, then $\widehat{\mathbf{v}}$ also belongs to $\mathcal{N}$. Due to ϕ^1 being an inverse of itself, the definition of $\mathbf{v}$ may be rewritten as $\mathbf{v}(\mathbf{y}) = (-\widehat{v}_1, \widehat{v}_2, \widehat{v}_3)^T(\phi^1(\mathbf{y}))$. Therefore, it holds that

$$\{\varepsilon(\mathbf{v})\}(\mathbf{y}) = \big(\varepsilon_{11}(\widehat{\mathbf{v}}), \varepsilon_{22}(\widehat{\mathbf{v}}), \varepsilon_{33}(\widehat{\mathbf{v}}), 2\varepsilon_{23}(\widehat{\mathbf{v}}), -2\varepsilon_{13}(\widehat{\mathbf{v}}), -2\varepsilon_{12}(\widehat{\mathbf{v}})\big)^T(\phi^1(\mathbf{y})). \tag{9.6}$$

Substitution in the bilinear form (9.2), application of the constitutive law (6.6) and the orthotropy Hypothesis (H.3), yields that

$$\begin{aligned}a(\widehat{\mathbf{u}}, \mathbf{v}) &= \int_Y \boldsymbol{\sigma}(\widehat{\mathbf{u}}) : \varepsilon(\mathbf{v})\, dV_{\mathbf{y}} = \int_Y ([\mathbf{C}]\{\varepsilon(\widehat{\mathbf{u}})\}) \cdot \{\varepsilon(\mathbf{v})\}\, dV_{\mathbf{y}} \\ &= \int_Y \big([\mathbf{C}](\mathbf{y})\{\varepsilon(\mathbf{u})\}(\phi^1(\mathbf{y}))\big) \cdot \{\varepsilon(\widehat{\mathbf{v}})\}(\phi^1(\mathbf{y}))\, dV_{\mathbf{y}},\end{aligned} \tag{9.7}$$

in virtue of (9.5) and (9.6). Since Hypothesis (H.2) on $\mathbb{C}$ implies that $c_{pq}(\mathbf{y}) = c_{pq}(\phi^1(\mathbf{y}))$ for any $p, q \in I_6$, the change of variable $\widehat{\mathbf{y}} = \phi^1(\mathbf{y})$ in the last integral in (9.7) leads to

$$a(\widehat{\mathbf{u}}, \mathbf{v}) = \int_Y \boldsymbol{\sigma}(\mathbf{u})(\phi^1(\mathbf{y})) : \varepsilon(\widehat{\mathbf{v}})(\phi^1(\mathbf{y}))\, dV_{\mathbf{y}} = \int_Y \boldsymbol{\sigma}(\mathbf{u}) : \varepsilon(\widehat{\mathbf{v}}) |\det J_{\phi^1}|\, dV_{\widehat{\mathbf{y}}}.$$

Then, since $|\det J_{\phi^1}| = 1$ and $\widehat{\mathbf{v}} \in \mathcal{N}$, it holds that

$$a(\widehat{\mathbf{u}}, \mathbf{v}) = a(\mathbf{u}, \widehat{\mathbf{v}}) = L(\widehat{\mathbf{v}}).$$

USC UNIVERSIDADE DE SANTIAGO DE COMPOSTELA

A similar relation to (9.6) involving the gradient of $\widehat{\mathbf{v}}$ defined on $\widehat{\mathbf{y}} = \phi^1(\mathbf{y})$ can be obtained. Hence, we consider $\widehat{\mathbf{v}}(\widehat{\mathbf{y}}) = (-v_1, v_2, v_3)^T(\phi^1(\widehat{\mathbf{y}}))$ for $\widehat{\mathbf{y}} \in Y$. Then, applying the change of variable $\mathbf{y} = \phi^1(\widehat{\mathbf{y}})$ and using the hypotheses (i) and (ii) on $\mathbf{L}$, it follows that

$$
\begin{aligned}
L(\widehat{\mathbf{v}}) &= \int_Y \mathbf{L} : \nabla\widehat{\mathbf{v}}\, dV_{\widehat{\mathbf{y}}} = \int_Y L_{ij}\frac{\partial \widehat{v}_i}{\partial \widehat{y}_j}\, dV_{\widehat{\mathbf{y}}} = \int_Y \Big[L_{11}(\phi^1(\widehat{\mathbf{y}}))\frac{\partial v_1}{\partial y_1}(\phi^1(\widehat{\mathbf{y}})) \\
&+ (-L_{12}(\phi^1(\widehat{\mathbf{y}})))(-\frac{\partial v_1}{\partial y_2}(\phi^1(\widehat{\mathbf{y}}))) + (-L_{13}(\phi^1(\widehat{\mathbf{y}})))(-\frac{\partial v_1}{\partial y_3}(\phi^1(\widehat{\mathbf{y}}))) \\
&+ (-L_{21}(\phi^1(\widehat{\mathbf{y}})))(-\frac{\partial v_2}{\partial y_1}(\phi^1(\widehat{\mathbf{y}}))) + L_{22}(\phi^1(\widehat{\mathbf{y}}))\frac{\partial v_2}{\partial y_2}(\phi^1(\widehat{\mathbf{y}})) + L_{23}(\phi^1(\widehat{\mathbf{y}}))\frac{\partial v_2}{\partial y_3}(\phi^1(\widehat{\mathbf{y}})) \\
&+ (-L_{31}(\phi^1(\widehat{\mathbf{y}})))(-\frac{\partial v_3}{\partial y_1}(\phi^1(\widehat{\mathbf{y}}))) + L_{32}(\phi^1(\widehat{\mathbf{y}}))\frac{\partial v_3}{\partial y_2}(\phi^1(\widehat{\mathbf{y}})) + L_{33}(\phi^1(\widehat{\mathbf{y}}))\frac{\partial v_3}{\partial y_3}(\phi^1(\widehat{\mathbf{y}}))\Big] dV_{\widehat{\mathbf{y}}} \\
&= \int_Y \mathbf{L} : \nabla\mathbf{v} |\det J_{\phi^1}|\, dV_{\mathbf{y}} = l(\mathbf{v}).
\end{aligned}
$$

Consequently, for any $\mathbf{v} \in \mathcal{N}$, $a(\widehat{\mathbf{u}}, \mathbf{v}) = l(\mathbf{v})$, so $\widehat{\mathbf{u}}$ solves $(\mathcal{VP}_A)$. Since the solution to $(\mathcal{VP}_A)$ is unique, then $\widehat{\mathbf{u}} = \mathbf{u}$ and thus, w.r.t. y_1, u_1 is odd whereas u_2 and u_3 are even.

Set ϕ^2 to be the reflection w.r.t. y_2. Moreover, let $\widetilde{\mathbf{u}}(\mathbf{y}) = (u_1, -u_2, u_3)^T(\phi^2(\mathbf{y}))$ and, for any given $\mathbf{v} \in \mathcal{N}$, set $\widetilde{\mathbf{v}}(\mathbf{y}) = (v_1, -v_2, v_3)^T(\phi^2(\mathbf{y}))$. Note that $\widetilde{\mathbf{v}} \in \mathcal{N}$. Analogous computations to those above for $\widehat{\mathbf{u}}$ lead to

$$
a(\widetilde{\mathbf{u}}, \mathbf{v}) = l(\mathbf{v}),
$$

for any $\mathbf{v} \in \mathcal{N}$. Hence, $\widetilde{\mathbf{u}} = \mathbf{u}$ and we obtain that u_2 is odd w.r.t. y_2 whereas u_1 and u_3 are even w.r.t. y_2. Similarly, using the reflection $\phi^3(\mathbf{y})$, we find that $\overline{\mathbf{u}}(\mathbf{y}) = (u_1, u_2, -u_3)^T(\phi^3(\mathbf{y}))$ is also a solution to $(\mathcal{VP}_A)$ and thus, u_3 is odd w.r.t. y_3 whereas u_1 and u_2 are even w.r.t. y_3. Therefore, $\mathbf{u} \in \mathcal{N}_S$. □

9.1.3. Tangential displacements

In Problem $(\mathcal{VP}_A)$, similar properties to those obtained for $V = \mathcal{N}$ can be established for a different choice of the functional space V. In particular, for $d \in I_3$, we define the following subspace of $\mathbf{H}^1(Y)$:

$$
\mathcal{T}^d := \{\mathbf{v} \in \mathbf{H}^1(Y) \mid \mathbf{v}_t = \mathbf{0} \text{ on } \partial Y \setminus \Gamma_d^{\pm}, v_d = 0 \text{ on } \Gamma_d^{\pm}\}, \tag{9.8}
$$

where $\mathbf{v}_t$ is the tangential displacement vector, i.e., $\mathbf{v}_t = \mathbf{v} - v_n\mathbf{n}$, v_n being the projection of the displacement in the outer normal direction, $\mathbf{n}$.

Remark 9.3. *Provided that the boundaries of the reference unit cell Y (7.1) are aligned with the coordinate axes, any $\mathbf{v} \in \mathcal{T}^d$ for a given index $d \in I_3$ satisfies that $v_d = 0$ on ∂Y, $v_l = 0$ on $\Gamma_k^{\pm}$ and $v_k = 0$ on $\Gamma_l^{\pm}$, where $l, k \in I_3$ such that $\gamma(l,k) - 3 = d$.*

With the choice $V = \mathcal{T}^d$, Problem $(\mathcal{VP}_A)$ for suitable data $\mathbf{L}$ becomes such that its solution induces a pure shear state in Y in a plane normal to the basis vector $\mathbf{e}_d$. Analogous results to Lemma 9.1 and Proposition 9.1 guarantee the existence and uniqueness of solution for problem $(\mathcal{VP}_A)$ in $\mathcal{T}^d$.

Lemma 9.3. *Let $\mathbf{v} \in \mathcal{T}^d \cap \mathcal{Z}(Y)$ for $d \in I_3$, with $\mathcal{Z}(Y)$ being the space of infinitesimal rigid motions of the unit cell Y, defined in (6.11). Then $\mathbf{v} \equiv \mathbf{0}$.*

Proof. In virtue of Remark 9.3, for any $d \in I_3$, the trace of each component v_i of $\mathbf{v} \in \mathcal{T}^d \cap \mathcal{Z}(Y)$ is zero at least on a pair of opposite faces of ∂Y. Hence, a similar argument to that used in Lemma 9.1 leads to $\mathbf{v} \equiv \mathbf{0}$. □

Proposition 9.3. *Let Y be the unit cell (7.1), $\mathbf{L} \in Lin$ such that $\mathbf{L} \in \mathbf{L}^2(Y)$ and $\mathbb{C} \in \mathcal{M}(\alpha, \beta, Y)$, for some $\alpha, \beta > 0$. Then Problem $(\mathcal{VP}_A)$ has a unique solution in $V = \mathcal{T}^d$, for $d \in I_3$.*

Proof. The proof is analogous to that of Proposition 9.1, since Lemma 9.3 allows to ensure the coerciveness of the bilinear form $a(\cdot,\cdot)$ (9.2) for any $\mathbf{v} \in \mathcal{T}^d$. □

An analogue result to Proposition 9.2 can be proved considering the unique solution to $(\mathcal{VP}_A)$ in $\mathcal{T}^d$ for any $d \in I_3$. In particular, we shall see that if the data satisfies specific symmetries, the solution belongs to the subsequent subspace of $\mathcal{T}^d$:

$$\mathcal{T}^d_S = \left\{ \mathbf{v} \in \mathcal{T}^d : \begin{array}{l} v_d \text{ is odd w.r.t. } y_i, i \in I_3. \\ v_j, j \neq d, \text{ is even w.r.t. } y_j, y_d \text{ and odd w.r.t } y_i \text{ such that } i \neq j \text{ and } i \neq d. \end{array} \right\}.$$

Similarly to the case for the space $\mathcal{N}_S$, we have the following direct consequence from the definition of $\mathcal{T}^d$ for any $d \in I_3$. Noting that those components of $\mathbf{u} \in \mathcal{T}^d$ that are not zero on the boundary of Y are even in Y, the proof is completely analogous to that of Lemma 9.2 and is thereby skipped.

Lemma 9.4. *Let $\mathbf{u} \in \mathcal{T}^d$. For any $d \in I_3$, it holds that*

(*i*) $\mathcal{M}_Y(\mathbf{u}) = \mathbf{0}$,

(*ii*) $\mathcal{M}_Y(\varepsilon(\mathbf{u})) = \mathbf{0}$.

Furthermore, the trace of $\mathbf{u}$ coincides on the opposite faces of Y. The extension $\mathbf{u}^\#$ of $\mathbf{u}$ belongs to $\mathbf{W}_{per}(Y)$.

Proposition 9.4. *Let Y, $\mathbf{L}$ and $\mathbb{C}$ satisfy the hypotheses of Proposition 9.3. Set $\mathcal{T}^d$ for any $d \in I_3$. Furthermore, assume that $\mathbb{C}$ satisfies Hypotheses (H.2)-(H.3) and $\mathbf{L}$ is such that:*

(*i*) *L_{dj} and L_{jd} are even w.r.t. y_j and odd w.r.t. y_i for $i \neq j$.*

(*ii*) *L_{jj} with $j \neq d$ is even w.r.t. y_d and odd w.r.t. y_i for $i \neq d$.*

(*iii*) *L_{ij} with $i \neq j$, $i \neq d$ and $j \neq d$ are even w.r.t. y_r $r \in I_3$.*

Then, the unique solution to $(\mathcal{VP}_A)$ in $\mathcal{T}^d$ is such that $\mathbf{u} \in \mathcal{T}^d_S$.

Proof. The proof mimics that of Proposition 9.2. For the sake of simplicity and without loss of generality, we set $d = 1$. The proof for the remaining cases is analogous. Let ϕ^1 denote the reflection w.r.t. the plane $y_1 = L_1/2$ and set $\widehat{\mathbf{u}}(\mathbf{y}) = (-u_1, u_2, u_3)^T(\phi^1(\mathbf{y}))$, with $\mathbf{u}$ being the unique solution to $(\mathcal{VP}_A)$ in $\mathcal{T}^1$. Set an arbitrary test function $\mathbf{v} \in \mathcal{T}^1$. Then, we define $\widehat{\mathbf{v}} \in \mathcal{T}^1$ such that $\widehat{\mathbf{v}}(\mathbf{y}) = (-v_1, v_2, v_3)^T(\phi^1(\mathbf{y}))$. Repeating the procedure followed in the proof of Proposition 9.2, using the orthotropy assumption and applying the chain rule, substitution of $\widehat{\mathbf{u}}$ in (9.2) leads to

$$a(\widehat{\mathbf{u}}, \mathbf{v}) = a(\mathbf{u}, \widehat{\mathbf{v}}) = l(\widehat{\mathbf{v}}).$$

Using the hypotheses (i), (ii) and (iii) on $\mathbf{L}$, the relation $\widehat{\mathbf{v}}(\widehat{\mathbf{y}}) = (-v_1, v_2, v_3)^T(\phi^1(\widehat{\mathbf{y}}))$ and applying the change of variable $\mathbf{y} = \phi^1(\widehat{\mathbf{y}})$, we find that $l(\widehat{\mathbf{v}}) = l(\mathbf{v})$. Consequently, for any $\mathbf{v} \in \mathcal{T}^1$, $a(\widehat{\mathbf{u}}, \mathbf{v}) = l(\mathbf{v})$, so $\widehat{\mathbf{u}}$ solves $(\mathcal{VP}_A)$. Since the solution of Problem $(\mathcal{VP}_A)$ is unique, then $\widehat{\mathbf{u}} = \mathbf{u}$ and thus, u_1 is odd w.r.t y_1 whereas u_2 as well as u_3 are even w.r.t y_1.

Analogously as in the proof of Proposition 9.2, we consider the reflections ϕ^2 and ϕ^3. Repeating the procedure above for $\widehat{\mathbf{u}}$, $\widetilde{\mathbf{u}}(\mathbf{y}) = (-u_1, u_2, -u_3)^T(\phi^2(\mathbf{y}))$ and $\overline{\mathbf{u}}(\mathbf{y}) = (-u_1, -u_2, u_3)^T(\phi^3(\mathbf{y}))$ also solve $(\mathcal{VP}_A)$ for $V = \mathcal{T}^1$. Hence, w.r.t. y_2, u_2 is even while u_1 and u_3 are odd and w.r.t. y_3, u_1 and u_2 are odd whereas u_3 is even. Thus, we conclude that $\mathbf{u} \in \mathcal{T}^1_S$.

□

9.2. Basic tests

In this section, two different types of problems on the reference cell Y are presented. They are similar to those discussed in Section 8.2. Their solutions will be used to obtain the homogenised material corresponding to the heterogeneous material defined by periodically repeating Y. We shall see that, as in the previous chapter, we need to solve six linear elasticity problems that induce three uniaxial traction (or compression) states and three shear states. The solution of these six basic tests will be

denoted as $\mathbf{u}^{lk}$, for $l,k \in I_3$. For simplicity, we shall refer to these problems as displacement basic tests (D-BT).

In the sequel, it shall be proven that the solution of the posed problems is related to the solutions of those stated in Section 9.1, with the particularity of having inhomogeneous Dirichlet conditions. Suitable lifting functions in $\mathbf{H}^1(Y)$ can be constructed such that the associated homogeneous problem has a right hand side term that satisfies the hypotheses of either Proposition 9.2 or Proposition 9.4.

9.2.1. Lifting functions

The lifting functions are defined as the following auxiliary vectorial functions for any $l,k \in I_3$ and $\mathbf{y} \in Y$:

$$\boldsymbol{\psi}^{lk}(\mathbf{y}) = -\frac{\eta}{2}\left(\frac{y_l}{L_l}\mathbf{e}_k + \frac{y_k}{L_k}\mathbf{e}_l\right), \tag{9.9}$$

where $\eta \in \mathbb{R}$ is a parameter.

Note that $\boldsymbol{\psi}^{lk}$ belongs to $\mathbf{H}^1(Y)$ and $\boldsymbol{\psi}^{lk} = \boldsymbol{\psi}^{kl}$. In particular, for $l = k$ it holds that

$$\boldsymbol{\psi}^{ll} \cdot \mathbf{n} = \begin{cases} -\eta, & \text{a.e. on } \Gamma_l^+, \\ 0, & \text{a.e. on } \partial Y \setminus \Gamma_l^+. \end{cases} \tag{9.10}$$

Moreover, if $l \neq k$, their normal components are

$$\boldsymbol{\psi}^{lk} \cdot \mathbf{n} = \begin{cases} \mp\dfrac{\eta y_l}{2L_l}, & \text{a.e. on } \Gamma_k^{\pm}, \\ \mp\dfrac{\eta y_k}{2L_k}, & \text{a.e. on } \Gamma_l^{\pm}, \\ 0, & \text{a.e. on } \Gamma_d^{\pm}, \end{cases} \tag{9.11}$$

with $d \in I_3 \setminus \{l,k\}$ Therefore, their tangential components, $\boldsymbol{\psi}_t^{lk} = \boldsymbol{\psi}^{lk} - (\boldsymbol{\psi}^{lk} \cdot \mathbf{n})\mathbf{n}$, are such that:

$$\boldsymbol{\psi}_t^{lk} = \begin{cases} -\dfrac{\eta y_k}{2L_k}\mathbf{e}_l, & \text{a.e. on } \Gamma_k^{\pm}, \\ -\dfrac{\eta y_l}{2L_l}\mathbf{e}_k, & \text{a.e. on } \Gamma_l^{\pm}, \\ \boldsymbol{\psi}^{lk}, & \text{a.e. on } \Gamma_d^{\pm}. \end{cases} \tag{9.12}$$

Let δ_{ij} denote the *Kronecker delta* function, i.e., the function such that $\delta_{ij} = 1$ if $i = j$ and $\delta_{ij} = 0$ otherwise. The subsequent lemma provides the expression satisfied by the stress generated by the lifting $\boldsymbol{\psi}^{lk}$ when the linear elastic material is orthotropic.

Lemma 9.5. *Let $\mathbb{C} \in \mathcal{M}(\alpha,\beta,Y)$ such that it also satisfies Hypothesis (H.3). Then, the associated stress tensor to the displacement $\boldsymbol{\psi}^{lk}$, defined in (9.9), is such that:*

$$\sigma_{ij}(\boldsymbol{\psi}^{lk}) = \begin{cases} -\dfrac{\eta}{L_l}C_{ijll}\delta_{ij}, & \text{if } l = k, \\ -\dfrac{\eta}{2}\left(\dfrac{1}{L_l} + \dfrac{1}{L_k}\right)C_{ijlk}(\delta_{il}\delta_{jk} + \delta_{jl}\delta_{ik}), & \text{if } l \neq k, \end{cases} \tag{9.13}$$

where no summation on the repeated subscripts is considered.

Proof. Let $\boldsymbol{\psi}^{lk}$ be such that $l = k$. Then, it holds that

$$\boldsymbol{\varepsilon}(\boldsymbol{\psi}^{ll}) = -\frac{\eta}{L_l}\mathbf{E}^{ll}, \tag{9.14}$$

without summation on the l index. Hence, the corresponding tensor field is directly obtained from the constitutive law (6.5):

$$\sigma_{ij}(\boldsymbol{\psi}^{ll}) = C_{ijrs}\varepsilon_{rs}(\boldsymbol{\psi}^{ll}) = -\frac{\eta}{L_l}C_{ijll}. \tag{9.15}$$

USC UNIVERSIDADE DE SANTIAGO DE COMPOSTELA

Hypothesis (H.3) implies that $\mathbb{C}$ corresponds to an orthotropic material. Thus, it holds that $C_{ijll} = 0$ if $i \neq j$ and, from (9.15), it follows that

$$\sigma_{ij}(\boldsymbol{\psi}^{ll}) = -\frac{\eta}{L_l} C_{ijll}\delta_{ij}.$$

Similarly, if $l \neq k$, the strain field induced by $\boldsymbol{\psi}^{lk}$ is such that

$$\boldsymbol{\varepsilon}(\boldsymbol{\psi}^{lk}) = -\frac{\eta}{2}\left(\frac{1}{L_l} + \frac{1}{L_k}\right)\mathbf{E}^{lk}, \tag{9.16}$$

without summation over the indices l, k. Thus, the corresponding stress is

$$\begin{aligned}\sigma_{ij}(\boldsymbol{\psi}^{lk}) &= -\frac{\eta}{2}\left(\frac{1}{L_l} + \frac{1}{L_k}\right) C_{ijrs}E^{lk}_{rs} = -\frac{\eta}{2}\left(\frac{1}{L_l} + \frac{1}{L_k}\right)\left(\frac{C_{ijlk}}{2} + \frac{C_{ijkl}}{2}\right)\\ &= -\frac{\eta}{2}\left(\frac{1}{L_l} + \frac{1}{L_k}\right) C_{ijlk},\end{aligned} \tag{9.17}$$

since $C_{ijlk} = C_{ijkl}$ as $\mathbb{C} \in \mathcal{M}(\alpha, \beta, \Upsilon)$.

Again, using that hypothesis (H.3) holds, (9.17) simplifies to

$$\sigma_{ij}(\boldsymbol{\psi}^{lk}) = -\frac{\eta}{2}\left(\frac{1}{L_l} + \frac{1}{L_k}\right) C_{ijlk}(\delta_{il}\delta_{jk} + \delta_{jl}\delta_{ik}),$$

since $C_{ijlk} \neq 0$ if and only if $(i, j) = (l, k)$ or $(i, j) = (k, l)$. □

Remark 9.4. *If $l = k$, expression (9.13) may be rewritten using the corresponding entries of the stiffness matrix, noting that $C_{iill} = c_{il}$:*

$$\boldsymbol{\sigma}_{ij}(\boldsymbol{\psi}^{ll}) = -\frac{\eta}{L_l} c_{il}\delta_{ij}. \tag{9.18}$$

Furthermore, the induced stress by $\boldsymbol{\psi}^{ll}$ on ∂Y satisfies that

$$\boldsymbol{\sigma}(\boldsymbol{\psi}^{ll})\mathbf{n} = \mp\frac{\eta}{L_l} c_{il}\mathbf{e}_i, \qquad \text{on } \Gamma_i^{\pm},$$

for each $i \in I_3$. Thus, it is a purely normal stress, being $\boldsymbol{\sigma}_t = \boldsymbol{\sigma}\mathbf{n} - \sigma_n\mathbf{n} = \mathbf{0}$ on ∂Y. For instance, if $l = k = 2$, then by (9.14) $\boldsymbol{\varepsilon}(\boldsymbol{\psi}^{22}) = -\eta/L_2\mathbf{E}^{22}$ and, using (9.18), the stress tensor induced by the lifting $\boldsymbol{\psi}^{22}$ simply becomes:

$$\boldsymbol{\sigma}(\boldsymbol{\psi}^{22}) = -\frac{\eta}{L_2}\begin{pmatrix} c_{12} & 0 & 0\\ 0 & c_{22} & 0\\ 0 & 0 & c_{32}\end{pmatrix}.$$

Conversely, if $l \neq k$, then on ∂Y it holds that

$$\boldsymbol{\sigma}(\boldsymbol{\psi}^{lk})\mathbf{n} = \begin{cases} \mp\dfrac{\eta}{2}\left(\dfrac{1}{L_l} + \dfrac{1}{L_k}\right) C_{lklk}\mathbf{e}_k, & \text{on } \Gamma_l^{\pm},\\ \mp\dfrac{\eta}{2}\left(\dfrac{1}{L_l} + \dfrac{1}{L_k}\right) C_{lklk}\mathbf{e}_l, & \text{on } \Gamma_k^{\pm},\\ \mathbf{0}, & \text{on } \Gamma_d^{\pm},\end{cases}$$

and, since $\boldsymbol{\sigma}\mathbf{n}\cdot\mathbf{n} = 0$, then $\boldsymbol{\sigma}_t = \boldsymbol{\sigma}\mathbf{n}$. In particular, if $l = 1$ and $k = 2$, then by (9.16) the corresponding strain tensor becomes $\boldsymbol{\varepsilon}(\boldsymbol{\psi}^{12}) = -\eta/2(1/L_1 + 1/L_2)\mathbf{E}^{12}$. Moreover, Lemma 9.5 yields that the induced stress is such that

$$\boldsymbol{\sigma}(\boldsymbol{\psi}^{12}) = -\frac{\eta}{2}\left(\frac{1}{L_1} + \frac{1}{L_2}\right)\begin{pmatrix} 0 & c_{66} & 0\\ c_{66} & 0 & 0\\ 0 & 0 & 0\end{pmatrix},$$

where it has been used that $C_{1212} = c_{66}$. Note that the stress corresponds to a shear state in the coordinate plane with normal vector $\mathbf{e}_3$.

USC

9.2.2. Traction tests

We start by presenting the strong and weak forms of the problem that induces a uniaxial traction state in the reference cell Y along the lth coordinate axis. Depending on the coordinate axis along which the stress state is generated, the corresponding solution displacement field is denoted as $\mathbf{u}^{ll}$, for $l \in I_3$. Set an arbitrary $\eta \in \mathbb{R}$. The strong formulation of the traction test problem is subsequently introduced.

Problem $(\mathcal{P}_\mathcal{N})^l$: Find $\mathbf{u}^{ll}$ such that:

$$\begin{aligned} -\operatorname{Div}(\boldsymbol{\sigma}(\mathbf{u}^{ll})) &= \mathbf{0}, && \text{in } Y, \\ \boldsymbol{\sigma}(\mathbf{u}^{ll}) &= \mathbb{C} : \boldsymbol{\varepsilon}(\mathbf{u}^{ll}), && \text{in } Y, \\ \mathbf{u}^{ll} \cdot \mathbf{n} &= \eta, && \text{on } \Gamma_l^+, \\ \mathbf{u}^{ll} \cdot \mathbf{n} &= 0, && \text{on } \partial Y \setminus \Gamma_l^+, \\ \boldsymbol{\sigma}_t &= \mathbf{0}, && \text{on } \partial Y. \end{aligned} \tag{9.19}$$

The following weak formulation is obtained multiplying (9.19) by a test function in $\mathcal{N}$, where $\mathcal{N}$ is the space (9.4), integrating in Y and applying a Green's formula.

Problem $(\mathcal{VP}_\mathcal{N})^l$. Find $\mathbf{u}^{ll} \in \mathbf{H}^1(Y)$ such that $\mathbf{u}^{ll} \cdot \mathbf{n} = \eta$ on Γ_l^+, $\mathbf{u}^{ll} \cdot \mathbf{n} = 0$ on $\partial Y \setminus \Gamma_l^+$ and

$$a(\mathbf{u}^{ll}, \mathbf{v}) = 0, \qquad \forall \mathbf{v} \in \mathcal{N},$$

where $a(\cdot,\cdot)$ is the bilinear form (9.2).

To obtain a result concerning the existence and uniqueness of solution to Problem $(\mathcal{VP}_\mathcal{N})^l$, we introduce the subsequent auxiliary problem.

Problem $(\widehat{\mathcal{VP}}_\mathcal{N})^l$. Find $\widehat{\mathbf{u}}^{ll} \in \mathcal{N}$ such that

$$a(\widehat{\mathbf{u}}^{ll}, \mathbf{v}) = l(\mathbf{v}), \qquad \forall \mathbf{v} \in \mathcal{N}, \tag{9.20}$$

where the functional $l(\mathbf{v})$ is defined as (9.3) with $\mathbf{L} = \boldsymbol{\sigma}(\boldsymbol{\psi}^{ll})$, i.e.:

$$l(\mathbf{v}) = \int_Y \boldsymbol{\sigma}(\boldsymbol{\psi}^{ll}) : \nabla \mathbf{v} \, dV. \tag{9.21}$$

Remark 9.5. *Let the second order tensor* $\mathbf{L}$ *be such that* $\mathbf{L} = \boldsymbol{\sigma}(\boldsymbol{\psi}^{ll})$. *Note that Problem* $(\widehat{\mathcal{VP}}_\mathcal{N})^l$ *is equivalent to Problem* $(\mathcal{VP}_A)$ *with* $V = \mathcal{N}$. *Since* $\mathbf{L} = \mathbf{L}^2(Y)$, *then Proposition 9.1 yields that there is a unique* $\widehat{\mathbf{u}}^{ll} \in \mathcal{N}$ *such that* (9.20) *holds.*

Proposition 9.5. *Let* Y *be the reference cell* (7.1) *and assume that* $\mathbb{C}$ *satisfies hypotheses* (H.1)-(H.3). *Moreover, let* $\widehat{\mathbf{u}}^{ll}$ *be the solution to Problem* $(\widehat{\mathcal{VP}}_\mathcal{N})^l$. *Then, it holds that* $\widehat{\mathbf{u}}^{ll} \in \mathcal{N}_S$ *and* $\mathcal{M}_Y(\widehat{\mathbf{u}}^{ll}) = \mathbf{0}$. *Furthermore,* $\mathbf{u}^{ll} = \widehat{\mathbf{u}}^{ll} - \boldsymbol{\psi}^{ll}$ *is the unique solution of Problem* $(\mathcal{VP}_\mathcal{N})^l$.

Proof. Set $\mathbf{u}^{ll} = \widehat{\mathbf{u}}^{ll} - \boldsymbol{\psi}^{ll}$. Since $\widehat{u}^{ll}, \boldsymbol{\psi}^{ll} \in \mathbf{H}^1(Y)$, it is clear that $\mathbf{u}^{ll} \in \mathbf{H}^1(Y)$. Substituting $\widehat{\mathbf{u}}^{ll} = \mathbf{u}^{ll} + \boldsymbol{\psi}^{ll}$ in the bilinear form $a(\cdot,\cdot)$ it follows that

$$a(\widehat{\mathbf{u}}^{ll}, \mathbf{v}) = a(\mathbf{u}^{ll}, \mathbf{v}) + a(\boldsymbol{\psi}^{ll}, \mathbf{v}) = a(\mathbf{u}^{ll}, \mathbf{v}) + \int_Y \boldsymbol{\sigma}(\boldsymbol{\psi}^{ll}) : \boldsymbol{\varepsilon}(\mathbf{v}) \, dV,$$

since $\boldsymbol{\sigma} \in Sym$ implies that (9.21) may be rewritten as

$$l(\mathbf{v}) = \int_Y \boldsymbol{\sigma}(\boldsymbol{\psi}^{ll}) : \boldsymbol{\varepsilon}(\mathbf{v}) \, dV,$$

for all $\mathbf{v} \in \mathcal{N}$.

Thus, from (9.20) we deduce that $\mathbf{u}^{ll}$ is such that

$$a(\mathbf{u}^{ll}, \mathbf{v}) = 0, \qquad \forall \mathbf{v} \in \mathcal{N}.$$

UNIVERSIDADE DE SANTIAGO DE COMPOSTELA

Consequently, given that $\widehat{\mathbf{u}}^{ll} \in \mathcal{N}$ and that $\boldsymbol{\psi}^{ll} \cdot \mathbf{n}$ satisfies (9.10), then $\mathbf{u}^{ll} \cdot \mathbf{n} = \eta$ on Γ_l^+. Therefore, $\mathbf{u}^{ll}$ solves problem $(\mathcal{VP}_{\mathcal{N}})^l$.

Assume that $\mathbf{u}_*^{ll}$ is another solution to Problem $(\mathcal{VP}_{\mathcal{N}})^l$. Then, the previous computations lead to $\widehat{\mathbf{u}}_*^{ll} = \mathbf{u}_*^{ll} + \boldsymbol{\psi}^{ll}$ being another solution to $(\mathcal{VP}_A)$ for $V = \mathcal{N}$ and $\mathbf{L} = \boldsymbol{\sigma}(\boldsymbol{\psi}^{ll})$. However, by Proposition 9.1 this solution is unique, so we conclude that $\widehat{\mathbf{u}}_*^{ll} = \widehat{\mathbf{u}}^{ll}$ and hence $\mathbf{u}_*^{ll} = \mathbf{u}^{ll}$, being $\mathbf{u}^{ll}$ the unique solution to $(\mathcal{VP}_{\mathcal{N}})^l$.

In virtue of Remark 9.5, it remains to see that the data $\mathbf{L} = \boldsymbol{\sigma}(\boldsymbol{\psi}^{ll})$ also satisfies the hypotheses of Proposition 9.2. In such a case, it directly follows that $\widehat{\mathbf{u}}^{ll}$ belongs to the space $\mathcal{N}_S$.

Note that Lemma 9.5 and Remark 9.4 guarantee that the stress induced by the lifting satisfies (9.18). Consequently, provided that $\sigma_{ij}(\boldsymbol{\psi}^{ll}) = 0$ if $i \neq j$, $\mathbf{L}$ satisfies hypothesis (ii) in Proposition 9.2. Moreover, since the elasticity tensor is even w.r.t. y_i, for $i \in I_3$, due to (H.1), then hypothesis (i) in Proposition 9.2 is also fulfilled. Thereby, $\widehat{\mathbf{u}}^{ll}$ belongs to $\mathcal{N}_S$. Corollary 9.2 yields that $\mathcal{M}_Y(\widehat{\mathbf{u}}^{ll}) = \mathbf{0}$ and $\mathcal{M}_Y(\boldsymbol{\varepsilon}(\widehat{\mathbf{u}}^{ll})) = \mathbf{0}$. □

9.2.3. Shear tests

Similarly as with the traction test introduced in Section 9.2.2, we state below a problem that induces a shear stress state in the reference cell Y. The shear is produced in the coordinate plane with normal vector $\mathbf{e}_d \in I_3$. The corresponding displacement field that is obtained as solution to the problem is denoted as $\mathbf{u}^{lk}$, where l, k with $l \neq k$ correspond to the indices of the canonical basis vectors $\mathbf{e}_l$ and $\mathbf{e}_k$ that span the plane, so, $l, k \in I_3 \setminus \{d\}$. For an arbitrary $\eta \in \mathbb{R}$, we pose the subsequent shear test problem.

Problem $(\mathcal{P}_{\mathcal{T}})^d$**:** Find $\mathbf{u}^{lk}$ such that:

$$
\begin{aligned}
&-\operatorname{Div}(\boldsymbol{\sigma}(\mathbf{u}^{lk})) = \mathbf{0}, && \text{in } Y, && (9.22)\\
&\boldsymbol{\sigma}(\mathbf{u}^{lk}) = \mathbb{C} : \boldsymbol{\varepsilon}(\mathbf{u}^{lk}), && \text{in } Y, &&\\
&\mathbf{u}_t^{lk} = \frac{\eta}{2L_k} y_k \mathbf{e}_l, && \text{on } \Gamma_k^{\pm}, && (9.23)\\
&\mathbf{u}_t^{lk} = \frac{\eta}{2L_l} y_l \mathbf{e}_k, && \text{on } \Gamma_l^{\pm}, && (9.24)\\
&\sigma_n = 0, && \text{on } \Gamma_l^{\pm} \cup \Gamma_k^{\pm}, &&\\
&\begin{cases} \mathbf{u} \cdot \mathbf{n} = 0, \\ \boldsymbol{\sigma}_t = \mathbf{0}, \end{cases} && \text{on } \Gamma_d^{\pm}. &&
\end{aligned}
$$

Remark 9.6. *The previous problem only depends on the index $d \in I_3$ and $\mathbf{u}^{lk} = \mathbf{u}^{kl}$. Provided that the tangential displacement $\mathbf{u}$ is defined as $\mathbf{u}_t = \mathbf{u} - (\mathbf{u} \cdot \mathbf{n})\mathbf{n}$, and since the faces forming the boundary of Y are aligned with the coordinate planes, then conditions (9.23) and (9.24) involve the lth and kth components of the solution $\mathbf{u}^{lk}$, respectively. Therefore, both of them implicitly impose that $u_d = 0$ on $\Gamma_k^{\pm} \cup \Gamma_l^{\pm}$.*

Also, note that the expressions involving the displacements simplify significantly in boundary conditions (9.23) and (9.24) if written separately for Γ_i^+ and Γ_i^-, $i \in \{l, k\}$. In particular, these boundary conditions force the lth and kth components of the solution to be 0 on $\Gamma_k^- \cup \Gamma_l^-$ and $\eta/2$ on $\Gamma_k^+ \cup \Gamma_l^+$, respectively.

To obtain a weak formulation of the problem for a given $d \in I_3$, we multiply (9.22) by a test function in the space $\mathcal{T}^d$, defined in (9.8), integrate in Y and apply a Green's formula. Noting Remark 9.3 and that $\boldsymbol{\sigma}_t = \boldsymbol{\sigma}\mathbf{n} - \sigma_n \mathbf{n}$, we obtain the subsequent weak problem.

Problem $(\mathcal{VP}_{\mathcal{T}})^d$. Find $\mathbf{u}^{lk} \in \mathbf{H}^1(Y)$ such that $\mathbf{u}_t^{lk} = \eta y_k/(2L_k)\mathbf{e}_l$ on $\Gamma_k^{\pm}$, $\mathbf{u}_t^{lk} = \eta y_l/(2L_l)\mathbf{e}_k$ on $\Gamma_l^{\pm}$, $u_d^{lk} = 0$ on $\Gamma_d^{\pm}$ and

$$
a(\mathbf{u}^{lk}, \mathbf{v}) = 0, \qquad \forall \mathbf{v} \in \mathcal{T}^d,
$$

where $a(\cdot, \cdot)$ is the bilinear form (9.2). In addition, we pose the following auxiliary problem.

USC UNIVERSIDADE DE SANTIAGO DE COMPOSTELA

Problem $(\widehat{\mathcal{VP}}_{\mathcal{T}})^d$. Find $\widehat{\mathbf{u}}^{lk} \in \mathcal{T}^d$ such that

$$
a(\widehat{\mathbf{u}}^{lk}, \mathbf{v}) = l(\mathbf{v}), \qquad \forall \mathbf{v} \in \mathcal{T}^d, \tag{9.25}
$$

where $l(\mathbf{v})$ is (9.3), setting that $\mathbf{L} = \boldsymbol{\sigma}(\boldsymbol{\psi}^{lk}) \in \mathbf{L}^2(Y)$.

Remark 9.7. *It holds that Problem* $(\widehat{\mathcal{VP}}_{\mathcal{T}})^d$ *is the same as* $(\mathcal{VP}_A)$ *for* $V = \mathcal{T}^d$. *Hence, Proposition 9.3 guarantees that there is a unique* $\widehat{\mathbf{u}}^{lk} \in \mathcal{T}^d$ *such that* (9.25) *holds.*

Below, an analogous result to Proposition 9.5 is given. It ensures that Problem $(\mathcal{VP}_{\mathcal{T}})^d$ has a unique solution using the lifting (9.9) and relates this solution to the displacement field $\widehat{\mathbf{u}}^{lk} \in \mathcal{T}_S^d$.

Proposition 9.6. *Let* Y *be the reference cell* (7.1) *and assume that* $\mathbb{C}$ *satisfies hypotheses* (H.1)-(H.3). *Set* $d \in I_3$ *and* $l, k \in I_3$ *such that* $\gamma(l,k) - 3 = d$. *Let* $\widehat{\mathbf{u}}^{lk}$ *be the solution to Problem* $(\widehat{\mathcal{VP}}_{\mathcal{T}})^d$. *Then, it holds that* $\widehat{\mathbf{u}}^{lk} \in \mathcal{T}_S^d$. *Furthermore,* $\mathbf{u}^{lk} = \widehat{\mathbf{u}}^{lk} - \boldsymbol{\psi}^{lk}$ *is the unique solution of Problem* $(\mathcal{VP}_{\mathcal{T}})^d$.

Proof. Let $\widehat{\mathbf{u}}^{lk}$ be the unique solution $\widehat{\mathbf{u}}^{lk}$ to Problem $(\widehat{\mathcal{VP}}_{\mathcal{T}})^d$. Then, set $\mathbf{u}^{lk} = \widehat{\mathbf{u}}^{lk} - \boldsymbol{\psi}^{lk}$. Again, using that $\boldsymbol{\sigma} \in Sym$ and following the lines of the proof of Proposition 9.5, it is straightforward to obtain that $\mathbf{u}^{lk}$ is the unique solution of Problem $(\mathcal{VP}_{\mathcal{T}})^d$. To this end, note that given (9.12), $\mathbf{u}_t^{lk}$ satisfies that $\mathbf{u}_t^{lk} = \eta y_l/(2L_l)\mathbf{e}_k$ on $\Gamma_l^{\pm}$ and $\mathbf{u}_t^{lk} = \eta y_k/(2L_k)\mathbf{e}_l$ on $\Gamma_k^{\pm}$. Furthermore, due to (9.11), $\mathbf{u}^{lk} \cdot \mathbf{n} = 0$ on $\Gamma_d^{\pm}$.

From Lemma 9.5, we deduce that the hypotheses on the data $\mathbf{L} = \boldsymbol{\sigma}(\boldsymbol{\psi}^{lk})$ of Proposition 9.4 are fulfilled. Indeed, since $L_{dj} = L_{jd} = 0$ and $L_{jj} = 0$ for any $j \in I_3$, hypotheses (i) and (ii) hold. In addition, invoking hypothesis (H.2), it holds that C_{lklk} is even w.r.t. y_r for $r \in I_3$. Hence, it follows that the unique solution $\widehat{\mathbf{u}}^{lk}$ to $(\mathcal{VP}_{\mathcal{T}})^d$ belongs to $\mathcal{T}_s^d$ in virtue of Proposition 9.4. □

9.3. Equivalence with the corrector problems

In this section, we obtain a mathematical justification of the technique presented in this chapter. With this purpose, we establish a result that relates the solutions to the displacement basic tests presented in Section 9.2, i.e., Problems $(\mathcal{VP}_{\mathcal{N}})^l$ and $(\mathcal{VP}_{\mathcal{T}})^d$, to the corrector functions of the linear elasticity system, obtained as the solution to Problem $(\mathcal{VP}_C)^{lk}$. Hence, the solutions to the D-BT can be used to obtain a fictitious homogeneous material whose macroscopic response is a good approximation of that of the heterogeneous material, as it is done following the classical homogenisation procedure presented in Chapter 7. We shall also prove that, under the previously introduced hypotheses, it holds that the homogenised material can be directly obtained by solving the system of 36 equations and unknowns (8.6), presented in the previous chapter to obtain a homogenised material using the stress basic tests (S-BT).

Before stating and proving these facts, assuming that the material is orthotropic, we establish an easy relation among the induced stress by the liftings $\boldsymbol{\psi}^{lk}$ and that produced by the displacements $\mathbf{p}^{lk}$, which appear in Problem $(\mathcal{VP}_C)^{lk}$.

Lemma 9.6. *Let* $\mathbb{C}$ *be such that it satisfies the hypotheses of Lemma 9.5 and set the displacement* $\boldsymbol{\psi}^{lk}$, *defined in* (9.9). *Then, the stress tensor associated to* $\mathbf{p}^{lk} = y_k \mathbf{e}_l$ *satisfies that*

$$\sigma_{ij}(\mathbf{p}^{lk}) = -\frac{2L_k L_l}{\eta(L_k + L_l)} \sigma_{ij}(\boldsymbol{\psi}^{lk}). \tag{9.26}$$

Proof. First, we observe that it holds that

$$\boldsymbol{\varepsilon}(\mathbf{p}^{lk}) = \mathbf{E}^{lk},$$

where we recall the second-order tensor $\mathbf{E}^{lk}$ was defined in (7.6). Clearly, the components of the stress tensor satisfy that

$$\sigma_{ij}(\mathbf{p}^{lk}) = C_{ijlk}.$$

From this expression, since $\mathbb{C}$ is orthotropic:

$$\sigma_{ij}(\mathbf{p}^{lk}) = \begin{cases} C_{ijll}\delta_{ij}, & \text{if } l = k, \\ C_{ijlk}(\delta_{il}\delta_{jk} + \delta_{jl}\delta_{ik}), & \text{if } l \neq k, \end{cases} \tag{9.27}$$

USC UNIVERSIDADE DE SANTIAGO DE COMPOSTELA

without summation on repeated indices.

Hence, Lemma 9.5 leads to

$$\sigma_{ij}(\boldsymbol{\psi}^{lk}) = -\frac{\eta}{2}\left(\frac{1}{L_l}+\frac{1}{L_k}\right)\sigma_{ij}(\mathbf{p}^{lk}),$$

and the assertion (9.26) follows directly. □

If the elasticity tensor satisfies hypotheses (H.1)-(H.3), it holds that the solution of the periodic problem corresponding to $\boldsymbol{\mathcal{X}}^{lk}$, which is sought in the space $\mathbf{W}_{per}(Y)$, belongs to $\mathcal{N}_S$ if $l = k$ and to $\mathcal{T}_S^d$ for $d = \gamma(l,k) - 3$. Below, we address the proof of this property, which is essentially analogous to that of Propositions 9.2 and 9.4.

Proposition 9.7. *Let Y be the reference cell (7.1) and assume that $\mathbb{C}$ satisfies hypotheses (H.1)-(H.3). If $\boldsymbol{\mathcal{X}}^{lk} \in \mathbf{W}_{per}(Y)$ is the solution to Problem $(\mathcal{VP}_C)^{lk}$, then it holds that*

(i) $\boldsymbol{\mathcal{X}}^{lk} \in \mathcal{N}_S$ *if* $l = k$,

(ii) $\boldsymbol{\mathcal{X}}^{lk} \in \mathcal{T}_S^d$ *if* $l \neq k$,

where $d \in I_3$ is such that $d = \gamma(l,k) - 3$.

Proof. Set $\boldsymbol{\mathcal{X}}^{lk} \in \mathbf{W}_{per}(Y)$ as the unique solution to Problem $(\mathcal{VP}_C)^{lk}$. Using that $\boldsymbol{\sigma} \in Sym$, note that the right hand side of (7.7), can be rewritten taking into account that

$$\int_Y \boldsymbol{\sigma}(\mathbf{p}^{lk}) : \varepsilon(\mathbf{v})\, dV = \int_Y \boldsymbol{\sigma}(\mathbf{p}^{lk}) : \nabla \mathbf{v}\, dV.$$

Therefore, the statement of the corrector problem is the same as that of Problem $(\mathcal{VP}_A)$, with the data $\mathbf{L} = \boldsymbol{\sigma}(\mathbf{p}^{lk})$ and choosing $V = \mathbf{W}_{per}(Y)$.

We first prove (i). Let $l = k$ and set $\widehat{\boldsymbol{\mathcal{X}}}^{lk}(\mathbf{y}) = (-\mathcal{X}_1^{lk}, \mathcal{X}_2^{lk}, \mathcal{X}_3^{lk})(\phi^1(\mathbf{y}))$. Also, set an arbitrary test function $\mathbf{v} \in \mathbf{W}_{per}(Y)$ and $\widehat{\mathbf{v}}(\mathbf{y}) = (-v_1, v_2, v_3)^T(\phi^1(\mathbf{y}))$, for almost all $\mathbf{y} \in Y$. Since the trace of any function in $\mathbf{W}_{per}(Y)$ coincides on the opposite faces of Y, it follows that $\widehat{\mathbf{v}} \in \mathbf{W}_{per}(Y)$. Then, following the lines of Proposition 9.2, it is straightforward to show that

$$a(\widehat{\boldsymbol{\mathcal{X}}}^{ll}, \mathbf{v}) = a(\boldsymbol{\mathcal{X}}^{ll}, \widehat{\mathbf{v}}) = l(\widehat{\mathbf{v}}).$$

In virtue of (9.26), notice that the second order tensor $\mathbf{L}$ defined as $\mathbf{L} = \boldsymbol{\sigma}(\mathbf{p}^{ll})$ satisfies the hypotheses on the data required in Proposition 9.2, as the only non-zero entries of $\boldsymbol{\sigma}(\mathbf{p}^{ll})$ are the diagonal ones, which are even w.r.t. y_i, $i \in I_3$ since hypothesis (H.2) on $\mathbb{C}$ holds. Hence, it follows that

$$l(\widehat{\mathbf{v}}) = l(\mathbf{v}).$$

Consequently, $\widehat{\boldsymbol{\mathcal{X}}}^{ll}$ is also a solution to Problem $(\mathcal{VP}_C)^{lk}$ and, as the solution is unique, then $\widehat{\boldsymbol{\mathcal{X}}}^{ll} = \boldsymbol{\mathcal{X}}^{ll}$. This leads to $\mathcal{X}_1{}^{ll}$ being odd w.r.t. y_1 as well as $\mathcal{X}_2{}^{ll}$ and $\mathcal{X}_3{}^{ll}$ being even w.r.t. y_1.

As in the proof of Proposition 9.2, now we set $\widetilde{\boldsymbol{\mathcal{X}}}^{ll}(\mathbf{y}) = (\mathcal{X}_1^{ll}, -\mathcal{X}_2^{ll}, \mathcal{X}_3^{ll})(\phi^2(\mathbf{y}))$ and $\overline{\boldsymbol{\mathcal{X}}}^{ll}(\mathbf{y}) = (\mathcal{X}_1^{ll}, \mathcal{X}_2^{ll}, -\mathcal{X}_3^{ll})(\phi^3(\mathbf{y}))$, which repeating the procedure above are shown to be also solutions to Problem $(\mathcal{VP}_C)^{lk}$. Therefore, $\mathcal{X}_i^{ll}$ is odd w.r.t. y_i and even w.r.t. y_j, $j \neq i$.

Lastly, since $\boldsymbol{\mathcal{X}}^{ll} \in \mathbf{W}_{per}(Y)$, in particular it holds that $\mathcal{X}_i^{ll}|_{\Gamma_i^+} = \mathcal{X}_i^{ll}|_{\Gamma_i^-}$. Furthermore, since $\mathcal{X}_i^{ll}$ is odd w.r.t. y_i, it follows that $\mathcal{X}_i^{ll} = 0$ on $\Gamma_i^{\pm}$ and thus $\boldsymbol{\mathcal{X}}^{ll} \cdot \mathbf{n} = \mathbf{0}$ on ∂Y. Therefore, $\boldsymbol{\mathcal{X}}^{ll} \in \mathcal{N}_S$.

Now, we prove (ii). Set $l, k \in I_3$ such that $l \neq k$. Without loss of generality, we consider the case $l = 2$ and $k = 3$, as the proof for the remaining ones is completely analogous. Then, since $d = \gamma(l,k) - 3$, set $d = 1$. As in the case above, using (9.27), it holds that $\mathbf{L} = \boldsymbol{\sigma}(\mathbf{p}^{lk})$ satisfies all the

hypotheses on the data required in Proposition 9.4. Hence, following the steps of its proof, it can be shown that

$$\widehat{\boldsymbol{\mathcal{X}}}^{23}(\mathbf{y}) = (-\mathcal{X}_1^{23}, \mathcal{X}_2^{23}, \mathcal{X}_3^{23})(\phi^1(\mathbf{y})),$$
$$\widetilde{\boldsymbol{\mathcal{X}}}^{23}(\mathbf{y}) = (-\mathcal{X}_1^{23}, \mathcal{X}_2^{23}, -\mathcal{X}_3^{23})(\phi^2(\mathbf{y})),$$
$$\overline{\boldsymbol{\mathcal{X}}}^{23}(\mathbf{y}) = (-\mathcal{X}_1^{23}, -\mathcal{X}_2^{23}, -\mathcal{X}_3^{23})(\phi^3(\mathbf{y})),$$

are also solutions to Problem $(\mathcal{VP}_C)^{lk}$ and, therefore, it must hold that $\mathcal{X}_1^{23}$ is odd w.r.t. y_i, $i \in I_3$, $\mathcal{X}_2^{23}$ is odd w.r.t. y_3 as well as even w.r.t. y_1, y_2, and $\mathcal{X}_3^{23}$ is odd w.r.t. y_2 and even w.r.t. y_1, y_3.

Finally, recalling Remark 9.3, the conditions that we need to prove to see that $\boldsymbol{\mathcal{X}}^{23} \in \mathcal{T}_S^1$ (i.e., that $\boldsymbol{\mathcal{X}}_t^{23} = \mathbf{0}$ on $\partial Y \setminus \Gamma_1^{\pm}$ and $\mathcal{X}_1^{23} = 0$ on $\Gamma_1^{\pm}$), can be equivalently stated as

$$\mathcal{X}_1^{23} = 0, \quad \text{on } \partial Y,$$
$$\mathcal{X}_2^{23} = 0, \quad \text{on } \Gamma_3^{\pm},$$
$$\mathcal{X}_3^{23} = 0, \quad \text{on } \Gamma_2^{\pm}.$$

Similarly as in the case $l = k$, we note that $\boldsymbol{\mathcal{X}}^{23}$ is such that its trace coincides on the opposite faces of ∂Y, but it is not necessarily zero. However, since $\mathcal{X}_1^{23}$ is odd w.r.t. y_i, $i \in I_3$, then it must hold that $\mathcal{X}_1^{23} = 0$ on ∂Y, and analogously for the remaining components. Therefore, we conclude that $\boldsymbol{\mathcal{X}}^{23} \in \mathcal{T}_S^1$. □

As a consequence of the previous result, the solutions to the D-BT can be connected to those of Problem $(\mathcal{VP}_C)^{lk}$ through the subsequent theorem.

Theorem 9.1. *Assume that the hypotheses of Proposition 9.7 hold. Set $l, k \in I_3$ and let $\mathbf{u}^{lk}$ be the solution to $(\mathcal{VP}_{\mathcal{N}})^l$ if $l = k$, and the solution to $(\mathcal{VP}_{\mathcal{T}})^d$ if $l \neq k$, for $d \in I_3$ and any $\eta \in \mathbb{R}$. Then, if $\boldsymbol{\mathcal{X}}^{lk}$ is the solution to $(\mathcal{VP}_C)^{lk}$:*

$$\widehat{\mathbf{u}}^{lk} = -\frac{\eta}{2}\left(\frac{1}{L_l} + \frac{1}{L_k}\right)\boldsymbol{\mathcal{X}}^{lk},$$

being $\widehat{\mathbf{u}}^{lk} = \mathbf{u}^{lk} + \boldsymbol{\psi}^{lk}$, with $\boldsymbol{\psi}^{lk}$ defined in (9.9).

Proof. Set $l, k \in I_3$. If $\boldsymbol{\mathcal{X}}^{lk}$ is the solution to $(\mathcal{VP}_C)^{lk}$, it holds that

$$a(\boldsymbol{\mathcal{X}}^{lk}, \mathbf{v}) = \int_Y \boldsymbol{\sigma}(\mathbf{p}^{lk}) : \boldsymbol{\varepsilon}(\mathbf{v})\, dV, \tag{9.28}$$

for all $\mathbf{v} \in \mathbf{W}_{per}(Y)$, being $a(\cdot,\cdot)$ the bilinear form introduced in (9.2).

If $l = k$, since Lemma 9.2 yields that $\mathcal{N}_S \subset \mathbf{W}_{per}(Y)$ in the sense described in Remark 9.2, then (9.28) holds for any $\mathbf{w} = \mathbf{v}$ such that $\mathbf{w} \in \mathcal{N}_S$:

$$a(\boldsymbol{\mathcal{X}}^{ll}, \mathbf{w}) = \int_Y \boldsymbol{\sigma}(\mathbf{p}^{ll}) : \boldsymbol{\varepsilon}(\mathbf{w})\, dV, \quad \forall \mathbf{w} \in \mathcal{N}_S. \tag{9.29}$$

Using Lemma 9.6, substituting in (9.29) and exploiting the linearity of the bilinear form $a(\cdot,\cdot)$, it readily follows that

$$a\left(-\frac{\eta}{L_l}\boldsymbol{\mathcal{X}}^{ll}, \mathbf{w}\right) = \int_Y \boldsymbol{\sigma}(\boldsymbol{\psi}^{ll}) : \boldsymbol{\varepsilon}(\mathbf{w})\, dV = \int_Y \boldsymbol{\sigma}(\boldsymbol{\psi}^{ll}) : \nabla \mathbf{w}\, dV, \quad \forall \mathbf{w} \in \mathcal{N}_S,$$

since $\boldsymbol{\sigma} \in Sym$.

On the other hand, let $\widehat{\mathbf{u}}^{ll}$ be the unique solution to Problem $(\widehat{\mathcal{VP}}_{\mathcal{N}})^l$. Hence, it holds that

$$a(\widehat{\mathbf{u}}^{ll}, \mathbf{v}) = \int_Y \boldsymbol{\sigma}(\boldsymbol{\psi}^{ll}) : \nabla \mathbf{v}\, dV, \quad \forall \mathbf{v} \in \mathcal{N}. \tag{9.30}$$

USC UNIVERSIDADE DE SANTIAGO DE COMPOSTELA

However, by Proposition 9.5, $\widehat{\mathbf{u}}^{ll} \in \mathcal{N}_S$ and since $\mathcal{N}_S$ is a subspace of $\mathcal{N}$, then (9.30) holds in particular for any $\mathbf{w} \in \mathcal{N}_S$. Therefore, as $\boldsymbol{\mathcal{X}}^{ll} \in \mathcal{N}_S$ by Proposition 9.7, we conclude that

$$\widehat{\mathbf{u}}^{ll} = -\frac{\eta}{L_l}\boldsymbol{\mathcal{X}}^{ll}.$$

Similarly, if $l \neq k$, Lemma 9.4 gives that $\mathcal{T}_S^d$ can be identified with a subspace of $\mathbf{W}_{per}(Y)$ for all $d \in I_3$. Thus, following the same steps outlined above for the case $l = k$, we obtain that

$$a\left(-\frac{\eta(L_k + L_l)}{2L_kL_l}\boldsymbol{\mathcal{X}}^{lk}, \mathbf{w}\right) = \int_Y \boldsymbol{\sigma}(\boldsymbol{\psi}^{lk}) : \nabla \mathbf{w}\, dV, \qquad \forall \mathbf{w} \in \mathcal{T}_S^d,$$

and, since $\boldsymbol{\mathcal{X}} \in \mathcal{T}_S^d$ by Proposition 9.7, it holds that

$$\widehat{\mathbf{u}}^{lk} = -\frac{\eta}{2}\left(\frac{1}{L_l} + \frac{1}{L_k}\right)\boldsymbol{\mathcal{X}}^{lk}.$$

□

9.3.1. Equivalent linear system

The solutions of the six different displacement basic tests and the corresponding liftings (9.9), presented in Section 9.2, can be denoted with a single superscript for clarity purposes. To this end, the transformation $\gamma(i,j)$, defined in (6.4), is used. In particular, given $l, k \in I_3$, we identify

$$\mathbf{u}^{lk} = \mathbf{u}^m, \qquad \boldsymbol{\psi}^{lk} = \boldsymbol{\psi}^m,$$

where $m = \gamma(l,k)$.

Recall the definition of matrix $\boldsymbol{\mathcal{E}}$, which was constructed in (8.4) using the solutions to the stress basic tests:

$$\boldsymbol{\mathcal{E}} = (\mathcal{E}_{mn}) = (\mathcal{M}_Y(\{\boldsymbol{\varepsilon}\}_n(\mathbf{u}^m))), \tag{9.31}$$

where $m, n \in I_6$.

In the following discussion, to assemble this matrix, we consider the displacement fields obtained as the solutions to the basic tests $(\mathcal{VP}_\mathcal{N})^l$ and $(\mathcal{VP}_\mathcal{T})^d$. In this case, the specific properties of these solutions allow to prove that solving the system of 36 equations and unknowns (8.3), proposed in the previous chapter, is equivalent to compute the homogenised material using (7.8). First, we address the subsequent auxiliary lemma, which ensures that the matrix (9.31) is diagonal.

Lemma 9.7. *Let $\mathbf{u}^{lk}$, $l, k \in I_3$ be the solutions to Problem $(\mathcal{VP}_\mathcal{N})^l$ if $l = k$ and to Problem $(\mathcal{VP}_\mathcal{T})^d$ otherwise, with $d = \gamma(l,k) - 3$. Then, the matrix $\boldsymbol{\mathcal{E}}$, defined in (9.31), is such that for $m, n \in I_6$:*

$$\mathcal{E}_{mn} = \frac{\eta}{2}\left(\frac{1}{L_l} + \frac{1}{L_k}\right)\delta_{mn},$$

where $l, k \in I_3$ satisfy that $\gamma(l,k) = m$.

Proof. Set $m \in I_6$ and l, k such that $\gamma(l,k) = m$. Set $\mathbf{u}^m = \widehat{\mathbf{u}}^m - \boldsymbol{\psi}^m$. If $m \leq 3$, Proposition 9.5 yields that $\widehat{\mathbf{u}}^m \in \mathcal{N}_S$. Conversely, if $m > 3$, from Proposition 9.6 it follows that $\widehat{\mathbf{u}}^m \in \mathcal{T}_S^d$. Thus, by Lemma 9.2 and Lemma 9.4, it holds that $\mathcal{M}_Y(\boldsymbol{\varepsilon}(\widehat{\mathbf{u}}^m)) = \mathbf{0}$ and it follows that

$$\mathcal{M}_Y(\boldsymbol{\varepsilon}(\mathbf{u}^m)) = \mathcal{M}_Y(\boldsymbol{\varepsilon}(\widehat{\mathbf{u}}^m)) - \mathcal{M}_Y(\boldsymbol{\varepsilon}(\boldsymbol{\psi}^m)) = -\mathcal{M}_Y(\boldsymbol{\varepsilon}(\boldsymbol{\psi}^m)).$$

Then, using (9.14) and (9.16) leads to

$$\boldsymbol{\varepsilon}(\boldsymbol{\psi}^m) = \boldsymbol{\varepsilon}(\boldsymbol{\psi}^{lk}) = -\frac{\eta}{2}\left(\frac{1}{L_l} + \frac{1}{L_k}\right)\mathbf{E}^{lk}.$$

Hence, for all $m \in I_6$:

$$\mathcal{E}_{mn} = -\mathcal{M}_Y(\{\boldsymbol{\varepsilon}\}_n(\boldsymbol{\psi}^m)) = \frac{\eta}{2}\left(\frac{1}{L_l} + \frac{1}{L_k}\right)\delta_{mn}.$$

□

USC UNIVERSIDADE DE SANTIAGO DE COMPOSTELA

Remark 9.8. *Lemma 9.7 means that $\boldsymbol{\mathcal{E}}$ is a diagonal matrix. Its entries are precisely the mean strain along the $\mathbf{e}_l$ direction in the solutions to $(\mathcal{VP}_{\mathcal{N}})^l$ and the mean strain in the plane with normal vector $\mathbf{e}_d$ for the D-BT $(\mathcal{VP}_{\mathcal{T}})^d$. Specifically, recalling the notation introduced in (8.2), it holds that*

$$\boldsymbol{\mathcal{E}} = \begin{pmatrix} \{\overline{\varepsilon}\}_1^1 & & & & & \\ & \{\overline{\varepsilon}\}_2^2 & & & & \\ & & \{\overline{\varepsilon}\}_3^3 & & & \\ & & & \{\overline{\varepsilon}\}_4^4 & & \\ & & & & \{\overline{\varepsilon}\}_5^5 & \\ & & & & & \{\overline{\varepsilon}\}_6^6 \end{pmatrix}.$$

Recall the statement of the linear system (8.3) in matrix form, using the 36×36 matrix $\widetilde{\boldsymbol{\mathcal{E}}}$, defined in (8.5) proposed in the previous chapter to obtain the homogenised material with the pure traction tests. The result below shows that, if the block-diagonal matrix is assembled using the solutions to the D-BT, the solution of the system of equations (8.6) coincides with the entries of the homogenised material elasticity tensor.

Proposition 9.8. *Let the hypotheses of Theorem 9.1 hold. Then, the vector $\mathbf{c}^0 \in \mathbb{R}^{36}$, obtained as the solution of the linear system with 36 equations and unknowns*

$$\widetilde{\boldsymbol{\mathcal{E}}}\mathbf{c}^0 = \mathbf{b},$$

coincides with the arrangement of the homogenised material elasticity matrix as a vector, where the components of $\mathbf{c}^0$ are defined as

$$c_p^0 = C_{ijlk}^0,$$

for $p \in I_{36}$ such that $\lceil p \rceil = \gamma(i,j)$, $(p) = \gamma(l,k)$, for $i,j,l,k \in I_3$.

Proof. Let $p,t \in I_{36}$. In virtue of Lemma 9.7, the inverse matrix of $\widetilde{\boldsymbol{\mathcal{E}}}$, $\widetilde{\boldsymbol{\mathcal{E}}}^{-1}$, is also a diagonal matrix with components

$$\widetilde{\mathcal{E}}_{pt}^{-1} = \frac{2L_kL_l}{\eta(L_k+L_l)}\delta_{pt}, \tag{9.32}$$

where $l,k \in I_3$ are such that $(p) = \gamma(l,k)$.

Let $m,n \in I_6$ be such that $(p) = n$ and $\lceil p \rceil = m$. Then, from (9.32), it follows that the pth component of the vector of solutions of the system becomes

$$c_p^0 = \widetilde{\mathcal{E}}_{pp}^{-1}b_p = \widetilde{\mathcal{E}}_{pp}^{-1}\mathcal{M}_Y(\{\boldsymbol{\sigma}\}_{\lceil p \rceil}(\mathbf{u}^{(p)})) = \frac{2L_kL_l}{\eta(L_k+L_l)}\mathcal{M}_Y(\{\boldsymbol{\sigma}\}_m(\mathbf{u}^n)).$$

Let $\widehat{\mathbb{C}}$ denote the following fourth order tensor, whose components $\widehat{C}_{ijlk}$ are defined as

$$\widehat{C}_{ijlk} = \frac{2L_kL_l}{\eta(L_k+L_l)}\mathcal{M}_Y(\sigma_{ij}(\mathbf{u}^{lk})), \tag{9.33}$$

for $i,j,l,k \in I_3$.

Thus, if $\gamma(i,j) = m$ and $\gamma(l,k) = n$ it holds that

$$\widehat{C}_{ijlk} = c_p^0.$$

Now, we show that $\widehat{\mathbb{C}}$ coincides with the homogenised fourth order elasticity tensor $\mathbb{C}^0$. Recall that $\mathbf{u}^{lk} = \widehat{\mathbf{u}}^{lk} - \boldsymbol{\psi}^{lk}$. Then, substitution in (9.33), using that Theorem 9.1 yields that $\widehat{\mathbf{u}}^{lk} = -\eta/2(1/L_l + 1/L_k)\boldsymbol{\mathcal{X}}^{lk}$. Hence, Lemma 9.6 leads to

$$\begin{aligned} c_p^0 = C_{ijlk}^0 &= \frac{2L_kL_l}{\eta(L_k+L_l)}\mathcal{M}_Y(\sigma_{ij}(\mathbf{u}^{lk})) \\ &= \frac{2L_kL_l}{\eta(L_k+L_l)}\frac{1}{\operatorname{meas}(Y)}\left(\int_Y \sigma_{ij}(\widehat{\mathbf{u}}^{lk})\,dV - \int_Y \sigma_{ij}(\boldsymbol{\psi}^{lk})\,dV\right) \\ &= \frac{1}{\operatorname{meas}(Y)}\left(\int_Y \sigma_{ij}(-\boldsymbol{\mathcal{X}}^{lk})\,dV + \int_Y \sigma_{ij}(\mathbf{p}^{lk})\,dV\right). \end{aligned} \tag{9.34}$$

USC UNIVERSIDADE DE SANTIAGO DE COMPOSTELA

Hence, using (7.8) and (7.9), it follows from (9.34) that

$$c_p^0 = \mathcal{M}_Y(C_{ijrs}\varepsilon_{rs}(\mathbf{w}^{lk})),$$

and therefores, $c_p^0 = C_{ijlk}^0$ for all $p \in I_6$. □

9.4. Numerical experiments

This section is devoted to assess the performance of the D-BT approach for some layouts of composite materials and masonries. To this end, an analogous procedure to that followed in Section 8.3 is adopted. Three different cells formed by compositions of two materials are analysed and, after obtaining the corresponding homogenised materials using the techniques that have been presented, the mechanical response predictions are compared to that of the real heterogeneous material numerically. To that end, the test problems presented in Section 8.3.1 are solved in assemblies of several reference cells for each configuration.

Again, as is Section 8.3, we refer to the most predominant material in each of the configurations as "brick" and to the less predominant one as "mortar". In all cases, the materials are linear isotropic, with the properties collected in Table 9.1. For all the computed solutions for the D-BT, the parameter η, appearing in the boundary conditions of the traction and shear basic tests, is chosen as $\eta = 1$.

9.4.1. Cell C. Layered composite

First, we return to Cell C, which corresponds to the layered composite already presented in Section 8.3.4. For this simple configuration, the S-BT approach led to a homogenised material stiffness matrix which was not a good approximation of that computed numerically solving the auxiliary periodic problems $(\mathcal{VP}_C)^{lk}$. It was also shown that the displacement prediction when solving Problem 1 was very inaccurate in comparison to the real heterogeneous material. This contrasted with the prediction using the equivalent orthotropic material yielded by the numerical approximation of the corrector functions $\boldsymbol{\chi}^{lk}$, which showed very good agreement with the heterogeneous assembly.

From Figure 8.12, we note that the layout of the two material components of Cell C is such that the cell can be oriented in such a way that the coordinate planes $y_i = L_i/2$ are symmetry planes. This ensures that hypothesis (H.2) is satisfied and, since both materials in the composition are linear isotropic, it can be concluded from the results previously presented in this chapter that the D-BT methodology yields, theoretically, the same homogenised material as solving the auxiliary periodic problems $(\mathcal{VP}_C)^{lk}$. In spite of this, we note that to solve these problems we use the saddle point formulation $(\mathcal{LP}_C)_h^{lk}$, using a direct method for the solution of the arising linear system from the discretisation. In contrast, the solutions to the displacement basic tests $(\mathcal{VP}_\mathcal{N})^l$ and $(\mathcal{VP}_\mathcal{T})^d$ are obtained through a much more efficient iterative solve, employing an AMG-preconditioned CG method in parallel. Thereby, the computed stifness matrices can slightly differ due to the particularities of the practical implementations of both methodologies. We start by addressing the homogenised material characterisation through both approaches and assessing if both coincide in practice.

Let $[\widehat{\mathbf{C}}_h]$ be the homogenised stiffness matrix computed by solving the D-BT. For the same hexahedral grid of the reference cell Y considered in Chapter 8, depicted in Figure 9.2a, and using first order

Table 9.1: Material properties for the numerical experiments.

	Cell C		Cell D		Cell E	
	E [Pa]	ν [·]	E [Pa]	ν[·]	E [Pa]	ν [·]
Brick	$1{\cdot}10^7$	0.25	$8{\cdot}10^{10}$	0.2	$1{\cdot}10^9$	0.08
Mortar	$1{\cdot}10^9$	0.1	$1{\cdot}10^7$	0.08	$1{\cdot}10^7$	0.2

Table 9.2: Cell C: leading order coefficients of the equivalent material stiffness matrix for stress basic tests (S-BT), displacement basic tests (D-BT) and rule of mixtures (Mixture). The number of cells assembled in each direction to solve the basic tests are indicated within parentheses.

	c_{11}	c_{22}	c_{33}	c_{23}	c_{13}	c_{12}	c_{44}	c_{55}	c_{66}
S-BT (1,1,1)	$1.59{\cdot}10^{7}$	$2.30{\cdot}10^{7}$	$2.30{\cdot}10^{7}$	$5.75{\cdot}10^{6}$	$5.27{\cdot}10^{6}$	$5.27{\cdot}10^{6}$	$8.91{\cdot}10^{6}$	$5.32{\cdot}10^{6}$	$5.32{\cdot}10^{6}$
D-BT (1,1,1)	$1.59{\cdot}10^{7}$	$2.62{\cdot}10^{8}$	$2.62{\cdot}10^{8}$	$2.85{\cdot}10^{7}$	$4.43{\cdot}10^{6}$	$4.43{\cdot}10^{6}$	$1.17{\cdot}10^{8}$	$5.32{\cdot}10^{6}$	$5.32{\cdot}10^{6}$
D-BT (2,2,2)	$1.59{\cdot}10^{7}$	$2.62{\cdot}10^{8}$	$2.62{\cdot}10^{8}$	$2.85{\cdot}10^{7}$	$4.43{\cdot}10^{6}$	$4.43{\cdot}10^{6}$	$1.17{\cdot}10^{8}$	$5.32{\cdot}10^{6}$	$5.32{\cdot}10^{6}$
Mixture	$2.91{\cdot}10^{8}$	$2.91{\cdot}10^{8}$	$2.91{\cdot}10^{8}$	$7.85{\cdot}10^{7}$	$7.85{\cdot}10^{7}$	$7.85{\cdot}10^{7}$	$1.06{\cdot}10^{8}$	$1.06{\cdot}10^{8}$	$1.06{\cdot}10^{8}$

Lagrange elements for the discretisation of the problem, we obtain that:

$$[\widehat{\mathbf{C}}_h] = \begin{pmatrix} \mathbf{1.59{\cdot}10^{7}} & \mathbf{4.43{\cdot}10^{6}} & \mathbf{4.43{\cdot}10^{6}} & 4.01{\cdot}10^{-8} & -2.60{\cdot}10^{-7} & -1.57{\cdot}10^{-6} \\ \mathbf{4.43{\cdot}10^{6}} & \mathbf{2.62{\cdot}10^{8}} & \mathbf{2.85{\cdot}10^{7}} & 4.39{\cdot}10^{-5} & 2.16{\cdot}10^{-6} & -1.29{\cdot}10^{-5} \\ \mathbf{4.43{\cdot}10^{6}} & \mathbf{2.85{\cdot}10^{7}} & \mathbf{2.62{\cdot}10^{8}} & -5.45{\cdot}10^{-5} & 1.68{\cdot}10^{-5} & -1.73{\cdot}10^{-6} \\ 3.03{\cdot}10^{-5} & -1.91{\cdot}10^{-5} & -2.34{\cdot}10^{-5} & \mathbf{1.17{\cdot}10^{8}} & 2.90{\cdot}10^{-5} & 2.38{\cdot}10^{-5} \\ -1.89{\cdot}10^{-5} & -1.59{\cdot}10^{-6} & -8.25{\cdot}10^{-6} & -3.78{\cdot}10^{-7} & \mathbf{5.32{\cdot}10^{6}} & 1.15{\cdot}10^{-6} \\ 4.36{\cdot}10^{-7} & -3.61{\cdot}10^{-6} & 1.22{\cdot}10^{-5} & -1.82{\cdot}10^{-6} & 7.22{\cdot}10^{-6} & \mathbf{5.32{\cdot}10^{6}} \end{pmatrix}.$$

As already noted in Section 8.3.4, we recall that the homogenised material is transversely isotropic. The computed leading order entries of the stiffness matrix for the D-BT approach are collected in Table 9.2, altogether with those computed using the S-BT and the coefficients computed in the previous chapter using a rule of mixtures.

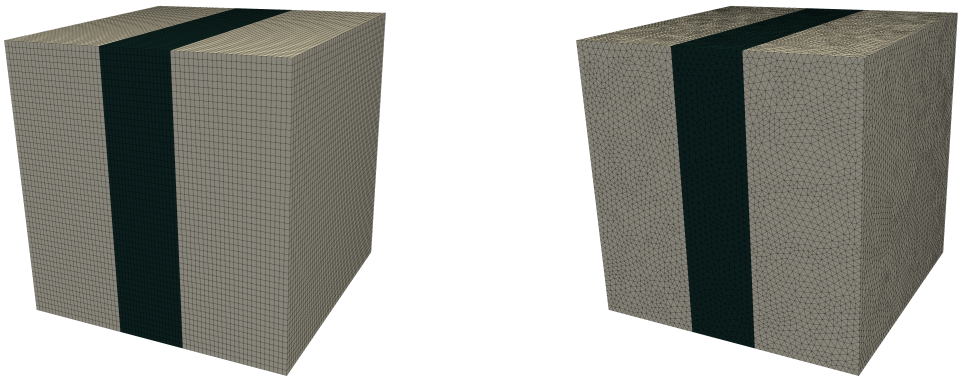
Recall that $[\mathbf{C}_h^0]$ denotes the homogenised elasticity tensor found by numerically approximating the corrector functions, computed by evaluating (7.8). If we compare this matrix to $[\widehat{\mathbf{C}}_h]$ we obtain the subsequent matrix of errors:

$$[\widehat{\mathbf{C}}_h] - [\mathbf{C}_h^0] = \begin{pmatrix} 8.50{\cdot}10^{-6} & -2.05{\cdot}10^{-5} & -1.54{\cdot}10^{-5} & -1.00{\cdot}10^{-7} & -3.00{\cdot}10^{-7} & -4.80{\cdot}10^{-6} \\ -1.23{\cdot}10^{-5} & -3.49{\cdot}10^{-4} & -1.07{\cdot}10^{-4} & -1.08{\cdot}10^{-5} & -4.00{\cdot}10^{-6} & 3.60{\cdot}10^{-5} \\ -1.34{\cdot}10^{-5} & -1.09{\cdot}10^{-4} & -3.33{\cdot}10^{-4} & 1.67{\cdot}10^{-5} & -3.97{\cdot}10^{-5} & 2.80{\cdot}10^{-6} \\ -1.84{\cdot}10^{-5} & 3.09{\cdot}10^{-5} & 1.60{\cdot}10^{-5} & -2.65{\cdot}10^{-4} & -2.00{\cdot}10^{-6} & -1.82{\cdot}10^{-5} \\ 1.40{\cdot}10^{-6} & 6.40{\cdot}10^{-6} & 2.28{\cdot}10^{-5} & 1.50{\cdot}10^{-6} & 2.07{\cdot}10^{-5} & 1.65{\cdot}10^{-5} \\ 7.70{\cdot}10^{-6} & 2.60{\cdot}10^{-6} & -4.20{\cdot}10^{-6} & 1.70{\cdot}10^{-6} & -1.50{\cdot}10^{-6} & 2.60{\cdot}10^{-5} \end{pmatrix}. \tag{9.35}$$

From the absolute error among the matrices, it is clear that both problems yield the same matrix numerically, since the leading order entries in the matrix (see Table 9.2) are from 10 to 12 orders of magnitude larger than the differences in (9.35). This error can be controlled by adjusting the tolerance of the iterative method and, if a direct solver is used to obtain the solution to the displacement basic tests, the absolute errors decrease upon reaching the limit of the double-precision floating point arithmetic. Hence, despite using widely different numerical methodologies the computed stiffness matrices are still the same, as shown by the theory presented in the prior sections.

Throughout the discussion in Section 8.3.4, another major shortcoming of the S-BT approach was that the considered size of the reference cell could heavily influence the computed homogenised stiffness matrix coefficients. In contrast, if the D-BT methodology is applied for larger reference cells, the results are essentially the same, as demonstrated by the coefficients computed for a $(2,2,2)$ Y reference cell with the displacement basic tests, showcased in Table 9.2. Recall that each component in the tuple means the number of repetitions of the original cell that is considered in each canonical basis direction.

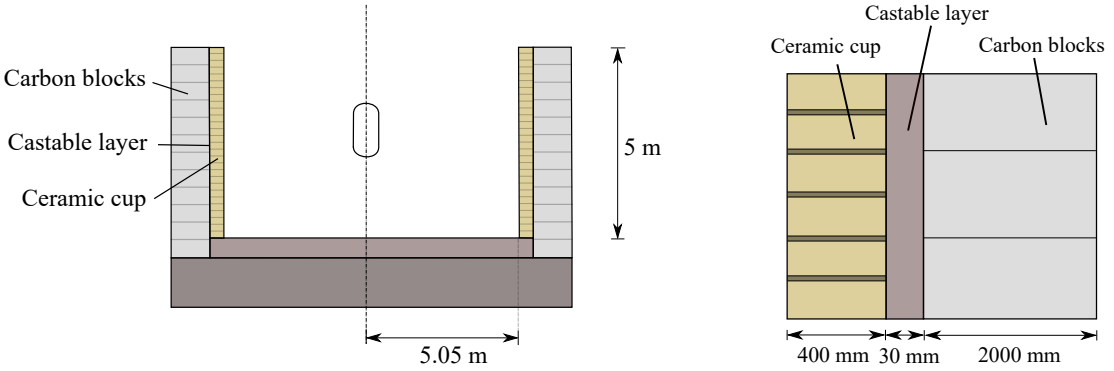
As introduced in previously, the main advantage of the basic test methodologies is that they eliminate the periodic boundary conditions and the need to introduce any constraints on the solution. While the periodic boundary condition is easily imposed numerically when the mesh is identical in the opposite faces of the boundary, arbitrary meshes require more complicated techniques (see V.-D. Nguyen et al., 2012). For ease of comparison among methodologies, symmetric hexahedral meshes



(**a**) Structured hexahedral.

(**b**) Unstructured tetrahedral.

Figure 9.2: Meshes of reference cell C.



(**a**) Lateral cut.

(**b**) Detail of the wall.

Figure 9.3: Schematic of the hearth of a BF.

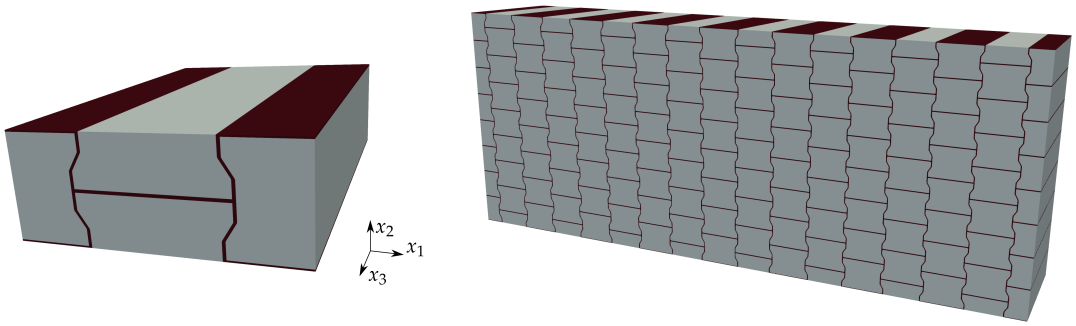
have been considered for most computations. For Cell C, the computed stiffness matrix for D-BT using a structured, symmetric hexahedral mesh is compared to that obtained for a unstructured tetrahedral mesh (for a similar discretisation parameter h), depicted in Figure 9.2. In this specific reference cell, we obtain that the modulus of the difference between both matrices is around $3.70{\cdot}10^{-6}$.

As evidenced by the discussed results, if the reference cell satisfies hypotheses (H.1)-(H.3), then the methodology for the D-BT yields the same material as solving the auxiliary periodic problems. The remaining cells analysed in Section 8.3, the square brick and mortar (Cell A) and the hexagonal brick layout (Cell B), satisfy such hypotheses. Thereby, we skip showing any further numerical results for them, since the equivalent material obtained through the D-BT is the same as that arising from the correctors.

9.4.2. Cell D. Blast furnace ceramic cup

In this section, we deal with a reference cell that corresponds to the industrial application that originally motivated this part of the manuscript. It is of great industrial interest to obtain predictions of the mechanical response of the wall of the hearth of the BF. Currently, the main limiting factor in BF longevity is precisely the hearth wall (Deng et al., 2018). Accurate numerical assessment of the thermo-mechanical behaviour of the BF hearth could lead to increasing operation safety and service life of the BF.

Although the specific materials, dimensions and layers of the BF wall depend widely on the specific furnace, most of them are composed of several protective refractory linings, designed to sustain the



(**a**) Reference cell (Y). (**b**) Masonry wall (Ω).

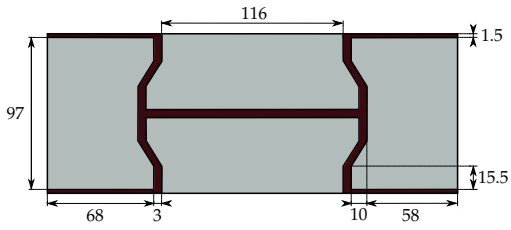
Figure 9.4: Ceramic cup of the BF (Cell D).

extremely harsh conditions within the hearth itself, reaching temperatures around 1500°C. A typical layout of the BF hearth wall is shown in Figure 9.3, with three distinct layers. The outermost layer is formed by large carbon blocks, while the innermost layer, known as the ceramic cup, is a masonry of bricks which, as opposed to the carbon blocks, are separated by joints. Both layers have a castable (unshaped) refractory lining joining them. Here, we focus only on the ceramic cup. A reconstruction of the ceramic cup of the BF was shown in Figure 1. Due to the small size of the joints and the large number of bricks, it is completely unfeasible to generate a conformal mesh of the entire structure. Nonetheless, since the layout repeats periodically, the presented mathematical tools can be useful to perform numerical simulations of the structure, substituting the masonry by an equivalent homogenised material that has a similar mechanical response.

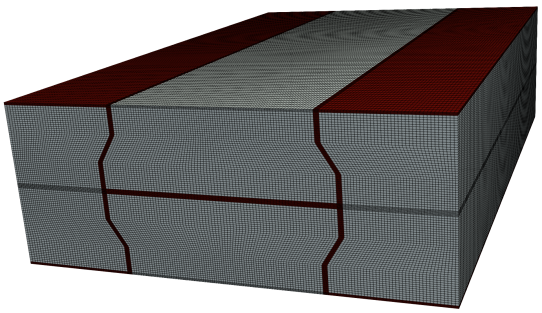
The ceramic cup that we address is formed by refractory bricks, which are made with corundum as main crystal phase. Hence, their aluminium oxide content is high, typically over 90%, and have a very large stiffness and crushing strength. In addition, their chemical composition remains with no significant changes in the operation temperature range at the BF wall (S. Yao et al., 2020). The corundum bricks and the joints forming the masonry are assumed to be linear elastic isotropic materials, characterised by the properties gathered in Table 9.1 for Cell D. These values are extracted from those collected in Shah (2022) for the materials at 1273 K.

Instead of considering the real cylindrical setting, we consider that the bricks and joints forming the ceramic cup are periodically repeating with the reference unit cell depicted in Figure 9.4a. The test masonry Ω, constructed by joining $\mathbf{k}^p = (8, 8, 1)$ reference cells, is shown in Figure 9.4b. Note that the joints separating the bricks are thin, with a thickness of 3 mm, and that the bricks have a complicated cross-section, resembling an inverted hexagon. In Figure 9.5a, the main dimensions in the cell cross-section are depicted. We consider that the length of Y ($\mathbf{e}_3$ direction) is $L = 0.4$ m, equal to the length of the bricks in the ceramic cup (see Figure 9.3b). Note that, since the material is isotropic in this particular direction, a smaller cell can be selected for the displacement basic tests (or to solve the auxiliary periodic problems). However, the stress basic tests become very inaccurate if the cell is shrank in this isotropy direction. Thus, we keep the whole brick as the reference unit cell size.

The solutions to the D-BT and S-BT are computed. Provided that the selected reference cell and the involved materials satisfy hypotheses (H.1)-(H.3), the solution to the auxiliary periodic problems coincides with the displacement basic tests and is skipped. In Figure 9.6, the contours of the von Mises stress norm are depicted in the deformed configuration for the displacement basic tests $m = 1$ and $m = 6$, i.e., the numerical approximation of the solution to Problem $(\mathcal{VP}_{\mathcal{N}})^l$ and Problem $(\mathcal{VP}_{\mathcal{T}})^d$ for $l = 1$ and $d = 3$, respectively. In Table 9.3, all the relevant coefficients in the computed stiffness matrices for the D-BT and S-BT methodologies are collected. In both cases, we find that the homogenised material is an orthotropic material. In addition, we also compute the Young's modulus and Poisson's ratio corresponding to a rule of mixtures. Specifically, bearing that $\alpha_b = 0.945$ and $\alpha_m = 0.0548$, it follows that $\widehat{E} = 7.78{\cdot}10^{10}$ Pa and $\widehat{\nu} = 0.0866$.

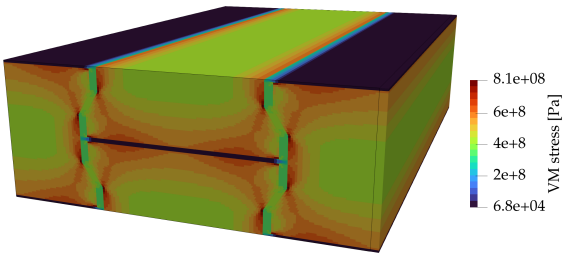


(**a**) Dimensions (in mm).

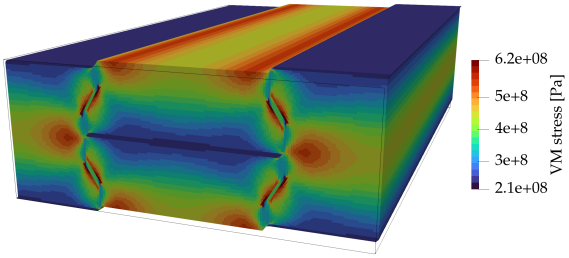


(**b**) Mesh.

Figure 9.5: Reference cell Y for the ceramic cup of the BF (Cell D); mesh and dimensions.



(**a**) $m = 1$.



(**b**) $m = 6$.

Figure 9.6: Contours of the VM stress norm corresponding to the solutions $\mathbf{u}^m$ for the D-BT.

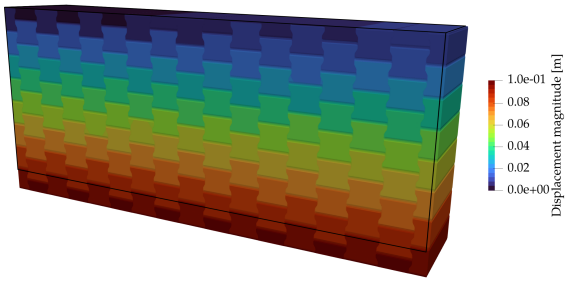
A remarkable finding is that, both the S-BT and the D-BT yield that the c_{12} coefficient takes a negative value. To illustrate the implications of this fact, let us consider the compliance matrix corresponding to the coefficients shown in Table 9.3 for the D-BT approach. From the relations in (6.10), the generalised Young's modulus, Poisson's ratio and shear modulus can be obtained. In particular, for the calculated values, since $E_1 = 4.89{\cdot}10^8$ Pa and $E_2 = 4.24{\cdot}10^8$ Pa, it follows that

$$\nu_{12} = -0.418, \qquad \nu_{21} = -0.0362.$$

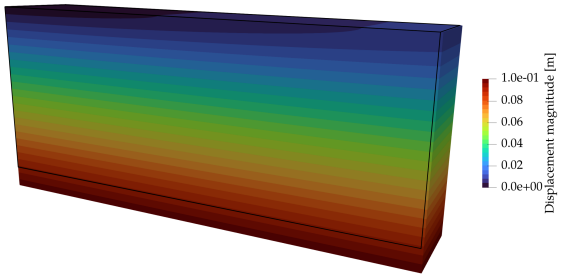
Hence, as $\epsilon \to 0$, from Theorem 7.1, we recover that the masonry corresponding to the ceramic cup should behave as an orthotropic material that has two *negative* generalised Poisson's ratios. This implies that, for instance, if the masonry is subjected to a uniaxial traction load in the direction $\mathbf{e}_1$, instead of having the usual shrinkage in the direction $\mathbf{e}_2$, the material will also expand in this direction. To better illustrate this behaviour, consider the subsequent linear elasticity problem, similar to Problem 2 in Section 8.3.1, but considering that the solid is subjected to a non-homogeneous normal displacement in the $\mathbf{e}_2$ direction.

Table 9.3: Cell D: leading order coefficients of the equivalent material stiffness matrix for stress basic tests (S-BT), displacement basic tests (D-BT) and rule of mixtures (Mixture).

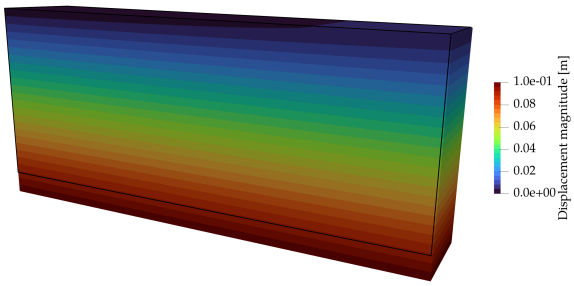
	c_{11}	c_{22}	c_{33}	c_{23}	c_{13}	c_{12}	c_{44}	c_{55}	c_{66}
D-BT	$4.90{\cdot}10^8$	$4.25{\cdot}10^8$	$7.78{\cdot}10^{10}$	$3.42{\cdot}10^7$	$3.94{\cdot}10^7$	$-1.77{\cdot}10^7$	$1.76{\cdot}10^8$	$1.98{\cdot}10^8$	$1.03{\cdot}10^8$
S-BT	$4.61{\cdot}10^8$	$4.12{\cdot}10^8$	$3.00{\cdot}10^{10}$	$4.42{\cdot}10^7$	$4.45{\cdot}10^7$	$-1.04{\cdot}10^7$	$1.64{\cdot}10^8$	$1.86{\cdot}10^8$	$8.69{\cdot}10^7$
Mixture	$7.91{\cdot}10^{10}$	$7.91{\cdot}10^{10}$	$7.91{\cdot}10^{10}$	$7.54{\cdot}10^9$	$7.54{\cdot}10^9$	$7.54{\cdot}10^9$	$3.58{\cdot}10^{10}$	$3.58{\cdot}10^{10}$	$3.58{\cdot}10^{10}$



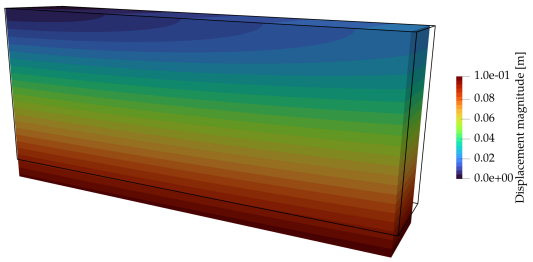
(**a**) Displacement, heterogeneous



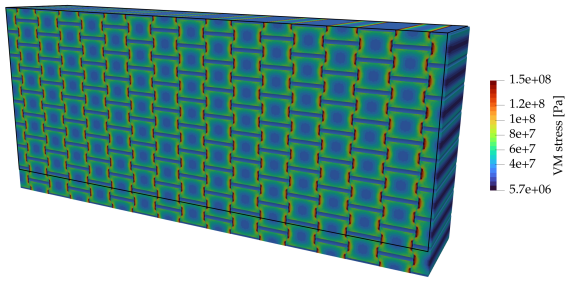
(**b**) Displacement, D-BT.



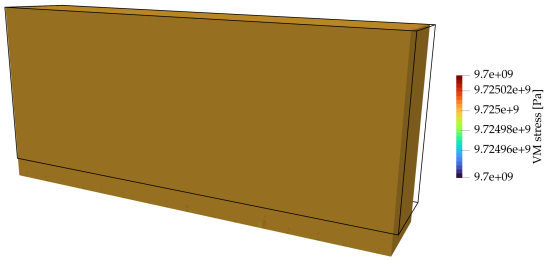
(**c**) Displacement, S-BT



(**d**) Displacement, mixture.



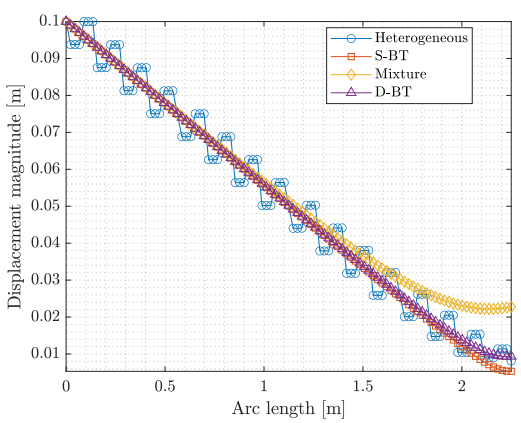
(**e**) VM stress, heterogeneous



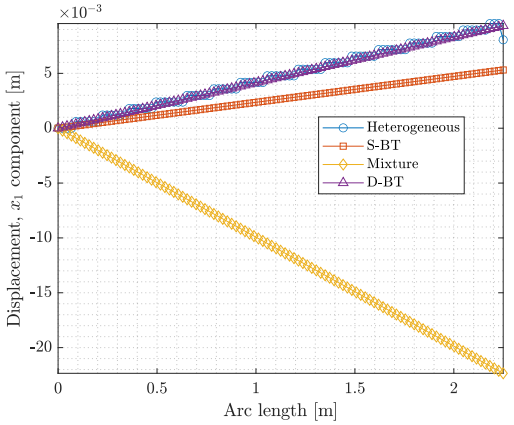
(**f**) VM stress, mixture

Figure 9.7: Cell D. Contours of the numerical solution to Problem 3.

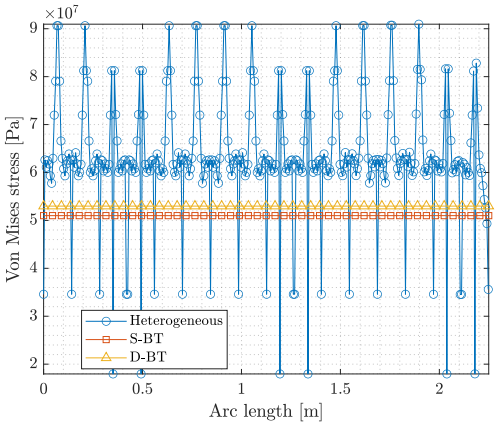
USC
UNIVERSIDADE
DE SANTIAGO
DE COMPOSTELA



(**a**) Displacement magnitude.



(**b**) Displacement, u_1 component.



(**c**) VM stress.

Figure 9.8: Cell D. Numerical solution to Problem 3 along the line $[\mathbf{x}_{min}, \mathbf{x}_{max}]$.

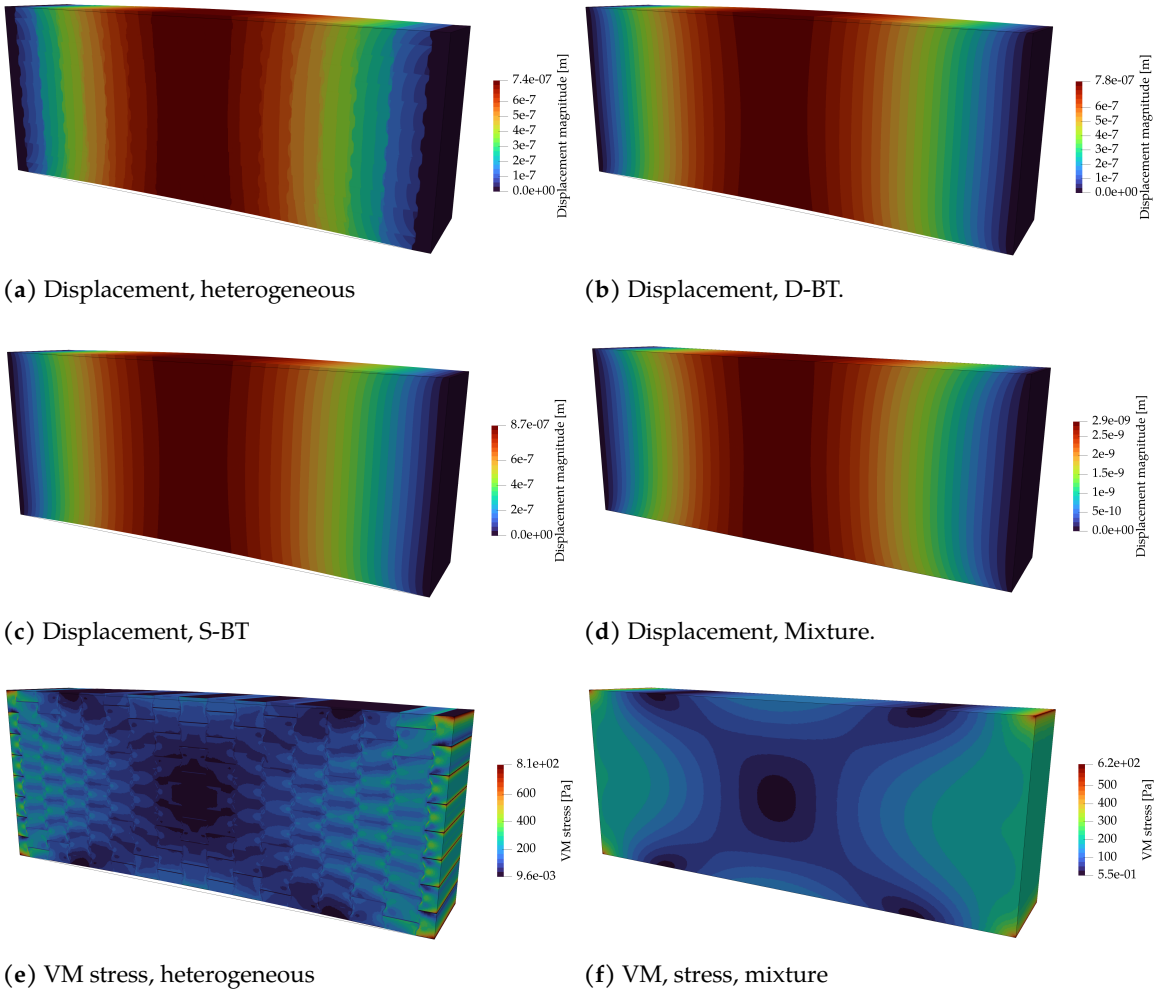
Problem 3. Find $\mathbf{u}$ such that:

$$
\begin{aligned}
-\operatorname{Div}(\boldsymbol{\sigma}(\mathbf{u})) &= \mathbf{0}, && \text{in } \Omega,\\
\boldsymbol{\sigma}(\mathbf{u}) &= \mathbb{C} : \varepsilon(\mathbf{u}), && \text{in } \Omega,\\
\mathbf{u}\cdot\mathbf{n} &= 0, \\
\boldsymbol{\sigma}_t &= \mathbf{0}, && \text{on } \Gamma_S,\\
\mathbf{u}\cdot\mathbf{n} &= -0.1 \text{ m}, \\
\boldsymbol{\sigma}_t &= \mathbf{0}, && \text{on } \Gamma_2^-,\\
\boldsymbol{\sigma}(\mathbf{u})\mathbf{n} &= \mathbf{0}, && \text{on } \Gamma_N,
\end{aligned}
$$

where we set $\Gamma_S = \Gamma_1^- \cup \Gamma_2^+ \cup \Gamma_3^+$ and $\Gamma_N = \partial\Omega \setminus (\Gamma_S \cup \Gamma_2^-)$.

In Figures 9.7a-9.7d, the displacement magnitude contours obtained as solution to Problem 3 are displayed. A masonry formed by $\mathbf{k}^p = (8, 8, 1)$ reference cells is considered as Ω and the predictions using various homogenised materials as well as the real heterogeneous are shown. Note how in all cases but the one corresponding to the mixture material, the deformed configuration stretches both in the $\mathbf{e}_2$ and $\mathbf{e}_1$ directions. Since the mixture homogenised material is a regular isotropic linear elastic body, the elongation induced in the $\mathbf{e}_2$ by the displacement boundary condition results in the usual behaviour for elastic materials, i.e., the body shrinks in the $\mathbf{e}_1$ and $\mathbf{e}_3$ directions.

Since the displacement is prescribed by the boundary conditions, we note that all the displacement magnitude curves shown in Figure 9.8a show fairly good agreement with the heterogeneous mate-



(**a**) Displacement, heterogeneous

(**b**) Displacement, D-BT.

(**c**) Displacement, S-BT

(**d**) Displacement, Mixture.

(**e**) VM stress, heterogeneous

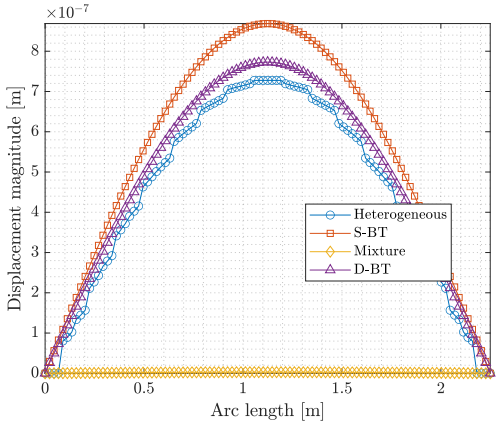
(**f**) VM, stress, mixture

Figure 9.9: Cell D. Contours of the numerical solution to Problem 1.

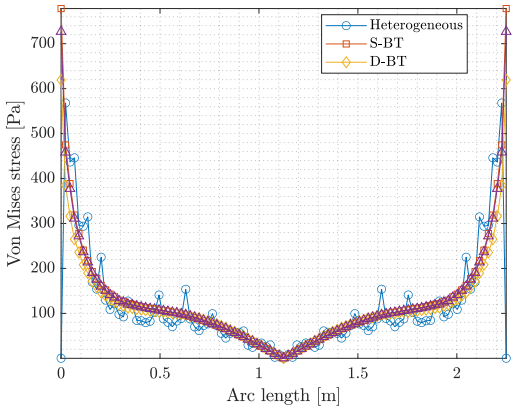
rial. Nevertheless, as clearly depicted in Figure 9.8b, if the component u_1 is analysed, we observe that the differences are large and, in accordance with the prior discussion, it is now clear that the mixture material predicts an u_1 displacement that goes in the opposite direction as the S-BT and D-BT homogenised materials, as well as the heterogeneous material. In particular, we remark that the agreement between the curves by the D-BT homogenised material and the heterogeneous masonry is very good.

Materials with a negative Poisson's ratio are uncommon, and are known in the engineering literature as *auxetic materials*. They are precisely characterised by the physical intuition previously described, i.e., if they are stretched in one direction, they become thicker in the perpendicular direction, instead of contracting. In Kolpakov (1985), a design of an auxetic with an inverted hexagonal periodicity cell was introduced, similar to the layout of the ceramic cup. Other examples of known auxetics are some hexagonal crystals (Gorodtsov & Lisovenko, 2019), α-cristobalite (Yeganeh-Haeri et al., 1992), and tendons (Gatt et al., 2015). For an overview of the implications, potential applications and thorough description of auxetics we refer to (Alderson & Alderson, 2007; Ren et al., 2018).

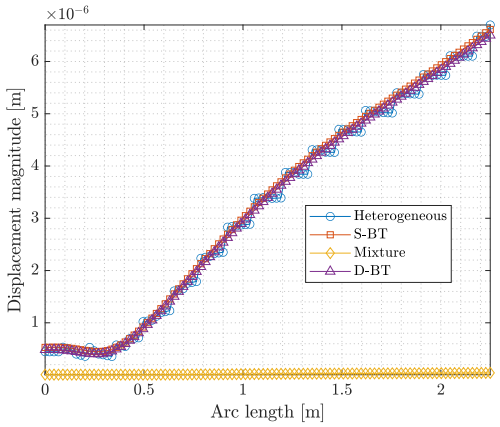
Concerning the computed stress, in Figures 9.7e and 9.7f, the VM stress norms calculated as solution to Problem 3 for the real heterogeneous material and the mixture material are displayed, respectively. For this problem, the stress and strain tensors for all equivalent materials are constant, in contrast with the heterogeneous material. Also, we remark that, despite the fairly reasonable agreement that was



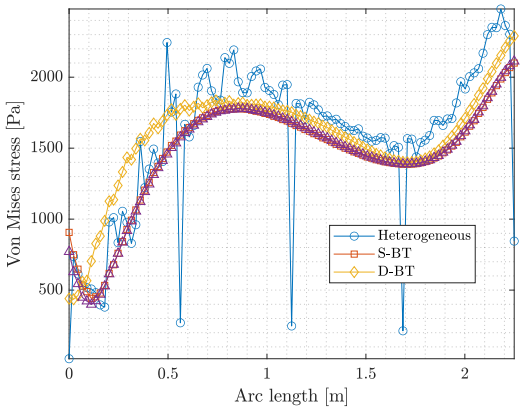
(**a**) Problem 1, displacement.



(**b**) Problem 1, VM stress.



(**c**) Problem 2, displacement.



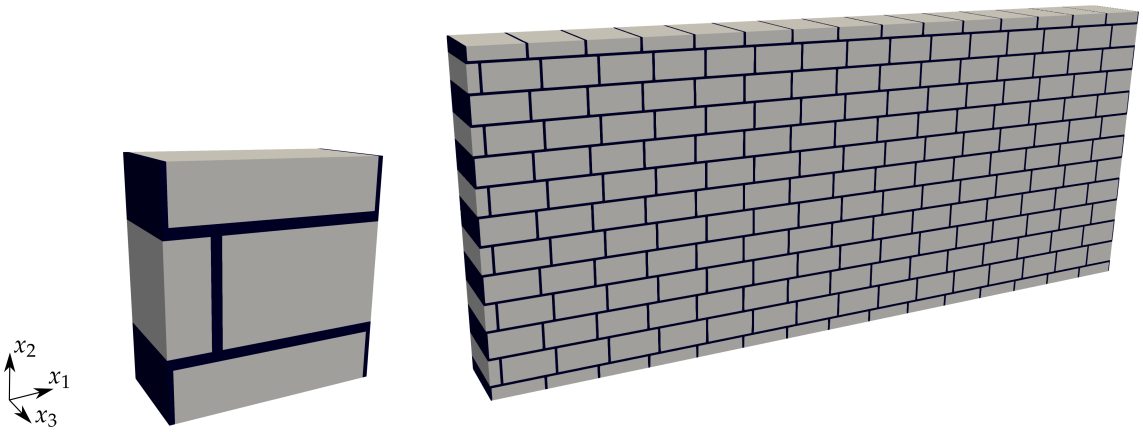
(**d**) Problem 2, VM stress.

Figure 9.10: Cell D. Solution to Problems 1 and 2 along the line $[\mathbf{x}_{min}, \mathbf{x}_{max}]$.

observed for the stress predictions with the mixture homogenised material in the numerical examples of Section 8.3, for Problem 3, we observe that the stress prediction is around two full orders of magnitude off. In particular, even the local maximum stress predicted in the corners of the heterogeneous material is much lower than the constant stress in the mixture material. Hence, we can conclude that when the stress is specified as a boundary condition, the mixture material yields inaccurate displacement predictions, whereas if the displacement is set instead, the stress prediction becomes incorrect. On the other hand, both the D-BT and S-BT yield reasonable predictions both for the stress and displacement in this example problem.

To conclude the analysis of the ceramic cup masonry cell, we briefly discuss the solutions to the test Problems 1 and 2 (see Section 8.3.1). In Figure 9.9, the contours of displacement magnitude and VM stress are displayed for the solution of Problem 1. The results are very similar to those already discussed in detail for Cells A and B in Chapter 8. The mixture material is clearly much stiffer than the other homogenised ones, which leads to a severe underestimation of the displacement of the real heterogeneous structure. On the other hand, the stress contours are similar for all approaches. The VM stress and displacement along the line $[\mathbf{x}_{min}, \mathbf{x}_{max}]$ are also displayed in Figure 9.10 for Problems 1 and 2, showing that the D-BT yields a fairly good estimation of the response of the ceramic cup for the selected test problems.

USC DE SANTIAGO DE COMPOSTELA



(**a**) Reference cell (Y). (**b**) Masonry wall (Ω).

Figure 9.11: Running bond masonry (Cell E).

9.4.3. Cell E. Running bond masonry

The last case that is analysed corresponds to a masonry of bricks and joints with a running bond, taken from the examples in Anthoine (1995). In Figure 9.11, the masonry as well as the reference cell Y are shown. Despite its apparent simplicity and similarity with the square brick and mortar masonry, addressed in Section 8.3.2, this layout has the particularity of not being representable by periodical repetition of a reference cell with the three symmetry planes that are required in hypothesis (H.2). Thus, there is no guarantee that the D-BT approach yields the same result as solving the periodic auxiliary problems and computing the homogenised elasticity tensor by evaluating (7.8).

The dimensions of the reference period Y are shown in Figure 9.12. As in the previous case, the material is isotropic in the direction $\mathbf{e}_3$ and the length of the cell in this direction can be chosen arbitrarily. In particular, we select that the size of Y in the $\mathbf{e}_3$ direction is 0.1 m.

To assess if the D-BT methodology still yields reasonable approximations, even if the hypotheses to ensure its mathematical rigour are not satisfied, we obtain the approximation of the corrector functions for the linear elasticity system. The D-BT and S-BT are also solved, and the corresponding homogenised materials are computed. The properties displayed in Table 9.1 for Cell E are considered. In addition, we compute the homogenised stiffness matrix coefficients through the rule of mixtures. Specifically, using that $\alpha_b = 0.866$ and $\alpha_m = 0.134$, we find that $\widehat{E} = 8.67{\cdot}10^8$ and $\widehat{\nu} = 0.096$.

Again, as the resulting homogenised materials are orthotropic, we gather all the relevant entries of the stiffness matrices in Table 9.4. We observe that, even though the homogenised material resulting from the D-BT is not the same as the one yielded by the correctors, the differences are small. Specifically, the maximum relative error in the approximation of these coefficients is committed for c_{44}, and is around 4%. Most of the relative errors are well below 1%. In this case, the coefficients obtained trough the solution of the stress basic tests are also quite close to those of the D-BT and the correctors. Nevertheless, there are some large differences in the approximation of some coefficients. In particular, the prediction of c_{33} using S-BT is approximately half of that obtained through D-BT and the

Table 9.4: Cell E: leading order coefficients of the equivalent material stiffness matrix for stress basic tests (S-BT), displacement basic tests (D-BT) and rule of mixtures (Mixture).

	c_{11}	c_{22}	c_{33}	c_{23}	c_{13}	c_{12}	c_{44}	c_{55}	c_{66}
D-BT	$1.99{\cdot}10^8$	$1.07{\cdot}10^8$	$8.70{\cdot}10^8$	$1.06{\cdot}10^7$	$1.78{\cdot}10^7$	$6.24{\cdot}10^6$	$4.14{\cdot}10^7$	$8.99{\cdot}10^7$	$3.37{\cdot}10^7$
Correctors	$1.93{\cdot}10^8$	$1.07{\cdot}10^8$	$8.70{\cdot}10^8$	$1.06{\cdot}10^7$	$1.73{\cdot}10^7$	$6.21{\cdot}10^6$	$4.14{\cdot}10^7$	$8.62{\cdot}10^7$	$3.36{\cdot}10^7$
S-BT	$1.83{\cdot}10^8$	$1.05{\cdot}10^8$	$4.33{\cdot}10^8$	$1.47{\cdot}10^7$	$1.76{\cdot}10^7$	$8.39{\cdot}10^6$	$4.01{\cdot}10^7$	$7.12{\cdot}10^7$	$3.12{\cdot}10^7$
Mixture	$8.85{\cdot}10^8$	$8.85{\cdot}10^8$	$8.85{\cdot}10^8$	$9.40{\cdot}10^7$	$9.40{\cdot}10^7$	$9.40{\cdot}10^7$	$3.96{\cdot}10^8$	$3.96{\cdot}10^8$	$3.96{\cdot}10^8$

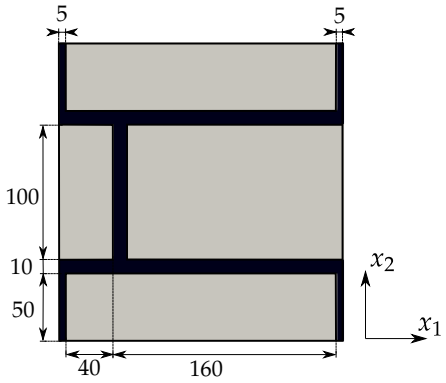
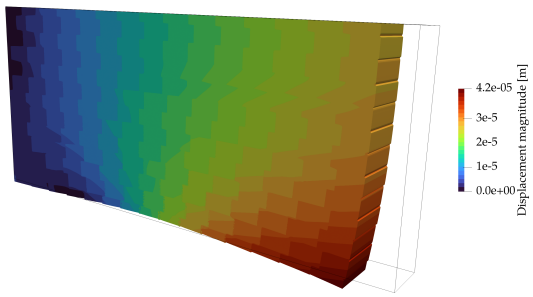
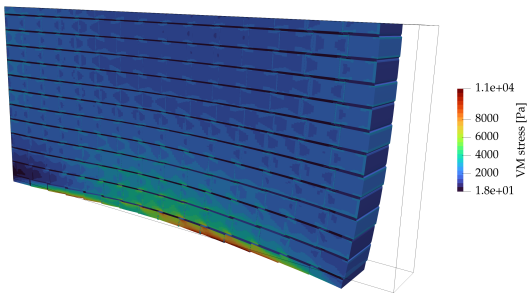


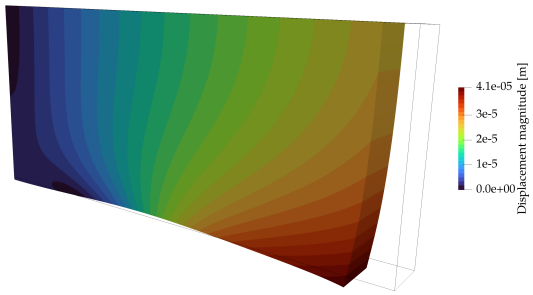
Figure 9.12: Dimensions (in mm) of the reference period for Cell E.



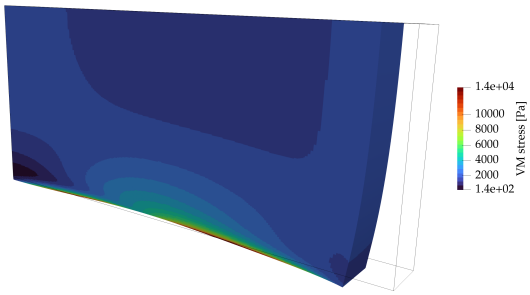
(**a**) Displacement, heterogeneous



(**b**) VM stress, heterogeneous.



(**c**) Displacement, D-BT

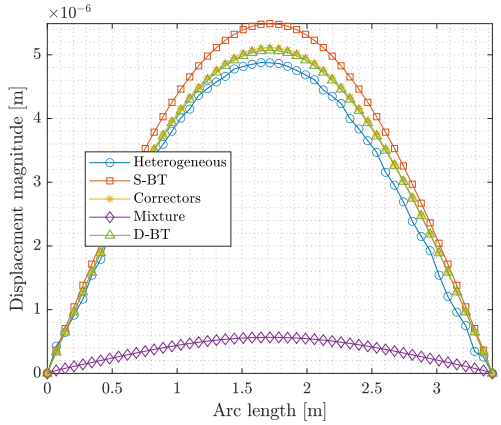


(**d**) VM stress, D-BT.

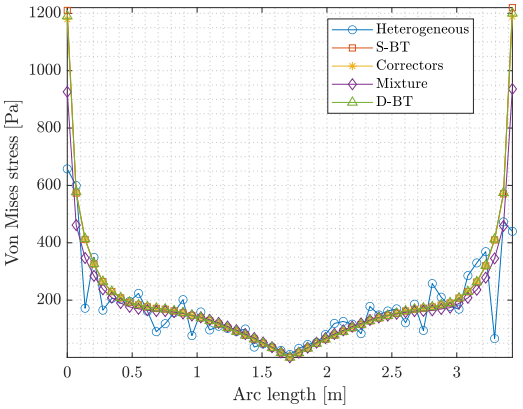
Figure 9.13: Cell E. Contours of the numerical solution to Problem 2.

correctors. Again, this error can be mitigated by considering a larger cell in the direction $\mathbf{e}_3$ to obtain the solution to the stress basic tests. However, it is unclear how to guarantee *a priori* that the selected cell is sufficiently large, rendering the S-BT approach unreliable in practice.

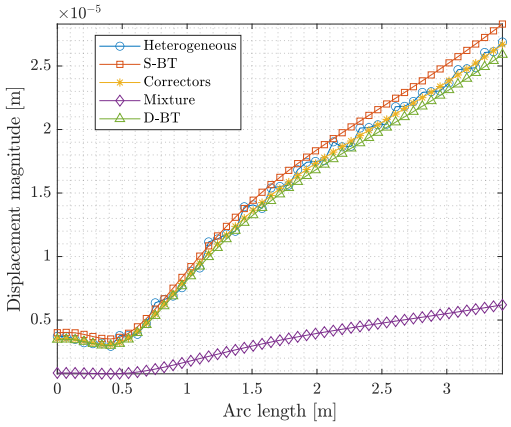
In Figure 9.13, the contours of the numerical solution to Problem 2, selecting Ω as a masonry formed by the repetition of $\mathbf{k}^p = (15, 6, 3)$ reference cells are presented. Only those of the heterogeneous material and the homogenised by D-BT are depicted, as the differences between the remaining results are similar to those already discussed previously. In Figure 9.14, the numerical solutions to Problems 1 and 2 are displayed. As in the previous examples, we observe that the displacement predictions with the mixture are not accurate, while those for the homogenised materials through D-BT and S-BT are fairly good. In the particular situation of Problem 1, it appears that the agreement between the displacement prediction with the D-BT homogeneous material is marginally better than that obtained through the correctors. However, it should be noted that this is most likely an effect of numerical errors.



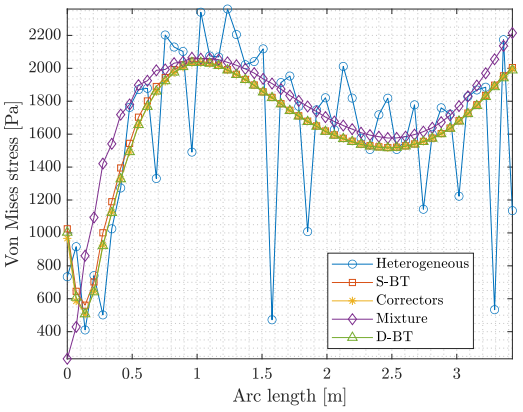
(**a**) Problem 1, displacement.



(**b**) Problem 1, VM stress.



(**c**) Problem 2, displacement.



(**d**) Problem 2, VM stress.

Figure 9.14: Cell E. Solution to Problems 1 and 2 along the line $[\mathbf{x}_{min}, \mathbf{x}_{max}]$.

USC
UNIVERSIDADE DE SANTIAGO DE COMPOSTELA

USC
UNIVERSIDADE
DE SANTIAGO
DE COMPOSTELA

Conclusions and perspectives

In this part of the manuscript, with the main motivation of obtaining a homogenous material with an equivalent mechanical response to the ceramic cup of the BF, two different techniques, the stress basic tests (S-BT) and displacement basic tests (D-BT), have been introduced. They allow to obtain the homogeneous equivalent material corresponding to a heterogeneous, periodically repeating material, under the assumption of a linear elastic mechanical response. With this purpose, each of the proposed methodologies poses a set of six problems –the *basic tests*– that are defined in the reference cell of the heterogeneous domain. The S-BT uses pure Neumann boundary conditions, whereas the D-BT imposes Dirichlet conditions on specifically selected displacement components.

To address the ill-posedness of the pure traction problems that are required to solve the S-BT technique, in Chapter 6, a saddle point formulation of the problem, obtained by the introduction of a Lagrange multiplier, was analysed in detail. The existence and uniqueness of solution was established, and the numerical performance of the formulation was compared with other solution strategies, such as pinning or directly using a suitable iterative solver. It was found that only the formulation considering the Lagrange multiplier preserved all the expected theoretical convergence rates.

In Chapter 8, the S-BT technique was presented. Despite the initial appeal of the S-BT due to its conceptual simplicity, this methodology was found to be unsuitable to approximate the heterogeneous material response. Although in some cases it yielded reasonable predictions, in general, it cannot be guaranteed to provide an accurate characterisation of heterogeneous materials. Furthermore, a relation with the mathematical results in the homogenisation theory could not be established. In particular, it was shown with numerical experiments that for a very simple setting, considering a laminated heterogeneous material, its performance was extremely poor.

In contrast, the D-BT methodology, analysed in Chapter 9, was found to perform much better. It was proved that, for orthotropic materials having a periodic reference cell with several symmetries, solving the D-BT and a suitable linear system relating the mean stress and strain in the basic tests solutions is the same as considering the corrector problems for classical periodic homogenisation. Furthermore, it was numerically demonstrated with a practical example that the D-BT also produces good characterisations even if the hypotheses to guarantee its equivalence with the correctors do not hold. The masonry forming the ceramic cup of the BF was characterised as an orthotropic material using the devised methodologies. One remarkable finding was that one of the generalised Poisson's ratios of the corresponding homogenised material was negative, i.e., the ceramic cup response is that of an auxetic material.

For future perspectives, we have ongoing work regarding the extension of the presented methodology for a thermo-elastic behaviour law, which would allow predicting the response of the ceramic cup when subjected to thermal stress due to the high temperature. In addition, for those cases that involve reference cells that do not satisfy the required hypotheses, it could be possible to obtain suitable bounds on the error among the correctors. Lastly, an interesting line of further research could be to extend the methodology to the layer formed by carbon blocks, which have no joints in between and are allowed to slide freely. A publication regarding the main results of this part is currently in preparation.

USC
UNIVERSIDADE DE SANTIAGO DE COMPOSTELA

USC
UNIVERSIDADE
DE SANTIAGO
DE COMPOSTELA

Resumo

O aceiro é un material moi arraigado na sociedade moderna. A principal fonte de demanda de aceiro é a infraestrutura, pero tamén é un ingrediente clave para varios medios de transporte, electrodomésticos e moitos outros artigos. A industria do aceiro xoga un papel crucial na economía global, con ingresos de máis de 2, 5 billóns de dólares e empregando a entorno a 6 millóns de persoas en todo o mundo. Desde 1970, a demanda mundial de aceiro triplicouse e prevese que medre máis dun terzo ata 2050 (International Energy Agency, 2020).

A fabricación de aceiro realízase principalmente cun material intermedio coñecido como *arrabio*, producido en grandes fornos metalúrxicos chamados Altos Fornos (AF) mediante a redución do mineral de ferro. Estos son responsables de preto do 70% da produción mundial de aceiro (Geerdes et al., 2015). Segundo Cameron et al. (2019), no futuro, os AF seguirán sendo a principal vía de produción de aceiro en todo o mundo, xa que o resto de rutas para a obtención de aceiro, coma os fornos de arco eléctrico, non poden igualar a escala e eficiencia dos AF. Para manter a economía de escala do proceso, tanto a súa produtividade como a extensión das súas campañas deben satisfacer requisitos cada vez máis esixentes. Isto impón condicións máis difíciles para os materiais refractarios utilizados como revestimento dos recipientes usados na industria do aceiro, xa que os maiores rendementos conducen a un incremento das taxas de erosión mecánica, ataque químico e tamén maiores tensións térmicas nos refractarios (Luomala et al., 2001).

Na acería integrada, a etapa do alto forno é a parte máis crítica do proceso, xa que o custo de obtención do arrabio no AF supón preto do 75% de todos os custos relacionados coa produción de aceiro (Cameron et al., 2019). Unha gran parte destes custos son gastos relacionados con materiais refractarios utilizados para protexer canais, cunchas e outros equipamentos empregados na industria siderúrxica, que sofren duras condicións de funcionamento, provocando elevadas taxas de degradación. Ademais, dado que a fabricación de aceiro é un proceso con altos consumos enerxéticos, existen importantes preocupacións ambientais en relación coa mellora da eficiencia e a redución da pegada de carbono do proceso. En concreto, a industria siderúrxica é responsable de aproximadamente o 7% das emisións mundiais de gases de efecto invernadoiro e o 11% das emisións mundiais de CO_2 (Hasanbeigi, 2022).

As condicións operativas hostís na maioría das fases do proceso e a dificultade de acceso encarecen a experimentación, tanto desde o punto de vista da seguridade como dos custos económicos. Por este motivo, a industria pode beneficiarse enormemente do uso de ferramentas matemáticas para obter predicións adecuadas que permitan caracterizar a resposta dos recipientes refractarios que interveñen nas diferentes etapas do proceso siderúrxico. Aínda que as múltiples complexidades do proceso adoitan levar a modelos que requiren unha idealización considerable das condicións reais, na maioría de casos é posible extraer conclusións de utilidade a pesar destas idealizacións.

Nos últimos anos fixéronse esforzos considerables para incorporar técnicas computacionais que proporcionen novos coñecementos sobre o proceso siderúrxico integral (véxase, por exemplo, Kuang et al., 2018). Estes desenvolvementos provocaron cambios importantes na industria, xa que nas últimas décadas se produciron cambios significativos no tamaño, tecnoloxía e prácticas operativas no AF, entre outros (Ranjan et al., 2022). De feito, estes desenrolos supuxeron un aumento considerable da eficiencia dos AF, posto que dende 1960 estímase que a enerxía necesaria para producir unha tonelada de aceiro bruto reduciuse aproximadamente nun 60%. Porén, aínda quedan moitas cuestións abertas e retos relacionados coa fabricación de aceiro que deberían abordarse para continuar optimizando o proceso nos próximos anos.

Este manuscrito divídese en dúas partes nas que se introducen diferentes metodoloxías matemáticas para estudar problemas relevantes no proceso de fabricación de ferro no alto forno. A continuación, descríbense os principais contidos de cada unha delas.

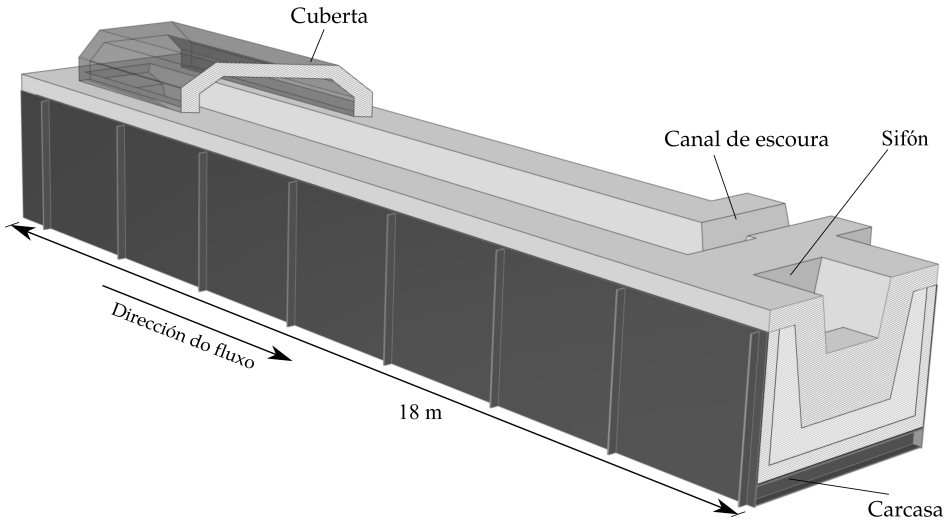


Figura 2: Esbozo do canal principal.

Parte I. Modelización matemática no canal principal do forno alto

O obxectivo da primeira parte é concibir modelos matemáticos axeitados para estudar o comportamento termohidrodinámico do canal ou corredor principal do AF. Trátase dunha estrutura recuberta de formigón refractario onde se recolle o chorro de arrabio e escoura extraído do crisol do AF. Na Figura 2, amósase un esbozo do canal principal, cortando a cuberta refractaria por claridade, xa que cubre a totalidade do canal. As súas dimensións e características específicas dependen en gran medida da disposición e necesidades particulares da planta. Non obstante, usualmente miden uns 18 m de longo e 3 m de ancho. A función do corredor non é simplemente transportar o arrabio líquido ao seguinte paso do proceso, senón tamén garantir a adecuada separación entre metal e escoura (Monteiro de Oliveira et al., 2020). A separación consíguese por diferenza de densidade, xa que o arrabio, máis denso, flúe por debaixo do sifón, o que obriga a que a escoura, máis lixeira, se acumule enriba del e drene a través dun corredor máis pequeno chamado canal de escoura. O encoro de ferro ao final do canal permite manter unha cantidade residual de arrabio e escoura entre as coladas do AF, que axuda a manter o calor no canal e facilita o proceso de separación.

A principal motivación desta parte é proporcionar unha mellor comprensión dos complicados fenómenos xerados no fluxo multifásico e turbulento de arrabio e escoura, así como avaliar a transferencia de calor no canal. Na zona de impacto do chorro, unha cantidade significativa de aire é arrastrada e penetra na balsa de fluídos, xerando unha zona de alta turbulencia cunha mestura de aire, escoura e arrabio. O canal está sometido a unha carga térmica cíclica durante a súa vida útil, que se cre que está relacionada coa degradación dos materiais refractarios. Ademais, o ataque químico da escoura e a erosión mecánica xogan un papel fundamental no desgaste do refractario (Ranjan et al., 2022). O deseño dos canais baséase a miúdo en métodos de proba e erro (Ouedraogo & Prompt, 2008). Polo tanto, a simulación numérica pode proporcionar información valiosa, permitindo substituír estes métodos. Para investigar os diversos fenómenos no canal, constrúese un modelo CAD dun canal principal operado por ArcelorMittal. As principais características do proceso, así como as dimensións do canal empregado nos modelos, recóllense no Capítulo 1.

A continuación, proponse unha xerarquía de diferentes modelos matemáticos que se resolven numericamente. En primeiro lugar, no Capítulo 2, utilízase un modelo de Dinámica de Fluídos Computacional (CFD) para analizar os patróns de fluxo no canal, similar aos que apareceron recentemente na literatura (véxase, por exemplo Ge et al., 2020; H. Yao et al., 2021). En particular, abórdanse diversas áreas non tratadas nos traballos existentes na literatura, como a evolución da posición estimada das interfaces de fluídos durante as coladas do forno e a caracterización precisa dos esforzos cortantes na parede. Os resultados amosan que as curvas de esforzos cortantes son similares ás que se

encontran en estudos tanto experimentais coma numéricos sobre chorros mergullados impactando en superficies planas. Obsérvase tamén que as estruturas do fluxo e os esforzos dependen da fracción de escoura que se está a drenar do forno. Ademais, os niveis de líquido evolucionan rapidamente a un estado estacionario durante cada colada, con cambios significativos de espesor da balsa de arrabio retida no canal. Estes cambios poden levar a un maior desgaste, xa que o revestimento refractario vese sometido ao ataque tanto por parte do arrabio como da escoura.

O perfil de velocidade obtido ao resolver o modelo anterior utilízase para proporcionar unha condición de contorno adecuada para un modelo matemático que pretende investigar a temperatura no canal, introducido no Capítulo 3. Para iso, asúmense condicións de estado estacionario. Ademais, só se inclúe a parte media e final da estrutura, onde a influencia do impacto do chorro sobre os fluídos retidos no canal é desprezable e o fluxo presenta características similares a un fluxo de tipo pistón (Kim & Ozturk, 1998). O modelo térmico pretende abordar a transferencia de calor conxugada entre as capas sólidas refractarias e os fluídos que circulan polo canal, así como o fluxo forzado xerado pola aspiración de vapores. Tamén se avalía a transferencia de calor radiativa, tendo en conta a radiación de superficie a superficie. Os resultados utilízanse para estudar se o deseño do canal provoca que as chamadas isotermas críticas se atopen dentro do revestimento de traballo, a capa refractaria máis externa, que está en contacto co arrabio e a escoura. Asemade, estúdase o efecto producido pola velocidade do fluxo de aire forzado na extracción de calor do canal. As predicións de temperatura son validadas cunha instantánea de temperatura dos termopares incrustados na revestimento illante do canal.

Porén, medicións da evolución da temperatura ao longo de campañas completas, proporcionadas posteriormente por ArcelorMittal, mostran oscilacións de temperatura significativas. Isto suxire que o campo de temperatura nas capas refractarias de apoio vese influenciada polas paradas do proceso de colada do forno e que a hipótese de que se alcanza o estado estacionario non é totalmente realista. Para investigar máis a fondo esta dificultade, no Capítulo 5 estúdase o influencia das paradas do AF na resposta térmica do canal durante un ciclo completo de campaña nunha sección 2D do canal. Para tal fin, mediante un novo modelo térmico transitorio, utilizando os resultados dos modelos matemáticos anteriores para establecer as condicións de contorno axeitadas, simúlase a transferencia de calor durante a campaña completa, de 2 meses de duración. O modelo inclúe a condución de calor con radiación non local acoplada, simplificando o comportamento dos fluídos para obter un modelo abordable numéricamente. A derivación do modelo, a discretización do mesmo e o algoritmo de resolución numérica descríbense e analízanse no Capítulo 4.

A metodoloxía proposta mellora os estudos previos similares que supoñían que se alcanza o estado estacionario, onde se consideraban condicións bastante idealizadas para a transferencia de calor por radiación (véxase, por exemplo Vázquez-Fernández et al., 2019). As temperaturas calculadas no Capítulo 5 mostran un acordo cualitativo coas medicións, pero con diferencias significativas nos valores observados. Emporiso, como hai un grao de incerteza elevado sobre a posición dos termopares, utilizouse unha técnica para atopar unha posición corrixida dentro dunha rexión factible para a posición de cada dispositivo, empregando un algoritmo de optimización global. Nas posicións corrixidas, alcanzáronse niveis de acordo moito mellores entre as medicións e as temperaturas calculadas. Tendo en conta que o modelo que se resolve non ten en conta o desgaste do refractario, as discrepancias entre os valores de temperatura calculados e as medicións, que crecen cara ao final das campañas, suxiren graves danos e perda de propiedades no revestimento de traballo. Os resultados tamén indican que a maior parte do desgaste localízase nas seccións laterais do canal, xa que as diferenzas de temperatura observadas son moito maiores para os termopares laterais, en acordo coa bibiografía existente relacionada co desgaste dos refractarios no canal (Begnis & Brandaleze, 2006).

Parte II. Material equivalente para a cunca cerámica do alto forno

USC

Na segunda parte, o foco trasládase ao propio alto forno. Na zona do crisol, as paredes dalgúns fornos teñen unha parte adicional chamada cunca cerámica, composta por un anel interior na parede formado por ladrillos refractarios separados por xuntas de morteiro. Este protexe a un anel exterior

de bloques de carbono. Para simular numericamente a resposta mecánica da devandita estrutura, non é computacionalmente viable incluír cada ladrillo e cada unión, o que motiva a necesidade de proporcionar unha metodoloxía que permita a simulación numérica da resposta mecánica da cunca cerámica como un material homoxéneo equivalente. Dado que a estrutura pode xerarse mediante a repetición periódica dunha cela de referencia, baixo o suposto de que a resposta de ambos materiais é elástica lineal, as ferramentas clásicas de homoxeneización periódica pódense utilizar para obter un material homoxeneizado cun comportamento mecánico similar ao da estrutura enteira (Cioranescu & Donato, 1999).

Non obstante, os problemas que deben resolverse para obter as entradas da matriz de rixidez efectiva do material homoxeneizado, requiren introducir unha condición de contorno de periodicidade en todas as caras da cela de referencia, así como restrinxir o desprazamento medio para que sexa nulo. A primeira condición establécese facilmente cando a malla é idéntica en caras opostas da cela. Porén, mallas arbitrarias requiren técnicas máis complicadas (V.-D. Nguyen et al., 2012). Ademais, estas restricións non sempre son sinxelas de aplicar na maioría dos paquetes de software utilizados frecuentemente en enxeñería.

En consecuencia, nesta parte propóñense dúas metodoloxías rápidas e máis doadas de usar, inspiradas na forma en que se realizan experimentalmente os ensaios de compresión e cizallamento uniaxial para caracterizar o comportamento de materiais. No Capítulo 6, recórdase a teoría clásica da elasticidade lineal e abórdanse algúns resultados relativos ao problema da de tracción pura. Para obter unha formulación ben plantexada do problema, introdúcese un multiplicador de Lagrange, utilizando unha formulación similar á proposta en Bochev & Lehoucq (2011); Kuchta et al. (2019), e preséntase unha técnica de preacondicionamento adecuada para a resolución do sistema lineal correspondente. O seu rendemento numérico analízase en comparación con outras dúas estratexias de solución populares mediante un par de tests académicos con solución analítica coñecida, observándose que só a formulación considerando o multiplicador de Lagrange preservou todas as taxas teóricas de converxencia.

A continuación, no Capítulo 8, preséntase unha técnica sinxela, chamada *stress basic tests* (S-BT) para a caracterización dos coeficientes do material equivalente homoxeneizado. Consiste na resolución de seis problemas de tracción pura, definidos na cela de referencia. Os resultados calculados coa metodoloxía avalíanse fronte aos obtidos a través da homoxeneización clásica en varios experimentos numéricos. A pesar do atractivo inicial dos S-BT debido á súa sinxeleza conceptual, esta metodoloxía resultou inadecuada para aproximar a resposta do material heteroxéneo. Aínda que nalgúns casos proporciona predicións razoables, en xeral, non se pode garantir unha caracterización precisa de materiais heteroxéneos, e non se puido establecer unha relación cos resultados na teoría da homoxeneización matemática. En concreto, demostrouse que para unha configuración moi sinxela, considerando un material laminado, o material homoxeneizado proporcionado polos S-BT non aproxima ben a resposta do material heteroxéneo.

En cambio, os denominados *displacement basic tests* (D-BT), propostos no Capítulo 9, substitúen a condición de contorno de Neumann pura dos S-BT, por condicións de contorno de Dirichlet, impostas en compoñentes do desprazamento coidadosamente seleccionadas. Baixo supostos adecuados de simetría xeométrica e para materiais ortotrópicos, demóstrase que as solucións destes novos ensaios básicos están relacionadas coas funcións correctoras do sistema elástico lineal, usadas na teoría clásica de homoxeneización. En particular, próbase que os D-BT son equivalentes a homoxeneización matemática sempre que estas hipóteses sexan satisfeitas, no sentido de que proporcionan a mesma matriz de rixidez efectiva do material homoxeneizado. Así, é posible obter os mesmos resultados que coa homoxeneización clásica, que ten garantizada a converxencia, pero resolvendo problemas moito máis sinxelos de tratar numéricamente.

Ademais, cun exemplo práctico, demostrouse numericamente que os D-BT tamén producen boas caracterizacións aínda que non se cumpran as hipóteses para garantir a súa equivalencia cos correctores. Finalmente, a resposta da cunca cerámica do alto forno caracterizouse usando todas as técnicas analizadas. Un descubrimento notable foi que un dos coeficientes xeneralizados de Poisson do material homoxeneizado é negativo, é dicir, a resposta da cunca cerámica a un esforzo compresivo na dirección correspondente é contraerse tamén nas direccións ortogonais, xusto ao revés que un material

estándar. Este tipo de materiais denomínanse auxéticos (véxase, por exemplo Alderson & Alderson, 2007), e teñen importantes aplicacións prácticas.

Parte dos modelos matemáticos propostos neste traballo resólvense numericamente mediante código propio, escrito na súa maioría na linguaxe *Python*. Asemade, úsanse as librarías de código aberto *FEniCS*, que permite obter facilmente a discretización por elementos finitos do sistema de ecuación en derivadas parciais (EDP) a partir da correspondente formulación variacional, e *PETSc*, utilizada para resolver os sistemas lineais correspondentes ás discretizacións. A simulación numérica dos modelos máis complicados, que implican a caracterización do fluxo no canal principal, realízase co paquete comercial de Dinámica de Fluídos Computacional *Ansys Fluent*. Para o posprocesamento e discusión posterior dos resultados calculados, utilizáronse varios paquetes, como *MATLAB*, a libraría de código aberto *Matplotlib* e o software *Paraview*. Para as tarefas relacionadas coa simulación numérica tívose acceso ao clúster de computadores *Mariscal*, formado por 21 nodos aloxados no Centro de Supercomputación de Galicia (CESGA).

Este traballo realizouse no marco dos proxectos *MTM2015-68275-R*, financiado polo Ministerio de Ciencia, Innovación y Universidades, e *PID2019-10561RB-I00/AEI/ 10.13039/501100011*, financiado pola Agencia Estatal de Investigación. En ambos proxectos, a empresa siderúrxica ArcelorMittal foi unha entidade colaboradora, que proporcionou datos reais relativos á xeometría do crisol do AF e do canal, así como as propiedades físicas dos materiais sólidos e fluídos implicados. Impulsouse o diálogo activo cos enxeñeiros da empresa para a identificación de parámetros, propiedades e estratexias adecuadas para a modelización dos distintos fenómenos físicos abordados neste manuscrito. Ademais, as medicións experimentais e os datos de operación do AF, tamén facilitados pola empresa, foron esenciais para axustar os modelos e validar os resultados numéricos obtidos.

USC
UNIVERSIDADE DE SANTIAGO DE COMPOSTELA

USC
UNIVERSIDADE
DE SANTIAGO
DE COMPOSTELA

Bibliography

Alderson, A., & Alderson, K. L. (2007). Auxetic materials. In *Proc. of the Institution of Mechanical Engineers, Part G: Journal of Aerospace Engineering* (Vol. 221, pp. 565–575). SAGE Publications.

Allaire, G. (1992). Homogenization and Two-Scale Convergence. *SIAM Journal on Mathematical Analysis*, *23*(6), 1482–1518.

Allaire, G. (2012). A brief introduction to homogenization and miscellaneous applications. In *ESAIM: Proceedings* (Vol. 37, pp. 1–49).

Almeida, B. V. d., Neves, E. S., Silva, S. N., & Vernilli Junior, F. (2017). Blast Furnace Hearth Lining: Post Mortem Analysis. *Materials Research*, *20*(3), 814–818.

Alnæs, M. S., Blechta, J., Hake, J., Johansson, A., Kehlet, B., Logg, A., ... Wells, G. N. (2015). The FEniCS project version 1.5. *Archive of Numerical Software*, *3*(100), 9–23.

Ansys, Inc. (2019). *Ansys Fluent Theory Guide, Release 19.5.*

Ansys, Inc. (2021). *Ansys Fluent User Guide, Release 21.2.*

Anthoine, A. (1995). Derivation of the in-plane elastic characteristics of masonry through homogenization theory. *International Journal of Solids and Structures*, *32*(2), 137–163.

Babich, A., & Senk, D. (2019). Coke in the iron and steel industry. In *New Trends in Coal Conversion: Combustion, Gasification, Emissions, and Coking* (pp. 367–404). Woodhead Publishing.

Balay, S., Abhyankar, S., Adams, M. F., Benson, S., Brown, J., Brune, P., ... Zhang, J. (2022). *PETSc/TAO Users Manual* (Tech. Rep. No. ANL-21/39 - Revision 3.17). Argonne National Laboratory.

Barral, P., Fanjul, M., Pérez-Pérez, L. J., Quintela, P., & Sánchez, M. (2018). Equivalent thermomechanical model for ceramic cups. In *Proc. of 139 ESGI* (pp. 85–101).

Barral, P., Nicolás, B., Pérez-Pérez, L. J., & Quintela, P. (2019). Numerical Simulation of Wear-Related Problems in a Blast Furnace Runner. In *Recent advances in differential equations and applications* (pp. 229–244). Springer.

Barral, P., Nicolás, B., & Quintela, P. (2021). Numerical simulation of the shear stress produced by the hot metal jet on the blast furnace runner. *Computers & Mathematics with Applications*, *102*(15), 146–159.

Barral, P., Pérez-Pérez, L. J., & Quintela, P. (2022a). Numerical simulation of the transient heat transfer in a blast furnace main trough during its complete campaign cycle. *International Journal of Thermal Sciences*, *173*, 107349.

Barral, P., Pérez-Pérez, L. J., & Quintela, P. (2022b). Transient thermal response with nonlocal radiation of a blast furnace main trough. *Applied Mathematical Modelling*, *105*, 197–225.

Begnis, J. S. S., & Brandaleze, E. (2006). Simulación del canal del alto horno nº2 por medio de modelos físicos. *Estudos Tecnológicos em Engenharia*, *2*(1), 1–12.

Beltaos, S., & Rajaratnam, N. (1974). Impinging circular turbulent jets. *Journal of the Hydraulics Division*, *100*(10), 1313–1328.

Bergman, T. L., Incropera, F. P., DeWitt, D. P., & Lavine, A. S. (2011). *Fundamentals of heat and mass transfer*. John Wiley & Sons.

Bermúdez, A. (2005). *Continuum Thermomechanics*. Progress in Mathematical Physics (PMP), 43. Springer Science & Business Media.

Bermúdez, A., Gómez, D., Muñiz, M. C., & Vázquez, R. (2011). A thermo-electrical problem with a nonlocal radiation boundary condition. *Mathematical and Computer Modelling*, *53*(1–2), 63–80.

Bermúdez, A., Gómez, D., Piñeiro, M., Salgado, P., & Venegas, P. (2017). Numerical Simulation of Magnetization and Demagnetization Processes. *IEEE Transactions on Magnetics*, *53*(12), 1–6.

Bermúdez, A., Gómez, D., Salgado, P., Rodriguez, R., & Venegas, P. (2013). Numerical solution of a transient nonlinear axisymmetric eddy current model with nonlocal boundary conditions. *Mathematical Models and Methods in Applied Sciences*, *23*(13), 2495–2521.

Bermúdez, A., Leira, R., Muñiz, M. C., & Pena, F. (2006). Numerical modelling of a transient conductive–radiative thermal problem arising in silicon purification. *Finite Elements in Analysis and Design*, *42*(10), 809–820.

Blackwell, B., Dowding, K., & Modest, M. (2009). Cylindrical geometry verification problem for enclosure radiation. *Journal of Thermophysics and Heat Transfer*, *23*(4), 711–715.

Bochev, P., & Lehoucq, R. (2011). Energy principles and finite element methods for pure traction linear elasticity. *Computational Methods in Applied Mathematics*, *11*(2), 173–191.

Bochev, P., & Lehoucq, R. B. (2005). On the finite element solution of the pure neumann problem. *SIAM review*, *47*(1), 50–66.

Bower, A. F. (2009). *Applied mechanics of solids*. CRC Press.

Boyd, S., & Vandenberghe, L. (2004). *Convex optimization*. Cambridge University Press.

Bredberg, J. (2000). *On the wall boundary condition for turbulence models.* Chalmers University of Technology, Department of Thermo and Fluid Dynamics. Internal Report 00/4.

Brenner, S., & Scott, R. (2008). *The Mathematical Theory of Finite Element Methods*. Texts in Applied Mathematics (TAM), 15. Springer Science & Business Media.

Brezzi, F. (1974). On the existence, uniqueness and approximation of saddle-point problems arising from lagrangian multipliers. *R.A.I.R.O. Analyse Numérique*, *8*(R2), 129–151.

Busto, S. (2018). *Contributions to the numerical solution of heterogeneous fluid mechanics models* (Doctoral dissertation). Universidade de Santiago de Compostela.

Cameron, I., Sukhram, M., Lefebvre, K., & Davenport, W. (2019). *Blast Furnace Ironmaking: Analysis, Control and Optimization*. Elsevier.

Cengel, Y. (2014). *Heat and mass transfer: Fundamentals and applications*. McGraw-Hill Higher Education.

Chacón Rebollo, T., & Lewandowski, R. (2014). *Mathematical and numerical foundations of turbulence models and applications*. Modeling and Simulation in Science, Engineering and Technology (MSSET). Springer.

Ciarlet, P. G. (1988). *Mathematical elasticity, volume I: Three-dimensional elasticity*. Studies in Mathematics and its Applications, 20. North-Holland.

Ciarlet, P. G. (2010). On Korn's inequality. *Chinese Annals of Mathematics, Series B*, *31*, 607–618.

USC UNIVERSIDADE DE SANTIAGO

Cioranescu, D., Damlamian, A., & Griso, G. (2018). *The Periodic Unfolding Method*. Series in Contemporary Mathematics 3. Springer.

Cioranescu, D., & Donato, P. (1999). *An introduction to homogenization*. Oxford Lecture Series in Mathematics and Its Applications, 17. Oxford University Press.

D'Altri, A. M., Sarhosis, V., Milani, G., Rots, J., Cattari, S., Lagomarsino, S., ... de Miranda, S. (2020). Modeling Strategies for the Computational Analysis of Unreinforced Masonry Structures: Review and Classification. *Archives of Computational Methods in Engineering*, *27*(4), 1153–1185.

Deng, Y., Zhang, J. L., & Jiao, K. X. (2018). Economical and efficient protection for blast furnace hearth. *ISIJ International*, *58*(7), 1198–1203.

Druet, P.-É. (2009). Weak solutions to a stationary heat equation with nonlocal radiation boundary condition and right-hand side in L^p ($p \geq 1$). *Mathematical Methods in the Applied Sciences*, *32*(2), 135–166.

Du, K.-L., & Swamy, M. (2016). Simulated annealing. In *Search and Optimization by Metaheuristics* (pp. 29–36). Springer.

Falgout, R. D., & Yang, U. M. (2002). hypre: A Library of High Performance Preconditioners. In *International conference on computational science* (pp. 632–641).

Ferrín, J. L. (1999). *Algunas contribuciones a la modelización matemática de procesos de combustión de carbón* (Doctoral dissertation). Universidade de Santiago de Compostela.

Garbers-Craig, A. (2008). Presidential address: How cool are refractory materials? *Journal of the Southern African Institute of Mining and Metallurgy*, *108*(9), 491–506.

Gasser, A., Terny-Rebeyrotte, K., & Boisse, P. (2004). Modelling of joint effects on refractory lining behaviour. In *Proc. of the Institution of Mechanical Engineers, Part L: Journal of Materials: Design and Applications* (Vol. 218, pp. 19–28). SAGE Publications.

Gatt, R., Wood, M. V., Gatt, A., Zarb, F., Formosa, C., Azzopardi, K. M., ... others (2015). Negative Poisson's ratios in tendons: An unexpected mechanical response. *Acta biomaterialia*, *24*, 201–208.

Ge, Y., Li, M., Wei, H., Liang, D., Wang, X., & Yu, Y. (2020). Numerical Analysis on Velocity and Temperature of the Fluid in a Blast Furnace Main Trough. *Processes*, *8*, 249.

Geerdes, M., Chaigneau, R., & Kurunov, I. (2015). *Modern Blast Furnace Ironmaking: An Introduction*. IOS Press.

Geyer, P., & Halifa, Z. (2014). Blast furnace tapping practice at ArcelorMittal South Africa, Vanderbijlpark Works. In *Proc. of Furnace Tapping Conference 2014* (pp. 97–112). Southern African Institute of Mining and Metallurgy.

Golub, G. H., & Van Loan, C. F. (2013). *Matrix computations*. JHU Press.

Gorodtsov, V. A., & Lisovenko, D. S. (2019). Extreme values of Young's modulus and Poisson's ratio of hexagonal crystals. *Mechanics of Materials*, *134*, 1–8.

Gurtin, M. E. (1982). *An introduction to continuum mechanics*. Mathematics in Science and Engineering, 158. Academic Press.

Hasanbeigi, A. (2022). *Steel Climate Impact – An International Benchmarking of Energy and CO2 Intensities* (Tech. Rep.). Global Efficiency Intelligence.

He, Q., Evans, G., Zulli, P., Tanzil, F., & Lee, B. (2002). Flow Characteristics in a Blast Furnace Trough. *ISIJ International*, *42*(8), 844–851.

Henriksson, M., Louwerse, G., Zeilstra, C., Bartusch, H., Kaymak, Y., Nechyporuk, O., ... Stel, J. (2016). *Blast furnace sustained tapping practice (SUSTAINTAP): final report*. Publications Office of the European Union. doi: 10.2777/988594

Hirt, C. W., & Nichols, B. D. (1981). Volume of fluid (VOF) method for the dynamics of free boundaries. *Journal of Computational Physics*, *39*(1), 201–225.

Höpker, M. (2016). *Extension operators for Sobolev spaces on periodic domains, their applications, and homogenization of a phase field model for phase transitions in porous media* (Doctoral dissertation). Universität Bremen.

Howell, J. R., Mengüç, M. P., Daun, K., & Siegel, R. (2015). *Thermal Radiation Heat Transfer*. CRC Press.

Hunter, J. D. (2007). Matplotlib: A 2D Graphics Environment. *Computing in Science & Engineering*, *9*(3), 90–95.

Iida, M., Ogura, K., & Hakone, T. (2008). Analysis of Drainage Rate Variation of Molten Iron and Slag from Blast Furnace during Tapping. *ISIJ international*, *48*(4), 412–419.

Ingber, L. (1993). Simulated annealing: Practice versus theory. *Mathematical and Computer Modelling*, *18*(11), 29–57.

International Energy Agency. (2020). *Iron and steel technology roadmap* (Tech. Rep.). https://www.iea.org/reports/iron-and-steel-technology-roadmap.

Jørgensen, J. B., Kristensen, M. R., & Thomsen, P. G. (2018). *A Family of ESDIRK Integration Methods*. (arXiv:1803.01613)

Khodabandeh, E., Ghaderi, M., Afzalabadi, A., Rouboa, A., & Salarifard, A. (2017). Parametric study of heat transfer in an electric arc furnace and cooling system. *Applied Thermal Engineering*, *123*, 1190–1200.

Kim, H., & Ozturk, B. (1998). Slag-metal Separation in the Blast Furnace Trough. *ISIJ International*, *38*(5), 430–439.

Kolpakov, A. (1985). Determination of the average characteristics of elastic frameworks. *Journal of Applied Mathematics and Mechanics*, *49*(6), 739–745.

Kou, M., Yao, S., Wu, S., Zhou, H., & Xu, J. (2019). Effects of Blast Furnace Main Trough Geometry on the Slag-Metal Separation Based on Numerical Simulation. *Steel Research International*, *90*(2), 1800383.

Kramer, S. C., Gritzki, R., Perschk, A., Rösler, M., & Felsmann, C. (2015). Fully parallel, OpenGL-based computation of obstructed area-to-area view factors. *Journal of Building Performance Simulation*, *8*(4), 266–281.

Kuang, S., Li, Z., & Yu, A. (2018). Review on Modeling and Simulation of Blast Furnace. *Steel Research International*, *89*(1), 1700071.

Kuchta, M., Mardal, K.-A., & Mortensen, M. (2019). On the singular Neumann problem in linear elasticity. *Numerical Linear Algebra with Applications*, *26*(1), e2212.

Kumar, A., Khan, S. A., Biswas, S., & Pal, A. (2010). Strategic steps towards longer and reliable blast furnace trough campaign –- Tata Steel experience. *Ironmaking & Steelmaking*, *37*(1), 15–20.

Kundu, P. K., Cohen, I. M., & Dowling, D. R. (2015). *Fluid Mechanics*. Academic Press.

Kværnø, A. (2004). Singly Diagonally Implicit Runge–Kutta Methods with an Explicit First Stage. *BIT Numerical Mathematics*, *44*(3), 489–502.

Laitinen, M., & Tiihonen, T. (2001). Conductive-radiative heat transfer in grey materials. *Quarterly of Applied Mathematics*, *59*, 737–768.

Laney, C. B. (1998). *Computational Gasdynamics*. Cambridge University Press.

Launder, B. E., & Spalding, D. B. (1974). The numerical computation of turbulent flows. *Computer Methods in Applied Mechanics and Engineering*, *3*(2), 269–289.

Lee, W. E., & Moore, R. E. (1998). Evolution of *in Situ* Refractories in the 20th Century. *Journal of the American Ceramic Society*, *81*(6), 1385–1410.

Lee, W. E., Vieira, W., Zhang, S., Ahari, K. G., Sarpoolaky, H., & Parr, C. (2001). Castable refractory concretes. *International Materials Reviews*, *46*(3), 145–167.

Levy, A. V., & Montalvo, A. (1985). The tunneling algorithm for the global minimisation of functions. *SIAM Journal on Scientific and Statistical Computing*, *6*(1), 15–29.

Li, Y., Cheng, S., & Wang, Z. (2015). Corrosion Behavior of Ceramic Cup of Blast Furnace Hearth by Liquid Iron and Slag. *High Temperature Materials and Processes*, *35*(9), 941–948.

Logg, A., Mardal, K.-A., & Wells, G. (2012). *Automated solution of differential equations by the finite element method: The FEniCS book*. Lecture Notes in Computational Science and Engineering (LNCSE), 84. Springer Science & Business Media.

Lourenço, P. B., Zucchini, A., Milani, G., & Tralli, A. (2006). Homogenisation approaches for structural analysis of masonry buildings. In *Structural analysis of historical constructions: Possibilities of numerical and experimental techniques* (Vol. 1, pp. 59–76). Macmillan.

Luomala, M. J., Paananen, T. T., Köykkä, M. J., Fabritius, J., Matti, T., Nevala, H., & Härkki, J. J. (2001). Modelling of fluid flows in the blast furnace trough. *Steel Research International*, *72*(4), 130–135.

Mathieu, N., Sab, K., & Zaïmi, S. (2012). An enhanced homogenization approach for masonry structures with compressible joints. Application to hearth thermomechanical computations. *International Journal for Numerical and Analytical Methods in Geomechanics*, *36*(9), 1102–1124.

Menter, F. (1994). Two-equation eddy-viscosity turbulence models for engineering applications. *AIAA Journal*, *32*(8), 1598–1605.

Menter, F., & Esch, T. (2001). Elements of industrial heat transfer predictions. In *Proc. of 16th Brazilian Congress of Mechanical Engineering (COBEM)* (Vol. 20, pp. 117–127).

Menter, F., Kuntz, M., & Langtry, R. (2003). Ten Years of Industrial Experience with the SST Turbulence Model. In *Proc. of 4th International Symposium on Turbulence, Heat and Mass transfer* (pp. 625–632). Begell House.

Mills, K. (2011). *The estimation of slag properties.* A short course presented as part of *Southern African Pyrometallurgy 2011*.

Modest, M. F. (2013). *Radiative heat transfer*. Academic Press.

Mohammadi, B., & Pironneau, O. (1994). *Analysis of the K-Epsilon Turbulence Model*. Research in Applied Mathematics (RAM). Wiley.

Monteiro de Oliveira, M. J., Rodrigues, G. F. R., Silva, I. A., Peixoto, J. J. M., & Silva, C. A. d. (2020). Modeling of Two-Phase Flow in Blast Furnace Trough. *Steel Research International*, *92*(3), 2000485.

Montiel, S., & Ros, A. (2009). *Curves and surfaces*. Graduate Studies in Mathematics, 69. American Mathematical Society.

Nguyen, T., Blond, E., Gasser, A., & Prietl, T. (2009). Mechanical homogenisation of masonry wall without mortar. *European Journal of Mechanics-A/Solids*, *28*(3), 535–544.

Nguyen, V.-D., Béchet, E., Geuzaine, C., & Noels, L. (2012). Imposing periodic boundary condition on arbitrary meshes by polynomial interpolation. *Computational Materials Science*, *55*, 390–406.

Oleïnik, O. A., Shamaev, A., & Yosifian, G. (1992). *Mathematical problems in elasticity and homogenization*. Studies in Mathematics and its Applications, 26. North-Holland.

Ouedraogo, E., & Prompt, N. (2008). High-temperature mechanical characterisation of an alumina refractory concrete for Blast Furnace main trough: Part II. Material behaviour. *Journal of the European Ceramic Society*, *28*(15), 2867–2875.

Ouedraogo, E., Roosefid, M., Prompt, N., & Deteuf, C. (2011). Refractory concretes uniaxial compression behaviour under high temperature testing conditions. *Journal of the European Ceramic Society*, *31*(15), 2763–2774.

Panton, R. L. (2013). *Incompressible flow*. John Wiley & Sons.

Phares, D. J., Smedley, G. T., & Flagan, R. C. (2000). The wall shear stress produced by the normal impingement of a jet on a flat surface. *Journal of Fluid Mechanics*, *418*, 351–375.

Prompt, N., & Ouedraogo, E. (2008). High temperature mechanical characterisation of an alumina refractory concrete for Blast Furnace main trough: Part I. General context. *Journal of the European Ceramic Society*, *28*(15), 2859–2865.

Quarteroni, A. (2009). *Numerical Models for Differential Problems*. MS&A, 8. Springer-Verlag.

Ranjan, S., Mazumdar, D., Chakraborty, I. N., Sinha, S., & Sarkar, R. (2022). Review and Analysis of Metallurgical Processes in Blast Furnace Main Trough and Trough Performances. *Transactions of the Indian Institute of Metals*, *75*, 589–611.

Ren, X., Das, R., Tran, P., Ngo, T. D., & Xie, Y. M. (2018). Auxetic metamaterials and structures: a review. *Smart Materials and Structures*, *27*(2), 023001.

Rezende, R. V. P., Silva, A. F. C., & Maliska, C. R. (2007). The blast furnace trough two-phase flow and its influence in the refractory lining wear: mathematical modeling and numerical simulation. In *Proc. of 19th International Congress of Mechanical Engineering (COBEM)*.

Roache, P. J. (2001). Code Verification by the Method of Manufactured Solutions. *Journal of Fluids Engineering*, *124*(1), 4–10.

Roubíček, T. (2013). *Nonlinear partial differential equations with applications*. International Series of Numerical Mathematics (ISNM), 153. Springer Science & Business Media.

Roy, C. J. (2005). Review of code and solution verification procedures for computational simulation. *Journal of Computational Physics*, *205*(1), 131–156.

Rudin, W. (2006). *Real and Complex Analysis*. Tata McGraw-Hill Education.

Rüther, H., & Lüngen, H. (1989). Refractory technology and operational experience with tapholes and troughs of blast furnaces in the Federal Republic of Germany. *Revue de Métallurgie*, *86*(2), 137–146.

Saad, Y. (2003). *Iterative Methods for Sparse Linear Systems*. SIAM.

Schacht, C. (2004). *Refractories handbook*. CRC Press.

Schwartz, L. (1966). *Théorie des distributions*. Hermann.

Seoane, M. (2016). *Modelización de fenómenos térmicos que afectan al canal principal del horno alto* (Master's thesis. M.Sc. Industrial Mathematics). Universidade de Santiago de Compostela.

Shah, N. V. (2022). *Coupled parameterized reduced order modelling of thermomechanical phenomena arising in blast furnaces* (Doctoral dissertation). Scuola Internazionale Superiore di Studi Avanzati.

Shao, L., & Saxén, H. (2011). A Simulation Study of Blast Furnace Hearth Drainage Using a Two-phase Flow Model of the Taphole. *ISIJ International*, *51*(2), 228–235.

Shao, L., & Saxén, H. (2012a). Model of Blast Furnace Hearth Drainage. *Steel Research International*, *83*(2), 197–204.

Shao, L., & Saxén, H. (2012b). Numerical Prediction of Iron Flow and Bottom Erosion in the Blast Furnace Hearth. *Steel Research International*, *83*(9), 878–885.

Shao, L., & Saxén, H. (2013a). Flow Patterns of Iron and Slag in the Blast Furnace Taphole. *ISIJ international*, *53*(10), 1756–1762.

Shao, L., & Saxén, H. (2013b). A Simulation Study of Two-Liquid Flow in the Taphole of the Blast Furnace. *ISIJ international*, *53*(6), 988–994.

Shestopalov, I., Denisov, A., Mel'nikov, P., Makarov, V., Unigovskii, L. B., Shul'man, V., ... Tsera, I. (1988). Improving the separation of smelting products in the main trough of a blast furnace. *Metallurgist*, *32*(6), 194–195.

Silva III, H., & Carnes, B. (2016). Fully Two-Dimensional Verification Problem for Coupled Heat Conduction and Enclosure Radiation. *Journal of Thermophysics and Heat Transfer*, *30*(4), 799–803.

Stevenson, P., & He, Q. (2005). Slug flow in a blast furnace taphole. *Chemical Engineering and Processing: Process Intensification*, *44*(10), 1094–1097.

Söderlind, G. (2003). Digital filters in adaptive time-stepping. *ACM Transactions on Mathematical Software*, *29*(1), 1–26.

Söderlind, G., & Wang, L. (2006). Adaptive time-stepping and computational stability. *Journal of Computational and Applied Mathematics*, *185*(2), 225-243.

Tennekes, H., & Lumley, J. L. (1972). *A First Course in Turbulence*. MIT press.

Tiihonen, T. (1997a). A nonlocal problem arising from heat radiation on non-convex surfaces. *European Journal of Applied Mathematics*, *8*(4), 403–416.

Tiihonen, T. (1997b). Stefan–Boltzmann Radiation on Non-convex Surfaces. *Mathematical Methods in the Applied Sciences*, *20*(1), 47–57.

Ting, T. C. (1996). *Anisotropic Elasticity: Theory and Applications*. Oxford Engineering Science Series, 45. Oxford University Press.

Trottenberg, U., Oosterlee, C. W., & Schuller, A. (2000). *Multigrid*. Elsevier.

Tryggvason, G., Scardovelli, R., & Zaleski, S. (2011). *Direct Numerical Simulations of Gas–Liquid Multiphase Flows*. Cambridge University Press.

Turkdogan, E. (1984). Physicochemical Aspects of Reactions in Ironmaking and Steelmaking Processes. *Transactions of the Iron and Steel Institute of Japan*, *24*(8), 591–611.

Van der Vorst, H. A. (2003). *Iterative Krylov methods for large linear systems*. Cambridge Monographs on Applied and Computational Mathematics, 13. Cambridge University Press.

Vázquez-Fernández, S. (2015). *Modelización Matemática y Simulación Numérica de la Transferencia de Calor de una ruta de Horno Alto* (Master's thesis. M.Sc. Industrial Mathematics). Universidade de Santiago de Compostela.

Vázquez-Fernández, S., García-Lengomín, A., Lausín-Gónzalez, C., & Quintela, P. (2019). Mathematical modelling and numerical simulation of the heat transfer in a trough of a blast furnace. *International Journal of Thermal Sciences*, *137*, 365–374.

Versteeg, H. K., & Malalasekera, W. (2007). *An Introduction to Computational Fluid Dynamics: The Finite Volume Method*. Pearson Education.

Wang, L., Pan, C.-N., & Cheng, W.-T. (2017). Numerical Analysis on Flow Behavior of Molten Iron and Slag in Main Trough of Blast Furnace during Tapping Process. *Advances in Numerical Analysis*.

Wang, L., Taniguchi, Y., & Seetharaman, S. (2012). Measurements of Solidus and Liquidus Temperatures of $CaO–Al_2O_3–SiO_2$ and $CaO–MgO–Al_2O_3–SiO_2$ Slags with MnO Additions. *Steel Research International*, *83*(2), 157–161.

Wang, Y.-J., & Zhang, J.-S. (2007). An efficient algorithm for large scale global optimization of continuous functions. *Journal of Computational and Applied Mathematics*, *206*(2), 1015–1026.

Wanner, G., & Hairer, E. (1996). *Solving Ordinary Differential Equations II: Stiff and Differential-Algebraic Problems*. Springer Series in Computational Mathematics (SSCM), 14. Springer-Verlag.

Wilcox, D. C. (2006). *Turbulence modeling for CFD*. DCW Industries.

World Steel. (2022). *Energy use in the steel industry. fact sheet.* (https://worldsteel.org/wp-content/uploads/Fact-sheet-energy-in-the-steel-industry-2021.pdf)

Yao, H., Chen, H., Ge, Y., Wei, H., Li, Y., Saxén, H., ... Yu, Y. (2021). Numerical Analysis on Erosion and Optimization of a Blast Furnace Main Trough. *Materials*, *14*(17), 4851.

Yao, S., Wu, S., Zhou, H., Song, B., Kou, M., & Xu, R. (2020). Influence of temperature on the microstructure and physical properties of corundum refractory brick in the blast furnace hearth. *Ironmaking & Steelmaking*, *47*(3), 263–270.

Yeganeh-Haeri, A., Weidner, D. J., & Parise, J. B. (1992). Elasticity of α-Cristobalite: A Silicon Dioxide with a Negative Poisson's Ratio. *Science*, *257*(5070), 650–652.

Yiu, K. F. C., Liu, Y., & Teo, K. L. (2004). A Hybrid Descent Method for Global Optimization. *Journal of Global Optimization*, *28*(2), 229–238.

Zhao, H., Cheng, S., & Zhao, M. (2007). Analysis of all-carbon brick bottom and ceramic cup synthetic hearth bottom. *Journal of iron and steel research, International*, *14*(2), 6–12.

USC UNIVERSIDADE DE SANTIAGO DE COMPOSTELA

Nomenclature

Part I

Greek symbols

α	Volume fraction
β	Thermal expansion coefficient
Γ	Boundary of Ω
$\widetilde{\Gamma}_{R,\mathbf{x}}$	Portion of Γ_R visible from point $\mathbf{x}$
γ	Boundary of ϖ
$\widehat{\gamma}$	Diagonal entries of ESDIRK scheme
ε	Emissivity
$\overline{\eta}$	Vector of radiosity unknowns
λ	Wavelength
μ	Dynamic viscosity
μ_T	Eddy viscosity
$\overline{\xi}$	Vector of temperature unknowns
ρ	Density
Σ	Interface between fluid phases or subdomains
σ	Stefan-Boltzmann constant
σ_Σ	Surface tension
ς	Scattering coefficient
τ_h	Triangulation of the computational domain
τ_w	Wall shear stress
$\boldsymbol{\tau}^R$	Reynolds stress tensor
Θ	Visibility factor
θ	Characteristic temperature
ϑ	Absorptivity
υ_{fp}	Relaxation parameter in fixed-point algorithm
ϕ	Scattering phase function
Ω	Three-dimensional computational domain
ϖ	Two-dimensional computational domain
ω	Specific dissipation rate

Latin symbols

a	Absorption coefficient
$\mathbf{b}$	Density of body force
$\mathcal{B}$	Body or reference configuration
$\mathcal{C}$	Feasible region
$\mathcal{C}_q$	Feasible region for qth thermocouple
c_p	Specific heat at constant pressure
c^n	Step size change ratio at nth time step
$\mathbf{D}(\mathbf{v})$	Symmetric part of the velocity gradient
D_{tap}	Taphole diameter
E	Total emissive power
E_λ	Spectral emissive power

USC UNIVERSIDADE DE SANTIAGO DE COMPOSTELA

E_{tot}	Specific total energy
e	Specific internal energy
f	Heat source
G	Irradiation
$\mathbf{g}$	Gravitational acceleration
g	Surface heat
$\mathcal{H}$	Specific enthalpy
h	Heat transfer coefficient
h_B	Height of the bottom of the main trough
h_{hm}	Height of the hot metal-slag interface
h^*_{hm}	Height of the hot metal-air interface, downstream of the skimmer
h_{jet}	Height of the jet
h_{slag}	Height of slag-air free surface
$\widehat{h}_{slag}$	Thickness of the slag pool in the trough
$\mathbf{I}$	Identity tensor
I	Total radiation intensity
$\mathcal{I}$	Identity operator
I_b	Black-body radiation intensity
I_T	Turbulence intensity
i	Spectral radiation intensity
K	Turbulent kinetic energy
$\mathcal{K}$	Integral operator for non-local radiation
k	Thermal conductivity
k_T	Turbulent thermal conductivity
$\mathscr{L}$	Length scale
M	Number of unit cycles in BF trough campaign
M_w	Molar mass mass
$\dot{m}$	Mass flow rate
N	Geometric dimension
N_h	Dimension of the discrete space
Nu	Nusselt number
$\mathbf{n}$	Outward-pointing unit normal vector
$\mathcal{P}_t$	Region of the space occupied by $\mathcal{P}$ at time t
p	Pressure
Pr	Prandtl number
$\mathcal{Q}$	Integral operator for radiative heat flux
$\mathbf{q}$	Heat flux
$\mathbf{q}_{rad}$	Radiative heat flux
q_{rad}	Radiative heat flux on the normal direction of the cavity boundary
R	Radiosity
R_g	Gas constant
$\mathcal{R}$	Universal gas constant
r	Radial coordinate
Ra	Rayleigh number
Re	Reynolds number
S	Strain rate magnitude
S^2	Unit sphere in $\mathbb{R}^3$
$S^2_+(\mathbf{x})$	Set of outgoing directions in S^2 at point $\mathbf{x}$
$S^2_-(\mathbf{x})$	Set of incoming directions in S^2 at point $\mathbf{x}$
$\mathbf{s}$	Generic vector in S^2
s	Density of surface force
s	Number of RK scheme stages
T	Temperature

USC UNIVERSIDADE DE SANTIAGO DE COMPOSTELA

$T^m_{D,cast}$	Dirichlet temperature during cast number m
T_{ext,c,n_c}	External temperature on boundary n_c for convection
T_{ext,r,n_c}	External temperature on boundary n_c for radiation
$T_{ext,R}$	External temperature on non-local radiation boundary
$\mathbf{T}$	Stress tensor
$\mathbf{T}_v$	Viscous part of stress tensor
$\mathcal{T}$	Time period of a Campaign cycle
$\mathscr{T}$	Time scale
t	Time
t_{end}	Final time value
t^n	nth time step
$\mathscr{V}$	Velocity scale
$\mathbf{v}$	Velocity
v	Test function
v_{air}	Inlet air velocity parameter
v_τ	Friction velocity
W	Three-dimensional Integral kernel for non-local radiation
w	Two-dimensional integral kernel for non-local radiation
$\mathbf{x}$	Vector of spatial coordinates
$\overline{\mathcal{X}}^n_l$	Vector of temperature unknowns at lth RK stage and nth time step
y^+	Wall dimensionless distance
y_w	Normal wall distance

Subscripts

A	Air
b	Black body
C	Convective boundary
c	Index of times at which BF activity changes from cast to stop
$cast$	Cast problem
D	Dirichlet
F	Fluid
h	Discretisation
hm	Hot metal
in	Insulation lining
L	Liquid subdomain (hot metal and slag)
l	lth RK stage
m	Index on unit cycles
n_c	Index on convective boundaries
R	Non-local radiation cavity boundary
S	Solid
$steady$	Steady-state
$stop$	Stop problem

Superscripts

A	Air
a	Manufactured solution test
$\mathcal{G}$	Restriction to the mesh of Γ_R
L	Liquid subdomain (hot metal and slag)
n	nth time step
T	Transpose

USC UNIVERSIDADE DE SANTIAGO DE COMPOSTELA

Acronyms

BF	Blast Furnace
CFD	Computational Fluid Dynamics
DNS	Direct Numerical Simulation
ESDIRK	Explicit Singly Diagonal Implicit Runge-Kutta
GRSA	Gradient Descent and Simulated Annealing
HRN	High-Reynolds Number
LES	Large Eddy Simulation
LRN	Low-Reynolds Number
ODE	Ordinary Differential Equation
PLIC	Piecewise Linear Interface Construction
RANS	Reynolds-Averaged Navier-Stokes
RK	Runge-Kutta method
RSM	Reynolds Stress Models
RTE	Radiative transfer equation
SST	Shear Stress Transport
TC	Thermocouple

Part II

Greek symbols

$\boldsymbol{\varepsilon}$	Linearised strain tensor
ϵ	Periodicity parameter
Γ_D	Dirichlet boundary
Γ_{int}	Interface between two subdomains
Γ_N	Neumann boundary
$\gamma(i,j)$	Index transformation
λ	First Lamé parameter
μ	Second Lamé parameter
ν	Poisson's ratio
ϕ^i	Reflection w.r.t. the plane $y_i = L_i/2$.
ψ^{lk}	Lifting function
$\boldsymbol{\sigma}$	Stress tensor
σ_{VM}	Von Mises norm of the stress tensor
Y	Reference period
Ω	Domain
$\partial\Omega$	Boundary of Ω
$\boldsymbol{\omega}$	Rotational tensor

Latin symbols

$\mathbb{C}$	Elasticity tensor
$[\mathbf{C}]$	Stiffness matrix
$[\overline{\mathbf{C}}]$	Homogenised (effective) stiffness matrix, S-BT
$[\mathbf{C}^0]$	Homogenised (effective) stiffness matrix, correctors
$[\widehat{\mathbf{C}}]$	Homogenised (effective) stiffness matrix, D-BT
E	Young's modulus
$\mathbf{f}$	Density of applied body forces
$\mathbf{g}$	Density of applied surface forces
I_N	Set of natural indices from 1 to N
$\mathcal{M}_\Omega(f)$	Mean value of f in Ω

USC UNIVERSIDADE DE SANTIAGO DE COMPOSTELA

$meas(\Omega)$	Measure of Ω
$\mathbf{n}$	Outward-pointing unit normal vector
$\mathbf{u}$	Displacement field
$[\mathbf{S}]$	Compliance matrix
$\mathcal{X}^{lk}$	Corrector function for the linear elasticity system
Y	Reference period
$\mathcal{Z}(\Omega)$	Space of infinitesimal rigid motions of Ω

Subscripts

D	Dirichlet boundary
ex	Analytical solution
h	Discretisation or numerical approximation
N	Neumann boundary
n	Normal projection
t	Tangential projection
S	Simmetry boundary

Superscripts

$\perp$	Orthogonal complement
ϵ	Dependency on the periodicity parameter ϵ
T	Transpose

USC UNIVERSIDADE DE SANTIAGO DE COMPOSTELA





This thesis is divided into two parts wherein different mathematical methodologies are introduced to study relevant problems in the Blast Furnace (BF) ironmaking process.

The scope of the first part is to analyse the thermo-hydrodynamical behaviour of the BF trough, with the primary motivation of providing valuable insights that allow to minimise the frequency of its repairs. A hierarchy of different mathematical models is proposed and numerically solved, with the aim of investigating several effects such as the influence of the tapping rates on the flow structures or the wall shear stress, as well as the impact that the tapping process stops have on the thermal response of the trough during a complete campaign cycle.

In the second part, various techniques that allow to numerically assess the mechanical behaviour of the ceramic cup of the BF are introduced. One of them is shown to be mathematically equivalent to the classical periodic homogenisation, with the advantage of being conceptually simpler and easier to implement numerically. The performance of the proposed methodologies is illustrated with multiple numerical experiments.